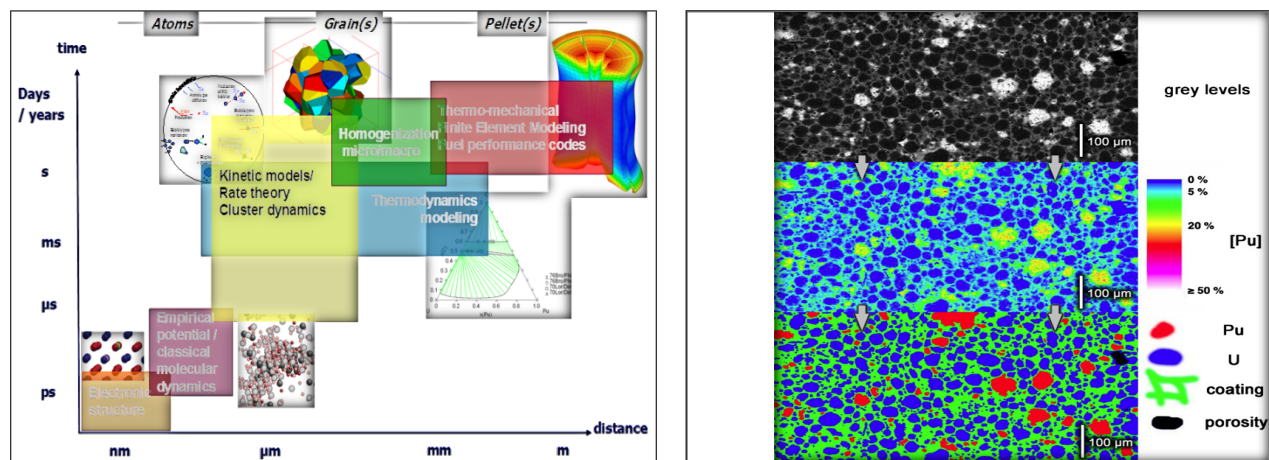


State-of-the-Art Report on Multi-scale Modelling of Nuclear Fuels

State-of-the-Art Report on Multi-scale Modelling of Nuclear Fuels



© OECD 2015

NUCLEAR ENERGY AGENCY

ORGANISATION FOR ECONOMIC CO-OPERATION AND DEVELOPMENT

ORGANISATION FOR ECONOMIC CO-OPERATION AND DEVELOPMENT

The OECD is a unique forum where the governments of 34 democracies work together to address the economic, social and environmental challenges of globalisation. The OECD is also at the forefront of efforts to understand and to help governments respond to new developments and concerns, such as corporate governance, the information economy and the challenges of an ageing population. The Organisation provides a setting where governments can compare policy experiences, seek answers to common problems, identify good practice and work to co-ordinate domestic and international policies.

The OECD member countries are: Australia, Austria, Belgium, Canada, Chile, the Czech Republic, Denmark, Estonia, Finland, France, Germany, Greece, Hungary, Iceland, Ireland, Israel, Italy, Japan, Korea, Luxembourg, Mexico, the Netherlands, New Zealand, Norway, Poland, Portugal, the Slovak Republic, Slovenia, Spain, Sweden, Switzerland, Turkey, the United Kingdom and the United States. The European Commission takes part in the work of the OECD.

OECD Publishing disseminates widely the results of the Organisation's statistics gathering and research on economic, social and environmental issues, as well as the conventions, guidelines and standards agreed by its members.

NUCLEAR ENERGY AGENCY

The OECD Nuclear Energy Agency (NEA) was established on 1 February 1958. Current NEA membership consists of 31 countries: Australia, Austria, Belgium, Canada, the Czech Republic, Denmark, Finland, France, Germany, Greece, Hungary, Iceland, Ireland, Italy, Japan, Korea, Luxembourg, Mexico, the Netherlands, Norway, Poland, Portugal, Russia, the Slovak Republic, Slovenia, Spain, Sweden, Switzerland, Turkey, the United Kingdom and the United States. The European Commission also takes part in the work of the Agency.

The mission of the NEA is:

- to assist its member countries in maintaining and further developing, through international co-operation, the scientific, technological and legal bases required for a safe, environmentally friendly and economical use of nuclear energy for peaceful purposes;
- to provide authoritative assessments and to forge common understandings on key issues, as input to government decisions on nuclear energy policy and to broader OECD policy analyses in areas such as energy and sustainable development.

Specific areas of competence of the NEA include the safety and regulation of nuclear activities, radioactive waste management, radiological protection, nuclear science, economic and technical analyses of the nuclear fuel cycle, nuclear law and liability, and public information.

The NEA Data Bank provides nuclear data and computer program services for participating countries. In these and related tasks, the NEA works in close collaboration with the International Atomic Energy Agency in Vienna, with which it has a Co-operation Agreement, as well as with other international organisations in the nuclear field.

This document and any map included herein are without prejudice to the status of or sovereignty over any territory, to the delimitation of international frontiers and boundaries and to the name of any territory, city or area.

Corrigenda to OECD publications may be found online at: www.oecd.org/publishing/corrigenda.

© OECD 2015

You can copy, download or print OECD content for your own use, and you can include excerpts from OECD publications, databases and multimedia products in your own documents, presentations, blogs, websites and teaching materials, provided that suitable acknowledgment of the OECD as source and copyright owner is given. All requests for public or commercial use and translation rights should be submitted to rights@oecd.org. Requests for permission to photocopy portions of this material for public or commercial use shall be addressed directly to the Copyright Clearance Center (CCC) at info@copyright.com or the Centre français d'exploitation du droit de copie (CFC) contact@cfcopies.com.

Foreword

The Working Party on Multi-scale Modelling of Fuels and Structural Materials for Nuclear Systems (WPMM) has been established, under the auspices of the NEA Nuclear Science Committee (NSC), to review multi-scale models and simulations as validated predictive tools for fuels and structural materials needed in the design of nuclear systems, for fuel fabrication and for understanding performance. The WPMM's objective is to promote the exchange of information on theoretical and computational methods, experimental validation, and other topics related to modelling and simulation of nuclear materials.

The Expert Group on Multi-scale Modelling of Fuels was established in 2009 to document the development of multi-scale modelling approaches for fuels in support of current fuel optimisation programmes and innovative fuel designs. This expert group aims to assess international multi-scale modelling approaches devoted to nuclear fuels from the atomic to the macroscopic scale, and to identify the most relevant experimental data or experimental characterisation techniques that are still needed for validation of fuel multi-scale models.

This report lays out the different classes of phenomena relevant to nuclear fuel behaviour, describes the techniques used to obtain material properties necessary for describing the phenomena and their assessment, and finally covers details relative to the principles and limits behind each modelling/computational technique.

Acknowledgements

The NEA wishes to express its sincere gratitude to the Chair and Vice-Chair of the Expert Group on Multi-scale Modelling of Fuels, Professor Dr Theodore M. Besmann (US) – who is also the current Chair of the Working Party on Multi-scale Modelling of Fuels and Structural Materials for Nuclear Systems (WPMM) – and Dr Carole Valot (France), to the members of the Expert Group and to the authors for their contribution to this report. Special thanks are also due to Dr Marius Stan (US), former Chair of the WPMM.

This report was co-ordinated by Professor Dr Theodore M. Besmann (US) and edited by Dr Simone Massara (NEA), with the precious contribution of Ms Reka Tarsi (NEA).

Thanks are expressed to Dr Jeffrey Powers (US) and Mr Robert Montgomery (US) for their review and helpful suggestions.

List of authors

T.M. Besmann (Univ. of South Carolina, US), Editor
T.J. Bartel (SNL, US)
M. Bertolus (CEA, France)
V. Blanc (CEA, France)
V. Bouineau (CEA, France)
G. Carlot (CEA, France)
A. Chernatynskiy (University of Florida, US)
K. Clarno (ORNL, US)
C. Desgranges (CEA, France)
R. Devanathan (PNNL, US)
R. Dingreville (SNL, US)
B. Dorado (CEA, France)
J.C. Dumas (CEA, France)
M. Dumont (CNRS, France)
A. El-Azab (Purdue University, US)
M. Freyss (CEA, France)
P. Garcia (CEA, France)
J.M. Gatt (CEA, France)
S.B. Gorti (ORNL, US)
C. Guéneau (CEA, France)
F.C. Iglesias (UOIT, Canada)
J. Julien (CEA, France)
M. Krack (PSI, Switzerland)
M. Kurata (JAERI, Japan)
K. Kurosaki (Osaka University, Japan)

R. Largenton (EDF, France)
R.A. Lebensohn (LANL, US)
B.J. Lewis (UOIT, Canada)
D. Littlewood (SNL, US)
S. Maillard (CEA, France)
L. Malerba (SCK•CEN, Belgium)
G. Martin (CEA, France)
R. Masson (CEA, France)
P. Maugis (CNRS, France)
B. Michel (CEA, France)
J.Y. Oh (KAERI, Korea)
S.R. Phillpot (University of Florida, US)
J.P. Piron (CEA, France)
J. Rachid (ANATECH, US)
B. Radhakrishnan (ORNL, US)
C. Sabathier (CEA, France)
R. Skorek (CEA, France)
M. Stan (ANL, US)
B. Sundman (KTH, Sweden)
V. Tikare (SNL, US)
C. Toffolon (CEA, France)
M.R. Tonks (INL, US)
J. S. Tulenko (University of Florida, US)
C. Valot (CEA, France)
L. Van Brutzel (CEA, France)
P. Van Uffelen (EC, JRC-ITE, Germany)
M.J. Welland (CNL, Canada)
R. Williamson (INL, US)
Y. Yun (PSI, Switzerland)

Table of contents

Executive summary	9
Introduction	17
Part I: Underlying Phenomena of Nuclear Fuel Behaviour	19
Chapter 1. Mechanisms of microstructural changes of fuel under irradiation	22
Chapter 2. Nuclear fuel deformation phenomena.....	59
Chapter 3. Fuel-cladding chemical interaction	80
Chapter 4. Fuel-coolant chemical interaction.....	91
Chapter 5. Clad-coolant chemical interaction.....	108
Chapter 6. Property-process relationships in nuclear fuel fabrication.....	123
Chapter 7. Phenomena in thermal transport in fuels	144
Part II: Methodologies for Determining Nuclear Fuel Properties	175
Chapter 8. Thermal expansion.....	177
Chapter 9. Atomic transport properties	185
Chapter 10. Free energy and heat capacity	197
Chapter 11. Elastic and viscoplastic properties.....	209
Part III: Principles of Modelling and Simulation Techniques for Nuclear Fuels	221
Chapter 12. Density functional theory	225
Chapter 13. Classical molecular dynamics simulation of nuclear fuel	236
Chapter 14. Assessment of current atomic scale modelling methods for the investigation of nuclear fuel under irradiation: Example of uranium dioxide....	246
Chapter 15. Dislocation dynamics method.....	277
Chapter 16. Phase field	282
Chapter 17. Modelling microstructural evolution under irradiation	291
Chapter 18. Rate theory.....	299
Chapter 19. Thermochemical modelling of multi-component systems	309
Chapter 20. Peridynamics.....	320
Chapter 21. Micromechanical modelling of fuel viscoplastic behaviour.....	327
Chapter 22. Finite element modelling.....	337

Chapter 23. Evaluation of thermal conductivity of multi-component and multi-phase nuclear fuels by the finite element method	344
Chapter 24. Use of advanced simulations in fuel performance codes	352
Chapter 25. Integrated multi-scale modelling and simulation of nuclear fuels	359
Conclusion.....	376

Executive summary

T.M. Besmann
University of South Carolina, US

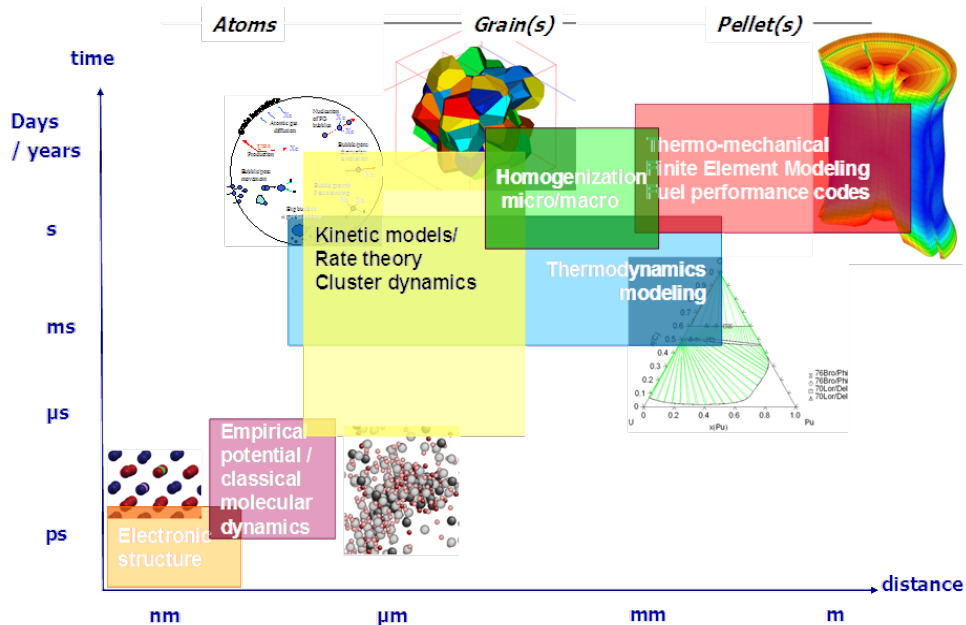
This report on *Multi-Scale Modelling of Nuclear Fuel* is one of a set of state-of-the-art reports on multi-scale modelling of fuels and structural materials commissioned by the Nuclear Science Committee (NSC) and its Working Party on Multi-Scale Modelling of Fuels and Structural Materials for Nuclear Systems (WPMM) of the Nuclear Energy Agency (NEA). The overall objective of the WPMM is to promote the exchange of information on models and simulations of nuclear materials including theoretical and computational methods, experimental validation, and related topics. To this end, the current report was developed through the contributions of an international expert group dedicated to a broad range of topics on multi-scale modelling of fuels, as well as to components on integration and validation. Ultimately, multi-scale modelling of fuel is seen as allowing a fuller understanding of fuel behaviour, including behaviour under irradiation, and as providing computational components for fuel performance codes for the development of advanced fuel systems, for the prediction of in-reactor performance and for the support of regulatory activity.

Multi-scale modelling implies the generation of models for fuel from the atomic scale, through the mesoscale, to the macroscopic scale. The figure below represents the enormous breadth of both time and length that needs to be considered to accommodate all phenomena. In addition, lower scale processes affect higher scale properties/behaviour, and in some cases the reverse can be true. Thus, any true simulation of fuel behaviour that is more than empirically based must allow for coupling among phenomena and across scales within fuel performance codes. For example, irradiation-induced defects can affect thermal conductivity, which, in turn, influences the thermal gradient in an oxide fuel pellet. This directly impacts concerns such as centreline temperature, and thus the margins for fuel melting, and grain growth, which, in turn, influences conductivity and fission product release. In addition, melting temperature is dependent on composition, atomic scale defects and microstructure. It is, therefore, apparent that behaviour is also dependent on various phenomena occurring across time and length scales, and can interact in a complex manner.

At the lowest scales of time and length it is necessary to develop quantitative representations of phenomena such as radiation-induced atomic displacements that disrupt crystal structures, electronic excitations that influence chemical bonding, and atomic-scale transport properties. Time intervals are of the order of picoseconds and lengths of the order of nanometers. Atomic transport properties govern a large range

of nuclear fuel properties, from controlling microstructure resulting from fabrication conditions to behaviour under irradiation. These affect grain growth, oxidation, fission product release, and gas bubble nucleation. Modelling approaches include static atomistic calculations, in which the migration mechanism is fixed and the corresponding migration energy barrier is calculated or molecular dynamics calculations and mesoscale rate theory models, for which the time evolution of the system is explicitly calculated. One challenge is to improve the coupling of phenomena for fission gas transport, which includes behaviour at both the atomic and the mesoscale. The study of radiation damage and atomic transport properties in nuclear fuels would also benefit from efficient accelerated dynamics schemes to access fuel evolution during longer timescales, and the application of *ab initio* molecular dynamics to actinide compounds.

Figure 1. Schematic representation of the scales/phenomena of effects spanning the thermomechanical, physical and chemical evolution of nuclear fuels from the atomic to the pellet and rod



Electronic structure calculations are based on quantum theory, require little prior knowledge and make use of very few adjustable parameters, yet they play a crucial role in the multi-scale modelling of materials. Not only do they enable one to accurately determine physical and chemical properties of materials, they also provide data for the adjustment of parameters (or potentials) at higher-scales, such as for classical molecular dynamics, kinetic Monte Carlo, cluster dynamics, etc. Most of the properties of a solid depend on the behaviour of its electrons, and in order to model or predict that behaviour it is necessary to have an accurate method for computing electronic structure. An increasingly accurate and useful methodology is density functional theory (DFT). DFT has been successfully applied to the determination of structural or dynamical properties (lattice structure, charge density, magnetisation, phonon spectra, etc.) of a wide variety of solids. The limitations of DFT in treating strong 5f

correlations are one of the main issues for DFT modelling of nuclear fuels. Various methods exist, however, to treat such strongly correlated materials better.

Classical molecular dynamics simulations use forces calculated from empirical potentials. They are well suited for studying primary damage production by irradiation, defect interactions with fission gas atoms, gas bubble nucleation, grain boundary influences on defect and gas bubble evolution, and the resulting changes in thermomechanical properties. This can enable insights into fundamental mechanisms governing the behaviour of nuclear fuel, as well as parameters that can be used as inputs for mesoscale models. The interaction potentials used for the force calculations are generated by fitting properties of interest to experimental data and electronic structure calculations. One of the current challenges is the need to refine the existing potentials to provide a better representation of the performance of polycrystalline fuel under a variety of operating conditions, develop models that are equipped to handle deviations from stoichiometry, and validate the models and assumptions used.

Atomic scale methods provide fundamental information to the higher scales. It is, therefore, essential to know the accuracy of the results computed at this scale to have confidence in their application within higher scale models. A specific assessment of electronic structure and empirical potentials for the description of nuclear fuel under irradiation has been performed within the WPMM Expert Group dedicated to Validation and Benchmarking of Methods (VBM), and is contained in this report. It has revealed that the numerous studies performed on UO₂ prove that the DFT+U method and current empirical potentials provide a good description of the properties of bulk UO₂. In addition, encouraging agreement is observed between modelling results and the experimental data for defect formation energies, oxygen self-diffusion and atomic diffusion of xenon in UO₂. The comparison between calculated and experimental results on the behaviour of defects and fission products, however, is extremely difficult since it requires a detailed knowledge of experimental conditions and involves additional models. Thus, a comparison should not be used for validation rather the results should be used to help in the interpretation of the experimental results and in the determination of elementary mechanisms. The assessment of formation, incorporation and migration energies should be performed through comparison with more precise approximations.

Two techniques that straddle the gap between the atomic scale and the mesoscale are rate theory and dislocation dynamics. Cluster dynamics, which is a particular application of mesoscopic rate theory, has been applied to investigating fuel behaviour under irradiation. The method simulates the evolution of the concentration of every type of point or aggregated defect in a grain of material. It produces rich information that sheds light on the mechanisms involved in microstructure evolution and gas behaviour that are not accessible through conventional models, yet can provide for improvements in those models. Cluster dynamics parameters are largely the energetic values governing basic evolution mechanisms in the material (diffusion, trapping and thermal resolution). In this sense, the model has general applicability to very different situations (irradiation, ion-beam implantation, annealing) provided they rely on the same basic mechanisms, without requiring additional data fitting as would be necessary for more empirical models. For use with more complex systems, a better knowledge of the real defects present in the material as a function of stoichiometry is needed, so that

the simplifying assumptions of self-defects being equivalent to Schottky or anti-Schottky is better justified or improved. Indeed, in the near future it can be expected that basic data will be routinely available from either atomistic calculations or dedicated experiments.

Dislocation-dynamics (DD) models the evolution of material plastic properties as a function of the microstructural transformation predicted at the atomic scale. Indeed, it is the only simulation method capable of taking into account the collective behaviour of a large number of dislocations inside a realistic microstructure. DD simulations are based on the elastic dislocation theory following rules inherent to the dislocation core structure, often called “local rules”. All the data necessary to establish the local rules for DD have to come directly from experiments or from simulations carried out at the atomic scale such as molecular dynamics or *ab initio* calculations. However, no precise information on the interaction between two dislocations or between dislocations and defects induced by irradiation are available for nuclear fuels, which presents a future goal for the application of this approach.

At the mesoscale or microstructure scale, the key phenomena are thermal and chemical transport, grain growth/evolution, thermochemical equilibria, and chemical interactions. In nuclear fuels, thermal transport is a key performance metric that affects not only the power output, but is also an important consideration in potential accident scenarios. While a largely mesoscale phenomenon, it in fact is also influenced by atomistic processes. Yet, for example, a fundamental understanding of the interplay between microstructure and thermal conductivity of irradiated uranium dioxide fuel is still lacking. Being computational in nature, modelling approaches to thermal transport can, at least in principle, describe in detail virtually all mechanisms at the atomistic level. They permit the coupling of the atomistic-level simulations to mesoscale continuum theory and thus enable the capture of the impact on thermal transport of microstructural evolution. A key challenge at the atomistic level is the absence of an interatomic potential that reliably reproduces the relevant phonon effects. Another is properly accounting for scattering due to large extended defects caused by irradiation. At the mesoscale, a problem that has yet to be solved is phonon transport across a microstructure ensemble.

While debatably either an atomistic or mesoscale phenomenon, the chemistry of nuclear fuel is treated as mesoscale as its influences are revealed at that scale. Chemical composition changes with time are due to the formation of fission products and depend on the temperature history within the fuel pellet and the clad during operation. The oxidation of zircaloy and its variants from reaction with urania fuel or coolant under high-temperature conditions are some of the most obvious effects. Large thermal gradients between the centre and the periphery of the pellet can induce radial redistribution of the fuel constituents, particularly in metal and oxide fast reactor fuels. The fuel pellet can react with the clad by different corrosion processes, which can involve actinide and/or fission product transport via gas, liquid and/or solid phases. One of the main challenges for modelling chemical interactions is the limited number of migrating constituents that are currently considered in codes. Fuel-cladding chemical interaction is a key issue for oxide and metallic fuels, yet mechanisms are not well understood, particularly for oxide fuels, and thus need further elucidation both from experiment and modelling.

Computational thermodynamics, also known as the Calphad method, is a standard tool in industry for the development of materials and improving processes and there is intense scientific development of new models and databases. The calculations are based on thermodynamic models of the Gibbs energy for each phase as a function of temperature, pressure and constitution. Model parameters are stored in databases that are developed in international scientific collaborations. In this way, consistent and reliable data for many properties such as heat capacity, chemical potential, solubility, etc. can be obtained for multi-component systems. Computational thermodynamics has historically been central to understanding nuclear fuel chemical behaviour, both under operating and accident conditions. Currently, there are substantial efforts to both advance the thermochemical models and develop accurate thermodynamic databases. Thermochemical phase determinations and activity calculations are most recently being included in advanced fuel performance codes, such as MOOSE-BISON-MARMOT and ALCYONE-ANGE.

Nuclear fuels are subjected to high levels of radiation damage mainly due to the slowing of fission fragments, which results in substantial modifications to the initial fuel microstructure. Microstructure changes alter practically all engineering fuel properties such as atomic transport or thermomechanical properties, so understanding these changes is essential to predicting the performance of fuel elements. Firmly within the mesoscale is the phase-field technique, which is an efficient simulation approach for modelling microstructural evolution. A distinct advantage of the technique is that there is no need to explicitly track the complex evolution of interfaces, such as grain boundaries or bubble surfaces. In the phase-field method, the individual phases and their crystallographic variants are described by a set of non-conserved order parameters. It has proven to be well suited to nuclear fuel microstructure evolution due to the ease with which various physical phenomena can be coupled to account for the impact of the large stress and temperature gradients present. A number of barriers to phase field informing the mesoscale to macroscale must still be overcome. First, several material properties and mechanisms that occur within the fuel are either not well understood or are unknown. Therefore, small-scale experiments and atomistic simulations are required to fill this gap. Second, the mesoscale models have not been well validated due to the difficulty in obtaining mesoscale data under reactor conditions. Thus, detailed separate effects experiments are needed to obtain data for validation. Finally, large time and length scales are needed to model the complex polycrystalline behaviour that takes place within the fuel and the clad.

The Potts kinetic Monte Carlo (kMC) model is a method that enables the simulation of various microstructural features in nuclear fuels during irradiation. For example, swelling or the aggregation of vacancies to form voids is observed in many materials including some fuel rod claddings. The production of extra atoms by fission in nuclear fuel can also strain the lattice leading to swelling, albeit to a lesser extent. Nuclear fuels also swell due to precipitation of fission gas (primarily Xe and Kr) into nanosized intragranular and submicron intergranular bubbles. The creation of extra atoms by fission or transmutation of atoms alters the chemistry of the fuel and results in microstructural evolution that is unique to nuclear materials. Another feature that is unique to some is a large temperature gradient present that can lead to variable microstructural evolution in regions and segregation of components. Finally, radiation-

induced segregation of constituents in two or more component materials can occur. The kMC tool is a statistical-mechanical model that populates a lattice with an ensemble of discrete particles to represent and evolve the microstructure, and thus lends itself to modelling fuel microstructural evolution. The particles in the Potts kMC model represent a discrete quantity of material that is much larger than an atom, thus all atomistic information about the material system is aggregated into mesoscale model parameters. In kMC, the particles evolve in a variety of ways to simulate microstructural changes due to short- and long-range diffusive processes. kMC methods have proven themselves to be versatile, robust and capable of simulating various microstructural evolution processes such as grain growth. Continued model development of kMC has taken the form of developing hybrid approaches that couple multiple materials physics that kMC alone cannot inherently treat.

At the macroscale, nuclear fuel encounters severe thermomechanical environments and responds through fuel deformation: creep, swelling, cracking, and pellet-clad interaction. Its mechanical response is profoundly influenced by the underlying heterogeneous microstructure, as well as inherently dependent on the temperature and stress level history. The ability to adequately elucidate the associated macroscopic behaviour in such extreme environments is crucial for predicting both performance and transient fuel mechanical response. There is an obvious need for a multi-physics and multi-scale approach to develop a fundamental understanding of properties of complex nuclear fuel materials. The development of such advanced multi-scale mechanistic frameworks should include either an explicit (domain decomposition, homogenisation,...) or implicit (scaling laws, hand-shaking, etc.) linkage between the different time and length scales involved, in order to accurately predict thermomechanical responses for a wide range of operating conditions and fuel types.

Peridynamics, a nonlocal extension of continuum mechanics, is a natural framework for capturing constitutive response, and modelling pervasive material failure and fracture. Unlike classical approaches incorporating partial derivatives, the peridynamic governing equations utilise integral expressions that remain valid in the presence of discontinuities such as cracks. The mathematical theory of peridynamics unifies the mechanics of continuous media, cracks, and discrete particles. The result is a consistent framework for capturing a wide range of constitutive responses, including inelasticity, in combination with robust material failure laws. Peridynamic modelling of nuclear fuels, however, will require the resolution of several open questions. The selection and calibration of peridynamic constitutive models and bond-failure laws for specific fuel materials must be addressed. In addition, while peridynamics has been applied to thermal-mechanical phenomena and to coupled mechanics-diffusion scenarios, the application of peridynamics within the multi-physics environments affecting nuclear fuels remains an open area of research.

The modelling of fuel viscoplastic behaviour is at the macroscale as well, where so-called micromechanical (also termed homogenisation) approaches are used. These aim at deriving effective properties of heterogeneous material from the properties of their constituents. They utilise full-field computations of representative volume elements of microstructures as well as mean-field semi-analytical models. For light water reactor fuels, these approaches have been applied to the modelling of the effect of two microstructural parameters: the porosity effects on the thermal creep of UO₂ fuels

(transient conditions of irradiation) and the effect of plutonium content on the viscoplastic behaviour (nominal conditions of irradiation) in mixed oxide fuels. A challenge for modelling the viscoplastic behaviour of oxide fuels lies in representing the strongly coupled mechanisms of void diffusion and grain boundary sliding. More generally, there is a challenge of modelling the effect of irradiation on the mechanisms of intragranular strain.

The ultimate macroscale modelling approach is the classical Finite Element Method (FEM). FEM is a numerical technique for finding approximate solutions to boundary value problems. While FEM is commonly used to solve solid mechanics problems, it can be applied to a large range of boundary value problems from many different fields. FEM has been utilised in reactor fuel modelling for many years. It is most often used for fuel performance modelling at the pellet and pin scale, however, it has also been used to investigate properties of the fuel material, such as thermal conductivity and fission gas release. FEM forms the basis of the MOOSE-BISON-MARMOT codes that are developing a multi-dimensional, multi-physics fuel performance capability that is massively parallel. A challenge comes in being able to perform massively parallel simulations with these models. Another challenge is modelling the contact between fuel and cladding, especially in three dimensions, which has been demonstrated in the PLEIADES code that now can represent cracking from pellet-clad mechanical interactions. An additional issue arises in bridging the disparate length and time scales in efforts to concurrently couple microstructure FEM models with fuel performance codes.

It is the main objective to apply the variety of models of nuclear fuel phenomena in fuel performance codes for the accurate simulation of in-reactor behaviour. Such tools solve the equations for the heat transfer, the stresses and strains in fuel and cladding, the evolution of important isotopes and the behaviour of various fission products in the fuel rod. Heat transfer is generally solved in a section or slice of fuel as a sequence of thermal transfers between different resistances: the fuel, the fuel-to-cladding gap, the cladding (and its outer corrosion layer) and finally the barrier between the cladding surface and the bulk of the coolant. The assessment of the stresses and strains in a section of the fuel rod is usually based on the solution of the equilibrium relation, the compatibility equation and the constitutive equations. The main difficulties arise from the cracking of the pellets and the relocation of fuel fragments. The fission product behaviour in each axial slice of the fuel rod is generally considered to occur in two steps. The first step consists of the production and subsequent migration in the grains. This is usually dealt with by means of a diffusion equation within a spherical geometry. The second step consists of the development of grain boundary bubbles that grow until they interlink and form a tunnel network through which the insoluble fission products can be released.

Apart from the main limitations caused by the geometrical assumptions, there are other limitations in fuel performance codes related to the empirical nature of material property models and some of the physical models noted above. These limitations apply to multi-dimensional codes as well. As a consequence of the use of empirical models, it is impossible to extrapolate material properties and models beyond the range of operating conditions from which they have been determined. Hence, when advanced materials are to be designed for innovative reactor types, new codes have to be

developed for each combination. Finally, conventional as well as advanced fuel performance codes should be extended to deal with the fuel and fission product chemistry.

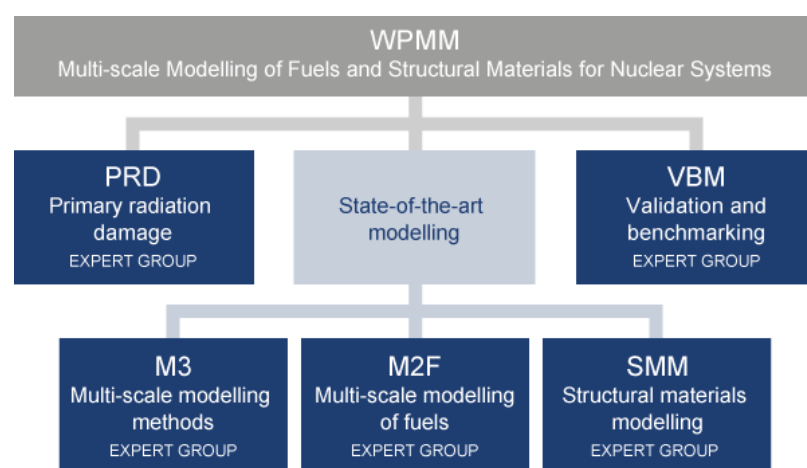
The integration of the various models at the multiple scales is an enormous challenge. The phenomena occurring in fuels is diverse, including physical and chemical transformations and evolution at various scales, such as cracking, fission gas bubble precipitation, restructuring, and fission product migration and interactions. Yet, without such integration it will not be possible to obtain truly predictive simulations based on more than empirical information. Fuel melting is a central nuclear safety issue, for example, and the phenomena that contribute to thermal conductivity and thus fuel temperature easily span multiple scales. Fuel fragmentation and pulverisation during a loss of coolant accident is a safety issue related to the effect of high temperature on the fission gas pressure in the gas bubbles within the grains and in grain boundaries, which combined with the loss of confinement due to cladding ballooning, causes instability in the fuel matrix. This is an ideal target for performing multi-scale modelling that couples the grain-scale with the macro/continuum scale. To date, this has been elusive, even though it is important for safety analyses that need to quantify the thermal conductivity of fragmented/pulverised pellets. Others phenomena that require integration over a variety scales include the effect of point and extended defects that ultimately influence fission gas bubble formation, macroscopic fuel-cladding interactions that result from atomistic phenomena such as stress corrosion, and thermodynamics and kinetics that in accidents govern fission product speciation and interactions with core internals.

The state-of-the-art of modelling phenomena related to nuclear fuel has advanced significantly in recent years. The representation of atomic level behaviour is increasingly becoming more accurate as capabilities to utilise larger sets of atoms evolve and empirical potentials improve. At the mesoscale, models for transport and microstructure evolution have also progressed with new techniques that well represent restructuring. At the macroscale, the lower scale representations inform models that reproduce observed fuel behaviour. Significant challenges do remain in both improving the models and in their multi-scale integration, and thus there is still much to be done. However, it is the expectation that as the problems of fuel modelling and simulation are solved, predictive models will increasingly find their way into advanced fuel performance codes and allow the eventual realistic simulation of nuclear fuel behaviour under normal and accident conditions that goes beyond empirical correlations.

Introduction

The Nuclear Science Committee (NSC) of the Nuclear Energy Agency (NEA) has undertaken an ambitious programme to document state-of-the-art of modelling for nuclear fuels and structural materials. The project is being performed under the Working Party on Multi-Scale Modelling of Fuels and Structural Material for Nuclear Systems (WPMM), which has been established to assess the scientific and engineering aspects of fuels and structural materials, describing multi-scale models and simulations as validated predictive tools for the design of nuclear systems, fuel fabrication and performance. The WPMM's objective is to promote the exchange of information on models and simulations of nuclear materials, theoretical and computational methods, experimental validation and related topics. It also provides member countries with up-to-date information, shared data, models, and expertise. The goal is also to assess needs for improvement and address them by initiating joint efforts. The WPMM reviews and evaluates multi-scale modelling and simulation techniques currently employed in the selection of materials used in nuclear systems. It serves to provide advice to the nuclear community on the developments needed to meet the requirements of modelling for the design of different nuclear systems. The original WPMM mandate had three components (Figure 1), with the first component currently completed, delivering a report on the state-of-the-art of modelling of structural materials. The work on modelling was performed by three expert groups, one each on Multi-Scale Modelling Methods (M3), Multi-Scale Modelling of Fuels (M2F) and Structural Materials Modelling (SMM).

Figure 1. Structure of the Working Party on Multi-scale Modelling of Fuels and Structural Materials for Nuclear Systems



At this writing, WPMM is now composed of three expert groups and two task forces providing contributions on multi-scale methods, modelling of fuels and modelling of structural materials. This structure will be retained, with the addition of task forces as new topics are developed.

The mandate of the Expert Group on Multi-Scale Modelling of Fuels is to document the development of multi-scale modelling approaches for fuels in support of current fuel optimisation programmes and innovative fuel designs. The objectives of the effort are:

- assess international multi-scale modelling approaches devoted to nuclear fuels from the atomic to the macroscopic scale in order to share and promote such approaches;
- address all types of fuels: both current (mainly oxide fuels) and advanced fuels (such as minor actinide containing oxide, carbide, nitride, or metal fuels);
- address key engineering issues associated with each type of fuel;
- assess the quality of existing links between the various scales and list needs for strengthening multi-scale modelling approaches;
- identify the most relevant experimental data or experimental characterisation techniques that are missing for validation of fuel multi-scale modelling;
- promote exchange between the actors involved at various scales;
- promote exchange between multi-scale modelling experts and experimentalists;
- exchange information with other expert groups of the wpmm.

This report is organised as follows:

- Part I lays out the different classes of phenomena relevant to nuclear fuel behaviour. Each chapter is further divided into topics relevant for each class of phenomena.
- Part II is devoted to a description of the techniques used to obtain material properties necessary for describing the phenomena and their assessment.
- Part III covers details relative to the principles and limits behind each modelling/computational technique as a reference for more detailed information.

Included within the appropriate sections are critical analyses of the mid- and long-term challenges for the future (i.e., approximations, methods, scales, key experimental data, characterisation techniques missing or to be strengthened).

Part I

Underlying Phenomena of Nuclear Fuel Behaviour

The first part of the report reviewing various fuel phenomena looks at *Mechanisms of microstructural changes of fuel under irradiation*, which is largely due to high-energy fission fragments. Changes in microstructure are extremely important as they substantially affect properties such as thermal and species transport and thermomechanical properties. In addition, the substantial thermal gradient across fuel pellets results in a diverse set of microstructures that are locally generated. Light Water Reactor (LWR) fuel also suffers from the rim effect, where a high burn-up region is located near the pellet periphery and results in major restructuring in that region. P. Garcia, G. Carlot, B. Dorado, S. Maillard, G. Martin, J.Y. Oh, C. Sabathier, and M.J. Welland discuss the problem of describing microstructure evolution over engineering length and timescales. While the emphasis is on oxide fuels due to the greatest amount of information available for this fuel form, there is consideration of carbides and metallic fuels as well, with examples of how modelling and experiment at various scales can provide for understanding and predicting microstructural evolution.

The second area reviewed involves *Nuclear fuel deformation phenomena* for fuel under irradiation. For LWR oxide pellets we see the familiar “hour-glass” effect from the severe thermomechanical environment in-reactor. L. Van Brutzel, R. Dingreville and T. Bartel address these issues, describing the mechanical response of fuels, influenced by their heterogeneous microstructure. They look at key phenomena and relate the status of current modelling techniques to evaluate and predict fuel deformation effects: creep, swelling, cracking and pellet-clad interaction. They note that there is a need for a multi-physics and multi-scale approach to develop a fundamental understanding of properties of these complex nuclear fuel materials. These include atomic structure and phase stability through diffusivity and bubble formation/motion to restructuring, fracture, and plastic deformation.

Chemical interactions play a large part in fuel performance from fuel/fission product redistribution to cladding oxidation. C. Guéneau, J.P. Piron, J.C. Dumas, V. Bouineau, F.C. Iglesias and B.J. Lewis have reviewed *Fuel-cladding chemical interaction* for LWR oxide fuel phenomena for both internal fuel chemical behaviour as well as cladding interactions with the environment. This includes a thermodynamic analysis of the uranium-oxygen system, and the effect of hydrogen-steam atmospheres and fuel-oxidation/reduction kinetics. Thus an understanding of both in-reactor behaviour and phenomena in defective fuel rods can be provided in models and they can be further extended to higher temperatures using a phase-field approach to simulate centre-line melting in defective fuel. Zircaloy oxidation is also considered in the assessment of kinetics in steam and air under prototypical accident conditions. *Fuel-coolant chemical interaction* and *Clad-coolant chemical interaction* are reviewed by B.J. Lewis, F.C. Iglesias, C. Desgranges and C. Toffolon, including the effect of internal oxidation due to UO₂ and low temperature water-side zircaloy corrosion.

V. Tikare has provided an overview of the complex *Property-process relationships in nuclear fuel fabrication* for a number of fuel types of interest. These include conventional LWR oxide fuels, fast reactor MOX fuel, metal fuel for Sodium Fast Reactors (SFR), and coated particle fuel designed for gas-cooled reactors. The oxide pellet fuels generally utilise conventional powder processing and consolidation, including pressing and sintering. Specific to the complex chemistry of urania is the need to control oxygen overpressure in the final processing steps to obtain specific oxygen-to-metal ratios. Design of

microstructure is also important as it directly affects significant issues such as fission gas retention. Metallic fuels offer different challenges, including understanding alloy formation and casting. Significant advances in modelling injection casting, for example, are needed to be able to effectively fill a narrow diameter fuel rod of substantial length needed for SFR applications. Finally, coated particle fuels have completely separate fabrication challenges, including formation of fissile kernels utilising internal or external gelation, reduction, and often conversion of oxide kernels to mixed oxide and carbide, or perhaps to nitride. The coatings on the kernels are fabricated by fluid bed chemical vapour deposition of alternate carbon and SiC coatings. Fuel in the form of rods or spheres is then produced by compacting the ~1 mm particles with graphite into the desired geometry.

One of the most critical aspects of nuclear fuel is the *Phenomena in thermal transport in fuels* as the effectiveness of fuel hinges on the ability to remove fission-generated heat. Yet, understanding and modelling thermal transport is tremendously challenging, especially for UO₂ as it depends on chemistry/stoichiometry, crystalline defects, microstructure, density, and geometry. For example, at this point, a fundamental theoretical understanding of the interplay between the microstructure and thermal conductivity of irradiated uranium dioxide fuel is still lacking. A. Chernatynskiy, A. El-Azab, J.S. Tulenko and S.R. Phillpot in their section summarise recent advances in modelling approaches that detail the mechanisms involved at the atomistic level which permit coupling to mesoscale continuum theory. This allows capturing the impact of microstructural evolution on thermal transport. Mastering representations for urania fuel are expected to allow extension to other fuel forms.

Chapter 1.

Mechanisms of microstructural changes of fuel under irradiation

**P. Garcia¹, G. Carlot¹, B. Dorado¹, S. Maillard¹, G. Martin^{1,2},
J.Y. Oh³, C. Sabathier¹, M.J. Welland⁴**

¹CEA, DEN, DEC, Centre de Cadarache, France,

²CEA, DEN, DER, Centre de Cadarache, France,

³Korea Atomic Energy Research Institute, Korea,

⁴Canadian Nuclear Laboratory, Canada

Abstract

Nuclear fuels are subjected to high levels of radiation damage mainly due to the slowing of fission fragments, which results in substantial modifications of the initial fuel microstructure. Microstructure changes alter practically all engineering fuel properties such as atomic transport or thermomechanical properties so understanding these changes is essential to predicting the performance of fuel elements. Also, with increasing burn-up, the fuel drifts away from its initial composition as the fission process produces new chemical elements. Because nuclear fuels operate at high temperature and usually under high-temperature gradients, damage annealing, foreign atom or defect clustering and migration occur on multiple time and length scales, which make long-term predictions difficult. The end result is a fuel microstructure which may show extensive differences on the scale of a single fuel pellet. The main challenge we are faced with is, therefore, to identify the phenomena occurring on the atom scale that are liable to have macroscopic effects that will determine the microstructure changes and ultimately the life-span of a fuel element. One step towards meeting this challenge is to develop and apply experimental or modelling methods capable of connecting events that occur over very short length and timescales to changes in the fuel microstructure over engineering length and timescales.

In the first part of this chapter, we provide an overview of some of the more important microstructure modifications observed in nuclear fuels. The emphasis is placed on oxide fuels because of the extensive amount of data available in relation to these materials under neutron or ion irradiation. When possible and relevant, the specifics of other types of fuels such as metallic or carbide fuels are alluded to.

Throughout this chapter but more specifically in the latter part, we attempt to give examples of how modelling and experimentation at various scales can provide us with theoretical frameworks for understanding and predicting these microstructure evolutions.

Introduction

Nuclear fuels are subjected to very high levels of radiation damage. This damage is mainly due to the slowing-down of fission fragments and produces various kinds of both point and extended defects in concentrations that lie far above the expected thermodynamic equilibrium. Under the effect of temperature and irradiation, point defects migrate and interact either with each other or with existing extended defects. The presence of these crystalline defects has far-reaching consequences because they substantially alter the material itself and the material properties. Indeed, in addition to macroscopic swelling, the presence of uranium-type defects may accelerate cation self-diffusion which will, for instance, modify the creep properties of the fuel or the extent to which minor actinide redistribution occurs.

The behaviour of defects also has a major influence on a class of fission products that may determine the life-span of a fuel element: rare gases. These particularly insoluble elements are produced in important quantities as a result of fission events or α decay of actinides. Extensive cladding loading may result either from over-pressurisation of the fuel element due to fission gas release or from fuel swelling due to rare gas bubble precipitation. Fission gas release and fuel swelling as a result of bubble nucleation and growth are both macroscopic consequences of complex and not fully understood radiation induced phenomena such as radiation enhanced atomic migration [117]. Fission gas bubble nucleation is thought to occur because rare gas atoms combine with radiation induced vacancy type defects. Gas bubbles then grow and become trapping sites for migrating vacancies or other gas atoms. As damage levels increase still further, oxide fuels in particular undergo a microstructural modification characterised by a drastic reduction in the grain size and the simultaneous development of a large micron size bubble population [74]. Still in oxide fuels, at high temperature and for large temperature gradients (typically of the order of 2 000 K and 2.5×10^5 K/m, respectively [104], the as-fabricated micron size pores migrate up the temperature gradient as a result of material evaporation from the hot side of the pore (towards the pellet centre) and condensation or re-crystallisation on the slightly cooler side (towards the pellet periphery). The central hole that appears has obvious consequences upon the temperature and stress distributions in the pellet. Also, depending on the fuel chemical properties and composition, plutonium enrichment may occur in the pellet centre which also modifies the fuel centreline temperature substantially at the beginning of life [14].

There are many reasons why these phenomena are difficult to study individually. Regarding equilibrium properties alone, actinide oxides for example are usually semiconductors which present a variety of defects in different charge states generally not particularly well characterised. Also, oxides and carbides present non-stoichiometric phases that are stable over wide ranges of thermodynamic conditions. In these materials, the nature of defects on both sublattices may change radically depending upon thermodynamic conditions. Under irradiation, fuels and oxides, in particular, are

susceptible to both elastic and inelastic damage processes, the latter again being poorly characterised and difficult to treat theoretically. In addition, when studied under neutron irradiation for instance, all fuels are subjected to many different but interacting phenomena which may be chemically, thermally or radiation induced. Understanding and controlling microstructural changes, therefore, requires a comprehensive approach which looks at all aspects of the material's behaviour from thermodynamic equilibrium to basic radiation damage processes and longer time and length scale changes to the material.

In the first part of this chapter, we look at studies mainly relating to neutron irradiated fuels which give an overall picture of the variety of microstructural observations of nuclear fuels at low and intermediate burn-up and temperatures. Based on this overview, we describe how kinetic models have been developed over the years in order to account for at least some of these microstructural features with an emphasis on fission gas behaviour. Higher temperature and burn-up effects such as the formation of a central void or oxide fuel restructuring are also discussed.

Often, models at the mesoscale have *ad hoc* hypotheses built in that are difficult to justify and that render any extrapolation to different conditions uncertain. This justifies adopting different approaches based on modelling and experimental techniques that are more analytical or separate effects more clearly than would emerge from a neutron irradiation and mesoscale kinetic models. In the second part of this chapter, we, therefore, look at a few recent studies based on modelling at different scales (from the scale of atoms to the mesoscale) and controlled electron or ion-irradiation experiments. These examples, which relate to oxide fuels in particular, demonstrate the ability of multi-scale approaches to explain some of the more salient observations relating to neutron or ion irradiated fuels.

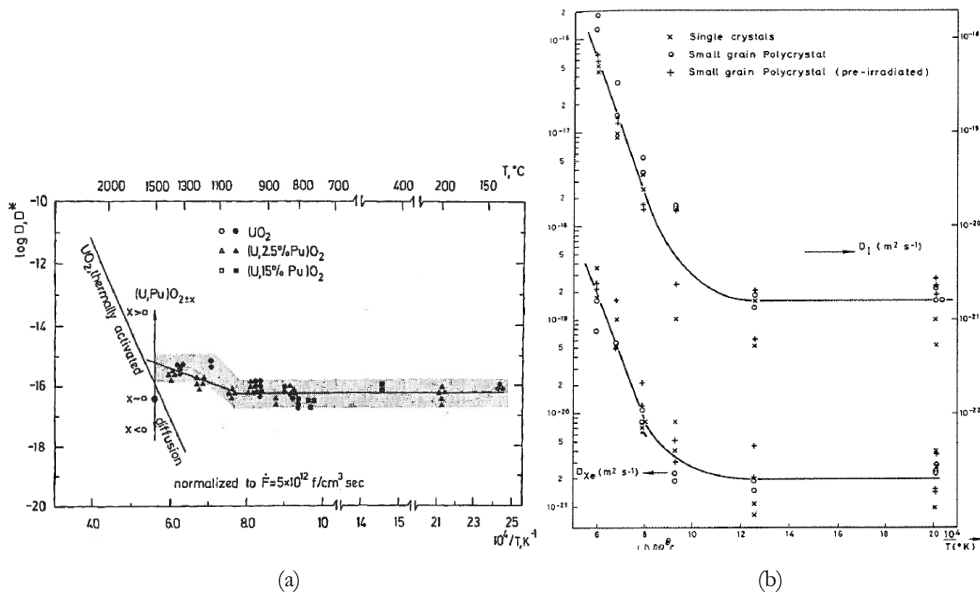
Observations relating to microstructural changes in nuclear fuels under neutron irradiation and associated kinetic modelling

Fuel behaviour at low and intermediate temperatures and burn-up

Because it was identified from an early stage that atomic transport properties likely controlled the kinetics of microstructure hence geometric changes in nuclear fuels, several basic studies were carried out in the 1970s and 1980s aimed to actually characterise the effect of neutron irradiation upon these properties. Several such studies emerge that were designed to assess quantitatively the effect of radiation upon uranium self-diffusion properties [140] and later [64] and fission gas diffusion [117]. Both studies involved isothermally irradiating single crystals and polycrystalline samples at fission rates of the order of $10^{19} \text{ m}^{-3} \text{ s}^{-1}$ for the fission gas study and between $7 \cdot 10^{18} \text{ m}^{-3} \text{ s}^{-1}$ and $6.4 \cdot 10^{19} \text{ m}^{-3} \text{ s}^{-1}$ for the cation studies. From the determination of diffusion profiles of ^{233}U tracer atoms deposited at the surface of the samples, Höh and Matzke observed an increase in the uranium self-diffusion coefficient of three to four orders of magnitude in comparison with thermally activated diffusion. Turnbull et al. monitored the release of both short- and long-lived volatile fission products and rare gases over a greater range of temperatures. The authors demonstrated that diffusion controlled release was effective at temperatures (down to 498 K) well below those at which substantial rare gas movement is expected to occur in the absence of neutron irradiation. The reported similarities between the rare gas and self-diffusion studies are striking. Both showed diffusion coefficients virtually independent of temperature below circa 1 273 K. Matzke [64] claimed a proportionality to

fission rate of the purely athermal component of the cation self-diffusion coefficient. This dependency, still commonly used in fuel behaviour applications, was applied to rationalise data relating to fission gas release. Probably because the numerical values for athermal rare gas and cation diffusion inferred from very different types of experiments were close (see Figures 1a and 1b from [64] and [117]), the phenomenon was commonly associated with thermal spike effects resulting from the high electronic stopping power of fission fragments. The evidence for this, however, is tenuous. In addition, a highly effective point defect theory was developed which very adequately explained results from experiments relating to radiation enhanced diffusion in metals [107]. Under simplifying assumptions of homogeneously distributed point defect sinks, kinetic equations for both vacancies and interstitial atoms were set up and solved assuming a steady-state situation is reached in which the defect production rate is balanced off by the rates at which defects recombine (mutual recombination) or are eliminated at sinks of prescribed concentration (elimination of point defects at fixed sinks). This theory [107] predicts that at lower temperatures, under steady-state conditions controlled by mutual recombination of Frenkel pairs, the enhanced diffusion coefficient is proportional to the square root of the defect production rate. The activation energy is given by half the migration enthalpy of the slowest moving point defect. At high defect sink concentrations, however, where concentrations are controlled by the rate at which defects are eliminated at internal sinks, there exists a range of temperatures in which enhanced diffusion is independent of temperature and proportional to the defect production rate. To what extent this theory also applies to cations when two interacting sublattices are present is impossible to check based upon neutron irradiations alone. Furthermore, basic experiments would also be required to ascertain the effect of oxygen potential on these phenomena. We will discuss these issues further in the latter part of the chapter.

Figure 1. Illustration of (a) estimated fission induced radiation-enhanced diffusion of cations in oxide fuels (b) and fission products xenon and iodine [64,117]



Note that units are in cm^2/s in Figure 1a and m^2/s in Figure 1b.

Atomic diffusion enhanced by radiation is a key property because it probably mirrors, albeit in a complex way, the changes in the microstructure on the atomic scale, but also it controls phenomena and properties that ultimately determine the dimensional changes of the fuel element. Although the next chapter is devoted to fuel properties among which creep plays a major role, it is worth mentioning similarities that this property bears with self-diffusion. Indeed, measured under isothermal conditions and neutron irradiation [141,143], radiation-induced creep displays an athermal behaviour under circa 1 273 K which appears to be proportional to fission rate. Both these characteristics could indicate that metal defect volume diffusion controls radiation creep. More work, however, is needed to ascertain the fundamental relationship between cation diffusion in general and creep properties. In polycrystalline materials, grain boundary diffusion is thought to play a major role in the observed high-temperature strain rates [142].

In-pile densification and pore behaviour

Clough [143] correlated initially high strain rates observed in irradiation creep tests to pore sintering. More generally, in-pile densification was shown to result in macroscopic modifications of the fuel geometry, such as reduction in fuel stack lengths, increase in the fuel cladding gap and increase in the hydrostatic fuel density. In-pile densification studies [144] also revealed that fuel resintering at temperatures too low for thermal resintering to occur was correlated to shifts in the pore size distribution due to significant reductions in the volume fraction of pores less than approximately one micron in size. Some efforts have also been reported that indicate a quantitative correspondence between hydrostatic fuel density measurements and micron size pore volumes measured from image analyses of SEM (Scanning Electron Microscopy) micrographs [145]. The less empirical models developed to describe in-pile resintering are based on kinetic equations, similar to those used for interpreting radiation enhanced diffusion, but with additional sink terms corresponding to the capture or emission of defects from fabrication pores. In-pile resintering models encountered may differ depending on the level of detail adopted for describing the pore population: single pore size [146,147] or pore size distribution function [148]. These models have in common the fact that fission spikes are assumed to interact with pores. A sputtering phenomenon is postulated, with each fission spike-pore encounter returning a set number of vacancies to the matrix. As vacancies are eliminated at internal sinks such as dislocations and grain boundaries, the pores eventually shrink. Values for the number of vacancies returned to the matrix per fission spike-pore encounter range between ~ 1 [149] and ~ 100 [150] but this phenomenon is only ever assumed. No direct demonstration of it has been reported to date.

Intragranular fission gas segregation and bubble formation

Although the observations presented previously are not fully understood, they are related to how radiation damage develops in the material and which the steady state the microstructure reaches. Rare gases are essential to the economy of point defects created under irradiation because, as they are highly insoluble, they combine with vacancies to form dense small size aggregates whereas interstitials appear to preferentially form dislocation loops [74]. The first systematic Transmission Electron Microscopy (TEM) observations of fission gas bubbles in low burn-up oxide fuel and at relatively low temperatures (1 073 K) are due to the work reported in [21] that described the presence of a high concentration (between 1 and $3 \times 10^{23} \text{ m}^{-3}$) of small rare gas bubbles of 2 to 3 nm in

diameter. The corresponding burn-up ranged between 1 and 15 GWd/Mt, which amounts to rare gas concentrations of approximately 100 and 1 000 ppm. The characteristics of bubbles were not reported to be much dependent upon burn-up or temperature. Since then, Kashibe et al. [50] made similar observations relating to UO₂ fuels irradiated at temperatures below 1 073 K and at burn-ups of 23 GWd/Mt and 44 GWd/Mt. The authors reported small 2 nm size bubbles at concentrations in the region of $9 \times 10^{23} \text{ m}^{-3}$ for the 23 GWd/Mt samples. At higher burn-up (44 GWd/Mt), a bimodal distribution was observed and a population of larger bubbles appeared, 10-20 nm in diameter, in addition to the initial smaller sized bubbles. Thomas et al. [115] subsequently reported TEM observations of areas irradiated to similar burn-ups (44 GWd/Mt) but that had experienced temperatures in excess of 1 173 K. Such samples showed much coarser intragranular bubbles 20-100 nm in size. These coarse bubbles were surrounded by dislocation tangles and were often, if not systematically, associated with similar size so-called ϵ -phase particles containing noble metals such as Mo, Ru, Pd, Tc and Rh. An Energy Dispersive X-Ray Spectrometry (EDS) analysis was applied from where xenon densities were found between 2 and 4 g/cm³. Such densities correspond to gas pressures in the GPa range (between ~ 0.1 GPa and ~ 1 GPa). This indicated (assuming a surface tension of circa 1 J m⁻² and a radius of 10 nm, which overestimates the radial stress induced by surface tension in the immediately surrounding lattice) that contrary to what was originally assumed by modellers, the pressures within fission gas bubbles are not necessarily balanced by their surface tension. Nogita and Une [75,76] provide a complementary description by using high-resolution TEM to examine samples taken from the peripheral region of pellets irradiated to average burn-ups of 30, 49 and 83 GWd/Mt and which had operated at around 873 K. The specimens examined revealed bubble sizes that tended to increase with burn-up (~ 1 nm for the lower burn-up to an average of around 4 nm for the 49 GWd/Mt samples). However, the bubble concentration remained close to $4 \times 10^{23} \text{ m}^{-3}$. In higher burn-up samples, nano-EDX was also performed on 4-10 nm bubbles. The xenon densities ranged between 3.8-6 g cm⁻³ which, for the higher values at least, would suggest xenon in a solid state. Bubbles were seen to be associated with 5 metal spherical particles.

To summarise, there is overwhelming TEM evidence which demonstrates that nanometre size bubbles form under neutron irradiation at low fission densities and that the bubble characteristics, i.e., size and concentration, are only marginally dependent upon burn-up or temperature. Bubble densities are in the 10^{23} - 10^{24} m^{-3} range. Bubbles contain high-pressure xenon and krypton in the GPa range and are often associated with five metal particles. Particle and bubble coarsening occur above 1 073 K as burn-up increases.

Higher scale microstructural changes in relation to fission gas behaviour

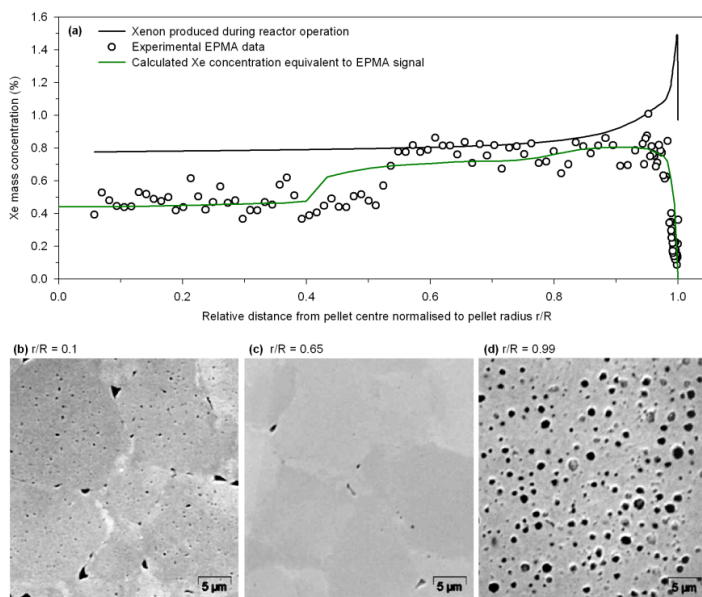
TEM has enabled microstructure characterisations of irradiated fuels on the scale of nanometres. Characterisations at higher scales (micron and above) require techniques such as SEM, EPMA (Electron Probe Micro-Analysis) and SIMS (Secondary Ion Mass Spectroscopy). Applying standard analytical tools to irradiated oxide fuels has revealed a comprehensive picture of the changes the fuel pellet undergoes as a function of burn-up and temperature. This sheds light on the role of specific features such as grain boundaries or inhomogeneity at that scale, particularly in relation to fission gas behaviour. Noirot et al. [78] have analysed a relatively high burn-up light water reactor (LWR) UO₂-based

rod irradiated to relatively high-fission densities (~ 60 GWd/Mt) using all three of the above mentioned tools. The picture that emerges is that the local fuel microstructure, which is burn-up and temperature dependent, is characterised by:

- the fraction of fission gas remaining at a given radial position in the pellet with respect to the total amount of gas produced by fission;
- the size, number density and pressure associated with the different fission gas bubble populations.

Figure 2 reproduced from [33] illustrates these results. At the fuel pellet rim (Figure 2d, here in the region of 100 GWd/Mt), the presence of micron sized pores is characteristic of the high burn-up structure [130]. Complementary xenon analyses using SIMS at that location show that the amount of fission gas detected is, within the experimental error, equal to the amount expected from the estimated local burn-up. At the mid-radius of the pellet (Figure 2c) and on the scale accessible with SEM, no differences can be detected compared with the microstructure of an un-irradiated sample. Comparison of the EPMA signal with the estimated total gas inventory shows that there is no measurable fission gas release in that region of the pellet (Figure 2a). One infers from this observation that fission gases are still present either as single gas atoms or contained in smaller, submicron size clusters probably similar to those described in the previous section. Towards the pellet centre (Figure 2b), which has operated at temperatures in excess of 1 073 K at least for some periods during the base irradiation, it is shown again from SIMS analyses that a small fraction of the gas has been released.

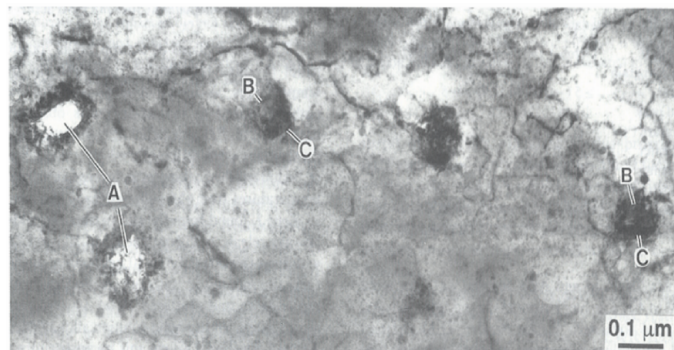
Figure 2. Experimental radial xenon distribution in a high burn-up pellet determined from EPMA



The dark line represents the calculated amount of xenon created. Calculation results corresponding to xenon in supersaturation and in small nanometre size bubbles are also indicated for comparison [78] (2a); SEM image of the central part of a fuel pellet (average pellet burn-up circa 61 GWd/Mt) revealing coarse intragranular porosity (2b); SEM image at a mid-radius location (2c); SEM image of the peripheral part of the pellet (local burn-up circa 100 GWd/Mt) revealing large micron size pores characteristic of the RIM structure (2d).

Release may be correlated to a visible change in the microstructure characterised by well-formed intra, lenticular intergranular fission gas bubbles 100 nm to 400 nm in diameter along with coarse porosity at the triple junctions of grains. The larger intragranular bubbles are shown to contain xenon at pressures in the GPa range, as observed for the similar size intra-granular objects reported previously (Figure 3 [115]).

Figure 3. TEM micrograph indicating the presence in high burn-up fuel of coarse intragranular bubbles surrounded by dislocation tangles and associated with five metal particle precipitates [115]



Although not characterised in the same material, there are similarities between the characteristics of intragranular bubbles illustrated in Figure 2b and the larger bubbles seen in Figure 3 [115]. In addition to this, the temperature and burn-up conditions in which these larger bubbles are observed are also comparable. This would suggest common nucleation and growth mechanisms. It was indicated that growth may occur via dislocation punching due to the high-gas pressures within the particle or a creep mechanism induced at lower temperatures than those required for plastic deformation to occur [151]. The former interpretation could be consistent with the abrupt microstructural changes seen in Figure 2, although how the pressure would build up in the first place remains unclear. As shown in Figure 3, large fission gas particles appear to be surrounded by dislocation tangles which could result in drainage to the particle of rare gases present in the matrix via a form of pipe diffusion.

In [79], the authors attempt to correlate gas release and hydrostatic swelling to microstructural modifications for even higher burn-up material. They show that upon further irradiation there is a sharp increase in the level of release in central areas of the pellet. Also, along the pellet radius, a large fission gas bubble population develops, with bubble sizes in excess of 100 nm.

Redistribution by carrier-gas assisted vapour transport

During fuel lifetime, regions of interconnected void space, for example cracks and tunnels, can develop in the fuel and act as channels for diffusion of gaseous species throughout the solid fuel matrix. At low temperatures, vapour pressures adjacent to the solid fuel are typically too low to move significant amounts of fuel components into the gas phase. However, if there are suitable gaseous species already in the void that fuel components may react with, appreciable amounts of an element may enter the gas phase and be transported along such channels in a much more efficient manner than by solid state transport. This carrier-gas assisted redistribution mechanism is thought to contribute to oxygen transport in MOX, and carbon transport in TRISO particle fuels [94,15,128].

The degree of oxygen (carbon) uptake into the gas phase is determined by the chemical potential of oxygen (carbon) in the solid phase, which depends on temperature and composition. The resulting effect is that components are seen to redistribute due to the temperature gradient, an effect also associated with thermodiffusion. Thermodiffusion, also known as the Soret effect and discussed later, is a different mechanism, which does not involve phase change and requires high temperature to be appreciable [109]. It should be emphasised that these are different phenomena, although the effect of carrier-gas assisted transport is sometimes quantified by an effective heat of transport [3].

Rand and Markin proposed oxygen in MOX could redistribute via a carrier-gas mechanism through reaction with hydrogen and/or carbon contaminations from the fuel, i.e., through reactions with H₂/H₂O or CO/CO₂ [94]. Even carbon contaminations at the level of 3 ppm in UO₂ were observed to have a considerable effect [1]. Depending on the local oxygen chemical potential, this reaction equilibrium will attempt to establish a local ratio of, for example, H₂ to H₂O. However, the gaseous species are also free to diffuse through interconnected porosity, and also attempts to establish an equilibrium along these channels which, in the absence of thermodiffusion in the gas phase, implies a constant ratio of H₂O to H₂. The competition between these two effects produces the carrier-gas transport mechanism. Aitken assumed that the diffusion of the carrier gas species was fast enough to reach equilibrium and proposed an effective heat of transport from thermodynamic parameters of the carrier gas species and the oxygen chemical potential in an assumed temperature gradient. In general, such an assumption is not valid for either hydrogen- or carbon-based carrier gasses due to poorly connected void space and competition with other transport mechanisms [3,2,83]. More complicated treatments may then be required such as kinetic models indefected fuel situations [42,105].

In TRISO particle fuels, the carbon buffer surrounding the kernel is considered to redistribute through this vapour transport mechanism for kernels of UO₂ [15,128]. In this case, oxygen present from contamination or liberation from the kernel develops a CO-CO₂ based carrier gas mechanism, transporting carbon from the hot side of the kernel to the cooler side. This effectively pushes the kernel up the temperature gradient, resulting in the so-called amoeba effect.

Description of standard intragranular models and usual modelling hypotheses

In this section, we have seen some important features relating to in-pile changes in oxide fuel microstructures prominent among which is the nucleation of small fission gas containing bubbles that grow depending upon burn-up and temperature. At the same time, a population of dislocation loops is also reported that evolves at sufficiently high burn-up and low enough temperature towards a dislocation network which gives way under certain conditions to complete restructuring of the fuel.

Efforts have been made to model these changes to the fuel microstructure based on rate theory models which account for point defect production, diffusion, annihilation and elimination at internal sinks such as fission gas bubbles and interstitial loops. Such models may also be used to describe the fuel microstructure leading up to fuel restructuring [97]. Although these approaches are interesting, they remain largely descriptive and fail to provide actual explanations for the reasons why actinide oxides are so remarkably radiation resistant in comparison to other oxide systems. Attempts have also been made over the years to rationalise some of the microstructural changes presented in this section

in relation to local or macroscopic fission gas release data through the development of intragranular fission gas behaviour models. We will now briefly describe the principles these models are based upon and try to circumscribe their limitations.

Basic assumptions in relation to single xenon atom and bubble behaviour

Most fission gas behaviour models [30,56,81,133] regard single atom intragranular xenon diffusion as the main rate determining factor for fission gas release. As a result, these models are usually constructed around an intragranular xenon diffusion equation in which the diffusion coefficient is generally taken as Turnbull et al.'s expression [117]. This despite the fact that the necessarily apparent xenon diffusion coefficient derived from Turnbull's original experiments is considered in part at least as resulting from a cation vacancy assisted mechanism. In this model, the vacancy concentration is given by rate theory equations solved under steady-state conditions. Although radiation assisted xenon migration is recognised as relevant, such models overlook this fact. In line with observations reported in previous sections, it seems that any comprehensive understanding of fission gas behaviour or release requires being able to calculate at all times the fraction of intragranular gas which is contained in intragranular bubbles and the remaining part in supersaturation, which can migrate to grain boundaries from where release can occur. Inevitably, therefore, comes the need to describe bubble characteristics, how they nucleate and grow, and also how migrating gas atoms interact with them. To this end, the time and space dependent rate of capture by bubbles of migrating gas atoms is expressed, assuming the bubble behaves as a perfect spherical sink of radius r_b , as: $4\pi r_b D_{Xe} C_b$.

A numerical estimate of this expression using Cornell's data [21] for a 1 GWd/Mt fuel at 1 273 K (i.e., $r_b \sim 1$ nm, bubble concentration $\sim 3 \times 10^{23} \text{ m}^{-3}$) and Turnbull's [117] data for the xenon diffusion coefficient D_{Xe} at that temperature (roughly $10^{-20} \text{ m}^2 \text{s}^{-1}$) shows that the inventory of gas in the matrix (outside bubbles) is divided by ten after less than a day. In the absence of some form of mechanism for transferring gas from the bubbles back to the matrix, virtually no fission gas release is possible. The original observation that the characteristics of the bubble population rapidly reached a narrow distribution was taken as a demonstration that thermal resolution was impossible. Indeed, this would have led to signs of Oswald ripening which there were not [20,72]. Nelson [72] suggested that in an irradiation environment fission gas atoms contained in bubbles could be resolved by direct elastic interaction with fission fragments. Based on the binary collision approximation (BCA), he evaluated the probability per second for this event to occur. Nelson's approach was then re-evaluated to take into account subsequent collisions with uranium recoil atoms, which increased the re-solution parameter by a factor of 40 approximately [86]. This resolution term enabled calculations to be carried out of the amount of gas reaching the grain boundaries, in super saturation in the oxide matrix and in intragranular bubbles at any time.

A set of experiments involving low-temperature irradiations and annealing sequences were reported at that period [118,120] and were considered as a demonstration that irradiation could disperse fission gas bubbles thus lending credence to Nelson's theoretical approach. Turnbull [119] later suggested that bubbles were formed continuously in the wake of fission fragments (coined heterogeneous nucleation) and that they grew until a subsequent encounter with a fission fragment destroyed them (heterogeneous re-solution).

The “heterogeneous” mechanism was mainly inferred from observations of small bubbles lying in strings of ~ 5 [119] and later [152].

Model principles

Although models incorporating bubble distribution densities based on rate theory have been developed over the years [136,38], we focus here on models that describe a single bubble population of which [81] is a typical example and which may be regarded as deriving from rate theory models. The basic intragranular model comprises four coupled conservation equations which describe atomic diffusion of gas through the grain (xenon conservation equation) with trapping at and emission from fission gas bubbles in the process, a bubble conservation equation which describes a balance between bubble nucleation and bubble destruction when the bubble radius lies below a threshold radius, an equation describing the rate at which the xenon atoms contained in bubbles changes over time and finally the rate at which the volume fraction of intragranular bubbles changes. An empirical treatment of fuel restructuring is also used which is based on a time dependent first order differential equation describing as a function of temperature the local dislocation density change. The parameters are chosen so that the model represents dislocation density measurements published by Nogita et al. [74]. The model also incorporates a specific treatment of grain boundary gas which is not described here.

Model performance and limitations

Such models when associated with fuel performance codes are capable of reproducing in-reactor data quite adequately. Figures 2a and 4 [81] show a comparison of modelled *vs.* experimental data obtained using characterisation techniques on the micron scale. Figure 4 is a comparison of the total porosity calculated and measured using SEM in association with image analysis techniques in a high burn-up fuel pellet (61 GWd/Mt). In Figure 2a, in addition to the EPMA xenon concentration signal, calculated fission gas concentrations are given, which correspond to xenon atoms in supersaturation and contained in nanometre size bubbles, which is what EPMA is sensitive to for reasons outlined previously.

Despite calculated values and experimental data being quite close, these models adopt a number of empirical approaches in relation to phenomena for which no satisfactory and/or comprehensive explanation exists. Fuel restructuring is by no means the only example:

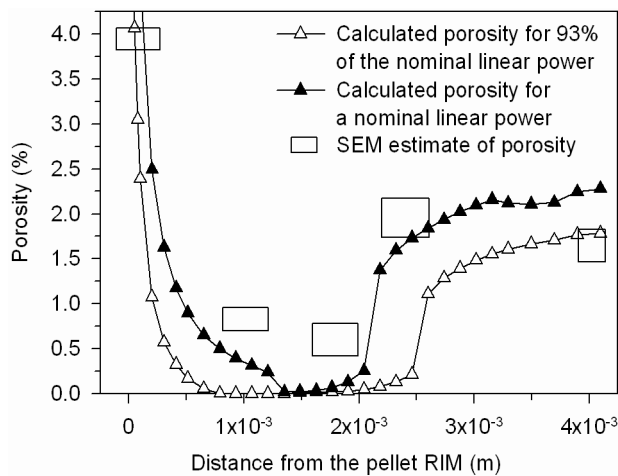
- Fission gas resolution has no other experimental demonstration than the fact that fission gases eventually reach grain boundaries. Nucleation or bubble destruction mechanisms are inferred from the fact that a nanometre size bubble population quickly reaches steady-state characteristics as irradiation proceeds. The terms used in fission gas behaviour models can in this respect be regarded as *ad hoc*.
- These models do not provide an adequate explanation for the emergence above 1 073 K of a coarser less abundant bubble population, although more complex size distribution approaches could help understand this phenomenon. According to our knowledge, there are no approaches that provide a predictive determination of the emergence of such a bubble population.

- The third point concerns release under thermal annealing conditions. One would expect fission gas behaviour models to predict release under less complex conditions than prevail during a neutron irradiation. In fuels irradiated at burn-ups greater than 6 GWd/Mt [9,121,138,123], substantial fission gas release during a post-irradiation annealing at temperatures above 1 573 K is widely reported. Modelling this release process requires a description of the interaction between nanometre size intragranular bubbles and diffusing gas atoms. If one assumes that intragranular bubbles act as perfect sinks (with no thermal resolution possible), then for fission gas bubble concentrations relevant to irradiated fuels, gas atoms homogeneously distributed within the grain initially are readily trapped resulting in calculated gas release fractions well below observed values [32]. No convincing explanation for this is available either.

Regarding this latter point, the fact that the underlying phenomena are not adequately taken into account in the *a priori* simpler context of out-of-pile annealing casts doubts as to whether they are under the more complex conditions of a neutron irradiation. The widely accepted scenarios based upon radiation induced bubble nucleation, resolution and fission gas trapping may, therefore, be substantially at fault.

Finally, in most cases, the models relied upon for describing fission gas behaviour leave little room for radiation-induced phenomena which along with atomic transport properties are a key to unravelling many aspects of the ageing of the material. When the models do account for some radiation effects, the approaches are usually so simplified that it is often difficult to justify modelling one phenomenon rather than another. A complementary, more detailed approach, which explicitly includes radiation effects shown to be relevant is, therefore, necessary and is described in the last section of this chapter.

Figure 4. Measured and calculated pore distribution across a high burn-up fuel pellet [81]



High-temperature effects

In cases such as fast reactor fuels, high temperatures can be reached at the fuel centreline (or, more accurately, the inner fuel surface). The high temperatures in the centre and cooled outer periphery result in large temperature gradients and can lead to a variety of matter transport phenomena and microstructural changes which can be modelled through application of thermodynamics of irreversible processes [131].

A schematic of the fuel restructuring process is shown in Figure 5 for a highly rated MOX element, as a function of burn-up (increasing clockwise) [17]. The fuel begins life with a homogeneous matrix of micron-sized grains and is fabricated such that some residual porosity is left so as to accommodate fission products. Immediately upon start-up cracks appear from thermal shock forming connected void regions throughout the radius of the fuel. The outermost region is too cool to experience significant grain growth, but at intermediate temperatures equi-axed grain growth can occur. In higher temperature regions, pores quickly migrate towards the centre as described below, consuming grains and cracks and leaving wakes of columnar grains. At the centre of the fuel, the central void develops as a consequence of direct transport of centreline material to the outer periphery and the coalescence of pores migrating from the columnar grain growth region. A cross-section of a real fuel pellet is shown in Figure 6 and clearly shows the as-fabricated, equi-axed grain growth, columnar grain growth and central void zones.

Figure 5. Schematic evolution of MOX microstructure evolution operating at 42.3 kW m⁻¹ and burn-up increases clockwise as labelled [17]

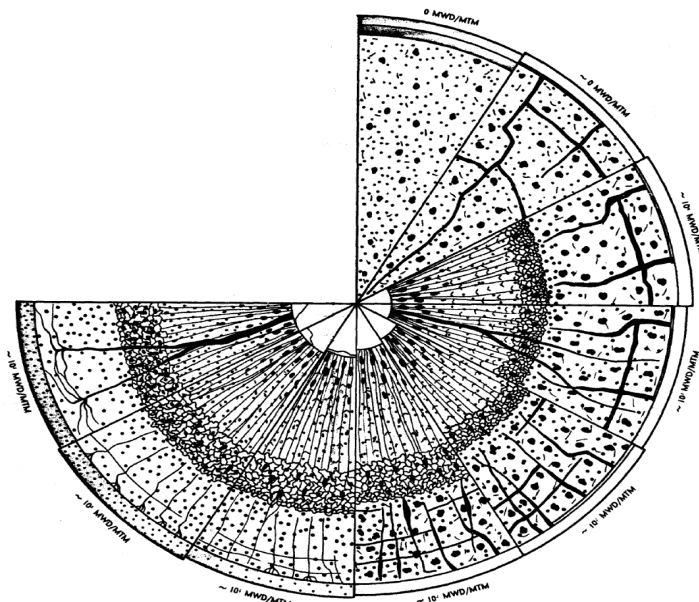
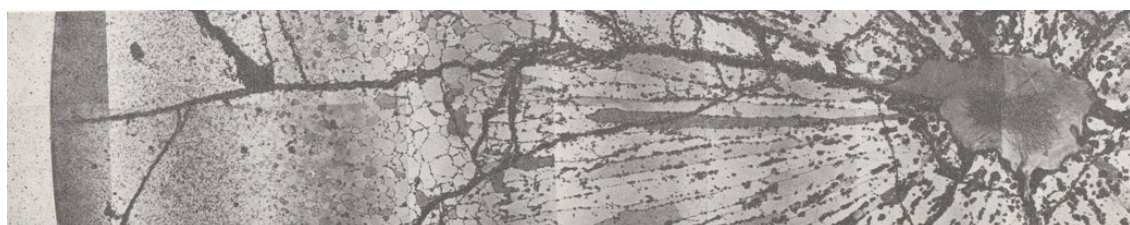


Figure 6. A cross-section of a MOX fuel pellet showing regions of as-fabricated porosity, equi-axed grain growth, columnar grains and the central void



Source: European Atomic Energy Community.

Matter is theorised to be driven by the temperature gradient by a number of superimposed forces. Firstly, thermodiffusion of atoms down the temperature (or likewise vacancies up), and its effects on void migration were considered [139]. Secondly, stress gradients, which develop as a consequence of temperature dependant densification as described previously, can drive matter from the centre to the periphery through creep mechanisms [68,127]. Finally, the evaporation-condensation mechanism can become of significant magnitude, which is important for redistribution as well as restructuring and, therefore, described separately below.

Evaporation-condensation transport

At high temperatures, significant vapour pressures may develop in available void space, moving fuel components into the gas phase where they can be transported through the free volume without the need of a carrier gas. Since even the host matrix components may be transported in this manner, significant restructuring of the fuel matrix may occur and produce very pronounced microstructural changes. The vapour in equilibrium with the condensed phase is not in general of the same composition and, therefore, this evaporation-condensation mechanism also can produce compositional shift at both the evaporation and condensation sites.

In MOX, vapourisation and transport of heavy elements, such as U, Pu and Am, can quickly transport large amounts of solid matrix material down the temperature gradient, leading to restructuring and redistribution [114]. Lackey et al. show results of restructuring of sphere-pac MOX elements in which uranium is clearly seen to have preferentially vapourised from the inner regions and condensed around the spheres at the outer region, leaving a central void with a plutonium rich periphery, and islands of Pu rich MOX in the outer region [53]. Redistribution also depends on the chemical state of the fuel with, for example, the ratio of U to Pu bearing species depending on the O/M ratio in the fuel. Bober et al. investigated this with samples of $(U_{0.85}Pu_{0.15})O_{2-x}$ with maximum temperatures 2 673 K and found that uranium preferentially evaporates for O/M ≥ 1.97 and plutonium for O/M ≤ 1.96 [13].

The evaporation-condensation mechanism is also noted in carbide and nitride fuels and contributes to their restructuring and redistribution. It was noted that the vapour adjacent to carbon rich fuels was rich in Pu-bearing species and, therefore, redistribution acts in the opposite fashion to MOX with Pu being transported down the temperature gradient [63,58]. In carbide and carbon rich fuels, small voids were observed to migrate up the temperature gradient, with an explanation proposed as a combination of vapour transport of (U, Pu) across the void with fast carbon diffusion in the matrix.

Pore migration

Small regions of gas filled voids may be present in the fuel as a result of residual porosity, accumulation of fission gases or from pinching off of crack tips. Bubbles, as discussed in this chapter, contain high-pressure gas, exist at submicron sizes and are spherical due to equilibrium with the isostatic pressure of the fuel matrix. The high-gas pressure inside the bubbles suppresses vapour transport leaving only solid state (or surface) diffusion mechanisms active.

Pores are a type of small, enclosed void, and play a major role in the restructuring of the solid fuel matrix. They are lenticular, with the minor axis aligned with the temperature gradient and contain low-pressure gas, primarily the cover gas used from fuel fabrication. Pores migrate up the temperature gradient primarily through vapour transport, thermodiffusion and stress-driven diffusion [104,68,127]. In the evaporation-condensation mechanism, matrix material vapourises on the hot surface, diffuses across the width of the pore, and condenses resulting in the void's progression towards the hottest region. In thermodiffusion and stress-driven diffusion, atoms are driven individually down the gradient (or vacancies up it) resulting in the net displacement of the pore towards the hottest point.

Pores are too big to be pinned to defects or grain boundaries and rather consume grains in their path, collecting new elements which were trapped in the matrix and building long, cylindrical, columnar grains in their wake, with a series of small regularly spaced bubbles along the circumference [87]. When they approach the fuel centreline, or rather the periphery of the central void, the temperature gradient becomes flat, which suppresses the evaporation-condensation mechanism. It is then considered that creep or sintering is responsible for the final merger of the pore with the central void where all the collected elements are deposited [68,127].

Pore migration and central void formation can occur quickly upon start-up and can remove the initial porosity in a matter of hours. Tanaka et al. irradiated MOX for 10 minutes and already observed central void formation and pore migration [114]. Following the removal of the initial porosity, pores may still be generated from cracks, and so may continue well into irradiation. Due to the high sensitivity of vapour pressure on temperature, the efficiency of vapour transport and, therefore, the pore migration velocity depends strongly upon temperature and the outer radius of the columnar grain region is fairly well predictable from the centreline temperature, as is the size of the central void [85, 18].

The predominance of the vapour transport mechanism in inducing pore migration and the previously discussed U-Pu redistribution, which is a consequence of this, raises the question of long-range redistribution of U-Pu from pore migration. The preferential vapourisation of, for example U, from the advancing surface implies an enrichment of Pu in the solid in front of the advancing pore, which can only diffuse a limited distance in the solid state due to slow diffusion. The higher concentration of Pu at the hot surface implies more vapourisation of Pu at that point, which balances the difference in vapour pressures across the pore. The macroscopic enrichment process is, therefore, limited to the Pu, which initially builds up at the advancing surface, the so-called “bow wave”, and the excess Pu vapour in the pore, akin to zone refinement. The cumulative effect of pore migration on actinide redistribution was calculated to be orders of magnitude smaller than the observed effects, implying that it was not the mechanism responsible for Pu enrichment at the inner surface, which instead might be preferential vapourisation and diffusion along the initial cracks in the fuel before they are healed [84,35,19].

Thermodiffusion

Another phenomenon partially responsible for redistribution and restructuring is that of thermodiffusion, also known as the Soret effect, which may occur in the solid or gas phase [14,139]. In the context of nuclear fuel, it is most often associated with redistribution of fuel components in the solid phase and for this reason requires high

temperatures and high-temperature gradients to produce fast enough kinetics and a large enough driving force to be appreciable. It is difficult to separate from the evaporation-condensation mechanism and carrier-gas assisted transport and is considered dominant in very dense solid regions, such as the columnar grain zone where pore migration has removed the initial porosity and cracks and, therefore, reduced vapour-phase transport.

In MOX, thermodiffusion in the solid state is considered to contribute to the redistribution of U and Pu. Experiments were performed on $U_{0.85}Pu_{0.15}O_2$ and $U_{0.85}Pu_{0.15}O_{1.98}$ at up to 2 800 K with linear temperature gradient of 1 500 K cm⁻¹ and found a profile which suggested overlapping effects of U vapourisation and U-Pu thermodiffusion [12,13,14]. In another experiment on (U, Ce)O₂, it was found that Ce is driven up the temperature gradient by thermodiffusion and counteracted by the vapour transport downwards [11].

Often, the lighter elements in fuels are several orders of magnitude more mobile than the heavy elements and so show more pronounced thermodiffusion effects. Such is the case with oxygen moving up the temperature gradient in non-stoichiometric MOX (of which $UO_{2\pm x}$ is a special case) [100], and carbon moving down the gradient in uranium carbide fuels [41,129]. The chemical state also influences the efficiency of this mechanism. Sari and Schumacher performed experiments on MOX samples of various U/Pu ratios and oxidations in which vapour phase transport was excluded by coating the samples in Mo [100]. They showed that oxygen is driven up the temperature gradient to varying degrees depending on the degree of oxidation (valence of U/Pu) but not the ratio of U/Pu [100]. Their results are partially questionable due to their technique, however, as they noted in their analysis, the metallic coating used to prevent vapour developing might be interfering with a thermoelectric effect which may be present in the normal fuel operation [45,70].

Modelling of high-temperature restructuring and redistribution processes

Modelling of the restructuring and redistribution phenomena includes matter transport driven by thermodiffusion, stress gradients, non-congruent vapourisation, and sintering. As of the time of this report writing, there does not appear to be a model which accounts for the interplay of these phenomena completely, which should then predict pore migration, central void growth and redistribution simultaneously and self consistently. Reasons for this may be the complexity of the problem, the range of length scales which must be considered (micrometre to centimetre), and frequent lack of basic material data (chemical diffusion or thermodiffusion coefficients) that such models require.

Higher burn-up effects

- The high burn-up structure in oxide fuels

A word must be said about a more radical microstructural change first coined as the RIM effect because it was initially observed in the periphery of UO₂ fuels [90]. This phenomenon is seen in all types of oxides both Pu-bearing Mixed [Pressurised Water Reactors (PWRs) or Fast Reactors (FRs)], Oxide Fuels (MOX) or UO₂ fuels below 1 273 K but at elevated local burn-ups (greater than 60 GWd/Mt). It first generated interest because of the characteristic radical change in the microstructure it brought about and concerns that this might lead to extensive fission gas release. Although the oxide retains its original fluorite structure as demonstrated by electron nano-diffraction [74,115,76,95],

the original grain size which is usually between 5 μm and 20 μm for sintered material is found in the 200 nm to 1 μm range following the transformation. It is also accompanied by the formation of micron size fission gas bubbles as seen in Figure 2d, although there is still debate about whether these bubbles precede or are a consequence of the restructuring process [113]. Other revealing TEM observations were instrumental in setting up scenarios for explaining this spectacular transformation. Nogita and Une [74] estimated the dislocation density in regions immediately adjacent to completely restructured zones. Their estimates led to extremely high values ($5\text{-}6 \times 10^{14} \text{ m/m}^3$) in un-restructured original grains and also found that within the new submicron grain structure, the interior of the grains showed no signs of the presence of dislocations or dislocation loops. The other finding confirmed in [115] was that nano electron diffraction revealed a random orientation of the new nano-grain structure. These observations led Nogita and Une [74] to suggest that this was a case of dynamic recrystallisation. The driving force for this is accumulation of radiation damage as fission events are assumed to lead to the formation of dislocation loops and vacancy clusters. Biased attraction of interstitials in comparison to vacancies for loops leads to their growth and eventually to the formation of dislocation networks. On the other hand, vacancies tend to form clusters in which fission gases in particular are likely to accumulate. In the authors' scenario, dislocations then reorganise into subdivided grains with high angle boundaries that constitute the nuclei for the subsequent recrystallised structure. At a critical damage level, recrystallisation occurs as a result of which defects and fission products are swept out and fission gases gather in micron size agglomerates. Another interesting finding which supports this interpretation is the fact that restructured grain regions are actually quite stable in the event of a continued burn-up increase and also that the restructured grain sizes appear to be dependent upon the temperature at which the transformation occurs [80]. In restructured MOX agglomerates that had operated at temperatures up to 1 273 K, grains of up to 1 μm in diameter have been observed whereas smaller grains are observed at the periphery of UO₂ fuels at high burn-up that operate at 673-773 K. This temperature dependence is typical of dynamic re-crystallisation. Also, the stability of restructured grain with burn-up may be an indication, as suggested in [134], that the sink efficiency of grain boundaries of small size grains has become predominant over the sink efficiency of internal sinks. Wiedersich indicates that the sink efficiency of grains with sizes between 100 nm and 1 μm is equivalent to that of dislocations at densities between 10^{14} and 10^{15} m/m^3 [134]. Based on different observations of similarly restructured regions, some authors favour a polygonisation mechanism to explain the reduction in grain size. Indeed, Ray et al. [95] observed diffraction patterns of restructured regions corresponding to low angled boundaries. Whatever the actual mechanism for restructuring interpretations always invoke the build-up of radiation damage [66]. A polygonisation mechanism is also supported by surface studies of ion irradiated single crystals [65,34].

Despite converging observations, other explanations for fuel restructuring have been suggested involving the role of so-called planar defects [51] that are not systematically reported or of high local stresses around pre-existing pressurised fission gas bubbles [113]. Other possible effects that have never really been studied analytically concern the role of fuel chemistry and oxygen redistribution and activity. There are indications for instance [80] that the local plutonium content may be essential in controlling fuel restructuring. Also, to conclude this section, recent characterisations of very high burn-up material (83 GWd/Mt) show restructured regions extending about 100 μm into the fuel pellet whereas previous

studies reported restructured regions more than three times as thick [79,57] at similar burn-ups and under similar irradiation conditions. No satisfactory explanations for these observations are yet available.

Microstructure evolution in research reactor fuel

The main purpose of research reactors is not to generate power, but to provide neutron sources which have diverse applications such as neutron research, fuel and material behaviour testing, radioisotope production, non-destructive testing. Research reactors are usually much simpler and operate at lower temperatures than commercial power reactors. The nuclear fuels for research reactors are much different from those for commercial power reactors and usually come in two geometries: plate and cylindrical types. They generally comprise what is known as the fuel meat and its surrounding cladding. The fuel meat is made up of fine fuel particles homogeneously dispersed in an aluminium matrix. Similar aluminium based alloys are used for the fuel meat matrix and as cladding material whilst different types of fuel particles are encountered in order to satisfy the fuel requirements.

To make a compact core with high neutron flux, many research reactors used high enriched uranium fuel (HEU, i.e., fuels with a ^{235}U enrichment in excess of 20%) up to the late 1970s. However, in order to abide by the international non-proliferation treaties, the US Department of Energy in 1978 initiated the Reduced Enrichment for Research and Test Reactors (RERTR) Program. The RERTR Program has developed technologies required to convert the HEU nuclear fuels to low enriched uranium fuels (LEU, i.e., fuels with a ^{235}U enrichment below 20%) in research reactors. The main concept of the RERTR is to develop LEU fuels which have identical ^{235}U densities to HEU fuels. It has been pursued through two approaches: one consists in increasing the amount of LEU fuel particles in the fuel to compensate the enrichment decrease. The other is to develop new fuel particle materials having higher uranium densities than those of existing fuel particles such as UAl_x , U_3O_8 , and UZrH_x . Because there is a practical limit to the increase in the amount of fuel particles, most efforts were spent on developing new fuel particle materials in the RERTR Program.

U_3Si_2 fuel particles dispersed in an aluminium matrix was a fuel type developed and qualified up to a density of 4.8 gU cm^{-3} in 1988 [122]. If the volume fraction of U_3Si_2 fuel particles in the fuel meat approaches its geometrical limit, the irradiation stability of U_3Si_2 is maintained up to a sufficiently high burn-up level as shown in Figure 7 [28]. However, the burn-up increase of the U_3Si_2 -Al fuel and the radiation damage it entails causes the microstructure to change substantially:

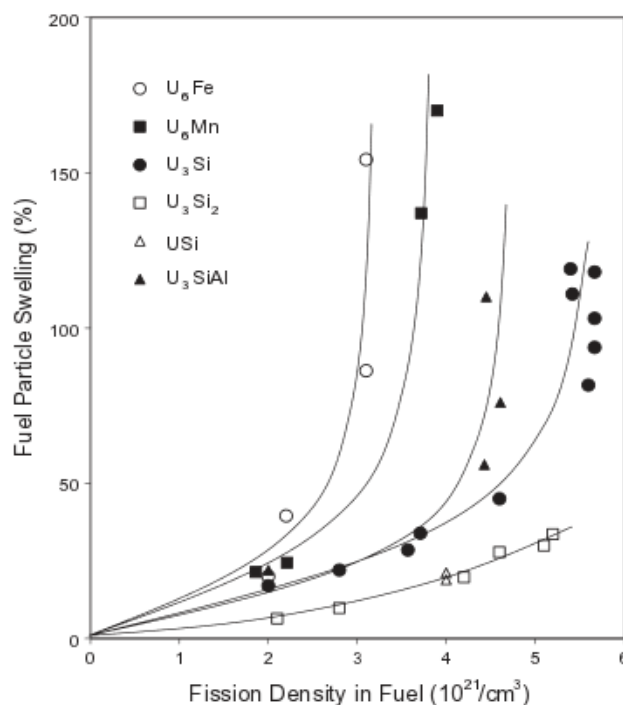
- The first phenomenon is the formation of an interaction layer between the U_3Si_2 fuel particles and the aluminum matrix which grows through radiation induced or enhanced diffusion controlled processes. Because the thermal conductivity of the interaction layer is less than that of the surrounding aluminium matrix, the overall conductivity of the fuel meat decreases with burn-up.
- The second phenomenon is the porosity change in the fuel meat which is due to two mechanisms. The unirradiated fuel meat contains voids left over from the manufacturing process which are liable to accommodate fuel swelling which occurs in the early stages of the irradiation process. As a result, the porosity in the fuel

meat decreases in the beginning. As irradiation proceeds, fission gas bubbles nucleate and coalesce thus affecting the pore size distribution. These processes are controlled by the apparent diffusivity of gas atoms and defects which are affected by temperature, fission density, fission gas resolution and trapping. The formation and coalescence of fission gas bubbles induces a degradation of the thermal conductivity of the fuel. In addition, the growth of fission gas bubbles into larger ones induces extensive fuel swelling. Hence, it is favourable to keep bubble sizes as small as possible from the viewpoint of fuel performance and integrity. Fortunately, reasonably small stable bubbles develop in U_3Si_2 fuel particles even at high burn-ups as shown in Figure 8, except in some extreme cases [54].

- The third phenomenon is the radiation induced amorphous phase change which may result in changes in fission gas diffusivity and fuel plastic flow rates for large swelling values. While it was widely recognised that U_3Si becomes amorphous at intermediate burn-up levels under irradiation, it was thought that U_3Si_2 remained crystalline under irradiation. Recent observations have revealed that U_3Si_2 can also become amorphous [28].

Despite these phenomena, the integrity of $\text{U}_3\text{Si}_2\text{-Al}$ fuels has been observed under most normal operating conditions in research reactors.

Figure 7. Fuel particle swelling of uranium silicides [28]



The microstructural evolution in research reactor fuels has been a big concern when the international study started on new research reactor fuels in 1996, which had much higher uranium density than U_3Si_2 . One of the most promising candidates is the U-Mo alloy fuel dispersed in an aluminium matrix and the monolithic U-Mo alloys. The U-Mo dispersion fuel showed a good performance up to a certain burn-up but an unexpected

breakaway swelling occurred at a high burn-up [43]. Post-irradiation examinations (PIE) correlated the unexpected breakaway swelling to the interaction between the U-Mo fuel particles and the aluminium matrix. Figure 9 shows the resulting microstructure with large pores. The unexpected breakaway swelling in U-Mo fuel is affected by various factors such as high fission rates, temperatures and burn-ups. Two options have been investigated to suppress the growth of an interaction layer between the U-Mo fuel particles and the aluminium matrix: one is to add at least 2 wt% silicon to the aluminium matrix. The irradiation test and PIE revealed that this decreased the growth rate of the interaction layer whilst guaranteeing the irradiation stability of U-Mo fuel even at high burn-up. The other is to coat the U-Mo particles with oxides. The oxide coating may work as a barrier to diffusion thus limiting interaction layer growth.

Figure 8. Fission gas bubble morphology in U_3Si_2 (96% burn-up) [28]

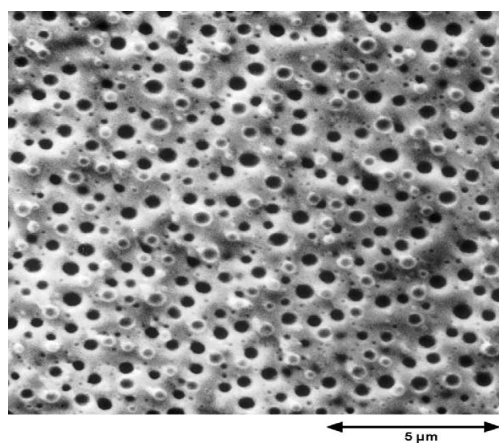
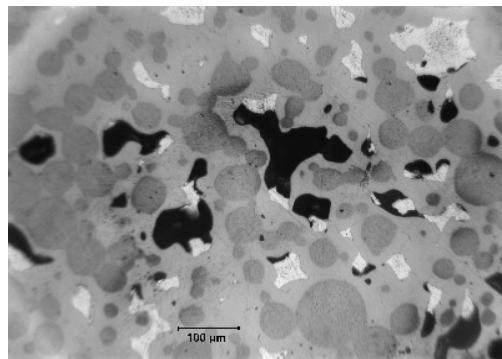


Figure 9. RERTR 4, mini-plate V6022M, U-10Mo, average burn-up 82% [43]



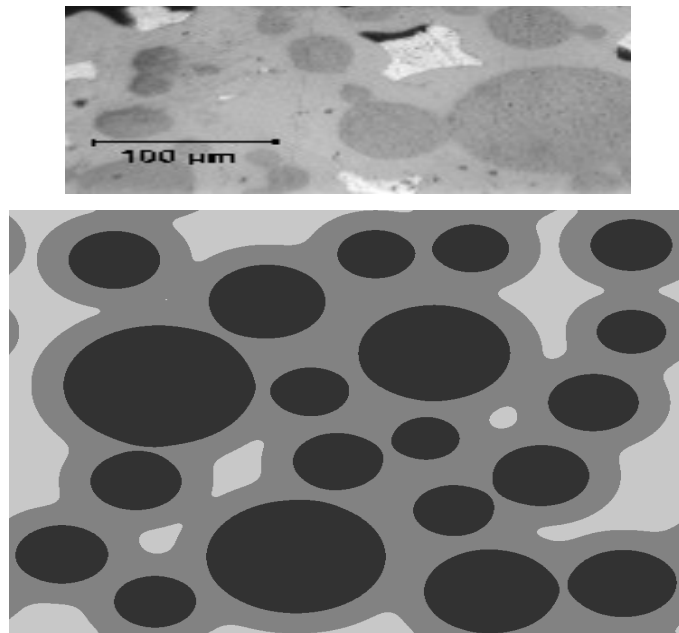
Dark areas correspond to fission gas containing pores, grey spherical structures are what remain of the original UMo fuel particles, surrounding lighter areas indicate the development of an interaction layer between the original fuel particle and the matrix.

Such microstructural changes in research reactor fuels were described using a combination of diffusion equations and correlations based upon experiment. The Dispersion Analysis Research Tool (DART), the main purpose of which is to predict fission-product-swelling in aluminium dispersion fuel, is the representative code in this field [96]. It calculates the closure of as-fabricated pores by accommodation of fuel particle swelling, interaction between fuel particles and aluminium matrix, amorphisation,

and recrystallisation. The resulting information on microstructure evolution is used for predicting macroscopic swelling and the thermal conductivity of fuel.

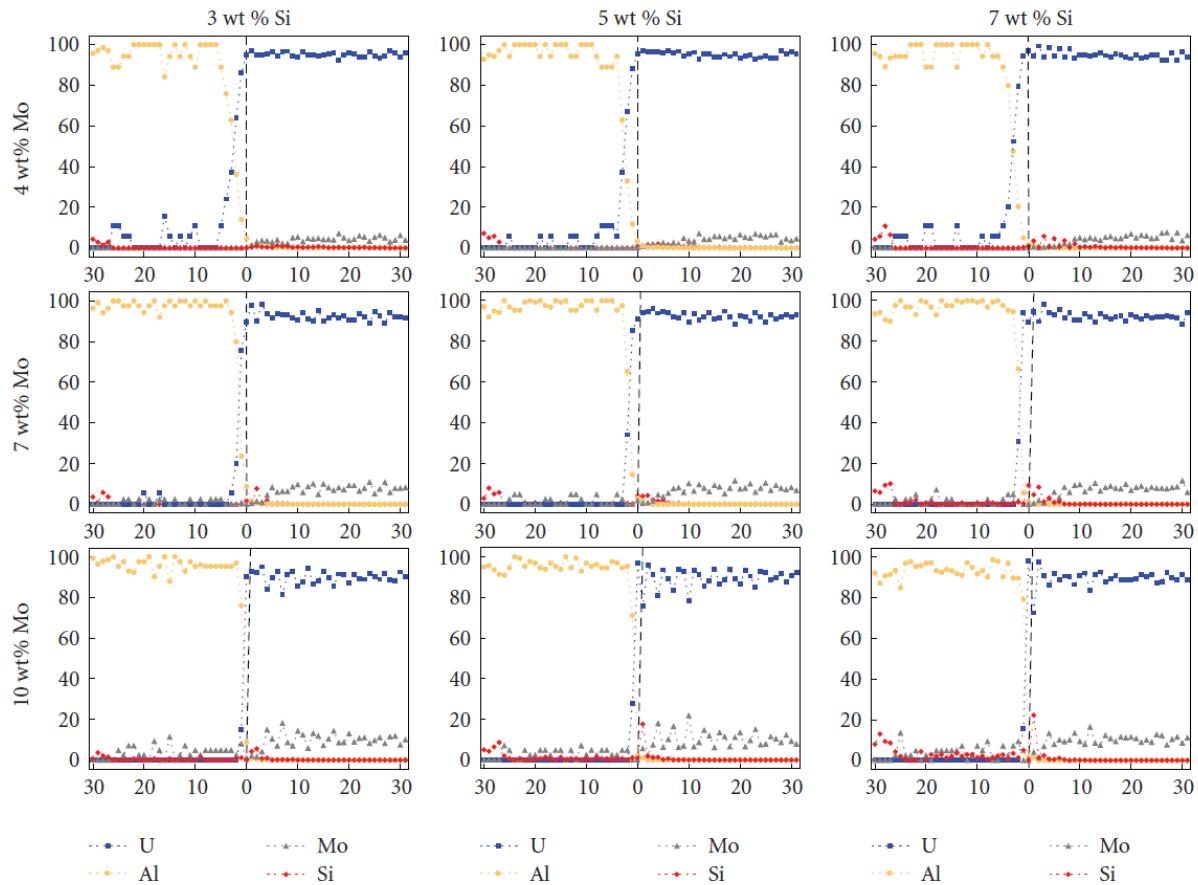
The microstructure evolution in U-Mo/Al dispersion fuel was also investigated using a phase-field model, which uses the free energy of a system to describe a system state [82]. Figure 10 shows the simulated microstructure of RERTR-3 V03 plate at 37.6% burn-up. It has 14.4% of unreacted Al matrix, which is very similar to a measured value, 17%. The simulated microstructures were used for evaluating thermal conductivity degradation as a result of the growth of an interaction layer.

Figure 10. Simulated microstructure of V03 plate at EOL by phase field model [82]



To study the effect of adding silicon to an aluminium matrix in U-Mo fuel, the Bozzole-Ferrante-Smith (BFS) method was applied to Al/U-Mo interface modelling [31]. It calculates the minimum amount of silicon addition for the diffusion barrier to be effective as shown in Figure 11. It is important to optimise the silicon content in U-Mo fuels because silicon is detrimental to the reprocessing process. The BFS method can be used to evaluate alternatives to silicon addition: silicon coating, zircaloy matrix, and carbon coating.

Figure 11. Composition profiles of the computational cells at U-Mo/Al interface at 450K [31]



An attempt at rationalising some of these observations based on separate effects experiments and atomistic scale modelling

Basic radiation damage processes and dislocation loop formation

Experimental results

In-reactor radiation damage mainly proceeds from the slowing down of fission fragments which induces both electronic excitation and ballistic effects although the material appears to be more sensitive to ballistic damage [77] in the range of stopping powers associated with fission fragments. This of course does not preclude that electronic excitation may have a substantial impact through modification of defect charge or mobility under irradiation as seen in other oxide systems [55].

Experimentally, fission fragment induced damage was studied by Whapham and Sheldon [132] who reported a number of interesting findings. Following low-dose irradiations of UO_2 samples, corresponding to fission densities four orders of magnitude less than the smallest fission density in Cornell's [21] study, the authors observed the presence of small interstitial type dislocation loops (lying on $\{1\ 1\ 0\}$ planes and with a Burgers vector of $a/2 <1\ 1\ 0>$) 2.5 nm in diameter. These dislocation loops quickly grow upon continued irradiation and eventually constitute a dislocation network. Some of these

findings were later confirmed by Soullard [110] in samples irradiated at slightly higher fission densities. The average dislocation loop size was nearly double (although difficulties were encountered due to the small loop sizes) that found in [132]. But in addition to the $a/2 <1\ 1\ 0>$ loops, $a/2 <1\ 1\ 1>$ loops are also reported; the latter corresponding to planes containing empty octahedral sites in which there is therefore some room to accommodate a stoichiometric array of uranium and oxygen atoms. The size distribution derived from TEM analyses showed a quasi-constant dislocation loop density between 5×10^5 fissions cm^{-3} and 3×10^{16} fissions cm^{-3} [110]. The author's favoured explanation for this is, as commonly assumed in the case of fission gas bubbles, fission spike induced resolution. We will see below that the author's second explanation which involves annihilation with vacancies produced through the fission process should by no means be overlooked. The last feature we should like to comment upon in relation to this work is the high radiation resistance of UO_2 . Soullard evaluated (based on a BCA estimate) that circa. Twenty-seven thousand uranium Frenkel pairs were formed at each fission event. And the fact remains that UO_2 preserves its crystal structure despite the level of ~ 2000 dpa readily reached in the periphery of a high burn-up oxide fuel.

For sake of completeness, three other types of studies should be cited in relation to radiation damage of a slightly different kind to that induced by fission fragments: they concern ^{238}Pu doped [48] or ion-irradiated UO_2 [99,101,108]. Regarding the former type of study α -decay of ^{238}Pu induces relatively high levels of radiation damage presumably through the ~ 100 keV recoil nucleus mainly. When observed after different storage times, dislocation loop formation and growth is clearly characterised which the authors interpret based on a rate theory model in terms of loop movement and coalescence and radiation induced resolution. This work focuses mainly on dislocation loop behaviour and no helium bubbles are reported. Following either 390 keV Xe or 300 keV Cs implantations, Sabathier et al. [99] describe a sequence of dislocation loop formation and growth and a change of the microstructure towards a dislocation network at fluences of 10^{15} ions cm^{-2} and 10^{16} ions cm^{-2} which is similar to that reported in neutron irradiated material [132]. By contrast in 7 keV He [101,61], irradiated samples, a regime of dislocation loops is observed when at similar fluences of ions characteristic of fission products, a dislocation network readily forms. This is quite obviously the result of the vastly differing radiation damage these two types of ions (7 keV He and 300-400 keV Xe or Cs) induce in the material.

Finally, the ion irradiation study presented in [108] also clarifies the susceptibility of UO_2 to electronic excitation effects in comparison to ceria and for several high electronic stopping powers. Ion tracks are characterised in ceria and uranium dioxide and as expected, in the high electronic stopping power ranges (between 15 and 30 keV nm^{-1}), uranium dioxide is much less susceptible to radiation damage than the more insulating cerium dioxide. For electronic stopping powers of roughly 20 keV nm^{-1} , the average track diameter is less than two nanometres in UO_2 as opposed to 7-8 nm in ceria. The other interesting finding is the fact that the scenario involving the build-up of a tangled dislocation network from dislocation loops is also observed following a 210 MeV Xe irradiation. It illustrates that this observation is not dependent upon the cause of radiation damage but a general mechanism through which the material accommodates this damage that could constitute a key stage in the evolution of the material towards a fully recrystallised microstructure (see the high burn-up effects section above).

Modelling

One of the most striking recent evolutions in fuel studies has been the wide spread development of modelling techniques at the atomic scale. Molecular dynamics based on empirical potentials in particular has extensively been used whether in relation to the study of radiation damage or not [39,71,124,37,60] as examples of applications. In the context of radiation damage studies it gives an insight into basic damage processes at scales in the main inaccessible to experiment. Before we look at what those techniques have revealed in relation to this, it should be noted that Monte-Carlo (MC) or analytical applications within the BCA can also provide essential insight into how energetic particles slow down in the material and how the subsequent damage is spatially distributed. The question is quite relevant to nuclear fuels because of the very high energies of fission fragments. Based on the BCA and recognising the fractal nature of collision cascades, Siméone and Lunéville [106], have defined a subcascade threshold energy E_c which represents the energy of, in the main, spatially separated subcascades into which a high-energy displacement cascade brakes down into. Intuitively, this energy can be seen as the energy for which the average distance travelled between two collision events is equivalent to the size of the subcascade. It is shown to depend upon the atomic number and the threshold displacement energy of the atoms it contains. Calculating E_c for UO_2 yields 25 keV using an atomic number averaged out to take into account composition and a 40 eV threshold displacement energy for U atoms [112]. Applying their theory to diatomic targets is still in progress but encouraging signs stem from the fact that this value is in good agreement with empirical potential molecular dynamics simulations of high-energy displacement cascades in UO_2 [125,62].

This latter modelling technique indeed provides details of the material's response to energetic ions and the previous comment justifies studying the effects of U recoil atoms in the 10 keV energy range. Van Brutzel et al. [126] have shown that a cascade develops in three distinct stages the first of which involves high-energy binary collisions and lasts a few tenths of picoseconds. As the recoil energy is deposited in the material, a thermal spike develops characterised by the short range movement of a large number of atoms within a roughly spherical volume which extends at the most over a diameter of approximately 5 nm for a 10 keV cascade. This lasts 1 to 3 ps. Then, as the heat is dissipated in the material, the zone affected by the thermal spike re-crystallises and reassumes, to a large extent, its original configuration, bar a few residual defects. It is interesting to note that above 10 keV, the recombination fraction (defined as the fraction of displaced atoms that settle at an ordinary lattice site once equilibrium is reached once again) reaches 90% for uranium atoms and circa 99% for oxygen atoms [62], in line with the high radiation resistance of this material. Defects are also mostly produced in stoichiometric composition as would be expected considering the fixed charged models that are employed and the fact that oxygen defects are rather mobile on the scale of the MD simulations; as a result of which, they are seen to recombine to form stable neutral clusters [62]. Finally, over a wide range of PKA energies, a majority of residual defects are found in defect clusters (circa 70% between 1 keV and 10 keV). This proportion appears to be little dependent upon temperature. Uranium defects are immobile at the temperatures studied on the scale of the simulations which would point to the fact that clustering may occur as a result of purely a-thermal radiation processes. At the end of the

re-crystallisation process, vacancies are found at the centre of what was the molten region whilst interstitials appear at the periphery of that area.

The last point in this section regards the effects of damage accumulation. Again, if the presumed cascade decomposition effects are correct, then the 7 000 keV deposited through nuclear collisions per fission event will lead to circa 700 10 keV cascades. In a volume corresponding to a cube with edges approximately 6 nm long, considering also a typical fission rate of 10^{19} fissions m^{-3} , 10 keV cascades will develop in approximately the same region of fuel every 10 minutes. Hence calculating cascade overlaps even though long time scale recombination is not taken into account is probably relevant. Van Brutzel et al. [126] and Martin et al. [61] report such calculation results. The authors analysed calculation results in terms of defect clustering and in [61] it is shown that cascade overlapping of thirty-six 10 keV events induces the growth of a large cluster containing roughly 200 vacancies and extending over a region approximately equivalent to the volume of a sphere 2 nm in diameter. The other point noted in [61] is the fact that the interstitial defects that appear at the periphery of the cascade eventually cluster to form small imperfect interstitial dislocation loops in {1 1 1} planes approximately 5 nm in diameter as reported above [111]. Such defect clustering observations have also been made in metals and the clustering processes studied. Kapinos and Bacon [49] suggest the vacancies cluster as the solid-liquid interface advances during the cooling stage of the cascade event, thus sweeping vacancies ahead of it. Whether the mechanism via which interstitials appear is akin to a dislocation punching is still a matter for debate, as is the role of the ballistic phase of the cascade upon the number of surviving defects [23]. However, the basic scenario whereby vacancies form small spherical like aggregates and interstitials dislocation loops is shown to be plausible and corroborates the experimental data.

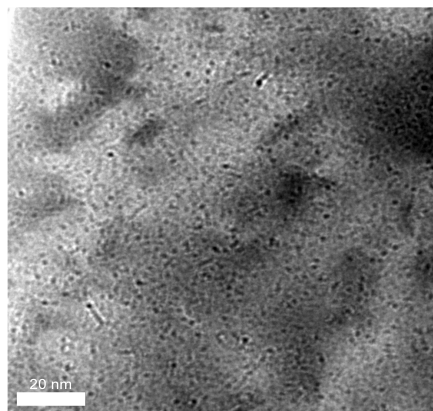
Bubble nucleation and growth studies

Bubble nucleation studies

It appears that insoluble fission product nucleation as reported extensively in previous sections results from this production of virtually stoichiometric vacancy and interstitial aggregates. In situ TEM experiments have recently been reported involving 390 keV Xe ion implantations in UO_2 thin foils irradiated at 873 K over fluences ranging between 3×10^{12} ions cm^{-2} and 7×10^{14} ions cm^{-2} [69] (experiment carried out at JANNUS-Orsay). The results show that small 1 nm size bubbles appear gradually at a fluence of 6×10^{12} ions cm^{-2} ; the bubble density stabilises at roughly 4×10^{23} bubbles m^{-3} beyond a fluence of 10^{14} ions cm^{-2} . There are striking similarities between these results and those of Cornell [21]. Cornell and subsequent workers reported bubble densities for samples irradiated at similar temperatures of between 10^{23} bubbles m^{-3} and 4×10^{23} bubbles m^{-3} in low burn-up samples. Fission product concentrations of approximately 10^{-3} at.% can be inferred from burn-up levels reported by Cornell, compared to a xenon concentration of between 10^4 at.% and 10^{-3} at.% in [69]. The higher value corresponds to the concentration levels at which the bubble density appears to level off. Bubble sizes are also similar although Cornell reported larger ~ 2 nm size bubbles. However, Cornell's data concerned slightly higher temperatures, probably higher cumulated damage levels and longer irradiation periods all conducive to bubble growth. Figure 12 shows a TEM micrograph of such a sample implanted with Xe atoms at 873 K. The figure shows small bubbles lying in straight lines

5 to 6 bubbles long. Because the nuclear energy losses are largely predominant under the ion irradiation conditions studied here, this observation seems to disprove the repeated claim [8,21,85,119] that bubbles form in fission fragment tracks in regions where electronic excitations predominate. Although no clear explanation can yet be provided for this observation, it does illustrate that controlled irradiation experiments can at least shed new light on old assumptions.

Figure 12. TEM micrograph of bubbles lying in straight lines following an irradiation with 390 keV Xe ions at 873 K, fluence 2.10^{14} ions cm^{-2} and under overfocused beam conditions [33]



At this stage, it becomes necessary to look at other ion-irradiation experiment results in order to identify the probably similar causes explaining the emergence of a steady-state nano-bubble size distribution in both neutron and ion irradiation experiments. To this end, we turn to the Xe, Cs and He implantations studies reported above [99,61]. In addition to the dislocation structure, it was found that following annealing at 673 K and 873 K for 20 minutes, nanometre size aggregates appeared in both the Xe or Cs implanted samples and at densities universally reported (10^{23} - 10^{24} bubbles m^{-3}), whereas no bubbles were observed even following annealing up to 1 023 K in helium implanted samples. As mentioned in [61], this points to chemical effects or indeed foreign atom concentrations having only a marginal impact on the initial size distribution of aggregates and conversely the level and nature of radiation damage playing a key role. Indeed a 7 keV He irradiation will generate U cascades at maximum energies of 200 eV, which based on a Threshold Displacement Energy (TDE) of 40 eV for U atoms will probably only lead to isolated Frenkel pairs; whereas a 390 keV Xe or a 300 keV Cs irradiation will produce damage cascades with maximum energies of roughly 180 keV that abide by the phenomenology described in the modelling section above. If one recalls the scenario which MD simulations provide (see Modelling Section above), it is quite natural to assume that the overlap of elementary cascades will lead to formation of nanometre size vacancy clusters that will act as sinks at which foreign, insoluble elements, will readily eliminate thus constituting a stable aggregate population. This is the exact definition of a heterogeneous nucleation mechanism i.e., a mechanism in which insoluble elements eliminate at defects in the crystal structure. In addition to constituting a credible explanation for ion-irradiation experiment results, it would also provide a reason why metallic fission product aggregates are so often found associated with rare gas bubbles. Metallic fission products just segregate at the same sinks as rare gas atoms because they

are insoluble. This mechanism differs substantially from that usually referred to in relation to nucleation in the wake of fission fragments which is often mentioned in the context of electronic excitation effects.

Another reported observation [132,110] that could be an indication of the necessary presence of insoluble atoms to stabilise vacancy aggregates is the fact that at low fission densities the dislocation loop distribution quickly reaches a steady state before loop growth resumes at higher fission densities. Indeed the initial dislocation loop distribution may be regarded as resulting from a radiation damage process. The vacancy aggregates which may be seen as the dislocation loop counterpart will act as sinks at which additional interstitials will annihilate until the foreign insoluble atom concentration is sufficient to stabilise the bubble nuclei. Once this concentration is reached and the nanometre size aggregates no longer act as sinks for migrating interstitials, the dislocation loops continue to absorb excess interstitials and loop growth resumes. This would suggest that if the nature of the damage is adequate (i.e., under displacement cascade conditions) then nucleation will indeed occur if foreign elements are present to stabilise the vacancy aggregates that are a basic consequence of the radiation damage process.

In conclusion, the dislocation loop and indeed the bubble size distributions and their evolution with dose are therefore probably dictated to a great extent by the radiation damage processes so long as the foreign element concentration exceeds a threshold value.

Why a steady-state bubble size distribution is established at temperatures below circa 1 273 K is still a matter for investigation. Also if vacancy clusters actually exist, they would be thermodynamically unstable because of surface tension effects. The question would remain as to whether they are kinetically stable, at what temperature and what concentrations of foreign insoluble elements are required to stabilise them.

Xenon content in bubbles

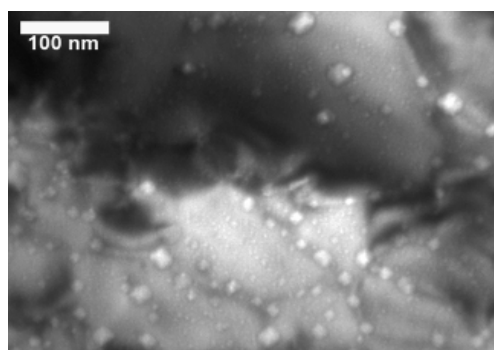
Assessing or validating models based on rate theory also requires ascertaining the quantity of rare gases that are liable to segregate to bubbles. X-Ray Absorption Spectroscopy (XAS) experiments at the xenon K-edge [32, 59] have been shown to enable this. A methodology has indeed been developed to characterise the pressure in ion-implanted specimens. This method is based on determining the local environment of xenon atoms and in particular the average Xe-Xe distance. The results of low-temperature (circa 5 K) characterisations of xenon implanted samples at fluences and energies such that the xenon concentration remained roughly equal to 2 at.% over 150 nm, showed that the Xe-Xe distance was of the order 3.97 Å as opposed to 4.34 Å had the xenon crystals been uncompressed at that temperature. Asaumi's equation of state for xenon [7] at low temperature enabled the xenon pressure within the aggregates to be estimated at 2.7 ± 0.3 GPa at 5 K in samples annealed for 30 minutes at 873 K. Further annealing for 12 hours showed the pressure dropped to approximately 2 GPa. An estimate may then be given of the fraction of gas contained in bubbles [99] based on TEM results of samples implanted and annealed under similar conditions. This estimate shows that less than 5% of the sample's gas content is contained in bubbles visible using TEM. A similar methodology has been applied to samples implanted at 10^{17} ions cm^{-2} with 400 keV krypton ions (corresponding to roughly 4 at.% average concentration) and annealed at 873 K for 12 hours. The pressure was estimated at 12 K at approximately 2.2 GPa confirming the very similar behaviour of Kr and characteristics of Kr bubbles. Thus, TEM and XAS at the rare gas K-edge are indeed

most complementary techniques, the development of which on neutron irradiated material would most enhance our knowledge of bubbles formed under those conditions.

Example of bubble growth studies

A last example of what may be obtained from ion irradiation experiments is given in the guise of a TEM thin foil implanted with 400 keV Xe ions to fluences 7×10^{15} ions cm⁻² such that the average concentration in the foil reached approximately 0.5 at.%. Figure 13 is a TEM micrograph of the foil following annealing at 1 773 K for 2 hours under a reducing atmosphere: dislocations have formed a network that separates the initial grain into smaller ones. Figure 13 also shows the presence of bubbles within the domains delineated by the dislocation structure. However, these bubbles (1-3 nm in size) remain small in comparison to those lying at the interfaces between two regions, most of which are faceted and have grown to sizes in the region of 20 nm. These observations are well in line with those carried out by Whapham and Sheldon [132] on neutron irradiated material further demonstrating the usefulness of ion irradiation experiments to develop model systems on which mechanisms can be studied without the difficulties associated with handling active material. It also suggests a scenario for gas to be released to grain boundaries during a power ramp or out-of-pile annealing experiments. The coarsened bubble network lying on the rearranged dislocation network would suggest higher transport properties at those dislocations and hence enhanced gas migration along the dislocation until it intersects a free surface or a grain boundary, in line with recent MD simulations [40] of Xe diffusion at dislocations in UO₂. The paradox outlined previously (large release fractions that are not predicted from standard rate theory approaches) could possibly be resolved considering that gas atoms have much less distance to travel to dislocations than to the grain boundary if no network was present.

Figure 13. TEM micrograph of bubbles lying along dislocations and a restructured dislocation network as a result of annealing at 1 773 K for 2 hours



The thin foil was irradiated at a dose of 7×10^{15} ions/cm² with 400 keV Xe ions. Note also the faceted nature of the bubbles [33].

Bubble stability

In this section, we look at certain aspects of the temperature and irradiation stability of rare gas bubbles guided by the paradox outlined above pertaining to in-pile and out-of-pile rare gas release from nuclear fuels. To this effect, a brief review is given of what first principles *ab initio* calculations based on Density Functional Theory (DFT) can contribute in relation to solubility of rare gases in UO₂. Then, we look at a few issues relating to the

radiation stability of rare gas bubbles investigated both using ion beams and MD simulations.

Rare gas solubility using first principles

One of difficulties related to modelling actinide compounds lies in the strong correlations between f-electrons. Unfortunately DFT in its standard formulation is not particularly well suited for this and a substantial effort has recently been devoted to improving our description of these strong correlations in a number of actinide compounds both using hybrid functionals [52] [91-93], [98,46] and the so-called DFT+U approximation [5,6] [24,25], [67,27]. In addition to providing an improved description of the electronic structure of actinide oxides, this latter approximation has further been demonstrated in UO₂ to yield defect formation and migration energies that tally well with diffusion experiments in UO₂ [27] carried out under controlled oxygen potential. Note that in general, the DFT+U approximation provides energies which are much closer to available experimental data than standard DFT [25-26]. Incorporation energies of Xe and Kr at various defect sites have been evaluated using DFT in the past and results initially suggested very low solubility.

Table 1. Kr and Xe incorporation energies in eV, using either standard DFT [22,29,16] or the DFT+U approximation [73,33,137]

	Octahedral site	U vacancy	Oxygen vacancy	Scotty trio (type 1)	Schottky trio (type 2)	Schottky trio (type 3)
Kr (Crocombette, 2002)	8.9	4	7.1	-	-	-
Kr (Garcia, 2012)	6.6	2.2	5.3	0.64	1.26	1.38
Xe (Freyss, 2006)*	11.2	13.9	9.4	-	-	-
Xe (Chartier, 2010)**	12.01	5.77	9.14	-	-	-
Xe (Nerikar, 2009)	11.11	2.5	9.5	1.38		
Xe (Yu, 2009)	8.07	5.18	9.01	2.90		
Xe (Garcia, 2012)	9.48	3.84	6.89	1.18	1.82	2.25

* 24 atom supercell, GGA approximation; ** 96 atom supercell, GGA approximation.

As shown in Table 1, Freyss et al. [29], Chartier et al. [16] had calculated the Xe incorporation energy in a uranium vacancy to be approximately 9.4 eV and 5.8 eV albeit using different calculation parameters (in particular exchange and correlation functionals, cut-off energies and supercell size). Crocombette [22] had estimated the Kr incorporation energy in a uranium vacancy to be 4 eV. Garcia et al. [33] calculated using the DFT+U approximation (calculation details identical to those described in [25]) using occupation matrix control [4,24,47,98], the incorporation energies of Kr and Xe at different defects including three types of Schottky defects. These three configurations depend upon the relative position of the two oxygen vacancies that constitute it. In this work, types 1, 2 and 3 correspond to oxygen vacancies in <1 0 0>, <1 1 0> and <1 1 1> directions, respectively.

This table illustrates that more recent methods tend to yield lower Kr and Xe incorporation energies. It is confirmed that Schottky defects, as pointed out in earlier work [39] tend to yield the lowest incorporation energies for fission gasses. At circa 1.2 eV

for xenon and even more so at a few tenths of eVs for Kr, these incorporation energies could point to thermal re-solution as playing a role in the high temperature removal of fission gasses from within the grain to the grain boundaries even in the absence of radiation; assuming of course that Schottky defects of the right type are created in sufficiently large quantities.

Radiation effects

We now turn to the radiation stability of fission gas bubbles which constitutes the corner stone of all fission gas behaviour modelling efforts to date. Recent publications reported on experiments [33] involving thinning UO₂ samples down to thicknesses conducive to TEM characterisation. Samples were then implanted on the IRMA accelerator at CSNSM/Orsay with 400 keV xenon ions at fluences of 10¹⁶ ions/cm² corresponding to an average Xe concentration of approximately 2 at.%. They were further annealed at 873 K under vacuum for 30 minutes which consolidates the bubble population at densities and sizes of roughly 4x10²³ m⁻³ and 2 nm, respectively. Thin foils were then irradiated with 8 MeV iodine ions at doses of up to 10¹⁶ ions/cm². Although at 3 keV/nm the electronic stopping power of an 8 MeV iodine ion traversing the thin foil is approximately 7 to 9 times less than the threshold value for track formation in UO₂ [135], it is reasonable to assume that at the highest irradiation dose, the material has been impacted at least once by impinging iodine ions. Despite this, no discernable modification of the characteristics of the initial bubble population was detected. Simple experiments could be carried out this way to prove or disprove the single impact bubble dissolution concept.

Empirical potentials MD techniques have recently been employed to investigate the impact of radiation on bubble stability under ballistic and electronic energy loss regimes [44,89,103]. Schwen et al. [103] combined MC simulations within the BCA with empirical potential MD simulations to determine a realistic estimate of Nelson's re-solution parameter. MC simulations were carried out to determine a detailed recoil spectrum of Xe atoms contained in small fission gas bubbles. MD simulations were used for calculating the effect of recoil energies greater than 200 eV and less than 12 keV, i.e., at energies for which a full MD cascade treatment is probably more realistic than the BCA. Weighting the Xe atom displacement histograms obtained from MD by the MC determined Xe recoil energy spectrum, an estimate of the re-solution probability in Nelson's model for small 1 nm radius bubbles is given. It lies a factor of 50 below Nelson's original estimate.

The same authors further investigated inelastic effects again using MD simulations [44]. They first used measured UO₂ sputtering yields for different incident ion stopping powers [102] to determine the electron-phonon coupling constant with the so-called Two Temperature Model (TTM) [116]. In this model, the coupling constant is characterised by a free parameter λ , which determines the efficiency with which energy is transferred from the hot electron sub-system to lattice atoms. Thermal spikes were simulated with MD for different (λ dependent) temperature profiles determined from application of the TTM. An optimal value of λ was thus determined. Next for this optimal value of λ , MD simulations of thermal spikes corresponding to different electronic stopping powers were modelled in the presence of small xenon bubbles as a result of which re-solution was noticeable only for stopping powers in excess of

35 keV/nm. Total bubble dispersion was not observed at any of the stopping powers studied.

Both these MD studies [44,103] would suggest that re-solution has only a marginal impact on bubble stability.

Conclusion and future challenges

A few of the more striking microstructural features of neutron irradiated UO₂ fuels are reviewed. Certain common observations may to some extent be rationalised based on results from more analytical ion irradiation experiments or atomic scale modelling techniques. In particular, it would appear that the initial size distribution of nanometre size fission product aggregates widely reported results from basic radiation damage effects. If damage is induced through displacement cascades then small vacancy aggregates are liable to form and constitute sinks for insoluble fission products. MD simulations offer a greater insight into the possible mechanisms involved. In simulations involving displacement cascades, vacancies are shown to form small voids and interstitial atoms small dislocation loops. Upon further damage, it is thought that these clusters will absorb migrating defects and gas atoms and grow.

It appears also that a number of commonly accepted precepts may be challenged by either analytical experiments or atomic scale simulations. This is the case for fission gas re-solution which is a corner stone for most fission gas behaviour models. In addition, under out-of-pile annealing conditions, these models are not capable of reproducing the observed levels of fission gas release. A number of mechanisms are suggested based on more recent *ab initio* results or ion-irradiated thin foil annealing experiments to explain these observations but clearly much more work is required if a general theory is to emerge capable of rationalising the plethora of experimental data available. There is overwhelming evidence to suggest that such a theory requires being capable of dealing both with radiation damage effects coupled to foreign insoluble element behaviour. Such models based on rate theory do exist for metallic systems [10,36] and should be applied to actinide oxides for interpreting ion-irradiation experiments quantitatively and neutron irradiations at least qualitatively. Quite naturally atomic scale modelling techniques have a central role to play in this effort since they constitute invaluable tools for determining quantities that are practically inaccessible through experimentation. However, even if the difficulties inherent to developing a coherent modelling approach at several different scales are overcome, there is, of course, no guarantee that the material's microstructural evolution will result from the behaviour of a single species: the interplay that exists between the oxygen and cation sublattices must be understood and the consequences of this interplay quantified. In addition, there exists very little knowledge of the extent to which the material is susceptible to certain radiation effects specific to insulators.

Finally, more work remains to acquire and understand actinide oxide basic properties since these are necessary for implementing rate theory based models. These properties both under irradiation and thermodynamic equilibrium conditions must be acquired so that progress may be made in the predictive capability of models describing microstructure evolutions over engineering time and length scales.

References

- [1] Adamson, M.G. (1971), *Journal of Nuclear Materials*, 38. pp. 213-216.
- [2] Adamson, M.G., R.F.A. Carney (1974), *Journal of Nuclear Materials*, 54. pp. 121-137.
- [3] Aitken, E.A. (1969), *Journal of Nuclear Materials*, 30. pp. 62-73.
- [4] Amadon, B, F. Jollet, M. Torrent (2008), *Physical Review B*, 77. 155104.
- [5] Andersson, D.A., J. Lezama, B.P. Uberuaga, C. Deo, S.D. Conradson (2009a), *Physical Review B*, 79. 024110.
- [6] Andersson, D.A., T. Watanabe, C. Deo, B. P. Uberuaga (2009b), *Physical Review B*, 80. 060101.
- [7] Asaumi, K. (1984), *Physical Review B*, 29.7026.
- [8] Baker, C. (1975), *Journal of Nuclear Materials*, 75 (1978) 105.
- [9] Baker, C., J.C. Killeen (1987), “Materials for nuclear reactor core applications”, *British Nuclear Energy Society*, p.153, London, UK.
- [10] Barbu, A., E. Clouet (2007), *Solid State Phenom.* 129.51.
- [11] Beisswenger, H., M. Bober, G. Schumacher (1967), *Journal of Nuclear Materials*, 21, pp. 38-52.
- [12] Bober, M., C. Sari, G. Schumacher (1971), *Journal of Nuclear Materials*, 39, pp. 265-284.
- [13] Bober, M., C. Sari, G. Schumacher (1971a), *Journal of Nuclear Materials*, 40, pp. 341-345.
- [14] Bober, M., G. Schumacher (1973), *Material Transport in the Temperature Gradient of Fast Reactor Fuels*, Academic Press, New York, 1973; Vol. 7, Chapter 2, p.121.
- [15] Bullock, R.E., J.L. Kaae (1983), *Journal of Nuclear Materials*, 115. pp. 69-83.
- [16] Chartier, A., L. Van Brutzel, M. Freyss (2010), *Physical Review B*, 81.174111.
- [17] Christensen, J.A., (1970), Technical Report, WHAN-SA-79; WADCO Corporation.
- [18] Christensen, J.A., (1972), *Transactions of the American Nuclear Society*, 15.214.
- [19] Clement, C.F., M.W. Finn (1978), *Journal of Nuclear Materials*, 75. pp. 193-200.
- [20] Cornell, R.M., M.V. Speight, B.C. Masters (1969), *Journal of Nuclear Materials*, 30.170.
- [21] Cornell, R.M. (1971), *Journal of Nuclear Materials*, 38.319.
- [22] Crocombette, J.P. (2002), *Journal of Nuclear Materials*, 305.29.
- [23] Crocombette, J.P. (2009), *Nuclear Instruments and Methods in Physics Research B*, 267.3152.
- [24] Dorado, B., B. Amadon, M. Freyss, M. Bertolus (2009), *Physical Review B*, 79.35125.
- [25] Dorado, B., G. Jomard, M. Freyss, M. Bertolus (2010a), *Physical Review B*, 82.035114.
- [26] Dorado, B., J. Durinck, P. Garcia, M. Freyss, M. Bertolus (2010b), *Journal of Nuclear Materials*, 400.103.

- [27] Dorado, B. et al. (2011), *Physical Review B*, 83.035126.
- [28] Finlay, M.R., G.L. Hofman, J.L. Snelgrove (2004), *Journal of Nuclear Materials*, 325 (2-3), pp. 118-128.
- [29] Freyss, M., N. Vergnet, T. Petit (2006), *Journal of Nuclear Materials*, 352.144.
- [30] Friskney, C.A., M.V. Speight (1976), *Journal of Nuclear Materials*, 62.89.
- [31] Garces, J.E., G. Bozzolo (2011), “Atomistic simulation of high-density uranium fuels”, *Science and Technology of Nuclear Installations*, Vol. 2011.
- [32] Garcia, P. et al. (2006), *Journal of Nuclear Materials*, 352.136.
- [33] Garcia, P. et al. (2012), *Nuclear Instruments and Methods B*, 277. pp. 98-108.
- [34] Garrido, F. et al. (1997), *Nuclear Instruments and Methods in Physics Research B*, 127-128.634.
- [35] Guarro, F., S. Guarro, D. R. Olander (1975), *Journal of Nuclear Materials*, 57. pp. 136-144.
- [36] Gohniem, N.M. (1989), *Physical Review B*, 39.11810.
- [37] Govers, K. et al. (2007), *Journal of Nuclear Materials*, 366 (1-2).161.
- [38] Griesmeyer, J.M., N.M. Gohniem, D. Okrent (1979), *Nuclear Engineering and Design* 55.69.
- [39] Grimes, R., C. Catlow (1991), *Philosophical Transactions of Royal Society A*, 335.609.
- [40] Grimes, R., D. Parfitt (2010), NUMAT conference, Karlsruhe 2010.
- [41] Gulden, T.D.J. (1972), *Journal of the American Ceramic Society*, 55. pp. 14-18.
- [42] Higgs, J.D. et al. (2007), *Journal of Nuclear Materials*, 366.99-128.
- [43] Hofman, G.L. et al. (2003), “Recent observations at the post-irradiation examination of low-enriched U-Mo miniplates irradiated to high burnup”, *International RERTR Meeting*, Chicago, Illinois, US.
- [44] Huang, M. et al. (2010), *Journal of Nuclear Materials*, 399.175.
- [45] Janek, J., H. Timm (1998), *Journal of Nuclear Materials*, 255. pp. 116-127.
- [46] Jollet, F. et al. (2009), *Physical Review B*, 80.235109.
- [47] Jomard, G. et al. (2008), *Physical Review B*, 78.075125.
- [48] Jonnet, J. et al. (2008), *Nuclear Instruments and Methods in Physics Research B*, 266.3008.
- [49] Kapinos, V.G., D.J. Bacon (1993), *Philosophical Magazine A*, 68.1165.
- [50] Kashibe, S., K. Une, K. Nogita (1993), *Journal of Nuclear Materials*, 206.22.
- [51] Kinoshita, M. et al. (2006), “Study of irradiation induced restructuring of high burnup fuel”, *The New Cross-over Project (NXO) to Study RIM-structure Formation*, TOPFUEL 2006 Salamanca, p. 248.
- [52] Kudin, K.N. et al. (2002), *Physical Review Letters*, 89, 266402.

- [53] Lackey, W.J. et al. (1972), *Journal of Nuclear Science and Technology*, 16. pp. 120-142.
- [54] Leenaers, A. et al. (2004), *Journal of Nuclear Materials*, 327. pp. 2-3.
- [55] Limoge, Y., A. Barbu (2005), Defect and Diffusion Forum 237. pp. 621.
- [56] Löösönen, P. (2002), *Journal of Nuclear Materials*, 304. pp. 29.
- [57] Manzel, R., C.T. Walker (2002), *Journal of Nuclear Materials*, 301.170.
- [58] Mardon, P.G., P.E. Potter (1970), *Nuclear Instruments and Methods*, 17.842.
- [59] Martin, P. et al. (2008), *Nuclear Instruments and Methods B*, 266.2887.
- [60] Martin, G. et al. (2009), *Journal of Nuclear Materials*, 385.351-357.
- [61] Martin, G. et al. (2010), *Physical Letters A*, 374.3038.
- [62] Martin, G. et al. (2011), *Nuclear Instruments and Methods B*, 269.1727-1730.
- [63] Matzke, Hj. (1975), *Journal of Nuclear Materials*, 57. pp. 180-186.
- [64] Matzke, Hj. (1983), “Radiation enhanced diffusion in UO₂ and (U, Pu)O₂”, *Radiation Effects*, Vol. 75, Issue 1-4.
- [65] Matzke, Hj., L.M. Wang (1996), *Journal of Nuclear Materials*, 231.155.
- [66] Matzke, Hj., M. Kinoshita (1997), *Journal of Nuclear Materials*, 247.108.
- [67] Meredig, B. et al. (2010), *Physical Review B*, 82.195128.
- [68] Meyer, R.O. (1974), *Journal of Nuclear Materials*, 52.326-328.
- [69] Michel, A. et al. (2012), “An in situ TEM study of the evolution of Xe bubble populations in UO₂”, *Nuclear Instruments and Methods B*, 272.218-22.
- [70] Millot, F., P. Gerdanian (1980), *Journal of Nuclear Materials*, 92. pp. 257-261.
- [71] Morelon, N.D. et al. (2003), *Philosophical Magazine*, 83.1533.
- [72] Nelson, R.S. (1969), *Journal of Nuclear Materials*, 31.153.
- [73] Nerikar, P.V. et al. (2009), *Journal of Physics: Condensed Matter*, 21.435602.
- [74] Nogita, K., K. Une (1995), *Journal of Nuclear Materials*, 226.302.
- [75] Nogita, K., K. Une (1998), *Nuclear Instruments and Methods in Physics Research B*, 141.481.
- [76] Nogita, K., K. Une (1997), *Journal of Nuclear Materials*, 250.244.
- [77] Nogita, K. et al. (1999), *Journal of Nuclear Materials*, 273.302.
- [78] Noirot, J. et al. (2004), Proceedings ANS International Meeting on LWR Fuel Performance, Orlando, US.
- [79] Noirot, J. et al. (2009), *Nuclear Engineering and Technology*, 41.155.
- [80] Noirot, J. et al. (2008), *Journal of Nuclear Materials*, 372.318.
- [81] Noirot, L. (2011), *Nuclear Engineering Design*, 241.2099-2118.

- [82] Oh, J.Y. et al. (2011), “Simulation of thermal conductivity degradation in U-Mo dispersion fuel”, *Materials Modeling and Simulation for Nuclear Fuels*, Aix-En-Provence, France.
- [83] Olander, D.R. (1971), *Journal of Nuclear Materials*, 44.116.
- [84] Olander, D.R. (1973), *Journal of Nuclear Materials*, 49.34-44.
- [85] Olander, D.R. (1976), “Nuclear reactor fuel elements”, *National Technical Information Services*, Document No. 26711.
- [86] Olander, D.R., D. Wongsawaeng (2006), *Journal of Nuclear Materials*, 354.94.
- [87] Oldfield, W., A. Markworth (1969), *Materials Science and Engineering*, 4.353-366.
- [88] Parfitt, D.C., C.L. Bishop, M.R. Wenman, R.W. Grimes (2010), *Journal of Physics: Condensed Matter*, 22.175004.
- [89] Parfitt, D.C., R.W. Grimes (2008), *Journal of Nuclear Materials*, 381.216.
- [90] Pati, S.R., A.M. Garde, L.J. Clink (1988), Proceedings ANS International Topical Meeting on LWR Fuel Performance, Williamsburg, Virginia, US.
- [91] Prodan, I.D. et al. (2005), *Journal of Chemical Physics*, 123.014703.
- [92] Prodan, I.D. et al. (2006), *Physical Review B*, 73.045104.
- [93] Prodan, I.D. et al. (2007), *Physical Review B*, 76.033101.
- [94] Rand, M.H., T.L. Markin (1967), *Thermodynamics of Nuclear Materials*; International Atomic Energy Agency, pp. 637-650, Vienna, Austria.
- [95] Ray, I.L.F. et al. (1997), *Journal of Nuclear Materials*, 245.115.
- [96] Rest, J. (1995), *The DART Dispersion Analysis Research Tool: A Mechanistic Model for Predicting Fission-Product-Induced Swelling of Aluminum Dispersion Fuels*, ANL-95/36, Argonne National Laboratory, US.
- [97] Rest, J., G.L. Hofman (2000), *Journal of Nuclear Materials*, 277.231.
- [98] Roy, L.E. et al. (2008), *Journal of Chemical Physics* 29.2288.
- [99] Sabathier, C. et al. (2008), *Nuclear Instruments and Methods B*, 266.3027.
- [100] Sari, C., G.J. Schumacher (1976), *Journal of Nuclear Materials*, 61.192-202.
- [101] Sattonnay, G. et al. (2006), *Journal of Nuclear Materials*, 355.131.
- [102] Schlutig, S. (2001), PhD Thesis, University of Caen, France.
- [103] Schwen, D. et al. (2009), *Journal of Nuclear Materials*, 392.35.
- [104] Sens, P.F. (1972), *Journal of Nuclear Materials*, 43.293-307.
- [105] Shaheen, K., B.J. Lewis (2009), “Platform-based modelling of intact and defective fuel behaviour”, *Proceedings of IAEA Symposium*, SFEN; pp. 654-667, Vienna, Austria.
- [106] Siméone, D. et al. (2010), *Physical Review E*, 82.011122.
- [107] Sizemann, R. (1978), *Journal of Nuclear Materials*, 69.386.

- [108] Sonoda, T. et al. (2010), *Nuclear Instruments and Methods in Physics Research B*, 268.3277-3281.
- [109] Soret, M.Ch. (1881), *Annals of Chemistry and Physics*, 22.293.
- [110] Soullard, J. (1977), PhD Thesis, CEA-R-4882.
- [111] Soullard, J. (1978), *Journal of Nuclear Materials*, 78.125.
- [112] Soullard, J. (1985), *Journal of Nuclear Materials*, 134.190.
- [113] Spino, J. et al. (1998), *Journal of Nuclear Materials*, 256.189.
- [114] Tanaka, K., S. Miwa, I. Sato (2009), *Journal of Nuclear Materials*, 385.407-412.
- [115] Thomas, L.E., C.E. Beyer, L.A. Charlot (1992), *Journal of Nuclear Materials*, 188.80.
- [116] Toulemonde, M. et al. (1993), *Radiation Effects and Defects in Solids*, 126.201.
- [117] Turnbull, J.A. et al. (1982), *Journal of Nuclear Materials*, 107.168.
- [118] Turnbull, J.A., R.M. Cornell (1970), *Journal of Nuclear Materials*, 36.161.
- [119] Turnbull, J.A. (1971a), *Journal of Nuclear Materials*, 38.203.
- [120] Turnbull, J.A., R.M. Cornell (1971b), *Journal of Nuclear Materials*, 41.156.
- [121] Une, K., S. Kashibe (1990), *Journal of Nuclear Science and Technology*, 27.1002-1016.
- [122] UNRC (1988), *Safety Evaluation Report related to the Evaluation of Low-Enriched Uranium Silicide-Aluminum Dispersion Fuel for Use in Non-Power Reactors*, NUREG-1313, US Nuclear Regulatory Commission.
- [123] Valin, S. (1999), PhD Thesis, DTP/SECC CEA Grenoble.
- [124] Van Brutzel, L. et al. (2003), *Philosophical Magazine*, 83.4083.
- [125] Van Brutzel, L. et al. (2006), *Journal of Nuclear Materials*, 354.28.
- [126] Van Brutzel, L., J.P. Crocombette (2007), *Materials Research Society Symposium Proceedings*, 981.
- [127] Veshchunov, M.S. (2011), *Journal of Nuclear Materials*, 415.96-103.
- [128] Wagner-Löffler, M. (1977), *Journal of Nuclear Science and Technology*, 35.392-402.
- [129] Wallace, T.C. et al. (1968), *Carbon Diffusion in the Carbides of Uranium*, Technical Report LA-DC-8840; Los Alamos National Laboratory: Los Alamos, US.
- [130] Walker, C.T. (1999), *Journal of Nuclear Materials*, 275.56.
- [131] Welland, M.J. (2012), “Matter transport in fast reactor fuels”, *Comprehensive Nuclear Materials*.
- [132] Whapham, A.D., B.E. Sheldon (1965), *Philosophical Magazine*, 12.1179.
- [133] White, R.J., M.O. Tucker (1983), *Journal of Nuclear Materials*, 118.1.
- [134] Wiedersich, H. (1972), *Radiation Effects*, 12.111.
- [135] Wiss, T. et al. (1997), *Nuclear Instruments and Methods B*, 122.583.
- [136] Wood, M.H. (1979), *Journal of Nuclear Materials*, 82.257.

- [137] Yu, J. et al. (2009), *Journal of Physics: Condensed Matter*, 21.435401.
- [138] Zacharie, I. (1997), PhD Thesis DMT/SEMI CEA Saclay, France.
- [139] Zhang, L. et al. (2012), *Computational Material Science*, 56.161-165.
- [140] Höh, A., Hj.Matzke (1973), *Journal of Nuclear Materials*, 48.157.
- [141] Milet, C., C. Piconi (1983), “Fluage en pile de l’oxyde mixte $\text{UO}_2\text{-PuO}_2$ ”, *Journal of Nuclear Materials*, 116.195,
- [142] Dherbey, F., F. Louchet, A. Mocellin, S. Leclercq (2002), *Acta Materialia*, 50.1495.
- [143] Clough, D.J. (1977), “Creep properties of oxide and carbide fuels under irradiation”, *Journal of Nuclear Materials*, 65. 24.
- [144] Freshley, M.D., D.W. Brite, J. L. Daniel, P.E. Hart (1976), *Journal of Nuclear Materials*, 62. 138.
- [145] Garcia, P., A. Bouloré, Y. Guérin, M. Trotabas, P. Goeuriot (2000), Proceedings of the International LWR Fuel Performance Meeting, Park City, US.
- [146] Dollins C.C. (1979), *Journal of Nuclear Materials*, 82.302.
- [147] Stehle, H., H. Assmann (1976), *Journal of Nuclear Materials*, 61.326.
- [148] Paraschiv, M.C., A. Paraschiv, V.V. Grecu (2002), *Journal of Nuclear Materials*, 302.109.
- [149] Small, G. (1985), *Proceedings of the Nuclear Fuel Performance Conference*, Stratford-on-Avon, UK.
- [150] Dollins, C.C. (1977), “In-pile Densification of oxide fuels (AWBA Development program)”, WAPD-TM-1293 DOE Research and Development Report.
- [151] Thomas, L.E. (1991), “Condensed phase of xenon and krypton in UO_2 spent fuel”, *Fundamental aspects of inert gases in solids*, Edited by S.E Donnelly and J. H. Evans, Plenum Press New-York.
- [152] Baker, E. (1978), *Journal of Nuclear Materials*, 75.105.

Chapter 2.

Nuclear fuel deformation phenomena

L. Van Brutzel¹, R. Dingreville², T.J. Bartel²

¹CEA, DEN, DPC, Centre de Saclay, France,

²Sandia National Laboratories, US

Abstract

Nuclear fuel encounters severe thermomechanical environments. Its mechanical response is profoundly influenced by an underlying heterogeneous microstructure but also inherently dependent on the temperature and stress level histories. The ability to adequately simulate the response of such microstructures, to elucidate the associated macroscopic response in such extreme environments is crucial for predicting both performance and transient fuel mechanical responses.

This chapter discusses key physical phenomena and the status of current modelling techniques to evaluate and predict fuel deformations: creep, swelling, cracking and pellet-clad interaction. This chapter only deals with nuclear fuel; deformations of cladding materials are discussed elsewhere. An obvious need for a multi-physics and multi-scale approach to develop a fundamental understanding of properties of complex nuclear fuel materials is presented. The development of such advanced multi-scale mechanistic frameworks should include either an explicit (domain decomposition, homogenisation, etc.) or implicit (scaling laws, hand-shaking,...) linkage between the different time and length scales involved, in order to accurately predict the fuel thermomechanical response for a wide range of operating conditions and fuel types (including Gen-IV and TRU).

Introduction

Fuel materials used in nuclear reactors are exposed to complex thermomechanical processes during their operation and storage resulting in deformation mechanisms such as swelling, creep, pellet-clad interaction (PCI) and cracking. Fuel deformation is clearly one of the important areas, which requires further understanding and model development for new fuel design and qualification programmes. The traditional experimentally-based paradigm requires several decades of development and is simply not a viable option for evaluating the multiple future fuel candidate designs.

Many of the aforementioned fuel mechanical responses are profoundly influenced by an underlying heterogeneous microstructure but also inherently dependent on the operating temperature and mechanical loading. During in-pile operation, the fuel chemical composition and its microstructure are strongly dependent on high-temperature gradients, neutron irradiation, transmutations and formation of fission products. In turn, these environmental factors affect the fuel chemistry (e.g., electronic excitations modifying the chemical bonds or fission and transmutation reactions altering the chemical composition), the fuel thermomechanical properties (e.g., irradiation creep or fuel cracking) and the fuel microstructure (e.g., nuclear interactions with neutrons and fission products inducing atomic displacements and disturbance of the crystallographic structure; irradiation effects changing and damaging the microstructure). Given these complicated processes, nuclear fuel is constantly transforming during its life (reactor operation and storage), but most of our present understanding and modelling of fuel deformation mechanisms remains empirical, and cannot be easily extrapolated to new fuel compositions, environments, or operating conditions. This is partly due to the fact that basic underlying mechanisms governing swelling, creep, PCI and cracking for this complex material remain for the most part poorly understood.

Figure 1 shows the results of a PIRT (Phenomena Identification and Ranking Table) process for identifying key phenomena associated with fuel deformation [12,81]. Both normal and abnormal situations are included in this figure. These phenomena are ranked based on both their importance and the current state of knowledge. What Figure 1 intelligibly shows is that items located in the upper right corner are the ones with the most impact per resource allocation on fuel deformation. It clearly appears that the most influential features are in fact associated with fission products, irradiation effects and fuel microstructure evolution.

As it will be discussed in the following of this chapter, numerous investigations have been conducted over the past 20 years and various mechanistic codes and models (mostly continuum) have been developed in an attempt to address and study fuel mechanical behaviour under various conditions (steady or transient). Table 1 summarises a brief list of representative mechanistic codes and their application. These codes generally consist of three main components [3]:

- a thermal analysis part dealing with the temperature distribution and the inventory of fission products within the fuel;

- a mechanical analysis part treating the mechanical interaction between pellet and cladding, and the stress and strain state in the fuel pellet and cladding;
- a material properties section referencing materials property libraries.

Figure 1. PIRT

System	Operational or design issue	Phenomena to be controlled	Mechanism to be understood
LWR	Under normal operating conditions : limitation of pressure inside the rod	Fission gas release Swelling (gaps collapse)	Fission gas transport and precipitation
	Under accidental conditions : limitation of the fission gas release	High burn up structure formation that can lead to large fission products release and actinide dissemination	Effect of irradiation on microstructure/transport of constitutive elements and solid FP's
HTR	Under normal conditions : limitation of mechanical loading of the coatings and FP's escape	Fission gas and CO pressure in the particles Chemical interactions between FP's and coatings elements	Fission product speciation in UO ₂ kernel and coatings
GFR	Know the operating limit temperature of U and Pu carbide fuels	Carbide dissociation/Pu vaporisation	Thermo chemical stability through phase diagram calculations
	Prediction of fuel element geometrical changes	Swelling of carbides	Irradiation damage/fission gas transport and swelling porosity/creep
SFR	Know the operating limit temperature of oxide fuels containing minor actinides	Thermo chemical stability of oxides with minor actinides	Impact of minor actinides on phase diagram/ actinide and O redistribution
	Control chemical interaction between fuel cladding and thermal bond	FP's compounds formation near the cladding	Thermo chemical stability of FP's compounds. FP's migration in the pellet
All fuel types	Under accidental conditions, limit the source term	FP's release and fuel behaviour	Thermo chemical stability of FP's compounds/FP's migration in fuel and coatings/swelling/creep

All these codes present diverse models with various degrees of refinement for the evolution of a variety of microstructural descriptors ranging from intragranular fission products transport to grain growth. The general strategy adopted for these codes is to lump various characteristics of the microstructure into effective properties or empirical laws and solve a set of coupled differential equations describing the coupled physics of the system. Although these codes are reasonably successful in predicting the fuel mechanical response where the empirical correlations are valid, as it was pointed out in the above, this response is impacted by sub-continuum phenomena. Improvements in this modelling approach are possible and require lower length scale modelling tools. These models span all time and length scales starting from the nuclear and electronic structure, to the atomistic and grain level and finally to the continuum level. Figure 2 illustrates this multi-scale paradigm. Such an approach brings further fundamental insight into the understanding of the physical, chemical and mechanical behaviour of nuclear fuel under various conditions (high temperatures and irradiation).

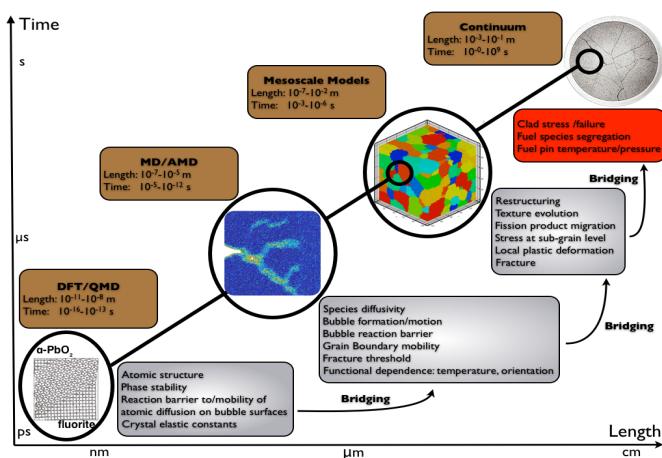
This chapter seeks to demonstrate the capabilities and challenges associated with modelling nuclear fuel deformation, both in terms of the current state-of-the-art and ongoing efforts to improve predictive modelling capabilities. In particular, in the reminder of this chapter, we will review various aspects of fuel mechanical deformation (creep, swelling, cracking, and PCI) in terms of the different mechanisms and physical

phenomena involved and their relevance. The status of current modelling strategies and on-going efforts for each of these deformation modes will be discussed. We will conclude this chapter by presenting future perspectives and research needs for the characterisation and modelling of thermomechanical response of nuclear fuel. Note that this chapter deals with the deformation of fuel materials only. Deformations of cladding materials are discussed elsewhere.

Table 1. Representative mechanistic codes for fuel mechanical behaviour and their application

Code	Application	Reference
BISON	Performance for light water reactor	Newman (2009) [48], Williamson (2011) [80]
AMP	Performance for oxide fuel in a light water reactor or metal fuel in a sodium-cooled fast reactor	Philip (2010) [56], Turner (2009) [72]
MFPR	Performance for light water reactor	Veshchunov (2006, 2009) [76,77]
FRAPCON	Performance for light water reactor	Berna (1997) [7]
FRAPTRAN	Transient behaviour for light water reactor	Cunningham (2001) [18]
FEMAXI-6	Performance and transient behaviour for light water reactor	Suzuki (2004) [69]
TRANSURANUS	Performance and transient behaviour for light water reactor	Lassmann (1992) [34], Van Uffelen (2008) [74]
ELESTRES	Performance code for CANDU fuel	Tayal (1996a,b) [70,71]
LIFE	Performance for fast breeder reactor	Jankus (1972) [30]
PLEIADES/ALCYONE	PWR: Nominal; transient and accidental behaviour	Sercombe (2009) [65], Sercombe(2010) [66], Marelle (2011) [39], Struzik (2012) [68]
PLEIADES/GERMINAL V2	SFR : Nominal; transient and accidental behaviour	Lainet (2011) [33], Bouineau(2011) [11]
PLEIADES/MAIA	MTR : Nominal and transient behaviour	Marelle (2007) [38]
PLEIADES/ATLAS	HTR&VHTR: Nominal and transient behaviour	Michel (2006) [41]

Figure 2. Paradigm of multi-scale modelling for nuclear fuel mechanical behaviour



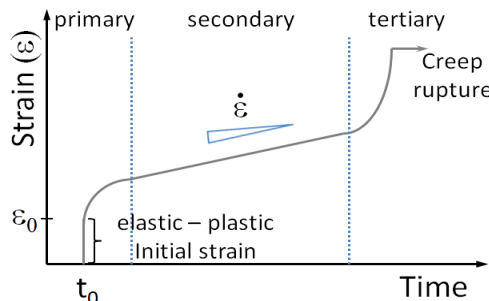
DFT: Density Functional Theory (*ab initio*), QMD: Quantum Molecular Dynamics (electronic structure), MD: Molecular Dynamic (atomistic), AMD: Accelerated MD (atomistic), Mesoscale models: grain-level techniques such as Monte Carlo, Phase Field, Mean Field, Continuum: Finite Element-like techniques.

Creep

In material science, creep defines a slow irreversible deformation process under the influence of stresses below the yield stress and has various origins, mechanical, thermal or irradiation. It must not be confused with plastic deformation, which relates to an instantaneous process. In a reactor, thermal creep and irradiation creep produce dimensional changes of the fuel element which can lead to severe deformation and reactor accidents. For long storage times even if the fuel temperature drops additional pressure may appear due to the increase of fissions gas products. For instance, for UO_2 fuel the additional pressure could be 1 MPa and 2 MPa after 100 and 300 years, respectively. For MOX fuel, which contains more α emitters, the helium pressure could be significantly higher: 7 and 12 MPa after 100 and 300 years [59]. Moreover, the temperature range is rather large and the duration that one needs to consider is much longer. Therefore, for reactor material design and safety assessment, creep is an important phenomenon that needs to be addressed and modelled.

With time, creep evolution is usually divided in three different stages (see Figure 3): (i) the primary creep presents high amplitude plastic deformation with strain rate that continuously decreases, (ii) the secondary creep or stationary creep is the stage where the strain rate is constant, and (iii) the tertiary creep relates a rapid increase of the strain rate during which the material is strongly degraded and leads to its failure.

Figure 3. Schematic representation of strain as a function of time due to constant applied stress

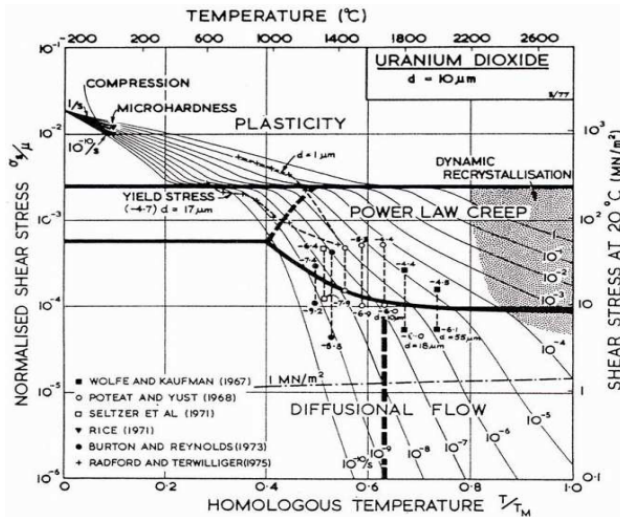


The primary creep corresponds to a small fraction of the total creep but it contributes more to the total strain at lower temperature and can play an important role on the fuel behaviour in pile during transient event. However, it was very little studied because of the experimental set-up difficulties and the absence of theoretical model. The secondary creep is the most important regime both in terms of time and accumulated strain and often the only one considered in an engineering assessment. Tertiary creep constitutes generally a very short time and therefore can often be neglected.

To summarise the creep behaviour in UO_2 , Ashby et al. [2] have gathered all the data available at the time in a data map (see Figure 4). This map gives a good overview of the deformation mechanisms, which take place in UO_2 during creep. It defines the temperature range at which the different mechanisms are predominant. This map shows that creep is greatly dependent on temperature. Below temperatures $0.4 T_m$ ($1\,000^\circ\text{C}$ for UO_2), the material is highly resistant; none or almost no permanent deformation has been measured below the

yield stress. This behaviour is common for most of the oxide materials. Above $0.4 T_m$, the oxide creeps with two different regimes according to the level of applied stress, which are separated with a threshold stress noted in the following σ_t . At the higher stresses, creep rate follows a power law, which is generally related to a dislocation diffusion mechanism. At lower stresses, creep rate is controlled by cation diffusion and follows a linear diffusion flow law.

Figure 4. Stress/temperature map for UO_2 with grain size of $10 \mu\text{m}$ [2]



To be used for engineering purpose, creep models need to be treated at the continuum level (macroscopic scale). From the standpoint of the continuum representation, solution of the creep problem requires statement of the mechanical equilibrium equations, appropriate constitutive equations for creep behaviour and suitable initial and boundary conditions. A commonly used equation of state representation for primary and secondary creep is provided by the Bailey-Norton law:

$$\dot{\epsilon} = A(T)\sigma^n \exp(-E_a/k_B T)$$

where $\dot{\epsilon}$ is the creep rate, A a material parameter that depends on the temperature T , σ the applied stress, E_a the creep activation energy, and k_B the Boltzmann constant. At applied stresses lower than σ_t , the exponent n , is close to 1, this corresponds to the diffusion flow regime. At applied stresses higher than σ_t , the exponent ranges from 4 to 7 implying that creep rate is greatly influenced with the applied stress. The creep response of materials is intimately related to microstructural processes that take place inside the material during deformation. These processes are included in the parameter A , which depends on the departure to the stoichiometry, the grain size, the density, and the fission products. Therefore the challenge for modelling is to describe accurately this parameter A .

In the literature, various models [37] have been proposed, however, they all have their restrained domain of application. One way to tackle this difficulty is to have a better knowledge of the physical phenomena involved in creep processes at the microscopic level, which could be approached with different modelling techniques. Table 2 summarises the different physical phenomena involved in creep processes and the modelling techniques with which they are susceptible to be treated.

To our knowledge, few simulations dedicated to creep have been carried out at the microscopic scale. We can acknowledge some work on grain boundary effect [20,50], on dislocation [19,22,52], on diffusion at high temperature [32,26,54], on migration of fission products in the fuel [82,29] [36,63,79], and lattice damage caused by irradiation [40,73]. Furthermore, most of the experimental studies available were carried out more than 30 years ago. In the following, we will list the issues that are currently under consideration or that still need to be modelled:

- Influence of stoichiometry: The creep activation energy is very sensitive to the evolution of the stoichiometry [62,64]. An excess of oxygen atom increases significantly the plastic deformation of UO_2 and hence increases the creep rate. The value of the threshold stress σ_t depends also on the stoichiometry because of the cation diffusion change with stoichiometry [13]. However, the cation diffusion coefficients are still imprecise.
- Influence of grain size: For stresses lower than σ_t , it is generally admitted that the creep rate is inversely proportional to the square of the grain size [1,10,13]. Conversely, for high stresses, the study carried out by Burton et al. [13] shows an increase of the creep rate with an increase of the grain size. The authors believe that the grain boundaries are acting as sliding barrier, which hardens the material (Cobble creep). No calculation of the grain boundary motion has been carried out yet. However, for big grain sizes, creep is dominated by dislocation motion even for low stresses (Nabarro-Herring diffusion). There is still some controversy about the influence of the grain size on the creep activation energy.
- Influence of density: Several studies [10,27,45] show that the creep rate increases with an increase of the porosity. However, the effect of the pore shape as well as the porosity self-healing intra- and intergranular have not yet been quantified and these parameters are not included in the creep models currently used.
- Irradiation effect: Several studies [16,23] show that creep appears at low temperatures (700-800°C) under irradiation. However, the microscopic physical phenomena behind this behaviour are not yet completely understood. It has been shown that creep decreases if the irradiation with heavy ions increases [17]. Conversely, older studies [55] carried out on spent fuels show that creep rate increases as the burn-up increases. Furthermore, the grain size effect has been studied on creep induced by irradiation but no clear effect arises from these studies [15]. More fundamental knowledge on irradiation effects is still needed to develop accurate model in order to embrace all the effects mentioned above.
- Irradiation effect – Fission products: The fission products as isolated defects or as precipitates reduce the fuel creep [1,9,27]. It is believed that the fission products at the grain boundaries disrupt the diffusion processes. The few available experiment data at high stresses are not sufficient to conclude if dislocation motion is affected by the presence of fission products.

Table 2. Available tools to study key physical phenomena involved in the mechanical response of nuclear fuel

Physical phenomenon	DFT	MD	Meso	Exp	PIE	CAL
Fission products	✓					
Point defects formation/diffusivity	✓	✓	✓			
Clusters of defect formation		✓	✓			
Dislocation loops formation/motion		✓	✓			
Grain boundary motion		✓	✓	✓	✓	
Fuel densification		✓	✓			
Fission gas bubbles nucleation / growth		✓	✓			
Recrystallisation		✓	✓		✓	
Phase transformation/stability		✓	✓	✓	✓	✓
Fission product's solubility	✓					✓

DFT: Density Functional Theory (*ab initio*), MD: Molecular Dynamics (atomistic), AMD: Accelerated Molecular Dynamics, Meso: Mesoscale modelling (grain-level techniques such as Monte Carlo, Phase Field, Mean Field, Dislocation Dynamics), Exp: Experiments, PIE: Post-Irradiation Examination, CAL: CALPHAD thermodynamic method.

Swelling

Accurate estimation of the dimensional changes of ceramic fuels during irradiation is of the utmost importance in predicting the mechanical performance, especially for fast reactor fuel elements. Fuel swelling is mainly due to replacement of heavy metal atoms by fission product atoms. Most of the fission products are solid and their contribution to swelling is commonly considered negligible. However, fission gasses are treated separately because they usually coalesce into bubbles within the fuel due to their very low solubility (Xenon, Krypton) and hence impact significantly fuel swelling.

Many individual physical processes contribute to the behaviour of fission gases in nuclear fuels. Each of them is important and needs to be understood in order to model correctly fuel swelling. We list in the following these behaviours and the attempts that have been achieved with different simulations techniques:

- Nucleation of gas bubbles. Either homogeneously by chance encounters of wandering gas atoms or heterogeneously on fission-fragment tracks or dislocation lines. Several atomistic simulations [46,25] but the full picture.
- Growth of gas bubbles by atomic migration of fission gas atoms to existing bubbles. Bubble growth can be affected by the availability of vacancies to permit the bubble to expand as gas is accumulated and by the effects of surface tension and the stress state of the surrounding fuel matrix, which determine the stable size of the bubble [47,35].
- Re-solution of the gas atoms in the matrix [51,63,24].
- Migration of the bubbles, either as a random-walk process in the absence of directed forces acting on the bubble or as biased motion when such forces are present. The forces that act on gas bubbles in solids are generally believed to be

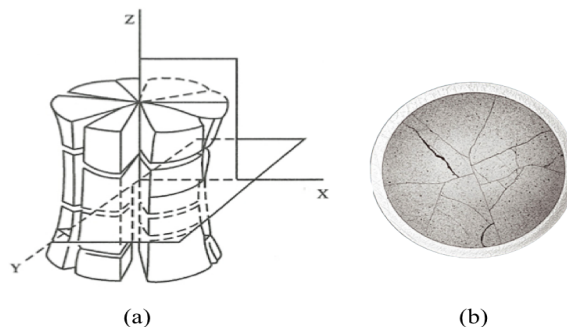
those due to the temperature or stress gradients, or restraining forces due to dislocations and grain boundaries [21].

- Coalescence of bubbles moving either in a random or directional fashion. Only very recently mesoscale simulations have been carried out in this topic [44].
- Interaction of bubbles with the crystal defects (dislocations and grain boundaries). To our knowledge no simulations were done on this topic.
- Release of the fission gases, either to external surfaces such as the central void, cracks in the fuel or the fuel-cladding gap or to internal surfaces such as grain boundaries. Most of the simulations have been done at the mesoscale or in fuel performance codes [48,28,67,53].

Cracking

Cracking of nuclear fuel has a direct impact on the release of fission products and thermal conductivity both during normal and abnormal operational conditions but also when spent fuel is used as the final disposal form. Indeed, a network of cracks increases the surface area of the fuel which, in turn, increases the rate at which fission products can leave the fuel and change thermal conductivity conditions. As such, cracking is an essential secondary phenomenon impacting important properties of the fuel. Immediately after the fuel rod power increases and before any significant swelling or creep can occur (see Section Creep and Swelling), a network of cracks due to thermal stresses is induced by the radial high-temperature gradients (a few hundreds Celsius per centimeter) [49].

Figure 5. Cracking of fuel pellet (a) schematic of a fuel pellet with a “hourgassing” shape due to the effect of thermal stresses, (b) macrograph of a PWR fuel pellet cracked by the thermal gradient [4]



As shown in Figure 5, these cracks are either oriented along radial planes passing through the fuel-pin axis (sometimes called θ cracks) or along horizontal planes perpendicular to the pellet axis (z cracks). Fracture orientations originate from the thermal stresses generated by the temperature gradient that exist between the centre ($1\text{ }200^{\circ}\text{C}$) and the outer part ($400\text{--}500^{\circ}\text{C}$) of the pellet. Pellet fragmentation during nominal loading is mainly characterised by radial and axial cracks. A second set of cracks appears during the power ramps (transient loading). Three-dimensional simulation of secondary crack network development is now possible with some fuel performance code [42]. The orientation of these secondary cracks is very similar to that of the primary cracks. The parabolic temperature gradient in the fuel induces tensile stresses in the radial and axial directions in

the outer region of the fuel where the fuel is brittle. In the inner core of the fuel, the thermal stresses are compressive, and therefore no cracking occurs inside.

As explained just above, because of high thermal gradients within the pellet, internal thermal stresses are developing in the fuel. These internal stresses can be evaluated by means of numerical methods (finite elements for example) but a good approximation can be obtained with an analytical solution. With the assumption of constant thermal power, thermal conductivity and thermal expansion coefficient, maximum tensile stresses $\sigma_{\theta,\max}$ are located at the pellet surface and are:

$$\sigma_{\theta,\max} = \frac{E_\alpha}{2(1-\nu)} (T_c - T_s)$$

where E is the fuel Young's modulus, α is the coefficient of thermal expansion, ν is the Poisson's ratio, T_c is the centreline temperature, and T_s is the temperature at the surface of the pellet. If one assume that UO_2 is a brittle material (at least for temperatures below half of the melting temperature), the fuel pellet will crack when $\sigma_{\theta,\max}$ exceeds the ultimate strength of the fuel $\sigma_{\theta,\text{frac}}$, i.e.:

$$T_c - T_s = 2 \frac{1-\nu}{E_\alpha} \sigma_{\text{frac}}$$

Note that the ultimate strength can vary notably according to the surface quality. For example, if one assumes that the average strength of a typical oxide fuel is about 130 MPa, one would find that the fuel pellet starts to fragment when $T_c - T_s > 100^\circ \text{C}$, i.e. during the first power increase to nominal conditions.

In addition, the fuel pellet is subject to thermoelastic deformation. This is due to the fact that the pellet has a finite length (between 10 and 14 mm). It can be shown that under the effect of thermal stresses, the pellet initially orthocylindric tends to a hourglassing shape with convex faces. This means that the approximation of plane deformation is not valid anymore in the vicinity of the pellet faces: the axial stress becomes zero on these faces and this behaviour needs to be corrected in the mesoscale models.

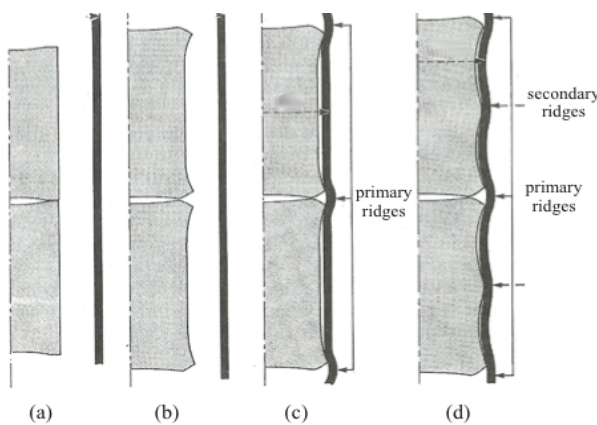
Furthermore, almost all the finite element codes take for approximation that the mechanical properties of the fuel are isotropic and assume that it is a brittle material. However, recent atomistic simulations [84] show that UO_2 can undergo phase transformation at the vicinity of the crack tip corresponding to a more plastic mechanical behaviour. Moreover, irradiation effects on the mechanical properties are seldom included in mesoscale model because they are not fully understood. More investigations in these two topics are then necessary to improve fuel cracking modelling.

Mechanical deformation in pellet-clad interaction

Nuclear fuel rods are fabricated with an initial pellet-cladding gap to offer space for radial thermal expansion and fission product swelling during operation. Pellet-clad interaction is a common fuel failure mechanism caused by fission-products (such as iodine and cadmium) induced stress corrosion cracking (SCC) of the cladding. At the beginning of irradiation, the clad is subjected to a differential pressure between the coolant pressure and the internal gas pressure leading to a compressive state. As illustrated in the schematic of Figure 6, the gap between the pellets and the clad progressively closes down (generally

between one to three years of burn-up, depending on the fuel type) under the combined effect of creep in the cladding material and swelling induced by the accumulation of fission products in the fuel pellet. As a consequence of the typical hourglass shape of the pellet, the first contact between the clad and the pellet occurs at the pellet-pellet interface where the gap is the smallest. Subsequently, the cladding will continue to deform in response to this non-uniform interaction to eventually take the exact shape of the hour-glassed pellet. This mechanism, known as *bambooing*, has been correlated with primary circumferential ridges identified on the cladding diametric measurements after irradiation (see Figure 6(c)).

Figure 6. Evolution of the gap between the cladding and the fuel pellet during irradiation
(a) start of irradiation, (b) first cycle and start of second irradiation cycle, (c) second half of second cycle: first cladding-pellet contact and appearance of primary ridges, (d) in the case of power ramp: appearance of secondary ridges [4]



While the gap closes, the cladding, initially loaded in compression due to the high coolant pressure, progressively gets in contact with the pellet and becomes loaded in tension. This tensile state of stress increases slowly to a stress level of about 20 to 30 MPa [6]. Therefore, in nominal conditions, the cladding material can easily accommodate the pellet swelling kinetics: the cladding is loaded by low PCI. During transients (power ramps), the thermal gradient increases rapidly and reaches within a few minutes a value almost three times higher than the nominal value (1 200°C over 4 mm in radius). The corresponding pellet swelling leads to high tensile stresses in the cladding, which cannot easily accommodate by viscoplasticity and can potentially result in the failure of the clad.

In addition, due to the high temperatures, the fuel viscoplasticity is also activated in the pellet centre and leads to a progressive filling of the transversal cracks. The fuel creep is correlated with the formation of secondary ridges at the median pellet plane level (Figure 6(d)). In such strong PCI conditions, the mechanical state of the pellet-cladding system is no more governed by the pellet deformation alone. In fact, the stiffness of the fragmented pellets and the cladding are not so different anymore and the strong cladding mechanical pre-stressing contributes to unbend the fragmented pellets.

The behaviour of pellets in their interactions with the cladding depends on many mechanisms potentially activated prior to or during PCI, namely:

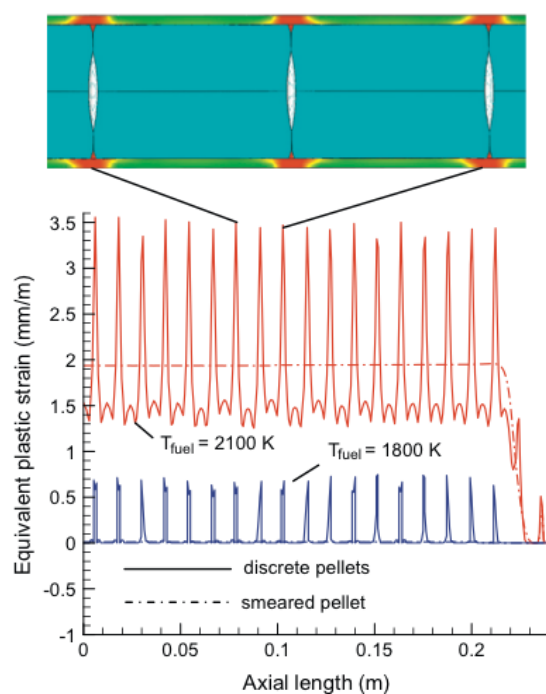
- swelling of solid and gaseous fission products due to burn-up;
- release of fission gases and volatile species;
- evolution of high-burn-up structure (HBS);
- evolution of thermal conductivity, elastic constants, thermal and irradiation creep, temperature-induced or microstructure-induced phenomena (porosity, recrystallisation);
- radiation damage;
- geometry of the pellets and their modifications by cracking;
- formation of contact materials or bonding layers at the interface of the fuel and the clad (zirconia/uranate compounds);
- oxidation, hybridiation;
- pellet-cladding interfacial friction.

The present state-of-the-art in modelling PCI predominantly involves modelling the fuel and clad as a single rod representation of the reactor core in an axisymmetric, axially-stacked one-dimensional (1D) representation with few examples of two-dimensional (2D) [61] and three-dimensional (3D) [6,58,43,48,80] simulations. The best known codes are FRAPCON [7] and FRAPTRAN [18] steady-state and transient codes, respectively, used by the Nuclear Regulatory Commission in the United States as audit codes. Industry codes include COPERNIC by AREVA [8], TRANSURANUS by ITU [34,74], or ENIGMA by British Energy [31]. In all the listed codes, the fuel rod is represented and meshed as a continuum divided in four domains: (i) the fuel pellets, (ii) the cladding, (iii) the fuel-cladding gap, and (iv) the cladding-coolant interface. The physical phenomena and processes affecting PCI and described above (at least part of them) are implemented with various degrees of details as correlational (with respect to experimental data) or empirical models and added to the set of equilibrium equations. The thermomechanical solutions representing the interaction between the clad and the pellets are obtained by time splitting the physics and a series of time marching iterative calculations in which the temperatures are calculated in both the pellets and the cladding (based on neutronics) followed by calculations of the state of stress and strain in the pellets and cladding (based on more or less refined constitutive models). The fidelity of the fuel constitutive model greatly influences the heat conductance within the pellet and across the pellet-clad gap which, in turn, affects the gap opening status and PCI contact pressure conditioning PCI failure. Inputs to these calculations are the power history (heat source) and the fast neutron flux and fluence (radiation damage).

For example, Newman et al. [48] from Idaho National Laboratory developed a 2D/3D fuel performance analysis capability (named BISON) which solves the fully coupled thermomechanics and mass diffusion equations, for both steady and transient regime. Implemented as a sub-routine in ABAQUS, this continuum code includes UO₂ temperature and burn-up dependent thermal properties, solid and gaseous fission product swelling, fuel densification, fission gas release, cladding thermal and irradiation creep, cladding irradiation growth, gap heat transfer, and gap/plenum gas behaviour during irradiation. As shown in Figure 7, comparisons between discrete and smeared-pellet

simulations reveal the importance of a multi-dimensional, multi-pellet, fully-coupled thermomechanical approach as opposed to 1D traditional/legacy codes lacking these features. Another example is the EPRI 2D fuel performance code Falcon [61], which computes the thermal, mechanical and chemical behaviour of a single fuel rod during irradiation. Similar to BISON, this continuum code includes empirical models for fission gas release, burn-up, fuel cracking, cladding and fuel viscoplasticity, densification and swelling. Of interest, this code was used to study PCI failure due manufacturing-induced missing pellet surface [60]. As shown in Figure 8, stress distribution predictions in the cladding obtained from these simulations appear to trace the crack propagation path seen in fuel rod failures where missing pellet surface is present.

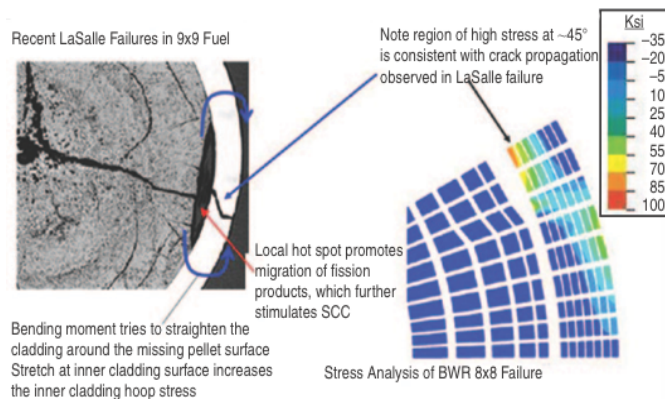
Figure 7. Clad mid-wall equivalent plastic strain, versus axial length, at two centreline fuel temperatures during the power-ramp



Results from both the discrete and smeared-pellet calculations are shown for comparison [48].

Regardless of the progresses made in recent years in the capabilities of these fuel codes where the empirical correlations are valid, these codes remain continuum representations of the fuel rod behaviour despite the fact that PCI is influenced by physical phenomena of several orders of magnitude smaller both in space and time. As such, higher resolution simulation techniques have been recently used to model lower length and time scales processes. These techniques include Density Functional Theory (DFT) and Molecular Dynamics. These atomistic-based modelling methodologies can be used to explicitly provide kinetic behaviours, including the probability of certain events like diffusion and alloying and capture mechanisms that cannot be resolved by coarser theories. Some of these processes are: migration of fission products in the fuel [29,36,63,82], lattice damage caused by fission products and neutron during irradiation [73,40], or the thermal conductivity of fuel pellets [5,57,79].

Figure 8. Manufactured-induced missing pellet surface induced failure pattern compared to calculation in falcon evaluating cladding hoop stress distribution [60]



The following articles illustrate the use of lower length scale modelling combined with theoretical understanding to improve empirical models of various properties of the fuel. For example, an opportunity has been shown to study the thermal conductivity using MD and show and quantify the variation of the thermal conductivity of UO₂ due to thermal and radiation effects [57]. Ichinomiya et al. [29] studied the migration dynamics of oxygen point defects in UO₂ using temperature-accelerated dynamics simulations giving insight into the formation mechanism of high-burn-up restructuring, including planar defects and grain subdivision (the rim structure), found in UO₂.

Clearly, integrating atomistic and mesoscale simulations results either by informing and improving empirical physical models or by substituting them would greatly benefit PCI modelling. Lower length scale simulations can help identify and inform key physical parameters influencing PCI such as diffusion coefficient used in fission products migration, defects/vacancies mobility or thermal conductivity. More importantly, the development of a multi-scale framework to study PCI would provide the following incentives:

- establish a basis for understanding fundamental phenomena;
- rank their relative importance;
- allow a credible prediction of PCI onset and demonstration of a safe operation of the fuel in-core when validated;
- define relevant experiments.

Conclusions and future challenges

One of the very important issues for the sustainability and the safety of the nuclear reactor is the knowledge of the nuclear fuel physical integrity. Fuel deformation is a complex problem, which includes several physical phenomena at different length and time scales. Therefore, modelling such behaviour involves the use of multi-scale and multi-physics approach with adequate bridge between the different scales and technics. Four key physical phenomena have been identified with their own on-going investigations:

- Creep is a long-term behaviour process, which is very difficult or impossible to study fully via experimental studies. Therefore, modelling and simulations are required. To this day, several models have been proposed but they all have their restrained domain of application. Furthermore, some fundamental knowledge on the stoichiometry and the irradiation effect including fission products on the mechanical properties are still needed to develop more accurate models.
- Fuel swelling is mainly due to the accumulation of inert gas bubbles. A lot of effort has been done in comprehending the nucleation and the growth of those gas bubbles and the fission gas release. However, data on the bubble migration and their interaction with extended crystal defects such as dislocations and grain boundaries are still missing.
- Concerning the fuel cracking and the mechanical deformation in pellet-clad-interaction, several codes in finite elements exist and predict correctly the main crack propagation behaviour seen in fuel rod failure and fuel cracking. However, the evolution of the mechanical properties under high burn-up or accidental conditions is still not fully understood. Insights from atomistic and mesoscale simulations on the lattice damage caused by irradiation or thermal conductivity evolution will provide useful understanding, which will improve the predictability of PCI codes.

References

- [1] Armstrong, W.M, W.R. Irvine, R.H. Martinson (1962), “Creep deformation of stoichiometric uranium dioxide”, *Journal of Nuclear Materials*, (2), 133-141.
- [2] Ashby, M.F, J. Frost (1982), *Deformation-mechanism maps, the Plasticity and Creep of Metals and Ceramics*, Oxford, Pergamon Press.
- [3] Aybar, H. S., P. Ortego (2005), “A review of nuclear fuel performance codes”, *Progress in Nuclear Energy*, 46 (2), 127-141.
- [4] Bailly, H., D. Ménessier, C. Prunier (1996), “Le combustible nucléaire des réacteurs à eau sous pression et des réacteurs à neutrons rapides”, *Conception et comportement*, volume Série Synthèses.
- [5] Basak, C.B., A.K. Sengupta, H.S. Kamath (2003), “Classical molecular dynamics simulation of UO₂ to predict thermophysical properties”, *Journal of Alloys and Compounds*, 360 (1-2), 210-216.
- [6] Bentejac, F., N. Hourdequin (2004), “TOUTATIS: An application of the cast3m element code for PCI three-dimensional modelling”, *Proceedings of the Pellet-clad Interaction in Water Reactor Fuels Seminar*, Aix-en-Provence, France.
- [7] Berna, G. A., G.A. Beyer, K.L. Davis, D.D. Lanning (1997), *FRAPCON-3: A Computer Code for the Calculation of Steady-state, Thermal-mechanical Behavior of Oxide Fuel Rods for High Burnup*, Technical Report NUREG/CR, 6534-Vol.2, Nuclear Regulatory Commission, Washington, DC (United States). Div. of Systems Technology; Pacific Northwest Lab., Richland, Idaho National Engineering Lab., Idaho Falls, ID, US.

- [8] Bernard, L. C., E. Van Schel, V. Rebeyrolle, C. Foissaud, D. Wesley (2000), “The FRAMATOME Copernic fuel rode performance code, recent high burn-up and advanced cladding developments”, *International Topical Meeting in Light Water Reactor Fuel Performance*, Park City, UT US.
- [9] Bibilashvili, Yu.K., A.V. Kuleshov, O.V. Milavanov, E.N. Mikheev, V.V. Novikov (2003), *Investigation of Thermal-physical and Mechanical Properties of Uranium Gadolinium Oxide Fuel*, IAEA, Technical committee meeting on improved fuel pellet materials and designs, Brussels, Belgium.
- [10] Bohaboy, P.E., R.R. Asamoto, A.E. Conti (1969), *Compressive Creep Characteristics of Stoichiometric Uranium Dioxide*, GEAP-10054, US Atomic Energy Commission, Springfield, US.
- [11] Bouineau, V., M. Lainet, A. Courcelle, M. Pelletier (2011), *Toward an Improved GERMINAL V2 Code to Model Oxide Fuel for SFR*, SMiRT 21, New Delhi, India.
- [12] Boyack, B., I. Catton, R. Duffey, P. Griffith, K. Katsma, G. Lellouche, S. Levy, G. Wilson, W. Wulff, N. Zuber (1989), *Quantifying Reactor Safety Margins: Application of Code Scaling, Applicability, and Uncertainty Evaluation Methodology to a Large-break, Loss-of Coolant Accident*, Technical Report NUREG/CR-5249.
- [13] Burton, B., G.L. Reynolds, J.P. Barnes (1973), “The influence of grain size on the creep of uranium dioxide”, *Journal of Materials Science*, 1973, 8, 1960-1964.
- [14] Chaperon, T., C. Duguay, A. Mocellin, P. Dehaudt (2003), *Programme FLOX, Lois de fluage stationnaires de l'UO₂ dopé à l'oxyde de chrome au-delà de la limite de solubilité: premières recommandations*, CEA, Note Technique DTP/SECC/LPCC n°97-057A.
- [15] Clough, D.J. (1977), “Creep properties of oxide and carbide fuels under irradiation”, *Journal of Nuclear Materials*, 65, 24.
- [16] Colin, C. (2003), *Etude du fluage du dioxyde d'uranium: caractérisation par essais de flexion et modélisation numérique*, Thèse de l'Ecole des Mines de Paris, Centre des Matériaux.
- [17] Colin, C., M. Boussuge, M. Beauvy (2006), *Fluage en flexion du dioxyde d'uranium après irradiation aux ions*, Communication, congrès Matériaux ,Dijon, France.
- [18] Cunningham, M. E. et al. (2001), *Fraptran: A Computer Code for the Transient Analysis of Oxide Fuel Rods*, Technical Report NUREG/CR- 7023-Vol.1, Nuclear Regulatory Commission, Washington, Pacific Northwest Lab., Richland, US.
- [19] Deng, B. et al. (2012), “Effects of edge dislocations on thermal transport in UO₂”, *Journal of Nuclear Materials*, 434.203-209.
- [20] Desai, T. et al. (2008), “Molecular dynamics study of diffusional creep in nanocrystalline UO₂”, *Acta Materialia*, 56, 4489-4497.
- [21] Desai, T., P. Millett, M. Tonks, D. Wolf (2010), “Atomistic simulations of void migration under thermal gradient in UO₂”, *Acta Materialia*, 58.330-339.
- [22] Fossati, P., L. Van Brutzel, B. Devincre (2013), “Molecular dynamics simulation of dislocations in uranium dioxide”, *Journal of Nuclear Materials*, 443.359-365.

- [23] Gatt, J.M. (2005), *Comportement thermomécanique du combustible sous irradiation*, CEA, Note Technique DEC/SESC/LLCC n°04-005.
- [24] Govers, K., C. Bishop, D. Parfitt, S. Lemehov, M. Verwerft, R. Grimes (2012), “Molecular dynamics study of Xe bubble re-solution in UO_2 ”, *Journal of Nuclear Materials*, 420.282-290.
- [25] Govers, K., M. Verwerft (2013), “Classical molecular dynamics investigation of microstructure evolution and grain boundary diffusion in nano-polycrystalline UO_2 ”, *Journal of Nuclear Materials*, 438.134-143.
- [26] Gridnev, A.A. et al. (1986), *A Study of the High-Temperature Creep in Coarse-grained Uranium Dioxide*, Soviet Atomic Energy, 1986, 59(1), 565-568.
- [27] Hough, A. (1988), *Compressive Creep in Nuclear Oxides*, United Kingdom Atomic Energy Authority, AERE R 13232.
- [28] Hu, S. et al. (2010), “Application of the phase-field method in predicting gas bubble microstructure evolution in nuclear fuels”, *International Journal of Materials Research*, 101 (4), 515-522.
- [29] Ichinomiya, T. et al. (2009), “Temperature accelerated dynamics study of migration process of oxygen defects in UO_2 ”, *Journal of Nuclear Materials*, 384 (3), 315-321.
- [30] Jankus, V. Z., R.W. Weeks (1972), “LIFE-II – A computer analysis of fast-reactor fuel-element behavior as a function of reactor operating history”, *Nuclear Engineering and Design*, 18(1), 83-96.
- [31] Kilgour, W. et al. (1991), “Capabilities and validation of the enigma fuel performance code”, *International Topical Meeting in Light Water Reactor Fuel Performance*, Avignon, France.
- [32] Kurosaki, K. et al. (2001), “Molecular dynamics study of mixed oxide fuel”, *Journal of Nuclear Materials*, 294 (1-2), 160-167.
- [33] Lainet, M., V. Bouineau, T. Helfer, M. Pelletier (2011), “Recent improvements of mechanical modelling in fuel performance code GERMINAL”, MMSNF, Aix-en-Provence, France.
- [34] Lassmann, K. (1992), “Transuranus: a fuel rod analysis code ready for use”, *Journal of Nuclear Materials*, 188, 295-302.
- [35] Li, Y., S. Hu, R. Montgomery, F. Gao, X. Sun (2012), “Phase-field simulations of intragranular fission gas bubble evolution in UO_2 under post-irradiation thermal annealing”, *Nuclear instruments and methods in physics research section b-beam interactions with materials and atoms*, 303.62-67.
- [36] X.-Y. Liu, B. P. Uberuaga, D. A. Andersson, C. R. Staneck and K. E. Sickafus (2011), “Mechanism for transient migration of xenon in UO_2 ”, *Applied Physics Letters*, vol 98, 151902.
- [37] Malygin, V. et al. (2010), *Recommendations for Calculating the Rate of Irradiation-induced Creep of Oxide Fuel when Analyzing Fuel-element Serviceability*, Atomic Energy 108 (2) 121-126.

- [38] Marelle, V. et al. (2007), “MTR plates modeling with MAIA”, *International RERTR Meeting*, Prague, Czech Republic.
- [39] Marelle, V., J. Sercombe, B. Michel, R. Tawizgant (2011), “Thermo-mechanical modeling of PWR fuel with ALCYONE”, T2-028, *Water Reactor Fuel Performance Meeting*, Chengdu, People’s Republic of China.
- [40] Martin, G. et al. (2009), “A molecular dynamics study of radiation induced diffusion in uranium dioxide”, *Journal of Nuclear Materials*, 385(2), 351-357.
- [41] Michel, F., P. Mailhe (2006), *ATLAS, A Code for VHTR Fuel Performance Evaluation*, Transactions of the ANS 94, 660-661.
- [42] Michel, B., J. Sercombe, G. Thouvenin, R. Chatelet (2008), “3D fuel cracking modelling in pellet cladding mechanical interaction”, *Engineering Fracture Mechanics*, 75 3581-3598.
- [43] Michel, B., J. Sercombe, C. Nonon, O. Fandeur (2011), “Modeling of Pellet Cladding Interaction (PCI)”, *Book Comprehensive Nuclear Material*, Chap 71, Ed. R. KONINGS, 26-05-2011.
- [44] Millett, P., M. Tonks, S. Biner, L. Zhang, K. Chockalingam, Y. Zhang (2012), “Phase-field simulation of intergranular bubble growth and percolation in bicrystals”, *Journal of Nuclear Materials*, 425, 130-135.
- [45] Mocellin, A. et al. (1998), “Influence de la densité et de la taille de grains sur les déformations de UO₂ en régime stationnaire”, *Compte rendu CEA Grenoble-DEC/SECC/LPCC N°98006A*.
- [46] Moore, E. et al. (2011), “Molecular dynamics simulation of Xe bubble nucleation in nanocrystalline UO₂ nuclear fuel”, *Journal of Nuclear Materials*, 419.140-144.
- [47] Murphy, S., A. Chartier, L. Van Brutzel, JP. Crocombette (2012), “Free energy of Xe incorporation at point defects and in nanovoids and bubbles in UO₂”, *Physical Review B*, 85.144102.
- [48] Newman, C. et al. (2009), “Three dimensional coupled simulation of thermomechanics, heat, and oxygen diffusion in UO₂ nuclear fuel rods”, *Journal of Nuclear Materials*, 392 (1), 6-15.
- [49] Olander, D.R. (1976), *Fundamental Aspects of Nuclear Reactor Fuel Elements*, Technical Report TID-26711-P1, Energy Research and Development Administration, Washington, US.
- [50] Pacull, J. et al. (2010), “Modèle numérique micromécanique d'agrégat polycristallin pour le comportement des combustibles oxydes”, *19^{ème} Congrès Français de Mécanique*, Marseille, France.
- [51] Parfitt, D., R.W. Grimes (2008), “Predicted mechanisms for radiation enhanced helium resolution in uranium dioxide”, *Journal of Nuclear Materials*, 381, 216-222.
- [52] Parfitt, D. et al. (2010), “Strain fields and line energies of dislocations in uranium dioxide”, *Journal of Physics: Condensed Matter*, 22, 175004.

- [53] Pastore, G., L. Luzzia, V. Di Marcellob, P. Van Uffelen (2013), “Physics-based modelling of fission gas swelling and release in UO_2 applied to integral fuel rod analysis”, *Nuclear Engineering and Design*, 256, 75-86.
- [54] Potashnikov, S., A. Boyarchenkov, K. Nekrasov, A. Kupryazhkin (2013), “High-precision molecular dynamics simulation of $\text{UO}_2\text{-PuO}_2$: Anion self-diffusion in UO_2 ”, *Journal of Nuclear Materials*, 433, 215-226.
- [55] Perrin, J.S. (1971), “Irradiation-induced creep of uranium dioxide”, *Journal of Nuclear Materials*, 39, 175-182.
- [56] Philip, B., K.T. Clarno, W.K. Cochran (2010), *Software Design Document for the AMP Nuclear Fuel Performance Code*, Technical Report ORNL/TM-2010/34, Oak Ridge National Laboratory, Oak Ridge, US.
- [57] Phillipot, S., A. El-Azab, A. Chernatynskiy, J. Tulenko (2011), “Thermal conductivity of UO_2 fuel: Predicting fuel performance from simulation”, *JOM Journal of the Minerals, Metals and Materials Society*, 63, 73-79.
- [58] Plancq, D. (2004), “Pleiades: A unified environment for multi-dimensional fuel performance modelling”, *International Meeting on LWR Fuel Performance*, Orlando, FL US.
- [59] Poinssot, C. et al. (2004), “Key scientific issues related to the evolution of spent nuclear fuel in long-term dry storage and geological disposal”, *Materials Research Society Symposia Proceedings*, Vol. 807, Materials Research Society.
- [60] Rashid, J.Y. et al. (2011), “Light water reactor fuel performance modeling and multi-dimensional simulation”, *JOM Journal of the Minerals, Metals and Materials Society*, 63(8), 81-88.10.
- [61] Rashid, Y.R. et al. (2004), *Falcon mod01: Fuel Analysis and Licensing Code New, Theoretical and Numerical Bases*, Technical Report ANA-04-0666, EPRI, Palo Alto, CA, and ANATECH Corp., San Diego, US.
- [62] Routbort, J.L. et al. (1973), “Creep of mixed-oxide fuel pellets at high stress”, *Journal of the American Ceramic Society*, 56(6) 330-333.
- [63] Schwen, D. et al. (2009), “Molecular dynamics simulation of intragranular Xe bubble re-solution in UO_2 ”, *Journal of Nuclear Materials*, 392(1), 35-39.
- [64] Seltzer, M.S., A.H. Clauer, B.A. Wilcox (1972), “The influence of stoichiometry on compression creep of polycrystalline UO_{2+x} ”, *Journal of Nuclear Materials*, 44, 331-336.
- [65] Sercombe, J., B. Michel, G. Thouvenin, B. Petitprez, R. Chatelet, D. Leboulch, C. Nonon (2009), “Multi-dimensional modeling of PCMI during base irradiation and ramp testing with ALCYONE V1.1”, *Proceedings Top Fuel 2009*, Paris, France.
- [66] Sercombe, J., E. Fédérici, M. Le Saux, B. Michel, C. Poussard (2010), “1D and 3D modeling of PCMI during a RIA with ALCYONE V1.1”, *Proceedings Top Fuel 2010*, Orlando, US.

- [67] Skorek, R., S. Maillard, A. Michel, G. Carlot, E. Gilabert, T. Jourdan (2011), “Modelling Fission Gas Bubble Distribution in UO₂”, *Diffusion in materials – DIMAT 2011*, Defect and Diffusion Forum 323-325, 209-214.
- [68] Struzik, C., V. Marelle (2012), “Validation of fuel performance CEA code ALCYONE, scheme 1D, on extensive data base”, *Proceedings Top Fuel 2012*, Manchester, UK.
- [69] Suzuki, M., H. Uetsuka, H. Saitou (2004), “Analysis of mechanical load on cladding induced by fuel swelling during power ramp in high burn-up rod by fuel performance code femaxi-6”, *Nuclear Engineering and Design*, 229(1), 1-14.
- [70] Tayal, M. (1986), *Elestres: Performance of Nuclear Fuel, Circumferential Ridging and Multiaxial Elastic-plastic Stresses in Sheaths*, Technical Report NUREG/CR, 6534-Vol.2; PNNL, 11513-Vol.2, Nuclear Regulatory Commission, Washington, DC Division of Systems Technology; Pacific Northwest Lab., Richland, WA Idaho National Engineering Lab., Idaho Falls, ID, US.
- [71] Tayal, M. (1986), *Modelling CANDU Fuel under Normal Operating Conditions: ELESTRES Code Description*, Technical Report 9331, AECL.
- [72] Turner, J. A., K.T. Clarno, G.A. Hansen (2009), *Roadmap to an Engineering-scale Nuclear Fuel Performance and Safety Code*, Technical Report ORNL/TM-2009/233, Oak Ridge National Laboratory, Oak Ridge, US.
- [73] van Brutzel, L., M. Rarivomanantsoa, D. Ghaleb (2006), “Displacement cascade initiated with the realistic energy of the recoil nucleus in UO₂ matrix by molecular dynamics simulation”, *Journal of Nuclear Materials*, 354 (1-3), 28-35.
- [74] van Uffelen, P., C. Györi, A. Schubert, J. van de Laar, Z. Hozer, G. Spykman (2008), “Extending the application range of a fuel performance code from normal operating to design basis accident conditions”, *Journal of Nuclear Materials*, 383 (1-2), 295-302.
- [75] Veshchunov, M., V. Ozrin, V. Shestak, V. Tarasov, R. Dubourg, G. Nicaise (2006), “Development of the mechanistic code MFPR for modelling fission-product release from irradiated UO₂ fuel”, *Nuclear Engineering and Design*, 236(2).179-200.
- [76] Veshchunov, M., R. Dubourg, V. Ozrin, V. Shestak, V. Tarasov (2007), “Mechanistic modeling of urania fuel evolution and fission product migration during irradiation and heating”, *Journal of Nuclear Materials*, 362 (2-3), 327-335.
- [77] Veshchunov, M., V. Shestak (2009), “Model for evolution of crystal defects in UO₂ under irradiation up to high burn-ups”, *Journal of Nuclear Materials*, 384(1), 12-18.
- [78] Veshchunov, M., V. Shestaka (2012), “Modelling of fission gas release from irradiated UO₂ fuel under high-temperature annealing conditions”, *Journal of Nuclear Materials*, 430, 82-89.
- [79] Watanabe, T., S.B. Sinnott, J.S. Tulenko, R.W. Grimes, P.K. Schelling, S.R. Phillpot (2008), “Thermal transport properties of uranium dioxide by molecular dynamics simulations”, *Journal of Nuclear Materials*, 375(3), 388-396.

-
- [80] Williamson, R. (2011), “Enhancing the ABAQUS thermomechanics code to simulate multipellet steady and transient LWR fuel rod behavior”, *Journal of Nuclear Materials*, 415(1), 74-83.
 - [81] Wilson, G., B. Boyack (1998), “The role of the PIRT process in experiments, code development and code applications associated with reactor safety analysis”, *Nuclear Engineering and Design*, 186(1), 23-37.
 - [82] Yun, Y., H. Kim, H. Kim, K. Park (2008), “Atomic diffusion mechanism of Xe in UO₂”, *Journal of Nuclear Materials*, 378(1), 40-44.
 - [83] Zhang, Y., X. Liu, P. Millett, M. Tonks, D. Andersson, B. Biner (2012), “Crack tip plasticity in single crystal UO₂: Atomistic simulations”, *Journal of Nuclear Materials*, 430, 96-105.

Chapter 3.

Fuel-cladding chemical interaction

C. Guéneau¹, J.-P. Piron², J.-C. Dumas², V. Bouineau², F.C. Iglesias³, B.J. Lewis³

¹CEA, DEN, DPC, Centre de Saclay, France,

²CEA, DEN, DEC, Centre de Cadarache, France,

³University of Ontario Institute of Technology, Canada

Abstract

The chemistry of the nuclear fuel is very complex. Its chemical composition changes with time due to the formation of fission products and depends on the temperature level history within the fuel pellet and the clad during operation. Firstly, in thermal reactors, zircaloy oxidation from reaction with UO₂ fuel under high-temperature conditions will be addressed. Then other fuel-cladding interaction phenomena occurring in fast reactors will be described. Large thermal gradients existing between the centre and the periphery of the pellet induce the radial redistribution of the fuel constituents. The fuel pellet can react with the clad by different corrosion processes which can involve actinide and/or fission product transport via gas, liquid or/and solid phases. All these phenomena are briefly described in the case of different kinds of fuels (oxide, carbide, nitride, metallic) to be used in fast reactors. The way these phenomena are taken into account in fuel performance codes is presented.

Introduction

Examples of fuel-cladding chemical interaction phenomena will be addressed. In a first part, zircaloy fuel sheathing internal oxidation by UO₂ fuel occurring in thermal neutron reactors under high-temperature reaction will be described. In fast reactors, chemical interaction between fuels and/or fission products (FPs) and cladding materials are factors limiting the lifetime of fuel pins. In a second part, examples of fuel-cladding reaction in fast neutron reactors operating with different types of fuels will be presented. Depending on the nature of the fuels (oxide, carbide, nitride or metal) and on the related operating conditions (fuel and clad temperature, thermal gradient, nature of clad and coolant, etc.), the chemical reactions differ. Recent reviews on Fuel-Clad Chemical Interaction (FCCI)

were recently published by Maeda for oxide, carbide and nitride fuels in [21] and by Keiser for metallic fuels in [17]. A brief summary on the way to take into account these chemical reactions in the models for different types of fuels is given mainly based on existing reviews.

Internal zircaloy oxidation due to zircaloy/uranium dioxide interaction in thermal reactors

Under high-temperature conditions, a combined external and internal oxidation of the fuel sheathing can occur due to a reaction of steam on the outside surface of the sheath and from the UO₂ on the inside surface. The UO₂ and Zr can interact chemically at temperatures as low as 1 273 K, leading to a complex series of reaction layers [5] where, from both internal and external oxidation, the following reaction layers can be formed: $[UO_2 + U] \rightarrow [\alpha\text{-Zr(O)}_a + (U,Zr)] \rightarrow (U,Zr)\text{alloy} \rightarrow \alpha\text{-Zr(O)}_b \rightarrow \beta\text{-Zry} \rightarrow \alpha\text{-Zr(O)}_c \rightarrow ZrO_2$. This internal interaction requires a substantial external overpressure to promote good solid-solid contact between the fuel and cladding. For instance, experiments have been conducted at overpressures of 4 MPa [5] and 1 MPa [15]. In the CANDU fuel design, the thin sheath will creep down onto the fuel under the conditions of the high pressure coolant. However, contact between the sheath and fuel can be lost during the transient with sheath lift off due to fission gas release into the (small) free void space of the fuel element and depressurisation with coolant blowdown, as well as with the eventual bursting of the sheath. Thus, with an open gap during an accident, any direct fuel/sheath interaction is suppressed and no uranium is transferred from the fuel to the sheathing as long as the sheath is solid. If the gap contains hydrogen, fuel reduction can occur as oxygen moves from the fuel to the sheathing by the H₂O-H₂ transport mechanism, driven by the difference in the oxygen potential between the fuel surface and the sheathing inner wall. However, the extent of fuel reduction and cladding oxidation by this mechanism is minor [28].

At temperatures above ~1 470 K, steam oxidation of zircaloy and stainless steel produces a significant temperature escalation. With the melting of the as received metallic zircaloy-4 cladding (2 030 K) or metallic oxygen-stabilised $\alpha\text{-Zr(O)}$ phase (2 245 K), the solid UO₂ may be partially dissolved and liquefied ~1 000 K below its melting temperature. The driving force for the reaction is diffusion of oxygen from the UO₂ into the sheathing. This process has been extensively studied in single-effect laboratory crucible experiments [5,7,35,13,14] [27,18,29,8,10,39] [25,37,30,1,11,12]. In hydrogen-rich regions of the core, the outer oxide scale is not present on the cladding, which is all-metal with oxygen in solid solution. On melting of the cladding, the liquid metal contacts the solid fuel and dissolution of the fuel begins. The endothermic reaction of UO₂ dissolution in U-Zr-O melts and the melting of $\alpha\text{-Zr(O)}$ sheathing is affected by the supply of heat. In addition to receiving additional oxygen, uranium from the fuel dissolves in the liquid metal forming a U-Zr-O melt. Dissolution continues until the melt is saturated in both oxygen and uranium [31]. The fuel dissolution process has been detailed, for example, in [30], where it is shown that diffusion in the growing U-Zr-O melt is rapid and the liquid phase concentration remains at saturation. Reduction of the fuel by oxygen diffusion affects the amount of oxygen in the melt. The effect of an oxide scale will also reduce the extent of fuel liquefaction because less metal is available to dissolve uranium

when a melt forms. In addition, the high concentration of oxygen in the oxide layer will increase the oxygen content of the melt, thus depressing the uranium solubility. It is suggested that the fraction of the fuel pellet that is dissolved by the initial liquefaction is small [30].

Fuel-cladding chemical interaction in fast reactors

Mixed oxide fuels

Chemical interaction between MOX ($\text{U},\text{Pu}\text{O}_2$) fuels and/or Fission Products (FPs) and cladding materials are key issues to address in fast reactors. Various types of steels or ODS steels (Oxide Dispersion Strengthened) are considered for the clad. The low thermal conductivity of the MOX fuels induces a large temperature gradient between the centre and the periphery of the fuel pellet. In normal operating conditions, the centreline temperature of the fuel will reach about 2 500 K and the inner clad temperature will go up to about 800-900 K. Therefore, large thermally driven mass transport phenomena are expected that will induce the redistribution of the constituent elements (U, Pu, oxygen, minor actinides and fission products) in the fuel. The mixed oxide fuel is manufactured to be hypo-stoichiometric (oxygen/metal ratio < 2). Excess oxygen due to irradiation implies the increase of the oxygen chemical potential of the fuel. The redistribution of oxygen along the radial temperature gradient induces the increase of the O/M (oxygen to metal) ratio at the fuel surface.

The increase in the oxygen potential due to the irradiation can be predicted using thermodynamic calculations. The fission products can be dissolved in the MOX solid solution or/and precipitate as separated phases (metallic or/and oxide phases). Thus, the fuel chemistry is very complex. Thermodynamic calculations using minimisation Gibbs energy codes and databases describing the thermodynamic properties of the fuel and fission product based phases are performed to predict the evolution of the chemical composition of the different phases constituting the irradiated fuel. By this way, the evolution of the oxygen potential of the fuel can be calculated versus burn-up. This type of calculation is limited to equilibrium conditions. The oxygen redistribution has to be calculated along the radial temperature gradient.

This is performed in the FEAST code developed by Karahan and Buongiorno [16]. This code aims at predicting the behaviour of MOX oxide fuel pins under irradiation in sodium-cooled fast reactors. In that code, a simplified thermodynamic model is used to calculate the fuel oxygen potential by solving the thermodynamic equilibrium between the fuel and fission products and the charge balance within the fuel. Molybdenum is an important fission product to consider in the calculations as it acts as a buffer to prevent the fuel from becoming hyperstoichiometric. The oxygen redistribution versus time under temperature gradient is determined by the OXIRED model based on thermo-transport theory [20]. The same type of model is also applied to predict the redistribution of Pu in the fuel.

The oxygen stoichiometry of the fuel (or the $\text{O}/(\text{U}+\text{Pu})$ ratio) is a key parameter. The chemical compatibility of MOX fuels with $\text{O}/(\text{U}+\text{Pu}) \leq 2$ and stainless steels is good. However, the cladding material is oxidised in the case of a hyperstoichiometric MOX ($\text{O}/(\text{U}+\text{Pu}) \geq 2$). To avoid the oxidation of the clad, the $\text{O}/(\text{U}+\text{Pu})$ ratio has to be

maintained below 2. In the case of oxidation, a stable protective layer of Cr_2O_3 forms on the inner wall of the clad.

However, post-irradiation observations show that the clad attack is accelerated by the presence of fission products. A chemical interaction between Cs, Te and O localised in the fuel to clad gap and the clad [34]. The corrosive environment is characterised by high temperatures and by a large axial and radial temperature gradient. The layer formed at the inner surface of the cladding material is mainly constituted of Fe, Ni, O, Cr, Te, Cs and Mo. The analysis of this layer shows that Te-Fe-Ni and Cs-O-Cr compounds are formed.

Different mechanisms are proposed in the literature.

For example, for high temperature ($>600^\circ\text{C}$) and oxygen potential ($\text{O}/\text{M}>1.97$), constituents of the cladding. Fe, Cr and Ni are dissolved in liquid Cs-Te and segregate in the fuel-cladding gap as a metallic layer separated from the cladding by a non metallic layer with Cr. The tellurium activity is a key parameter. It is determined by the following reaction:



The decomposition requires a high oxygen potential to destabilise Cs_2Te . The free tellurium in the gap can lead to the cladding attack by the formation of tellurides of iron, nickel and chromium. As a function of the ratio Cs/Te, different corrosion products are observed: (i) deep intergranular penetration with dissolution of the metal, (ii) uniform attack of the alloy matrix with the formation of successive layers, (iii) intergranular attack without dissolution of the metal [33]. Thermodynamic calculations involving reactions of formation of various compounds that form between fission products and cladding constituents and oxygen are used to interpret experimental observations.

The key parameters that control these attacks of the clad are:

- the concentration of corrosive fission products;
- the fuel-cladding gap width;
- the oxygen to metal ratio of the fuel;
- the clad temperature;
- the fuel temperature;
- the temperature gradient.

The influence of these parameters has been assessed from post-irradiation observations.

As the mechanisms of cladding attack are not enough clearly demonstrated and understood, in most of the cases, only empirical equations rather than fundamental relations are used in models for the fuel pin design. For example, this was the case up to now into the French code GERMINAL dedicated to the calculation of fast fuel behaviour for 20 years today [24]; an empirical correlation reproducing the corrosion zone thickness observed on irradiated Phénix fuel pins by metallographic examinations was considered up to now. This law will be reassessed with complementary experimental and theoretical studies in the future version of the code.

These equations give the penetration depth in the cladding related to irradiation and fabrication parameters of the fuel pins. A review of the different available equations is given in [21].

However, a model has been incorporated in the FEAST code to take into account caesium migration within the fuel and in the gap region [16]. In fact, this element, which is the most important of the volatile fission products (Cs,I,Te), is observed to deposit mainly as molybdate (Cs_2MoO_4) in the gap between the fuel pellet and the clad with increasing burn-up. The formation of this layer of fission products associated with oxygen, called JOG, as ‘‘Joint Oxyde Gaine’’ [38], improves the gap conductance and thus is expected to decrease the centreline temperature of the fuel. The caesium radial migration model within the fuel in the FEAST code is based on the thermo-transport theory. The JOG layer thickness is then computed. The caesium axial migration is also treated in the FEAST code. The transport of caesium is described by an evaporation/condensation process [6]. In the French GERMINAL code, the JOG layer thickness is also calculated from caesium migration. In this case, the release of caesium outside the fuel pellet is linked to the model for fission gas (Xe and Kr) release, based on experimental observations performed on irradiated fuel pins [23,24]. A similar approach is considered to the Japanese CEPTAR code [32], which is focused on annular fuel pellets.

Carbide fuels

A review on the carbide fuel properties has been recently published by Sengupta et al. [36]. The main reaction between carbide fuels and cladding consists of the clad carburisation [21]. The maximum temperature of the fuel surface is generally below 1 000°C. The centreline temperature is quite lower than in oxide fuel due to the higher thermal conductivity of carbide fuel. In this case, the fission products are less reactive than for oxide fuels. The fuel is designed to be slightly hyperstoichiometric (carbon/metal >1) to avoid the formation of metal phases. Thus the carbide fuel is mainly constituted of the monocarbide $(\text{U},\text{Pu})\text{C}$ with a small fraction of sesquicarbide $(\text{U},\text{Pu})_2\text{C}_3$ located at the grain boundaries. The carbon stoichiometry of the fuel is a key parameter as well as oxygen and nitrogen that are present in the fuel as impurities arising from the fabrication. These impurities are dissolved in the monocarbide phase.

There are two mechanisms for the clad carburisation [22]:

- by transport of carbon from (or to) the fuel and to (or from) the clad depending on the difference in carbon chemical potential between the fuel and the clad; the comparison of the carbon potential in the steel and in the fuel allows concluding that the clad may not be carburised in normal conditions for a fuel with $(\text{Pu}/(\text{U}+\text{Pu}))=0.70$;
- by transport of CO(g) to cooler fuel regions along the temperature gradient, depending on the gradient of CO(g) pressure within the fuel pin. CO(g) pressures can be calculated by thermodynamic calculations using Gibbs energy minimisation methods on the U-Pu-O-C-N system [22]. A thermodynamic analysis considering the reaction between carbon coming from the clad or from the fuel and the CO/CO_2 equilibrium shows that even in the case of low carbon potential in the fuel, the carburisation of the clad is possible. The carburisation process will be

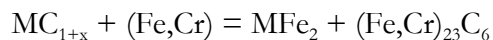
enhanced in the case of a lower Pu content in the fuel. For this type of fuel, the oxygen content has to be kept as low as possible.

In hypostoichiometric mixed carbide fuels, (U,Pu) metal will form as a secondary phase which may cause low temperature eutectics with Fe and Ni-based cladding alloys. Once a metal phase is formed in the fuel, it will react with the cladding material. The reaction between carbide fuels and different cladding alloys leads to the formation of intermetallic compounds such as (U,Pu)Ni₅, (U,Pu)Fe₂.

As an example, the following reaction has been proposed:



The carburisation increases with the carbon activity in MC_{1+x} fuel. Thus, the presence of the sesquicarbide phase enhances the carburisation of the clad. The carbon transport from the fuel to the cladding is controlled by gradient of carbon chemical potential between both materials. The reaction is as follows:



The solubility of carbon in the matrix being very low, carbides precipitate. In austenitic stainless steels, this precipitation leads to a depletion of chromium at the grain boundaries. The limited existing data show that cladding materials with high Ni and/or Ti content are more reactive than the austenitic steels. The precipitation of these carbides will cause a loss of ductility and mechanical strength and can determine the fuel lifetime as well as an excessive cladding swelling.

The key parameters that control the carburisation process are:

- the carbon activity in the fuel (and the oxygen content);
- the cladding and fuel temperatures;
- the bonding material (helium or sodium).

Diffusion models were developed to predict kinetics of the carburisation process in steels. The clad carburisation can directly occur in contact with fuel but also through the bonding medium (helium or sodium). It has been observed in sodium-bonded fuels where excessive clad carburisation can occur with hyperstoichiometric carbide fuel. The depth of carburisation is two or three times less extensive in helium medium. The carbon solubility in liquid sodium is very low. Carbon is probably transported in sodium as carbon atoms and transferred to the clad.

The oxygen potential is too low to form fission product oxides. Fission products mainly form mono, di and sequicarbides. Thus with increasing burn-up, the carbon/metal ratio of the fuel decreases. Thermodynamic calculations have been performed by Agarwal and Venugopal [2] to predict the chemical state of the fission products versus burn-up. The authors showed that rare earth metals play a crucial role in controlling the carbon activity of the fuel.

No severe attack of the cladding by the fission products is expected. An intergranular attack for high concentration of Te in the fuel was observed. Thin reaction layers containing Ni, Fe, U, Pu and rare earths were found at high linear heating rates. Thus no severe interactions were expected nor observed. At temperatures above ~950°C, the

reaction between the fuel and stainless steel or PE16 cladding can lead to liquid phase formation according to the following reaction:

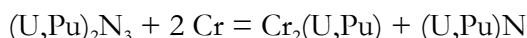


Except thermodynamic calculations, no models were found to predict the fuel/cladding chemical interaction for carbide fuels.

Nitride fuels

A review of the properties of nitride fuels was recently published by Arai [4]. The chemical interaction between nitride fuels and the cladding material is similar to that one observed for carbide fuels: clad nitriding, slight reactions with fission products and formation of intermetallic compounds occur. The available data are more limited in the case of nitride fuel compared to carbides. Thermodynamic calculations have been performed to predict the chemical form of the different products [3].

Nitride fuels are usually specified to be single-phased mononitrides (U, Pu) N. No chemical interaction of stoichiometric (U,Pu)N or single-phased mononitride were observed with stainless steel. The sesquinitride phase (U,Pu)₂N₃ can form. In that case, a stainless steel clad can be nitrided. The reaction is as follows:



The N/(U+Pu) ratio is expected to increase with burn-up. But even at high burn-up, the compatibility of nitride fuels with stainless steel clad was observed.

The oxygen impurity plays a positive role as it stabilises the sesquinitride phase and thus reduces clad nitriding.

There is no modelling for nitride fuels clad chemical interaction. Only thermodynamic calculations were performed to predict the phases to be formed.

Metallic fuels

A review of metal fuel-cladding interaction was very recently published by Keiser [17]. Under irradiation, metallic fuels swell and enter in contact with the clad at ~1-2 at.% burn-up. Interdiffusion can then occur between fuel, fission product and cladding constituents.

Even if the interdiffusion process occurs under irradiation, thus deviates from thermodynamic equilibrium conditions, phase diagrams can be used to predict the nature of the phases to be formed during chemical interaction between fuel and cladding. The U-Pu-Zr-Fe system is of great interest to predict chemical interaction between (U,Pu,Zr) fuel and steel. Nakamura et al. [26] performed phase diagram calculations in this quaternary system in order to interpret the interdiffusion zones observed in diffusion couples U-Pu-Zr/ Fe-based cladding materials. From the chemical analysis of the interdiffusion zones, diffusion paths were proposed in the phase diagram to help the interpretation of the couple diffusion tests. The results show that at 800°C (accidental conditions), the interdiffusion zone is constituted of liquid and intermetallic compounds (Fe_xZr_y and Fe_xU_y).

For the U-Pu-Zr metallic fuels, the redistribution of fuel elements is a key issue to address to predict the fuel performance under irradiation. The redistribution of the

elements leads to the existence of three distinct zones: (i) a zircaloy-enriched central zone, (ii) a zircaloy-depleted and uranium-enriched intermediate zone, (iii) a slightly zircaloy-enriched zone at the periphery. The migration of the fuel elements is caused by the radial temperature gradient in the fuel. Kim et al. [19] developed a computer model to calculate zircaloy redistribution by solving diffusion equations using a simplified pseudo-binary phase diagram. Pu is considered as non-diffusing species. The one-dimensional continuity equation for zircaloy in cylindrical coordinates is solved. The input data for this model are: the phase diagram, diffusion coefficients, enthalpy of solution and effective heats of transport of zircaloy and uranium in the ternary alloy.

Kim's model [19] for fuel element redistribution was incorporated by Karahan and Buongiorno [16] in the FEAST code to predict the irradiation behaviour of U-Zr and U-Pu-Zr metallic fuel pins.

Minor actinides are foreseen to be added in the fuel. The redistribution of these elements and their possible chemical reaction with the cladding has to be studied.

Tests were also performed under irradiation. The results show that the fuel-clad chemical interaction leads to the formation of a reaction zone constituted of Fe, Ni, Cr (from the clad), U, Zr, Pu and lanthanide fission products (from the fuel). Pd and Ru are also observed in some cases. Low melting point alloy can form in the reaction zone. The experimental data show that the growth rate of the interaction layer is proportional to the square root of time. Thus the process is diffusion-controlled. A kinetics model has been incorporated in the FEAST code developed by Karahan and Buongiorno [16]. In the model, the clad wastage layer thickness is calculated versus time and temperature. The input data are the concentrations of lanthanide atoms in the fuel and the diffusion coefficient of lanthanides at fuel-clad interface. The diffusion coefficient data were fitted on experimental results. A similar model was used in FEAST to predict the liquid formation at the fuel-clad interface [16].

Conclusion and future challenges

The fuel-cladding chemical interaction for fuels for fast reactors depends on the nature of the fuel (oxide, carbide, nitride or metallic) and on the operating condition of the reactor. The first step consists of the modelling of the "irradiated fuel chemistry". The fuel chemistry is very complex due to the large number of elements to consider. It is generally performed by thermodynamic calculations based on simple models for the description of the different phases containing fuel, fission product elements and minor actinides. In a second step, the redistribution of these elements within the fuel along the radial temperature gradient has to be predicted. This type of calculation is performed in codes developed for oxide and metallic fuels (for example in the FEAST code). But the number of migrating constituents is generally limited. The chemical interaction between the fuel and the clad is generally treated using empirical equations that give the thickness of the wastage as a function of operating parameters. These equations are assessed on in-pile experimental results. The FEAST code uses a more sophisticated model that couple thermodynamics and kinetics and thus calculates the flux of the migrating species within the fuel and in the JOG layer. The fuel-cladding chemical interaction is a key issue for oxide and metallic fuels. The mechanisms are not already well understood in the case of the oxide fuels and thus need further development both on experiments and modelling.

References

- [1] Adroguer, B. et al. (2005), “Core loss during a severe accident (COLOSS),” *Nuclear Engineering and Design*, 235(2-4).173-198.
- [2] Agarwal R., V. Venugopal (2006), *Journal of Nuclear Materials*, 158, 122.
- [3] Arai Y. et al. (1994), *Journal of Nuclear Materials*, 210, 161.
- [4] Arai Y. (2012), “Nitride fuel”, Chapter 3.02, *Comprehensive Nuclear Materials*, published by R.J.M. Konings, Elsevier.
- [5] Dienst, W., P. Hofmann, D. Kerwin-Peck (1984), “Chemical interactions between UO₂ and zircaloy from 1000 to 2000°C”, *Nuclear Technology*, 65, 109.
- [6] Furuya H. et al. (1993), *Journal of Nuclear Materials*, 201, 46.
- [7] Hayward, P.J., I.M. George (1994), “Dissolution of UO₂ fuel by molten zircaloy-4, Part 1: Solubility from 2000 to 2200°C”, *Journal of Nuclear Materials*, 208, 35 (a).
- [8] Hayward, P.J., I.M. George (1994), “Dissolution of UO₂ fuel by molten zircaloy-4, Part 2: Phase Evolution during Dissolution and Cooling,” *Journal of Nuclear Materials*, 208, 43.
- [9] Hayward, P.J., I.M. George (1996), “Dissolution of UO₂ fuel by molten zircaloy-4, Part 3: Solubility from 2000 to 2500°C,” *Journal of Nuclear Materials*, 232.1(a).
- [10] Hayward, P.J., I.M. George (1996), “Dissolution of UO₂ fuel by molten zircaloy-4, Part 4: Phase Evolution during Dissolution and Cooling of 2000 to 2500°C Specimens,” *Journal of Nuclear Materials*, 232.13(b).
- [11] Hayward, P.J., I.M. George (1999), “Dissolution of ZrO₂ in molten zircaloy-4,” *Journal of Nuclear Materials*, 265.69-77(a).
- [12] Hayward, P.J., P. Hofmann, J. Stuckert, M.S. Veshchunov, A.V. Berdyshev (1999), *UO₂ Dissolution by Molten Zircaloy: New Experimental Results and Modelling*, FzK Report FZKA-6379 / INV-CIT-99-P029, (b), Karlsruhe, Germany.
- [13] Hofmann, P., H. Uetsuka, A.N. Wilhelm, E.A. Garcia (1988), “Dissolution of solid uo₂ by molten zircaloy and its modelling”, *IAEA/OECD International Symposium on Severe Accidents in Nuclear Power Plants*, Sorrento, Italy, 21-25 March 1988 (IAEA-SM-296/99), p. 3.
- [14] Hofmann, P., J. Stuckert, A. Miassoedov, M.S. Veshchunov, A.V. Berdyshev, A.V. Boldyrev (1999), *ZrO₂ Dissolution by Molten Zircaloy and Cladding Oxide Shell Failure: New Experimental Results and Modelling*, FzK Report FZKA-6383 /INV-CIT-98-P026, (in English).
- [15] Hutchings, W.G., H.E. Rosinger (1984), “The UO₂/Zircaloy interaction: A metallographic examination”, *Proc. ASM Metals Congress*, Detroit, IL.
- [16] Karahan A., J. Buongiorno (2010), *Journal of Nuclear Materials*, 396, 272.
- [17] Keiser D.D. (2012), “Metal fuel-cladding interaction”, Chapter 3.15 in *Comprehensive Nuclear Materials*, published by R.J.M. Konings, Elsevier.

- [18] Kim, K.Y., D.R. Olander (1988), “Dissolution of UO₂ by molten zircaloy,” *Journal of Nuclear Materials*, 154, 85.
- [19] Kim Y.S., S.L. Hayes, G.L. Hofman, A.M. Yacout (2006), *Journal of Nuclear Materials*, 359, 17.
- [20] Lassmann K. (1987), *Journal of Nuclear Materials*, 150, 10.
- [21] Maeda K. (2012), “Ceramic fuel-cladding interaction”, Chapter 3.16 in *Comprehensive Nuclear Materials*, published by R.J.M. Konings, Elsevier.
- [22] Mathews C.K. (1995), *Pure and Applied Chemistry*, 67, 1011.
- [23] Melis J-C., J-P. Piron, L. Roche, J. Truffert (1992), *Journal of Nuclear Materials*, 188, 303.
- [24] Melis J-C., J-P. Piron, L. Roche (1993), *Journal of Nuclear Materials*, 204, 188.
- [25] Mueller, K., A.V. Goryachev, V.P. Smirnov, A.M. Svyatkin, J. Stuckert, M.S. Veshchunov, A.V. Berdyshev (2004), *Simultaneous Dissolution of UO₂ and ZrO₂ by Molten Zircaloy. New Experiments and Modelling*, FzK/EU Report FZKA-6947/SAM-COLOSS-P-074, Jan 2004.
- [26] Nakamura, K., T. Ogata, M. Kurata (2005), *Journal of Physics and Chemistry of Solids*, 66, 643.
- [27] Nikolopoulos, P., P. Hofmann, D.K. Kerwin-Peck (1984), “Determination of the interfacial energy and work of adhesion in the UO₂/zircaloy-4 diffusion couple”, *Journal of Nuclear Materials*, 124, 106.
- [28] Olander, D.R. (1994), “Materials chemistry and transport modeling for severe accident analysis in light-water reactors, II: Gap processes and heat release”, *Nuclear Engineering and Design*, 148.273-292(b).
- [29] Olander, D.R. (1995), “Interpretation of laboratory crucible experiments on UO₂ dissolution by liquid uranium”, *Journal of Nuclear Materials*, 224, 254(a).
- [30] Olander, D.R. (1996), “Materials chemistry and transport modeling for severe accident analyses in light-water reactors III. Fuel dissolution by molten cladding”, *Nuclear Engineering and Design*, 162, 257-270.
- [31] Olander, D.R. (1995), “Thermodynamics and transport processes in reactor fuel”, *Pure and Applied Chemistry*, Vol. 67, No. 6, pp. 1003-1010, 1995(b).
- [32] Ozawa T., T. Abe (2006), *Nuclear Technology*, 156, 39.
- [33] Pulham R.J., M.W. Richards (1990), *Journal of Nuclear Materials*, 172.2, 206.
- [34] Ratier J-L., M.F. Boidron Boussard, J-P. Piron, M. Tourasse M. (1992), “Fast neutron cladding corrosion”, *Proceedings in: Eurocorr 92 Conference*, Espoo, Finland.
- [35] Rosinger, H.E., R.K. Rondeau, K. Demoline, K.J. Ross (1985), “The Interaction and dissolution of solid UO₂ by molten zircaloy-4 cladding in an inert atmosphere or steam”, *6th Annual Conference of the Canadian Nuclear Society*, Ottawa, Ontario, p. 16.33.
- [36] Sengupta A.K. et al. (2012), “Carbide fuel”, Chapter 3.03 in *Comprehensive Nuclear Materials*, published by R.J.M. Konings, Elsevier.

- [37] Stuckert, J., A. Miassoedov, P.J. Hayward, P. Hofmann, M. Veshchunov (2002), “ZrO₂ and UO₂ dissolution by molten zircaloy”, *Proceedings of the International Conference Nuclear Energy in Central Europe 2002*, Kranjska Gora, Slovenia, p.8.
- [38] Tourasse, M., M. Boidron, B. Pasquet (1992), *Journal of Nuclear Materials*, 188, 49.
- [39] Veshchunov, M.S., P. Hofmann, A.V. Berdyshev (1996), “Critical evaluation of uranium dioxide dissolution by molten zircaloy in different crucible Tests,” *Journal of Nuclear Materials*, 231.1.

Chapter 4.

Fuel-coolant chemical interaction

B.J. Lewis, F.C. Iglesias

University of Ontario Institute of Technology, Canada

Abstract

A thermodynamic analysis of the uranium-oxygen system is used to determine the equilibrium state of oxidised fuel as a function of the atmospheric oxygen potential (i.e., hydrogen-to-steam partial pressure ratio) as required for the development of fuel-oxidation kinetics models. Annealing experiments have been performed to investigate the oxidation kinetics of fuel in a steam atmosphere at high temperature as well as the fuel-reduction kinetics. Mathematical treatments of these phenomena, coupled with heat and mass transport theory, can be used to describe the oxidation behaviour of uranium dioxide fuel in operating defective rods for water-cooled nuclear reactors. Model predictions are consistent with the observed oxygen-to-metal ratios seen in commercial defective rods as measured post-test using a coulometric titration technique. Such models can be further extended to higher temperature using a phase-field approach to simulate centreline melting in defective fuel. Fuel oxidation effects in air and water at low temperature are also discussed.

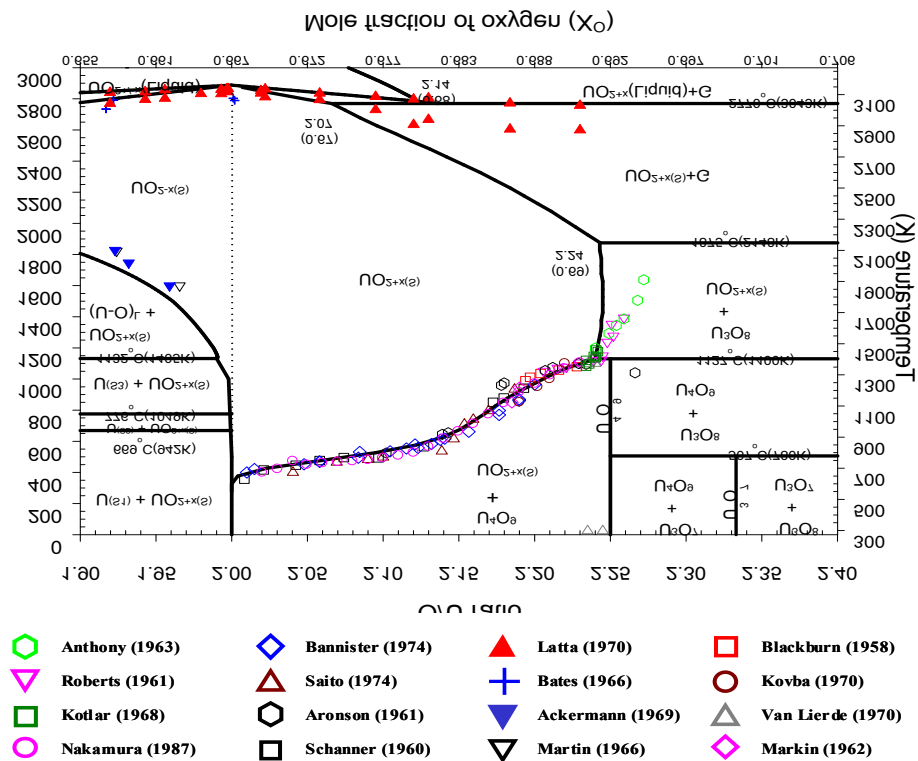
Introduction

Fuel oxidation is an important phenomenon which can affect the nuclear fuel performance of defective rods during normal reactor operations, as well as impact fuel volatilisation and fission product release behaviour during reactor accident conditions. In addition, it can influence the transfer and storage of defective fuel in the fuel bays. It also has important consequences in the long-term storage of spent fuel.

For instance, with the rare occurrence of a fuel failure, the cladding no longer provides a barrier between the fuel and primary coolant so that coolant can contact the fuel, permitting oxidation of the fuel. The presence of steam in the fuel-to-clad gap and the consequential effect of fuel oxidation will affect both the thermal performance of the fuel rod and the associated fission product release into the primary coolant [34]. The rod

performance is directly affected by fuel oxidation as a result of: (i) a degraded fuel thermal conductivity with continued oxidation, and (ii) a lower incipient melting temperature for the hyperstoichiometric fuel [56,57,36,37]. Fuel restructuring (i.e., columnar grain growth) may also be greater in defective fuel because of the higher fuel temperatures and the possibility of a higher partial pressure of UO_3 in the hyperstoichiometric fuel [26]. Fuel loss from defective fuel can also result from grain boundary oxidation under the defect site with coolant erosion [35]. The release behaviour of volatile fission products can be further enhanced with a greater mobility in the hyperstoichiometric fuel [46,47,28]. The oxygen potential also affects the chemical form of the fission products that determines their respective volatility [14,33,39]. Hence, knowledge of the oxidation state of the fuel is important in order to determine the thermomechanical performance of defective fuel and the fission product release behaviour.

Figure 1. Calculated phase diagram for the U-O system, highlighting the UO_{2+x} region, shown against experimental phase boundary determinations



U-O binary phase diagram analysis

A thermodynamic model of the equilibrium state of the oxidised fuel is required as a boundary condition for use in a kinetics model. A thermodynamic treatment of the U-O system (Figure 1) yields an expression for the oxygen partial pressure p_{O_2} in the fuel over the entire range of UO_{2+x} (652 to 3 100 K) [23]:

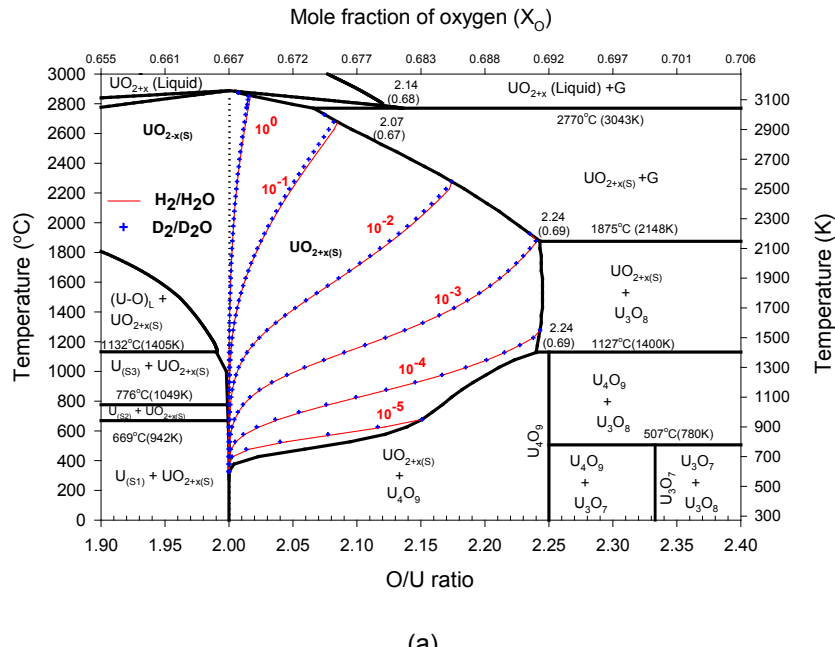
$$\log p_{O_2} = -11414.6 - 0.249 T + 1.096 \times 10^{-5} T^2 + 3103.86 \log T - 8617063 T^{1.1} + 3.118607 \times 10^8 T^{-2} + 3545460 (\log T) / T - 2 \log ((1-x_e) / x_e) + 1.832 x_e + 32.15 x_e^2 - 150.31 x_e^3 + 503.02 x_e^4 \quad (1)$$

where T is the temperature in K and x_e is the stoichiometry deviation. The placement of the phase boundary in Figure 1 is reasonable agreement with the published thermodynamic values for U_3O_8 [11]. An expression relating the hydrogen-to-steam partial pressure ratio, temperature T (in K) and equilibrium stoichiometric deviation x_e follows from this thermodynamic analysis:

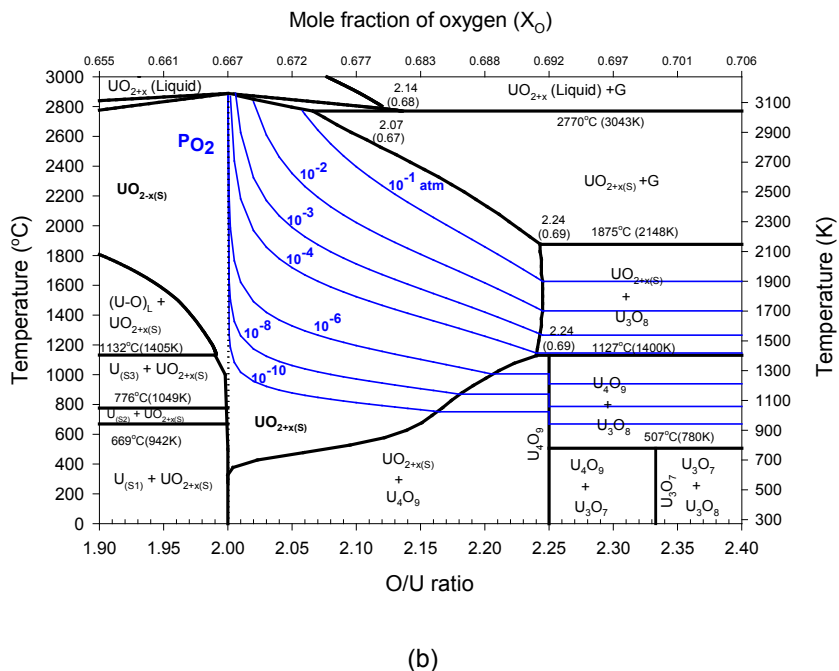
$$\begin{aligned} \log\left(\frac{p_{H_2}}{p_{H_2O}}\right) = & 5706.8 + 0.1245T - 5.482 \times 10^{-6} T^2 + \frac{4296016}{T} - 1550.95 \log(T) \\ & - \frac{1772730 \log(T)}{T} - \frac{155930360}{T^2} + \log\left(\frac{1-x_e}{x_e}\right) - 0.9158x_e - 16.08x_e^2 + 75.15x_e^3 - 251.51x_e^4 \end{aligned} \quad (2)$$

Equation 2 is in excellent agreement with the thermodynamic treatments of [42] and [8]. A similar analysis can be performed for a heavy water system as shown in Figure 2(a) and (b) [23], which indicates that there is very little difference in the estimate of the equilibrium stoichiometry deviation between light and heavy water. Moreover, burn-up effects can be neglected since the degree of oxygen binding to the fuel is small as demonstrated with a multi-component Gibbs energy minimisation calculation considering the addition of fission products and actinides that are produced at typical fuel burn-ups [70].

Figure 2. Calculated U-O binary phase diagram, (a) highlighting the UO_{2+x} region, with isobaric lines of oxygen partial pressure, and (b) lines of equivalent H_2/H_2O and comparable points of constant D_2/D_2O ratios



(a)



(b)

Fuel oxidation kinetics

Self-diffusion studies for UO_2 indicate that the anionic mobility exceeds that of the cations by many orders of magnitude so that changes in the fuel stoichiometry are a result of oxygen migration in the solid fuel [45]. The kinetics of the fuel oxidation process in steam has been studied in many out-of-pile experiments. In the temperature range 1 158 to 2 108 K, it was suggested that oxidation is controlled by oxygen diffusion through the solid fuel matrix [7]. However, it was subsequently shown that this process was controlled by a decomposition reaction of the H_2O at the solid/gas interface [10]:



Here O (solid) is the oxygen absorbed by the solid, which quickly converts to the stable ionic form O^{2-} by picking up electrons from the U^{4+} ions and converting this metal cation to a higher oxidation state. For electrical neutrality, the addition of one O^{2-} ion requires a change in the uranium valence state where either two U^{4+} ions must be converted to U^{5+} or one U^{4+} ion to U^{6+} . Excess oxygen in the UO_{2+x} is accommodated in interstitial sites of the fluorite structure with the formation of Frenkel defects on the oxygen-ion sublattice of the crystal [54].

For the surface-exchange process, an expression for the kinetics of oxidation of UO_2 in CO/CO_2 atmospheres was proposed [7]:

$$\frac{dx}{dt} = \left(\frac{S}{V} \right) \alpha p_{\text{H}_2\text{O}}^m (x_e - x(t)) \quad (4)$$

In this “phenomenological” type of model, α is the surface-exchange coefficient of oxygen (cm s^{-1}), x_e is the equilibrium stoichiometry deviation determined by the oxygen potential in the gas phase, $x(t)$ is the deviation from stoichiometry in UO_{2+x} at time t , and S/V is the surface-to-volume ratio of the solid (cm^{-1}). The surface-exchange coefficient

has been determined in the temperature range of 1 073 to 1 873 K for pure steam and in steam/argon/hydrogen mixtures at atmospheric pressure (see Table 1).

In the original Carter-Lay model, the exponent m in Equation 4 was assumed to be unity, while for experiments at atmospheric pressure no exponential dependence could be deduced. However, in more recent experiments in H₂O/Ar/H₂-mixtures from 1 273 to 1 623 K (H₂O partial pressure of 0.25 to 1 atm) and steam-helium mixtures (H₂O partial pressure of 0.01 to 0.03 atm), m is equal to 0.5 implying an approximate square-root dependence on the H₂O partial pressure [32,1]. A thermogravimetric technique was used to investigate UO₂ oxidation in defective light water reactor rods at much higher pressures of 7 and 70 atm in pure steam in the lower-temperature range of 773 to 873 K in which a similar dependence on the steam pressure was suggested [57]. To explain this pressure dependence, more mechanistic treatments have been suggested employing adsorption theory with Langmuir or Freundlich isotherms to fundamentally describe the surface-exchange mechanism [1,5,57,13,16,36].

Table 1. Surface-exchange coefficient for the phenomenological model for steam oxidation of UO₂ obtained in various experiments

Work	Surface-exchange coefficient ^(a)	
	Activation energy Q (K)	Pre-exponential factor α_0 (cm s ⁻¹)
(Cox, 1986)	23 500	36.5
Bittel's results reanalyzed by (Cox, 1986)] [12]	19 900	6.96
(Abrefah, 1994) (single crystal – pure steam)]	22 350 ± 1540	75.2 ± 2.8
(Abrefah, 1994) (polycrystal – pure steam)]	22 080 ± 1330	45.6 ± 2.5
(Abrefah, 1994) (polycrystal – steam/Ar/H ₂ mixtures)]	20 000 ± 2900	16.6 ± 6.4

a. $\alpha = \alpha_0 \exp(-Q/T(K))$ (cm s⁻¹).

As observed in the annealing experiments at the University of California – Berkeley (UCB) with polycrystalline and single crystal UO₂ specimens at 1 273 to 1 623 K, the oxygen-to-uranium (O/U) ratio increases with continued fuel oxidation in steam at a given temperature but decreases more rapidly when the gas stream is switched from pure steam to 95%-Ar/5%-H₂. The initial rate of fuel oxidation is seen to correlate roughly with the temperature dependence of the partial pressure of atomic oxygen (p_o) (in atm) in the atmosphere [5]:

$$p_o = p_{H_2O}^{1/3} 10^{\left[\frac{A}{T} + B \right]} \quad (\text{pure steam}) \quad (5)$$

where p_{H_2O} is the steam partial pressure (= 1 atm in the UCB experiments), T is the temperature (K), $A = -1.756 \times 10^4$ and $B = 4.289$. A dependence of the initial oxidation rate on the atomic oxygen partial pressure is consistent with a requirement for atomic oxygen at the surface via the reaction in Equation 3. It is also interesting to note that the oxygen partial pressure depends directly on the steam partial pressure. As such, a more mechanistic approach can be adopted from mass-transfer theory (compare with Equation 4):

$$c_U \frac{dx}{dt} = \left(\frac{S}{V} \right) \alpha_{ox} \{ p_o - p_o(x) \} \quad (6)$$

where $c_U = 0.041 \text{ mol cm}^{-3}$ is the molar density of uranium in UO_2 , S/V is the surface-to-volume ratio of the solid (cm^{-1}) and $\alpha_{ox}(T)$ is a mass transfer coefficient ($\text{mol cm}^{-2} \text{ s}^{-1} \text{ atm}^{-1}$) that accounts for the effect of adsorption/desorption of atomic oxygen on the fuel surface. The $p_o(x)$ is the partial pressure (in atm) of atomic oxygen in the fuel for the UO_{2+x} phase at temperature in Figure 2. A fitting of the mechanistic model in Equation 6 to data from the UCB experiments with thin disk samples yields the expression: $\alpha_{ox} = 3.532 \times 10^{-6} \exp \{19700/T(\text{K})\} \text{ mol cm}^{-2} \text{ s}^{-1} \text{ atm}^{-1}$. This model in fact yields a similar result to the empirical representation of Equation 4.

For the surface-exchange model of Equation 4, the following reaction rate in moles O (or H_2) $\text{m}^{-2} \text{ s}^{-1}$ for fuel oxidation R_f^{ox} (i.e., when $x < x_e$) results:

$$R_f^{ox} = \left(\frac{V}{S} \right) c_U \frac{dx}{dt} = c_U \alpha \sqrt{(1-q)p_t} (x - x_e), \quad \text{for } x < x_e \quad (7)$$

where q is the hydrogen gas mole fraction and p_t is the total system pressure. The faster kinetics for fuel reduction seen in the UCB experiments suggest a different rate-determining mechanism, which may be controlled by either solid-state diffusion of oxygen through the solid, hydrogen mass transport through the surface-boundary layer or chemical reaction/mass transfer at the fuel surface [1]. For instance, for a rate-controlling process of simple oxygen diffusion through a thin disk of thickness l_e , the average stoichiometry deviation in the fuel specimen as a function of time t follows:

$$\frac{\bar{x}}{x_o} = \frac{8}{\pi^2} \sum_{n=0}^{\infty} \frac{e^{-(2n+1)^2 \pi^2 D t / l_e^2}}{(2n+1)^2} \quad (8)$$

where D is the chemical diffusion coefficient for interstitial oxygen diffusion. However, the quantity (\bar{x}/x_o) predicted with Equation 8 for the UCB experiment P/S-623 C (with $l_e = 7 \times 10^{-4} \text{ m}$) falls off considerably more rapidly as compared to the data in Figure 3 using the diffusion coefficient in [49] at 1 623 K. This result indicates that interstitial diffusion alone is not rate-limiting. Alternatively, one can consider a combined diffusion/mass transfer model analogous to the Newton's law of cooling [9] where the average stoichiometry deviation in the slab is:

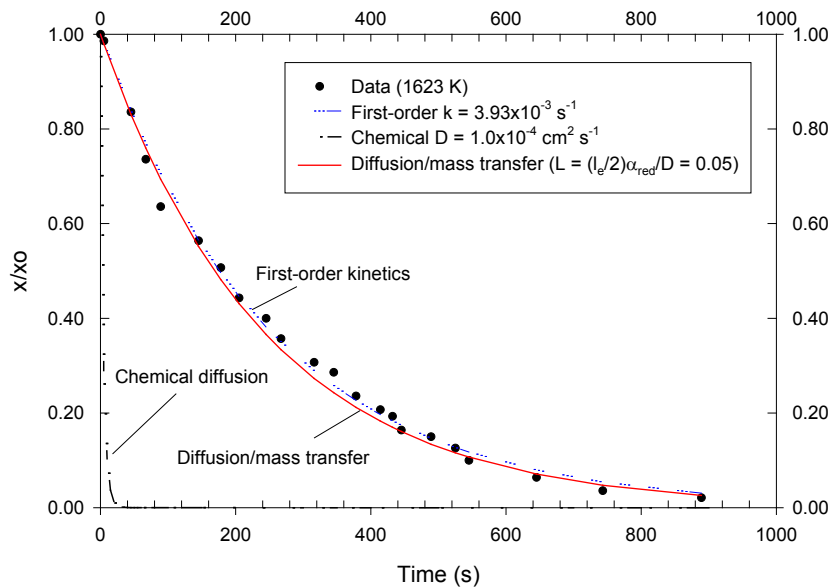
$$\frac{\bar{x}}{x_o} = \sum_{n=1}^{\infty} \frac{2L^2}{\alpha_n^2 [L(L+1) + \alpha_n^2]} e^{-\alpha_n^2 T} \quad (9)$$

Here the dimensionless variables are defined as $L = (l_e/2)\alpha_{red}/D$ and $T = Dt/(l_e/2)^2$, α_{red} is an effective rate constant (cm s^{-1}) and α_n ($n = 1, 2, \dots$) are the positive roots of $\alpha \tan \alpha = L$. As seen in Figure 3, the combined diffusion/mass transfer model is in excellent agreement with the observed data for a fitted value of $L = 0.05$ with a chemical diffusion coefficient of $D = 1.0 \times 10^{-4} \text{ cm}^2 \text{ s}^{-1}$. Interestingly, a first-order kinetic model is further suggested by the form of Equation 9, where the higher-order harmonic terms rapidly die out and the pre-exponential term is approximately equal to unity:

$$\bar{x} = x_o e^{-kt} \quad (10)$$

As expected, a fitted parameter of $k = 3.93 \times 10^{-3} \text{ s}^{-1}$ for the first-order kinetics model also yields excellent agreement with the UCB data.

Figure 3. Comparison of fuel reduction models based on chemical diffusion, diffusion/mass transfer and first-order kinetics versus UCB data from experiment P/S-623C in an Ar/H₂ atmosphere



Fuel oxidation kinetics in defective fuel

Modelling of the interrelated processes for fuel oxidation and sheath oxidation/hydriding is a complicated problem. Previous models have been proposed to describe the fuel oxidation behaviour in defective fuel. A one-dimensional model was initially developed to estimate the oxygen-to-uranium (O/U) ratio of the radial profile by assuming a constant hydrogen/steam ratio [34,36]. Similarly, in 1997, the UCB developed a semi-mechanistic model, which coupled steam/hydrogen reactions in the fuel-to-sheath gap to the oxidation state of the fuel sample, where the fuel oxidation reaction was only assumed to occur at the fuel surface [58]. This model was extended further with the development of a one-dimensional treatment to predict non-stoichiometry in defective fuel by considering fuel oxidation with steam and hydrogen/steam transport within the fuel with a fixed hydrogen/steam ratio in the gap. Likhanskii [40] considered sheath and fuel oxidation, with coupled heat transfer and oxygen diffusion in the fuel, but neglected hydrogen/steam transport along the gap or within the fuel cracks. Although the effect of fuel microstructure and temperature have been investigated in several in-reactor fuel defect experiments by [27] and [41], no quantitative correlation to the oxidation state of the fuel was proposed. A more sophisticated treatment, however, was developed by [23] to account for the various coupled processes:

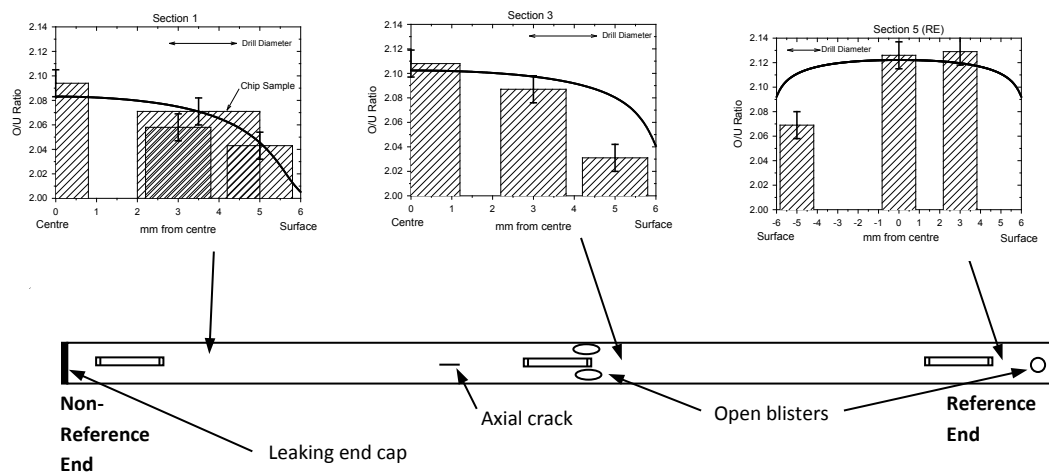
- hydrogen/steam gas-phase transport along the fuel-to-clad gap to account for the oxygen potential in the gap, including a steam source at the defect site with hydrogen production from the fuel and sheath oxidation reactions;
- hydrogen/steam transport within the cracks of the fuel pellet;

- interstitial oxygen diffusion in the fuel matrix accounting for normal (concentration-driven) diffusion and diffusion in a temperature gradient (Soret effect);
- heat conduction in the solid to determine the temperature distribution in the fuel element (which accounts for a feedback effect due to a reduced thermal conductivity in the hyperstoichiometric fuel).

A time-dependent treatment is needed for such an analysis since the ratio of the thermal diffusivity-to-mass diffusivity, which characterises the characteristic times of heat and oxygen diffusion, can play an important role in the transient behaviour of fuel that has defected under sudden changes in operating conditions [60]. A three-dimensional coupled simulation that takes into account thermomechanics, heat conduction and oxygen diffusion in nuclear fuel rods has been incorporated into the Bison fuel performance code, for instance, which specifically accounts for interstitial oxygen diffusion [52].

A typical comparison of the O/U prediction using the fuel oxidation model of Higgs et al. with coulometric titration measurements of the oxygen-to-metal (O/M) ratio from a commercial defective fuel element is shown in Figure 4.

Figure 4. Model predictions and O/M measurements for element X5



Low-temperature effects of fuel oxidation behaviour

The presence of oxides higher than UO_{2+x} are often observed in the post-irradiation examination of defective fuel. Enhanced oxidation kinetics may occur from coolant radiolysis processes. If the fuel cool-down is not too fast, higher-oxide phases could also arise during reactor shutdown as a result of U_4O_9 precipitation [78]. In addition, continued fuel oxidation can also result from out-reactor effects.

In-reactor radiolysis effects

Grain-boundary oxidation has been observed in defective fuel under the defect site(s) and in the fuel crack regions of defective rods. Steam oxidation to higher oxide phases is

precluded on thermodynamic grounds with the presence of hydrogen (see Figure 2 (a)). However, fuel oxidation could be enhanced by coolant radiolysis with the formation of the highly-reactive hydrogen peroxide species. In fact, this reactive metastable species can equilibrate with the fuel and oxidise it even in the presence of hydrogen [43]. However, hydrogen liberated in the H_2O_2 oxidation reaction could also neutralise the tendency of the oxidising counterparts to increase the stoichiometry of the fuel. Energy-deposition calculations also suggest that radiolysis does not substantially enhance the fuel oxidation kinetics at high pressure in operating defective rods [36]. At higher temperatures, radiolytic effects should become insignificant in comparison to thermal effects as the thermal reactions and the recombination of transient species become faster. It is therefore expected that any radiolysis-enhanced oxidation would be limited and localised at or near the fuel surface and close to the defect site [36,23].

$U_4O_{9,y}$ Nonstoichiometry

The thermodynamic treatment in Figure 2 is in agreement with a large body of experimental data. The calculated U-O phase diagram, as well as a recent evaluation of this system [11], takes the U_4O_9 phase to be stoichiometric as a reasonable approximation. Many investigators, however, have shown that U_4O_9 is a narrowly non-stoichiometric phase ($U_4O_{9,y}$), where three phases exist: α - $U_4O_{9,y}$ (below $\sim 80^\circ C$), β - $U_4O_{9,y}$ (between $\sim 80^\circ C$ and $\sim 550^\circ C$) and γ - $U_4O_{9,y}$ (above $\sim 550^\circ C$) [51]. In-situ neutron diffraction experiments at the Los Alamos Neutron Science Center (LANSCE) investigated the U_4O_9 non-stoichiometry from room temperature up to a maximum of $1\ 150^\circ C$ [24]. Rietveld refinement of the diffraction patterns indicated $U_4O_{9,y}$, (where y is 0.064), which provides evidence that U_4O_9 has a non-stoichiometric field at elevated temperature [44]. Although the U_4O_9 phase is slightly hypo-stoichiometric, this observation does not significantly affect the thermodynamic analysis of Figure 1.

If the UO_{2+x} is rapidly quenched from high temperatures, a single phase UO_{2+x} can be “frozen in” when there is little time for diffusion or other processes of structural rearrangement of ions to take place [19]. However, as observed in the LANSCE experiment, the $U_4O_{9,y}$ was observed to precipitate out of the UO_{2+x} at a relatively low temperature (200 to $400^\circ C$), where this system approached thermodynamic phase equilibrium in less than one hour.

Out-reactor effects

Fuel oxidation can occur post-irradiation from: (i) low-temperature oxidation in air with possible fuel transfer operations and (ii) long-term storage of defective fuel in the fuel bays in which there is dissolved oxygen in the bay water.

(i) Low-temperature oxidation effects in air

The air oxidation of UO_2 proceeds via a two-step reaction [6]:



This process has been studied because of its importance to dry storage and disposal of used nuclear fuel [4,25,62,53,20-22] [17,74,75,63-65].

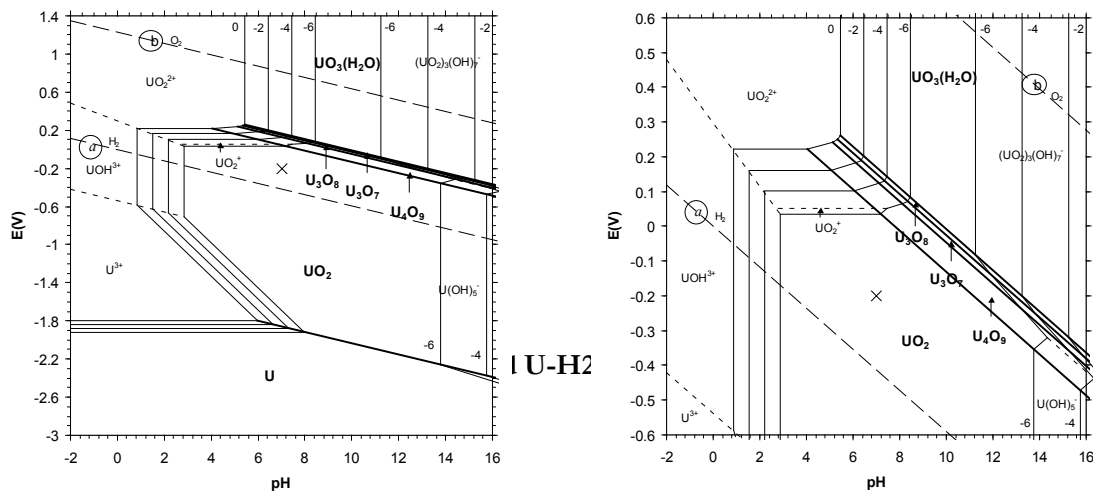
The “intermediate” phase(s), U_4O_9/U_3O_8 , forms as a discrete layer on the surface of the UO_2 sample that thickens with time. Since the reaction rate is limited by oxygen

diffusion through the surface layer, this process has been modelled as a moving-boundary problem [4,25,17]. In the second step of the reaction in Equation 11, grain-boundary diffusion is relatively rapid compared to the rate of U_3O_8 formation since three-dimensional bulk formation of U_3O_8 will be slower than unhindered oxidation along the surface [48]. Enhanced fuel oxidation may also occur due to the production of nitrogen oxides formed by radiolysis of air [48]. The nucleation-and-growth mechanism for U_3O_8 formation has been described by [48]. Higher-oxide formation (post-shutdown) is not an important consideration during normal refuelling operations because of a limited time in air at low temperature [31]. With irradiated fuel, water is also a potential source of radiolytic oxidation products; however, moisture has less of an effect on irradiated fuel samples (at relative humidity (RH)<33%) [63]. At RH <40%, the mechanisms are the same as that for dry oxidation, yielding the bulk products shown in Equation 11 [68]. In aerated water (i.e., RH >40%), mixtures of U_3O_8 and dehydrated schoepite (DS) have been observed [65,68,69,67,66]. High-moisture (100% RH) limited-air tests on irradiated CANDU fuel at 150°C further suggest that moisture enhances the extent of grain boundary oxidation [18].

(ii) Low-temperature oxidation effects in water (fuel bay storage)

Spent defective Candu fuel bundles, for instance, may be stored for long periods of time (i.e., at least several years) in water bays at ~30°C. The water bays are oxygenated since they are open to the air surface. Experiments conducted in a closed autoclave with fresh fuel specimens, i.e., in aerated water for ~20 d at ~200°C, have indicated that fuel oxidation can occur via: (i) solid-state diffusion to U_3O_7 (similar to dry oxidation as described above), (ii) oxidative dissolution and precipitation of U (VI) as $\sim(\text{UO}_3)\cdot0.8\text{H}_2\text{O}$ and (iii) back-reduction of dissolved U(VI) on the $\text{UO}_2/\text{U}_3\text{O}_7$ surface to form U_3O_8 [69]. These species are also consistent with a Pourbaix analysis of Redox potential E versus pH in Figure 5 [38], which shows the dissolution/precipitation product of UO_3 (H_2O). Corrosion experiments with fragments taken from irradiated boiling water reactor (BWR) fuel pellets (~34 $\text{GWD}\cdot(\text{tU})^{-1}$) that were conducted at 340°C and 15 MPa for up to ~50 hours indicated the occurrence of microcracks along the grain boundaries due to preferential U_4O_9 formation (i.e., in water with more than several ppm of dissolved oxygen) [72].

The contribution of out-reactor oxidation in fuel bays is generally small compared to in-reactor oxidation of defective fuel [23].

Figure 5. FACT generated U-H₂O Pourbaix diagram at 298.15 K

Impact of radiolysis of water on the oxidative dissolution of UO₂

Studies have been performed in the framework of the PRECCI programme to assess the impact of radiolysis of water on the oxidative dissolution of spent fuel. Indeed, for a potential performance assessment of direct disposal of spent fuel in a nuclear waste repository, the chemical reactions between the fuel and possibly intruding water (normal scenario) must be understood and the resulting radionuclide release quantified. It is important to emphasise that although uranium is sparingly soluble ($\approx 10^{-9} \text{ mol}\cdot\text{L}^{-1}$) under reducing conditions (-200 mV/ESH) similar to those encountered in a repository site (European concepts – granitic or clayey site), its solubility can increase significantly at the UO₂/water interface because of the very long-lasting α irradiation field. Alpha radiolysis of the water can result in oxidising conditions at the UO₂/water interface (redox disequilibrium with the environment) and accelerate the dissolution of the spent fuel matrix. As leaching experiments with spent nuclear fuel cannot specifically address the effects of α radiation on alteration (strong $\beta\gamma$ irradiation predominates for more than a hundred years), leaching experiments were performed under different conditions with UO₂ fuel pellets doped with alpha-emitters (^{238/239}Pu). These materials simulating the radiation field of spent fuel of various ages were synthesised in the framework of the PRECCI project [50] but also in the framework of European projects (SFS project) [59]. Results show that the effects of alpha radiolysis are highly dependent on environmental conditions. In simple systems, there is a specific alpha activity threshold between two behaviour patterns for uranium release in solution. Either the uranium release increases because radiolysis creates oxidising conditions in the homogeneous solution accompanied by higher uranium solubility, or the release remains constant as the uranium solubility limit is quickly reached under less oxidising conditions. The steady-state concentration can then vary depending on the phase present at the interface: apparently UO₂(xH₂O) for the lowest activities, if the sample preparation protocol successfully restores the surface stoichiometry, otherwise U₄O₉ or U₃O₇. The threshold value lies between 18 and 33 MBq·gUO₂⁻¹ in a carbonate solution ($10^{-3} \text{ mol}\cdot\text{L}^{-1}$) under anoxic conditions.

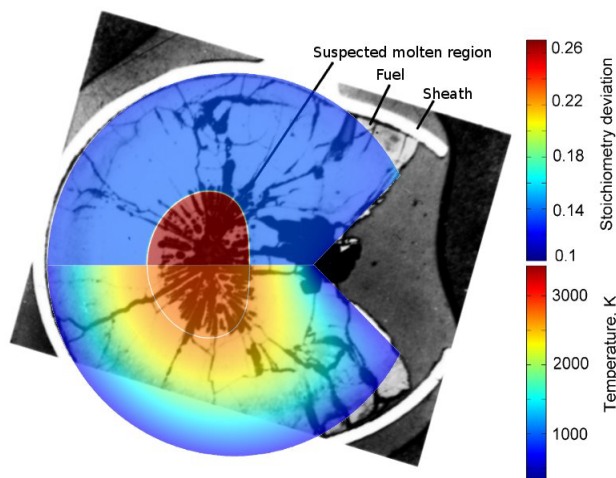
($O_2 < 0.1$ ppm). This threshold depends on the environmental conditions [71]. In contrast to simple systems (pure water), no significant activity dependence is observed for uranium concentrations in the presence of electroactive species like hydrogen or iron provided by the environment. To conclude the effect of alpha, radiolysis is expected to be negligible under geological disposal given the low alpha flux and the presence of electroactive species in the environment.

Phase-field modelling of incipient melting behaviour in defective fuel

With steam penetration into the fuel-to-sheath gap of defective rods, the thermal performance may be affected due to a reduced gap heat transfer coefficient and the possibility of fuel oxidation. In particular, oxidised fuel exhibits a reduced thermal conductivity in addition to a lower incipient melting point, thus lowering the power rating for which fuel melting may occur. Transient analysis codes such as ELOCA, TRANSURANUS, and SCDAP/RELAP often employ simplifying assumptions in regards to their assessment of fuel melting phenomena [61,3,30,73].

Hyperstoichiometric UO_{2+x} melts non-congruently, implying the oxygen solubility in the solid and liquid may differ and depend on the melting temperature. Melting will therefore redistribute oxygen [29], where, for instance, enrichment of oxygen in the previously molten region of UO_{2+x} has been observed [2]. A phase-field approach developed from the Theory of Irreversible Processes has been used to describe molten fuel behaviour in defective fuel rods containing oxidised fuel [76,77]. The heat and mass fluxes involve Fourier and Fickian diffusion, respectively, that are coupled through Onsager reciprocal relations [15].

Figure 6. Simulation result compared with metallography of an irradiated element



Top and bottom scales show the degree of oxidation and the temperature, respectively.

A phase-field model has in fact been applied to the analysis of a high-powered defected Candu fuel element that was severely hydrided [35,76]. The results of the simulation shown in Figure 6 overlap with the metallographic post-irradiation examination, showing the distribution profile with the oxygen and fuel temperature in the

upper and lower half of the diagram, respectively. The extent of the molten zone is depicted by the white contour line derived from the phase field analysis. Interestingly, this work shows that centreline melting is a self-regulating process since the formation of a liquid reduces the potential for more liquid to form due to the non-congruent phase change. In particular, the difference in oxygen concentration between the solidus and liquidus lines on the O-U binary phase diagram shows an enrichment of oxygen in the liquid so that the remaining solid is reduced in oxygen content, which raises the local melting temperature and increases the thermal conductivity of the solid.

References

- [1] Abrefah, J. et al. (1994), "High temperature oxidation of UO_2 in steam-hydrogen mixtures", *Journal of Nuclear Materials*, 208, 98.
- [2] Adamson, M.G., R.F.A. Carney (1974), "Mechanistic study of oxygen thermal diffusion in hyperstoichiometric urania and urania-plutonia solid solutions", *Journal of Nuclear Materials*, 54, 121.
- [3] Allison C.M. et al. (1985), *Draft Preliminary Report for Comment: SCDAP/MOD1 Theory and Models*, Idaho National Engineering Laboratory informal report.
- [4] Aronson, S. et al. (1957), "Kinetic study of the oxidation of uranium oxide", *Journal of Chemical Physics*, 27, 137.
- [5] Bale, C.W. et al. (1995), *Facility for the Analysis of Chemical Thermodynamics*, McGill University and École Polytechnique.
- [6] Belle, J. (1961), *Uranium Dioxide: Properties and Nuclear Applications*, Naval Reactors, Division of Reactor Development, USAEC.
- [7] Bittel, J.T. et al. (1968), *Journal of the American Ceramic Society*, 52(8).446.
- [8] Blackburn, P.E. (1973), "Oxygen pressures over fast breeder reactor fuel (I), A model for $\text{UO}_{2\pm x}$ ", *Journal of Nuclear Materials*, 46, 244-252.
- [9] Carslaw, H.S., J.C. Jaeger (1980), *Conduction of Heat in Solids*, Second Edition, Oxford University Press, Oxford, UK.
- [10] Carter, R.E., K.W. Lay (1970), *Journal of Nuclear Materials*, 36, 77.
- [11] Chevalier, P.-Y. et al. (2002), "Progress in the thermodynamic modelling of the U-O binary system", *Journal of Nuclear Materials*, 303, 1-28.
- [12] Cox, D.S. et al. (1986), "Oxidation of UO_2 in air and steam with relevance to fission product releases", *Proc. Symp. on Chemical Phenomena Associated with Radioactivity Releases during Severe Nuclear Plant Accidents*, NUREG/CP-0078, Anaheim, CA, 1986, pp. 2-35 to 2-49, US Nuclear Regulatory Commission.
- [13] Cox, D.S. et al. (1990), "High temperature oxidation behaviour of UO_2 in air and steam", *Proc. Int. Symp. on High-Temperature Oxidation and Sulphidation Process*, Hamilton, Ontario, Canada.
- [14] Cubicotti, D. (1981), "A model for release of fission gases and volatile fission products from irradiated UO_2 in steam environment", *Nuclear Technology*, 53, 5-7.

- [15] De Groot, S.R., P. Mazur (1984), *Non-equilibrium Thermodynamics*, General Publishing Company, Ltd., Toronto, Canada.
- [16] Dobrov, B.V. et al. (1998), “Kinetics of UO₂ oxidation in steam atmosphere”, *Journal of Nuclear Materials*, 255, 59.
- [17] Einziger, R.E., R.E. Woodley (1987), “Predicting spent fuel oxidation states in a tuff repository”, *Proc. Workshop on Chemical Reactivity of Oxide Fuel and Fission Product Release*, Vol. 2, Berkeley Nuclear Laboratories, Berkeley, Gloucestershire, UK.
- [18] Frost, C.R., K.M. Wasywich (1987), “UO₂ oxidation in air at 50°C to 400°C and the implications for CANDU irradiated fuel dry storage”, *Proc. Workshop on Chemical Reactivity of Oxide Fuel and Fission Product Release*, Vol. 2, Berkeley Nuclear Laboratories, Berkeley, Gloucestershire, UK.
- [19] Grønvold, F. (1955), “High temperature X-ray study of uranium oxides in the UO₂-U₃O₈ region”, *Journal of Inorganic and Nuclear Chemistry*, 1, 357.
- [20] Hastings, I.J. et al. (1985), “Postirradiation dimensional stability and fission product behavior of deliberately defected UO₂ fuel at 200 and 400°C”, *Nuclear Technology*, 70, 268(a).
- [21] Hastings, I.J. et al. (1985), “Postirradiation behavior of naturally and artificially defected UO₂ fuel elements at 250°C in air”, *Nuclear Technology*, 68, 418(b).
- [22] Hastings, I.J. et al. (1985), “Postirradiation behavior of UO₂ fuel II: Fragments at 175 to 275°C in air”, *Nuclear Technology*, 68, 40(c).
- [23] Higgs, J.D. et al. (2007), “A conceptual model for the fuel oxidation of defective fuel”, *Journal of Nuclear Materials*, 366, 99-128 (a).
- [24] Higgs, J.D. et al. (2007), “Kinetics of precipitation of U₄O₉ from hyperstoichiometric UO_{2+x}”, *Journal of Nuclear Materials*, 366, 297-305(b).
- [25] Hoekstra, H.R. et al. (1961), “The low-temperature oxidation of UO₂ and U₄O₉”, *Journal of Inorganic and Nuclear Chemistry*, 18, 166.
- [26] Hoffmann, H. (1974), “Crack formation, crack healing and porosity redistribution during irradiation of UO₂ and (U,Pu)O₂”, *Journal of Nuclear Materials*, 54, 9-23.
- [27] Karlsson, J. et al. (2004), “In-pile testing of liner cladding and pellet performance in failed fuel rods”, *Proc. American Nuclear Society, 2004 International Meeting*, LWR Fuel Performance, Orlando, Florida, US.
- [28] Killeen, J.C., J.A. Turnbull (1987), “An experimental and theoretical treatment of the release of ⁸⁵Kr from hyperstoichiometric uranium dioxide”, *Proc. Workshop Chemical Reactivity of Oxide Fuel and Fission Product Release*, Gloucestershire, UK.
- [29] Lackey, W.J. et al. (1972), “Porosity and actinide redistribution during irradiation of (U,Pu)O₂”, *Nuclear Technology*, 16, 120.
- [30] Lassmann, K., J. (1992), *Nuclear Materials*, 188, 295.
- [31] Leenaers, A. et al. (2003), “Oxidation of spent UO₂ stored in moist environment”, *Journal of Nuclear Materials*, 317, 226.

- [32] Lewis, B.J. et al. (1995), “Modelling the release behaviour of cesium during severe fuel degradation”, *Journal of Nuclear Materials*, 227, 83-109.
- [33] Lewis, B.J. et al. (1998), “Low volatile fission product release and fuel volatilization during severe reactor accident conditions”, *Journal of Nuclear Materials*, 252, 235-256.
- [34] Lewis, B.J. et al. (1990), “A model for fission gas release and fuel oxidation behaviour for defected UO₂ fuel elements”, *Nuclear Technology*, 92, 353-362.
- [35] Lewis, B.J. et al. (1993), “Fuel performance and fission product release studies for defected fuel elements”, *Nuclear Technology*, 103, 220-245.
- [36] Lewis, B.J. et al. (2002), “Fuel oxidation and thermal conductivity model for operating defective fuel rods”, *Journal of Nuclear Materials*, 306, 30-43.
- [37] Lewis, B.J. et al. (2004), “Thermodynamic and kinetic modelling of the fuel oxidation behaviour in operating defective fuel”, *Journal of Nuclear Materials*, 328, 180-196.
- [38] Lewis, B.J. et al. (2005), “Thermodynamic considerations and prediction of the primary coolant activity of ⁹⁹Tc”, *Journal of Nuclear Materials*, 340, 69-82.
- [39] Lewis, B.J. et al. (2011), “Fission product chemistry in oxide fuels”, *Comprehensive Nuclear Materials*, Editor-in-Chief, Rudy Konings, Elsevier.
- [40] Likhanskii, V. et al. (2004), “Modeling of fission product release from defective fuel rods under WWER operation conditions and in leakage tests during refueling”, *Proc. American Nuclear Society*, 2004 International Meet. LWR Fuel Performance, Orlando, Florida, US.
- [41] Limbäck, M. et al. (2004), “Test-reactor study of the phenomena involved in secondary fuel degradation”, *Proc. American Nuclear Society*, 2004 International Meeting, LWR Fuel Performance, Orlando, Florida, US.
- [42] Lindemer, T.B., T.M. Besmann (1985), “Chemical thermodynamic representation of <UO_{2±x}>”, *Journal of Nuclear Materials*, 130, 473-488.
- [43] Markowitz, J.M. (1963), *Internal Zirconium Hydride Formation in Zircaloy Fuel Element Cladding Under Irradiation*, WAPD-TM-351, Bettis Atomic Power Laboratory.
- [44] Masaki, N., K. Doi (1972), “Analysis of the superstructure of U₄O₉ by neutron diffraction”, *Acta Crystallographica B*, 28, 785-791.
- [45] Matzke, Hj. (1987), *Journal of Chemical Society*, Faraday Trans. 2 83,1121.
- [46] Matzke, Hj. (1986), “Diffusion in ceramic oxide systems”, *Advances in Ceramics*, Vol. 17, Fission-Product Behavior in Ceramic Oxide Fuel, ed. Hastings, I.J., American Ceramic Society, Columbus, Ohio, US.
- [47] Matzke, Hj. (1981), “Radiation damage in crystalline insulators, oxides and ceramic nuclear fuels”, *Radiation Effects*, 64 [1-4].3-33.
- [48] McEachern, R.J., P. Taylor (1998), “A review of oxidation of uranium dioxide at temperatures below 400°C”, *Journal of Nuclear Materials*, 254, 87.
- [49] Meachen, J.A. (1989), “Oxygen diffusion in uranium dioxide”, *Nuclear Energy*, 28, No. 4, August, 221-226.

- [50] Muzeau B. et al. (2009), “Radiolytic oxidation of UO₂ pellets doped with alpha-emitters (238/239Pu)”, *Journal of Alloys and Compounds*, Vol. 467, pp. 578-589.
- [51] Naito, K. (1974), “Phase Transitions of U₄O₉”, *Journal of Nuclear Materials*, 51, 126-135.
- [52] Newman, C. et al. (2009), “Three dimensional coupled simulation of thermomechanics, heat, and oxygen diffusion in UO₂ nuclear fuel rods”, *Journal of Nuclear Materials*, 392, 6-15.
- [53] Novak, J. et al. (1983), “Postirradiation behaviour of UO₂ fuel I: Elements at 220 to 250°C in air”, *Nuclear Technology*, 63, 254.
- [54] Olander, D.R. (1976), *Fundamental Aspects of Nuclear Reactor Fuel Elements*, TID-26711-p1, US Department of Energy.
- [55] Olander, D.R. (1998), “Mechanistic interpretations of UO₂ oxidation”, *Journal of Nuclear Materials*, 252, 121.
- [56] Olander, D.R. (1986), “Oxidation of UO₂ by high-pressure steam”, *Nuclear Technology*, 74, 215-217.
- [57] Olander, D.R. et al. (1999), “Steam oxidation of fuel in defective LWR rods”, *Journal of Nuclear Materials*, 270, 11-20.
- [58] Olander, D.R. et al. (1997), *Chemistry of Defective Light Water Reactor Fuel*, Electric Power Research Institute Report TR-107074.
- [59] Poinssot C. et al. (2005), *Final Report of the European Project Spent Fuel Stability under Repository Conditions*, Contract N°FIKW-CT-2001-00192 SFS.
- [60] Ramirez, J.C. et al. (2006), “Simulations of heat and oxygen diffusion in UO₂ nuclear fuel rods”, *Journal of Nuclear Materials*, 359, 174-184.
- [61] Sills, H.E. (1979), *ELOCA Fuel Element Behaviour During High-Temperature Transients*, Atomic Energy of Canada Limited report, AECL-6357.
- [62] Simpson, K.A., P. Wood (1983), “Uranium dioxide fuel oxidation below 350°C”, *Proc. NRC Workshop on Spent Fuel/Cladding Reaction during Dry Storage*, Gaithersburg, MD, (1983) (NUREG/CP-0049), 70.
- [63] Sunder, S., N.H. Miller (1996), “Oxidation of CANDU uranium oxide fuel by air in gamma radiation at 150°C”, *Journal of Nuclear Materials*, 231, 121.
- [64] Taylor, P. (2005), “Thermodynamic and kinetic aspects of UO₂ fuel oxidation in air at 400-2000 K”, *Journal of Nuclear Materials*, 344, 206-212.
- [65] Taylor, P. et al. (1993), “The influence of moisture on air oxidation of UO₂: Calculations and observations”, *Nuclear Technology*, 104, 164.
- [66] Taylor, P. et al. (1995), “Microstructures of corrosion films on UO₂ fuel oxidized in air-steam mixtures at 225°C”, *Journal of Nuclear Materials*, 223, 316.
- [67] Taylor, P. et al. (1989), “Formation of uranium trioxide hydrates on UO₂ fuel in air-steam mixtures near 200°C”, *Journal of Nuclear Materials*, 168, 70.

- [68] Taylor, P. et al. (1991), *Microstructure and Phase Relationship of Crystalline Oxidation Products Formed on Unused CANDU Fuel Exposed to Aerated Steam and Water near 200°C*, Atomic Energy of Canada Limited report AECL-10476, COG-91-292.
- [69] Taylor, P. et al. (1991), “Crystallization of U_3O_8 and hydrated UO_3 on fuel in aerated water near 200°C”, *Journal of Nuclear Materials*, 183, 105(b).
- [70] Thompson, W.T. et al. (2007), “Thermodynamic treatment of uranium dioxide based nuclear fuel”, *International Journal of Materials Research*, 98, 10 1004-1011.
- [71] Tribet M. et al. (2010), “Leaching of UO_2 pellet doped with alpha emitters (238/239Pu) in synthetic deep Callovo-Oxfordian groundwater”, *Actinides Conference 2009 San Francisco, CA JUL 12-17, IOP Conference Series-Materials Science and Engineering*, Vol. 9.
- [72] Une, K., S. Kashibe (1996), “Corrosion behavior of irradiated oxide fuel pellets in high temperature water”, *Journal of Nuclear Materials*, 232, 240.
- [73] van Uffelen P., C. Györi, A. Schubert, J. van de Laar, Z. Hózer, G. Spykman (2008), “Extending the application range of a fuel performance code from normal operating to design basis accident conditions”, *Journal of Nuclear Materials*, 383, 137.
- [74] Wasylwich, K.M., C.R. Frost (1982), “Update on the Canadian experimental program to evaluate used-fuel integrity under dry-storage conditions”, *Proc. 2nd International Conference CANDU Fuel*, Pembroke, Ontario, Canada.
- [75] Wasylwich, K.M. et al. (1993), “Differences in oxidation behavior of used CANDU fuel during prolonged storage in moisture-saturated air and dry at 150°C”, *Nuclear Technology*, 104, 309.
- [76] Welland, M.J. et al. (2011), “Review of high temperature thermochemical properties and application in phase-field modelling of incipient melting in defective fuel”, *Journal of Nuclear Materials*, 412, 342-349.
- [77] Welland, M.J. et al. (2008), “A comparison of Stefan and phase field modelling techniques for the simulation of melting nuclear fuel”, *Journal of Nuclear Materials*, 376, 229.
- [78] Whillock, S., J.H. Pearce (1990), “A method of determining the distribution of U_4O_9 in oxidized UO_2 ”, *Journal of Nuclear Materials*, 175, 121-128.

Chapter 5.

Clad-coolant chemical interaction

F.C. Iglesias¹, B.J. Lewis¹, C. Desgranges², C. Toffolon³

¹University of Ontario Institute of Technology, Canada,

²CEA, DEN, DPC, Centre de Saclay, France,

³CEA, DEN, DANS, Centre de Saclay, France

Abstract

This paper provides an overview of the kinetics for zircaloy clad oxidation behaviour in steam and air during reactor accident conditions. The generation of chemical heat from metal/water reaction is considered. Low-temperature oxidation of zircaloy due to water-side corrosion is further described.

Introduction

The prediction of high-temperature fuel rod behaviour is of particular importance for nuclear safety analysis. An understanding of fuel rod behaviour has been well advanced through many decades of experimental research and efforts in modelling and code development [79]. Various types of component and system computer codes have been developed by the international fuel community to describe nuclear fuel rod behaviour and performance during normal, up-set and severe accident conditions [38,27,16,4,70,82,14]. These various codes describe the complex and linked phenomena associated with the thermomechanical and chemical behaviour of the fuel rod/bundle.

Zircaloy oxidation will affect the behaviour of fuel cladding during normal reactor operation. More importantly, it is also a key source of chemical heat due to metal-water reaction at high temperature during reactor accident situations. The uptake of oxygen can also embrittle the zircaloy sheath. For instance, if the oxygen concentration over half of the clad wall thickness exceeds ~0.7 wt%, it can fail upon rewet during the introduction of emergency core cooling in a reactor accident [68,28], or fail by overstrain under oxide cracks at strains as low as ~2% [67].

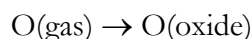
Zircaloy clad oxidation

The oxidation of the zircaloy cladding is an important consideration in light water/heavy water reactor accidents because this reaction will release heat and produce hydrogen/deuterium gas:



With a sufficient amount of water vapour, the cladding can be fully oxidised to ZrO_2 before the melting point of the metal is reached. On the other hand, as a significant amount of hydrogen gas can be produced in Equation 1 with a large mass of zirconium in the reactor core, the gas phase can become depleted in water vapour in the downstream locations of the fuel rods/bundle. In this case, the cladding does not completely oxidise and the ZrO_2 scale can be reduced and the oxygen dissolves into the remaining metal.

In the physical process of sheath oxidation [54], with the absorption of oxygen by the sheathing, the steam mole fraction in the gas at the surface of the clad is smaller than that in the bulk gas, and the oxygen uptake rate by the solid depends on the water flux through the external gas phase boundary layer on the cladding surface where it decomposes. The O/Zr ratio in the solid at the surface is related to the water vapour-H₂ ratio in the adjacent gas by the thermochemistry of the O-Zr system. Oxygen in the solid at the surface moves through the oxide scale:



The oxygen that arrives reacts with the substrate metal at the oxide/metal interface to produce the stoichiometric oxide ZrO_2 , which equilibrates with the substrate α -Zr. The O/Zr ratio in the metal at the interface is the terminal solubility of oxygen in α -Zr. Oxygen diffuses into the substrate metal from the oxide-metal interface.

$\text{O(metal at interface)} \rightarrow \text{O(bulk metal)}$ at a rate determined by the Fick's second law of diffusion.

Large accident modelling codes [27,16,4,21] generally describe the zircaloy oxidation process using parabolic corrosion rate theory developed from laboratory experiments [78,65,22,62,52,69,7,20,2,81]. For the parabolic rate law:

$$w^2 = k_w t \quad (2)$$

where w is the mass of zircaloy reacting per unit area with steam (kg m^{-2}), k_w is the reaction rate constant ($\text{kg m}^{-4} \text{ s}^{-1}$), and t is time (s). The parabolic rate constant k_w , has the form:

$$k_w = k_{wo} \exp\left(-\frac{Q}{RT}\right) \quad (3)$$

where k_{wo} and Q are constants (see Table 1), R is the ideal gas constant ($= 8.31 \text{ J mol}^{-1} \text{ K}^{-1}$), and T is the temperature (in K) [41].

Table 1. Parametric values for parabolic rate constant for zircaloy oxidation in steam

Investigators	Temperature range (K)	k_{wo} ($\text{kg}^2 \text{m}^{-4} \text{s}^{-1}$)	Q ($\times 10^3 \text{ J/mol}$)
Baker and Just	1273 to melting point	3.33×10^3	190
Urbanic and Heidrick	1323 to 1853	2.96×10^1	140
	1853 to melting point	8.79×10^1	138
Pawel et al.	1273 to 1773	2.94×10^2	167
Prater and Courtright	1783 to 2773	2.68×10^4	220

Recent experiments at 700 to 900°C with steam pressures from 0.1 MPa to 15 MPa suggest that the oxidation rate of zircaloy-4 increases with the steam pressure; however, this pressure dependence does not appear at 1 100°C [60,57]. Zircaloy oxidation tests have also been conducted in various steam-hydrogen mixtures at temperatures between 1 223 K and 1 373 K [23,24,25]. In these latter tests, the total weight gain varied with the hydrogen volume fraction and significantly decreased at a critical level of the hydrogen fraction. Hydrogen absorption occurred above a critical hydrogen fraction with the presence of a porous oxide. The hydriding resulted in a reduction of the zircaloy-4 ductility. In addition, the oxidation kinetics of low-Sn zircaloy-4 cladding has been investigated in the lower temperature range of 773 to 1253 K, where a cubic oxidation rate law is suggested [50]:

$$w^3 = k_w t \quad (4)$$

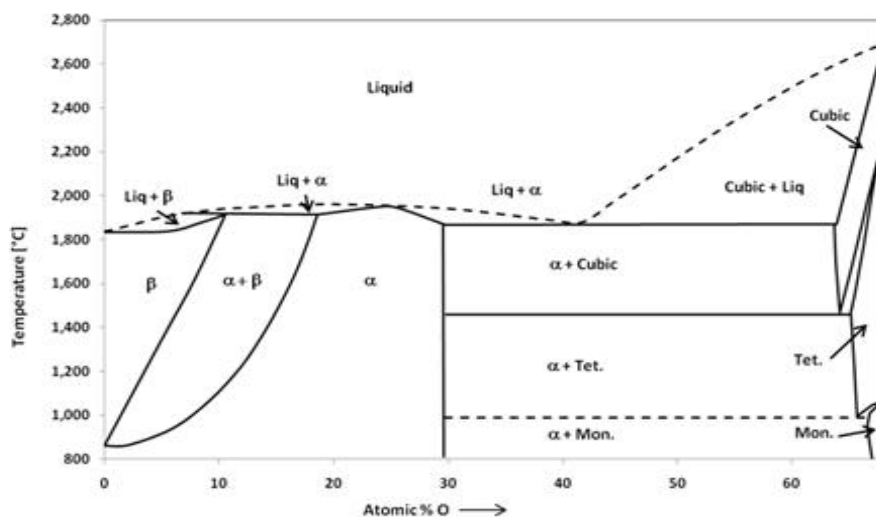
The rate constant obtained in these experiments in steam is shown in Figure 1.

In parabolic corrosion rate theory, the increment in the oxygen absorbed in a time step Δt is taken to be the minimum of $\dot{w}\Delta t$, n_{zr} or $n_w/2$, where \dot{w} is the molar rate of oxygen absorption per square centimeter of cladding, given by parabolic rate theory, and n_{zr} and n_w are the moles of zirconium and H₂O (or D₂O) per unit cladding surface area in the node at the start of the time step. These three conditions represent parabolic corrosion in unlimited steam, zirconium availability, and steam availability, respectively. The laboratory corrosion experiments that underlie the above method are isothermal, usually conducted in unlimited steam environments, and are restricted to metal specimens whose thickness is large compared with the scale thickness. Under these conditions, the rates of oxygen uptake and of growth of the oxide scale are theoretically inversely proportional to the square root of time as shown in Equation 2 at high temperature [62]. However, with steam-H₂ gas present in a degraded reactor accident and finite sheath thickness, the conditions required for a parabolic behaviour may not be fulfilled. The effect of scale dissolution in the substrate metal, which occurs in steam-starved gases as well as the effect of oxygen concentration reaching the solubility limit across the sheath volume, cannot be modelled by parabolic kinetics. A stage of scale dissolution at high temperature (HT) could also be observed in the case of a thick low-temperature pre-oxide scale (due to long-time oxidation in service conditions) being present at the surface of the clad before a HT transient [9,40]. The presence or absence of a ZrO₂ scale on the cladding has also an important effect on the uptake of hydrogen by the metal, which can affect the course of the fuel dissolution process [53] when the metal melts in higher temperature accident scenarios.

The oxidised cladding has a complex morphology. For instance, two other contiguous metallic phases of zirconium can exist for the partially-oxidised zircaloy cladding in addition to the zirconia layer. Since the mechanical properties of these layers are strongly influenced by oxygen distribution [6], an accurate prediction of the layer thicknesses, oxygen profile and reaction rates are needed. In summary, a more complicated model is needed to predict the zircaloy oxidation behaviour to more accurately predict the oxidation kinetics, as well as the sheath deformation behaviour and time of failure. In addition, as mentioned, parabolic kinetics cannot handle the scale dissolution behaviour in reducing environments.

A variety of structures result in oxidised zircaloy that depends on the temperature and oxygen concentration [33]. At temperatures below 1 144 K, an outer layer of zirconia results adjacent to a layer of alpha Zr (α) that contains oxygen in solid solution. On the other hand, at temperatures above 1 255 K, at least three layers are observed: (i) an external zirconia layer, (ii) an intermediate “oxygen-stabilised” α layer and (iii) an inner layer of base metal comprised of transformed beta Zr (β). Between this temperature range, the transformed β forms at the triple point of the α grains, where three structures form: (i) an outside layer of zirconia, (ii) an α layer adjacent to the zirconia layer and (iii) an internal layer of transformed β combined with undissolved α . With cooling, the β phase will transform back to the α phase in which the oxygen concentration is significantly different from that of the oxygen-stabilised α and “prior β ”. Moreover, under certain conditions, the α layer can also consist of two sublayers (α_1 and α_2) [33]. The prior β material can also reveal structural changes where, if enough oxygen is absorbed, “ α incursions” may form with a growth of oxygen-enriched α into β . Although the boundaries between the different phases are generally planar, irregular boundary surfaces can be formed at low temperatures or by the appearance of the secondary phenomenon previously mentioned. Figure 2 shows the boundaries for the existing phases [66].

Figure 1. Rate constant for cubic oxidation kinetics in steam from 773 to 1 253 K [50]

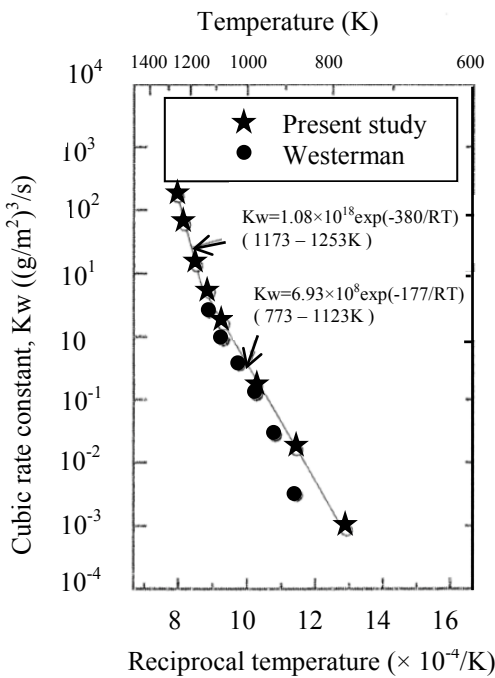


Several analytical models have been developed to predict HT oxidation of metal alloys. First, Debuigne [15] has proposed an analytical model for zirconium oxidation. In this model, a steady-state hypothesis in a semi-infinite geometry was considered. In a more recent work, Ma et al. have applied Debuigne's analytical model to low-tin zircaloy-4 steam oxidation between 1 100°C and 1 250°C [43]. Because these analyses made the assumption of a semi-infinite sample, the finite size of cladding tubes could not be simulated. This is a major drawback because the thickness of nuclear fuel cladding is quite limited (close to 600 µm), and because oxygen rapidly reaches the internal surface of the cladding wall. As mentioned, diffusion theory has been applied to describe the corrosion of cladding for general transient conditions for finite specimens [61,33,44,31,11,19]. These accurate models require the numerical solution of partial differential equations representing Fickian diffusion in each layer:

$$\frac{\partial C}{\partial t} = D \frac{\partial^2 C}{\partial x^2} \quad (5)$$

Here D is the diffusion coefficient, C is the oxygen concentration and x is the spatial coordinate. These partial differential equations are also subject to specified oxygen concentration values at each of the layer boundaries and oxygen conservation relationships as the boundaries move. This moving boundary problem has been solved as the FROM (Full Range Oxidation Model) computer code, which predicts the various corrosion layer thicknesses, transition from two phase to three phase oxidation and oxygen concentration profiles in the zircaloy sheath [33]. This latter treatment also incorporates non-equilibrium boundary concentrations that improve the prediction of the oxide layer thickness during fast temperature transients.

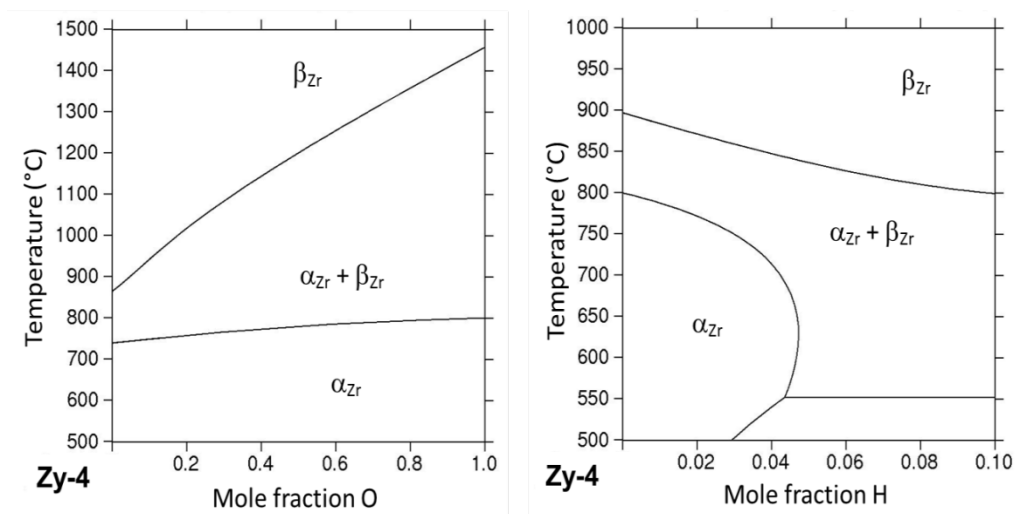
Figure 2. Zirconium-oxide phase diagram



Berdyshev et al. proposed another numerical model for cladding oxidation as a part of the SVECHA package [3]. The numerical model is also based on Fick's law and oxygen flux for interface displacements. The model succeeded in accurately simulating the growth kinetics of the $\alpha\text{Zr}(\text{O})$ phase with specific consideration for oxygen boundary conditions. Since 2006, the French Institut de Radioprotection et de Sécurité Nucléaire (IRSN) has developed the DIFFOX model in order to describe the oxidation of the cladding tube during a loss of coolant accident (LOCA) [19]. Once more it is based on solving Fickian equation for O diffusion with moving boundaries. The DIFFOX model is able to simulate double sided oxidation of cladding tubes with different conditions on each side.

Since a decade, a thermodynamic database named ZIRCOBASE has been developed in the CALPHAD formalism for zircaloy alloys [17]. In particular, it accounts for the variation of O solubility in each phase taking into consideration the different alloy compositions. Hence, a corresponding kinetics model EKINOX-Zr (Estimation KINetics OXidation) has been developed with equilibrium conditions on moving boundaries that are obtained from the thermodynamics database zircobase. It showed that differences in the O solubility result in a change in the O profile in the clad, and the critical time before a total loss of clad ductility [11]. This calculation tool is also able to reproduce the low-temperature oxide scale dissolution phenomena occurring in the early stage of the high-temperature dwell in the case of a thick pre-oxide scale [75]. In recent work [45], EKINOX-Zr was improved to take into account hydrogen and to exchange data with ThermoCalc (coupled with the zircobase database) during the simulation. One observes opposite effects of O and H on $\alpha\text{Zr} \leftrightarrow \beta\text{Zr}$ allotropic phase transition temperatures in zircaloy-4 alloy as illustrated on the zircaloy-4 isopleth sections as calculated using thermocalc/zircobase, i.e., as shown in Figure 3, O is an α -stabiliser element whereas H is a β -stabiliser element [75]. These kinetics calculations showed that even in the case of very low variations of hydrogen content in the alloy this can modify equilibrium oxygen concentrations and affect the diffusion profile in the βZr phase.

Figure 3. Calculated isopleth sections of zircaloy-4 alloy as a function of, respectively, O and H content showing the opposite effects of both elements on $\alpha\text{Zr} \leftrightarrow \beta\text{Zr}$ allotropic phase transition temperatures



An “integral diffusion technique” has been further developed as a compromise between the computationally simple yet physically oversimplified parabolic kinetic technique and the highly descriptive but analytically complex full diffusion theory treatment [54]. In this method, the exact concentration distribution of oxygen in the metal phase is replaced by an approximate distribution that fits the boundary and initial conditions. This distribution is coupled to the linear oxygen concentration profile in the oxide layer (and ultimately to the steam mole fraction in the bulk gas). However, this treatment oversimplifies the duplex α -Zr and β -Zr metal phase as a single metal layer (with the diffusion properties of α -Zr). Thus, this technique fails to accurately model the structural properties of the sheath, which is particularly important in order to determine the timing of sheath failure. The detailed morphological state of the sheathing is important because it determines: (i) the mechanical properties of the clad and thus the timing of clad failure; (ii) the heat released by the oxidation process and hydrogen dissolution in the cladding, and (iii) the capacity of the metal to dissolve fuel when the cladding melts at $\sim 2\ 000^\circ\text{C}$.

Oxidation of the zircaloy sheath in air is also an important phenomenon because of the possibility of fuel handling accidents. Single-effects experiments with air oxidation from ~ 500 to $1\ 000^\circ\text{C}$, as well as multi-element testing in the CODEX facility simulating air ingress for Pressurised Water Reactor (PWR)-type fuel, have been performed [80,51,18,74,32]. In the reaction between zircaloy-4 and air and in steam and nitrogen-containing atmospheres at temperatures above 800°C , there is a degradation of the cladding material with formation of zirconium nitride and its re-oxidation [73]. Breakaway oxidation in air shows similar characteristics to that of steam, where the only difference is due to the formation of zirconium nitrides that affect the characteristics of the zirconia phase. This is supported by the experimental evidence that the oxide thickness at transition is similar for oxidation in steam or air [39,18]. Although parabolic correlations may be applied for oxidation in air, this is only appropriate for high temperatures ($>1\ 400^\circ\text{C}$) and for pre-oxidised cladding ($\geq 1\ 100^\circ\text{C}$), i.e., under all other conditions, faster kinetics are observed to occur [73] probably due to a less protective oxide layer by the crystallographic mismatch between zirconia and zirconium nitrides. This is consistent with similar behaviour reported for zircaloy oxidation in environmental mixtures of steam and nitrogen [73].

Measurements have also been made on the loss of ductility and embrittlement of zircaloy-4 cladding by oxidation and hydriding under LOCA conditions and with a water quench [25,26,77,76] [49,48,35,36]. In particular, the LOFT FP-2 test was a relatively large in-reactor experiment to determine the effect of reflood for a severely damaged core assembly [34,30]. A large fraction of the bundle inventory of the LOFT FP-2 bundle was available for subsequent oxidation during reflooding. This experiment showed that significant H_2 generation can be expected during reflooding, which is largely dependent on the degree of prior oxidation and reflood thermalhydraulic conditions. An upper debris bed was also observed in the LOFT FP-2 test when coolant was introduced into the hot bundle, resulting in a thermal shock and fragmentation of the oxidised fuel rods.

Acceptance criteria for preventing fuel failure due to oxygen and hydrogen embrittlement with water quench by the emergency core coolant system has been proposed by a number of investigators [68,26,20,8,47].

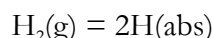
Chemical heat generation by clad oxidation/hydriding

All transient reactor analysis codes compute the oxidative heat release from the standard enthalpy change for the reaction in Equation 1 [27,16,4,70]. However, during a substantial portion of the accident, the corrosion product is not the stoichiometric oxide [55]. In the steam-starved regions, the principal final state is oxygen dissolved in the metal so that the heat release is in accordance with the reaction:



The partial molar enthalpy of solution of oxygen in zircaloy depends on the O/Zr ratio of the metal, where calorimetric data permit estimation of this quantity [5]. For typical oxygen contents in the metal, the heat of solution of oxygen is 3-5% more negative than the heat of formation of stoichiometric ZrO_2 . Hence, after subtracting the heat of formation of $\text{H}_2\text{O(g)}$, the heat release for the reaction in Equation 6 is 6-10% larger than that for Equation 1 [55,56].

It is generally assumed that the hydrogen solubility in zircaloy is negligible at high temperatures. Although the phase diagram of the H-Zr system shows that zirconium hydrides do not form at temperatures above about 1 200 K [37], measurements of the high-temperature solubility of hydrogen in zircaloy, however, show that dissolution as interstitial atoms is significant particularly at a higher system pressure [46,83,84]. For high steam flow rates, the outer sheath surface is covered with a protective ZrO_2 scale. Hence, because of the low solubility of hydrogen in ZrO_2 [58], H absorption is restricted to just the pick-up fraction that results during zircaloy oxidation. This amount is quite small because of the low hydrogen permeability of the coherent oxide scale produced by oxidation above $\sim 1\ 300$ K. When a ZrO_2 scale separates the external gas from the metal, the gas in the gap consists of only He and Xe, except for short distances from a rupture site with rod failure, where some hydrogen and, to a lesser extent, steam are present. On the other hand, with a low steam flow rate, the external gas quickly becomes steam-starved and, shortly thereafter, the oxide scale dissolves into the metal. Downstream regions of the reactor core that contain zircaloy without an oxide scale are inevitably in contact with a gas that is nearly pure H_2 , which dissolves in the metal according to the reaction:



The equilibrium of this reaction is given by Sievert's law:

$$\frac{C_H}{\sqrt{P_{H_2}}} = \exp\left(\frac{\Delta S_H}{R}\right) \exp\left(-\frac{\Delta H_H}{RT}\right) \quad (7)$$

where C_H is the H/Zr ratio of the metal in equilibrium with the gas containing H_2 at a hydrogen gas partial pressure p_{H_2} (atm). The thermochemical properties of hydrogen dissolution in zircaloy are given in Table 2 [46,83,72]. However, some discrepancy is seen in the measured values shown in Table 2. Hydrogen dissolution is typically neglected in accident analysis even though the above data suggest that the solubility is significant at temperatures as high as 2 000°C. The principal consequences of hydrogen retention by the metal are twofold [55,56]:

- the unoxidised metal acts as a sink of hydrogen, which can alter the timing of hydrogen release; hydrogen absorbed in the metal in the steam-starved regions of the core is released on subsequent oxidation, because of the low solubility of hydrogen in zirconia;
- hydrogen absorption by zirconium releases heat.

Table 2. Thermophysical properties for hydrogen dissolution in zircaloy

Investigator	ΔH_H (kJ/mol)	ΔS_H (J/mol·K)
(Moalem, 1991)	-63	-54
(Yamanaka, 1995)	- 246 (alpha), -252 (beta)	- 38 (alpha), -25 (beta)
(Steinbrück, 2004)	-65	-101

The normal approach for estimating heat release in accident codes is by oxidative heating, which is valid during the early stages of a transient because the principal oxidation product is ZrO_2 , where the oxide scale has not appreciably dissolved in the metal so that no hydrogen is absorbed in this time period. This oxidative heating is based on the total amount of oxygen absorbed, assuming that the heat released per gram atom of oxygen absorbed by the metal is one-half of the standard enthalpy of the reaction in Equation 1. As previously discussed, in steam-starved regions, one must further consider the effect of hydrogen absorption in metallic zircaloy. Moreover, hydrogen absorption can result in a sharp increase in the heat release with dissolution of only 10% of the corrosion-product hydrogen in cladding without an oxide scale, i.e., while not as exothermic as oxidative heating, hydrogen uptake can nearly double the contribution from oxidation alone [55]. This additional heating effect is the sum of the product of the hydrogen content of the metal and the enthalpy of solution of hydrogen. The cumulative heat release will decrease with a reduction in the solubility of hydrogen in zircaloy as the temperature increases [55]. Desorption of hydrogen from the cladding is endothermic, which consumes more heat than is typically provided by the continuing oxidation process.

Zircaloy corrosion at low temperature

During normal reactor operation, the outer cladding surface of the fuel rods will corrode very slowly on the waterside of the cladding. This reaction at low temperature proceeds through the reaction in Equation 1. Part of the hydrogen generated in this reaction diffuses into the metal. At the start of the oxidation process, all of the hydrogen may be absorbed. However, the rate of absorption readily decreases from a maximum during the first 10 mg dm⁻² oxidation to a typical plateau [10,12,13]. The pick-up fraction (defined as the amount of hydrogen in the metal to the total amount produced during the corrosion reaction) for zircaloy-4 is usually between 5 and 25%. In the case of defective fuel, with the addition of internal clad corrosion, the hydrogen that is not absorbed by the cladding is released into the fuel-to-clad gap of the defected rod, thereby enriching the steam atmosphere in hydrogen, which will affect the oxygen potential in the fuel-to-clad gap thereby inhibiting the fuel oxidation reaction [29].

The kinetics for the waterside corrosion have been extensively studied [59,71,63,1]. In the 523 to 673 K temperature range, the corrosion process of zircaloy starts with the formation of a thin protective oxide that grows with an approximate cubic rate law. After a certain thickness is reached, a transition occurs where cracks develop in the oxide film structure. These cracks provide easier access of the oxygen to the oxide-metal interface, resulting in a breakaway regime that is characterised by linear kinetics. An enhancement factor for water-side corrosion is seen for in-reactor conditions, with a factor ranging from 1 to 3 in pressurised water reactors, and 10 for boiling water reactors [64]. For a defected fuel element operating at $\sim 50 \text{ kW m}^{-1}$, an enhancement of ~ 50 has been suggested for enhanced corrosion on the inside cladding surface due to bombardment by energetic fission fragments [42].

References

- [1] Almarshad, A.I.A., A.C. Klein (1991), “A model for waterside oxidation of zircaloy fuel cladding in pressurized water reactors”, *Journal of Nuclear Materials*, 183, 186.
- [2] Baker, L., L.C. Just (1962), *Studies of Metal-water Reactions at High Temperatures*, Report, ANL-6548, Argonne National Laboratory, Argonne, US.
- [3] Berdyshev A. V., M.S. Veshchunov (2010), “Model for high-temperature oxidation of Zr cladding in steam under fast transient conditions”, *Proceeding of Nuclear Safety Institut*, (IBRAE-RAS), 1.
- [4] Berna, G.A. et al. (1985), *RELAP5/SCDAP/MOD0 Code Manual*, EGG-RTH-7051, EG&G.
- [5] Boureau, G., P. Gerdanian (1984), *Journal of Physics and Chemistry of Solids*, 4, 141.
- [6] Brachet J.-C. et al. (2008), *Journal of ASTM International*, 5, n°5, Paper ID JAI101116.
- [7] Causey, R.A. et al. (2005), *Review of Oxidation Rate of Zirconium Alloys*, SAND2005-6006, Sandia Repot.
- [8] Chung, H. M. (2005), “Fuel behavior under loss-of-coolant accident situations”, *Nuclear Engineering and Technology*, Vol. 37, No.4.
- [9] Chuto T. et al. (2009), “High-temperature oxidation of Nb-containing Zr alloy cladding in LOCA conditions”, *Nuclear Engineering and Technology*, 41, 163-170.
- [10] Clayton, J.C. (1989), “Internal hydriding in irradiated defected zircaloy fuel rods”, *Proc. 8th Int. Sym. Zirconium in the Nuclear Industry*, STP 1023, p. 266, American Society for Testing and Materials.
- [11] Corvalan C. et al. (2010), *Journal of Nuclear Materials*, 400, 196.
- [12] Cox, B. (1963), *Some Factors Which Affect the Rate of oxidation and Hydrogen Absorption of Zircaloy-2 in Steam*, AERE-R4348, Atomic Energy Research Establishment.
- [13] Cox, B. (2005), “Some thoughts on the mechanisms of in-reactor corrosion of zirconium alloys”, *Journal of Nuclear Materials*, 336, 331-368.
- [14] Cunningham, M.E. et al. (2001), *FRAPTRAN: A Computer Code for the Transient Analysis of Oxide Fuel Rods*, NUREG/CR-6739, Vol. 1, PNNL-13576.

- [15] Debuigne J. (1966), *Contribution to Study of Zirconium Oxidation and Oxygen Diffusion into the Oxide and the Metal*, PhD Thesis, Faculté des sciences de Paris, France.
- [16] Dosanjh, S. S. (Ed.) (1989), *MELPROG-PWR/MOD1: A Two-Dimensional, Mechanistic Code for Analysis of Reactor Core Melt Progression and Vessel Attack Under Severe Accident Conditions*, Sandia National Laboratories, NUREG/CR-5193, SAND88-1824.
- [17] Dupin N. et al. (2004), *Journal of Nuclear Materials*, 275, 481.
- [18] Duriez, C. et al. (2005), “The MOZART Program on air cladding oxidation: Results on bare zircaloy-4 in the range 600-1000°C”, *Proceedings of the 25th Meeting of the Phebus FP Bundle Interpretation Circle*, Aix-en-Provence, France.
- [19] Duriez C. et al. (2010), *Journal of ASTM International*, 2, n°8 (2010), Paper ID JAI103156.
- [20] Erbacher, F. J., S. Leistikow (1987), “Zircaloy fuel cladding behavior in a loss-of-coolant accident: A Review”, *ASTM-STP 939, American Society for Testing and Materials*, pp. 451-488.
- [21] Fauske and Associates (1990), *MAAP3.0B Computer Code Manual*, EPRI Report NE-7071-CCML.
- [22] Fichot, F. et al. (2004), “Advanced treatment of zircaloy cladding high-temperature oxidation in severe accident code calculations, Part III. Verification against representative transient tests”, *Nuclear Engineering and Design*, 232(1), pp. 97-109.
- [23] Furuta, T., S. Kawasaki (1982), “Reaction behavior of zircaloy-4 in steam-hydrogen mixtures at high temperature”, *Journal of Nuclear Materials*, 105(2/3).119-131.
- [24] Furuta, T. et al. (1978), “Zircaloy-clad fuel rod burst behavior under simulated loss-of-coolant condition in pressurized water reactors”, *Journal of Nuclear Science and Technology*, 15[10], pp. 736-744.
- [25] Furuta, T. et al. (1981), “Ductility loss of zircaloy cladding by inner-surface oxidation during high temperature transient”, *Journal of Nuclear Science and Technology*, 18(10),802-810.
- [26] Furuta, T. et al. (1984), “Estimation of conservatism of present embrittlement criteria for zircaloy fuel cladding under LOCA”, *ASTM-STP 824, American Society for Testing and Materials*, pp. 734-746.
- [27] Gauntt, R. et al. (2000), *MELCOR Computer Code Manuals*, Version 1.8.5, NUREG/CR-6119, SAND-2417/2.
- [28] Grandjean, C., G. Hache (2008), *A State-of-Art Review of Past Programmes Devoted to Fuel Behaviour Under Loss-of-Coolant Conditions*, Part 3: Cladding Oxidation Resistance to Quench and Post-Quench Loads, IRSN Technical Report, DPAM/SEMCA 2008-093.
- [29] Higgs, J.D. et al. (2007), “A conceptual model for the fuel oxidation of defective fuel”, *Journal of Nuclear Materials*, 366, 99-128
- [30] Hobbins, R.R., G.D. McPherson (1991), *Proceedings of the Open Forum on the OECD/LOFT Project, Achievements and Significant Results*, Madrid, Spain.

- [31] Hofmann, P., H.J. Neitzel (1987), “Experimental and theoretical results of cladding oxidation under severe fuel-damage conditions”, *7th Symposium, ASTM STP 939*, pp. 504-538.
- [32] Hozer, Z. et al. (2006), “Behavior of VVER fuel rods tested under severe accident conditions in the CODEX Facility”, *Nuclear Technology*, 154, 302-317.
- [33] Iglesias, F.C. et al. (1985), “Verification of the FROM model for zircaloy oxidation during high temperature transients”, *Journal of Nuclear Materials*, 130, 3644.
- [34] Jensen, S.M. et al. (1989), *Postirradiation Examination Data and Analysis for OECD LOFT Fission Product Experiment LP-FP-2*, OECD LOFT-T-3810, Vol. 1, Paris, France.
- [35] Kim, J. et al. (2006), “Effects of oxide and hydrogen on the behavior of zircaloy-4 cladding during the loss of coolant accident (LOCA)”, *Nuclear Engineering and Design*, 236, 2386-2393.
- [36] Kim, J.H. et al. (2005), “Embrittlement behavior of zircaloy-4 cladding during oxidation and water quench”, *Nuclear Engineering and Design*, 235(1), 67-75.
- [37] Kubaschewski, O. (1976), *Zirconium: Physico-chemical Properties of its Compounds and Alloys*, IAEA Special Issue 6, Vienna, Austria.
- [38] Lassmann, K. (1992), “TRANSURANUS: A fuel rod analysis code ready for use”, *Journal of Nuclear Materials*, 188, 295-302.
- [39] Leistikov, S. et al. (1978), *Kinetics and Morphology of Isothermal Steam Oxidation of Zircaloy at 700-1300°C*, KfK-2587.
- [40] Le Saux, M. et al. (2011), “Influence of the pre-transient oxide on LOCA high temperature steam oxidation and post-quench mechanical properties of zircaloy-4 and M5™ cladding”, *Proceedings of 2011 Water Reactor Fuel Performance Meeting*, Chengdu, People’s Republic of China.
- [41] Lewis, B.J. et al. (1993), “A kinetic model for fission-product release and fuel oxidation behaviour for zircaloy-clad fuel elements under reactor accident conditions”, *Journal of Nuclear Materials*, 207, 228-241 (a)
- [42] Lewis, B.J. et al. (1993), “Fuel performance and fission product release studies for defected fuel elements”, *Nuclear Technology*, 103, 220-245 (b).
- [43] Ma, X. et al. (2008), *Journal of Nuclear Materials*, 377, (359).
- [44] Malang, S. (1975), *SIMTRAN I-A Computer Code for the Simultaneous Calculation of Oxygen Distributions and Temperature Profiles in Zircaloy during Exposure to High-temperature Oxidizing Environments*, Report ORNL-5083, Oak Ridge National Laboratory, Oak Ridge, US.
- [45] Mazères B. et al. (2013), “Contribution to the modelling of hydrogen effect on oxygen diffusion in Zy-4 alloy during high temperature steam oxidation”, *Oxidation of Metals*, 79, 121.
- [46] Moalem, M., D.R. Olander (1991), “The high-temperature solubility of hydrogen in pure and oxygen-containing zircaloy”, *Journal of Nuclear Materials*, 178, 61.

- [47] Nagase, F. et al. (2009), “Behavior of high burn-up fuel cladding under LOCA conditions”, *Journal of Nuclear Science and Technology*, Vol. 46, No. 7, PP. 763-769.
- [48] Nagase, F., T. Fuketa (2005), “Behavior of pre-hydrided zircaloy-4 cladding under simulated LOCA conditions”, *Journal of Nuclear Science and Technology*, 42(2), 209-218.
- [49] Nagase, F., T. Fuketa (2004), “Effect of pre-hydriding on thermal shock resistance of zircaloy-4 cladding under simulated loss-of-coolant accident conditions”, *Journal of Nuclear Science and Technology*, 41(7), 723-730.
- [50] Nagase, F. et al. (2003), “Oxidation kinetics of low-sn zircaloy-4 at the temperature range 773 to 1,573 K”, *Journal of Nuclear Science and Technology*, 40(4), 213-219.
- [51] Natesan, K., W.K. Soppet (2004), *Air Oxidation Kinetics for Zr-Based Alloys*, NUREG/CR-6846.
- [52] NEA (2010), *Nuclear Fuel Behaviour under Loss-of-Coolant Accident (LOCA) Conditions*, NEA No. 6846, Paris, France.
- [53] Olander, D.R. (1995), “Interpretation of laboratory crucible experiments on UO₂ dissolution by liquid uranium”, *Journal of Nuclear Materials*, 224, 254 (a).
- [54] Olander, D.R. (1994), “Materials chemistry and transport modeling for severe accident analyses in light-water reactors, I: External cladding oxidation”, *Nuclear Engineering and Design*, 148, 253-271 (a).
- [55] Olander, D.R. (1994), “Materials chemistry and transport modeling for severe accident analysis in light-water reactors, II: Gap processes and heat release”, *Nuclear Engineering and Design*, 148, 273-292 (b).
- [56] Olander, D.R. (1995), “Thermodynamics and transport processes in reactor fuel”, *Pure and Applied Chemistry*, Vol. 67, No. 6, pp. 1003-1010.
- [57] Park, K. et al. (2001), “High temperature oxidation of zirconium base alloy in steam”, *7th International CANDU Fuel Conference*, Kingston, Ontario, Canada.
- [58] Park, K.H., D.R. Olander (1991), “Hydrogen dissolution in and release from nonmetals: III, tetragonal zirconia”, *Journal of the American Ceramic Society*, 74, 72.
- [59] Parry, G.W., P.G. Smerd (1980), *Review of PWR Fuel Rod Waterside Corrosion Behavior*, NP-1472, Electric Power Research Institute.
- [60] Pawel, R.E. et al. (1979), “The oxidation of zircaloy-4 at 900 and 1100°C in high pressure steam”, *Journal of Nuclear Materials*, 82(1), 129-139 (a).
- [61] Pawel, R.E., J.J. Campbell (1980), “The observation of effects of finite specimen geometry on the oxidation kinetics of Zircaloy-4”, *Journal of the Electrochemical Society*, 127, 2188-2194.
- [62] Pawel, R.E. (1979), *Journal of the Electrochemical Society*, 126, 1111 (b).
- [63] Peters, H.R. (1984), “Improved characterization of aqueous corrosion kinetics of zircaloy-4”, *Proceedings 6th Int. Sym. Zirconium in the Nuclear Industry, ASTM-STP 824*, p. 507, *American Society for Testing and Materials*.

- [64] Pickman, D. O. (1994), “Zirconium alloy performance in light water reactors: A Review of UK and Scandinavian experience”, *ASTM-STP 1245, American Society for Testing and Materials*, pp. 19-32.
- [65] Prater, J.T., E.L. Courtwright (1987), “Oxidation of zircaloy-4 in steam at 1300°C to 2400°C”, *Proceedings 7th Int. Symp. on Zirconium in the Nuclear Industry, ASTM Spec. Tech. Pobl.*, 939.489 (a).
- [66] Prater, J.T., E.L. Courtwright (1987), *Properties of Reactor Fuel Rods Material at High Temperatures*, NUREG/CR-4891.
- [67] Sagat, S. et al. (1982), “Deformation and failure of zircaloy fuel sheaths under LOCA conditions”, *6th International Conference on Zirconium in the Nuclear Industry*, Vancouver, Canada.
- [68] Sawatzky, A. (1978), “A proposed criterion for the oxygen embrittlement of zircaloy-4 fuel cladding”, *4th International Conference on Zirconium in the Nuclear Industry*, pp. 479-496, Stratford-upon-Avon, UK.
- [69] Schanz, G. et al. (2004), “Advanced treatment of zircaloy cladding high-temperature oxidation in severe accident code calculations Part I. Experimental database and basic modelling”, *Nuclear Engineering and Design*, 232(1), pp. 75-84.
- [70] Sills, H.E. (1979), *ELOCA Fuel Element Behaviour during High-Temperature Transients*, AECL Report AECL-6357.
- [71] Stehle, H. et al. (1984), “Characterization of ZrO₂ films formed in-reactor and ex-reactor to study factors contributing to the in-reactor waterside corrosion of zircaloy”, *Proceedings 6th Int. Sym. Zirconium in the Nuclear Industry, ASTM-STP 824*, p. 483, *American Society for Testing and Materials*.
- [72] Steinbrück, M. (2004), “Hydrogen absorption by zirconium alloys at high temperatures”, *Journal of Nuclear Materials*, 334, 58-64.
- [73] Steinbrück, M. (2009), “Prototypical experiments relating to air oxidation of zircaloy-4 at high temperatures”, *Journal of Nuclear Materials*, 392.531-544.
- [74] Suzuki, M., S. Kawasaki (1986), “Oxidation of zircaloy cladding in air”, *Journal of Nuclear Materials*, 140(1), 32-43.
- [75] Toffolon-Masclet, C. et al. (2011), *Solid State Phenomena*, 172, 652.
- [76] Uetsuka, H. et al. (1983), “Failure-bearing capability of oxidized zircaloy-4 cladding under simulated loss-of-coolant condition”, *Journal of Nuclear Science Technology*, 20(11), 941-950.
- [77] Uetsuka, H. et al. (1981), “Zircaloy-4 cladding embrittlement due to inner surface oxidation under simulated loss-of-coolant condition”, *Journal of Nuclear Science and Technology*, 18(9), 705-717.
- [78] Urbanic, V.F., T.R. Heidrick (1978), “High-temperature oxidation of zircaloy-2 and zircaloy-4 in steam”, *Journal of Nuclear Materials*, 75, pp. 251-261 (also AECL Report AECL-6149).

- [79] Van Uffelen, P. (2006), *Modelling of Nuclear Fuel Behaviour*, European Commission Directorate-General Joint Research Centre Institute for Transuranium Elements, EUR 22321 EN ISSN 1018-5593.
- [80] Vermoyal, J.J. et al. (2001), "In situ characterization of zircaloy-4 oxidation at 500°C in dry air", *Journal of Nuclear Materials*, 298(3), 297-308.
- [81] Volchek, A. et al. (2004), "Advanced treatment of zircaloy cladding high-temperature oxidation in severe accident code calculations Part II. Best-fitted parabolic correlations", *Nuclear Engineering and Design*, 232(1), pp. 85-96.
- [82] Williams, A.F. (2005), "The ELOCA fuel modelling code: Past, Present And Future", *9th International CNS Conference on CANDU Fuel*, Belleville, Ontario, Canada.
- [83] Yamanaka, S. et al. (1995), "Hydrogen solubility in zirconium alloys", *Journal of Alloys and Compounds*, 231, 503-507.
- [84] Yamanaka, S. et al. (1997), "Study on the hydrogen solubility in zirconium alloys", *Journal of Nuclear Materials*, 247, 315-321.

Chapter 6.

Property-process relationships in nuclear fuel fabrication

V. Tikare

Sandia National Laboratories, US

Abstract

Nuclear fuels are fabricated using many different techniques as they come in a large variety of shapes and compositions. The design and composition of nuclear fuels are predominantly dictated by the engineering requirements necessary for their function in reactors of various designs. Other engineering properties requirements originate from safety and security concerns, and the easy of handling, storing, transporting and disposing of the radioactive materials. In this chapter, the more common of these fuels will be briefly reviewed and the methods used to fabricate them will be presented. The fuels considered in this paper are oxide fuels used in LWRs and FRs, metal fuels in FRs and particulate fuels used in HTGRs. Fabrication of alternative fuel forms and use of standard fuels in alternative reactors will be discussed briefly. The primary motivation to advance fuel fabrication is to improve performance, reduce cost, reduce waste or enhance safety and security of the fuels. To achieve optimal performance, developing models to advance fuel fabrication has to be done in concert with developing fuel performance models. The specific properties and microstructures necessary for improved fuel performance must be identified using fuel performance models, while fuel fabrication models that can determine processing variables to give the desired microstructure and materials properties must be developed.

Introduction

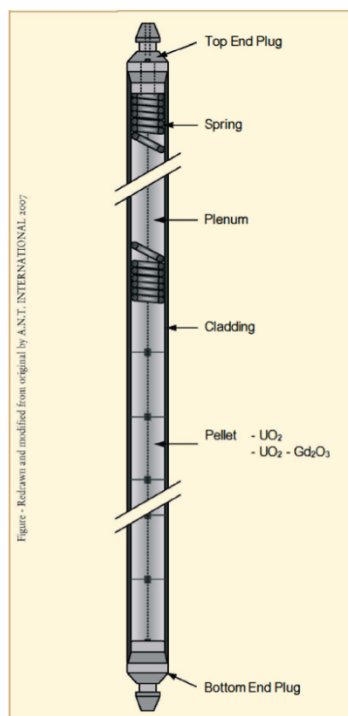
The purpose of a nuclear fuel is to generate heat, which can be used to do work. Thus, the primary function that a nuclear fuel is required to perform is to generate heat in a controlled and sustainable manner and transfer it to power generating facility. In addition, this power generation must be done safely and economically. These basic requirements translate to surprisingly few materials performance requirements for fuels:

- The density of fissionable nuclei must be sufficiently high to sustain a controlled chain reaction.

- High thermal conductivity is necessary to transfer the heat from the fuel to the power generation systems.
- Radioactive materials that are inherent to the fuel as well as those generated during fission must remain safely sequestered within the fuel.
- The cost of the complete fuel life cycle, from fabrication to disposal or reuse, must be economically comparable to competing energy technologies.

In compliance with these materials requirements, a number of nuclear fuel forms have been developed. The overwhelming majority of the nuclear fuels is UO₂ in the form of fuel pellets in zircaloy clad used in LWRs. Other major nuclear fuels are UO₂ fuel for fast reactors, mixed UO₂ and PuO₂ called MOX for use in both LWRs and FRs, metal fuels for use in FRs, particulate fuels and many other specialty fuels. In this work, the fabrication of these fuel forms will be described. The engineering properties that dictate optimisation of the fabrication process to achieve them will be reviewed. Finally, improved processing and fabrication technologies will be suggested.

Figure 1. Schematic diagram of a PWR fuel rod [1]



Fuel rod

Nuclear fuel is packaged in the form of long, thin, hollow metal rods with cylindrical pellets stacked inside the rods. The rods are made with a small gap between the fuel pellets and the clad. The gap is filled with He gas to promote thermal conductive from the pellets to the clad. In the PWRs, the He gas is pressurised to match the pressure of the primary coolant on the external surface of the rods. In BWRs rods, the He gas in the rod

is slightly pressurised to maintain good contact between the pellets and the clad. A schematic diagram showing a PWR rod is shown in Figure 1 [1]. The UO_2 cylindrical pellets are approximately 1 cm in height and 2 cm in diameter. The clad is zircaloy with typical composition of 98% Zr alloyed with other additives. The choice of zircaloy for the clad is due to chemical stability in the boiling water in BWR and pressurised steam in PWRs. It is also highly resistance to irradiation damage and maintains its structural and dimension properties under the conditions encountered in LWRs. The clad is formed by hot and cold rolling to form a continuous long hollow tube. The ends are welded with plugs to contain the fuel pellets and fission products especially fission gases that are generated during service.

In sodium-cooled fast reactors, the geometry of the rod is similar to that of LWRs, however; there are substantial differences. The rod is thinner to accommodate the fuel pellets, which are still cylindrical, but have a smaller diameter of 0.5 cm. The clad have been traditionally made of stainless steel as it has good chemical stability when in contact with the molten sodium coolant; however other alloys and materials are sometimes used today. Again, the rod is manufactured with a gap between the fuel pellet and clad with a He gas filling it. The clad is discussed in another section of this report. The fuel pellets are the topic of this section. Their fabrication will be discussed in detail for the remainder of this section.

Figure 2. Numerous minerals contain uranium are found in many parts of the world uranium mining and UO_2 powder processing

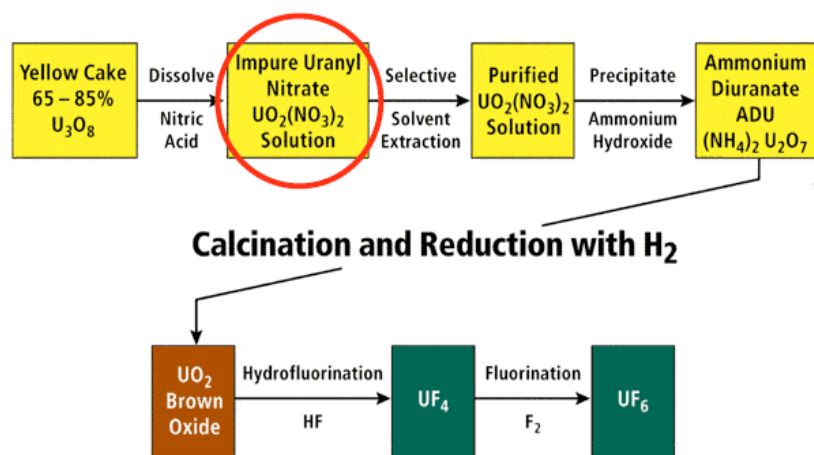


The first step in making UO_2 is the mining of uranium minerals, which comes in many different types; some are shown in Figure 2. Of these minerals a few qualify as uranium ores as their content is sufficiently high and chemical structure is such as to enable economical extraction. Among these uraninite, pitchblende and davideite are the primary ores used for uranium extraction [2]. Uranium is extracted from the crushed ores by chemical extraction and refining to form yellowcake, a coarse powder with 70 to 90% U_3O_8 and some UO_2 and UO_3 . The next step is to convert the yellow cake to UF_6 by a series of chemical processes schematically summarised in Figure 3 [3]. UF_6 is used in uranium processing because it exists in all three phases at pressures and temperature that are common to industrial processes. In the gaseous form, it can be enriched to the desired

content of ^{235}U . In the liquid form it can be filled and emptied from shipping containers and it can be stored as a solid.

Fuel fabrication for nuclear reactors typically begins with receipt of enriched uranium hexafluoride (UF_6) from an enrichment plant. The UF_6 , in solid form, in containers, is heated to gaseous form, and the UF_6 gas is chemically processed to form uranium dioxide (UO_2) powder. Conversion of UF_6 to UO_2 can be performed by one of three processes. In the first, UF_6 is reduced and hydrolyzed to UO_2 using hydrogen and steam. In the second, UF_6 is hydrolysed by solution in water, ammonia is added to precipitate ammonium diuranate, and the diuranate is reduced to UO_2 with hydrogen at 820°C . In the third process, gaseous UF_6 , CO_2 , and NH_3 are combined in water, precipitating ammonium uranyl carbonate. The ammonium uranyl carbonate is combined with steam and hydrogen at $500\text{--}600^\circ\text{C}$ to yield UO_2 . UF_6 to UO_2 conversion is often performed as the first stage of a fuel fabrication plant [4].

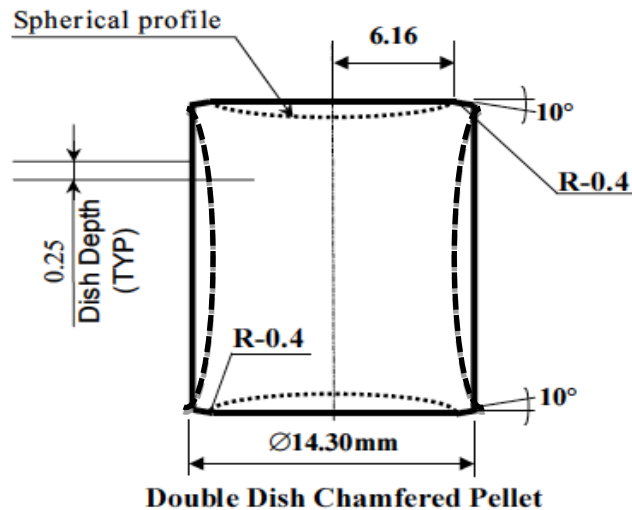
Figure 3. A schematic diagram showing the conversion of yellow cake to UF_6



Uranium dioxide pellet processing

Once the powder is made, standard powder compaction and sintering methods are used to make the fuel pellet. The UO_2 powder is either crushed or agglomerated to obtain the optimum size distribution for die filling and pressing. The powder is uniaxially cold pressed to form a cylindrical pellet. Next the pressed pellet is sintered in a reducing atmosphere at temperatures around $1\ 500^\circ\text{C}$, but can be as high as $1\ 700^\circ\text{C}$, for approximately four hours. Finally, the pellet is machined to have a disc shaped volume removed from both ends and the edges are ground to be smoothly chamfered as shown in Figure 4. Note the shape shown in Figure 4 is an example, the final dimensions vary depending on the reactor design and fuel used in it. Some pellets are also ground to have an hour glass shape shown in the same figure. While this process appears simple, the variations are numerous to give improved performance during service in a reactor. The details of the process variations will be elaborated in this section.

Figure 4. An LWR fuel pellet with discs removed from the ends and chamfered along the edges and materials removed to form a slight hour-glass shape along the cylindrical axis



LWR fuel pellets, UO₂ fuel pellets

Among the four criteria list at the beginning of this document, density of fissile isotopes, thermal conductivity, retention of radioactive materials and cost, the one that is most influenced by UO₂ pellet processing is the retention of fission gases and products. Sustaining a chain reaction is controlled by enrichment and reactor design; thermal conductivity is relatively low in UO₂ especially with the presence of pores and other defects and can only be influenced slightly by processing. Thus, the primary focus of pellet processing is to optimise the microstructure to retain fission gases and other fission products while reducing porosity to improve thermal conductivity and reducing swelling to maintain structural integrity of the clad.

The fission gas release mechanism is a combination of diffusion of the gas atoms to the grain boundaries followed by a percolating event that release the gas into the gap between the fuel pellets and the clad. Fission and the subsequent decay results in formation of some Xe, Kr, I and other gases that contain some radioactive isotopes. These atoms are dissolved in the fuel lattice structure, but have very low solubility. Thus, they precipitate from the fuel lattice to form nano-sized bubbles within grains as well as at grain boundaries. As more gas atoms are generated, the intragranular bubbles become more numerous and grow larger. However, the gas in the bubbles is periodically re-dissolved into the fuel lattice when the passing of a high-energy fission fragment disorders the fuel lattice at the surface of the bubble. This dissolved gas re-precipitates out to form nano-bubbles, but some of it also diffuses to the grain boundaries where it forms grain boundary bubbles. As these grain boundary bubbles grow and become more numerous, they link together to form a percolating path to the external surface or a crack thus releasing the gas. For optimal retention of the fission gases, it is best to keep the gases either dissolved in the lattice or within grains as nano-bubbles.

A secondary benefit to retaining gas in the intragranular nano-sized bubbles rather than in the larger grain boundary bubbles is that it minimises swelling of the fuel pellet. Minimising swelling of the fuel pellet is desirable as it reduces the physical and chemical interaction of the fuel with the clad. The pressure of the gas in the nano-sized bubbles is much higher than in the larger grain boundary bubbles due to the Gibbs-Thomson effect. This, in turn, means the volume occupied by the gas in nano-bubbles is much lower leading to less swelling of the fuel.

Retaining the gas with the grains is accomplished by enlarging the UO_2 grains and reducing the porosity in the fuel. A simple relationship describing the fractional release of fission gas, F , is developed using a modified Booth analysis [5]:

$$F = \frac{4}{r} \sqrt{\frac{Dt}{\pi}} \quad (1)$$

where r is the grain size, D is the diffusion coefficient and t is time. One can see that as the grain size r increases, the release of fission gas to the grain boundaries F decreases. Simplistically, one can attribute this to the greater distance that the gas must diffuse to reach grain boundaries. The emphasis on retention of fission gases within the UO_2 fuel grains has driven fuel vendors to manufacture LWR fuel pellets to have very large grains. Traditional LWR fuels were characterised by 12 to 15 mm grains. More recently, the fuels are doped with a variety of oxides to increase grain size. Grain sizes of UO_2 with dopants have been reported to grow to be as large as 50 to 100 mm, unusually large grain sizes for ceramic materials. Some of the dopants that have been reported are TiO_2 [6-8], V_2O_3 [9], NbO_2 [10-12], Al_2O_3 [13] [14], Cr_2O_5 [14-17] and MgO [14]. Another consist result reported is that the density of the oxide doped UO_2 is higher than that of the undoped UO_2 [6]. While the exact mechanisms leading to grain growth and higher densification rates are not known, many speculate that it is due to increased diffusivity [18]. Virtually all the dopants listed above form solid solutions with UO_2 in small quantities (≤ 0.2 to 0.3 wt%) with associated defects. At higher concentrations, they form a second, liquid phase. In some cases, the dopants at high concentrations form a second phase in the form of nano-size intragranular precipitates. The effect of additives on performance is also mixed with some finding no difference in FGR [10] [17] and other reporting decreased FGR [19].

The same diffusive mechanisms that enhance grain growth and densification also increase diffusivities of the dissolved fission gas atoms. Thus, the increase in gas retention due to the larger grain size r is off-set by the increase in diffusivity D as described by Equation 1. However, there appears to be another mechanism that is enabling gas retention in the large-grained UO_2 . Some of the additives, such as Cr_2O_3 , form nano-sized precipitates within the grains. These precipitates serve as nucleation sites for fission gas bubbles. Thus, many more nano-sized bubbles form in the larger grains at the precipitates thus increasing the FG retention.

Thermal conductivity of fresh oxide fuels is low to begin with and continually decreases as burn-up proceeds. This decrease is generally attributed to the accumulation of fission products and irradiation damage in the fuel [20]. The formation of gas bubbles, both inter- and intragranular, also decrease thermal conductivity. There is little that can be done to mitigate this decrease. One of the few materials properties that can be controlled

is the initial density of the fuel. Thermal conductivity as a function of porosity is given by the Maxwell-Eucken relationship:

$$\lambda = \lambda_o \frac{1-P}{1+\beta P} \quad (2)$$

Where λ is the thermal conductivity, λ_o is the theoretical thermal conductivity of the fully dense material, P is the fraction of porosity and β is a constant related to the geometry of the pores. Fabricating fuels of higher density will increase the thermal conductivity as shown by Equation 2. Retaining the fission gas in intragranular nanobubbles rather than in intergranular submicron-sized bubbles will also help in maintaining higher thermal conductivity.

MOX fuel pellets

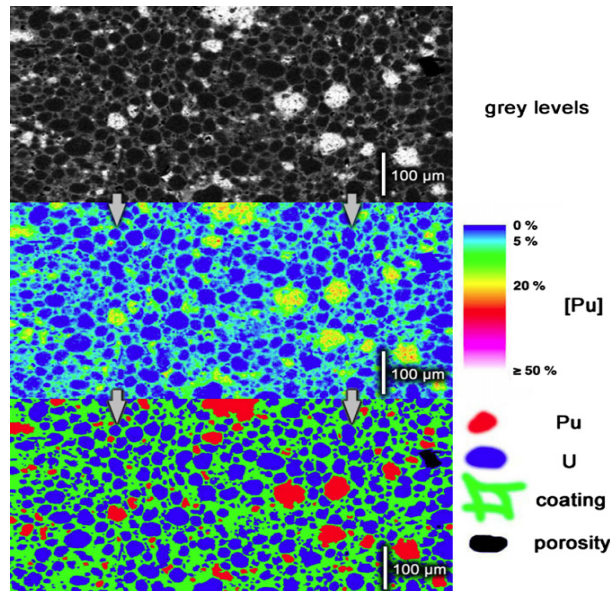
While MOX fuel pellets have not been used commercially in the US, they have been extensively used by the French commercially and researched for use in LWRs [21]. The original purpose of using MOX was to conserve and extend uranium resources. However, the discovery of many new uranium deposits coupled with improved mining techniques has resulted in unlimited supply of uranium for all practical purposes. The current purpose of MOX is to deplete the large stores of weapons-grade plutonium that have been amassed by recycling used fuel [22,23]. In the past, rather than use PuO_2 fuel pellets with substantially different properties, relatively small quantities of PuO_2 of $\leq 6\%$ are mixed with the UO_2 in the hope that the resulting fuel will perform similarly to traditional UO_2 fuel [24,25,26]. Indeed, irradiation of the low- PuO_2 -content MOX in LWRs has shown very similar behaviour to that of UO_2 [21,27,28]. In more recent years, much higher PuO_2 content MOX, ranging up to 20% PuO_2 , has been studied and used successfully in LWRs. In this range, there are quantitative differences in fuel performance and behaviour, however, qualitatively these high- PuO_2 MOX fuels behave similarly to the low- PuO_2 MOX fuels [29].

PuO_2 has the same crystal structure as UO_2 with comparable lattice parameters. Thus the two compounds form a complete solid solution. MOX can be fabricated by co-precipitation or by mixing the two powders with the later being more, however, virtually all MOX fuel is produced by mixing the two powders. The MIMAS (Micronized MAster blend) process is one process used for mixing UO_2 and PuO_2 powder in two different mixing steps. In the first step, PuO_2 and UO_2 powders and sintered scraps of UO_2 are ball milled for several hours to obtain a homogeneous mixture. The amount of Pu concentration in the master mix can vary between 20 and 40 mol% of heavy metal, but is typically 30 mol%. The second step consists of blending the master mix with depleted or natural UO_2 to obtain the desired final enrichment [30]. This process results in a heterogeneous distribution of Pu and U, as shown in Figure 5 [31] showing Pu rich region consisting of $\sim 30\%$ Pu, U-rich areas of almost 100% U and the “coating” region where interdiffusion has resulted in region with $\sim 5\%$ Pu.

Another process used to produce MOX is SBR, Short Binderless Route. In this process, PuO_2 , UO_2 , and possibly sintered scraps are assembled with the desired enrichment and milled in an attritor mill [30]. Like MIMAS, SBR also results in fuel with PuO_2 -rich regions, but these regions are small with PuO_2 enrichment being only

marginally more than the matrix [30]. Powders prepared by MIMAS or SBR are pressed and sintered under the same conditions used for fabricating traditional UO₂ fuel.

Figure 5. The distribution of U and Pu in MIMAS MOX fuel



LWR oxide fuels are made using standard powder processing techniques. Powders are milled, mixed, sieved and combined with sintering aids. The powders are formed by uniaxial, cold, dry pressing into pellets. The pellets are sintered at approximately 1 600°C for 1 to 4 hours to the desired density. Finally, the pellets are machined to have the final shape, a haystack shaped-pellet which mitigates the mechanical interaction with the clad due to swelling.

While processing a monolithic piece of UO₂ or MOX to the approximate pellet shape and desired density is routine and relatively easy with present-day technology, obtaining the exact dimensions, and matching the microstructure and composition to performance properties remains challenging. The ability to sinter the pellet to the desired end shape to minimise or even eliminate grinding the pellet to the final shape and size would simplify the processing greatly. Near-net shaping to eliminate grinding can be achieved by developing predictive modelling enabled by experiments that characterise sintering as a function of the starting powder characteristics (particle size and shape distributions, and composition and composition distribution), the powder compact characteristics (density variation in the compact after pressing). Near net shaping is routinely achieved in many metallic products as sufficient control can be exerted over all aspects of powder processing. For LWR fuels, the feed stock materials for synthesising powders can vary greatly. Thus, more research is needed to develop near-net shape sintering.

Like almost all engineering materials, the microstructure and composition of the materials must be optimised to obtain the desired performance properties during service. Nuclear fuels are no exception. The exact role of additives on diffusion processing during sintering and irradiation is not well understood. The role of precipitates on fission gas retention is also not well understood. The distribution of phases and composition on

MOX performance is poorly understood. The bulk of the research necessary in fuel fabrication is not the fabrication itself, but in identifying the desired microstructure, phases and composition; then developing the powder processing methods to obtain this microstructure at the end of powder synthesis, pressing and sintering.

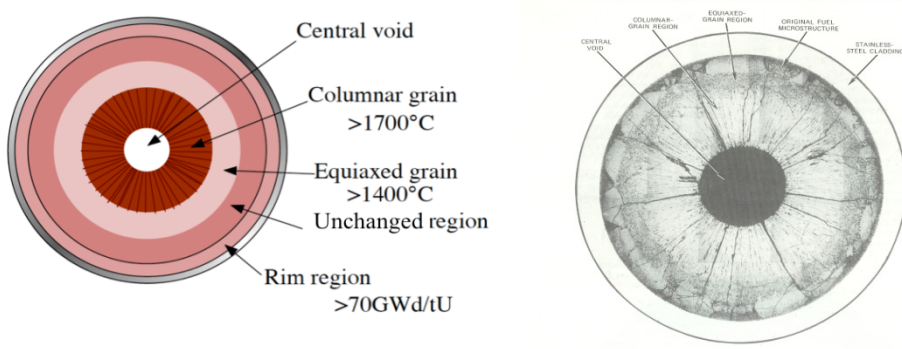
Fast reactor oxide fuel pellets

The neutronics of a fast reactor require that the fuel pellet have a smaller diameter approximately 0.5 cm as compared to the 1 cm diameter of LWR fuel pellets. While this does not have great implications for pellet processing, it does require slightly better control during the powder compaction as the aspect ratio of the die is higher. Otherwise, the basic pressing and sintering of FR pellets is very similar to LWR fuel pellets.

Another requirement imposed by FR neutronics is that enrichment of FR fuels have much higher enrichment with typical enrichments of 19% and some research fuels having PuO₂ of 44% [32]. This does complicate powder processing as the higher alpha-emissions do charge the powders more, but more controlled powder processing can overcome these complications easily.

The conditions that the fuel pellet experiences in a fast reactor are substantially different from those experienced by LWR fuels. Both the absolute temperature and the temperature gradients in a FR fuel pellet are much higher. This leads to substantial restructuring of the fuel within a couple of days of service in-reactor. The fresh fuel pellet has uniform grain size and density, but very quickly becomes restructured to have the features shown in Figure 6 [28,29]. The porosity in the central portion of the pellet diffuses up the temperature gradient due to the Soret effect. It forms a central void that traverses the length of the entire pellet. In the region immediately adjacent to the void, grain growth under the large temperature gradient results in columnar grains. The third region experiences equi-axed grain growth. The outer most region remains unchanged as the temperature is low. However, at high burn-up >70 GWD/tU, the high-burn-up rim structure does form in ²³⁸U containing fuels.

Figure 6. Fast reactor fuels restructure to form a central, axial pore with grain structure as shown schematically on the left and in a micrograph on the right



3.22 Cross section of mixed-oxide fuel rod irradiated to 2.7% burnup. No melting. [From D. R. O'Boyle et al., *J.*

Fission gas retention in FR pellets is difficult to achieve. In the central region of the fuel where the columnar grains form, the fission gas like the gas in the pores diffuses up the temperature gradient to the central void and is released. In the next layer where the

equi-axed grains form, the temperature is high and fission gas diffusivity is high, leading to a release by diffusion to grain boundaries, followed by percolation along the boundaries. In the outer, cooler region fission gas is retained much like it is in LWR fuels.

Thus the goals of the FR fuel pellet processing to optimise performance are different than that of LWR fuel pellets. Oxygen retention within the fuel is more important than it is for LWR fuels. Each fission event removes a U atom from the UO_2 lattice, leaving two oxygen atoms available to nominally oxidise the steel clad. Oxidation of the clad would substantially degrade the chemical and mechanical properties of the clad making it more susceptible to releasing radio-nuclides. In order to retain the oxygen atoms release by fission in the fuel, FR fuels are made with oxygen hypo-stoichiometry UO_{2-x} with x ranging from 0.03 to 0.08. Hypo-stoichiometry is achieved primarily by sintering the UO_2 pellet in highly reducing environments. In LWR fuels, oxygen can and does diffuse to oxidise the clad. However, far fewer oxygen atoms are released as the enrichment in LWRs fuels is much lower. The lower temperatures in the fuel and especially at the clad result in lower oxygen diffusion rates. Lower diffusivity of fewer oxygen atoms leads to less oxidation of the clad. Thus, little effort is made to lower the oxygen stoichiometry of LWR fuels.

Reducing the fuel-clad mechanical interaction by reducing fuel pellet swelling is another goal of FR fuel design. As discussed above, the high temperatures and high-temperature gradients of the fuel lead to very little retention of fission gases within grains either in the form of dissolved gas or nano-sized bubbles. While nano-sized intragranular bubbles do form, they retain much less fission gas than in LWR fuels [35]. Thus, unlike LWR fuels, no attempt to trap gas bubbles at metal oxides precipitates in large-grained structures is made. Rather the fuel rod is designed with a large plenum to retain the fission gas rather than allow it to pressurise the clad by filling the gap between the fuel pellets and clad. The plenum is normally very long, typically the same height as the core and can be located either above or below the core [36].

Due to the high neutron absorption cross-section of Pu in the fast neutron energy spectrum and the high enrichment necessary for FR, mixed UO_2 and PuO_2 MOX is frequently used. Unlike LWR MOX fuel, FR MOX has a much higher fraction of Pu. Other compositional differences in FR fuels may be driven by the need to consume TRU elements such as Np, Cm and Am formed during irradiation. The separation and use of these long-lived TRU elements would not only provide energy, but also reduce the burden of sequestering them for many thousands of years or even longer. While sintering of FR UO_2 or MOX fuel with minor quantities of NpO_2 , AmO_2 , and CmO_2 is not substantially different than the standard process of milling, mixing, pressing and sintering, some complications may arise. Achieving hypo-stoichiometry in FR oxide fuels with TRU may require some modification to the sintering process such the composition of the reducing atmosphere used during sintering. The differences in diffusivities due to TRU additions may drive the development of a modified time-temperature cycle. The TRU elements, particularly Am, have high volatility. This requires modification either to the sintering cycle or the furnace to control the loss of the TRU elements.

Fast reactor oxide fuels operate at very high temperatures with the centreline temperature that is close to its melting point. These high temperatures drive microstructural evolution and compositional changes that is specific to the fuel and design.

There is little one can do to effect these changes during service by fabrication. Thus, the opportunity to develop improved FR oxide fuel and the attending fabrication methodologies is limited.

Metallic fuels

Metallic fuels have been used in SFRs and offer some advantages over oxide fuels. The primary one being the higher thermal conductivity of the fuel which allows the operational temperatures to be lower and requires less cooling under accident conditions. Other advantages are high fissile and fertile density capability and low Doppler broadening yielding lower reactivity feedback. However, metal fuels do have the disadvantage of having lower melting temperatures and high chemical interaction with the clad than do oxide fuels.

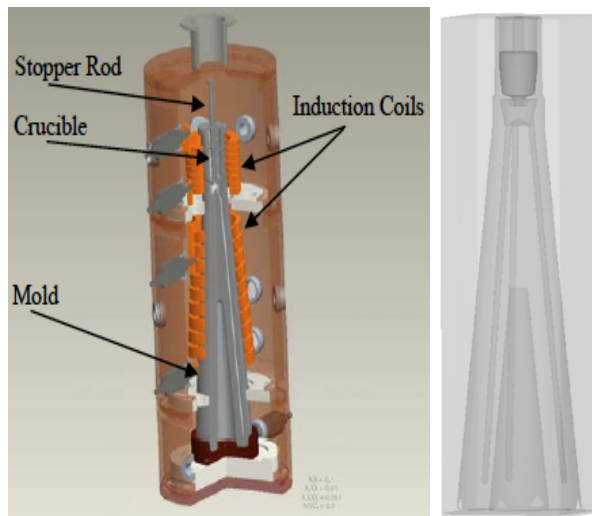
For optimal performance and safer operation during off-normal or accident condition, high melting temperature is desired. Alloying with components that do not lower the melting temperature of uranium and plutonium is important. Another necessary property of the alloying component is that it does not moderate the neutrons. Early attempts to alloy with iron [37-39], cobalt [40,41], aluminum [42,43] and other metals proved unsustainable [44]. Alloying with zirconium [45,46] proved to be the best option as it has the desirable neutronic properties, has a much higher melting temperature than those of Pu and U and mitigates chemical interaction with the clad. It also has the advantage of stabilising the desired phase in Pu [44,42]. A possible route for disposition of many of the long-lived TRU elements such as Np, Cm and Am, is to alloy them with U-Pu-Zr fuel. While little data exists for Cm, all other TRU elements, Am, Pu and Np, have higher vapour pressure than U at fabrication temperatures. Americium in particular has a very high vapour pressure [47]. Their high volatility present some challenge during fabrication. Another complication of alloying TRU elements with U-Pu-Zr is that they are gamma emitters; thus requiring greater shielding during fabrication and handling during and post-service.

Metal fuels for FR have traditionally been fabricated by melting and casting into long pins which are clad in stainless steels with sodium filling the gap between the fuel and clad. The fuel rod is designed with a large plenum to retain fission gas released during operation. A number of methods have been used to fabricate the metal pins. Several molten metal casting techniques, continuous casting, centrifugal casting, injection casting, vacuum casting [48,49] and others [50], have been attempted. Other methods such as co-extrusion with clad and hot rolling have also been tried. Injection casting into quartz molds has emerged as the primary fabrication of metal fuels. Injection casting of U-Pu-Zr fuels consists of melting the feedstock in the desired alloy ratio at a temperature of approximately 1 500°C in an induction furnace. To fabricate EBR-II fuel, Y_2O_3 coated graphite crucibles were used for the melt. Once the fuel is molten, the atmosphere in the furnace is evacuated and the quartz molds were lowered into to the melt until they were fully submerged. After several seconds when the molds have preheated, the furnace was rapidly pressurised with argon gas to inject the metal into the molds [47].

This injection casting technique has proven effective in making the long, thin metal pins with uniform isotropic microstructure that is desired. Furthermore, it is conducive to remote operation as it is easily built and operated. However, the need for retaining highly volatile components such as Am during casting is driving development of improved

injection casting for advanced metallic fuels. The casting process and equipment is being designed to minimise evaporation of the volatile components by minimising their exposure time to high temperature, reducing application of vacuum and keeping the crucibles closed. A schematic model of one such system being developed at INL is shown in Figure 7 [50,51].

Figure 7. Schematics of the bench-scale metal casting being developed at INL (in this system the three molds extend down at small angles from the crucible)



Particulate fuels

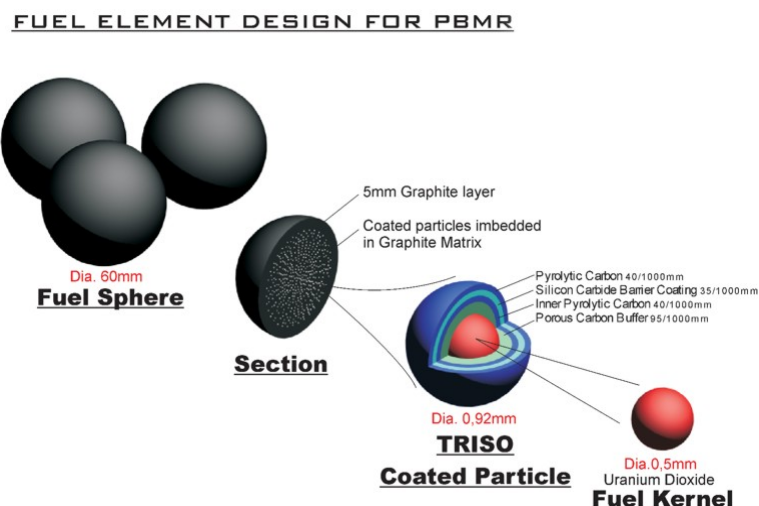
Particulate fuels are a class of fuels consisting of a spherical kernel of fissile fuel enveloped in concentric coatings. Nominally, the coatings function much like cladding for pellets; they provide a barrier against release of radioactive ions. The overall dimension of the spherical fuel particle ranges from 0.7 to 1.0 mm. Among the particulate fuels, TRISO, tristructural-isotropic, has emerged as the predominant fuel. While there are a few variants of TRISO, the basic particle consists of the UO₂ or UCO kernel with four layers consisting of three isotropic materials. The first layer, a porous carbon buffer over the kernel, serves to contain fission products that escape the kernel by recoil or the knock out effect. It also provides open space for the swelling fuel kernel and fission gases to fill, thus reducing the pressure on the outer layers. The next three layers are inner dense pyrolytic carbon (iPyC), SiC and outer dense pyrolytic carbon (oPyC). They contain all the radioactive materials, fuel and fission products, from being released. These three layers are often referred to as the pressure vessel as they contain the pressurised fission gases. Pyrolytic carbon is composed of graphene sheets in planar order with some bonding between the sheets. Depending on the deposition conditions a wide range of microstructures from isotropic to lamellar can result [52]. Note that the deposition conditions are not just of the PyC layer in question, but of subsequent outer layers as well. Thus the inner iPyC layer is usually more anisotropic than the outer one. The desirable PyC microstructure for TRISO fuel particles is a dense, isotropic one. Under irradiation, PyC will develop irradiation defects resulting in volume change. Anisotropic volumetric

changes will crack the PyC layers, but isotropic PyC with uniform and dense microstructure will remain protective under irradiation [53]. The SiC layer, like all the layers, is chemically deposited. A “good” SiC layer is dense, equi-axed (as opposed to columnar) and small-grained with no defects such as pores or inclusion.

The variations in TRISO are the exact composition and size of the kernel. The most common kernels are either UO₂ or UCO, however, other fissile materials can also be used to form the kernel, such as MOX or oxides with other transuramics. The size of the kernel can range from 350 to 500 mm and the exact thickness of the outer layers can also vary with typical layer being 35 to 90 mm thick.

These particles can be packed in various configurations to constitute a fuel element. The two most widely used are pebbles in a pebble bed reactor and fuel compacts in prismatic, graphite fuel elements. These are schematically shown in Figures 8a and b. The fuel in Figure 8a was a TRISO product developed by Pebble Bed Modular Reactor, Pty. Ltd. [54]¹. The fuel element, called a pebble, is a sphere approximately the size of a tennis ball. The pebble consists of fuel particles embedded in a graphite matrix which is ~5 cm in diameter surrounded by another cm of fuel free graphite for a total pebble diameter of 6 cm. The number of fuel particles in each pebble is on the order of 15 000.

Figure 8a. Schematic of a TRISO particle in a graphite pebble



For the Prismatic Modular Reactor (PMR), the TRISO particles are embedded in a “fuel compact”, also composed of graphite matrix, which are cylinders ~5 cm in height by 1.27 cm in diameter. These cylinders are inserted into graphite fuel elements, as shown in Figure 8b [55]. Both the types of fuel elements were designed to be used in high-temperature gas-cooled reactors. He gas is used as the coolant.

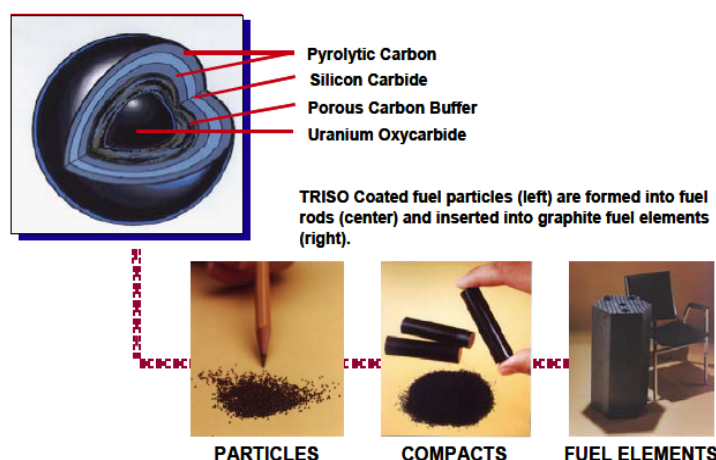
Other fuel and reactor designs for particulate fuels have been proposed. These will not be reviewed here; however, one example of an alternative particulate fuel design is to use them in currently operational LWRs. The design consists of replacing current oxide pellets with pellets formed by TRISO particles dispersed in a carbon matrix. The advantages of

¹ Pebble Bed Modular Reactor , Pty. Ltd. is a subsidiary of EskomHoldings and is a state of Care and Maintenance.

this design are increased safety, higher burn-ups, reduced waste and reduced waste handling. The fission products and gases are retained in the fuel particles even under accident conditions making the fuel safer. The fuel kernels can be made of TRU fuels, thus reducing the amount of waste for disposal. The handling, transport and storage of these fuels is more robust as the fission products are hermetically sealed within each particle.

The kernel is fabricated using a sol gel process. The layers are deposited by CVD. Sol gel has been used to form spherical particles for many years [56]. Using it to form the kernel of TRISO particles was a natural extension of this technology. A sol is a dispersion of colloidal particles in a liquid. A gel is an interconnected, rigid network of long polymeric chains. The basic sol-gel process is the reaction of a nitrate salt with ammonia to produce a spherical gel. The ammonia is produced internally by the decomposition of HMTA, $(\text{CH}_2)_6\text{N}_4$. An aqueous solution of uranyl nitrate is made. The active chemical reagents for UO_2 internal gelation are the uranyl nitrate salt combined with urea $(\text{NH}_2)_2\text{CO}$ and HMTA $(\text{CH}_2)_6\text{N}_4$ inside an inert heat transfer medium, such as silicone. At the low temperature of 0°C , urea combines with the nitrate salt to stabilise the solution and prevent early gelation. The temperature is raised to 100°C and the solution is introduced into the silicone oil using a needle in the form of drops. The drops spheroidise and gelation proceeds to produce a solid sphere of hydrated uranium oxide with ammonia. The detailed process with the accompanying chemical reactions are reviewed by Jeong et al. [57]. The spheres are sintered to form the dense kernel of the TRISO particle [58,59]. The spherical kernels are coated using Chemical Vapour Deposition (CVD), to form the porous carbon, pyrolytic carbon and SiC layers over the kernel.

Figure 8b. Schematic of a TRISO particle formed into graphitic, cylindrical compacts in prismatic fuel elements



The advantage of TRISO fuel particles is that they contain the radioactive material, both the initial fissile material and the resulting fission products, within the particles. The outer layers of C and SiC serve as the containment and are often called the pressure vessel as the fission products, particularly the gases, pressurise the particle. The goal of the fabrication process is to produce highly spherical kernels and high strength, defect free coatings to ensure radioactive nuclides remain contained during service, and storage and

transportation of the used fuel. Improved processing resulting near-perfect particles is needed. Due to criticality concerns, the kernels must be processed in small batches. Scaling fabrication operations to manufacturing scales while ensuring safety and quality of the particles is another goal.

Modelling to enable advanced fuel fabrication

A necessary component of designing fabrication methods for developing advanced fuels is to know the desired characteristics of the resulting fuel that will perform optimally during service and later during storage and/or disposal conditions. Fuel fabrication must be constantly informed by how fabrication conditions affect the resulting fuel performance. Thus, adapting and developing models for fuel fabrication must be designed under these constraints. The fuel characteristics that can be controlled by fabrication can be separated into microstructural and chemical. The chemical composition will determine the thermodynamic stability, thermomechanical properties, irradiation response and other performance characteristics. Microstructure will influence kinetic rates, release of fission products, swelling, thermal conductivity degradation and many more properties. Thus, fabrication models must be able to predict these fuel characteristics and how they evolve during fabrication.

Oxide fuel fabrication models

Oxides are fabricated by pressing or otherwise shaping powder compacts that are sintered to form stronger more dense ceramics. Models that simulate these processes at multiple length scales could aid either in improving the fabrication process or the development of advanced oxides fuels. An example of the former may be the ability to make near-net shape oxides that do not require machining after sintering. Examples of the latter are when the composition of the fuel is changed by adding transuranics to UO₂ or additives to control microstructure, tailoring the sintering process to ensure only the desired microstructural and compositional changes occur. This requires simulation capabilities at the microstructural and continuum scale. At the pellet-scale, engineering models that simulate the macro-dimensional size and shape changes in the powder compact from pressing to final sintering are necessary as a function of powder characteristics such as particle size and shape, particle chemical composition, additives composition and distribution, and variation in density in the pressed pellet as well as processing conditions such as die geometry, pressing variables, sintering time and temperature. At the mesoscale level, models are needed to predict microstructural evolution and variations in the composition at the grain size scale from pressed powder compact to sintering pellet. Engineering scale models of powder compaction and sintering are highly developed. Their precision to predict macroscale changes is dependent of the accuracy of the constitutive materials models they use. The development of constitutive materials models that give the shrinkage, grain growth, porosity evolution, changes in chemistry and other microstructural during oxide fabrication are the key to advancing oxide fuel fabrication modelling. Development of microstructural evolution models that can be used to obtain material models for the continuum models would be the most effective way to promote fuel fabrication.

Metal fuel fabrication models

Metal fuels are fabricated by melting the metal and pouring into to mold to cast fuel pins that have very high aspect ratios of length to diameter and must be straight. Both the casting process and models to simulate it are highly developed. Adapting these models for the geometry of materials used for metal fuel casting could be accomplished readily. Mold design and optimisation of the casting process would be most useful for metal fuel design when the geometry or composition of the fuel needs to be modified. For example, if the fuel pin requires that the porosity in the cast fuel pin should be 4% and distributed evenly through the entire length of the cast pin, the casting model can be used to bracket the casting process conditions to be tested. Such modelling would greatly reduce process development time and expense by narrowing the casting process variables to obtain the desired porosity. If the composition of the metal is changed it may change the viscosity, which, in turn, may change the metal flow and filling into the mold. Again, a casting model that can simulate pin fabrication by casting would greatly improve efficiency, cost and performance of the fuel. The investment to further metal fuel fabrication is in the adaptation of casting models to fuel geometries and materials rather than in development of the casting models themselves. Again, the emphasis should be on mesoscale microstructural models that give details of grain size and shape given cooling conditions, formation of voids given pouring conditions and other such characteristics.

Particulate fuel fabrication models

Particulate fuels are fabricated by using sol-gel techniques to form the kernel and CVD is used to form the outer coatings. “Good” particles are ones that have kernels of concise size and shape with defect free coatings of even thickness with no cracks or voids. There is little that process modelling has to offer in fabricating these fuels. However, models that address the chemical and structural stability and thermomechanical performance of the particles during reactor service and later are necessary to continue to develop better designs of the particulate fuels.

Conclusion and future challenges

The fabrication of all engineering materials is intimately tied to obtaining the desired composition, microstructure and performance properties of that component. Nuclear fuels are the same. Their fabrication methods are a direct result of their performance characteristics during assembly of fuel elements, irradiation during service under normal and off-normal conditions, and during post-service handling, transportation and storage. The fabrication techniques of fuels are highly developed to meet the needs of current commercial nuclear reactors. The current fabrication processes are sufficiently advanced to enable obtaining the desired fuel macro-form with a minimal development effort. The motivation for developing improved fuel fabrication techniques for fuels in current commercial reactors is to lower cost or to improve safety and security. However, more than 50 years of LWR fuel development has optimised fuel fabrication to meet its performance requirements. Powder synthesis and powder processing have likewise continuously improved, thus oxide fuel fabrication is highly developed and not difficult to achieve. Likewise, melt and casting of metal fuels is also readily achievable with today’s technologies. Thus, the objective of improved fuel fabrication research is to develop

fabrication techniques to obtain the desired microstructure, composition distribution and other fuel characteristics.

The ability to tailor fabrication processes and or variables with sufficient control to obtain the desired fuel characteristics is the key. The desired fuel characteristics may be large grains of UO_2 with 50 nm precipitates of a particular oxide that are spaced approximately 100 nm apart. Or they may be to have Am in a metal fuel rod at a radial distance $r = 0.7$ (where $r = 1.0$ is the external surface) from the centre of the fuel axis where the temperature is relatively low, but Am is not readily able to vapourise from the surface. The fabrication variables and processes that would allow one to meet these can range from simple changes like adjusting the additives or particle size distribution to casting in a sealed furnace to very complex fabrication techniques like melt casting in layered structures to obtain the variable composition in the desired radial distributions.

A consequence of this type of fuel fabrication development to improve performance is that fuel fabrication research cannot be separated from fuel performance research. They two are closely tied thus requiring the need to design research programmes that recognise the overlap between fuel fabrication and fuel performance. This is the classic materials paradigm of fabrication-microstructure-properties link that enables progress in engineering performance of any component.

Acknowledgements

Sandia National Laboratories is a multi-programme laboratory managed and operated by Sandia Corporation, a wholly owned subsidiary of Lockheed Martin Corporation, for the US Department of Energy's National Nuclear Security Administration under contract DE-AC04-94AL85000.

References

- [1] Rudling, P. et al. (2007), *Welding of Zr Alloys*, IZNA7 Report.
- [2] Nininger, Robert D. (1954), *Minerals For Atomic Energy*, Inc. New York, <http://www.dangerouslaboratories.org/radore.html>.
- [3] <http://web.ead.anl.gov/uranium/guide/prodhand/sld008.cfm>.
- [4] <http://www.nrc.gov/reading-rm/doc-collections/cfr/part110/part110-appj.html>.
- [5] Booth, A. (1957), *A Method of Calculating Fission Gas Diffusion from UO_2 Fuel and its Application to the X-2-f Test Loop*, AECL-496.
- [6] Ainscough, J. et al. (1974), “The effect of titania on grain growth and densification of sintered UO_2 ”, *Journal of Nuclear Materials*, 52, 191-203.
- [7] Amato, I. et al. (1966), “Grain growth in pure and titania-doped uranium dioxide”, *Journal of Nuclear Materials*, 18, 252-260.
- [8] Sengupta, A.K., C.B. Basak, T. Jarvis, R.K. Bhagat, V.D. Pandey, S. Majumdar (2004), “Effect of titania addition on hot hardness of UO_2 ”, *Journal of Nuclear Materials*, 325, 141-147.

- [9] Amato, I., M. Ravizza (1967), “The effect of vanadium oxide additions on sintering and grain growth of uranium dioxide”, *Journal of Nuclear Materials*, 23, 103-106.
- [10] Assmann, H. et al. (1981), “Doping UO₂ with niobia beneficial or not?”, *Journal of Nuclear Materials*, 98, 216-220.
- [11] Harada, Y. (1996), “Sintering behaviour of niobia-doped large grain UO₂ pellet”, *Journal of Nuclear Materials*, 238, 237-243.
- [12] Song, K.W., S.H. Kim, S.H. Na, Y.W. Lee, M.S. Yang (1994), “Effects of Nb₂O₅ addition on grain growth and densification in UO₂ pellets under reducing and/or oxidizing atmospheres”, *Journal of Nuclear Materials*, 209, 280-285.
- [13] Aybers, M. et al. (2004), “Grain growth in corundum-oxides doped uranium dioxide and effects of grain growth to the mechanical properties of uranium dioxide such as elasticity determined by ultrasonic methods”, *Key Engineering Materials*, 264-268, 985-988.
- [14] Kashibe, S., K. Une (1998), “Effect of additives (Cr₂O₃, Al₂O₃, SiO₂, MgO) on diffusional release of Xe-133 from UO₂ fuels”, *Journal of Nuclear Materials*, 254, 234-242.
- [15] Bourgeois, L. et al. (2001), “Factors governing microstructure development of Cr₂O₃-doped UO₂ during sintering”, *Journal of Nuclear Materials*, 297, 313-326.
- [16] Delafoy, C. et al. (2007), “AREVA NP Cr₂O₃-doped fuel development for BWRs”, *Proceedings of the 2007 International LWR Fuel performance Meeting*, San Francisco, US.
- [17] Killeen, J. (1980), “Fission gas release and swelling in UO₂ doped with Cr₂O₃”, *Journal of Nuclear Materials*, 88, 177-184.
- [18] Une, K., I. Tanabe, M. Oguma (1987), “Effects of additives and the oxygen potential on the fission gas diffusion in UO₂ fuel”, *Journal of Nuclear Materials*, 150, pp. 93-99.
- [19] Sawbridge, P.T., C. Baker, R.M. Cornell, K.W. Jones, D. Reed, J.B. Ainscough (1980), “The irradiation performance of magnesia-doped UO₂ fuel”, *Journal of Nuclear Materials*, 95, 119-128.
- [20] Ronchi, C., M. Sheindlin, D. Staicu, M. Kinoshita (2004), “Effect of burn-up on the thermal conductivity of uranium dioxide up to 100,000 MWd/t”, *Journal of Nuclear Materials*, 327, 58-76.
- [21] Fisher, S.B., R.J. White, P.M.A. Cook, S. Bremier, R.C. Corcoran, R. Stratton, C.T. Walker, P.K. Ivison, I.D. Palmer (2002), “Microstructure of irradiated SBR MOX fuel and its relationship to fission gas release”, *Journal of Nuclear Materials*, 306, 153-172.
- [22] <http://georgewbush-whitehouse.archives.gov/omb/expectmore/summary/10003238.2006.html>.
- [23] <http://www.anl.gov/research/fmd/>.
- [24] Carbajo, J.J., G.L. Yoder, S.G. Popov, V.K. Ivonov (2001), “A review of the thermophysical properties of MOX and UO₂ fuels”, *Journal of Nuclear Materials*, 299, 181-198.

- [25] Walker, C.T., W. Goll, T. Matsumura (1996), “Effect of inhomogeneity on the level of fission gas and caesium release from OCOM MOX fuel during irradiation”, *Journal of Nuclear Materials*, 228, 8-17.
- [26] Sasahara, A., T. Matsumura (2008), “Post-irradiation examination focused on fuel integrity of sent BWR-MOX and PWR-UO₂ fuels stored for 20 years”, *Nuclear Engineering and Design*, 238, 1250-1259.
- [27] Bairiot, H., P. Deramaix (1992), “MOX fuel development: yesterday, today and tomorrow”, *Journal of Nuclear Materials*, 188, 10-18.
- [28] Fisher, S.B., R.J. White, P.M.A. Cook, S. Bremier, R.C. Corcoran, R. Stratton, C.T. Walker, P.K. Ivison, I.D. Palmer (2002), “Microstructure of irradiated SBR MOX fuel and its relationship to fission gas release”, *Journal of Nuclear Materials*, 306, 153-172.
- [29] Massih, A.R. (2006), *Models for MOX Fuel Behaviour*, SKI Report, ISSN 1104-1374.
- [30] White, R.J., S.B. Fisher, P.M.A. Cook, R. Stratton, C.T. Walker, I.D. Palmer (2001), “Measurement and analysis of fission gas release from BNFL's SBR MOX fuel”, *Journal of Nuclear Materials*, 288, 43-56
- [31] Oudinet, G., I. Munoz-Viallard, L. Aufore , M. Gotta, J.M. Becker, G. Chiarelli, R. Castelli (2008), “Characterization of plutonium distribution in MIMAS MOX by image analysis”, *Journal of Nuclear Materials*, 375, 86-94.
- [32] Sengupta, A.K., K.B. Khan, Jose Panakkal, H.S. Kamath, S. Banerjee (2008), “Evaluation of high plutonia (44% PuO₂) MOX as a fuel for fast breeder test reactor”, *Journal of Nuclear Materials*, 385, 173-177.
- [33] Idemitsu, K. “Nuclear fuel engineering”, <http://idemitsu.nucl.kyushu-u.ac.jp>.
- [34] O’Boyle, D.R., F.L. Brown, J.E. Sanecki (1969), “Solid fission product behavior in uranium-plutonium oxide fuel irradiated in a fast neutron flux”, *Journal of Nuclear Materials*, 29, 27-42
- [35] Maeda, K., K. Katsuyama, T. Asaga (2005), “Fission gas release in FBR MOX fuel irradiated to high burnup”, *Journal of Nuclear Materials*, 346, 244-252.
- [36] Waltar A.E., A.B. Reynolds (1981), *Fast Breeder Reactors*, Pergamon Press, Elmsford New York, US.
- [37] Okamoto, H. (1993), “Fe-Pu (iron-plutonium)”, *Phase Diagrams of Binary Iron Alloys*, H. Okamoto, ed., ASM International, Materials Park, pp. 337-39.
- [38] Okamoto, H. (1993), “Fe-U (Iron-Uranium)”, *Phase Diagrams of Binary Iron Alloys*, pp. 429-32.
- [39] Kurata, M., T. Ogata, K. Nakamura, T. Ogawa (1998), “Thermodynamic assessment of the Fe-U, U-Zr and Fe-U-Zr systems”, *Journal of Alloys and Compounds*, 271-273, 636-40.
- [40] Rough, F.A., A.A. Bauer (1958), *Constitution of Uranium and Thorium Alloys*, Report BMI-1300, Battelle Memorial Institute, Columbus, pp. 23.

- [41] Ellinger, F.H., W.N. Miner, D.R. O'Boyle, F.W. Schonfeld (1968), *Constitution of Plutonium Alloys*, LA-3870, Los Alamos Scientific Laboratory, p. 29.
- [42] Ellinger, F.H., W.N. Miner, D.R. O'Boyle, F.W. Schonfeld (1968), *Constitution of Plutonium Alloys*, LA-3870, Los Alamos Scientific Laboratory, p. 5.
- [43] Rough, F.A., A.A. Bauer (1958), *Constitution of Uranium and Thorium Alloys*, Report BMI-1300, Battelle Memorial Institute, Columbus, p. 11.
- [44] Hecker, S.S., M. Stan (2008), *Properties of Plutonium and its Alloys for Use as Fast Reactor Fuels*, JNM 383.112-118.
- [45] Kurata, M. (2000), *Thermodynamic Assessment of the Pu-U, Pu-Zr and Pu-U-Zr Systems*, Calphad, 23, 305-37.
- [46] Kittel, J.H., B.R.T. Frost, J.P. Mustelier, K.Q. Bagley, G.C. Crittenden, J. Van Dievoet (1993), "History of fast reactor fuel development", *Journal of Nuclear Materials*, 204, 1.
- [47] Burkes, D.E., R.S. Fielding, D.L. Porter (2009), "Metallic fast reactor fuel fabrication for the global nuclear energy partnership", *Journal of Nuclear Materials*, 393, 158-163.
- [48] Burkes, D., R.S. Fielding, D.L. Porter, D.C. Crawford, M.K. Meyer (2009), "A US perspective on fast reactor fuel fabrication technology and experience, Part I: Metal fuels and assembly design", *Journal of Nuclear Materials*, 389, 458-469.
- [49] Wu, X., R. Clarksean, Y. Chen, M.K. Meyer (2002), "Design and analysis for melt casting metallic fuel pins", *International Congress on Advanced Nuclear Power Plants*, Florida, US.
- [50] Fielding, R., K. Marsden, B. Grover, G. Preslar (2008), "Advanced bench-scale metal fuel casting system development", *Reactor Fuels and Mat'l., Transactions of the American Nuclear Society*, 99, 305-306.
- [51] Korzekwa, D., J. Crapps (2011), *Metal Fuel Casting Simulation*, LA-UR-11-05601, Los Alamos National Laboratory, US.
- [52] Hunn, J.D. et al. (2008), "Increase in pyrolytic carbon optical anisotropy and density during processing of coated particle fuel due to heat treatment", *Journal of Nuclear Materials*, 374, 445-452.
- [53] Snead, L.L. et al. (2007), "Handbook of SiC properties for fuel performance modeling", *Journal of Nuclear Materials*, 371, 329-377.
- [54] <http://www.pbmri.com/index.asp?Content=213&GState=Image&CatId=0&Image=44&Page=1>.
- [55] Sterbentz, J.W., B. Phillips, G.S. Chang, P.D. Bayless (2004), *Reactor Physics Parametric and Depletion Studies in Support of TRISO Particle Fuel Specification for the Next Generation Nuclear Plant*, INEEL/EXT-04-02331, Idaho National Engineering and Environmental Laboratory, US.
- [56] Hench, L.L., J.K. West (1990), "The sol-gel process", *Chemical Reviews*, 90, 33-72.

-
- [57] Jeong, K-C., S-C. Oh, Y-K. Kim, Y-W. Lee (2007), “ADU compound particle preparation for HTGR nuclear fuel in Korea”, *Journal of Industrial and Engineering Chemistry*, 13, 744-750.
 - [58] Rabu, B. et al. (2008), *State-of-the-Art Transmutation Fuels and Fuel Fabrication Facilities*, F16W – Contract Number 036418, PATEROS.
 - [59] Wegener, J.J. (2008), *Production of Cerium Oxide Microspheres by an Internal Gelation Sol-gel Process*, Masters Thesis, Texas, US.

Chapter 7.

Phenomena in thermal transport in fuels

A. Chernatynskiy¹, A. El-Azab², J.S. Tuleenko¹, S.R. Phillpot¹

¹University of Florida, US,

²Purdue University, US

Abstract

Thermal transport in nuclear fuels is a key performance metric that affects not only the power output, but is also an important consideration in potential accident situations. While the fundamental theory of the thermal transport in crystalline solids was extensively developed in the 1950s and 1960s, the pertinent analytic approaches contained significant simplifications of the physical processes. While these approaches enabled estimates of the thermal conductivity in bulk materials with microstructure, they were not comprehensive enough to provide the detailed guidance needed for the in-pile fuel performance. Rather, this guidance has come from data painfully accumulated over 50 years of experiments on irradiated uranium dioxide, the most widely used nuclear fuel. At this point, a fundamental theoretical understanding of the interplay between the microstructure and thermal conductivity of irradiated uranium dioxide fuel is still lacking. In this chapter, recent advances are summarised in the modelling approaches for thermal transport of uranium dioxide fuel. Being computational in nature, these modelling approaches can, at least in principle, describe in detail virtually all mechanisms affecting thermal transport at the atomistic level, while permitting the coupling of the atomistic-level simulations to the mesoscale continuum theory and thus enable the capture of the impact of microstructural evolution in fuel on thermal transport. While the subject of current studies is uranium dioxide, potential applications of the methods described in this chapter extend to the thermal performance of other fuel forms.

Introduction

In a nuclear power plant, energy is generated inside the reactor core in the form of heat, which is then transported out of the core by a working fluid and ultimately used to drive turbines and generate electricity. In the reactor core itself, heat is generated in the nuclear fuel by two processes: the fission of fissile (and fissionable) elements and radioactive decay of fission products. The fission process is the main contributor to heat generation under reactor operation. In shut-down mode, heat is mainly generated by radioactive decay [47,29].

Uranium dioxide (UO_2) is the most commonly used fuel form, especially in Light Water Reactors (LWRs). Aside from minor variations that depend on the reactor design, all LWRs utilise UO_2 fuel made of small pellets stacked and clad by thin walled tubes of zirconium alloy. Clad tubes filled with pellets are known as fuel elements. These elements are assembled in bundles, which are further grouped to form the fuel assembly inside the reactor core [47,29]. During reactor operation, the cooling water passes through the core to transport the heat out and keep the fuel temperature under control. The fuel assembly has to be thermomechanically and chemically stable so as to maintain the cooling process uninterrupted. The fuel conducts all heat generated to the coolant. This process depends on the thermal conductivity of the fuel, thermal conductivity in the gap region, fuel-clad interface conductance, clad thermal conductivity and the condition of the outer clad surface. Of these, the conductivity of the fuel is most critical because, being a ceramic, UO_2 has a low thermal conductivity of typically only a few W/mK at the temperature range of interest to reactor operation. The thermal conductivity decreases with increasing temperature, and deteriorates irreversibly during service. This deterioration is the result of a large number of microscopic and microstructural processes, including the change in composition due to fission and subsequent fission product decay, the formation and evolution of microstructure features such as dislocations, gas bubbles and precipitates, and fuel restructuring. The connection between these processes and the conductivity changes have long been a concern within the fuel design community, and many empirical models have been developed and/or adopted to describe such changes [63].

Most fuel performance codes use semi-empirical models to capture the effect of irradiation-induced microstructure on the thermo-physical properties of UO_2 , most especially the thermal conductivity. A variety of such models exist [63,65,71] [31,70,84], the review of which is beyond the scope of this chapter. Most such models, however, start with the conductivity of the pristine, unirradiated UO_2 , which has a thermal conductivity that decays slowly as $1/(a+bT)$, with T being the absolute temperature, up to temperatures close to 2 000 K; a and b are empirical constants. At any given temperature, irradiation lowers the conductivity values for UO_2 below the pristine value. The conductivity models available in the literature treat this reduction of conductivity by including corrections associated with various defects and microstructure features: dissolved fission products, porosity (voids and bubbles), dislocation loops, precipitates, and grain boundary evolution, etc. Since there is currently no theoretical framework to include such defects on a rigorous basis, various levels of approximations have been used. Typical semi-empirical models can be found in [9] and [65], which attempt to reproduce the experimental observations. The salient experimental observations of conductivity degradation are as follows: the conductivity decreases as a function of measurement temperature, irradiation temperature

and burn-up, while it shows some improvement as a function of annealing temperature due to defect recovery. These observations imply that the conductivity is strongly dependent on the temperature-history and is in general a dynamical quantity [65]. As such, physics-based models are highly desirable to capture the conductivity of UO_2 during reactor operation.

In this chapter, we assess the state-of-the-art modelling techniques of thermal transport in UO_2 , taking into consideration the impact of defects and microstructure on that important fuel property. Specifically, we address the issues related to the impact of defects and microstructure on the thermal conductivity of UO_2 and discuss available modelling approaches. These issues are conveniently categorised and discussed in the next two sections under *atomistic* and *mesoscale* modelling approaches. The chapter ends with a discussion of further modelling needs in this important area.

Recent progress in atomistic simulation of thermal transport in UO_2

As with all electrically insulating crystalline solids, thermal transport in UO_2 is mediated by lattice vibrations, the quanta of which are known as phonons. At very high temperatures (above $\sim 1\ 500$ K), contributions from polarons (localised structures of phonons and electrons) lead to a slow increase in the thermal conductivity [17]. Since this temperature range is outside of the operating conditions of the typical nuclear reactor, we concentrate our discussion here on the phonon-mediated lattice thermal transport. Above the Debye temperature (~ 400 K), thermal transport is primarily affected by the phonon-phonon interactions and by phonon scattering by defects of the crystal. We therefore discuss the nature of the phonon-phonon interactions in UO_2 first. Of the various defects, point defects seem to be the most important in degrading thermal conductivity; hence we continue with the discussion of the phonons interactions with the point defects. UO_2 fuel is a polycrystalline ceramics with some porosity (typically around 5% for a fresh pellet). Porosity is further developed during burn-up of the fuel, in the form of the helium bubbles. The polycrystallinity of UO_2 results in additional Kapitza resistance across grain boundaries and interfaces with second phases. In the subsequent sections, we outline the effect of these microstructural features on thermal conductivity. Finally, we discuss a contribution of the dislocations to the overall thermal transport. We remark here that the studies of UO_2 itself are rather limited and, therefore, we discuss the advances in the simulation of the thermal conductivity of ceramics and, where available, examples of the applications to UO_2 will be discussed. In particular, a ceramic solid that has the same crystal structure as UO_2 and which has been extensively studied is yttria-stabilised zirconia.

Phonons and their interactions

The concept of phonon-mediated thermal transport is briefly outlined here [8,94]. The pertinent theoretical formalisms represent the starting point of the classical topics of lattice dynamics and the theory of heat of crystalline solids [11]. The starting point of such formalisms is expanding the potential energy of the crystal into a Taylor series around equilibrium atomic positions. In the harmonic approximation, this series is truncated after the quadratic term. Using the translational symmetry of the crystal, the resulting Hamiltonian can be diagonalised in a plane wave basis, with the frequencies of the waves determined by the eigenvalues of the dynamical matrix. Looking at the problem from a different perspective, each of the plane waves can be viewed as a propagating harmonic

oscillator (crystal) mode; hence the dynamics of the crystal is described as a set of harmonic oscillators for which the quantum solution is readily available. In the quantum view, each of the eigenstates of the system corresponds to a phonon and the thermal energy in the solid can be viewed as the energy of ideal gas of non-interacting phonons. Since phonons are bosons, the number of phonons in the system at a given temperature is given by the Bose-Einstein distribution.

Using standard statistical mechanics, one can immediately deduce the formula for the thermal conductivity tensor of such phonon gas:

$$k_{ij} = \sum_{\lambda} C_{\nu}^{\lambda} v_i^{\lambda} v_j^{\lambda} \tau_{\lambda} \quad (1)$$

In this expression, λ denotes individual phonon modes, C_{ν}^{λ} is the heat capacity of a given mode, v_i^{λ} is the i -th component of the phonon group velocity and τ_{λ} is the phonon lifetime. In the harmonic approximation, the thermal conductivity of a solid is infinite (the analogy with the atomic ideal gas is not absolute, since head-on collisions are not present in the phonons case, hence the infinite phonon lifetime). In order to produce interactions among phonons, one retains high-order anharmonic terms in the Taylor expansion of the potential energy and treats them by the means of perturbation theory [51]. In this description, the phonon-phonon interactions result in both an energy shift and a non-zero linewidth Γ_{λ} of each phonon state. The linewidth Γ_{λ} is related to the phonon lifetime $\tau_{\lambda} = 1/2\Gamma_{\lambda}$, and therefore is the fundamental quantity describing phonon-mediated thermal conductivity. To leading order, the cubic and quartic terms in the expansion of the crystal energy contribute approximately the same amount to the shift in the phonon energy, while only the cubic term contributes to the linewidth.

To this point, the analysis has been for a statistical phonon system under thermodynamic equilibrium, whereas thermal transport is a non-equilibrium process. The standard vehicle to treat non-equilibrium phonon transport is to use the Boltzmann Transport Equation (BTE), which governs the phonon distribution in the crystalline solid. For small deviations from equilibrium, the BTE (see next section) can be linearised and solved under various simplifications. For example, the relaxation time approximation [42] leads to the expression for the thermal conductivity in Equation 1. The resulting non-equilibrium distribution function can support non-zero heat current, and from which one can, by using Fourier's law, extract the thermal conductivity of the solid. Moreover, the presence of defects in the crystalline solid of interest can also be treated within the relaxation time approximation, taking advantage of the fact that various types of crystal defects provide additional scattering mechanisms for phonons, each associated with a corresponding relaxation time. Treating different scattering mechanisms as independent from each other, it is possible to use Mathiessen's rule to compute overall relaxation time, τ , as follows:

$$\frac{1}{\tau} = \frac{1}{\tau_u} + \frac{1}{\tau_d} + \frac{1}{\tau_b} \dots \quad (2)$$

Here τ_u is the relaxation time associated with phonon-phonon scattering mechanism; τ_d and τ_b is associated with the scattering on the point defects and boundaries correspondingly. This programme was actively developed in the 1950s and 1960s with great success in the works of Klemens, Ziman, Carruthers, Callaway and others [42,16,14,94,8]. The major difficulty, however, is that in order to obtain analytical expressions some significant

simplifying approximations have to be made (for example, the Debye approximation for the phonon density of states neglects most of the detailed information about interatomic interactions).

Atomistic level simulation of thermal transport in crystalline solids has been pursued to gain further insight into the impact of various scattering mechanisms on thermal transport. The pertinent methods can be divided into two broad classes: Lattice Dynamics (LD) based methods and Molecular Dynamics (MD) based methods. Lattice dynamics methods follow the analysis described above, but because they are largely numerical rather than analytic, they can be carried out without the approximations described above; most notably, the phonon structure of the solid is typically computed explicitly without relying on the Debye model. A number of approximate techniques for solving the BTE were proposed in the 1950s and 1960s and have been further developed, including the relaxation time approximations [42,83] and the variational method [94,67]. However, renewed interest in thermal conductivity and advances in computational power have allowed for the development of the full solution to the BTE by numerical methods [64,12,21]. In particular, it was demonstrated [20] that in the case of UO_2 the relaxation time approximation works very well. While providing a wealth of information on the fundamental details of the thermal transport, these methods are limited by the level of the anharmonicity one takes into account, and are therefore applicable only at relatively “low” temperature (some fraction of the melting temperature). Another limitation of LD methods is their reliance on the translational symmetry of the crystal, and hence the capability for explicitly describing the effect of defects of any kind is limited. The standard apparatus of imposing periodic boundary conditions fails due to a poor scaling of the computational time with the number of atoms in the system [83,21].

In the MD based methods, simulations are performed either in thermal equilibrium (Green-Kubo method) or in non-equilibrium (direct method) conditions [73]. In the first case, the decay of the heat current correlation function is computed and related to the thermal conductivity through linear response theory. In the second case, a thermal gradient is established throughout the simulation cell and, by measuring this gradient and the heat current, one can deduce the thermal conductivity from Fourier law. Limitations of the MD based methods include size effects (simulation cells are by many orders of magnitude smaller than real macroscopic samples) and the fact that in MD simulations ions move in accord with the classical equations of motion; hence quantum effects are not taken into account. The latter means that MD methods are effective at temperatures above Debye temperature of the solid. Since the Debye temperature of UO_2 is quite low (~ 400 K), application of these methods for studying thermal conductivity effects in UO_2 fuel is reasonable. While not providing detailed information about phonon properties of the system, these methods are capable of analysing systems with point defects, and interfacial systems.

One can see that the two classes of methods described above are complementary to each other: LD methods work well at low temperature and for ideal crystals; MD methods work well at high temperature and can take into account structural defects. The common limitation of these techniques, however, is the description of the interatomic interactions. While development of high-fidelity first-principles methods has made great strides in the last two decades [37], as discussed below, their application for thermal transport is still limited due to the high computational expense. The majority of simulations of thermal

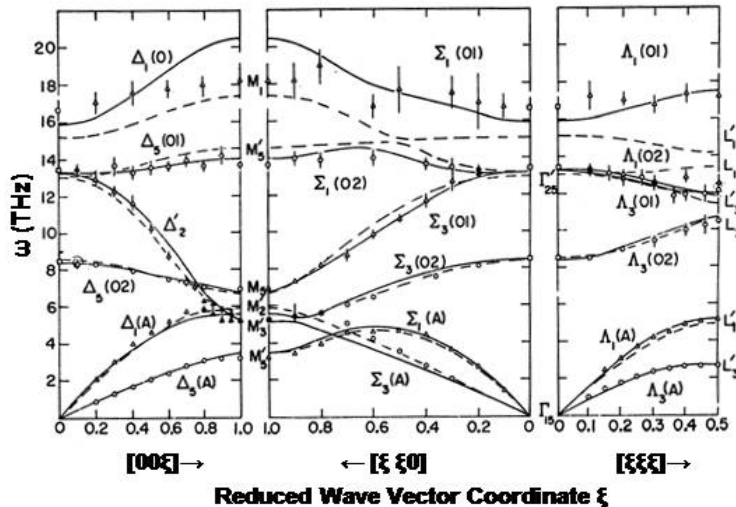
transport therefore employ classical semi-empirical potentials. While such classical potentials have had great success in representing thermomechanical properties, their reliability in thermal transport calculations is less impressive. The main reason is that thermal transport properties are largely determined by the third derivatives of the potential energy with respect to atomic position, while the empirical database for these potentials typically consists only of the properties that are sensitive to the energy itself (relative energies of different phases) or its second derivatives (elastic constants and/or phonon dispersion curves). In the case of UO_2 , development of high-fidelity potentials for thermal transport properties is parallel to the development of potentials for the radiation damage simulations. In the latter case, due to the deposition of the large amounts of kinetic energy in the crystal, atoms routinely probe much shorter interatomic distances than in normal equilibrium or near-equilibrium conditions. The total energy typical database typically does not include properties that probe such short interatomic separations. A possible solution is to include such short-range interactions. One example of this approach was implemented by [81]. However, while having some success in description of the defects in fluorite UO_2 , this model also predicts that fluorite is not the ground state of UO_2 [20], a flaw that limits its applications.

Phonon-phonon interactions

We begin this discussion of the phonon-phonon interaction in UO_2 with a description of its phonon structure. Phonon properties were measured in the 1960s [26] by the inelastic neutron scattering technique. The phonon dispersion along the [001], [011] and [111] directions is shown in Figure 1. Since UO_2 has 3 atoms in the primitive cell, there are a total of nine phonon branches, some of which are degenerate along high symmetry directions. The two transverse acoustic modes show very little dispersion, with the energy about half that of the longitudinal modes. Six optical modes occupy the higher range, with the cut-off frequency at about 18 THz. Of these optical modes, the $\Delta_5(\text{O}1)$ and Δ'_2 modes are a longitudinal/transverse pair that do not have an LO/TO splitting at the gamma point, while the $\Delta_5(\text{O}2)$ and $\Delta_1(\text{O})$ modes are split at the gamma point due to the long-range electrostatic interactions. While optical modes typically are not considered to be important for thermal transport, we will argue below that they make significant contribution to the overall thermal conductivity. The typical reasoning for their unimportance is the relatively small group velocity of these modes in comparison with the acoustic modes, which according to Equation 1 should markedly decrease the thermal conductivity. Looking at Figure 1, however, one readily observes that mode Δ'_2 , for example, has a group velocity, given by its slope, which is very close to or even larger than that of the acoustic modes.

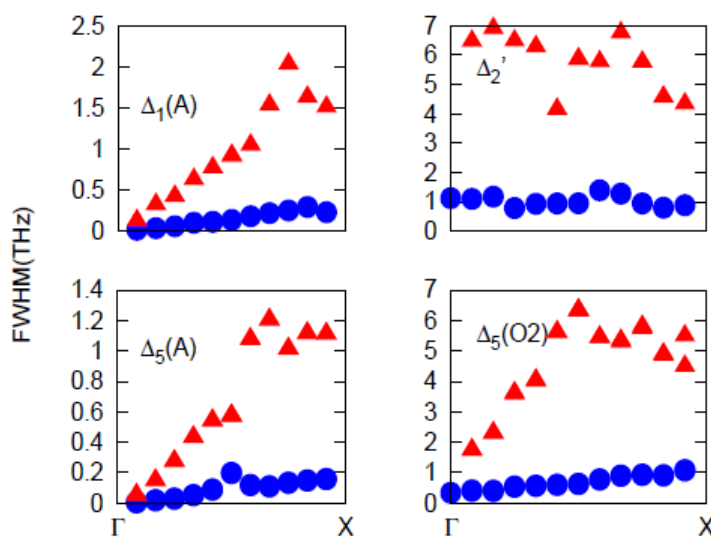
From the simulation perspective, the UO_2 phonon band structure can be reproduced rather well by first principles methods [92,79] despite the well-known difficulties of the proper representation of the highly correlated f-electrons of uranium [28]. Classical potentials generally reproduce the phonon structure less well, with the most typical problems being the highest optical mode, Δ_1 , being pushed to the 20-25 THz range, an excessively high group velocity for the $\Delta_5(\text{O}1)$ mode, and a very low frequency for the Δ'_2 mode at the zone boundary. In spite of these difficulties, the shell model [25] potential proposed by Catlow [18] reproduces the phonon structure rather well.

Figure 1. Phonon dispersion curves for UO_2 as measured by the inelastic neutrons scattering [26]



While details of the phonon band structure are known in UO_2 , the information about phonon-phonon interactions that define thermal conductivity of the ideal UO_2 crystal is essentially non-existent. The thermal conductivity itself was studied by [20] using lattice dynamics of the basis of the classical interatomic potentials; the main outcome that works is that none of the classical potentials reliably predicts thermal conductivity even in the relatively narrow temperature range between 300 K and 1 000 K. More detailed calculations on the basis of the first principles theory are currently underway, as are inelastic phonon scattering measurements of the phonon lifetimes.

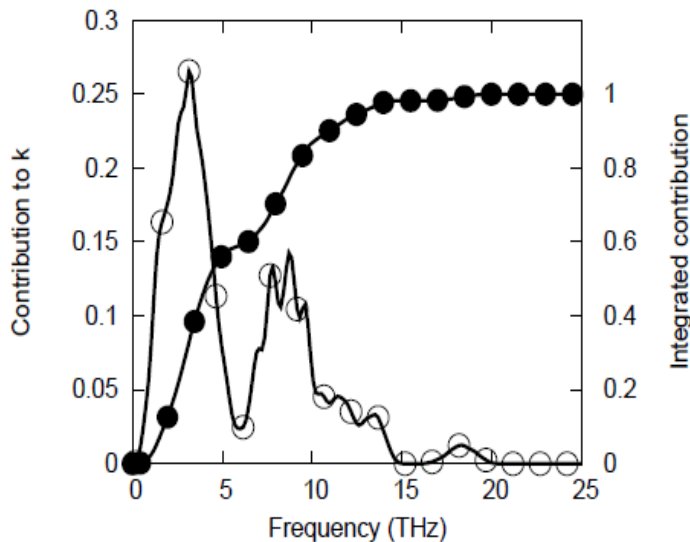
Figure 2. Phonon linewidths (FWHM) in UO_2 at two different temperatures: 300 K (blue circles) and 1 200 K (red triangles) based on Catlow interatomic potential



Interactions between phonon modes are much less understood. Inelastic neutron scattering can, in principle, be used to measure the phonon linewidths that according to the theory described in the previous chapter should be directly connected with the

thermal conductivity. Unfortunately, no experiments of this type have been published on UO_2 so far. Theoretical calculations of the phonon linewidths along [001] direction based on the Catlow [18] interatomic potential are presented in Figure 2 for the acoustic branches and two lowest optical branches at two different temperatures: 300 K and 1 200 K. First, one observes that as the temperature increases, the phonon linewidths also increases, roughly proportionally to temperature. This is indicative of the typical $\sim 1/T$ dependence of the thermal conductivity. The acoustic modes show almost monotonic increase of the linewidths with the k -vector, while optical modes show quite a complex structure. The acoustic modes clearly have smaller linewidth than optical modes; however, the Δ'_2 mode has a larger group velocity than any of the acoustic modes. This difference in the velocity is even more significant since acoustic modes have the largest group velocity near the Γ -point of the Brillouin zone, while for the Δ'_2 mode maximum is at about halfway between Γ - and X-points. To understand the significance of this, an isotropic approximation should be considered. In that case, the contribution from the states of wave vector k will be proportional to $\sim k^2 dk$; therefore the contribution of the phonons with large k -vector will have larger weight. As a result, the optical modes contribute to the thermal conductivity to a comparable extent as the acoustic modes, as shown in Figure 3.

Figure 3. Differential contribution to thermal conductivity (open circles, left axis) and integrated contribution to thermal conductivity (solid circles, right axis) normalised to unity in UO_2



These calculations, however, were performed on the basis of the Catlow empirical interatomic potential, with all the shortcomings discussed above. In particular, while this potential predicts thermal conductivity at 300 K to be 8.9 W/mK, in accord with the experimental values, it underestimates it strongly at high temperature: 1.7 W/mK vs. the experimental value of 3.3 W/mK. One therefore expects that phonon linewidths at 1 200 K to be an overestimate. There is a clear need for the simulations of the linewidths using more realistic interatomic constants, such as those produced by first principles methods, as well as experimental measurements of the phonon linewidths in UO_2 . The first such measurements have been very recently reported in the literature [66], together with the first principles simulations at the DFT+U level. While experiment and theory

both qualitatively agree and confirm that optical phonons are crucial for the accurate description of the thermal transport in UO_2 , quantitatively phonon lifetimes are only in fair agreement. This might indicate the limitations of the DFT+U methodology for the description of the fine details of the highly correlated systems.

Phonon-point defect interactions

Most simulation studies of the effects of point defects on thermal transport have been performed by molecular dynamics. Equilibrium defects include isotopic point defects, associated with the fact that both uranium and oxygen each have three long-lived, naturally-occurring isotopes, point defects related to off-stoichiometry of the UO_2 and impurities of other chemical elements that result from the sintering process. In addition to the naturally occurring isotopes, nuclear fuel is also enriched with the fissile ^{235}U to the level of 3-4% [34]. In this group, points defects associated with off-stoichiometry have the most pronounced effect on thermal transport. These defects appear because the oxygen interstitial has a negative formation energy in UO_2 [32]; therefore UO_2 can easily oxidise and become hyper-stoichiometric. Under irradiation, the fission products of the uranium decay provide a plethora of various point defects [63]. At the same time, irradiation damage also results in formation of large number of Frenkel pairs as well as more complex defect clusters [1,3], some of which can be very stable. Finally, we mention that mixed-oxide fuels (MOX) for breeder reactors provide a possible path to recycle the nuclear fuel from LWR's. MOX consists of heavy-element products (plutonium, americium and others) together with the UO_2 matrix. From a heat-transport perspective it is essentially uranium dioxide with large admixture of point defects, with thermal transport performance defined by the same physics.

The basic understanding of the effect of point defects on thermal conductivity was developed in the works of Klemens [41]. In his approach, one treats a point defect as a perturbation to the harmonic Hamiltonian that adds additional scattering mechanism with the corresponding phonon relaxation time τ_d . For the simplest case of isotopic substitution in the dilute limit (concentration is so low that each scattering event is independent from others), the result reads:

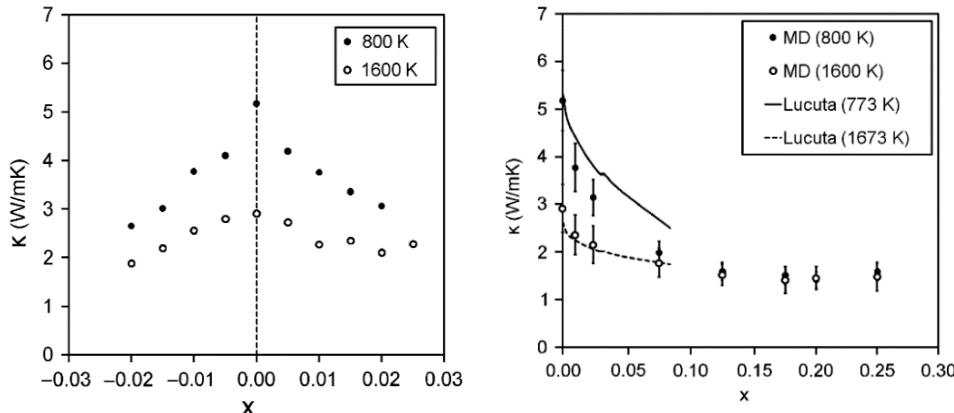
$$\frac{1}{\tau_d} = V_a c_i \left(\frac{m_i - m_{ave}}{m_{ave}} \right)^2 \frac{\omega^4}{4\pi v^3} \quad (3)$$

In this expression m_i is the mass of the isotope, c_i is its concentration, and m_{ave} is the average mass of the atoms in the system. V_a is an atomic volume and v is the speed of sound. While this formula is obtained within Debye approximation (which approximates only very roughly the actual phonon structure of the solid), it is very useful, as it allows for a transparent physical interpretation: scattering of the lattice waves (phonons) on the point defects can be viewed as a Rayleigh scattering process with a characteristic $\sim\omega^4$ dependence of the scattering strength. This interpretation permits the treatment of the more complicated case of the substitutional defect, or a small defects cluster: the relaxation time is declared to have the same frequency dependence as in Rayleigh scattering, $\tau_d^{-1} \sim \omega^4$, however, the proportionality coefficient is difficult to deduce, and it is most often treated as an adjustable parameter. Finally, we note that if the concentration of defects is so large that the dilute limit does not apply, the dependence on the

concentration becomes less pronounced: instead of the linear dependence, the inverse relaxation time is proportional to the square root of concentration [43].

The effect of the isotopic defects on thermal transport was considered in a recent publication [88] and was found to be negligible (3% reduction of the thermal conductivity at 300 K for 5% concentration of ^{235}U , a result well within the error bars for the thermal conductivity calculations by the MD methods). Off-stoichiometry has been studied in a number of publications [88,89], yielding rather consistent results. The latter work considers both effects of the hypo- and hyper-stoichiometry with the change of thermal conductivity as a function of oxygen content presented in Figure 4 for two different temperatures. First, one immediately observes a very strong dependence of thermal conductivity on oxygen excess/deficit. Just one percent excess or deficit ($x = \pm 0.02$) reduces the thermal conductivity by a factor of two at 800 K. Second, the concentration dependence is in agreement with the Klemens theory: for low point-defect concentrations, the thermal conductivity follows a linear dependence with the defects concentration. At high concentrations, there is a much weaker dependence, especially observed at the higher temperature and larger oxygen excess. Lastly, the thermal conductivity of stoichiometric and near-stoichiometric UO_2 is about a factor of two smaller at 1 600 K than at 800 K – representing the expected $\sim 1/T$ dependence. As the defect concentration increases (right panel), the difference between the thermal conductivities at 800 K and 1 600 K decreases.

Figure 4. Thermal conductivity in $\text{UO}_{2\pm x}$ at two different temperatures, as determined by MD [88]



Indeed, at $x=0.125$ (not obtainable experimentally in the fluorite structure, but conceptually instructive) the thermal conductivity becomes independent of both temperature and composition. Such a temperature-independent thermal conductivity is characteristic of an amorphous material. Indeed, by analysing the phonon modes present in the system, Watanabe and co-workers [87] demonstrated that at $x=0.125$ the majority of the vibrational modes present in the system are non-propagating modes, and that heat is transported diffusively via a mechanism proposed by Allen and Feldman [2] in the context of amorphous Si. Thus, UO_{2+x} exhibits a transition from the crystal-like thermal transport impeded by the point defects ($x < 0.02$) to that of the amorphous solid ($x > 0.1$). Very similar results were obtained by Yamasaki and co-workers [88]. Since different interatomic potential were used for the two studies, this points to these results and conclusions as being robust.

There are almost no theoretical studies in the literature of the effects of the light fission products. In a rare exception, Higuchi [36] studied a “generic” defect atom whose properties are identical to those of uranium, except its mass, which was varied over a rather wide range. Only a single, rather large, 6% concentration of defects was considered. In agreement with the perturbation theory formulas [43] for point defects, the thermal conductivity was found to decrease with increasing mass difference between the substituting atom and the average mass of atoms in the system. Rather surprisingly, although derived from perturbation theory, and hence assuming small mass differences, the Klemens formula produced good agreement with the simulation results even for very large mass differences. As an estimate, if all of the 6% concentration of fission products ended up being elements with the mass approximately half of that of uranium, then thermal conductivity was found to decrease threefold compared to stoichiometric UO_2 .

The effect of an admixture of plutonium was studied by Arima and co-workers [4,5]. In that work, it was found that Pu has very little effect on the thermal conductivity: compositions of $\text{U}_{1-y}\text{Pu}_y\text{O}_2$ with $y=0\text{--}0.3$ were studied and the thermal conductivity was found to be essentially independent of y . The same work also discussed the effect of the hypo-stoichiometry, and found it to be far more significant: reduction of the oxygen content by $y=0.03$ reduces the thermal conductivity by a factor of two. The effect of the addition of americium to MOX was discussed by Kurosaki et al. [45]: $\text{U}_{0.7-y}\text{Pu}_{0.3}\text{Am}_y\text{O}_2$ $y=0\text{--}0.15$; again, the thermal conductivity was found to be essentially independent of the concentration of americium. Such behaviour might be explained by the similar properties of U, Pu and Am: all these elements are actinides, with the chemistry largely determined by the same outer electron shell. Moreover, since they have large atomic masses, the relatively small differences in mass do not have a large effect; this is also consistent with the weak effect of isotopic defects in UO_2 itself.

Phonon-dislocation interactions

Understanding the effect of dislocations on the thermal conductivity is a longstanding problem and remains largely unresolved. Since the early work of Klemens [42] and others [16,62], dislocations have been recognised as possible scatterers of phonons. In addition, in many materials, impurities segregate to dislocations and these impurities within the Cottrell atmosphere can also cause additional phonon scattering. In the simplest form of the theory, one considers the interaction of the incident phonons with the static strain field associated with the dislocations as a dominant scattering mechanism. Following the same line of thought as discussed previously for the point defects, a number of different models have been introduced to represent these scattering mechanisms in terms of appropriate relaxation times. The contribution of the dislocation strain field to phonon scattering was calculated by Klemens to be:

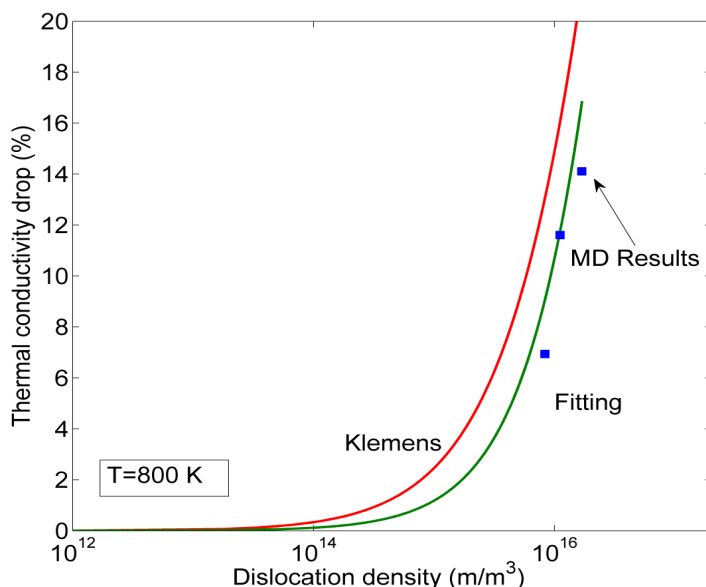
$$\frac{1}{\tau_s} = \frac{2^{3/2}}{3^{7/2}} N_d b^2 \gamma^2 \omega \quad (4)$$

In this expression, N_d is the dislocation density, b is Burgers vector and γ is the Grüneisen parameter. The numerical prefactor has different values depending on the details of the particular derivation. The straightforward application of this formula for the case of UO_2 demonstrates that at 800 K dislocations begin to significantly reduce the thermal conductivity only if $N_d > 10^{16} \text{ m}^{-2}$. This would seem to indicate that dislocations

should not be very important for the reactor operation, as the highest concentrations reached are of the order of $10^{15-16} \text{ m}^{-2}$ [23]. However, there is still a controversy whether expression in Equation 4 is universally applicable as there are reports that it can underestimate the dislocation effect by 2-3 orders of magnitude [77].

In order to elucidate the effect of dislocations on the thermal conductivity in UO_2 , in a recent study [23], we have used the non-equilibrium molecular dynamics method. Restrictions on the simulation cell size mean that only large ($\sim 10^{16} \text{ m}^2$) concentrations of dislocations can be studied. For this study, the Busker interatomic potential [13] was chosen. Results for the edge dislocation ($\{110\} < 110 >$ slip system) are presented in Figure 5. As expected, the presence of the dislocations reduces the thermal conductivity. In accord with the Klemens predictions, the effect is not temperature dependent (not shown). In Figure 5, we demonstrate the comparison between MD simulations and Klemens theory (see Equation 4). One can see that MD simulations produce an effect smaller than predicted from the theory. We recall that the numerical factor in Equation 4 is strongly dependent on the derivations details. We therefore use it as an adjustable parameter to verify if functional dependence of Equation 4 can fit the (limited) simulation data. We therefore conclude that the Klemens model is satisfactory for the description of the effect of dislocations on thermal conductivity in UO_2 . The limitation of the current simulations approach, however, is the type of the dislocations considered (linear edge dislocation), that are completely immobile. Studies of the microstructure of the irradiated MO_2 materials [91] indicate large concentration of the dislocation loops that might have different effect on the thermal conductivity. In addition, possible mobility of the dislocations (although this probably is small effect in UO_2 , as dislocations are very stable in ionic compounds) were implicated [44,59] in the underestimate of contribution to the thermal conductivity reduction by the Klemens theory.

Figure 5. Thermal conductivity reduction in UO_2 as a function of the dislocation density at 800 K: Klemens theory (red) vs. fit to MD simulations (green)

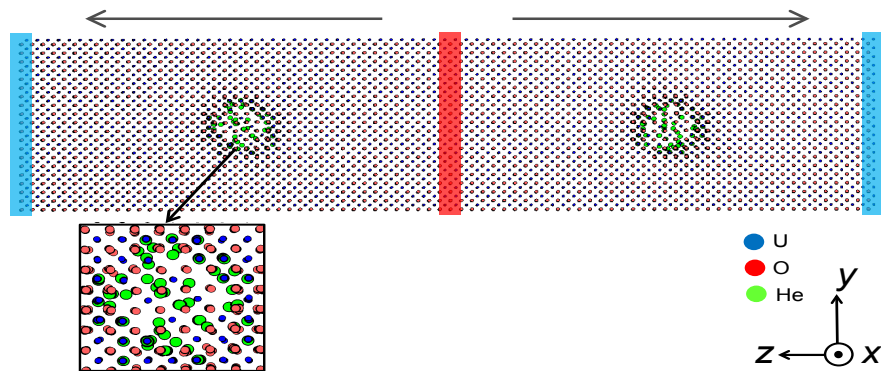


Courtesy of Bowen Deng.

Phonon-void/bubble interactions

Porosity is another important element of the microstructure evolution of the UO_2 nuclear fuel. It is present both in the fresh pellet, as well a result of the radioactive decay. Moreover, since the decay produces significant amounts of the inert gases (He , Xe), these gases tend to accumulate in the voids and therefore can also affect the thermal conductivity of the overall system. Experimental observations have resulted in empirical models for the porosity effect [6,22,69]. However, these studies could not control the size of the pores. There are also a number of models based on the continuum approximations [7]. The non-equilibrium molecular dynamics technique is again an appropriate technique to investigate this effect. We investigated systematically the effect of the size of the pores on the effective thermal conductivity and compared these results to both empirical and continuum models. In addition, we investigated the effect of the presence of the helium in the pores. [49]. This latter study required potential that can describe interaction of the UO_2 with He ; hence the Grimes parameterisation [33] of the Buckingham potential was used. The size of the pores was varied up to 1.2 nm, still significantly smaller than experimentally observed pores: typical pore size distribution in sintered UO_2 pellet ranges from 1 to 10 μm [76], while irradiated fuels develop smaller gas-filled bubbles with the size of the order of 100 nm [93]. An example of the simulation set-up is represented in Figure 6. Periodic boundary conditions are applied in all three dimensions, effectively creating an ordered array of pores.

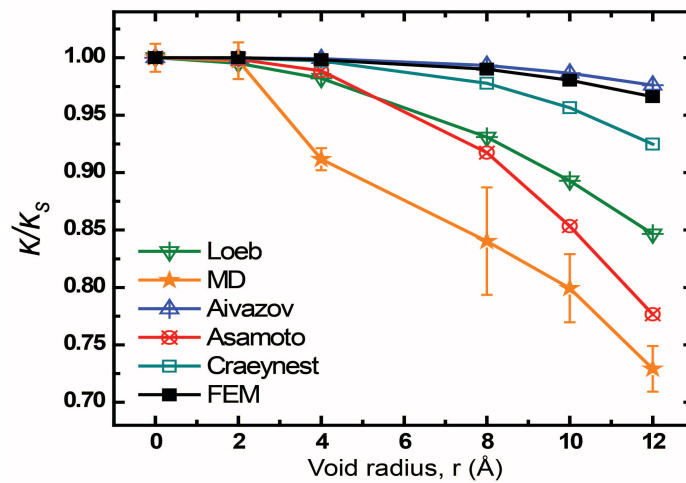
Figure 6. Simulation set-up for the thermal conductivity calculations by the NEMD method [49]



Results of the calculations in comparison with the empirical and continuum models are presented in Figure 7. All of the empirical models were essentially constructed in terms of the porosity concentration, which can be recast as a function of the void radius. All models show that an increase in the void radius leads to a reduction of the thermal conductivity; interestingly, the MD data show the strongest decrease. The empirical model of Asamoto and co-workers [6] comes closest to reproducing the MD model. It is also interesting that straightforward finite element analysis (black squares in Figure 7) of exactly the same system produced significantly smaller effects than is demonstrated in the MD simulations. This is attributed to the complete neglect of the phonon scattering of the boundary/strain field in the continuum modelling. Finally, the presence of the helium

in the void produces a rather small effect on the effective thermal conductivity. However, somewhat counter-intuitively, the thermal conductivity of these small voids actually decreases when helium is present. One would expect a slight increase in thermal conductivity since the helium in the bubble can serve as an additional heat carrier. Instead, it turns out that some of the He atoms dissolve into a shell of the UO_2 matrix surrounding the void, and behave as additional point defects scatterers, further degrading the overall thermal conductivity. This effect can be expected to disappear as the bubble size increases.

Figure 7. Effect of the porosity on the thermal conductivity as a function of the pore size [49]



Phonon-interface interactions

Since nuclear fuel is a polycrystalline material, the thermal resistance of interfaces (also called the Kapitza resistance) also contributes to the degradation of the overall thermal conductivity. The Kapitza resistance is manifested as a finite temperature drop at the interface between two different materials, or in our case, between grains of different orientations of the same material. This effect is especially important at high burn-up (more than ~ 60 MWd/kgU) around the rim of the fuel pellet. In this region [48,72], due to the resonance neutron absorption of ^{328}U , fissile ^{239}Pu is produced resulting in much higher burn-up than in the rest of the pellet. The high burn-up structure is characterised by the subdivision of the original UO_2 grains into very fine ($0.1\text{--}0.5 \mu\text{m}$) subgrains and relatively high concentrations of the intergranular bubbles ($\sim 15\%$ porosity). Since grain boundaries behave as sinks for point defects, these subgrains are almost free of defects. As a result, the interfacial resistance becomes a dominant mechanism for the thermal conductivity reduction in this region. Experiment has demonstrated that due to low defect concentration in the subgrains, the *lattice* thermal conductivity (omitting the porosity effect) is actually larger than in the lower burn-up regions [71]. The thermal interfacial resistance is conveniently characterised by the Kapitza length that is defined as the thickness of the perfect crystal that provides the same drop in temperature as an interface. Consequently, the effect of the grain boundaries on the thermal conductivity depends on the relationship between two length scales: the Kapitza length and the characteristic grain size. If the grain size is much larger than the Kapitza length, then interface does not contribute significantly to the interface.

There are two standard models of the boundary thermal resistance: the Diffuse Mismatch Model (DMM) and Acoustic Mismatch Model (AMM) [80]. In the DMM, each phonon arriving at the interface “forgets” where it came from and is re-emitted on either side of the interface with probability proportional to the available phonon density of states. For the grain boundary, therefore, the DMM predicts the probability of transmission through the boundary to be 50% for all phonons and for all grain boundaries, a result found to be qualitatively incorrect from computational studies [74]. In contrast to the DMM, the AMM predicts the transmission probability based on the mismatch of the acoustic impedances on the both sides of the interface. However, this means that for some grain boundaries, such as symmetric tilt grain boundaries, the AMM would predict that the interface would have no effect on thermal transport at all, a result again refuted by simulation [50]. Thus, the two prevalent models are not able to capture fully the effect of interfaces; atomistic simulations therefore are necessary to fully characterise the effects of interfaces on thermal transport.

Studies of the grain boundary resistance in UO_2 also have limitations. Watanabe and co-workers [87] considered the thermal conductivity of the polycrystalline sample and deduced the average interface conductance in UO_2 to be 0.15-30 $\text{GW}/\text{m}^2\text{K}$. This yields a Kapitza length of ~ 50 nm at 300 K and ~ 10 nm at 1000 K; these relatively long lengths arise from the low intrinsic bulk thermal conductivity. It is an open question, however, as to how the interfacial resistance depends on the type of the grain boundaries. One indication comes from the studies of the grain boundaries in diamond [86]. In this work, a strong positive correlation was observed between the grain boundary energy and its Kapitza resistance. Coupling these results with the models for the formation energies of the grain boundaries as a function of orientation, one might be able produce an entire map of the interfacial resistance based on just a few simulations. Construction of such a model would provide a very useful for a link to the mesoscale modelling of the thermal transport in UO_2 .

Recent progress in mesoscale simulation of thermal transport in UO_2

The macroscopic thermal conductivity models used in current fuel design and performance codes are motivated by the classical physics models of thermal conductivity as a function of temperature and density of defects in single crystals. As discussed above, these classical models also cover the effect of extended defects, such as dislocations and grain boundaries [8,15,19,41-43,62,85]. While, as the simulations discussed above show, that the contribution of each type of lattice defects (point defects, isotopes, dislocations and grain boundaries) can be handled using atomic scale models with reasonable levels of accuracy, the hierarchical nature of the material microstructure in a real fuel pellet requires a top-down modelling strategy, whereby the roles of various microstructure features are logically defined within the context of the overall thermal transport problem. This section therefore highlights the microstructural issues related to thermal transport in UO_2 , and the impact of microstructure on conductivity model selection.

Conductivity models at the pellet scale

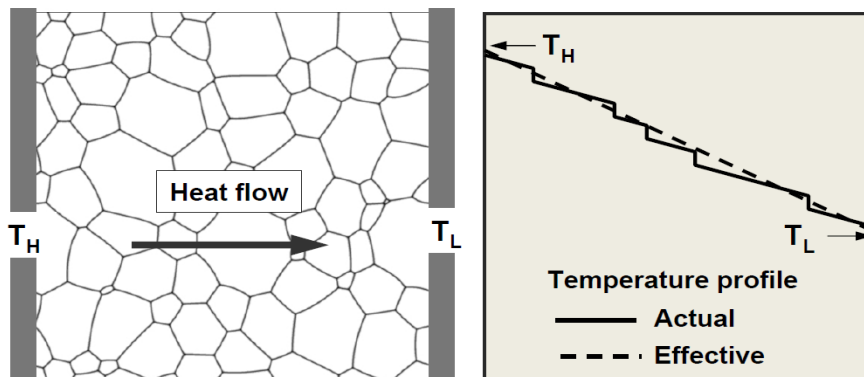
Let us first consider an unirradiated polycrystalline UO_2 . A macroscale model of the effective thermal conductivity can be constructed as a problem of heat transport through an aggregate of UO_2 grains having well-defined conductivity and bonded together via a

network of grain boundaries of specific thermal resistance. This pristine material will also contain porosity. The theoretical context within which the problem of finding the conductivity of such a material lies is the theory of effective properties of heterogeneous media [58,82]. While such theory is limited by how accurately the microstructure can be represented, a method of finding the effective properties of heterogeneous media based on direct numerical simulation (DNS) has also been established [38,40]. The latter method has become popular because of the availability of large amounts of computing power and the ease with which thermal conductivity can be simulated. By applying a temperature drop across a sample of the heterogeneous material and solving for the heat flow within this domain, the effective conductivity, k_{eff} , can be computed by Fourier law:

$$k_{\text{eff}} = -\frac{q_{\text{ave}}}{(\nabla T)_{\text{ave}}} \quad (5)$$

where q_{ave} is the imposed heat flux and $(\nabla T)_{\text{ave}}$ is the average temperature gradient. Here the terms “effective” and “average” refer to microstructure averaged quantities. This problem is schematically illustrated in Figure 8. At this stage, all that is needed are the conductivity of the grains and the grain boundary (Kapitza) resistance. The former might encompass the effects of lower scale defects within the grains (e.g., dislocations and point defects) and the latter may include the effects of grain boundary segregation. Voids can also be added systematically to the model.

Figure 8. A representative volume element of a polycrystalline material (left) and a line profile of the temperature across the volume element showing small localised drops across grain boundaries



The conductivity of the individual grains used as input for the above mode comes from either MD method [88] or from classical phonon-based models [15,19,41-43,62,85]. The simplest model in this regard is that of Klemens [41-43]. In this model, Debye's model of dispersion, which lumps all phonons as one group moving with the velocity of sound in the solid, is used along with the Bose-Einstein distribution for the phonon population [8]. This model is discussed later in the context of Monte Carlo solution of the Boltzmann transport equations for phonons in the next subsection.

The above continuum-based model of conductivity of a polycrystalline fuel can, in principle, work at finite burn-up with only a minor modification; additional microstructures feature such as gas bubbles can be added to the polycrystalline model, both at the grain boundaries and within the grains. Assuming that a conductivity value can be assigned to these bubbles (see above discussion of the atomistic simulations), the

effective conductivity of the fuel sample can be evaluated numerically. An advantage of this approach is that the statistical variability of the microstructure can be automatically included by varying the microstructure realisations used as input to the simulations. Numerical modelling of the thermal conductivity of a polycrystalline fuel with gas bubbles along grain boundaries and at triple junctions was recently attempted [55]; the grain boundaries were assigned a Kapitza conductance, $G_k = 10 \text{ MW/m}^2\text{K}$, and the UO_2 matrix was assigned a single crystalline conductivity, $k_{\text{Bulk}} = 4.5 \text{ W/mK}$. The effect of bubbles was considered through the relationship [75]:

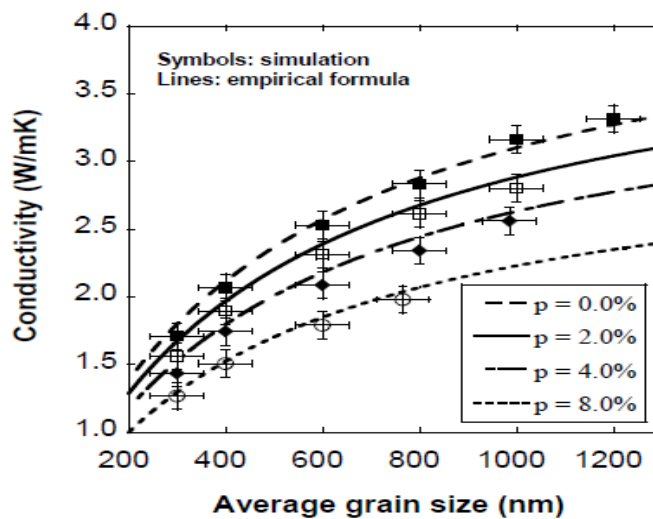
$$k_{\text{eff}} = k_{\text{Bulk}} (1 - p)^{\beta} \Psi \quad (6)$$

where p is the porosity volume fraction, β is a fitting parameter whose value is ~ 3 , and Ψ is a correlation factor relating two- and three-dimensional results for conductivity. The combined effect of porosity and grain boundary resistance on the overall conductivity can then be given by [54,90]:

$$k_{\text{eff}} = \frac{k_{\text{bulk}}}{1 + k_{\text{bulk}}/G_k d} (1 - p)^{\beta} \Psi \quad (7)$$

with d being the average grain size. A sample solution adopted from [55] is shown in Figure 9. This figure compares the results of a numerical solution of heat conduction problem over a representative microstructure (see Figure 8) with the effective conductivity computed via Equation 5, to that calculated with Equation 7. The results show the suitability of the latter model for computing the conductivity of porous UO_2 , provided that the pore size is well above the average phonon wavelength. Most fuel codes include thermal conductivity models of similar nature as that in Equation 7, in the sense that the effect of porosity is approximated on a geometrical basis.

Figure 9. Direct numerical simulation (symbols) versus the empirical formula (lines) for the conductivity of polycrystalline UO_2 with various levels of porosity [55]



The analytical and computational models discussed above fix the effective conductivity of the heterogeneous fuel at the macroscale under the assumption that the thermal transport characteristics of the constituents, namely, the conductivity of the grains,

grain boundary conductance and the thermal properties of the pores (bubbles) and precipitates are prescribed. The results of these models depend strongly on the grain size and porosity distributions, which all evolve during irradiation. It is known, for example, that UO_2 fuel undergoes a significant restructuring during reactor operation [52,60,61,68]. The main feature of this process is the formation of various texture zones in the fuel, as well as a complex bubble size and density distributions that vary along the radial direction of the pellet. The pellet restructuring process is driven by the temperature difference between the centre of the pellet and its periphery, and it is manifested in the formation of a fine grained region at the outer periphery, known as the rim region, and a coarser- or columnar-grain region towards the centre, with a transition of grain size in the intermediate region. The restructuring and bubble formation processes in fuel occur simultaneously. In the rim region, irradiated UO_2 fuel also exhibits a complex dislocation and subgrain structure, which evolves due to the intense fission process, grain size evolution and the accommodation of high density of fission gas bubbles.

The microstructure-based conductivity approach discussed above provides the local continuum-scale conductivity of fuel in engineering scale codes, where the conductivity values are resolved along the radial direction in the pellet and as a function of time [10,65]. Fixing the values of the conductivity at any radial position requires knowledge of the local microstructure and defects. The microstructure itself evolves as a function of temperature, and as such, the thermal performance of the fuel is tightly coupled with its microstructure performance. In current codes, the conductivity dependence on the radial position is captured in the temperature dependence part of the intrinsic conductivity and by taking into consideration the porosity evolution along the radial direction and as a function of time.

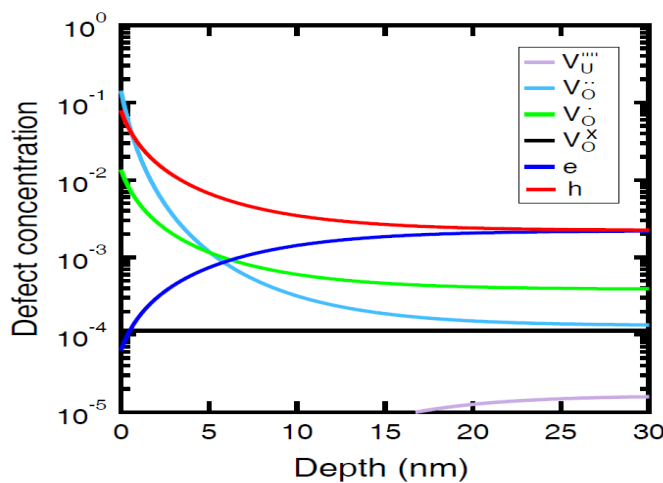
Transition from atomistic to continuum scale at the single crystal level

From a continuum scale perspective, the grain structure and larger scale porosity in fuel define a mesoscopic length scale range relevant to the effective conductivity models at the pellet scale. There is a lower scale regime in which the defects within a single grain, many of which were discussed in the context of the MD simulations, play a critical role in determining the conductivity of these grains (or crystals, in the sequel). Such intergranular defects include, but are not limited to, dislocations and dislocation loops, small point-defect clusters, small voids, segregated species or small precipitates, as well as local off-stoichiometry. From a single crystal point of view, these defects are perturbations of the lattice, with size and/or separation distances on the order of the mean free path of phonons. A continuum representation of these features is thus not possible. However, fully-resolved, atomic-scale type models of thermal transport at such a scale are also not viable because the size of a material volume containing an appropriate ensemble of such defects is beyond the capabilities of molecular dynamics simulation. The scale of a single crystal with extended structural defects thus defines a unique mesoscale regime that can only be tackled with the theoretical tools of phonon physics.

In order to motivate the need for a careful look at the just-identified crystalline mesoscale in the context of thermal transport, we recall the fact that the conductivity of UO_2 single crystals is sensitive to minor off-stoichiometry levels [88]. A recent investigation of off-stoichiometry near a free surface shows that the concentration of oxygen vacancies can vary over a significant mesoscopic distance of few to several tens of nm from the

surface (see Figure 10). The origin of such variation is the strong electro-chemical coupling in the free energy of the system. In irradiated UO_2 , however, it is anticipated that such mesoscopic variations of the density of defects will occur near cavity surfaces, interfaces as well as dislocation loops. This will result in an indirect effect of such crystalline microstructure features on thermal transport, in addition to their direct influence on phonons.

Figure 10. Spatial variation of intrinsic defect concentrations in UO_2 as a function of distance from a free surface at 1 900 K and $\log p_{\text{O}_2} = -16$ [35]



The depth over which off-stoichiometry level varies is on the order of a few tens of nm.

Investigating the collective phonon dynamics in single crystals opens up the possibility for modelling all mesoscopic effects, both those due to the microstructure features resulting from irradiation and those arising from the off-stoichiometry distribution in the crystalline space between these microstructure features. While this work is still in progress, we discuss below an important step of the relevant framework, which is the description of phonon dynamics in a fresh, stoichiometric single crystalline UO_2 based on the Boltzmann Transport Equation (BTE). As mentioned in the previous section, the collective behaviour of a phonon population in crystals can be described by the space and time evolution of a distribution function $f(\mathbf{r}, \mathbf{K}, t)$, with \mathbf{r} and \mathbf{K} being the spatial position and wavevector of the phonons, respectively. The space and time evolution of this function is described by the BTE as [8] [19]:

$$\frac{\partial f}{\partial t} + \mathbf{v}_g \cdot \nabla f = \left[\frac{\partial f}{\partial t} \right]_{\text{scat}} = \sum_{\mathbf{K}'} [\varphi(\mathbf{K}', \mathbf{K}) f(\mathbf{K}') - \varphi(\mathbf{K}, \mathbf{K}') f(\mathbf{K})] \quad (8)$$

where $\mathbf{v}_g = \nabla_{\mathbf{K}} \omega$ is the group velocity. The functions $\varphi(\mathbf{K}', \mathbf{K})$ and $\varphi(\mathbf{K}, \mathbf{K}')$ are the probability rates for scattering of phonons from one point to another in \mathbf{K} -space; specifically, $\varphi(\mathbf{K}', \mathbf{K}) f(\mathbf{K}')$ is the rate of scattering of phonons from \mathbf{K}' to \mathbf{K} . In order to solve the above equation, the probability rate functions $\varphi(\mathbf{K}', \mathbf{K})$ and $\varphi(\mathbf{K}, \mathbf{K}')$ must be specified throughout \mathbf{K} -space for all types of scattering processes. Owing to the difficulties in determining these scattering kernels, a relaxation time approximation of the BTE is typically used, as has already been mentioned. In this approximation, the

distribution function $f(\mathbf{r}, \mathbf{k}, t)$ is assumed to be close enough (but not equal) to its thermal equilibrium value, f_o , appropriate to the local temperature, such that the role of scattering is to relax that function closer to its thermal equilibrium value. With this approximation, the BTE can be reduced to the form [19]:

$$\frac{\partial f}{\partial t} + \mathbf{v}_g \cdot \nabla f = \frac{f - f_o}{\tau} \quad (9)$$

where τ is the relaxation time that accounts for all scattering mechanisms operating in the system. Classical literature distinguishes the mechanisms of phonon-phonon scattering as normal and umklapp processes [8,19]; phonon scattering by lattice defects is also included [15,19,41,43,85]. As discussed above, expressions of the relaxation times associated with these processes are usually combined to give the overall relaxation time via Mathiessen's rule (see Equation 2).

The above formulation of the phonon transport problem has been solved by Monte Carlo (MC) [53,46,56] and Lattice Boltzmann (LB) [57,30] techniques. In the former, a sample of phonons is created following the Bose-Einstein distribution. These phonons are allowed to stream according to their group velocities over the prescribed time step. At the end of each step, it is determined which phonons have undergone a scattering event based on a probability given by the expression $P = 1 - \exp(-\Delta t / \tau)$. The outcome of a scattering event is a phonon or phonons with an energy and possibly polarisation and direction different from the original phonons [53,46,56]. The simulation is continued until a steady-state distribution of phonons is reached in the domain of solution, which may be at a uniform temperature or under a temperature gradient.

The MC scheme of solving the BTE for phonons works well when phonon scattering occurs from other phonons or from impurities distributed uniformly in the crystal. The results of the simulations have been compared with experiments, and the efforts made in that direction show that the MC method (as well as the LB method) for solving the BTE can yield reasonably accurate results [53,46,56]. Figure 11 shows typical frequency spectra of phonons in a silicon crystal at 300 K and 500 K, along with the time evolution of the temperature profile across a thin film of silicon with a thickness of 0.8 μm , in contact with two thermal reservoirs at 310 K and 290 K at its surfaces. The frequency spectrum in Figure 11 (a) takes into consideration the transverse and longitudinal acoustic branches of silicon only. The temperature profile evolution is computed using MC with a Debye model. It is shown that the profile across the films becomes nearly linear after 2.5 ns. The fluctuations about the linear part are due to the stochastic nature of the MC method, by virtue of the fact that a discrete phonon system is being simulated, and averaging over an ensemble, an appropriate number of simulated samples should reduce or eliminate these fluctuations.

A first attempt at computing the thermal conductivity in UO_2 using the MC solution of BTE has been carried out. The conductivity can be found by imposing a linear temperature gradient across the sample and computing the resulting heat flux using from the data of the phonon population being simulated – the heat flux is basically the sum of the product of phonon energies and velocities resolved in the direction of the temperature gradient. The conductivity is then computed using Fourier law. A sample calculation of the conductivity is shown in Figure 12. The predicted conductivity is in good agreement

with MD simulations [87], with both being slightly higher than reported experimental values. The temperature dependence of the conductivity is captured well. It should be noted that the conductivity values fluctuate slightly about a smooth decay trend; these fluctuations originate from the finite number of phonon trajectories used in the simulation. Further work in this area is on-going.

Figure 11. (a) Phonon frequency spectrum in a silicon crystal at 300 K and 500 K, (b) Monte Carlo simulation of the time-dependent temperature profile in a silicon thin film of thickness 0.8 μm in contact with thermal reservoirs at a 310 K and 290 K at its two surfaces [24]

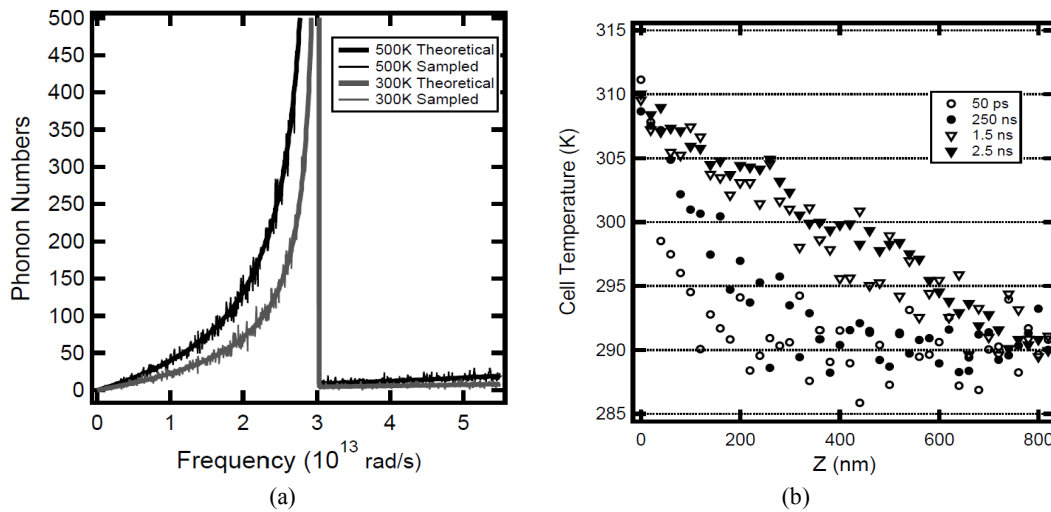
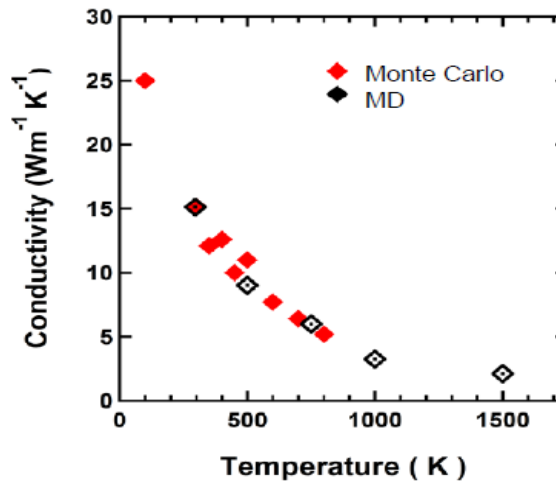


Figure 12. Preliminary prediction of the thermal conductivity of UO_2 using MC solution of BTE [88]



The results are compared with the MD simulation of UO_2 conductivity using Yamada potential.

Irradiation introduces two complexities. The first is that the field of point defects, e.g., impurities or vacancies associated with off-stoichiometry, for example, can be both non-uniform and time dependent. In such a case, the local relaxation time can be taken to be spatially dependent throughout the domain of the simulation. The second complexity is

the introduction of extended defects with complex configurations, e.g., dislocation loops, dislocation walls, small voids, gas bubbles, precipitates and subgrains, which require new theoretical formulations that do not currently exist.

Conclusion and future challenges

Modelling thermal transport in polycrystalline, irradiated UO_2 provides an example problem where the complexity of microstructure is dominant. The microstructure of the material is hierarchical in nature with multiple mesoscale levels to be handled between the atomistic and continuum regimes. The following levels of microstructure (or states of the fuel materials) can be easily identified, at each level of which a different set of issues and physics laws are used to study thermal transport. We conveniently classify these levels as follows:

a. Single crystal UO_2

Thermal transport at the level of a fresh single crystal is governed by the phenomenological heat equation shown below, with the thermal diffusivity being the only constitutive quantity needed to completely solve the heat equation:

$$\frac{\partial T}{\partial t} = \alpha \nabla^2 T. \quad (10)$$

The thermal diffusivity is given by $\alpha = k / \rho c$, with the k , ρ and c being the conductivity, density and specific heat, respectively. These three fundamental properties of the crystal, as well as the heat law itself can be derived from statistical physics (classical or quantum). In particular, the temperature dependence of the conductivity and specific heat is a classical problem in the theory of heat of crystalline solids [78]. When size effects are involved, heat transport in single crystals can be studied in terms of phonon transport. This level of understanding of the problem of thermal transport is well documented in the classical literature.

The key challenge at this level is the absence of an interatomic potential that reliably reproduces the relevant phonon effects. While Density Functional Theory (DFT) has proved itself in many contexts, the presence of strongly correlated electrons in f-electrons such as U leads conceptual issues that are not yet fully resolved. Progress in this direction in the form of extensions to DFT, such as DFT+U or hybrid functionals have led to better reproduction of experimental results; however, great care need to be exercised in performing calculations with these methods, as they exhibit multiple energy minima in the electronic structure [27,39]. More advanced approaches, such as Dynamical Mean Field Theory (DMFT) are yet to enter the mainstream of the computational techniques.

b. Single crystal with defects

Point defects and dislocations are commonly studied in the classical literature related to thermal transport in crystals. In particular, the modification of the temperature dependence of the conductivity by such defects has received most attention [8]. At this level, the crystal contains an ensemble of non-interacting defects, each of which contributes to scattering in the same fashion. As such, only the density of these defects appears in all related formulae. The effect of such isolated defects can be studied by MD [88] or using a phonon-based framework [15,41-43,62,85]. Thermal transport in this

case is studied in essentially the same way as in a perfect crystal. It is important to point out that the classical works related to impact of defects on thermal conductivity did not look at the way such defects arise in the matrix. For example, in compound solids, e.g., oxides, significant composition variations may occur, which leads to high density of intrinsic point defects that interact in the lattice. In this case, treating such defects as isolated, and adding their effects using simple statistics may not apply.

c. Irradiated single crystals

Irradiation brings in a different level of complexity in UO_2 , namely the concurrent presence of point defects, dislocation loops and voids (with or without gas). Depending on the level and type of irradiation, precipitates may also form. A very important factor to consider is the interaction of these defects and the possible off-stoichiometry that might arise in the crystal lattice between the extended defects. Considering also the potential elastic and electrostatic interactions in the material, the ensemble of defects in irradiated UO_2 represents a realm of lattice dynamic situations that has not been tackled to this point. Large-scale MD simulations can be performed to investigate thermal transport across an ensemble of defects. This task is, however, difficult at present time because of the lack of interatomic potentials that work reliably under off-stoichiometric situations, and because of the lack of a theoretical framework to synthesise the MD data beyond computing the conductivity as the outcome of dividing the heat flux into the imposed temperature gradient. This first level of mesoscale complexity can be handled using a BTE-based approach in which the scattering events involving extended defects are computed atomistically or using lattice dynamics. This suggested paradigm has not been considered before, but at present time it seems to be a viable conceptual framework. Again, the challenge here lies in the need to modify the BTE approach to represent the scattering by the irradiation-induced large extended defects consistently. Ground breaking theoretical work is required here.

d. Unirradiated polycrystalline UO_2 (baseline mesoscale problem)

Without irradiation, polycrystalline UO_2 contains grain boundaries with, at most, some level of porosity left from the manufacturing step. A continuum theory of heat transport based on the heat equation can be employed in this regard, with the conductivity of the grains (single-crystal conductivity) plus grain boundary conductance being the only thermal properties required. Such conductivities can be computed using MD or a phonon-based approach. At this level, dilute concentrations of point defects can be handled systematically within these frameworks. An atomistically-informed continuum approach is thus possible. In fact, given an interatomic potential with well characterised predictions of thermal properties at the single crystal level, coupling atomistic and continuum approaches can be a tractable baseline problem of mesoscale thermal transport through a microstructure. Finite element simulations can be easily used to extract effective conductivities, which can be then used in continuum engineering simulations.

e. Irradiated polycrystalline UO_2 (fuel sample testing regime)

Irradiation introduces yet another level of complexity to the baseline mesoscale thermal transport scenario described above, simply due to the complex microstructure evolution that takes place. In this regard, it is important to differentiate between two scenarios, fuel samples irradiated in a uniform temperature field and actual fuel in which the temperature

gradient plays a significant role in determining the microstructural evolution, and hence the local thermal transport characteristics. As far as the microstructure is concerned, the two scenarios differ in the sense that a fuel sample has a uniform microstructure while the actual fuel has a gradient in the microstructure. In the case of a fuel sample, a thermal-transport model can be mesoscale in nature, i.e., one in which the fully developed microstructure is represented explicitly (as under level d above), while lower scale MD and/or phonon-based models are used to predict the thermal transport properties of the individual phases and interfaces. While the mesoscale solution of the heat equation poses no difficulty, it is the lower scale problem that was never solved before, for example phonon transport across a microstructure ensemble.

f. Actual UO₂ fuel

The problem of thermal transport in actual UO₂ fuel represents the highest level of complexity; in this problem the microstructure evolution and microstructure gradients pose a challenge to the continuum level simulations because the underlying thermal transport properties are strongly coupled with the microstructure. A microstructure simulation model taking the local temperature as an input should in principle provide the microstructure information required to model thermal transport. A continuum model in which local thermal transport properties can be computed on the fly seems to be a necessary approach to tackle the problem of thermal transport in fuel. As a part of this strategy, a thermal conductivity model at every point is needed as input at the continuum scale. Such modelling approach of the local thermal conductivity will naturally consider the local microstructure as dictated by the local temperature history. The main challenge here will be the modelling of the concurrent evolution of microstructure and thermal transport properties, and the need to solve the pertinent models simultaneously with the macroscale thermal transport problem.

Acknowledgements

We would like to thank Bowen Deng, Chan-Woo Lee and Ryan Deskins for sharing unpublished work. This work was authored by subcontractors (AC, AE-A, SRP) of the US Government under DOE Contract No. DE-AC07-05ID14517, under the Energy Frontier Research Center (Office of Science, Office of Basic Energy Science, FWP 1356). Accordingly, the US Government retains and the publisher (by accepting the article for publication) acknowledges that the US Government retains a nonexclusive, paid-up, irrevocable, world-wide license to publish or reproduce the published form of this manuscript, or allow others to do so, for US Government purposes.

References

- [1] Aidhy, D.S. et al. (2009), “Kinetically evolving irradiation-induced point defect clusters in UO₂ by molecular dynamics simulation”, *Physical Review B*, 80, 104107.
- [2] Allen, P.B., J.L. Feldman (1993), “Thermal conductivity of disordered harmonic solids”, *Physical Review B*, 48, 12581-12588.
- [3] Andersson, D.A. et al. (2009), “Cooperativity among defect sites in AO_{2+x} and A₄O₉ (A=U,Np,Pu): Density functional calculations”, *Physical Review B*, 79, 024110.

- [4] Arima, T. et al. (2008), “Equilibrium and nonequilibrium molecular dynamics simulations of heat conduction in uranium oxide and mixed uranium-plutonium oxide”, *Journal of Nuclear Materials*, 376, 139-145.
- [5] Arima, T. et al. (2006), “Evaluation of thermal conductivity of hypostoichiometric $(U, Pu)O_{2-x}$ solid solution by molecular dynamics simulation at temperatures up to 2000 K”, *Journal of Alloys and Compounds*, 415, 43-50.
- [6] Asamoto, R. et al. (1969), “The effect of density on the thermal conductivity of uranium dioxide”, *Journal of Nuclear Materials*, 29, 67-81.
- [7] Bauer, T.H. (1993), “A general analytical approach toward the thermal conductivity of porous media”, *International Journal of Heat and Mass Transfer*, 36, 4181-4191.
- [8] Berman, R. (1976), *Thermal Conduction in Solids*, Clarendon Press, Oxford.
- [9] Berna, G. et al. (1997), *FRAPCON-3: A Computer Code for the Calculation of Steady-State, Thermal Mechanical Behavior of Oxide Fuel Rods for High Burnup*, Vol. 2 of NUREG/CR-6534. PNNL-11513, Pacific Northwest National Laboratory, Richland, Washington, US.
- [10] Beyer, C., D. Lamnning (1999), “Review of fuel thermal conductivity data and models”, *Thermal Performance of High Burn-Up LWR Fuel, Seminar Proceedings*, pp. 57-70, CEA, Caradache, France.
- [11] Born, M., K. Huang (1998), *Dynamical Theory of Crystal Lattices*, Oxford University Press.
- [12] Broido, D.A. et al. (2005), “Lattice thermal conductivity of silicon from empirical interatomic potentials”, *Physical Review B*, 72, 014308.
- [13] Busker, G. (2002), PhD thesis, Imperial College of Science, Technology and Medicine.
- [14] Callaway, J. (1959), “Model for lattice thermal conductivity at low temperatures”, *Physical Review*, 113, 1046-1051.
- [15] Callaway, J., H.C. von Baeyer (1960), Effect of point imperfections on lattice thermal conductivity. *Physical Review*, 120, 1149–1154.
- [16] Carruthers, P. (1961), “Theory of thermal conductivity of solids at low temperatures”, *Reviews of Modern Physics*, 33, 92.
- [17] Casado, J.M. et al. (1994), “Small-polaron hopping in mott-insulating UO_2 ”, *Journal of Physics: Condensed Matter*, 6, 4685.
- [18] Catlow, C.R.A. (1977), “Point defect and electronic properties of uranium dioxide”, *Proceedings of the Royal Society A, Mathematical Physical*, 353, 533-561.
- [19] Chen, G. (2005), *Nanoscale Energy Transport and Conversion: A Parallel Treatment of Electrons, Molecules, Phonons and Photons*, Oxford University Press, New York, US.
- [20] Chernatynskiy, A. et al. (2012), “Critical assessment of UO_2 classical potentials for thermal conductivity calculations”, *Journal of Materials Science*, pp. 1-10.

- [21] Chernatynskiy, A., S.R. Phillpot (2010), “Evaluation of computational techniques for solving the Boltzmann transport equation for lattice thermal conductivity calculations”, *Physical Review B*, 82, 134301.
- [22] Craeynest, J.C.V., J.P. Stora (1970), “Effet de la porosité sur la variation de conductibilité thermique du bioxyde d’uranium en fonction de la température: Application à l’oxyde mixte (U-Pu)O₂”, *Journal of Nuclear Materials*, 37, 153-158.
- [23] Deng, B. et al. (2012), “Effects of edge dislocations on the thermal conductivity of UO₂”, *Journal of Nuclear Materials*, 434, 203.
- [24] Deskins, W.R., A. El-Azab (2013), “Monte Carlo simulation of phonon transport in UO₂ single crystals”, *Modelling and Simulation in Materials Science and Engineering*, 21, 025013.
- [25] Dick, B.G., A.W. Overhauser (1958), “Theory of the dielectric constants of alkali halide crystals”, *Physical Review*, 112, 90.
- [26] Dolling, G. et al. (1965), “The crystal dynamics of uranium dioxide”, *Canadian Journal of Physics*, 43, 1397-1413.
- [27] Dorado, B. et al. (2009), “DFT+U calculations of the ground state and metastable states of uranium dioxide”, *Physical Review B*, 79, 235125.
- [28] Dudarev, S.L. et al. (1997), “Effect of mott-hubbard correlations on the electronic structure and structural stability of uranium dioxide”, *Philosophical Magazine Part B*, 75, 613-628.
- [29] El-Wakil, M.M. (1981), “Nuclear heat transport”, *American Nuclear Society*.
- [30] Escobar, R. et al. (2006), “Lattice Boltzmann modeling of subcontinuum energy transport in crystalline and amorphous microelectronic devices”, *Journal of Electronic Packaging*, 128, 115-124.
- [31] Fink, J.K. (2000), “Thermophysical properties of uranium dioxide”, *Journal of Nuclear Materials*, 279, 1-18.
- [32] Freyss, M. et al. (2005), “Point defects in uranium dioxide: Ab initio pseudopotential approach in the generalized gradient approximation”, *Journal of Nuclear Materials*, 347, 44-51.
- [33] Grimes, R.W. et al. (1990), “The behaviour of helium in UO₂: Solution and migration energies”, *Journal of Nuclear Materials*, 172, 123-125.
- [34] Gupta, C.K. (1989), *Materials in Nuclear Energy Applications*, CRC Press, Boca Raton.
- [35] Hassan, A.-R. (2011), *Surface-Bulk Electrochemical Coupling and Off-Stoichiometry in Uranium Dioxide*, M.S. Thesis, Florida State University.
- [36] Higuchi, S. (1998), “A molecular dynamics study of the thermal conductivity of UO₂ with impurities”, *Journal of Nuclear Science and Technology*, 35, 833-835.
- [37] Huang, P., E.A. Carter (2008), “Advances in correlated electronic structure methods for solids, surfaces, and nanostructures”, *Annual Review of Physical Chemistry*, 59(1)261-290.

- [38] Hui, P. et al. (1999), “Thermal conductivity of graded composites: Numerical simulations and an effective medium approximation”, *Journal of Materials Science*, 34, 5497-5503.
- [39] Jollet, F. et al. (2009), “Hybrid functional for correlated electrons in the projector augmented-wave formalism: Study of multiple minima for actinide oxides”, *Physical Review B*, 80, 235109.
- [40] Kari, S. et al. (2007), Computational evaluation of effective material properties of composites reinforced by randomly distributed spherical particles”, *Composite Structures*, 77, 223-231.
- [41] Klemens, P.G. (1955), “The scattering of low-frequency lattice waves by static imperfections”, *Proceedings of the Physical Society A*, 68, 1113.
- [42] Klemens, P.G. (1958), “Thermal conductivity and lattice vibrational modes”, *Solid State Physics*, 7, 1-98.
- [43] Klemens, P.G. (1960), “Thermal resistance due to point defects at high temperatures”, *Physical Review*, 119, 507-509.
- [44] Kneeze, G.A., A.V. Granato (1982), “Effect of independent and coupled vibrations of dislocations on low-temperature thermal conductivity in alkali halides”, *Physical Review B*, 25, 2851-2866.
- [45] Kurosaki, K. et al. (2006), “Molecular dynamics studies of americium-containing mixed oxide fuels”, *Journal of Nuclear Science and Technology*, 43, 1224-1227.
- [46] Lacroix, D. et al. (2005), “Monte Carlo transient phonon transport in silicon and germanium at nanoscales”, *Physical Review B*, 72, 064305.
- [47] Lamarch, J.R., J.A. Baratta (2001), *Introduction to Nuclear Engineering*, Prentice Hall, Third edition.
- [48] Lee, C.B., Y.H. Jung (2000), “An attempt to explain the high burnup structure formation mechanism in UO₂ fuel”, *Journal of Nuclear Materials*, 279, 207-215.
- [49] Lee, C.W., A. Chernatynskiy, P. Shukla, R.E. Stoller, S.B. Sinnott, S.R. Phillpot. (2012), “Effect of pores and He bubbles on the thermal transport properties of UO₂ by molecular dynamics simulation”, *Journal of Nuclear Materials*, 456, 253-259.
- [50] Maiti, A. et al. (1997), “Dynamical simulations of nonequilibrium processes: Heat flow and the Kapitza resistance across grain boundaries”, *Solid State Communications*, 102, 517-521.
- [51] Maradudin, A.A., A.E. Fein (1962), “Scattering of neutrons by an anharmonic crystal”, *Physical Review*, 128, 2589-2608.
- [52] Matzke, H., J. Spino (1997), “Formation of the rim structure in high burnup fuel”, *Journal of Nuclear Materials*, 248, 170-179.
- [53] Mazumder, S., Majumdar, A. (2001), “Monte carlo study of phonon transport in solid thin films including dispersion and polarization”, *Journal of Heat Transfer*, 123, 749-759.

- [54] Millett, P.C., M. Tonks (2011), “Meso-scale modeling of the influence of intergranular gas bubbles on effective thermal conductivity”, *Journal of Nuclear Materials*, 412, 281-286.
- [55] Millett, P.C. et al. (2008), “Phase-field simulation of thermal conductivity in porous polycrystalline microstructures”, *Journal of Applied Physics*, 104, 033512.
- [56] Mittal, A., S. Mazumder (2010), “Monte carlo study of phonon heat conduction in silicon thin films including contributions of optical phonons”, *Journal of Heat Transfer*, 132, 052402.
- [57] Narumanchi, S. et al. (2006), “Boltzmann transport equation-based thermal modeling approaches for hotspots in microelectronics”, *Heat Mass Transfer*, 42, 478-491.
- [58] Nemat-Nasser, S., M. Hori (1999), *Micromechanics: Overall Properties of Heterogeneous Materials*, Elsevier, Second edition.
- [59] Ninomiya, T. (1968), “Dislocation vibration and phonon scattering”, *Journal of Physical Society of Japan*, 25, 830-840.
- [60] Noirot, J. et al. (2009), “High burnup changes in UO₂ fuels irradiated up to 83 Gwd/t in M5 claddings”, *Nuclear Engineering and Technology*, 41, 155-162.
- [61] Noirot, J. et al. (2008), “Detailed characterisations of high burn-up structures in oxide fuels”, *Journal of Nuclear Materials*, 372, 318-339.
- [62] Ohashi, K. (1968), “Scattering of lattice waves by dislocations”, *Journal of Physical Society of Japan*, 24, 437-445.
- [63] Olander, D.R. (1976), *Fundamental Aspects on Nuclear Reactor Fuel Elements*, University of Michigan Library.
- [64] Omini, M., A. Sparavigna(1997), “Heat transport in dielectric solids with diamond structure”, *Nuovo Cimento D*, 19, 1537-1563.
- [65] Palagin, A. (2007), “Analysis of thermal conductivity of irradiated UO₂ fuel”, Transactions, SmiRT 19, Toronto, Paper # C04/2.
- [66] Pang, J. et al. (2013), “Phonon lifetime investigation of anharmonicity and thermal conductivity of UO₂ by neutron scattering and theory”, *Physical Review Letters*, 110, 157401.
- [67] Pettersson, S. (1991), “Solving the phonon Boltzmann equation with the variational method”, *Physical Review B*, 43, 9238-9246.
- [68] Ray, I. et al. (1997), “An electron microscopy study of the rim structure of a UO₂ fuel with a high burnup of 7.9% FIMA”, *Journal of Nuclear Materials*, 245, 115-123.
- [69] Rhee, S. (1975), “Porosity-thermal conductivity correlations for ceramic materials”, *Materials Science and Engineering*, 20, 89-93.
- [70] Ronchi, C. et al. (1999), “Thermal conductivity of uranium dioxide up to 2900 K from simultaneous measurement of the heat capacity and thermal diffusivity”, *Journal of Applied Physics*, 85, 776-789.

- [71] Ronchi, C. et al. (2004), “Effect of burn-up on the thermal conductivity of uranium dioxide up to 100.000 MWdt⁻¹”, *Journal of Nuclear Materials*, 327, 58-76.
- [72] Rondinella, V.V., T. Wiss (2010), “The high burn-up structure in nuclear fuel”, *Materials Today*, 13, 24-32.
- [73] Schelling, P.K. et al. (2002), “Comparison of atomic-level simulation methods for computing thermal conductivity”, *Physical Review B*, 65, 144306.
- [74] Schelling, P.K. et al. (2004), “Kapitza conductance and phonon scattering at grain boundaries by simulation”, *Journal of Applied Physics*, 95, 6082-6091.
- [75] Schulz, B. (1981), “Thermal conductivity of porous and highly porous materials”, *High Temperatures – High Pressures*, 13, 649-660.
- [76] Song, K.W. et al. (2000), “Reduction of the open porosity of UO₂ pellets through pore structure control”, *Journal of Nuclear Materials*, 279, 253-258.
- [77] Sproull, R.L. et al. (1959), “Effect of dislocations on the thermal conductivity of lithium fluoride”, *Journal of Applied Physics*, 30, 334-337.
- [78] Srivastava, G. (1999), *The Physics of Phonons*, Taylor & Francis Group.
- [79] Stan, M. et al. (2007), “Models and simulations of nuclear fuel materials properties”, *Journal of Alloys and Compounds*, 445, 415-423.
- [80] Swartz, E.T., R.O. Pohl (1989), “Thermal boundary resistance”, *Reviews of Modern Physics*, 61, 605-668.
- [81] Tiwary, P. et al. (2009), “Ab initio construction of interatomic potentials for uranium dioxide across all interatomic distances”, *Physical Review B*, 80, 174302.
- [82] Torquato, S. (2002), *Random Heterogeneous Materials: Microstructure and Macroscopic Properties*, Springer-Verlag.
- [83] Turney, J.E. et al. (2009), “Predicting phonon properties and thermal conductivity from anharmonic lattice dynamics calculations and molecular dynamics simulations”, *Physical Review B*, 79, 064301.
- [84] Walker, C. et al. (2006), “On the thermal conductivity of UO₂ nuclear fuel at a high burn-up of around 100 MWd/kgHM”, *Journal of Nuclear Materials*, 350, 19-39.
- [85] Walker, C.T., R.O. Pohl (1963), “Phonon scattering by point defects”, *Physical Review*, 131, 1433-1442.
- [86] Watanabe, T. et al. (2007), “Thermal conductance across grain boundaries in diamond from molecular dynamics simulation”, *Journal of Applied Physics*, 102, 063503.
- [87] Watanabe, T. et al. (2008), “Thermal transport properties of uranium dioxide by molecular dynamics simulations”, *Journal of Nuclear Materials*, 375, 388-396.
- [88] Watanabe, T. et al. (2009), “Thermal transport in off-stoichiometric uranium dioxide by atomic level simulation”, *Journal of the American Ceramic Society*, 92, 850-856.
- [89] Yamasaki, S. et al. (2007), “Evaluation of thermal conductivity of hyperstoichiometric UO_{2+x}; by molecular dynamics simulation”, *International Journal of Thermophysics*, 28, 661-673. 10.1007

-
- [90] Yang, H.S. et al. (2002), “Interfacial thermal resistance in nanocrystalline yttria-stabilized zirconia”, *Acta Materialia*, 50, 2309-2317.
 - [91] Ye, B. et al. (2011), “TEM investigation of irradiation damage in single crystal CeO₂”, *Journal of Nuclear Materials*, 414, 251-256.
 - [92] Yin, Q., S.Y. Savrasov (2008), “Origin of low thermal conductivity in nuclear fuels”, *Physical Review Letters*, 100, 225504.
 - [93] Zacharie, I. et al. (1998), “Thermal treatment of uranium oxide irradiated in pressurized water reactor: Swelling and release of fission gases”, *Journal of Nuclear Materials*, 255, 85-91.
 - [94] Ziman, J. (1962), *Electrons and Phonons*, Clarendon Press, Oxford, UK.

Part II

Methodologies for Determining Nuclear Fuel Properties

In the second major part of this report, the methodologies for developing and assessing material properties are briefly addressed for the critical areas of determining *Thermal expansion*, including thermal conductivity, transport/chemical diffusivity, free energy/heat capacity and mechanical properties. Y. Yun discusses the theoretical determination of thermal expansion behaviour in fuels, looking at a prototypical oxide pellet. Expansion of the pellet over time can cause detrimental pellet-clad mechanical interactions and affect gap conductivity. While expressions for behaviour have been developed, large scatter in measured data makes validation problematic. This is thus driving the improvement in theoretical methodologies, including first-principles and molecular dynamics (MD) simulations which are contributing to reliable predictions.

Atomic transport properties that affect microstructure, oxidation, fission product release, bubble nucleation, and other properties are another important area of materials properties that needs accurate modelling methodologies. The modelling of atomic transport is a key to understanding and predicting material properties under irradiation or in storage. M. Freyss discusses modelling approaches which span static atomistic calculations, in which the migration mechanism is fixed and the corresponding migration energy barrier is calculated, to MD calculations and kinetic Monte-Carlo (kMC) simulations, for which the time evolution of the system is explicitly calculated. Fundamental to many properties of fuels are the *Free energy and heat capacity*. Methods for measuring and estimating these values are discussed by M. Kurata and R. Devanathan, who note their importance in determining phase equilibria, phase-field modelling and other techniques. The last contribution to the second part of the report deals with assessing *Elastic and viscoplastic properties* of fuels. These are basic to predicting deformation and cracking, and thus to the mechanical integrity of fuel systems. R.A. Lebensohn describes mean-field formulations which enable the prediction of the mechanical behaviour of polycrystalline aggregates based on the heterogeneous and/or directional properties of their constituent single crystal grains and phases. These are ideal tools for establishing relationships between microstructure and properties of these materials.

Chapter 8.

Thermal expansion

Y. Yun

Paul Scherrer Institut, Switzerland

Abstract

Thermal expansion of fuel pellet is an important property which limits the lifetime of the fuels in reactors, because it affects both the pellet and cladding mechanical interaction and the gap conductivity. By fitting a number of available measured data, recommended equations have been presented and successfully used to estimate thermal expansion coefficient of the nuclear fuel pellet. However, due to large scatter of the measured data, non-consensus data have been omitted in formulating the equations. Also, the equation is strongly governed by the lack of appropriate experimental data. For those reasons, it is important to develop theoretical methodologies to better describe thermal expansion behaviour of nuclear fuel. In particular, first-principles and molecular dynamics simulations have been certainly contributed to predict reliable thermal expansion without fitting the measured data. Furthermore, the two theoretical techniques have improved on understanding the change of fuel dimension by describing the atomic-scale processes associated with lattice expansion in the fuels.

Introduction

Upon being heated in reactor, nuclear fuels thermally expand with temperature. Uranium dioxide (UO_2), which is a representative nuclear fuel in light water reactors (~95% of all fuel), has a cubic crystal structure, with uranium in a face centred array and the oxide ions occupying the tetrahedral holes. This cubic structure gives the uranium oxide pellet uniform expansion properties. The thermal expansion of fuel pellet contributes to pellet-clad mechanical interaction, which is known to cause fuel rod failure under operation condition. As manufactured, a roughly axisymmetric gap exists between the outer radius of cylindrical UO_2 fuel pellets and the inner surface of the cladding in fuel rods. The gap thickness is decreased during the operation by the thermal expansion of fuel pellet as well as the cladding creep down due to the high coolant pressure, causing the pellet-cladding mechanical interaction (PCMI) at power transient conditions [1]. In addition, due to

relatively low thermal conductivity of oxide fuel materials, such as ThO₂, UO₂, and mixed oxide of (U,Pu)O₂, a steep radial temperature gradient appears in the fuel pellet and leads to differential thermal expansion along the radial direction. The thermal expansion results in the liner strain of fuel and takes part in the degradation of thermal conductivity of fuel in a recurrent manner. As a result of the non-uniform thermal expansion by the radial temperature gradient, the circumferential thermal stress is developed in the pellet, causing radial cracking [2]. The cracks strongly influence on both thermal and mechanical performance of the fuel, altering temperature distribution and causing an anisotropic degradation of the fuel thermal conductivity by the pellet relocation [3]. Owing to these characteristics of fuel pellet, the thermal expansion is one of important parameters in determining the fuel performance during reactor operation. Furthermore, it is essential to predict accurately the thermal expansion of fuel pellet to design and prevent the fuel rod failure in operating condition.

In this report, representative modelling methodologies are encapsulated, which have been satisfactorily used to elucidate thermal properties of nuclear fuels. First, measured data fitting is reviewed and equations to estimate thermal expansion of fuels are recommended. Subsequently, the application of first-principles techniques is described to calculate the expansion coefficient of UO₂. Molecular dynamics (MD) methods are also summarised and the results are compared with experiments. Finally, the current status of first-principles and MD simulations is discussed, considering existing limitations such as the application of the approximations for high-temperature behaviour and the determination of parameters in potential functions.

Theoretical methodologies

Empirical correlation

The thermal expansion is typically measured either by a macroscopic length change or by a microscopic change of lattice parameter. A number of measured data, especially for UO₂, have been reported in the literature, and equations of thermal expansion have been recommended by comparing the macroscopic length change with the lattice parameter measurements [4]. Using a weighted least-squares minimisation procedure, D.G. Martin has fit the macroscopic length changes with the lattice parameter measurements and recommended the equations of the thermal expansion for solid UO₂ [5], as written in Equations 1 and 2:

For 273 K ≤ T ≤ 923 K:

$$L = L_{273} \left(9.9734 \times 10^{-1} + 9.802 \times 10^{-6} T - 2.705 \times 10^{-10} T^2 + 4.391 \times 10^{-13} T^3 \right) \quad (1)$$

For 923 K ≤ T ≤ 3120 K:

$$L = L_{273} \left(9.9672 \times 10^{-1} + 1.179 \times 10^{-5} T - 2.429 \times 10^{-9} T^2 + 1.2119 \times 10^{-12} T^3 \right) \quad (2)$$

where L and L_{273} are the lengths at temperature T (K) and 273 K, respectively. J.K. Fink has also summarised the measurement of fractional change in length of UO₂ with the recommended uncertainties and the data fit [6]. Although the thermal expansion data from macroscopic and the lattice parameter measurements are overall good agreement with each other, there are non-dispensable problems in assessing the quality of the available data due to the fact that the two principal methods are each subject to

possible errors. For example, it has been known that the lattice parameter measurements obtained from X-ray diffraction can be subject to error at high temperature, because of difficulties in measuring sufficiently the temperature of samples in the high-temperature diffraction camera [5]. Consequently, some of data do not agree with the common consensus and accordingly were excluded in the fitting for formulating Equations 1 and 2. Apart from the difficulties, the contribution of Schottky defects to the macroscopic expansion becomes significant above around 2 700 K and leads to increasing the difference of macroscopically measured data with lattice parameter measurements [7]. Furthermore, the fitting to formulate the recommended equations of thermal expansion is largely governed by appropriate experimental data. Because of those technical difficulties of measurement as well as the lack of appropriate experimental data, it is definitely essential to improve theoretical methods to understand the thermal expansion behaviour of nuclear fuels. Recently, big efforts have been made to develop databases of materials properties by applying atomistic modeling techniques [8,9]. Most of all, assessment of the measurements as well as a step forward in understanding the thermal properties of nuclear fuels can be gained from a better description of atomic-scale processes in nuclear fuels.

First principles modelling

The change of lattice parameter with temperature is directly related to thermodynamics of a system containing particles within molecule or crystals. In thermodynamics, the total free energy of the system at a certain temperature has contributions from the lattice vibrations and the thermal excitation of electrons. To obtain the temperature dependence of the lattice parameter, the Helmholtz free energy, $F(V,T)$, is used at the temperature.

$$F(V,T) = U(V) + F^{phon}(V,T) + F^{el}(V,T) \quad (3)$$

where $U(V)$ the static lattice energy, $F^{phon}(V,T)$ the phonon contribution to the free energy, and $F^{el}(V,T)$ the free energy of the electronic subsystem. The static lattice energy is the potential energy associated with the static constituent of material and is equal to the total free energy at absolute zero temperature. With increased temperature, the phonon energy due to the lattice vibration as well as the electron contribution becomes significant to the total free energy. First, the static lattice energy can be obtained using various first-principles methods, typically density functional theory (DFT) calculations, at the equilibrium volume at $T=0K$. Calculating the static lattice energy by the DFT method is explained in Chapter 12 (by M. Freyss) in more detail. The free energy contribution of phonon, $F^{phon}(V,T)$, is expressed as follows:

$$F^{phon}(V,T) = \int_0^{\infty} d\omega g(\omega) \left[\frac{\hbar\omega}{2} + k_B T \ln(1 - e^{-\hbar\omega/k_B T}) \right] \quad (4)$$

The phonon density of states (DOS), $g(\omega)$, the force constant matrix can be extracted from the Hellman-Feynman forces, which are calculated by using either the linear response theory or the direct approach, is used. In the former approach, a perturbation of the atomic positions with the periodicity of the original lattice is treated with standard perturbation theory, and first-order corrections are computed [10,11]. In the direct approach, or so-called supercell method, a finite displacement of several atoms is employed in a supercell to compute atomic force constants and the phonon spectrum [12,13]. The free electron energy has been approximated using the following expression:

$$F^{el}(V, T) = -(\pi k_B)^2 / 6D(E_F)T^2 \quad (5)$$

where $D(E_F)$ is the electron DOS at the Fermi level. When the phonon and electrons DOSs are calculated, the thermal expansion coefficient is obtained very straightforward. First, the phonon and electrons DOSs with static lattice energy is calculated for a number of volumes around the $T=0\text{K}$ equilibrium. Then, the total free energies are calculated for the different volumes at constant temperature using Equations 3-5. Once the free energy is calculated, the corresponding equilibrium volume is obtained. By repeating the process for different temperatures, the thermal expansion coefficient, α , defined by:

$$\alpha = \frac{1}{a} \frac{da}{dT} = \frac{1}{3V} \frac{dV}{dT} \quad (6)$$

where a is the lattice constant. Figure 1(a) shows the thermal expansion coefficient of UO_2 calculated by Yun et al. [9] using the first-principles DFT method. To obtain the phonon free energy as written in Equation 5, the phonon density of state of UO_2 was calculated using a 96-atom supercell based on the direct method. They presented that the electronic contribution was not included in the calculation, because the electronic contribution can be negligible in the temperature range up to 1 000 K, which is the range of interest in the work. In Figure 1(a), the calculated thermal expansion coefficient considering only the phonon contribution is in good agreement with experimental data [20] especially up to 500 K, and the deviation becomes significant at around 1 000 K. This might be due to an increased electronic contribution to the thermal expansion. It is important to note that the phonon calculation from first-principles is based on the harmonic lattice approximation that the atomic deviations are assumed to be so small, and this is generally a good approximation, at least at relatively low temperatures [14].

Molecular dynamics with empirical potentials

Molecular Dynamics (MD) is useful in the study of non-equilibrium dynamic processes at the atomic level. Especially, in extreme conditions of high temperature or high pressures, the MD simulation is often the best way to obtain the necessary information [15]. In recent years, a number of studies on thermophysical and transport properties of nuclear fuels have been published using classical potentials in the MD simulations. The MD results have been overall in good agreement with experimental data. It should be noted that in the MD simulations it is crucial to select well-established interatomic potential function to obtain reliable results, because it requires technically many fitting parameters or coefficients of interatomic potentials. A number of interatomic potentials developed over the past decades are categorised into two kinds of functions [16]: (1) rigid-ion model and (2) shell model. T. Arima et al. calculated the lattice constant of UO_2 with temperature applying two different sets of rigid-ion potentials [17]. One is the Born-Mayer-Huggins (BMH) potentials with the fully ionic model (FIM), which assumes that UO_2 crystal is fully ionic-bonded with 100% of the ion valence. The BMH potential with FIM is given by:

$$U_{FIM}(r_{ij}) = \frac{z_i z_j e^2}{r_{ij}} + A_{ij} \exp\left(-\frac{r_{ij}}{\rho_{ij}}\right) - \frac{C_{ij}}{r_{ij}^6} \quad (7)$$

where r_{ij} is the distance between ions of types i and j , z_i is the charge of type i . A_{ij} , ρ_{ij} and C_{ij} are potential parameters. The other function developed by T. Arima et al. is the BMH potential with the partially ionic model (PIM) and is written by:

$$U_{PIM}(r_{ij}) = \frac{z_i z_j e^2}{r_{ij}} + f_0(b_i + b_j) \exp\left\{-\left(\frac{a_i + a_j - r_{ij}}{b_i + b_j}\right) \times \left(-\frac{r_{ij}}{\rho_{ij}}\right)\right\} - \frac{c_i c_j}{r_{ij}^6} \quad (8)$$

where f_0 is the adjustable parameter. Potential parameters, a_i , b_i , c_i are given to the ion of types i . In this equation, z_i is the effective charge of type i ion. Following the Pauling's equation, T. Arima et al. assumed the ionic bonding of 67.5% for UO_2 .

Figure 1. Lattice constants of UO_2 using the first-principles DFT method [9] and (b) using MD [17] and compared with experimental data: a) [20], b) [21], c) [5]

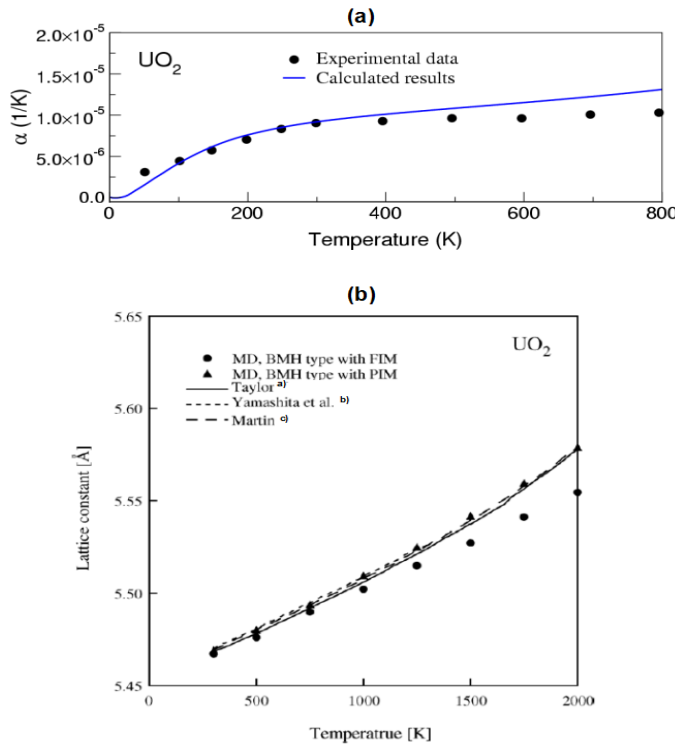


Figure 1 shows the lattice constants of UO_2 using both the BMH potential with the FIM and PIM, and compared the results with experimental data. The results obtained for the FIM are comparable with experimental data up to 1 000 K, but above 1 000 K, the PIM better reproduced the experimental data than the FIM. It is because the depressing Coulomb force between uranium and oxygen ions leads to the relatively large thermal expansion at high temperature. On the other hand, the Morse potential successfully explained the temperature dependence of the thermal expansion coefficient, especially for fluorite-type compounds [18], such as ThO_2 , UO_2 , and PuO_2 .

$$V(r) = D[\exp\{-2a(r - r_0) - 2\exp\{-a(r - r_0)\}\}] \quad (9)$$

where D is the depth of the potential, r is the interatomic separation, r_0 is the interatomic separation at the potential minimum, and α is the inverse line width of the potential. H. Inaba presented the thermal expansion coefficients calculated by the morse potential for ThO_2 and UO_2 .

The calculated thermal expansion coefficients are overall in good agreement with the experimental data below around 1 300 K for ThO_2 and 1 000 K for UO_2 , but the difference is increased above the temperatures both for ThO_2 and UO_2 . It is considered that the larger experimental values of the thermal expansion coefficient at high temperature are mainly due to the contribution of vacancies created.

Conclusion and future challenges

Along with the consistent development of interatomic potentials, the description on thermal expansion behaviour of nuclear fuels has also been improved for the past decades. However, the parameters in the potential functions have been fitted on different experimental data, and are normally difficult to apply to other materials. Hence, it is still challenging to establish potentials which can be applied to various nuclear fuel materials at broad temperature ranges. In addition, system size (up to few million atoms) and time (up to a few nanoseconds) is a major limitation required to be improved in the MD simulations[16]. The application of first-principles methods is even more demanding. The first-principles calculation is fundamentally to describe the ground states of materials, and the harmonic lattice approximation is valid at relatively low temperature. Therefore, there are limits to extending the application of the first-principles method at high temperature [8], in particular, over 1 000°C that nuclear fuels are exposed to under reactor operation. For a better description of temperature-dependent properties including thermal expansion, DFT-based MD simulations have been successfully applied over a wide range in temperature, up to about 2 700°C [19]. Despite a significant step forward in development of temperature-dependent DFT in combination with MD simulations, it has not yet been employed to nuclear fuels, especially no application result yet for thermal expansion behaviour of the fuel materials. In order to successfully apply DFT-MD methods for thermodynamic properties of nuclear fuel, both the first-principles and MD methods need further improvement, with the primary need being associated with the ability to scale up to larger numbers of atoms and to develop high-temperature predictions of nuclear fuel behaviour.

With increased temperature, the free energy of electrons became significant. To take into account for the contribution of electrons on the total free energy, a finite temperature DFT functional is needed, such as Mermin functional [22], rather than the ordinary DFT energy functional to treat the thermal excitation of electrons. Beside the thermal expansion of fuel itself, the fuel expansion originates from swelling due to fission products. Therefore, fuel burn-up is also needed to be considered to accurately estimate the fuel expansion during irradiation.

It is challenging to describe the thermal expansion of nuclear fuel during irradiation because of the complex environment in reactor and various parameters affecting to fuel behaviour, such as temperature, burn-up, stoichiometry, fission products, and correlations between the parameters. Therefore, broader consideration is required from the fundamentals of thermal properties of fuel to the macroscopic thermal behaviour in

reactors to accurately estimate the thermal expansion of fuel. To achieve this, it is necessary to improve the theoretical estimation techniques and a multi-length and -time scale approach will be an appropriate method to assess such a complex fuel behaviour.

References

- [1] NEA (2005), “Pellet-clad interaction in water reactor fuels”, *Seminar Proceedings*, Aix-en-Provence, France.
- [2] Gehl, S.M. et al. (1978), NUREG/CR-0088, ANL-77-80, Argonne National Laboratory, Argonne, US.
- [3] Sumi, Y. (1981), “Thermally induced radial cracking in fuel element pellets”, *Journal of Nuclear Materials*, 96. pp. 147-159.
- [4] Olsen, C.S. (1979), *Fuel Thermal Expansion (FTHEXP) in MATPRO-Version 11: A Handbook of Materials Properties for Use in the Analysis of Light Water Reactor Fuel Rod Behaviour*, ed. Hagraman, D.G., G.A. Reymann, US Nuclear Regulatory Commission Rep. NUREG/CR-0497.
- [5] Martin, D.G. (1988), “The thermal expansion of solid UO₂ and (U,Pu) mixed oxides – A review and recommendations”, *Journal of Nuclear Materials*, 152. pp. 94-101.
- [6] Fink, J.K. (2000), “Thermophysical properties of uranium dioxide”, *Journal of Nuclear Materials*, 279. pp. 1-18.
- [7] IAEA (2006), *Thermophysical Properties Database of Materials for Light Water Reactors and Heavy Water Reactors*, IAEA-TECDOC-1496.
- [8] Yun, Y., Oppeneer, P.M. (2011), “First-principles design of next-generation nuclear fuels”, MRS Bulletin, 36, pp.178- 184.
- [9] Yun, Y., D., Legut, P.M. Oppeneer (2012), “Phonon spectrum, thermal expansion and heat capacity of uo₂ from first-principles”, *Journal of Nuclear Materials*, 426, pp. 109-114.
- [10] Yin, Q., S.Y. Savrasov (2008), “Origin of low thermal conductivity in nuclear fuels”, *Physical Review Letters*, 100. pp. 225504-225507.
- [11] Dai, X. et al. (2003), “Calculated phonon spectra of plutonium at high temperatures”, *Science*, 300(2003) 953-955.
- [12] Parlinski, K. (2005), *Phonon Software*, Cracow, Poland.
- [13] Piekarz, P. et al. (2005), *Physical Review B*, 72(1)014521.
- [14] Petros, P. (2007), *Electronic Structure and Lattice Dynamics of Elements and Compounds*, Ph.D. Thesis, Uppsala Universitet, pp 79-109.
- [15] Potashnikov, S.I. et al. (2011), “High-precision molecular dynamics simulation of UO₂-PuO₂: pair potentials comparison in UO₂”, *Physical Review B*, 83, 094104.
- [16] Govers, K. et al. (2007), “Comparison of interatomic potentials for UO₂. Part I: Static calculations”, *Journal of Nuclear Materials*, 366, pp. 166-177.

- [17] Arima, T. et al. (2005), “Evaluation of thermal properties of UO_2 and PuO_2 by equilibrium molecular dynamics simulations from 300 to 2000 K”, *Journal of Alloys and Compounds*, 400, pp. 43-50.
- [18] Inaba, H. (2000), “Semiempirical estimation of thermal expansion coefficients and isobaric heat capacities of fluorite-type compounds”, *International Journal of Thermophysics*, 22, pp. 249-268.
- [19] Mattsson, T.R. et al. (2009), “Quantifying the anomalous self-diffusion in molybdenum with first-principles simulations”, *Physical Review B*, 80.
- [20] Taylor, D. (1984), British Ceramic Transactions and Journal, 83, pp. 32.
- [21] Yamashcita, T. et al. (1997), “Thermal expansions of NpO_2 and some other actinide dioxides”, *Journal of Nuclear Materials*, 245, pp. 72-78.
- [22] Mermin, N.D. (1965), “Thermal properties of the inhomogeneous electron gas”, *Physical Reviews*, 137, A1441.

Chapter 9.

Atomic transport properties

M. Freyss

CEA, DEN, DEC, Centre de Cadarache, France

Abstract

As presented in the first chapter of this book, atomic transport properties govern a large panel of nuclear fuel properties, from its microstructure after fabrication to its behaviour under irradiation: grain growth, oxidation, fission product release, gas bubble nucleation. The modelling of the atomic transport properties is therefore the key to understanding and predicting the material behaviour under irradiation or in storage conditions. In particular, it is noteworthy that many modelling techniques within the so-called multi-scale modelling scheme of materials make use of atomic transport data as input parameters: activation energies of diffusion, diffusion coefficients, diffusion mechanisms, all of which are then required to be known accurately. Modelling approaches that are readily used or which could be used to determine atomic transport properties of nuclear materials are reviewed here. They comprise, on the one hand, static atomistic calculations, in which the migration mechanism is fixed and the corresponding migration energy barrier is calculated, and, on the other hand, molecular dynamics calculations and kinetic Monte-Carlo simulations, for which the time evolution of the system is explicitly calculated.

Introduction

In nuclear materials, atomic transport properties can be a combination of radiation effects (atom collisions) and thermal effects (lattice vibrations), this latter being possibly enhanced by vacancies created by radiation damage in the crystal lattice (radiation enhanced-diffusion). Thermal diffusion usually occurs at high temperature (typically above 1 000 K in nuclear ceramics), which makes the transport processes difficult to model at lower temperatures because of the low probability to see the diffusion event occur in a reasonable simulation time. In this chapter, some methods will be reviewed that

enable one to apprehend atomic transport properties in solids and which are currently used for nuclear materials or which show great potential.

The basic equation to express the thermal contribution to the atomic transport properties (in particular self-diffusion) is the Fick law, giving the atom flux \mathbf{J} in the crystal:

$$\mathbf{J} = -D \cdot \nabla c \quad (1)$$

where c is the atom concentration and D is the diffusion coefficient (assumed isotropic in Equation 1). Diffusion is strongly affected by the microstructure and composition of the material. Atomic transport properties can be strongly dependent on the stoichiometry of the compound, the presence of grain-boundaries or surfaces, the concentration of point defects or impurities, etc. The diffusion equation 1 has to take into account these various effects by additional terms, in particular in the case of materials under irradiation, terms describing the contribution of intragranular and intergranular diffusion, sink efficiency of point defects, bubble nucleation and re-solution of fission gases, etc. These various effects make the determination (experimental or theoretical) of diffusion coefficients for a given species difficult. For instance, a large dispersion of experimental data exists for atomic self-diffusion coefficients in UO_2 [1-5].

For a given element and a fixed composition (or stoichiometry) of the compound, the temperature-activated diffusion coefficient in Equation 1 is expressed as:

$$D = f \cdot a^2 \cdot v \cdot \exp\left(-\frac{\Delta G}{k_B T}\right), \text{ with } \Delta G \text{ the Gibbs free energy (or free enthalpy) associated}$$

with the diffusion, f is a correlation factor accounting for the fact that successive atom jumps can be related to one another, v the jump frequency, a is a characteristic diffusion length in the crystal depending on the lattice parameter, T the temperature and k_B the Boltzmann constant. The diffusion coefficient D is often found to obey an Arrhenius law:

$$D = D_o \cdot \exp\left(-\frac{\Delta H}{k_B T}\right) \quad (2)$$

in which ΔH is the enthalpy (or the diffusion activation energy $\Delta H = E_a$) associated with the diffusion, D_o the diffusion pre-factor. The activation energy E_a is generally identified as the sum of the migration energy E_m and the defect formation energy, depending on the diffusing element, on the diffusion mechanism and on the nature of the point defects which mediate the diffusion. The temperature-independent pre-factor D_o then depends on the migration and the defect formation entropies ΔS_f and ΔS_m :

$$D_o = f \cdot a^2 \cdot v \cdot \exp\left(-\frac{\Delta S_f + \Delta S_m}{k_B}\right) \quad (3)$$

The knowledge of atomic transport events, even of rare events, is required in order to set up a so-called multi-scale modelling scheme for the evolution of the material [6] and to provide physics-based data for nuclear fuel performance codes [7]. The challenge is then, using state-of-the-art modelling techniques, to calculate the diffusion coefficient D directly or determine separately its various contributions: the possible diffusion mechanisms, the corresponding activation energies, the pre-exponential factor D_o .

including its several components (jump frequency, entropy terms, correlation factor). Several modelling approaches exist to reach this goal, based on atomistic first-principles or empirical potential calculations, or Monte Carlo simulations.

Dynamical calculations: Diffusion coefficients

Molecular dynamics (either *ab initio* or classical) and kinetic Monte Carlo simulations are techniques which enable one to simulate the evolution in time of the system and to directly access the diffusion coefficient of a given species in a material.

a. Molecular dynamics

The time evolution of the system is obtained by solving the Newton equation of motion for all the atoms of the system. The trajectory as a function of time for each particle of the system is obtained. The accuracy of the calculations is determined by the accuracy with which the interaction potentials between the atoms can be described. The interaction potentials can be either calculated using the electronic structure of the system from first-principles calculations (*ab initio* molecular dynamics) or using interatomic empirical potentials (classical molecular dynamic). For more details on classical molecular dynamics, (see Chapter 13). The accuracy chosen will limit the time scale of the simulation: a few picoseconds for *ab initio* molecular dynamics, and a few nanoseconds for classical molecular dynamics. Most of the transport processes involved in the evolution of nuclear materials (point defect or fission product migration) exhibit, however, energy barriers too high to occur within the time scale of *ab initio* simulation. Most of the molecular dynamics studies of nuclear materials, especially actinide compounds, are still performed using empirical potentials.

Using molecular dynamics, atomic transport properties are determined by the analysis of the trajectories of the atoms as a function of time. Thermal vibrations or complex concerted motions of the atoms can, however, make the determination of elementary migration paths difficult. But one can access the coefficient D, which is expressed as the mean square displacement of an atom species:

$$D = \lim_{t \rightarrow \infty} \frac{1}{6t} \langle |\mathbf{r}(t) - \mathbf{r}(0)|^2 \rangle \quad (4)$$

By performing simulations at various temperatures, one can plot the evolution of D as a function of the temperature and extract the pre-exponential factor D_0 by a fit to the Arrhenius law equation 2. The activation energy of a particular diffusion mechanism can, however, hardly be extracted from molecular dynamics simulations because of the concerted motion of all the atoms of the system. Generally, the diffusion mechanism is identified in a molecular dynamics simulation and its activation energy is subsequently calculated using a static calculation method, such as the Nudged Elastic Band (NEB) method presented below.

There are several limitations in the use of *ab initio* or classical molecular dynamics for atomic transport properties. *Ab initio* calculations can only reach simulation times of the order of a few picoseconds with a limited number of atoms involved (several hundreds at most), while in classical molecular dynamics calculations, the number of atoms involved can reach billions and the timescale is significantly increased to around 10-100 ns. But in

many cases, it is still not enough to observe diffusion events that are too slow and involve a large energy barrier, like for instance uranium or xenon diffusion in UO₂. For such processes, either static migration methods have to be used (see below) or accelerated dynamics algorithms.

b. Accelerated dynamics

Accelerated dynamics methods such as temperature-accelerated dynamics simulations [8] introduce a fictitious temperature to the system in order to ease the climbing of potential barriers and thus artificially accelerate the time evolution of the system. The temperature can be raised typically to 3 000 K, the challenge being the conservation of the correct dynamics at the original temperature. Similarly, in hyperdynamics [9] or metadynamics [10] calculations, a bias potential raises the energy in regions other than the transition states between potential basins, enabling the exploration of the potential energy surface and making transitions occur at an accelerated rate without the prior knowledge of the states through which the system may evolve.

Classical molecular dynamics calculations have been used to model various aspects of atomic transport properties of point defects and fission products in nuclear fuel materials. For instance, in the case of UO₂: defect recombination [11,12], diffusion induced by displacement cascades [13-16], influence of grain boundaries and dislocations [17,18], rare gas diffusion and resolution [19-23], etc.

c. Kinetic Monte Carlo

KMC simulations [24] are another approach to determine the time evolution of a system from which diffusion coefficients may be directly extracted. Its advantage over classical molecular dynamics is that it enables to access larger timescales, but it is based on the prior knowledge of all the various mechanisms by which the system can evolve. It cannot predict a migration mechanism by itself. A list of migration mechanisms and their associated migration barriers are input data of the simulation. These data are often provided by *ab initio* or empirical potential calculations or extracted from experimental data. Kinetic Monte Carlo is based on the calculation of the probabilities of all the possible transitions of the system (see Chapter 17). KMC has only been recently applied to the study of atomic transport properties in nuclear fuels. An example is the calculation of oxygen diffusivity in UO₂ as a function of the stoichiometry [25].

Static calculations: Migration barriers

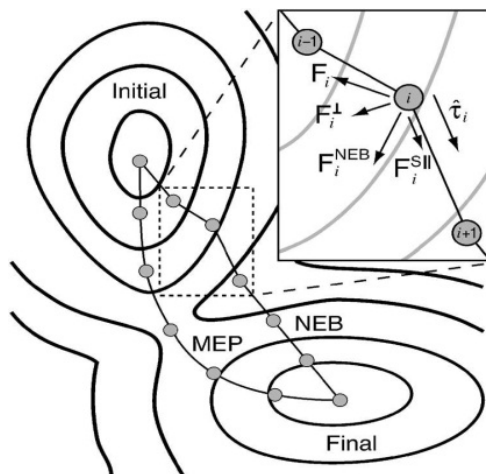
Static calculations are an alternative to dynamical simulations for the study of transport properties in materials. The goal of static migration calculations is to determine the energy barrier that the migrating atom has to overcome in order to hop from one position in the crystal to the next. In this approach, the time evolution of the system does not come into play. The migration energy is determined by the calculation of the energy of the system upon displacement of the migrating atom in the crystal. The challenge for static migration calculations is to find the most favourable migration mechanism, the minimum-energy path (MEP), which is starting from a local energy minimum and leading to another local energy minimum, passing through a saddle point. The energy of the saddle point relative to the local energy minimum is defined as the migration energy E_m. Several such static methods have been developed, among them the Nudged Elastic Band (NEB) method [26],

the string method [27,28], the dimer method [29], the Activation-Relaxation Technique (ART) [30-33].

a. The Nudged Elastic Band (NEB) and the string methods

These methods are used to find reaction pathways when both the initial and final states are known. An initial migration path is interpolated and discretised into a set of images between the known initial and final states. The total energy of the images, corresponding to intermediary configuration of the migrating atom along the migration path, is then minimised. The NEB method is based on a spring interaction between adjacent images which is added to ensure continuity of the path, thus mimicking an elastic band. The forces acting on each image that should be minimised are the normal component of the potential force and the tangential component of the spring force (see Figure 1). In the string method, an elastic chain of configurations joining the initial and final states is progressively driven to the minimum energy path using an iterative procedure consisting of two steps: (1) evolution step: the images are moved following the atomic forces, (2) reparametrisation step: the images are equally redistributed along the string. In both NEB and string methods, the atomic positions of the system are optimised at each step of the migration to ensure that the minimum energy path is found. The climbing-image method [33] is an improvement of these methods to make one of the images correspond to the saddle point of the migration path for a more accurate determination of the energy barrier. The drawback of the NEB and the string methods is that the final state of the migration has to be known: one has to explore many migration mechanisms in order to find the diffusion process with the lowest migration barrier that will be thus the most probable to occur.

Figure 1. Two components making up the nudged elastic band force F^{NEB} : the spring force $F^{S//}$ along the tangent and the perpendicular force F^{\perp} due to the potential [35]



b. The dimer method and Activation-Relaxation Technique (ART)

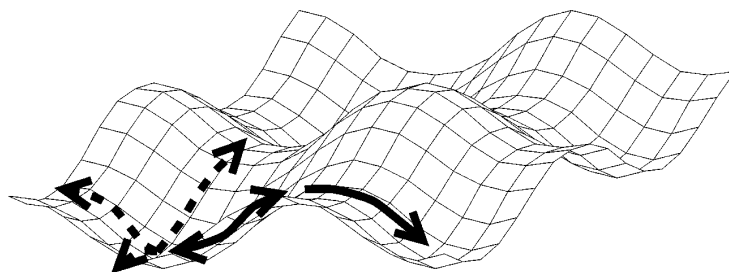
Contrary to the NEB or the string methods, these methods require the knowledge of neither the final state of migration nor the saddle points: it allows the system to evolve following well-defined paths between local energy minima, starting from the knowledge of only one local minimum. The dimer method [27,28] is used to find saddle points by defining two replicas (dimer) of the system with slightly displaced coordinates in order to

explore the curvature of the potential energy surface. The ART method [30-33] proceeds in two steps starting from a local minimum:

- activation: the configuration is moved from a local minimum to a nearby local saddle point;
- relaxation: the system is pushed over the saddle point and relaxed to a new minimum.

The first step is achieved by defining a modified force field in which the saddle is a minimum. The dimer and the ART methods allow one to jump over much higher energy barriers than allowed by standard molecular dynamic techniques and can thus predict migration mechanisms and activation energies in complex local atomic arrangements or in disordered materials. For nuclear materials such as UO_2 , such methods should be, however, used with caution because of the large difference between oxygen and uranium migration barrier: only migration events involving oxygen ions would most probably be obtained.

Figure 2. Illustration of the activation and relaxation steps in ART for a two-dimensional energy landscape [30]



From each energy minimum, the system can reach several saddle points. The down-pointing arrows from the saddle point indicate the directions of the force toward a minimum energy. The full line arrows show the path for a single event.

In the static migration approaches, the interatomic interactions can be calculated from either first-principles or empirical potential calculations. ART has been recently applied to point defects in metals [36], silicon carbide [37], amorphous silica [31]. For nuclear fuel applications, the NEB method has been mostly used so far in order to determine migration mechanisms and to calculate migration energies of point defects and fission products. For instance, in the case of UO_2 , using the first-principles DFT+U method, the migration of oxygen [25,38] uranium [39,40] and xenon [39] atoms has been studied. These studies follow many previous works making use of standard DFT [41,42], which is unfortunately not appropriate for a correct description of the electronic properties of UO_2 (see Chapter 12). Using empirical potentials, pioneering works in the eighties and early nineties were already able to identify migration mechanisms of point defects [43] and xenon atoms [44,45] in UO_2 with static migration calculations. They were later completed by the use of several empirical pair-potentials for the study of transport properties of point defects [46], dislocations [47], fission gases and helium [48] in UO_2 .

Vibrational properties: Pre-exponential factor

a. Entropic contributions to the pre-exponential factor

Atomic transport properties can be apprehended by the calculation of the vibrational properties of the system. The diffusion prefactor D_o is indeed expressed as a function of migration and defect formation entropy ΔS_f and ΔS_m (Equation 3 – in which the electronic entropy contribution is generally neglected). The formation entropy is related to the phase-space volume accessible to the defects and involves configurational and vibrational contributions: $\Delta S_f = \Delta S_{f,conf} + \Delta S_{f,vib}$. The configurational contribution is purely geometric and depends on the number of configurations Ω that the diffusing defect can take in the lattice: $\Delta S_{f,conf} = k_B \ln \Omega$. The vibrational contribution $\Delta S_{f,vib}$ is the difference between the vibrational entropy of the system containing the defect and the vibrational entropy of the perfect system without defect. In the harmonic approximation, it can be expressed as a function of the phonon frequencies ν_i^0 of the perfect system (containing N atoms) and the phonon frequencies ν_i' of the defective system, which can be calculated using first-principles or empirical potential calculations:

$$\Delta S_{f,vib} = k_B \ln \frac{\prod_{i=1}^{3N} \nu_i^0}{\prod_{i=1}^{3N} \nu_i'} \quad (5)$$

The migration entropy ΔS_m is defined as the difference in entropy between the system in which the diffusing atom is at a local stable position (local minima 0) and at a saddle-point position (or transition state TS): $\Delta S_m = S_{vib}^{TS} - S_{vib}^0$. The migration entropy can again be calculated from the phonon spectra of the system. In the harmonic approximation ΔS_m can be expressed, similarly to the formation entropy, as a function of the phonon frequencies ν of the system at the equilibrium and transition states:

$$\Delta S_m = k_B \ln \frac{\prod_{i=1}^{3N} \nu_i^0}{\prod_{i=1}^{3N-1} \nu_i^{TS}} \quad (6)$$

The denominator specifically excludes the frequency in the direction of the motion corresponding to an unstable mode at the transition state.

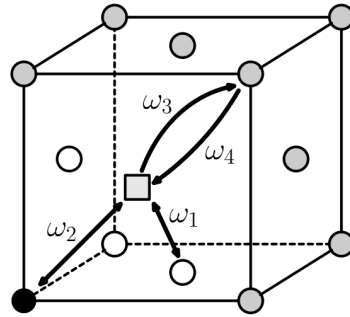
b. Five-frequency model for impurity diffusion

The diffusion pre-exponential factor for impurities can also be determined using a model describing the diffusion mechanisms of the impurity (in dilute concentration) called the five-frequency model. Assuming that the impurity jumps are affected by the presence of vacancies only in the immediate vicinity, A.D Le Claire and A.B. Lidiard [49] expressed the diffusion coefficient D_2 of an impurity in a face-centered cubic crystal in terms of five jump frequencies w and of the self-diffusion coefficient of the pure host element D_o :

$$\frac{D_2}{D_0} = \frac{f_2}{f_0} \frac{w_4}{w_0} \frac{w_1}{w_3} \frac{w_2}{w_1} \quad (7)$$

where w are the atom jump frequencies, as illustrated in Figure 3; w_0 is the host atom jump frequency in the absence of the impurity, w_1 is the jump frequency for a host atom nearest neighbour to the impurity, w_2 is the impurity atom jump frequency, w_3 is the host atom jump frequency whose jump dissociate the impurity and the vacancy, w_4 is the host atom jump frequency which associates the impurity and the vacancy (reverse of jump w_3). The impurity diffusion correlation factor f_2 can be expressed as a function of the probability of the impurity atom to jump back to its previous position and the jump frequencies [50,51]. Thus, the determination of the diffusion coefficient of the impurity mostly resides in the calculation of the various jump frequencies w.

Figure 3. Illustration of the atom jump frequencies involving the impurity (black circle) and the vacancy (grey square), as defined in the five-frequency model



Based on transition state theory (TST), the jump frequencies can be expressed as:

$w = w^* e^{-\frac{\Delta H_m}{k_B T}}$, where ΔH_m is the change in enthalpy of the system between the states in which the diffusing atom is in its initial equilibrium state and at the saddle point of the diffusion path (transition state). This migration barrier can be calculated by static migration calculations as presented in this chapter (the NEB method for instance). w^* is the effective frequency defined by G.H. Vineyard [52] as a function of the vibrational frequencies in the initial equilibrium state ν_i^0 and in the transition state ν_i^{TS} of a system with N atoms and one vacancy:

$$w^* = \frac{\prod_{i=1}^{3N-3} \nu_i^0}{\prod_{i=1}^{3N-4} \nu_i^{TS}} \quad (8)$$

The vibration frequencies ν_i^0 and ν_i^{TS} can be determined by the explicit calculations of the phonon spectrum of the impurity at the equilibrium state and transition state. This can be achieved using first-principles calculations (usually in the harmonic or quasi-harmonic approximations) or empirical potential calculations.

Examples of diffusion prefactor calculations using first-principles methods associated to the determination of the entropic contributions or to the five-frequency model exist for

SiC [53] and metallic alloys [54], among others. Applications to UO₂ are still hampered by the computational cost of phonon spectrum calculations for defect systems.

Conclusions and future challenges

The modelling of atomic transport properties in nuclear fuel materials has much benefited from the increase in computer resources available and from the recent progress made in the coupling of atomistic methods (DFT, empirical potential, kMC, etc). Atomic transport is a key phenomenon in the multi-scale modelling scheme of nuclear fuels.

One of the challenges for the future consists in tightening even more the links between the modelling techniques at the atomic scale and the mesoscale, in particular for fission gas transport. The study of radiation damage and atomic transport properties in nuclear fuels would also benefit from efficient accelerated dynamics schemes to access fuel evolution during longer timescale and the application of *ab initio* molecular dynamics to actinide compounds.

References

- [1] Belle, J. (1969), “Oxygen and uranium diffusion in uranium dioxide”, *Journal of Nuclear Materials*, 30, 3.
- [2] Marin, J.F., P. Contamin (1969), “Uranium and oxygen self-diffusion in UO₂”, *Journal of Nuclear Materials*, 30, 16.
- [3] Auskern, A.B., J. Belle (1961), “Oxygen ion self-diffusion in uranium dioxide”, *Journal of Nuclear Materials*, 3, 267.
- [4] Hadari, Z., M. Kroup, Y. Wolfson (1971), “Self diffusion measurement of oxygen in UO₂ by the nuclear reaction $^{18}\text{O}(\text{p}, \gamma)^{19}\text{F}$ ”, *Journal of Applied Physics*, 42, 534.
- [5] Dorado, B. et al. (2011), “First-principles and experimental study of oxygen diffusion in uranium dioxide”, *Physical Review B*, 83, 035126.
- [6] Devanathan, R. et al. (2010), “Modeling and simulation of nuclear fuel materials”, *Energy and Environmental Science* 3, 1406.
- [7] Noirot, L. (2011), “MARGARET: A comprehensive code for the description of fission gas behavior”, *Nuclear Engineering and Design*, 241, 2099.
- [8] Sørensen, M.R., A.F. Voter (2000), “Temperature-accelerated dynamics for simulation of infrequent events”, *Journal of Chemical Physics*, 112, 9599.
- [9] Voter, A.F. (1997), “Hyperdynamics: Accelerated molecular dynamics of infrequent events”, *Physical Review Letters*, 78, 3908.
- [10] Iannuzzi, M., A. Laio, M. Parrinello (2003), “Efficient exploration of reactive potential energy surfaces using Car-Parrinello molecular dynamics”, *Physical Review Letters*, 90, 238302.
- [11] van Brutzel, L., A. Chartier, J.P. Crocombette (2008), “Basic mechanisms of Frenkel pair recombinations in UO₂ fluorite structure calculated by molecular dynamics simulations”, *Physical Review B*, 78, 024111.

- [12] Devynck, F., M. Iannuzzi, M. Krack (2012), “Frenkel pair recombinations in UO₂: Importance of explicit description of polarizability in core-shell molecular dynamics simulations”, *Physical Review B*, 85, 184103.
- [13] van Brutzel, L., M. Rarivomanantsoa, D. Ghaleb (2006), “Displacement cascade initiated with the realistic energy of the recoil nucleus in UO₂ matrix by molecular dynamics simulation”, *Journal of Nuclear Materials*, 354, 28.
- [14] Martin, G. et al. (2009), “A molecular dynamics study of radiation induced diffusion in uranium dioxide”, *Journal of Nuclear Materials*, 385, 351.
- [15] Devanathan, R., J. Yu, W. J. Weber (2009), “Energetic recoils in UO₂ simulated using five different potentials”, *Journal of Chemical Physics*, 130, 174502.
- [16] Bishop, C.L., R.W Grimes, D.C. Parfitt (2010), Establishing the isotropy of displacement cascades in UO₂ through molecular dynamics simulation, *Nuclear Instruments and Methods in Physics Research B*, 268, 2915.
- [17] Vincent-Aublant, E., L. van Brutzel, J.M. Delaye (2009), “Self-diffusion near symmetrical tilt grain boundaries in UO₂ matrix: A molecular dynamics simulation study”, *Journal of Nuclear Materials*, 392, 114.
- [18] Nerikar, P.V. et al. (2011), “Segregation of xenon to dislocations and grain boundaries in uranium dioxide”, *Physical Review B*, 84 174105.
- [19] Govers, K. et al. (2010), “On the solution and migration of single Xe atoms in uranium dioxide – An interatomic potentials study”, *Journal of Nuclear Materials*, 405, 252.
- [20] Yakub, E., C. Ronchi, D. Staicu (2010), “Diffusion of helium in non-stoichiometric uranium dioxide”, *Journal of Nuclear Materials*, 400, 189.
- [21] Parfitt, D.C., R.W. Grimes (2009), “Predicting the probability for fission gas resolution into uranium dioxide”, *Journal of Nuclear Materials*, 392, 28.
- [22] Govers, K. et al. (2012), “Molecular dynamics study of Xe bubble resolution in UO₂”, *Journal of Nuclear Materials*, 420, 282.
- [23] Parfitt, D.C., R.W. Grimes (2008), “Predicted mechanisms for radiation enhanced helium resolution in uranium dioxide”, *Journal of Nuclear Materials*, 381, 216.
- [24] Voter, A.F. (2005), *Introduction to the Kinetic Monte Carlo Method, in Radiation Effects in Solids*, K.E. Sickafus, E.A. Kotomin (Eds.), Springer, NATO Publishing Unit, Dordrecht, The Netherlands.
- [25] Andersson, D.A., T. Watanabe, C. Deo, B.P. Uberuaga (2009), “Role of di-interstitial clusters in oxygen transport in UO_{2+x} from first principles”, *Physical Review B*, 80, 060101R.
- [26] Henkelman, G., H. Jónsson (2000), “Improved tangent estimate in the nudged elastic band method for finding minimum energy paths and saddle points”, *Journal of Chemical Physics*, 113, 9978.
- [27] Ren, W., E. Vanden-Eijnden (2002), “String method for the study of rare events”, *Physical Review B*, 66, 052301.

- [28] Ren, W., E. Vanden-Eijnden (2007), “Simplified string method for computing the minimum energy path in barrier-crossing events”, *Journal of Chemical Physics*, 126, 164103.
- [29] Henkelman, G., H. Jónsson (1999), “A dimer method for finding saddle points on high dimensional potential surfaces using only first derivatives”, *Journal of Chemical Physics*, 111, 7010.
- [30] Barkema, G., N. Mousseau (1996), “Event-based relaxation of continuous disordered systems”, *Physical Review Letters*, 77, 4358.
- [31] Mousseau, N., G. Barkema (1998), “Traveling through potential energy landscapes of disordered materials: The activation-relaxation technique”, *Physical Review E*, 57, 2419.
- [32] Mousseau, N., G. Barkema (2000), “Activated mechanisms in amorphous silicon: An activation-relaxation-technique study”, *Physical Review B*, 61, 1898.
- [33] Malek, R., N. Mousseau (2000), “Dynamics of Lennard-Jones clusters: A characterization of the activation-relaxation technique”, *Physical Review E*, 62, 7723.
- [34] Henkelman, G., B.P. Uberuaga, H. Jónsson (2000), “A climbing image nudged elastic band method for finding saddle points and minimum energy paths”, *Journal of Chemical Physics*, 113, 9901.
- [35] Sheppard, D., R. Terrell, G. Henkelman (2008), “Optimization methods for finding minimum energy paths”, *Journal of Chemical Physics*, 128, 134106.
- [36] Marinica, M.-C., F. Willaime, N. Mousseau (2011), “Energy landscape of small clusters of self-interstitial dumbbells in iron”, *Physical Review B*, 83, 094119.
- [37] Gao, F. et al. (2003), “Finding possible transition states of defects in silicon-carbide and alpha-iron using the dimer method”, *Nuclear Instruments and Methods in Physics Research B*, 202, 1.
- [38] Dorado, B. et al. (2011), “First-principles and experimental study of oxygen diffusion in uranium dioxide”, *Physical Review B*, 83, 035126.
- [39] Andersson, D.A. et al. (2011), “U and Xe transport in $\text{UO}_{2\pm x}$: Density functional theory calculations”, *Physical Review B*, 84, 054105.
- [40] Dorado, B. et al. (2012), “First-principles calculations of uranium diffusion in uranium dioxide”, *Physical Review B*, 86, 035110.
- [41] Yun, Y. et al. (2009), “First-principles theory for helium and xenon diffusion in uranium dioxide”, *Journal of Nuclear Materials*, 385, 364.
- [42] Dorado, B. et al. (2010), “An atomistic approach to self-diffusion in uranium dioxide”, *Journal of Nuclear Materials*, 400, 103.
- [43] Jackson, R.A. et al. (1986), “The calculation of defect parameters in UO_2 ”, *Philosophical Magazine A*, 53, 27.
- [44] Ball, R.G.J., R.W. Grimes (1990), “Diffusion of Xe in UO_2 ”, *Journal of the Chemical Society, Faraday Transactions*, 86, 1257.

- [45] Ball, R.G.J., R.W. Grimes (1992), “A comparison of the behaviour of fission gases in $\text{UO}_{2\pm x}$ and $\alpha\text{-U}_3\text{O}_{8-z}$ ”, *Journal of Nuclear Materials*, 188, 216.
- [46] Govers, K. et al. (2007), “Comparison of interatomic potentials for UO_2 . Part I: Static calculations”, *Journal of Nuclear Materials*, 366, 161.
- [47] Parfitt, D.C. et al. (2010), “Strain field and line energies of dislocations in uranium dioxide”, *Journal of Physics: Condensed Matter*, 22, 175004.
- [48] Govers, K. et al. (2009), “Molecular dynamics simulation of helium and oxygen diffusion in $\text{UO}_{2\pm x}$ ”, *Journal of Nuclear Materials*, 395, 131.
- [49] Le Claire, A.D., A.B. Lidiard (1956), “Correlation effects in diffusion in crystals”, *Philosophical Magazine*, 1, 518.
- [50] Manning, J.R. (1964), “Correlation factors for impurity diffusion. bcc, diamond, and FCC structures”, *Physical Review*, 136, A1758.
- [51] Mehrer, H. (1972), “Correlation factor for impurity diffusion by a divacancy mechanism in an FCC lattice”, *Journal of Physics F: Metal Physics*, 2, L11.
- [52] Vineyard, G.H. (1957), “Frequency factors and isotope effects in solid state rate processes”, *Journal of Physics and Chemistry of Solids*, 3, 121.
- [53] Bedoya-Martinez, O.N., G. Roma (2010), “Activation entropies for diffusion in cubic silicon carbide from first principles”, *Physical Review B*, 82, 134115.
- [54] Mantina, M., Y. Wang, L.Q. Chen, Z.K. Liu, C. Wolverton (2009), “First-principles impurity diffusion coefficients”, *Acta Materialia*, 57, 4102.

Chapter 10.

Free energy and heat capacity

M. Kurata¹, R. Devanathan²

¹Central Research Institute of Electric Power Industry/Japan Atomic Energy Agency, Japan,

²Pacific Northwest National Laboratory, US

Abstract

Free energy and heat capacity of actinide elements and compounds are important properties for the evaluation of the safety and reliable performance of nuclear fuel. They are essential inputs for models that describe complex phenomena that govern the behaviour of actinide compounds during nuclear fuels fabrication and irradiation. This chapter introduces various experimental methods to measure free energy and heat capacity to serve as inputs for models and to validate computer simulations. This is followed by a discussion of computer simulation of these properties, and recent simulations of thermophysical properties of nuclear fuel are briefly reviewed.

Introduction

During the operation of nuclear fuel under normal or accident condition, such as loss of coolant, several interacting mechanisms determine the changes in the chemical and physical condition of the fuel. There are calculation codes for describing the fuel behaviour that contain individual models for describing each chemical interaction. Free energy and heat capacity are essential parameters for these models. The former can indicate the chemical stability for various species and provide the driving force to change the chemical condition. The latter is directly related to heat transfer or temperature variation in the fuel. Reliable determination of free energy and heat capacity are important for improving the accuracy of numerical thermodynamic modelling. In the case of calculation of phase diagrams, the numerical solution model is introduced to evaluate the free energy of mixing for solution phases and the free energy of formation for compounds. These values can be calculated only from phase boundary data, such as liquidus/solidus. Furthermore, *ab initio* and classical molecular dynamics (MD) can be used to evaluate heat capacity and free energy. The accuracy is enhanced if reliable free

energy data can be obtained using experimental methods, such as vapour pressure and electro-motive force. In the following sections, major experimental methods are introduced with a discussion of experimental error in each method, which is important from the viewpoint of a thermodynamic database. Computational methods are then discussed with a review of recent MD simulations of free energy and heat capacity.

Heat capacity

Adiabatic calorimetry is generally applied for measuring low-temperature heat capacity and, on the other hand, drop calorimetry, differential scanning calorimetry or laser flash method for high temperatures. Work up to 1975 has been reviewed by F.L. Oetting et al. [1] and further studies were reviewed by J.W. Ward et al. [2] and by R.J.M. Konings et al. [3]. Heat capacity of actinide elements through Es at 298 K is summarised in Table 1.

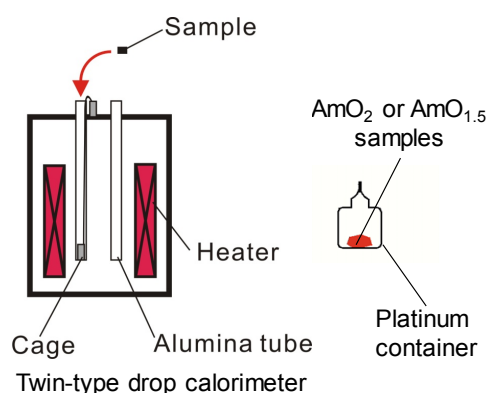
Table 1. Heat capacity of actinide elements (at 298 K, J/K/mol)

	Ac	Th	Pa	U	Np	Pu	Am	Cm	Bk	Cf	Es
solid	26	26.23	28.2	27.66	29.62	31.49	25.5	28.8	26.1	28.0	26.7
gas	20.82	20.79	22.91	23.69	20.82	20.85	20.79	28.11	20.79	20.79	20.79

There are several methods for measuring the high-temperature heat capacity. Figure 1 indicates a schematic image of the drop calorimetry method. Two systems are considered. The first system is constructed as follows:

- a sample at a prescribed high temperature is dropped into a low temperature heat sink;
- a decrease in enthalpy is measured via the small variation in heat flow from the heat sink to the sample.

Figure 1. Schematic image of drop calorimetry using a Pt-container to avoid interaction of sample and atmosphere or crucible



	AmO ₂	AmO _{1.5}
Weight (mg)	72.80	61.77
Pt weight (mg)	489.77	357.64

The second system is: (i) a sample at room temperature is dropped into a high-temperature heat sink maintained at a prescribed temperatures, (ii) an increase in enthalpy is measured. Figure 1 indicates the latter system. Since this method gives a relationship between heat capacity and temperature, the specific heat capacity can be calculated. The enthalpy for phase transition can also be evaluated. However, the temperature measurement is discontinuous and this method needs a long time, and generates only a few data points per day. Major concerns of the drop calorimetry method are (i) heat transfer between the sample and atmosphere during the drop process and (ii) chemical interaction between sample and atmosphere or crucible. Sample damage can be avoided by encapsulating the sample in a small container made by platinum. However, it decreases the accuracy of measurement because one has to compensate for the variation in the container material.

Figure 2. Variation in heat flow just after drop-in Am_2O_3 sample into a heat

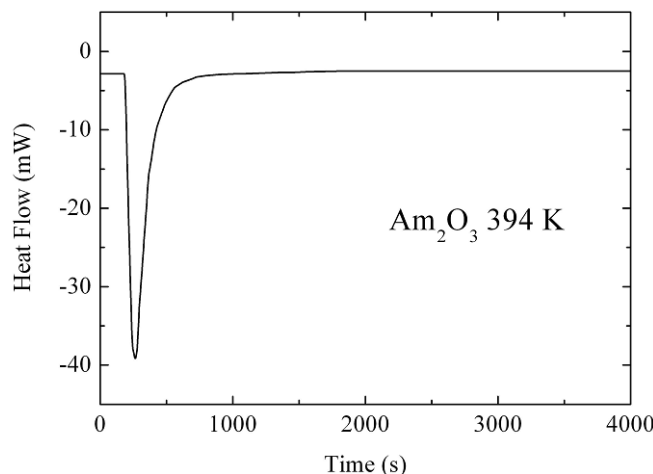


Figure 2 shows an example of the variation in the heat flow into the sample just after the drop-in. The heat flow is evaluated from accurate measurement of the difference in temperature between the sample and the reference. As for the reference material, chemically stable materials, such as alumina, are generally used. The heat flow decreases abruptly just after the drop-in of the sample into the heat sink. Then, it recovers by heat transfer from the heat sink surrounding the sample. The heat capacity is calculated from the sample weight and the area originated from the variation in the heat flow.

Regarding Differential Scanning Calorimetry (DSC), there are two methods, namely power-compensation and heat-flux systems. Since relatively high temperature is necessary in the case of nuclear materials, the heat-flux system method is generally used. Figure 3 shows a schematic of the working principle of Differential Thermal Analysis (DTA) and DSCs [5]. The system of the heat-flux DSC is mostly similar to that of DTA, except for the preparation of the heat sink surrounding the sample and the reference. The temperature of the entire system is gradually changed with a fixed rate and the difference in temperature between sample and reference is continuously measured using thermocouples. If the heat flow is forced to occur only between the sample or the reference and the heat sink, the difference in the heat-flux, $\delta q/\delta t$, can be evaluated from $\Delta T/R$ in case of the heat-flux DSC, in which R indicates thermal resistance between the

reference and the heat sink. On the other hand, $\delta q/\delta t$ can be directly measured in the case of the power-compensation DSC.

Figure 3. Schematic diagram of working principle of DTA and DSCs [5]

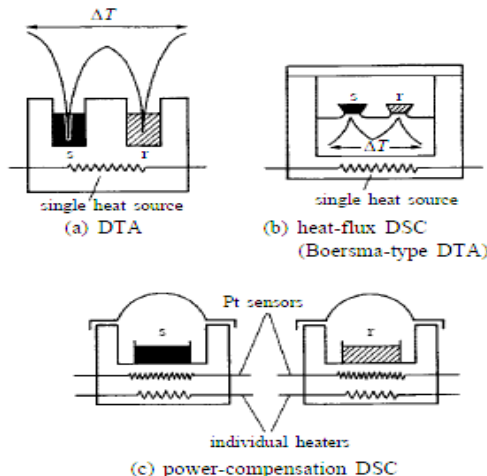
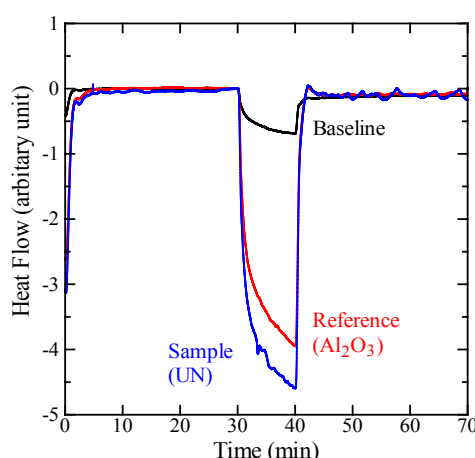


Figure 4 shows an example of DSC-measurement, in which a relationship is drawn between the heat flow, $\Delta T/R$, and time [6]. When increasing temperature by a fixed temperature interval, the heat flows to the sample (UN: uranium nitride) and the reference (Al_2O_3) are measured respectively. The difference in the variation is drawn in the figure with respect to the baseline, which was drawn from the measurement of an empty tantalum crucible. Provided that the heat capacity of the reference material is already known, the heat capacity of the sample can be calculated from these variations and the sample weights. It must be ensured that the heat capacity evaluated in this manner is an averaged value in each temperature range. The major experimental concern is how to prepare the closed system. Usually, an empirical constant, which depends on the apparatus, is introduced from the measurement of the reference material. Nevertheless, in the case of high temperature, usually greater than $\sim 1\ 000\text{ K}$, the accuracy of measurement decreases significantly due to heat loss.

Figure 4. Variation in heat flow of sample and reference when increasing temperature form 323 K to 426 K [6]



There is another method for measuring the heat capacity, which uses a laser flash [7]. Figure 5 shows the principle. A small amount of heat absorber material, such as glassy carbon, is pasted on the front surface of the reference material with known heat capacity. The temperature increase is measured based on the response on the rear surface of the sample after laser beam irradiation. The heat induced by the laser beam, Q , is calculated from the heat capacity of the reference material and temperature increase (ΔT). Then, the sample is measured in a similar manner. The heat capacity is calculated from $Q/\Delta T$. In the high-temperature condition, the correction of heat loss is necessary for reference and sample. In Figure 6, black solid circles indicate the data obtained by the laser flash method. Open circles indicate the data measured by DSC. Both values are mostly overlapped.

Figure 5. Principle of laser flash method for measuring heat capacity [7]

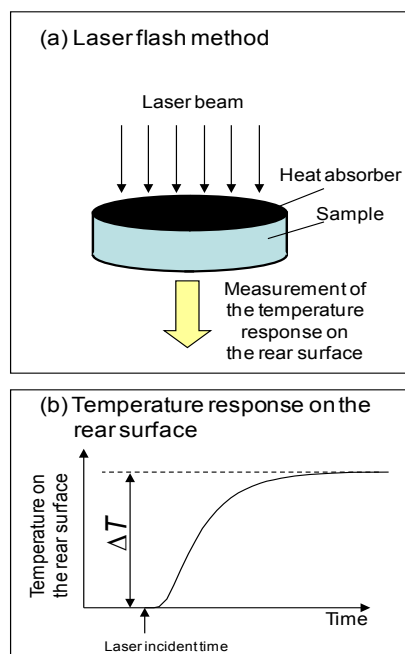
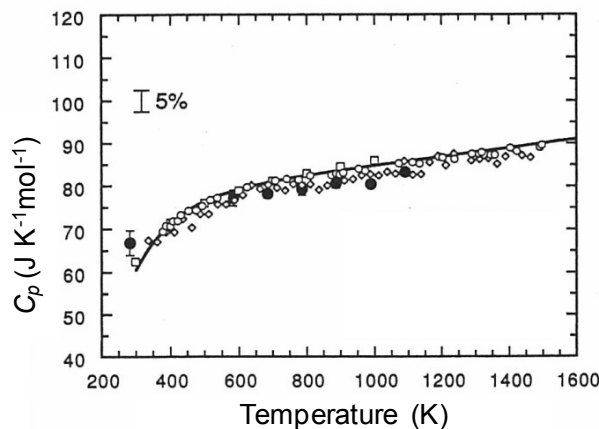


Figure 6. Heat capacity of UO_2 measured by laser flash method [7]



Free energy

Classical methods for measuring free energy include electro-motive force measurement, Knudsen cell method, and chemical equilibrium method. Figure 7 illustrates experimental apparatus for measuring the oxygen potential using a zirconia solid electrolyte [8]. By coupling a zirconia plate and an oxide sample, the variation in the electro-motive force can be measured as a function of temperature. Oxygen potential or the partial free energy of formation of the oxide is evaluated using the following equation:

$$\Delta G(O_2) = RT \ln P(O_2) (\text{sample}) - nFE + RT \ln P(O_2) (\text{air})$$

Here $\Delta G(O_2)$ is the oxygen potential, R gas constant, T temperature (K), $P(O_2)$ oxygen partial pressure, F Faraday constant, and E electro-motive force (V).

Figure 7. Oxygen potential measurement system by the EMF-method [8]

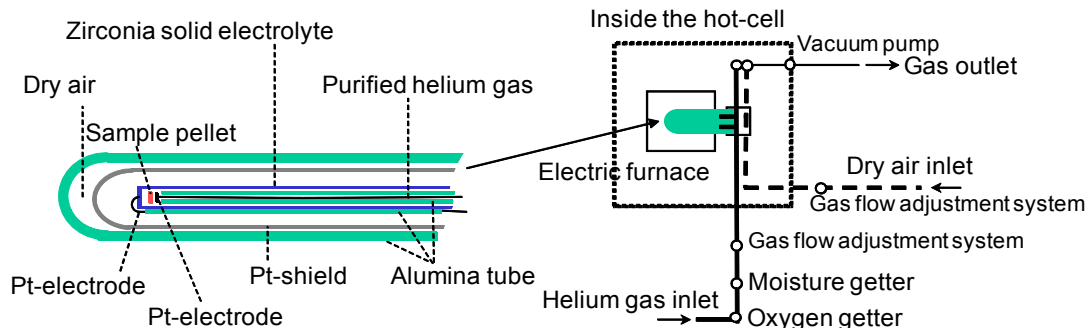


Figure 8 shows an example of experimental data for the measurement of the oxygen potential using the EMF-method [9]. Variation in the oxygen potential is given as a function of the O/M ratio of the oxide. The gradual change in the value indicates that the sample consists of a single phase. When the oxygen potential is maintained at any fixed value, it is supposed that two phases exist at that condition. The most important concern of this method is how to determine the accurate O/M ratio of the sample. The degree of the error on the O/M is far larger than that of the oxygen potential value. When comparing the data given in the literature, the accuracy on the O/M ratio is extremely important.

Figure 8. Oxygen potential of Am-Np mixed oxide as a function of O/M at 1 333 K

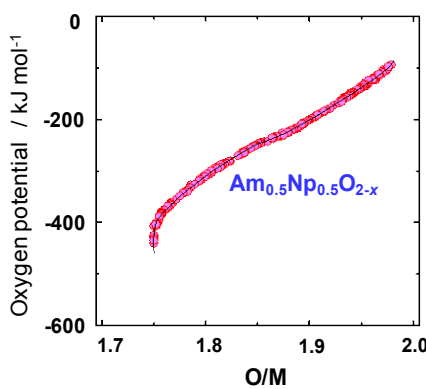


Figure 9 illustrates an example of the system using a molten salt bath as an electrolyte, in which various electrodes are inserted to measure potentials. In the present example, a small amount of uranium metal was deposited by electrolysis on the surface of zirconium plate to form a uranium-zirconium compound. Then, the electro-motive force was determined from the difference in the electrode potential between the uranium-zirconium compound and the uranium metal. This value gives the free energy of formation of the compound.

Figure 9. EMF-measurement system using a molten salt

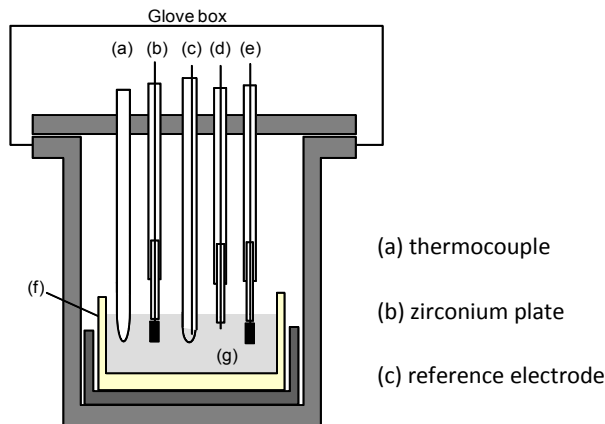


Table 2 summarises the experimental result [10], in which various thermodynamic properties of the uranium-zirconium compound are given, such as the electro-motive force, partial free energy of formation, activity of uranium, partial entropy and partial enthalpy. As given in the table, the electro-motive force values in the present example are very small, of the order of mV. This may cause a relatively larger experimental error for the free energy in comparison to cases with a larger value.

Table 2. Thermodynamic properties of U-Zr compound, δ -phase

T(K)	E_d (mV vs. U^{3+}/U)	(kJ mol ⁻¹ U)	a_U	(J K ⁻¹ mol ⁻¹ U)	(kJ mol ⁻¹ U)
700.1	5.71	-1.65	0.753		
743.6	4.51	-1.31	0.810		
758.1	3.71	-1.07	0.843	-8.56	-7.62
775.0	3.46	-1.00	0.856		
800.5	2.23	-0.645	0.908		
839.0	1.82	-0.527	0.927		

Figure 10 shows the schematic image of the Knudsen cell. In a fixed temperature condition, a small amount of volatilised species is discharged from the sample and introduced into a mass-spectrometer thorough an orifice. Variation in mass of the volatilized species can be detected.

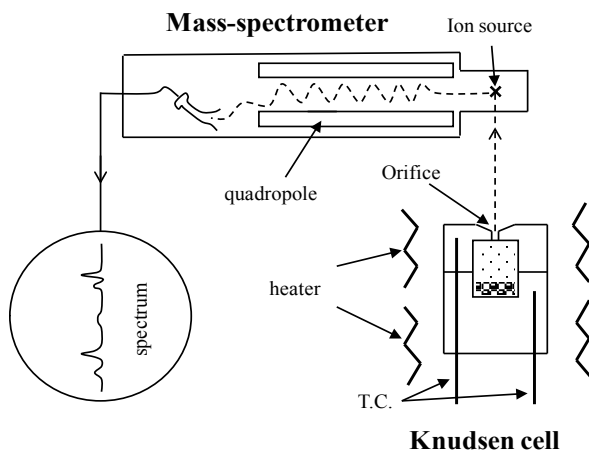
Figure 10. Schematic image of Knudsen cell method

Figure 11 indicates an example of the result for the vapour pressure measurement of americium-plutonium binary alloy [11]. The vapour pressure of americium in the alloy is approximately one order smaller than that of pure americium metal. Considering the concentration of americium in the sample, americium and plutonium are expected to be soluble as a regular solution. The slope of the present data is different from that of pure americium, suggesting the activity of americium in the binary alloy changes gradually with increasing temperature. Major concerns of the vapour pressure measurement are the effect of atmosphere, especially for the measurement of the sample which is easily oxidised. Since several vapour species are generally discharged from the sample, the determination of the dominant species is important to evaluate the free energy. The oxidation condition of the sample might be changed with changing the atmosphere and temperature. It is important to avoid interaction between the sample and cell to increase the accuracy. Nevertheless, the vapour pressure measurement is a quite useful way to evaluate the free energy in the high-temperature region.

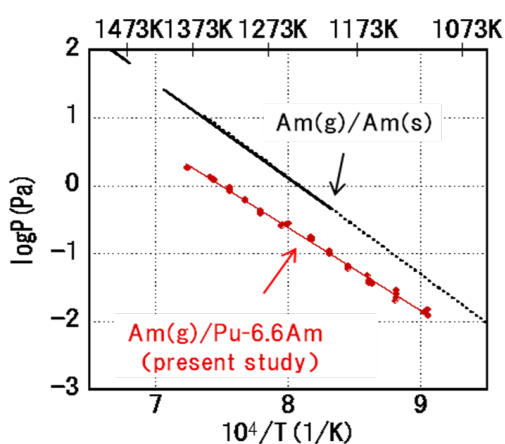
Figure 11. Vapour pressure of Am (g) on a Pu-6.6% Am sample [11]

Figure 12 illustrates the chemical equilibrium method using a molten salt/liquid metal system. After adding two kinds of solute material, *A* and *B*, into the system, the differences in the concentration of *A* and *B* in the molten salt and the liquid metal phases

are measured, respectively, by chemical analysis. Electro-motive force of M^iCl_n in molten salt for the cell, $M^i | M^iCl_n, LiCl-KCl || AgCl, LiCl-KCl | Ag$, is given by:

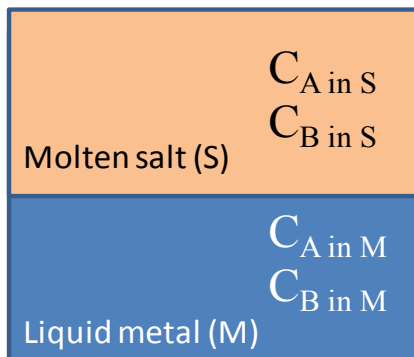
$$E = {}^0E_{Mi} + RT/nF \ln(a_{MiCl_n}/a_{Mi}) - E_{AgCl},$$

in which 0E : standard redox potential with respect to chlorine electrode, R: gas constant, T: temperature (K), F: Faraday constant, n: valence, a_{MiCl_n} : activity in molten salt, a_{Mi} : activity on metal electrode, E_{AgCl} : potential of $Ag/AgCl$ electrode with respect to chlorine electrode ($i = A$ or B). On the other hand, electro-motive force of M in liquid metal for the $M^i | M^iCl_n, LiCl-KCl | M$ in liquid metal, is given by:

$$E = RT/nF \ln(a_{M \text{ in liquid metal}}),$$

in which $a_{M \text{ in liquid metal}}$ activity of M^i in liquid metal. Provided that three of the four thermodynamic properties are known, such as electro-motive force of A and B in the molten salt or in the liquid metal, the rest one can be calculated from the difference in the distribution of A and B in the system. Sometimes it is difficult to confirm the attainment of equilibrium, which is a major concern of this method.

Figure 12. Variation in concentration in solute A and B in a molten salt/liquid metal system



Modelling of free energy and heat capacity

Free energy and heat capacity can be calculated from atomistic simulation [12-15] or using simple physical models of phonon and electron spectra [16]. The results of the model can be validated using experimental data obtained as discussed in the preceding sections. The validated models, in turn, can be used to evaluate physical properties in cases where experimental data are not available and to design new experiments. The Helmholtz free energy $F(V,T)$ for a compound is given by:

$$F(V,T) = E_0(V) + F_{\text{vib}}(V,T) + F_{\text{el}}(V,T), \quad (1)$$

where $E_0(V)$ is the internal energy of the compound at 0 K, $F_{\text{vib}}(V,T)$ and $F_{\text{el}}(V,T)$ are the vibration and thermal electron contribution to the Helmholtz free energy, respectively. Based on the quasi-harmonic approximation, $F_{\text{vib}}(V,T)$ can be calculated from the density of state (DOS) of phonons.

$$F_{\text{vib}}(V,T) = k_B T \int_0^\infty g_{\text{vib}}(\omega, V) \ln \left(2 \sinh \frac{\hbar \omega}{2k_B T} \right) d\omega, \quad (2)$$

where $g_{\text{vib}}(\omega, V)$ is the phonon DOS at phonon frequency ω and volume V . The thermal electron contribution is given by $F_{\text{el}} = E_{\text{el}} - TS_{\text{el}}$, where:

$$E_{\text{el}} = \int n(E)fEdE - \int^{E_F} n(E)fEdE \quad (3)$$

E and f represent the energy Eigen-value and the Fermi distribution function, respectively.

$$f = \frac{1}{\exp\left(\frac{E-\mu}{k_B T}\right)+1}, \quad (4)$$

where μ is the chemical potential. The entropy term is expressed by:

$$S_{\text{el}} = -k_B \int n(E) [f \ln f + (1-f) \ln (1-f)] dE \quad (5)$$

In MD simulation [17], the free energy difference between two states of the simulation cell cannot be calculated merely from the coordinates of the atoms in the two systems. Instead, one typically uses thermodynamic integration [18]. In this method, the free energy difference between two states is determined by first identifying a thermodynamic path between the states. A parameter (λ) is defined to couple the two states such that one goes from the first state to the second state as λ changes from 0 to 1. The enthalpy changes along the path (λ going from 0 to 1) are calculated and integrated to compute the free energy change. A recent review has discussed free energy calculations in detail [19].

Regarding heat capacity, $C_v(T)$ is calculated from the phonon DOS.

$$C_v(T) = k_B \int_0^{\infty} g_{\text{vib}}(\omega) \left(\frac{\hbar\omega}{k_B T} \right)^2 \frac{\exp\left(\frac{\hbar\omega}{k_B T}\right)}{\left[\exp\left(\frac{\hbar\omega}{k_B T}\right)-1\right]^2} d\omega \quad (6)$$

and $C_p(T)$ is given by:

$$C_p(T) = C_v(T) + \alpha(T)^2 B(T) V(T) T \quad (7)$$

where $\alpha(T)$ and $B(T)$ are linear thermal expansion coefficient and bulk modulus, respectively.

In MD simulations [17], C_v is calculated from the variation of the internal energy with temperature at constant volume (constant NVT ensemble) and C_p is calculated from the variation of internal energy with temperature at constant pressure (constant NPT ensemble) [12]:

$$C_v(T) = \left(\frac{\partial E}{\partial T} \right)_V \quad (8)$$

$$C_p(T) = \left(\frac{\partial E}{\partial T} \right)_P \quad (9)$$

Classical MD simulations follow the time evolution of a system of ions, whose interactions are represented by a combination of long-range Coulombic terms and short-

range terms to account for dispersion, repulsion, and covalency. Several interatomic potentials have been developed to model the ionic interactions in actinide compounds. These potentials can be broadly classified as rigid-ion models that treat ions as massive points with formal or partial charges and shell models that represent ions as massive point charges connected to a massless charged shell by a spring. A recent study [14] has systematically compared the temperature dependence of C_v and C_p from MD simulation using several rigid-ion and shell model potentials with experimental observations. The C_v value was found to be almost constant over the temperature range from 100 K to 3 000 K and equal to the classical value of Dulong and Petit for all potentials studied. This incorrect behaviour at low temperatures is due to the fact that classical MD does not include quantum mechanical effects. At temperatures above 1 500 K, rigid-ion potentials with non-formal charges show an increase in specific heat with increasing temperature in a manner consistent with experimental findings due to the creation of temporary anion Frenkel pairs [14]. In general, some rigid-ion potentials, such as those developed by Morelon [20] and Yakub [21], provide a good representation of thermal expansion, C_v , and C_p between 300 K and about 2 000 K. These potentials are also known to represent thermal conductivity of UO_2 reasonably well [22]. There is scope for improvement of these potentials to expand their range of applicability by rigorous fitting to a large database of results from experiment and *ab initio* calculations. A good understanding of experimental error is needed to achieve reliable fitting.

Conclusion and future challenges

Atomistic simulations and analytical models can provide valuable information about thermophysical properties of actinides and actinide compounds including temperature dependence of heat capacity, especially in cases where experimental data is lacking. The accuracy and reliability of these models can be improved by generating input data using a host of experimental methods discussed in this chapter. Existing rigid-ion potentials provide a satisfactory representation of thermophysical properties over a narrow temperature window from 300 K to 1 500 K. Further improvement in potentials will have to balance the conflicting requirements of matching known equilibrium properties, on the one hand, and representing the behaviour of charged defects and property changes under far-from-equilibrium conditions on the other hand.

Acknowledgements

R. Devanathan was supported by the US Department of Energy (DOE), Nuclear Energy Advanced Modeling and Simulation (NEAMS) Program at Pacific Northwest National Laboratory – a multiprogram laboratory operated for DOE by Battelle.

References

- [1] Oetting, F.L. et al. (1976), *The Chemical Thermodynamics of Actinide Elements and Compounds, Part 1, The Actinide Elements*, IAEA, Vienna, Austria.
- [2] Ward, J.W. et al. (1986), “Thermodynamical properties of the actinide elements and selected actinide-noble metal intermetallics”, *Handbook on the Physics and Chemistry of the Actinides*, North-Holland.

- [3] Konings, R.J.M., L.R. Morss, J. Fuger (2006), “Thermodynamic properties of actinides and actinides compounds”, *The Chemistry of the Actinide and Transactinide Elements, Part 4*, Springer.
- [4] Nishi, T., A. Itoh, K. Ichise, Y. Arai (2011), *Journal of Nuclear Materials*, 414, 109-113.
- [5] Todoki, M. *Netsu Sokutei* 31 (5) 241-248.
- [6] Nakajima, K., Y. Arai (2002), *Journal of Nuclear Science and Technology*, Suppl. 3, 620-623.
- [7] Amaya, M., H. Hirai, unpublished work, Private communication.
- [8] Otobe, H., M. Akabori, K. Minato (2008), *Journal of the American Ceramic Society*, 91, 1981-1985.
- [9] Otobe, H., M. Akabori, Y. Arai, K. Minato (2009), *Journal of the American Ceramic Society*, 92, 174-178.
- [10] Murakami, T., T. Kato, M. Kurata, H. Yamana (2009), *Journal of Nuclear Materials*, 394, 131-135.
- [11] Nakajima, K., M. Kurata, non-published data.
- [12] Kurosaki, K., K. Yamada, M. Uno, S. Yamanaka, K. Yamamoto, T. Namekawa (2001), *Journal of Nuclear Materials*, 294, 160-167.
- [13] Arima, T., S. Yamasaki, Y. Inagaki, K. Idemitsu (2005), *Journal of Alloys and Compounds*, 400, 43-50.
- [14] Govers, K., S. Lemehov, M. Hou, M. Verwerft (2008), *Journal of Nuclear Materials*, 376, 66-77.
- [15] Shibata, H., T. Tsuru, T. Nishi, M. Hirata, Y. Kaji (2012), *Journal of Nuclear Science and Technology*, 49, 328-333.
- [16] Sobolev, V. (2005), *Journal of Nuclear Materials*, 344, 198-205.
- [17] Haile, J.M. (1992), “Molecular Dynamics Simulation”, *Elementary Methods*, Wiley.
- [18] Sprik, M., G. Ciccotti (1998), *Journal of Chemical Physics*, 109, 7737.
- [19] Crist, C.D., A.E. Mark, W.F. van Gunsteren (2010), *Journal of Computational Chemistry*, 31, 1569-1582.
- [20] Morelon, N.D., D. Ghaleb, J. M. Delaye, L. Van Brutzel (2003), *Philosophical Magazine*, 83, 1533-1555.
- [21] Yakub, E., C. Ronchi, D. Staicu (2007), *Journal of Physical Chemistry*, 127, 094508.
- [22] Chernatynskiy, A. et al. (2012), *Journal of Materials Science*, 47, 7693-7702.

Chapter 11.

Elastic and viscoplastic properties

R.A. Lebensohn

Los Alamos National Laboratory, US

Abstract

In this chapter, we review crystal elasticity and plasticity-based self-consistent theories and apply them to the determination of the effective response of polycrystalline aggregates. These mean-field formulations, which enable the prediction of the mechanical behaviour of polycrystalline aggregates based on the heterogeneous and/or directional properties of their constituent single crystal grains and phases, are ideal tools to establish relationships between microstructure and properties of these materials, ubiquitous among fuels and structural materials for nuclear systems.

Introduction

Mean-field theories linking microstructure and properties of heterogeneous materials can be used for the development of efficient algorithms for the prediction of the elastic and plastic response of polycrystals. In this chapter, we will review crystal elasticity and crystal plasticity-based self-consistent theories, and show applications of these formulations to the prediction of microstructure-property relations of polycrystalline aggregates.

The self-consistent (SC) approximation, one of the most commonly used homogenisation methods to estimate the mechanical response behaviour of polycrystals, was originally proposed by A.V. Hershey [3] for linear elastic materials. For nonlinear aggregates (as those formed by grains deforming in the viscoplastic regime), the several SC approximations that were subsequently proposed differ in the procedure used to linearise the local non-linear mechanical behaviour, but eventually all of them end up making use of the original linear SC theory. In general, SC estimates of the effective behaviour of heterogeneous materials are between the iso-strain upper-bound (i.e., Voigt and Taylor approximations in the elastic and viscoplastic regimes, respectively) and the iso-stress lower-bound (Reuss and Sachs approximations in the elastic and viscoplastic regimes, respectively).

This chapter is organised as follows: in Sections 2 and 3, we present the elastic self-consistent (ELSC) and viscoplastic self-consistent (VPSC) formulations, respectively. In Section 4, we show examples of the use of ELSC for the prediction of: (i) effective elastic behaviour of isotropic composites with increasing volume fractions of hard and soft phases, respectively and (ii) effective elastic anisotropy developing in an FCC polycrystal as crystallographic texture evolves. Finally, we show a classical benchmark for the different non-linear SC approaches in terms of the predicted effective behaviour of a random FCC polycrystal as a function of its rate-sensitivity.

Local constitutive behaviour and homogenisation

Let us consider a macroscopic strain \mathbf{E} applied to an elastically heterogeneous material. The elastic behaviour at each material point \mathbf{x} is given by:

$$\boldsymbol{\sigma}(\mathbf{x}) = \mathbf{C}^{(r)} : \boldsymbol{\epsilon}(\mathbf{x}) \quad (1)$$

where $\mathbf{C}^{(r)}$ is the elastic stiffness of mechanical phase (r) . Let us homogenise the behaviour of a linear heterogeneous medium whose local behaviour is described by Equation 1 by the following macroscopic linear relation:

$$\boldsymbol{\Sigma} = \overline{\mathbf{C}} : \mathbf{E} \quad (2)$$

where $\boldsymbol{\Sigma}$ and \mathbf{E} are the effective stress and tensors, respectively, and $\overline{\mathbf{C}}$ is the stiffness of an a priori unknown Homogeneous Equivalent Medium (HEM). The problem underlying the SC method is that of an inhomogeneous domain (r) of modulus $\mathbf{C}^{(r)}$ embedded in an infinite medium of modulus $\overline{\mathbf{C}}$. Invoking the concept of the equivalent inclusion [13], the local constitutive behaviour in domain (r) can be rewritten as:

$$\boldsymbol{\sigma}(\mathbf{x}) = \overline{\mathbf{C}} : (\boldsymbol{\epsilon}(\mathbf{x}) + \boldsymbol{\epsilon}^*(\mathbf{x})) \quad (3)$$

where $\boldsymbol{\epsilon}^*(\mathbf{x})$ is an eigenstrain field, which follows from replacing the inhomogeneity by an equivalent inclusion and the symbol “~” denotes local deviations from macroscopic values of the corresponding magnitudes. Using the equilibrium condition $\sigma_{ij,j}(\mathbf{x}) = 0$ and the relation $\tilde{\epsilon}_{ij}(\mathbf{x}) = \frac{1}{2}(\tilde{u}_{i,j}(\mathbf{x}) + \tilde{u}_{j,i}(\mathbf{x}))$ between the strain and displacement gradient fields we obtain:

$$\overline{C}_{ijkl} \tilde{u}_{k,lj}(\mathbf{x}) + \varphi_{ij,j}(\mathbf{x}) = 0 \quad (4)$$

where:

$$\varphi(\mathbf{x}) = -\overline{\mathbf{C}} : \boldsymbol{\epsilon}^*(\mathbf{x}) \quad (5)$$

is a polarisation field. Differential Equation 5 can be solved using the Green function method. If $\mathbf{G}_{km}(\mathbf{x})$ is the Green function associated with $\tilde{u}_k(\mathbf{x})$, which solves the auxiliary problem of a unitary volumetric force, with a single non-vanishing m-component:

$$\overline{C}_{ijkl} \mathbf{G}_{km,lj}(\mathbf{x} - \mathbf{x}') + \delta_{im} \delta(\mathbf{x} - \mathbf{x}') = 0 \quad (6)$$

Once the solution of Equation 7 is obtained, the displacement:

$$\begin{aligned}\tilde{u}_k(\mathbf{x}) &= \int_{\mathbb{R}^3} G_{ki}(\mathbf{x} - \mathbf{x}') f_i(\mathbf{x}') d\mathbf{x}' \\ \tilde{u}_{k,l}(\mathbf{x}) &= \int_{\mathbb{R}^3} G_{ki,jl}(\mathbf{x} - \mathbf{x}') \varphi_{ij}(\mathbf{x}') d\mathbf{x}'\end{aligned}$$

An inclusion of volume Ω in an infinite medium takes the form:

$$\tilde{u}_{k,l}^{(r)} = \left(-\frac{1}{\Omega} \int_{\Omega} \int G_{ki,jl}(\mathbf{x} - \mathbf{x}') d\mathbf{x} d\mathbf{x}' \right) \bar{C}_{ijmn} \varepsilon_{mn}^{*(r)} \quad (7)$$

where $\tilde{u}_{k,l}^{(r)}$ and $\varepsilon_{mn}^{*(r)}$ are averages inside the inclusion and the expression of tensor T_{klj} solution of the above integral expression, can be found in [1].

The Eshelby tensor, a function of \bar{C} and the shape of the ellipsoidal inclusion, is given by:

$$S_{ijkl} = \frac{1}{4} (T_{ijmn} + T_{jimn} + T_{ijnm} + T_{jinm}) \bar{C}_{mnkl} \quad (8)$$

Thus, taking symmetric part in Equation 9 gives:

$$\tilde{\boldsymbol{\epsilon}}^{(r)} = \mathbf{S} : \boldsymbol{\varepsilon}^{*(r)} \quad (9)$$

Interaction, localisation and self-consistent equations

Taking volume averages over the domain of the inclusion on both sides of Equation 4 and replacing the eigenstrain given by Equation 10, we obtain the interaction equation:

$$\tilde{\boldsymbol{\sigma}}^{(r)} = -\bar{C} : \mathbf{S}^{-1} : (\mathbf{I} - \mathbf{S}) \tilde{\boldsymbol{\epsilon}}^{(r)} = -\tilde{C} : \tilde{\boldsymbol{\epsilon}}^{(r)} \quad (10)$$

Replacing the constitutive relations of the inclusion and the effective medium in the latter and after some manipulation, one can write the following localisation equation:

$$\boldsymbol{\epsilon}^{(r)} = (\mathbf{C}^{(r)} + \tilde{C})^{-1} : (\bar{C} + \tilde{C}) : \mathbf{E} = \mathbf{A}^{(r)} : \mathbf{E} \quad (11)$$

The previous solution for an equivalent inclusion embedded in an effective medium can be used to construct a homogenisation model, consisting in regarding each mechanical phase (r) as heterogeneity embedded in an effective medium that represents the polycrystal. The properties of such medium are not known *a priori* but have to be found through an iterative procedure. Replacing the stress localisation equation (Equation 11) in the averaged local constitutive equation (Equation 1) we obtain:

$$\boldsymbol{\sigma}^{(r)} = \mathbf{C}^{(r)} : \mathbf{A}^{(r)} : \boldsymbol{\Sigma} \quad (12)$$

Taking volumetric average (denoted $\langle \cdot \rangle$), enforcing the condition that the average stress over the aggregate has to coincide with the corresponding macroscopic magnitude and using the macroscopic constitutive relation (Equation 2), we obtain the following self-consistent equation for the HEM's stiffness:

$$\bar{C} = \langle \mathbf{C}^{(r)} : \mathbf{A}^{(r)} \rangle \quad (13)$$

To illustrate the use of this ELSC formulation, we describe here the steps required to predict the local and overall elastic response of an elastically heterogeneous materials. We start, for convenience, from an initial Voigt guess, i.e.: $\dot{\boldsymbol{\epsilon}}^{(r)} = \dot{\mathbf{E}}$ for all phases, and:

$\bar{\mathbf{C}} = \langle \mathbf{C}^{(r)} \rangle$. Next, the Eshelby tensor \mathbf{S} can be calculated for the ellipsoidal shape of the mechanical phases. Subsequently, the interaction tensor $\tilde{\mathbf{C}}$ (Equation 10), and the localisation tensors $\mathbf{A}^{(r)}$ for each phase (Equation 11), are obtained. With these, an improved estimate of $\bar{\mathbf{C}}$ can be calculated, using the self-consistent fix-point equation (Equation 13). After achieving convergence on the macroscopic stiffness (and, consequently, also on the interaction and localisation tensors), a new estimation of average grain strain and stresses can be obtained, e.g., using the localisation relation and the averaged local constitutive equation (Equation 1).

Viscoplastic self-consistent method

In what follows, the SC formalism described in the previous section will be extended to the case of viscoplastic polycrystals. Each SR grain will be treated as an ellipsoidal viscoplastic inclusion embedded in an effective viscoplastic medium. Deformation in the grains is accommodated by dislocation glide activated by a resolved shear stress.

Local constitutive behaviour, linearisation and homogenisation

Let us consider that a macroscopic strain-rate $\dot{\mathbf{E}}$ is applied to the polycrystal. Let us assume that the plastic component of the deformation is much larger than the elastic part and therefore the flow is incompressible. The viscoplastic constitutive behaviour at each material point is described by means of the following non-linear, rate-sensitive equation:

$$\dot{\boldsymbol{\epsilon}}(\mathbf{x}) = \sum_{k=1}^{N_k} \mathbf{m}^k(\mathbf{x}) \dot{\gamma}^k(\mathbf{x}) = \dot{\gamma}_0 \sum_{k=1}^{N_k} \mathbf{m}^k(\mathbf{x}) \left(\frac{|\mathbf{m}^k(\mathbf{x}) : \boldsymbol{\sigma}'(\mathbf{x})|}{\tau_0^k(\mathbf{x})} \right)^n \times \text{sgn}(\mathbf{m}^k(\mathbf{x}) : \boldsymbol{\sigma}'(\mathbf{x})) \quad (14)$$

where the sum runs over all N_k slip and twinning systems. τ_0^k and $\mathbf{m}^k(\mathbf{x}) = \frac{1}{2} (\mathbf{n}^k(\mathbf{x}) \otimes \mathbf{b}^k(\mathbf{x}) - \mathbf{b}^k(\mathbf{x}) \otimes \mathbf{n}^k(\mathbf{x}))$ are the threshold resolved shear stress and the symmetric Schmid tensor associated with slip or twinning system (k) (with \mathbf{n}^k and \mathbf{b}^k being the normal and Burgers vector direction of such slip or twinning system), $\dot{\boldsymbol{\epsilon}}$ and $\boldsymbol{\sigma}'$ are the deviatoric strain-rate and stress tensors, $\dot{\gamma}_0$ is the local shear-rate on slip or twinning system (k), $\dot{\gamma}_0$ is a normalisation factor and n is the rate-sensitivity exponent.

Let us assume that the following linear relation (i.e., an approximation of the actual non-linear relation, Equation 26) holds between the strain-rate and stress in the SR grain (r):

$$\dot{\boldsymbol{\epsilon}}(\mathbf{x}) = \mathbf{M}^{(r)} : \boldsymbol{\sigma}'(\mathbf{x}) + \dot{\boldsymbol{\epsilon}}^o(r) \quad (15)$$

where $\mathbf{M}^{(r)}$ and $\dot{\boldsymbol{\varepsilon}}^{o(r)}$ are respectively a viscoplastic compliance and a back-extrapolated term (stress-free strain-rate) of SR grain (r). Different choices are possible for the linearised behaviour at grain level, and the results of the homogenisation scheme depend on this choice. The *secant approximation* [4,5] consists in assuming $\dot{\boldsymbol{\varepsilon}}_{\text{sec}}^{o(r)} = 0$, and the following linearised modulus:

$$\mathbf{M}_{\text{sec}}^{(r)} = \dot{\gamma}_o \sum_k \frac{\mathbf{m}^{k(r)} \otimes \mathbf{m}^{k(r)}}{\tau_o^{k(r)}} \left(\frac{\mathbf{m}^{k(r)} : \boldsymbol{\sigma}'^{(r)}}{\tau_o^{k(r)}} \right)^{n-1} \quad (16)$$

where the index (r) in $\mathbf{m}^{k(r)}$ and $\tau_o^{k(r)}$ indicates uniform (average) values of these magnitudes, corresponding to a given orientation and hardening state associated with SR grain (r). Under the *affine approximation* [10], the moduli are given by:

$$\mathbf{M}_{\text{aff}}^{(r)} = n\dot{\gamma}_o \sum_k \frac{\mathbf{m}^{k(r)} \otimes \mathbf{m}^{k(r)}}{\tau_o^{k(r)}} \left(\frac{\mathbf{m}^{k(r)} : \boldsymbol{\sigma}'^{(r)}}{\tau_o^{k(r)}} \right)^{n-1} \quad (17)$$

$$\dot{\boldsymbol{\varepsilon}}_{\text{aff}}^{o(r)} = (1-n)\dot{\gamma}_o \sum_k \left(\frac{\mathbf{m}^{k(r)} : \boldsymbol{\sigma}'^{(r)}}{\tau_o^{k(r)}} \right)^n \times \text{sgn}(\mathbf{m}^{k(r)} : \boldsymbol{\sigma}'^{(r)}) \quad (18)$$

The secant and affine models, together the *tangent approximation* of A. Molinari et al. [11] and R.A. Lebensohn et al. [6] (which combines aspects of the former two), [8] are first-order approximations, since they are based on linearisation schemes that at grain level make use of information on field averages only, disregarding higher-order statistical information inside the SR grains. However, the above assumption may be not sufficient, especially when strong directionality and/or large variations in local properties are to be expected. To overcome the above limitations, P. Ponte Castañeda et al. have developed more accurate nonlinear homogenisation methods, using linearisation schemes at grain level that also incorporate information on the second moments of the field fluctuations in the mechanical phases. These more elaborate SC formulations are based on the use of so-called linear comparison methods, which express the effective potential of the nonlinear VP polycrystal in terms of that of a linearly viscous aggregate with properties that are determined from suitably-designed variational principles [2,9,14,15]. Once a specific type of linearisation is chosen, the viscoplastic self-consistent method can be constructed following similar procedure as in the elastic case. The homogenised behaviour is given by Equation 2:

$$\dot{\mathbf{E}} = \overline{\mathbf{M}} : \boldsymbol{\Sigma}' + \dot{\mathbf{E}}^o \quad (19)$$

where $\dot{\mathbf{E}}$ and $\boldsymbol{\Sigma}'$ are the macroscopic deviatoric strain-rate and stress tensors and $\overline{\mathbf{M}}$ and $\dot{\mathbf{E}}^o$ are respectively the compliance and back-extrapolated term of the *a priori*

unknown viscoplastic HEM. The average strain-rate deviation in the ellipsoidal domain $\tilde{\dot{\epsilon}}^{(r)} = \dot{\mathbf{E}} - \dot{\epsilon}^{(r)}$ is given by Equation 9:

$$\tilde{\dot{\epsilon}}^{(r)} = \mathbf{S} : \dot{\epsilon}^{*(r)} \quad (20)$$

The interaction equation is given by Equation 10:

$$\tilde{\dot{\epsilon}}^{(r)} = -(\mathbf{I} - \mathbf{S})^{-1} : \mathbf{S} : \bar{\mathbf{M}} : \dot{\sigma}'^{(r)} = -\tilde{\mathbf{M}} : \dot{\sigma}'^{(r)} \quad (21)$$

The localisation equation is then written as Equation 11:

$$\dot{\sigma}'^{(r)} = (\mathbf{M}^{(r)} + \tilde{\mathbf{M}})^{-1} \left((\bar{\mathbf{M}} + \tilde{\mathbf{M}}) : \Sigma' + (\dot{\mathbf{E}}^o - \dot{\epsilon}^{o(r)}) \right) = \mathbf{B}^{(r)} : \Sigma' + \mathbf{b}^{(r)} \quad (22)$$

The self-consistent equations are then given by Equation 13:

$$\bar{\mathbf{M}} = \langle \mathbf{M}^{(r)} : \mathbf{B}^{(r)} \rangle \text{ and } \dot{\mathbf{E}}^o = \langle \mathbf{M}^{(r)} : \mathbf{b}^{(r)} + \dot{\epsilon}^{o(r)} \rangle \quad (23)$$

Numerical implementation

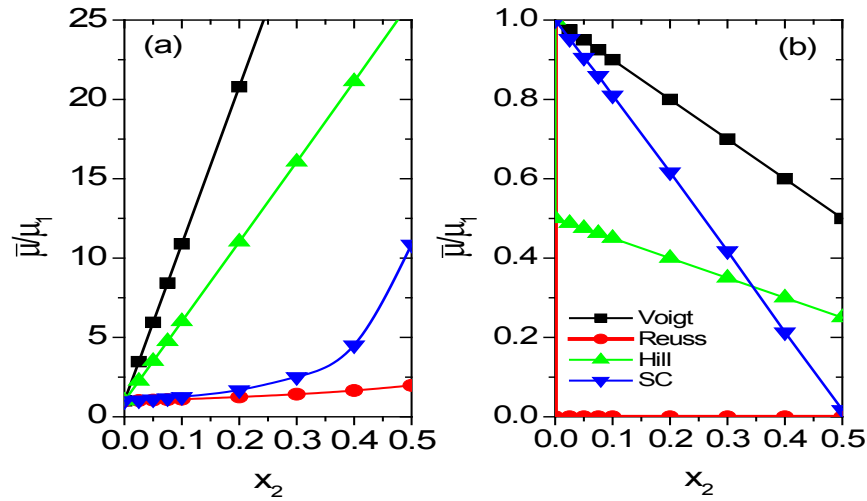
Starting, e.g., from an initial Taylor guess: $\dot{\epsilon}^{(r)} = \dot{\mathbf{E}}$ for all grains, a non-linear equation can be solved to get $\dot{\sigma}'^{(r)}$ and, using an appropriate linearisation scheme, the initial values of $\mathbf{M}^{(r)}$ and $\dot{\epsilon}^{o(r)}$ can be obtained, for each SR grain (r). Next, initial guesses for the macroscopic moduli $\bar{\mathbf{M}}$ and $\dot{\mathbf{E}}^o$ can be obtained as simple averages of the local moduli. With them and the applied strain-rate, the initial guess for the macroscopic stress Σ' can be obtained. The Eshelby tensors can be calculated using the macroscopic moduli and the ellipsoidal shape of the SR grains. Subsequently, the interaction tensor (Equation 21), and the localisation tensors (Equation 22), can be calculated as well, and new estimates of the macroscopic moduli can be obtained, by solving iteratively the self-consistent equation (Equation 23). After achieving convergence on the macroscopic moduli (and, consequently, also on the macroscopic stress and the interaction and localisation tensors), a new estimation of the average grain stresses is obtained, using the localisation relation. If the recalculated average grain stresses are different (within certain tolerance) from the input values, a new iteration should be started, until convergence is reached.

Applications

We show an application of the ELSC model to the prediction of the effective elastic shear modulus of isotropic two-phase composites made of: phase #1 with shear modulus and Poisson ratio $\mu_1 = 1$ and $\nu_1 = 1/3$, and phase #2 being either a hard phase with $\mu_2 = 100$ and $\nu_2 = 1/3$, or a void phase, i.e. $\mu_2 = 0$. Figure 1, corresponding to the case of equiaxed phase morphologies, shows the shear modulus of the composite as a function of phase #2 content. Together with the ELSC estimate, we show the Voigt, Reuss and Hill (defined as the arithmetic average between the Reuss and Voigt values) predictions. From Figure 1a (phase #2 100 times harder than phase #1) shows the huge spread existing between the bounds, and also the large difference between the SC estimate and the Hill average. Figure 1b (phase #2 void) shows similar results, as well as the “percolation limit”

of the SC theory at 50% volume fraction, at which the presence of a void phase determines a vanishing load-bearing capacity of the aggregate.

Figure 1. Voigt, Reuss, Hill and ELS predictions of the effective shear modulus as a function of phase #2 content (x_2), for isotropic two-phase composites made of phase #1 with shear modulus and Poisson ratio $\mu_1 = 1$ and $\nu_1 = 1/3$, and phase #2 being either: a) a hard phase with $\mu_2 = 100$ and $\nu_2 = 1/3$, and b) a void phase, i.e., $\mu_2 = 0$

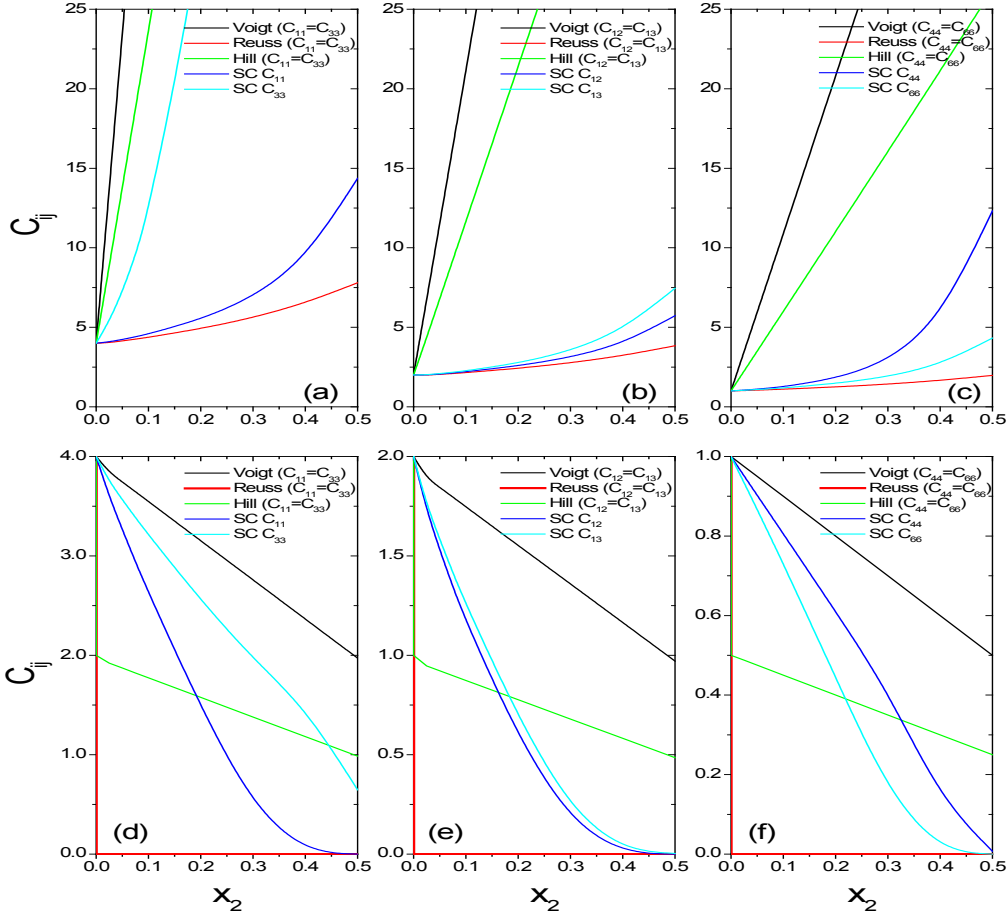


All cases correspond to equi-axed phase morphologies.

Figure 2 exemplifies how the ELS formulation naturally captures the effect of morphologic anisotropy. The cases shown correspond to the same materials as before, except that the morphology of the phases is represented by oblate spheroids with their short axis 10 times shorter than the long ones aligned with direction x_3 . It can be seen that: (i) the (isotropic) elastic constants for the homogeneous phase #1 material are $C_{11} = C_{22} = C_{33} = 4$, $C_{12} = C_{13} = C_{23} = 2$ and $C_{44} = C_{55} = C_{66} = 1$, and (ii) the effective response predicted by ELS (unlike the Voigt, Reuss and Hill predictions) are anisotropic (axisymmetric), e.g., in Figures 2a and 2d (hard and soft phase #2, respectively), note the very different evolution of the directional moduli $C_{11}(=C_{22})$ along the long morphologic directions, with respect to C_{33} , giving the response along the short direction.

Texture-induced anisotropy is also captured by the ELS approach. Figure 3 shows the evolution of the nine independent orthotropic elastic constants for the case plane strain deformation (extension along x_1 and shortening along x_3) of an initially random austenitic steel polycrystal (single crystal elastic constants: $C_{11} = 204.6 \text{ GPa}$, $C_{12} = 137.7 \text{ GPa}$ and $C_{44} = 126.2 \text{ GPa}$) as a function of the true strain along x_1 (texture evolution calculated with the affine VPSC approach). It should be noted that the orthotropic symmetry and relative values of the polycrystal elastic constants follow naturally from the texture evolution, e.g., the prediction of $C_{22} > C_{11} > C_{33}$ reflects the strong alignment of the hard $<111>$ crystallographic directions with x_2 as texture evolves.

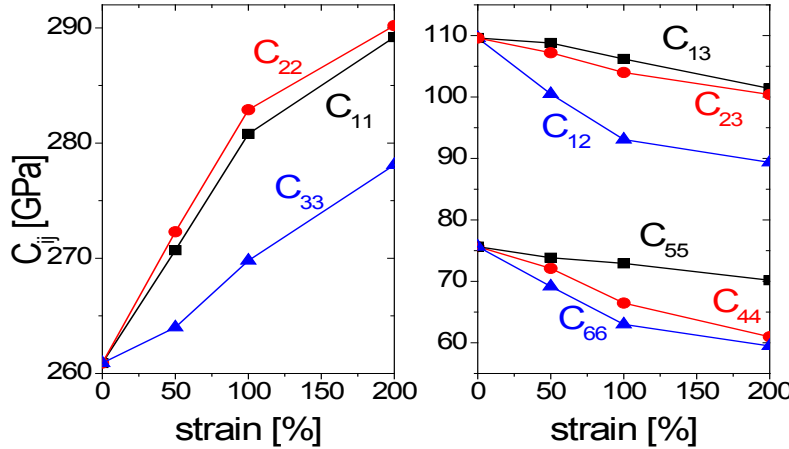
Figure 2. Same as Figure 1, except that the morphology of the phases is represented by oblate spheroids with their short axis ten times shorter than the long ones aligned with direction x_3



Upper row: case of hard phase #2, lower row: case of voided phase #2. a,d) C_{11}, C_{22}, C_{33} , b,e), C_{12}, C_{13}, C_{23} and c,f)
 C_{44}, C_{55}, C_{66} .

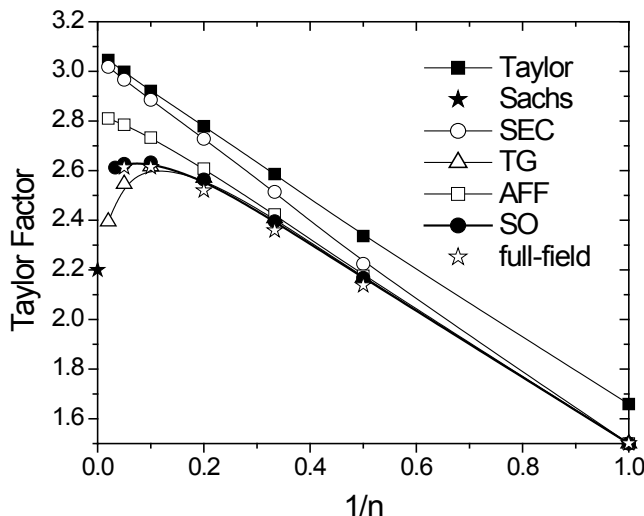
The advantage of SC schemes to get improved predictions of the mechanical behaviour of viscoplastic polycrystals, becomes evident as the contrast in local properties increases. The prediction of the effective properties of a random FCC polycrystal as the rate-sensitivity of the material changes is a classical benchmark for the different non-linear SC approaches. Figure 4 shows a comparison between average Taylor factor vs. rate-sensitivity ($1/n$) curves, for a random FCC polycrystal under uniaxial tension [8]. The Taylor factor is calculated as $\Sigma_{\text{eq}}^{\text{ref}} / \tau_0$, where τ_0 is the threshold stress of the $(111)\langle 110 \rangle$ slip systems, and $\Sigma_{\text{eq}}^{\text{ref}}$ is the macroscopic equivalent stress corresponding to an applied uniaxial strain-rate with a Von Mises equivalent value $E_{\text{eq}}^{\text{ref}} = 1$.

Figure 3. Evolution of the nine independent orthotropic elastic constants for the case of plane strain deformation of an initially random austenitic steel polycrystal, as a function of the true strain along the extension direction x_1



The curves in Figure 4 correspond to the Taylor model, the different first-order SC approximations, and the second-order procedure [9]. The solid star indicates the rate-insensitive Sachs lower-bound. The open stars correspond to reference solutions, obtained from ensemble averages of full-field solutions performed on random polycrystals using a Fast Fourier Transform-based method [12,7]. These ensemble averages were calculated over the outcome of “numerical experiments” performed on 100 unit cells generated alike, i.e., by random assignation of orientations to a given array of grains, but which differ at micro level due to the inherent stochastic character of such generation procedure. The averages over a sufficiently large number of configurations should give the effective properties of a polycrystal with random microstructure. From the comparison between the different mean-field and the full-field estimates, it can be observed that: (i) the Taylor approach gives the stiffest response, consistent with the upper-bound character of this model; (ii) all the SC estimates coincide for $n=1$, i.e., the linear SC case; (iii) in the rate-insensitive limit, the secant and tangent models tend to the upper- and lower-bounds, respectively, while the affine and second-order approximations remain intermediate with respect to the bounds; (iv) the best match with the exact solutions corresponds to the second-order approach.

Figure 4. Average Taylor factor for a random FCC polycrystal under uniaxial tension, calculated with the different SC approaches (lines+symbols) and reference values (stars) obtained by means of ensemble averages of full-field solutions [8]



Conclusion and future challenges

We have presented the ELS and VPSC formulations, and exemplified their use to establish relationships between microstructure and properties of composites and polycrystalline materials. The elastic model is a mature formulation that can be readily applied to fuels and structural materials for nuclear systems to predict effective elastic properties if the single crystal elastic constants, morphology, texture and phase distribution are known. The viscoplastic model can be applied to predict the effective anisotropic plastic response as a function of single crystal plastic properties and morphologic and crystallographic texture. For other inelastic deformation regimes of relevance, like thermal and irradiation creep, the formulation should be modified with pertinent constitutive relations at grain level (Equation 14) that reflect the single crystal response in such regimes. The presented methodology can be applied to predict the effective behaviour of polycrystalline aggregates deformation in such regimes.

References

- [1] Berveiller, M., O. Fassi-Fehri, A. Hihi (1987), "The problem of 2 plastic and heterogeneous inclusions in an anisotropic medium", *International Journal of Engineering Science*, 25, 691-709.
- [2] de Botton, G., P. Ponte Castañeda (1995), "Variational estimates for the creep-behavior of polycrystals", *Proceedings of the Royal Society of London A*, 448, 121-142.
- [3] Hershey, A.V. (1954), "The elasticity of an isotropic aggregate of anisotropic cubic crystals", *Journal of Applied Mechanics*, 21, 236-240.
- [4] Hill, R. (1965), "Continuum micro-mechanics of elastoplastic polycrystals", *Journal of the Mechanics and Physics of Solids*, 13, 89.

- [5] Hutchinson, J.W. (1976), "Bounds and self-consistent estimates for creep of polycrystalline materials", *Proceedings of the Royal Society of London A*, 348, 101-127.
- [6] Lebensohn, R.A. et al. (1993), "A self-consistent approach for the simulation of plastic deformation and texture development of polycrystals: Application to zirconium alloys", *Acta Metallurgica et Materialia*, 41, 2611-2624.
- [7] Lebensohn, R.A. (2001), "N-site modelling of a 3D viscoplastic polycrystal using Fast Fourier Transform", *Acta Materialia*, 49, 2723-2737.
- [8] Lebensohn, R.A. et al. (2007), "Self-consistent modeling of the mechanical behavior of viscoplastic polycrystals incorporating intragranular field fluctuations", *Philosophical Magazine*, 87, 4287-4322.
- [9] Liu, Y., P. Ponte Castañeda (2004), "Second-order theory for the effective behavior and field fluctuations in viscoplastic polycrystals", *Journal of the Mechanics and Physics of Solids*, 52, 467-495.
- [10] Masson, R. et al. (2000), "Affine formulation for the prediction of the effective properties of nonlinear composites and polycrystals", *Journal of the Mechanics and Physics of Solids*, 48, 1203-1227.
- [11] Molinari, A. et al. (1987), "Self consistent approach of the large deformation polycrystal viscoplasticity", *Acta Metallurgica*, 35, 2983-2994.
- [12] Moulinec, H., P. Suquet (1998), "Numerical method for computing the overall response of nonlinear composites with complex microstructure", *Computer Methods in Applied Mechanics and Engineering*, 157, 69-94.
- [13] Mura, T. (1987), *Micromechanics of Defects in Solids*, Martinus-Nijhoff Publishers, Dordrecht.
- [14] Ponte Castañeda, P. (1991), "The effective mechanical properties of nonlinear isotropic composites", *Journal of the Mechanics and Physics of Solids*, 39, 45-71.
- [15] Ponte Castañeda, P. (2002), "Second-order homogenization estimates for nonlinear composites incorporating field fluctuations: I- 'Theory'", *Journal of the Mechanics and Physics of Solids*, 50, 737-757.

Part III

Principles of Modelling and Simulation Techniques for Nuclear Fuels

The final section of this report covers modelling and computational principles in a number of areas. M. Freyss provides an introduction to *Density functional theory* (DFT) as it is applied to nuclear fuel materials. Electronic structure calculations enable accurate determination of physical and chemical properties, and provide data for the adjustment of parameters in empirical methods such as MD and kMC. The limitations of DFT in treating strong 5f correlations are one of the main issues for modelling of nuclear fuels. Various methods exist to better accommodate strongly correlated materials and are presented in this section. R. Devanathan, M. Krack and M. Bertolus review *Classical molecular dynamics simulation of nuclear fuel* as a means of representing damage production by irradiation, defect interactions with fission gas atoms, bubble nucleation, and grain boundary effects. MD simulations can also provide parameters that can be used as inputs for mesoscale models. They note, however, the need for refining interaction potentials and to develop models that can handle off-stoichiometry.

The use of atomic scale modelling techniques has been the subject of a benchmarking activity under the Expert Group on Validation and Benchmarking of Methods now subsumed under the current Expert Group on Multi-Scale Modelling of Fuels. That report is included in this volume and looks at whether these methodologies indeed provide accurate representations of nuclear materials. M. Bertolus, M. Krack, M. Freyss and

R. Devanathan have performed an *Assessment of current atomic scale modelling methods for the investigation of nuclear fuel under irradiation: Example of uranium dioxide*. Interestingly, they conclude that indeed, for UO₂, the techniques can accurately represent properties of the phase and can be seen as powerful tools for investigating many systems.

The evolution of material plastic properties is exclusively modelled by the *Dislocation dynamics method*. The simulations are based on elastic dislocation theory following rules inherent to the dislocation core structure, often called “local rules.” In this contribution, L. Van Brutzel presents the technique and gives some examples of what can be achieved with using related methodologies, although for fuel materials sufficient basic information on dislocation mobility is still not available.

The *Phase field* technique is an efficient simulation approach for evolving microstructural evolution due to phase transformations. In describing the methodologies, B. Radhakrishnan, S.B. Gorti, K. Clarno and M.R. Tonks utilise the example of simulating the formation and the stress induced re-orientation of zirconium hydride during dry storage of spent fuel. However, the modelling effort to-date is far from adequate and several issues remain to be addressed before the simulations can be used as a predictive tool for the behaviour of, for example, clad during long term dry storage.

Modelling microstructural evolution under irradiation is exceptionally difficult given the compositional changes, large thermal gradients and radiation field. One of the current approaches uses the Potts kMC model, which is a statistical-mechanical model that populates a lattice with an ensemble of discrete particles to represent and evolve the microstructure. V. Tikare summarises the approach, noting that the particles in the Potts kMC model represent a discrete quantity of material that is much larger than an atom, thus all atomistic information about the material system is aggregated into mesoscale model parameters. In kMC, the particles evolve in a variety of ways to simulate microstructural changes due to short- and long-range diffusive processes.

Rate theory, and the particular case of cluster dynamics, is discussed by S. Maillard, R. Skorek, P. Maugis and M. Dumont as a complementary method to mean field models. It can reveal mechanisms involved in microstructure evolution and gas behaviour that are not accessible through conventional models, but yet can provide for improvements in those models. The derived parameters can be seen as essentially the energetic values governing the basic evolutionary mechanisms in materials such as diffusion, trapping and thermal resolution. It can, for example, represent fission product release and be used to assess migration mechanisms for low solubility gases.

As noted in the first part of the report, the *Thermochemical modelling of multi-component systems* is fundamental to predicting the formation of phases and species within fuel. The Calphad (Calculation of Phase Diagrams) method was developed to utilise a wide variety of chemical and phase information to generate thermochemical representations that produce phase equilibria and chemical activities. B. Sundman and C. Guéneau describe the Calphad approach, where calculations are based on thermodynamic models of the Gibbs energy for each phase as a function of temperature, pressure and composition.

Peridynamics, a nonlocal extension of continuum mechanics, is a natural framework for capturing constitutive response, and modelling pervasive material failure and fracture. Unlike classical approaches incorporating partial derivatives, the peridynamic governing equations utilise integral expressions that remain valid in the presence of discontinuities such as cracks. While it has promise for modelling fuel mechanical behaviour, D. Littlewood in his discussion of the technique, notes that work remains to be done to integrate it into the multi-physics environment of nuclear fuels.

The structural integrity of fuel depends on its mechanical properties, which can be modelled using finite element calculations to provide an understanding of thermal strains, irradiation induced swelling and other phenomena. The viscoplastic range corresponds to the occurrence of inelastic strain called viscoplastic strain. A viscoplastic model allows one to compute these strains as a function of time, temperature and stress. R. Masson, V. Blanc, J.M. Gatt, J. Julien, R. Largentot and B. Michel review *Micromechanical modelling of fuel viscoplastic behaviour* including full, mean and transformation field approaches and their application to fuel behaviour.

Finite element modelling (FEM) is a numerical technique for finding approximate solutions to boundary value problems. FEM has been used for reactor fuels modelling for many years. It is now being developed for use in the multi-dimensional MOOSE-BISON-MARMOT suite of fuel performance codes as described by M.R. Tonks, R. Williamson and R. Masson. FEM is widely applied to thermal modelling, and K. Kurosaki provides an *Evaluation of thermal conductivity of multi-component and multi-phase nuclear fuels by the finite element method*, as an example.

The section continues with a review of the *Use of advanced simulations in fuel performance codes* to predict fuel rod behaviour and lifetime in a reactor. The codes must take into account a wide variety of phenomena including the coupled effects of heat transfer, the mechanical interaction between the fuel and its surrounding protection, the isotopic evolution caused by irradiation and the chemical interactions between fuel, fission products, cladding and coolant. Yet, the complexity of the problem and the ubiquitous lack of data and fully representative models require simplifying assumptions including a less than three-dimensional rendering. P. Van Uffelen briefly reviews fuel performance

codes noting the computational domains and the issues involved in accurate representation of fuel behaviour, with current approaches to dealing with the limitations.

The report concludes with a description of the *Integrated multi-scale modelling and simulation of nuclear fuels* approach to how the tools representing the thermomechanical, physical and chemical evolution combine modelling from the atomic scale through the intermediate grain scale up to the pellet/rod scale. Tying together the models described in the report is a discussion on the integration of the models and how they potentially interact by C. Valot, M. Bertolus, L. Malerba, J. Rashid, T. Besmann, R. Masson, S. Phillipot and M. Stan. Information and relevant mechanisms relate the behaviour of fuel at a certain scale to the higher scale, so that models at a higher level can be more physically representative and more accurate. It is important to stress that the multi-scale approach does not only build links between scales, but also across various technical approaches and between basic research and applied technology.

Chapter 12.

Density functional theory

M. Freyss

CEA, DEN, DEC, Centre de Cadarache, France

Abstract

This chapter gives an introduction to first-principles electronic structure calculations based on the density functional theory (DFT). Electronic structure calculations have a crucial importance in the multi-scale modelling scheme of materials: not only do they enable one to accurately determine physical and chemical properties of materials, they also provide data for the adjustment of parameters (or potentials) in higher-scale methods such as classical molecular dynamics, kinetic Monte Carlo, cluster dynamics, etc. Most of the properties of a solid depend on the behaviour of its electrons, and in order to model or predict them it is necessary to have an accurate method to compute the electronic structure. DFT is based on quantum theory and does not make use of any adjustable or empirical parameter: the only input data are the atomic number of the constituent atoms and some initial structural information. The complicated many-body problem of interacting electrons is replaced by an equivalent single electron problem, in which each electron is moving in an effective potential. DFT has been successfully applied to the determination of structural or dynamical properties (lattice structure, charge density, magnetisation, phonon spectra, etc.) of a wide variety of solids. Its efficiency was acknowledged by the attribution of the Nobel Prize in Chemistry in 1998 to one of its authors, Walter Kohn. A particular attention is given in this chapter to the ability of DFT to model the physical properties of nuclear materials such as actinide compounds. The specificities of the $5f$ electrons of actinides will be presented, i.e., their more or less high degree of localisation around the nuclei and correlations. The limitations of the DFT to treat the strong $5f$ correlations are one of the main issues for the DFT modelling of nuclear fuels. Various methods that exist to better treat strongly correlated materials will finally be presented.

From the Schrödinger Equation to the one-electron Kohn-Sham Equation

The electronic structure of a material is in principle obtained by solving the Schrödinger Equation $H\Psi = E\Psi$ of the system described by the wave-function $\Psi(\mathbf{r}, \mathbf{R})$ of interacting electrons (with positions \mathbf{r}) and nuclei (with positions \mathbf{R}). Such a many-body problem can, however, not be solved exactly and one usually assumes that the movement of the electrons can be decoupled from the movement of the nuclei. It is the *Born-Oppenheimer approximation*, justified by the much greater velocities of the electrons compared to the velocities of the heavier nuclei: electrons respond quasi instantaneously to the movement of the nuclei and one can consider that electrons remain in their ground state during the displacement of the nuclei. As a consequence, the electron wave-function $\Psi(\mathbf{r})$ is determined for fixed positions \mathbf{R} of the nuclei and the dependence in \mathbf{R} can be omitted. This approximation can be considered valid in most cases and in particular as long as the electron-phonon coupling is not fundamental in the properties studied. The Hamiltonian H of the system therefore becomes that of interacting electrons moving in the external field created by the nuclei.

The many-body character of the electron-electron interactions requires further simplification and the next transformation constitutes the fundament of DFT: the Schrödinger Equation is expressed for an equivalent system of independent electrons characterised by single-electron wave functions $\varphi_i(\mathbf{r})$ and whose electron density is the same as the one of the system with interacting electrons. Two theorems by Hohenberg and Kohn [1] show that the single-particle charge density $n(\mathbf{r})$ can be chosen as the fundamental variable for the description of the ground state of a system of interacting electrons. This density $n(\mathbf{r})$ is only a function of the three space coordinates, which simplifies greatly the many-body problem. The two theorems by Hohenberg and Kohn are as follows:

- All physical quantities are a functional of the electron density $n(\mathbf{r})$ of the system, in particular the total energy.
- The physical (or « real ») electron density of a system is the one minimising the total energy functional of the system (variational principle).

The total energy functional is defined as follows:

$$E[n] = -\frac{1}{2} \sum_i \int \varphi_i^*(\mathbf{r}) \nabla^2 \varphi_i(\mathbf{r}) d\mathbf{r} + \frac{1}{2} \iint \frac{n(\mathbf{r}) n(\mathbf{r}')}{|\mathbf{r} - \mathbf{r}'|} d\mathbf{r} d\mathbf{r}' + \int V_{ext}(\mathbf{r}, \mathbf{R}) n(\mathbf{r}) d\mathbf{r} + E_{xc}[n(\mathbf{r})] \quad (1)$$

where the first term corresponds to the kinetic energy of non-interacting electrons. The corrections to this term due to the many-body interaction of the electrons are included in the last term, the exchange-correlation term. The second term corresponds to the electron Coulomb interactions. The Coulomb interactions between electrons and nuclei are included in the external potential term $V_{ext}(\mathbf{r}, \mathbf{R})$.

The electron charge density is determined from the single electron wave functions $\varphi_i(\mathbf{r})$ according to the expression:

$$n(\mathbf{r}) = \sum_i^N |\varphi_i(\mathbf{r})|^2 \quad (2)$$

with N the number of occupied states for all atoms of the system.

The minimisation of the energy functional relative to the electron density yields an eigenvalue problem, called the Kohn-Sham Equation [2], which has the form of a single-particle Schrödinger Equation:

$$\left(-\frac{\hbar^2}{2m} \nabla^2 + V_{\text{eff}}(\mathbf{r}) \right) \varphi_i(\mathbf{r}) = \varepsilon_i \varphi_i(\mathbf{r}) \quad (3)$$

The effective potential V_{eff} is given by:

$$V_{\text{eff}}(\mathbf{r}) = V_{\text{ext}}(\mathbf{r}, \mathbf{R}) + \int \frac{n(\mathbf{r}')}{|\mathbf{r} - \mathbf{r}'|} d\mathbf{r}' + v_{xc}(\mathbf{r}) \quad (4)$$

with v_{xc} the exchange-correlation potential defined by:

$$v_{xc}(\mathbf{r}) = \frac{\partial E_{xc}}{\partial n(\mathbf{r})} \quad (5)$$

The derivation of the single-particle Kohn-Sham Equation (3) from the many-body Schrödinger Equation is formally exact. Were all interaction terms in Equation 4 known, the solution of the problem would be exact. Unfortunately, the exact analytical expression of the exchange-correlation interaction v_{xc} is not known. Various approximations can be used for this term and they usually determine the accuracy of the calculations. The most usual approximations are the Local Density Approximation (LDA) and the Generalised Gradient Approximation (GGA), which are presented below.

The Bloch theorem and the electron basis set

The resolution of the Kohn-Sham Equation (3) can be simplified by taking advantage of the periodicity of the system. In bulk crystalline systems, the periodicity of the effective potential is straightforward and can be expressed as the condition $V_{\text{eff}}(\mathbf{r} + \mathbf{T}) = V_{\text{eff}}(\mathbf{r})$, where \mathbf{T} is a translation vector of the crystal lattice. The Bloch theorem then states that all solutions of the Kohn-Sham Equation can be written in the form of a product of a plane wave with a function u that has the periodicity of the crystal: $\varphi_i(\mathbf{k}; \mathbf{r}) = u_{i,\mathbf{k}}(\mathbf{r}) e^{i\mathbf{k}\cdot\mathbf{r}}$. Due to the periodicity of the crystal, the \mathbf{k} vectors are limited to a primitive cell of the reciprocal lattice, the first Brillouin Zone. In practice, the Brillouin zone has to be sampled by a finite number of \mathbf{k} -points, which is usually achieved by the Monkhorst-Pack scheme [3]. For systems containing point defects or impurities (fission products, helium, oxygen...), the periodicity of the system is retained by the use of the *supercell* method.

In order to solve the Kohn-Sham Equation (3), one needs to choose the analytical form of the electron basis set on which the wave functions will be expanded. The wave

function φ_i is a linear combination of the basis functions χ : $\varphi_{ik}(\mathbf{r}) = \sum_j c_{j,ik} \chi_{jk}(\mathbf{r})$ where the basis functions χ fulfill the Bloch theorem.

The various methods based on the DFT differentiate by the choice of the basis functions χ , which usually defines the name of the method. The basis functions can be plane waves (in pseudopotentials methods) [4,5] augmented or orthogonalised plane waves (in the PAW [6], the OPW [7] or the APW [8] methods), augmented spherical waves (ASW) [9], Muffin-Tin orbitals (in the LMTO method) [10], linear combination of atomic (LCAO) or Gaussian (LCGO) orbitals, etc. The Korringa-Kohn-Rostoker (KKR) [11,12] method makes use of the Green's function of the system instead of the wave function.

For the study of radiation damage in nuclear fuels, which requires large supercells to accommodate point defects or impurities and the relaxation of the atomic positions around the defects, a plane-wave method such as the PAW method is one of the most adapted and accurate. This method is widely used with the code VASP [13] and ABINIT [14].

The Kohn-Sham Equation (3) is solved in a self-consistent manner: an initial charge density (usually calculated by the superposition of atomic densities) is used to derive the various terms of the effective potential (4). The eigenvalue problem is solved for this trial density, and a new electron density is obtained from the eigenvectors according to expression (2). An appropriate mixing of the new and previous densities (or potentials) is used to build the new effective potential in order to solve again the Kohn-Sham Equation. This process is repeated until the results (total energy, charge density, or potential) are converged, i.e., they do not vary anymore (or less than a chosen limit) during the iterative process.

Approximations for the exchange-correlation interaction

The Local Density Approximation (LDA) is one of the first and most standard approximation for the exchange-correlation interaction. It assumes that the exchange-correlation energy of the system is equal to the one of a homogeneous electron gas with the density $n(\mathbf{r})$. The exact expression of the exchange-correlation energy of such a homogeneous electron gas is known:

$$E_{xc}[n] = \int n(\mathbf{r}) \varepsilon_{xc}^{\text{hom}}[n(\mathbf{r})] d\mathbf{r} \quad (6)$$

where $\varepsilon_{xc}^{\text{hom}}$ is the exchange-correlation energy per electron of a homogeneous electron gas of density n . $\varepsilon_{xc}^{\text{hom}}$ can be expressed in various analytical parameterised forms, among which one finds those by Hedin-Lundqvist [15], Barth-Hedin [16], Vosko-Wilk-Nusair [17], Ceperley-Alder [18], Perdew-Zunger [19], etc. The LDA approximation is, in principle, adequate for system with a low spatial varying electron density, but it revealed good for a wider variety of materials. It, however, significantly fails in the description of many properties of *d* and *f* compounds. Binding energies are in particular overestimated [20].

The Generalised Gradient Approximation (GGA) is a more elaborate approximation of the exchange-correlation interaction, which consists in taking into account the non-uniform character of the electron density by replacing $\epsilon_{xc}^{\text{hom}}$ by a semi-local function of the electron density and the magnitude of its gradient:

$$E_{xc}[n] = \int f(n(\mathbf{r}), |\nabla n(\mathbf{r})|) d\mathbf{r} \quad (7)$$

where f is an analytical function which can also be parameterised in various ways. The most common ones are the Perdew-Burke-Ernzerhof (PBE) [21] and the Perdew-Wang [22] parametrisations. For most materials, GGA improves the LDA overbinding. However, both GGA and LDA approximations are known to underestimate the band gap of semiconductors by about 30 to 80% and to inaccurately describe the band structure of strongly correlated materials. In the case of UO_2 , which is a Mott insulator, LDA and GGA predict a metallic behaviour. The failure of standard DFT (LDA and GGA) is generally attributed to the use of a local potential to treat exchange or to the inadequate treatment of the many-body electron correlations.

Beyond DFT to treat the strong correlations of the $5f$ electrons in actinide compounds

Most nuclear fuels consist of actinide oxides, which are strongly correlated materials. In UO_2 , the $5f$ electrons of the uranium atoms are strongly localised in space around the nuclei. The standard DFT does not accurately reproduce the thus induced strong correlations of the $5f$ electrons. This flaw is revealed by the metallic behaviour of the actinide oxides obtained by DFT, whereas these materials are insulators. Several methods exist to better treat the correlations of $5f$ electrons: the self-interaction correction (SIC) method, the DFT+U method, hybrid functionals, the DFT+DMFT method:

a. The self-interaction correction (SIC) [23,24]: The unphysical electron self-interaction in DFT is explicitly subtracted from the DFT energy, orbital by orbital, for all the occupied orbitals, namely: $E_{SIC} = E_{DFT} - \sum_{\alpha} \delta_{\alpha}^{SIC}$. Since for the itinerant (delocalised) electrons the self-interaction vanishes, the above sum runs only over localised orbitals (α). The SIC method thus enables one to select the number of electrons that are considered localised or itinerant. In this approach, the localised and itinerant orbitals are treated on an equal footing, the global energy minimum of the system with different localised/itinerant configurations gives the ground-state valence state of the correlated atoms. The SIC method has been applied to bulk properties of actinide metals [25], oxides [26], carbides and nitrides [27].

b. The DFT+U method [28]: An on-site Hubbard like Coulomb interaction term U is added as a correction to the DFT Hamiltonian to increase the Coulomb repulsion between the localised electrons and better account for their enhanced correlations. The corrective term is only applied for the correlated orbitals (d or f) and the total energy functional takes the following form:

$$E_{DFT+U}[n(\mathbf{r})] = E_{DFT}[n(\mathbf{r})] + E_U[n_m^{I,\sigma}] - E_{dc}[n_d^{I,\sigma}] \quad (8)$$

where E_{DFT} is the DFT (LDA or GGA) energy term as in Equation 1, $n(\mathbf{r})$ the electron density and $n_m^{I\sigma}$ the atomic-orbital occupations with spin σ for the correlated atom I . E_U takes the following form:

$$E_U[n(\mathbf{r})] = \frac{1}{2} \sum_{\{m\}, I, \sigma} [\langle m, m'' | V_{ee} | m', m''' \rangle n_{mm'}^{I, \sigma} n_{m'm''}^{I, -\sigma} + (\langle m, m'' | V_{ee} | m', m''' \rangle - \langle m, m'' | V_{ee} | m'', m' \rangle) n_{mm'}^{I, \sigma} n_{m'm''}^{I, \sigma}] \quad (9)$$

and it can be expressed as a function of the screened on-site Coulomb and exchange parameters U and J :

$$U = \frac{1}{(2l+1)^2} \sum_{m, m'} \langle m, m' | V_{ee} | m, m' \rangle \quad \text{and} \quad J = \frac{1}{2l(2l+1)} \sum_{m \neq m', m'} \langle m, m' | V_{ee} | m', m \rangle \quad (10)$$

E_{dc} is the “double counting term”, i.e., a mean-field evaluation of the Hubbard term removing the same amount of Coulomb repulsion from the DFT part of the Hamiltonian. E_{dc} can be assessed using the Around Mean Field (AMF) scheme [29] or the Fully-Localised Limit (FLL) scheme which is better adapted for strongly correlated materials [30].

There exist two formulations of the DFT+U approach. In Dudarev’s approach [31], only the difference ($U - J$) comes into play in the energy functional whereas in Liechtenstein’s formulation [32] both U and J parameters separately come into play. Thus either the value of the difference ($U - J$) or both U and J parameters have to be chosen. This choice can be based on an adjustment on the material properties or on an analysis of experimental spectroscopic data. Such an approach requiring parameter adjustment can thus be seen as a phenomenological many-body corrections. There, however, exist methods based on a linear response approach [33] or on the Random-Phase Approximation (RPA) [34] to calculate the interaction parameters U and J entering the DFT+U functional from first-principles.

In the case of UO_2 , the values of the parameters U and J widely used in the literature were deduced from photoemission spectra [35] and do not need further adjustment. Their use in DFT+U simulations gives very good bulk properties for UO_2 [36-38]: lattice parameter, elastic constants, cohesive energy, energy gap, non-collinear antiferromagnetic order, Jahn-Teller distortion. Even point defect properties, such as oxygen activation energy of diffusion, are well described [39,40].

c. Hybrid Functionals [41]: Hybrid functionals combine a part of the Hartree-Fock (HF) exact exchange with LDA or GGA exchange-correlation functionals. For instance, the PBE0 hybrid functional [42] yields the following expression for the total energy of the system: $E_{XC} = E_{XC}^{PBE} + \frac{1}{4} [E_x^{HF} - E_x^{PBE}]$, where PBE refers to the Perdew-Burke-Ernzerhof GGA exchange-correlation functional. Another example of hybrid functional is the HSE06 one, in which the exchange energy term is split into short- range and long-range components and the HF long range is neglected but compensated by the PBE long range [43]. A comparison of those functionals with the standard LDA and GGA functionals for UO_2 , PuO_2 and $\beta\text{-Pu}_2\text{O}_5$ is given in [44].

The results yielded by hybrid functionals are comparable or better than DFT+U calculations with the advantage of having no system-dependent parameters U and J . The

$\frac{1}{4}$ ration is considered as adequate for most, if not all, materials. Hybrid functional calculations are computationally much more demanding than DFT+U calculations and are not achievable yet for large systems containing point defects or impurities. Recently, however, P. Novák et al. [45] proposed the Exact Exchange for Correlated Electrons method (EECE) in which the exact exchange functional is only applied to a restricted subspace formed by the correlated electrons. This method is therefore much faster and was applied to the study of actinide oxides [46] and charged defects in UO_2 [47].

It should finally be emphasised that the localisation of the correlated electrons yielded by the above-described methods induces the existence of local energy minima (or metastable states) towards which the calculation can converge, missing thus the ground state of the system. This issue was evidenced in $4f$ [48] and $5f$ systems [46,49,50,51]. For the study of radiation damage in UO_2 using DFT+U, several solutions have been proposed [35,52,53] to avoid such local energy minima.

d. Combination of DFT with Dynamical Mean Field Theory (DFT+DMFT) [54,55]: This method is an extension of the DFT+U method and goes beyond the static mean field approximation. The local correlations are described exactly for each single atom, the effect of the other atoms being gathered in an effective field. The resolution of the problem is based on its mapping onto a single-impurity Anderson model using a Quantum Monte Carlo solver [56] or the Hubbard I approximation [57]. The DFT+DMFT method requires choosing a Hubbard-type U term in the same way as in the DFT+U method (by constrained U-calculations or adjustments to experiments). Besides being able to correctly describe Mott insulators, the DFT+DMFT method is the only method up to now that is able to describe strongly correlated paramagnetic metals. This method is very time-consuming, making the study of radiation damage hardly possible. Only point defects in very small supercells containing few tens of atoms can currently be considered.

Relativistic effects: Spin-orbit coupling

In order to accurately describe the electronic structure of compounds containing heavy elements, relativistic effects must be taken into account. Usually only the Darwin and the mass-velocity relativistic corrections are taken into account, corresponding to the *scalar relativistic approximation*. In the fully relativistic description of the system, the Kohn-Sham Equation should be replaced by its relativistic analogue, the Dirac Equation, in which the spin-orbit coupling is also taken into account. The spin-orbit coupling has a significant influence on the electronic structure of actinide compounds (it accounts in particular for the $5f_{5/2}$ and $5f_{7/2}$ splitting of the actinide $5f$ states) but its effect on the modelling of radiation damage in fuels (formation or migration energies of point defects...) has not been assessed so far due to the increased computational cost.

DFT and Van der Waals interactions

Another limitation of the local and semi-local LDA and GGA approximations of the DFT is that they cannot describe long-range van der Waals interactions (or dispersive interactions). This is a significant flaw for the modelling of nuclear fuels in which rare gas fission products (xenon, krypton) and helium are abundant and tend to aggregate into clusters or bubbles. Such clusters will not be correctly described by these approximations

(energetically and structurally) since the dispersive bonding between rare gas atoms is non-local. The question also arises not only for bonds between rare gas atoms but also for the bonds between a rare gas atom and the host crystal. Improvement of the DFT to describe dispersive bonds is an active field of research. Non-local correlation functionals such as the vdW-DF [58] or the VV09 functionals [59] have been developed recently and have shown success on a wide range of materials. Another way to treat dispersive bonds is by introducing an empirical pair-potential correction to the total energy, as developed in the DFT-D method [60] or the vdW-MLWF method (Maximally Localised Wannier Function) [61] or the DFT-ulg (universal low gradient) approach [62].

Finite temperature effects

DFT is formulated for zero K calculations, i.e., without lattice vibrations. Finite temperature effects can be modelled either by *ab initio* molecular dynamics, in which the forces acting on each atom of the system are calculated from first-principles calculations and the temperature is controlled by a thermostat rescaling the atom velocities, or by the calculation of the phonon spectrum of the material (see Chapter 8). The phonon spectrum can be calculated from the forces that arise due to small displacements of selected atoms from their equilibrium positions in the supercell (frozen phonons in the harmonic approximation) [63] or by the linear response theory (density-functional perturbation theory - DFPT) in which the linear-order variation of the electronic charge density can be calculated using the unperturbed wave-functions [64]. From the phonon spectrum, the vibrational free energy can be obtained, and the link can then be made between first-principles calculations and thermodynamic calculations (using CALPHAD for instance), as already widely done for metallic alloys [65]. Phase diagrams, formation energies of compounds, free energy, heat capacity C_v , thermal expansion, etc. can be predicted and can complete thermodynamic database. For actinide compounds, first-principles thermodynamic calculations, using *ab initio* molecular dynamics or phonon spectra calculations, are only an emerging field due to the difficulties to accurately describe the electronic structure of actinide compounds and to the great computational resources required.

Conclusion and future challenges

DFT-based studies of nuclear fuels have much progressed in the last 15 years, in terms of the complexity of the phenomena which can be treated, and in terms of the approximations which have become available for a more accurate description of the electronic structure of actinide compounds. The importance of DFT calculations in the multiscale modelling scheme of fuel materials is now widely recognised.

It is, however, still a challenge for future studies of radiation damage in nuclear fuels to develop and use first-principles methods beyond the local and semi-local approximations for the exchange-correlation interaction, in particular without a parameterised term to account for the strong correlations. The use of the DFT+DMFT method coupled to the Random Phase Approximation (RPA) [66] is promising to this respect.

References

- [1] Hohenberg, P., W. Kohn (1964), *Physical Review*, 136, B864.
- [2] Kohn, W., L. J. Sham (1965), *Physical Review*, 140, A1133.
- [3] Monkhorst, H.J., J.D. Pack (1976), *Physical Review B*, 13, 5188.
- [4] Bachelet, G.B., D.R. Hamann, M. Schlüter (1982), *Physical Review B*, 26, 4199.
- [5] Payne, M.C., M.P. Teter, D.C. Allan, T.A. Arias, J.D. Joannopoulos (1992), *Reviews of Modern Physics*, 64, 1045.
- [6] Blöchl, P. (1994), *Physical Review B*, 50, 17953.
- [7] Herring, C. (1940), *Physical Review*, 57, 1169.
- [8] Schwarz, K., P. Blaha, G.K.H. Madsen (2002), *Computer Physics Communications*, 147.
- [9] Williams, A.R., J. Kübler, C.D. Gelatt (1979), *Physical Review B*, 19, 6094.
- [10] Andersen, O.K. (1975), *Physical Review B*, 12.
- [11] Korringa, J. (1947), *Physica*, 13, 392.
- [12] Kohn, W., N. Rostoker (1954), *Physical Review*, 94, 1111.
- [13] <http://cms.mpi.univie.ac.at/vasp/>.
- [14] <http://www.abinit.org>.
- [15] Hedin, L., B.I. Lundqvist (1971), *Journal of Physics C*, 4, 2064.
- [16] von Barth, U., L. Hedin (1972), *Journal of Physics C: Solid State Physics* 5, 1629.
- [17] Vosko, S.H., L. Wilk, M. Nusair (1980), *Can. Journal of Physics*, 58, 1200.
- [18] Ceperley, D.M., B.J. Alder (1980), *Physical Review Letter*, 45, 566.
- [19] Perdew, J.P., A. Zunger (1981), *Physical Review B*, 23, 5048.
- [20] Koch, W., M.C. Holthausen (2001), *A Chemist's Guide to Density Functional Theory*, 2nd edition, Wiley VCH Verlag GmbH.
- [21] Perdew, J.P., K. Burke, M. Ernzerhof (1996), *Physical Review Letter*, 77, 3865.
- [22] Perdew, J.P., Y. Wang (1992), *Physical Review B*, 45, 13244.
- [23] Perdew, J.P., A. Zunger (1981), *Physical Review B*, 23, 5048.
- [24] Svane, A. (1996), *Physical Review B*, 53, 4275.
- [25] Svane, A., L. Petit, Z. Szotek, W.M. Temmerman (2007), *Physical Review B*, 76, 115116.
- [26] Petit, L., A. Svane, Z. Szotek, W.M. Temmerman, G.M. Stocks (2010), *Physical Review B*, 81, 045108.
- [27] Petit, L., A. Svane, Z. Szotek, W.M. Temmerman, G.M. Stocks (2009), *Physical Review B*, 80, 045124.

- [28] Anisimov, V.I., F. Aryasetiawan, A.I. Liechtenstein (1997), *Journal of Physics: Condensed Matter*, 9, 767.
- [29] Czyzyk, M.T., G. Sawatzky (1994), *Physical Review B*, 49, 14211.
- [30] Petukhov, A.G., I.I. Mazin, L. Chioncel, A.I. Lichtenstein (2003), *Physical Review B*, 67, 153106.
- [31] Dudarev, S.L., G.A. Botton, S.Y. Savrasov, C.J. Humphreys, A.P. Sutton (1998), *Physical Review B*, 57, 1505.
- [32] Liechtenstein, A.I., V.I. Anisimov, J. Zaane (1995), *Physical Review B*, 52, R5467.
- [33] Cococcioni, M., S. de Gironcoli (2005), *Physical Review B*, 71, 035105.
- [34] Aryasetiawan, F., K. Karlsson O. Jepsen, U. Schönberger (2006), *Physical Review B*, 74, 125106.
- [35] Kotani, A., H. Ogasawara (1993), *Physica B*, 186, 16.
- [36] Dorado, B., G. Jomard, M. Freyss, M. Bertolus (2010), *Physical Review B*, 82, 035114.
- [37] Yun, Y., H. Kim, H. Kim, K. Park (2005), *Nuclear Engineering and Technology*, 37, 293.
- [38] Gryaznov, D., E. Heifets, D. Sedmidubsky (2010), *Physical Chemistry Chemical Physics*, 12, 12273.
- [39] Dorado, B., P. Garcia, G. Carlot, M. Fraczkiewicz, B. Pasquet, M. Freyss, M. Bertolus, G. Baldinozzi, D. Siméone (2011), *Physical Review B*, 83, 035126.
- [40] Andersson, D.A., T. Watanabe, C. Deo, B.P. Uberuaga (2009), *Physical Review B*, 80, 060101.
- [41] Becke, A.D. (1993), *Journal of Chemical Physics*, 98, 5648.
- [42] Ernzerhof, M., G.E. Scuseria (1999), *Journal of Chemical Physics*, 110, 5029.
- [43] Heyd, J., G.E. Scuseria (2004), *Journal of Chemical Physics*, 121, 1187.
- [44] Prodan, I.D., G.E. Scuseria, R.L. Martin (2006), *Physical Review B*, 73, 045104.
- [45] Novák, P., J. Kunes, L. Chaput, W.E. Pickett (2006), *Physica Status Solidi B*, 243, 563.
- [46] Jollet, F., G. Jomard, B. Amadon, J.P. Crocombette, D. Torumba (2009), *Physical Review B*, 80, 235109.
- [47] Crocombette, J.P., D. Torumba, A. Chartier (2011), *Physical Review B*, 80, 184107.
- [48] Larson, P., W.R.L. Lambrecht, A. Chantis, M. van Schilfgaarde (2007), *Physical Review B*, 75, 045114.
- [49] Amadon, B., F. Jollet, M. Torrent (2008), *Physical Review B*, 77, 155104.
- [50] Jomard, G., B. Amadon, F. Bottin, M. Torrent (2008), *Physical Review B*, 78, 075125.
- [51] Dorado, B., B. Amadon, M. Freyss, M. Bertolus (2009), *Physical Review B*, 79, 235125.
- [52] Meredig, B., A. Thompson, H.A. Hansen, C. Wolverton, A. van de Walle (2010), *Physical Review B*, 82, 195128.

-
- [53] Geng, H.Y., Y. Chen, Y. Kaneta, M. Kinoshita, Q. Wu (2010), *Physical Review B*, 82, 094106.
 - [54] George, A., G. Kotliar, W. Krauth, M.J. Rozenburg (1996), *Reviews of Modern Physics*, 68, 13.
 - [55] Amadon, B., F. Lechermann, A. Georges, F. Jollet, T.O. Wehling, A.I. Lichtenstein (2008), *Physical Review B*, 77, 205112.
 - [56] Hirsch, J.E., R.M. Fye (1986), *Physical Review Letter*, 56, 2521.
 - [57] Shick, A.B., J. Kolorenč, A.I. Lichtenstein, L. Havela (2009), *Physical Review B*, 80, 085106.
 - [58] Dion, M., H. Rydberg, E. Schröder, D.C. Langreth, B.I. Lundqvist (2004), *Physical Review Letter*, 92, 246401.
 - [59] Vydrov, O.A., T. van Voorhis (2009), *Physical Review Letter*, 103, 063004.
 - [60] Grimme, S. (2010), *Journal of Chemical Physics*, 132, 154104.
 - [61] Silvestrelli, P.L. (2008), *Physical Review Letter*, 100, 053002.
 - [62] Kim, H., J.-M. Choi, W.A. Goddard (2012), *Journal of Physical Chemistry Letters*, 3, 360.
 - [63] Parlinski, K., Z.Q. Li, Y. Kawazoe (1997), *Physical Review Letter*, 78, 4063.
 - [64] Baroni, S., P. Gianozzi, A. Testa (1987), *Physical Review Letter*, 58, 1861.
 - [65] Turchi, P.E.A. et al. (2007), *Computer Coupling of Phase Diagrams and Thermochemistry*, 31, 4.
 - [66] Ren, X., P. Rinke, C. Joas, M. Scheffler (2012), *Journal of Materials Science*, 47, 7447.

Chapter 13.

Classical molecular dynamics simulation of nuclear fuels

R. Devanathan¹, M. Krack², M. Bertolus³

¹Pacific Northwest National Laboratory, US,

²Paul Scherrer Institute, Switzerland,

³CEA, DEN, DEC, Centre de Cadarache, France

Abstract

Molecular dynamics simulation using forces calculated from empirical potentials, commonly called classical molecular dynamics, is well suited to study primary damage production by irradiation, defect interactions with fission gas atoms, gas bubble nucleation, grain boundary effects on defect and gas bubble evolution in nuclear fuel, and the resulting changes in thermomechanical properties. This enables one to obtain insights into fundamental mechanisms governing the behaviour of nuclear fuel, as well as parameters that can be used as inputs for mesoscale models. The interaction potentials used for the force calculations are generated by fitting properties of interest to experimental data and electronic structure calculations (see Chapter 12). We present here the different types of potentials currently available for UO₂ and illustrations of applications to the description of the behaviour of this material under irradiation. The results obtained from the present generation of potentials for UO₂ are qualitatively similar, but quantitatively different. There is a need to refine these existing potentials to provide a better representation of the performance of polycrystalline fuel under a variety of operating conditions, develop models that are equipped to handle deviations from stoichiometry, and validate the models and assumptions used.

Introduction

Classical molecular dynamics (CMD) simulation of nuclear fuel occupies an important niche between more accurate but computationally intensive density functional theory (DFT) studies that are restricted to a few hundred atoms and coarse grained mesoscale models that have to be extensively parameterised [9]. In the study of nuclear fuel, CMD can shed light on the primary damage state produced by energetic recoils and thermal spikes in single and polycrystalline materials; point defect accumulation, clustering, and interaction with grain boundaries and impurities [23], fission gas bubble formation and

resolution [20]; and changes in the thermal conductivity and mechanical properties under prolonged irradiation [24].

At the core of the CMD method is the interatomic potential, also known as the force field. It is a mathematical function that describes the interaction energy between the atoms/ions in the simulation and is parameterised based on available data from experiment and DFT. At present, CMD simulations can be used to study systems of ~ 10 million atoms for 1 ns or smaller systems for 1 μ s. This report will focus on UO₂, because most of the simulation studies to date have examined UO₂. These simulations of point defect clusters, fission products and gas bubbles in polycrystalline nuclear fuel can be used to establish defect and gas bubble distributions and thermodynamic parameters as input for mesoscopic simulations capable of approaching longer time and length scales. Thus, CMD simulations have a crucial role to play in studies of fission gas bubble evolution, and changes in microstructure and thermomechanical behaviour of irradiated fuel.

Empirical potentials

The use of empirical potentials to model nuclear fuel was initiated more than half a century ago [4]. The potential energy of a system of n atoms with coordinates r_i, r_j, \dots, r_n can be written in terms of one-, two-, and many-body terms as:

$$V(r) = \sum_i^n V_1(r_i) + \sum_i^n \sum_{j>i}^n V_2(r_i, r_j) + \sum_i^n \sum_{j>i}^n \sum_{k>j>i}^n V_3(r_i, r_j, r_k) + \dots \quad (1)$$

Four-body and higher terms make a smaller contribution to $V(r)$ but become more computationally expensive. Even an explicit evaluation of three-body terms is often avoided, which is a common approximation performed for ceramic materials with a dominantly ionic character like UO₂. This reduces the computational effort significantly. For materials, however, which exhibit a pronounced covalent bonding character like silicon carbide (SiC), an explicit inclusion of three-body terms is required. However, an implicit inclusion of average three-body (and even higher) effects is often performed via an effective pair potential as follows. This is the case for most UO₂ empirical potentials.

$$V(r) \approx \sum_i^n V_1(r_i) + \sum_i^n \sum_{j>i}^n V_2^{eff}(r_{ij}) \quad \text{with } r_{ij} = |r_i - r_j| \quad (2)$$

The effective potential $V_2^{eff}(r_{ij})$ can be decomposed into long-range Coulombic interaction of the ionic particles and a short-range part.

$$V_2^{eff}(r_{ij}) = V_{LR}(r_{ij}) + V_{SR}(r_{ij}) \quad (3)$$

The long-range term, $V_{LR}(r_{ij})$, between charges q_i and q_j separated by distance r_{ij} is given in atomic units by:

$$V_{LR}(r_{ij}) = \frac{q_i q_j}{r_{ij}}. \quad (4)$$

Fission gas atoms are considered neutral ($q_i = 0$) and their interactions with each other and with U and O typically include only short-range repulsion and dispersion interactions [12]. The short-range part can be written as a sum of three terms as follows:

$$V_{SR}(r_{ij}) = A_{ij} e^{-B_{ij}r_{ij}} - \frac{C_{ij}}{r_{ij}^6} + D_{ij} \left[e^{-2\beta_{ij}(r_{ij}-r_{ij}^0)} - 2e^{-\beta_{ij}(r_{ij}-r_{ij}^0)} \right] \quad (5)$$

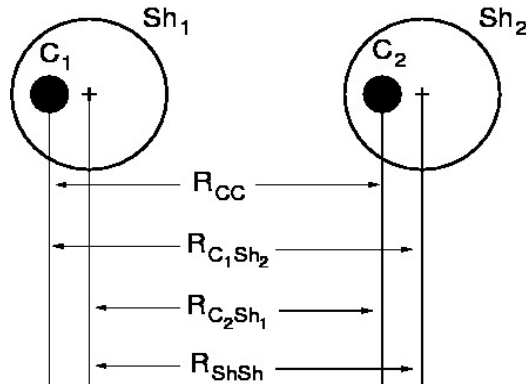
The first term represents Pauli repulsion, the second dispersion, and the third covalency. An additional repulsive potential term for short interatomic distances is used in collision cascade simulations for technical reasons due to the potentially high kinetic energy of some atoms, e.g., the potential, $V_{ZBL}(x)$, of Ziegler, Biersack, and Littmark [28]. If Z_i and Z_j are the atomic numbers of two atoms and a_0 is the Bohr radius, then the repulsive potential fitted to an universal screening function can be expressed as:

$$V_{ZBL}(x) = 0.1818e^{-3.2x} + 0.5099e^{-0.9423x} + 0.2802e^{-0.4029x} + 0.02817e^{-0.2016x} \quad (6)$$

$$\text{with } x = \frac{r_{ij}(Z_i^{0.23} + Z_j^{0.23})}{0.8854a_0}. \quad (7)$$

Interatomic potentials available for UO_2 can be broadly classified [13] as rigid-ion models or core-shell models. The former treat ions as point charges, while the latter include ionic polarisability by considering ions as cores connected to charged shells [10]. In the latter formalism, each ion is represented by two particles of opposite charge, namely a core and a shell particle which are linked by a (typically harmonic) spring. The core particle is a massive point, which is much heavier than the shell particle as it represents the nucleus and its inner (filled) electron shells, whereas the shell particle represents the valence electrons. Consequently, the lighter shell particle moves much faster than the core particle and thus it mimics the motion of the outer valence electrons. In this way, the shell particle responds quickly to changes in the electric field acting on the ion and due to the opposite charges of core and shell particles a dipole is created which can describe the polarisation of the electron cloud by the external electric field. Due to the split of each ion into two particles, four interactions instead of one interaction per atom pair have to be evaluated, as shown in Figure 1. However, the short-range interatomic potential acts only between the shell particles to reduce the computational effort for the non-bonded interactions. The electrostatic interaction between a core and its own shell is explicitly excluded.

Figure 1. Illustration of the interactions in the core-shell model



C and Sh stand for Core and Shell, respectively while R represents distance.

There are two variants of the core-shell model. The original core-shell model of Dick and Overhauser [10] employs massless shells. The shells follow instantaneously their respective cores. This requires a tight optimisation of the shells to their zero-force positions for each atomic configuration, e.g., in each time step of a molecular dynamics (MD) run. A significant computational overhead is introduced due to the iterative optimisation of the shell positions. Unfortunately, small energy drifts are observed even for tight optimisation settings due to small residual forces. In the adiabatic (dynamical) core-shell model, the shells are treated as particles with very small mass compared to the mass of the corresponding core particle. The sum of core and shell mass is given by the actual atomic mass. The shells are treated as fictitious dynamical variables in the spirit of the Car-Parrinello method and explicit dynamics is also imposed for the shell particles. Core and shell particles are propagated concurrently in each MD time step. However, the MD time step is limited by the core-shell motion. This requires smaller MD time steps compared to rigid-ion models to ensure the adiabaticity. On the other hand, an explicit thermostat for the shell particles can be applied which allows for CMD runs at higher target temperatures.

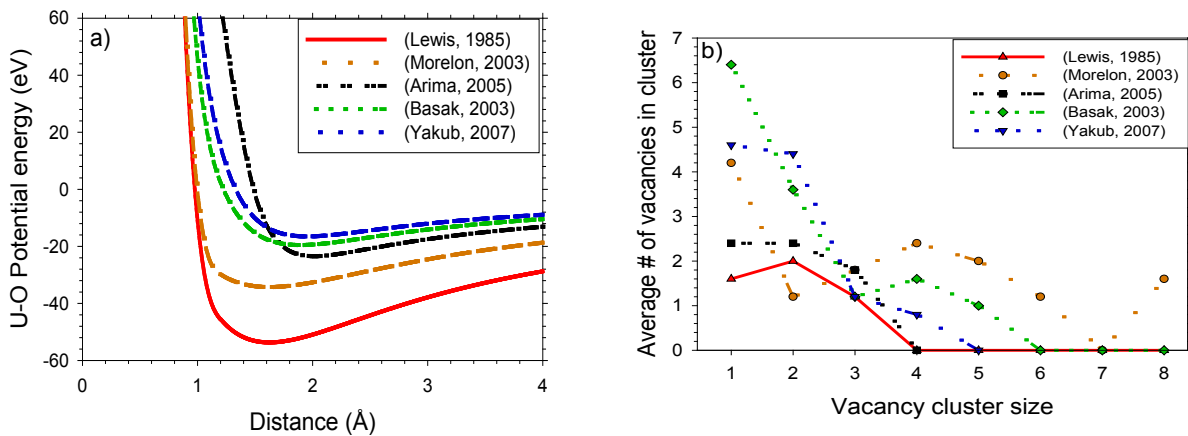
The shell-core interaction can become unstable in simulations of energetic processes [6]. A polarisation catastrophe can occur [5] when dynamic processes drive two ions to approach each other closely. At short separations, the strong Coulomb attraction between the core of one ion and the shell with opposite charge of a nearby ion can cause a structural collapse. This possibility limits core-shell potentials to low-temperature simulations and restricts the simulation of displacement cascades and thermal spikes.

Rigid-ion potentials are less computationally intensive than core-shell models and offer greater stability for dynamic simulations. In these models, the ions can be assigned formal charges (+4 for U and -2 for O) or partial charges based on the best fit to experimental data. The shell models give a better representation of the equilibrium properties including the elastic constants in static calculations [13]. However, rigid-ion potentials with non-formal charges have been shown to provide the best fit to the melting temperature and the change in lattice parameter and mechanical properties with changing temperature [14].

Since the use of shell model potentials in MD simulations of highly energetic non-equilibrium processes is limited, the rest of this discussion will focus on rigid-ion potentials. The form of the U-O interaction for five rigid-ion potentials is shown in Figure 2(a). Potentials have also been developed for mixed oxide fuel [26], hypostoichiometric $(U,Pu)O_{2-x}$ solid solutions, and hyperstoichiometric UO_{2+x} fuel [27]. A shortcoming of many of these potentials is that the dispersion term results in an unrealistic attractive interaction for small values of r_{ij} , typically less than 1 Å. This is remedied in an *ad hoc* fashion by splining V_{ij} to a repulsive potential, such as the Ziegler-Biersack-Littmark potential [28] for $r_{ij} < 1$ Å as discussed previously. In an effort to overcome the ambiguity created by the choice of the functional form and range of operation of the spline, interaction potentials valid for all values of r_{ij} have been developed for $(U,Pu,Np)O_2$ by fitting to a database of energies of different structures calculated using DFT [22]. The potentials reproduce the experimental results for the variation of lattice constants and enthalpy with temperature from 300 to 1 500 K.

Molecular statics calculations of defect energies [5] have shown large variations in the calculated values depending on the choice of potential. The Schottky defect formation energy varies from 2.5 to 8.2 eV, while the corresponding value from DFT with the Hubbard U correction (DFT+U) is 4.6-6.4 eV and the experimental value is about 6.5 eV [5]. The oxygen vacancy migration energy was found to be in the range of 0.0-0.6 eV as opposed to DFT+U value of 0.7 eV [5]. Dynamic simulations of the pre-melting transition [11], melting and defect creation by 1 keV recoils in UO_2 using five different rigid-ion potentials [16,3,19,1,25] have also revealed significant differences in the size, spatial distribution and clustering of defects [8]. Figure 2(b) shows that the Lewis potential produces fewer vacancies and small clusters while the Morelon potential produces nearly three times as many vacancies and much larger vacancy clusters. Since potentials are not fitted to properties that affect thermal conductivity, many existing potentials reproduce the experimental value of the thermal conductivity of UO_2 poorly [7]. There is no potential for UO_2 that is uniformly superior, and the choice of potential is based on the reproduction of experimental or DFT data for the property of interest, such as melting temperature, oxygen vacancy migration energy, coefficient of thermal expansion, or thermal conductivity.

Figure 2. (a) U-O interaction energy for five rigid-ion potentials, (b) the average number of vacancies in clusters containing one to eight vacancies produced by 1 keV U recoils in UO_2 for these potentials



Calculation of thermal properties

Classical molecular dynamics enables the calculation of the heat capacity and thermal conductivity. A detailed review of the results obtained for the thermal properties is given in [5]. The value of heat capacity at constant pressure calculated by CMD simulation of UO_2 shows good agreement with experimental results, while there is some discrepancy between CMD simulation and experiment for PuO_2 [1].

The calculation of thermal conductivity (κ) in MD simulations can be accomplished by equilibrium molecular dynamics (EMD) using the Green-Kubo relationship based on the fluctuation dissipation theorem [27] or by non-equilibrium molecular dynamics (NEMD). CMD simulations tend to overestimate the thermal conductivity of UO_2 and PuO_2 at room temperature), but the agreement with experimental data is improved in the temperature range 800 to 2 000 K [1,15]. EMD simulations of UO_{2+x} show that κ decreases with increasing temperature in the range of temperature from 900 to 2 000 K and oxygen parameter x ranging from 0 to 0.09 [27]. The change in κ with x was attributed to scattering by excess oxygen ions, while the temperature dependence for $x = 0$ was attributed to the anharmonic Umklapp process. In real nuclear fuel, the thermal conductivity will also be influenced by voids, bubbles, grain boundaries and extended defects, which have been mostly neglected in simulations to date. A recent NEMD simulation has made a start in this direction by considering polycrystalline, albeit pure, UO_2 [24].

Simulation of radiation damage

Simulations of radiation damage in UO_2 have been recently reviewed [9]. CMD simulations of primary damage in pure monocrystalline UO_2 induced by recoils with energy from 1 to 80 keV reveal that there is no amorphisation [17,9]. The damage consists mainly of point defects and defect clusters. The effect of temperature on damage in the temperature range from 300 to 700 K was found to be minimal. Due to the high mobility of oxygen vacancies, oxygen defect annihilation is effective and residual oxygen defects combine with uranium defects that are immobile on the picoseconds time scale to form neutral clusters. Vacancy clusters were found to be larger on the average than the interstitial clusters, and the size of the largest defect clusters was found to increase linearly with the number of 10 keV overlapped recoils (or their dimension was found to increase following the number of recoils with a power law with an exponent of 1/3) [17]). The observed characteristics of defect clusters may be specific to the potential used in this work. CMD studies of 1 keV displacement cascades in UO_2 with five different potentials have shown drastically different vacancy and interstitial distributions [8]. It has been observed that the damaged region lies within a volume that varies with recoil energy according to a power law with exponent of 3/2, and this has been attributed to the multifractal nature of the damage zone [18]. Studies of displacement damage by 0.4 to 10 keV recoils in pure monocrystalline UO_2 using two different potentials show that the damage becomes more isotropic with increasing energy [6]. Simulations of 10 keV recoils directed perpendicular to the interface in UO_2 bicrystals show that the nature of the interface plays an important role in displacement damage evolution [23]. More defects were found in the grain interior than were observed in UO_2 monocrystals under the same conditions. Vacancies appear to be preferentially created in the grain interior while interstitials prefer the grain boundaries [23]. The grain boundaries become more disordered due to point defect accumulation [9].

Swift heavy ion damage in nuclear fuel can be simulated using a simple thermal spike model that represents the deposition of electronic energy in the material by a cylinder of radius of 3 to 6 nm within which all the atoms are given excess kinetic energy corresponding to a certain value of electronic stopping (dE/dx). Simulation of spikes with dE/dx between 4 and 66 keV/nm [9] reveals the primary damage state to be isotropic as reported based on displacement cascade simulations [6]. The threshold value of dE/dx to create point defects appears to be between 4 and 16 keV/nm. For dE/dx value of 66 keV/nm, stable dislocation loops are produced. However, these simulations do not take into account electron-phonon coupling.

Modelling fission gas bubbles

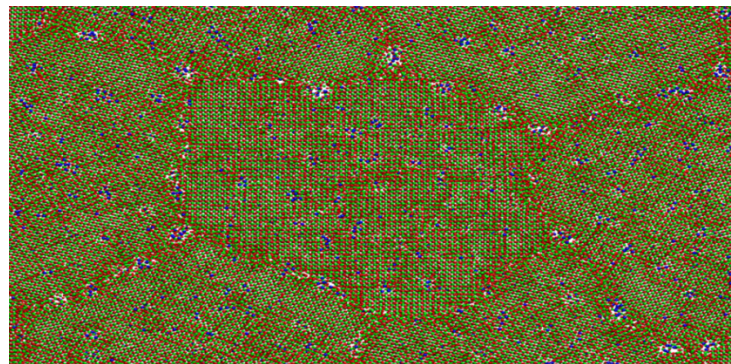
The restructuring of nuclear fuel has been related to gas bubble formation. Fission gas atoms (Xe and Kr) are insoluble in UO_2 and give rise to lattice strain. CMD simulations of Xe clustering in UO_2 show that the bubble geometry is favoured, but planar clusters are possible. In these clusters, Xe exists in a liquid state. When the Xe is released, a planar loop is left behind [12]. This has been attributed to the mechanical stability of solid UO_2 . Recently, CMD simulation has been used to study the formation of Xe clusters from isolated Xe atoms in polycrystalline UO_2 containing a supersaturation of Schottky defects, which served to enhance Xe mobility over the CMD time scale [20]. The simulation cell was made of uniform columnar grains with a grain diameter of 20 nm and it was maintained at 2 500 K for several nanoseconds. The elevated temperature was needed to ensure defect mobility in this short timescale. The Xe atoms agglomerated into clusters with the largest cluster containing 8 Xe atoms. There was no appreciable difference in cluster distribution between the grain interior and bulk, as shown in Figure 3, and grain boundary motion was not a factor in Xe aggregation at this early stage of bubble nucleation [20]. Recently, CMD simulations have identified a thermodynamic driving force for Xe bubble nucleation arising from the decrease in free energy of Xe in bubbles compared to Xe incorporated at point defects [21]. The variation of free energy of Xe in small bubbles (0.6 nm in radius) with Xe density was found to be different from that in pure Xe. Such simulations provide insights into transient processes over short length scales that are not easily accessed by experiment. Much work remains to be done in modelling fission gas evolution in polycrystalline UO_2 . In order to extend these studies to realistic grain sizes (tens of μm) and timescales (second), there is a need to connect with mesoscale models through parameter passing.

Validation of molecular dynamics simulations

The use of empirical potential-based simulations to shed light on physical processes in complex driven systems requires a thorough understanding of the approximations inherent in the models and the limitations of the methods employed. A potential that will satisfactorily reproduce all the relevant properties of irradiated nuclear fuel appears, however, to be out of reach at present, and one has to judiciously choose a potential that is tailored to a subset of properties of interest for the simulation. It is, in addition, essential to establish the validity of the simulation by comparing to experimental data or results of more accurate calculations, e.g., DFT, for the property of interest [5]. Experimental data from neutron and X-ray diffraction, spectroscopy, and microscopy are often not readily available for making direct comparisons. Uncertainties in measurement

need to be understood while validating simulation data. If the relevant experimental dataset is not available, more accurate calculations on representative model systems and DFT (or DFT+U) data from the literature can be used to validate CMD simulations. By the same logic, CMD simulations can be used to validate coarser grained simulations and continuum models. Ultimately, the comparison between calculated and experimental results on the behaviour of defects and fission products in nuclear fuel is challenging due to the need for a detailed knowledge of the experimental conditions and may involve the use of additional models. Such comparisons are quite useful in the interpretation of experimental results and determination of elementary mechanisms [5].

Figure 3. Distribution of Xe bubble nuclei and voids in polycrystalline UO₂ from CMD simulation [20]



Xe, U, and O are represented in blue, green and red, respectively.

Conclusions and future challenges

Molecular dynamics simulation using empirical potentials is an invaluable method for simulating energetic recoil and swift heavy ion damage, fission gas bubble evolution, and changes in thermomechanical properties in polycrystalline nuclear fuel. Mixed oxide fuel and deviations from stoichiometry can be simulated with existing potentials. However, there is a need to improve interatomic potentials by considering more complex functional forms and fitting to data from electronic structure calculations and experiments to predict properties relevant to nuclear fuel performance, such as thermal conductivity. There is also a need to improve our understanding of fission product diffusion, fission gas bubble nucleation, growth, re-solution, microstructural response and evolution of thermomechanical properties. One needs to understand the underlying assumptions and limitations of the model used and validate the results using experimental data or more accurate calculations for model systems. Molecular dynamics simulations can serve as a bridge between density functional theory and continuum models. With constant improvement in computational power and algorithms for linking models, the prospect of realistic modelling of nuclear fuel starting at the atomistic level is growing brighter.

Acknowledgements

R. Devanathan was supported by the US Department of Energy (DOE) Nuclear Energy Advanced Modeling and Simulation (NEAMS) program at Pacific Northwest National Laboratory – a multiprogram laboratory operated for DOE by Battelle.

References

- [1] Arima, T. et al. (2005), “Evaluation of thermal properties of UO_2 and PuO_2 by equilibrium molecular dynamics simulations from 300 to 2000 K”, *Journal of Alloys and Compounds*, 400, 43.
- [2] Arima, T. et al. (2007), “Evaluation of thermal conductivity of hypostoichiometric ($\text{U}, \text{Pu}\text{O}_{2-x}$) solid solution by molecular dynamics simulation at temperatures up to 2000 K”, *Journal of Alloys and Compounds*, 415, 43.
- [3] Basak, C.B. et al. (2003), “Classical molecular dynamics simulation of UO_2 to predict thermophysical properties”, *Journal of Alloys and Compounds*, 360, 210.
- [4] Benson, G.C. et al. (1963), “Calculation of cohesive and surface energies of thorium and uranium dioxides”, *Journal of the American Ceramic Society*, 46, 43.
- [5] Bertolus, M. et al. (2014), “Assessment of current atomic scale modelling methods for the investigation of nuclear fuel under irradiation: Example of uranium dioxide”, NEA Report, *Multi-scale Modelling of Nuclear Fuels*.
- [6] Bishop, C.L. et al. (2010), “Establishing the isotropy of displacement cascades in UO_2 through molecular dynamics simulation”, *Nuclear Instruments and Methods in Physics Research B*, 268, 2915.
- [7] Chernatynskiy, A. et al. (2012), “Critical assessment of UO_2 classical potentials for thermal conductivity calculations”, *Journal of Materials Science*, 47, 7693.
- [8] Devanathan, R. et al. (2009), “Energetic recoils in UO_2 simulated using five different potentials”, *Journal of Chemical Physics*, 130, 174502.
- [9] Devanathan, R. et al. (2010), “Modeling and simulation of nuclear fuel materials”, *Energy and Environmental Science*, 3, 1406.
- [10] Dick Jr., B.G., A.W. Overhauser (1958), “Theory of the dielectric constants of alkali halide crystals”, *Physical Review*, 112, 90.
- [11] Dworkin, A.S., M.A. Bredig (1968), “Diffuse Transition and melting in fluorite and anti-fluorite type of compounds: Heat content of potassium sulfide from 298 to 1260 K”, *Journal of Physical Chemistry*, 72, 1277.
- [12] Geng, H.Y. et al. (2007), “Molecular dynamics study on planar clustering of xenon in UO_2 ”, *Journal of Alloys and Compounds*, 457, 465.
- [13] Govers, K. et al. (2007), “Comparison of interatomic potentials for UO_2 . Part I: Static calculations”, *Journal of Nuclear Materials*, 366, 161.
- [14] Govers, K. et al. (2008), “Comparison of interatomic potentials for UO_2 . Part II: Molecular dynamics simulations”, *Journal of Nuclear Materials*, 376, 66.

- [15] Kurosaki, K. et al. (2001), “Molecular dynamics study of mixed oxide fuel”, *Journal of Nuclear Materials*, 294, 160.
- [16] Lewis, G.V., C.R.A. Catlow (1985), “Potential models for ionic oxides”, *Journal of Physics C: Solid State Physics*, 18, 1149.
- [17] Martin, G. et al. (2010), “Irradiation-induced heterogeneous nucleation in uranium dioxide”, *Physical Letter A*, 374, 3038.
- [18] Martin, G. et al. (2011), “Effect of the cascade energy on defect production in uranium dioxide”, *Nuclear Instruments and Methods in Physics Research B*, 269, 1727.
- [19] Morelon, N.D. et al. (2003), “A new empirical potential for simulating the formation of defects and their mobility in uranium dioxide”, *Philosophical Magazine*, 83, 1533.
- [20] Moore, E. et al. (2011), “Molecular dynamics simulation of Xe bubble nucleation in nanocrystalline UO₂ nuclear fuel”, *Journal of Nuclear Materials*, 419, 140.
- [21] Murphy, S.T. et al. (2012), “Free energy of Xe incorporation at point defects and in nanovoids and bubbles in UO₂”, *Physical Review B*, 85, 144102.
- [22] Tiwary, P. et al. (2011), “Interatomic potentials for mixed oxide and advanced nuclear fuels”, *Physical Review B*, 83, 094104.
- [23] Van Brutzel, L., E. Vincent-Aublant (2008), “Grain boundary influence on displacement cascades in UO₂: A molecular dynamics study”, *Journal of Nuclear Materials*, 377, 522.
- [24] Watanabe, T. et al. (2008), “Thermal transport properties of uranium dioxide by molecular dynamics simulations”, *Journal of Nuclear Materials*, 375, 388.
- [25] Yakub, E. et al. (2007), “Molecular dynamics simulation of pre-melting and melting phase transitions in stoichiometric uranium dioxide”, *Journal of Chemical Physics*, 127, 094508.
- [26] Yamada, K. et al. (2000), “Evaluation of thermal properties of mixed oxide fuel by molecular dynamics”, *Journal of Alloys and Compounds*, 307, 1.
- [27] Yamasaki, S. et al. (2007), “Evaluation of thermal conductivity of hyperstoichiometric UO_{2+x} by molecular dynamics simulation”, *International Journal of Thermophysics*, 28, 661.
- [28] Ziegler, J. et al. (1985), *The Stopping and Range of Ions in Matter*, Pergamon, New York.

Chapter 14.

Assessment of current atomic scale modelling methods for the investigation of nuclear fuels under irradiation: Example of uranium dioxide

M. Bertolus¹, M. Krack², M. Freyss¹, R. Devanathan³

¹CEA, DEN, DEC, Centre de Cadarache, France,

²Paul Scherrer Institute, Switzerland,

³Pacific Northwest National Laboratory, US

Introduction

Why do we need to validate atomic scale methods for the description of structural materials and nuclear fuel?

Multi-scale approaches are developed to build more physically based kinetic and mechanical mesoscale models to enhance the predictive capability of fuel performance codes and increase the efficiency of the development of the safer and more innovative nuclear materials needed in the future. Atomic scale methods, in particular electronic structure calculations and empirical potential-based models, form the basis of this multi-scale approach. It is therefore essential to know the accuracy of the results computed at this scale if we want to feed them into higher scale models.

Atomic scale calculations have been used extensively on molecular and solid systems for the last thirty years. Electronic structure calculation methods, and in particular those based on Density Functional Theory (DFT), are powerful tools which yield precise and predictive results for a large number of solid and molecular systems [1-5]. Empirical potential-based methods, especially those associated with the use of molecular dynamics simulations, are effective to investigate thermodynamic and out-of equilibrium properties at finite temperature [6,7,8]. Numerous assessments of these methods have been performed over the years.

The application to nuclear materials under irradiation and especially to fuels, however, is more delicate and calls for bespoke developments. On the one hand, actinide compounds are systems with strongly correlated electrons. This strong correlation, which is due partly to the localisation of the electrons near the nuclei, is difficult to model using standard electronic structure methods and empirical potentials, especially in solids. Newer and more expensive approximations must be used but their applications are limited by

their infrequent implementation in available codes, the efficiency of these codes and the current computational power at our disposal. On the other hand, irradiation induces complex phenomena in materials, in particular the creation of defects and fission products. The study of such complex systems, for which a large number of atoms should be considered, is again limited by the efficiency of the codes used and the available computational resources.

A specific assessment of the atomic scale methods for the description of nuclear fuel under irradiation is therefore necessary.

What do we need to validate?

We need to assess the validity of the main approximations used in atomic scale modelling methods for the description of nuclear materials under irradiation. In particular, three aspects need to be investigated:

- the quality of the description of interatomic interactions using electronic structure or empirical potential methods;
- the validity of the methods used to calculate properties of interest, for instance to simulate radiation damage;
- the effectiveness of the methods employed for the configuration space exploration, which yield the equilibrium structures and the energies of perfect and defective materials, as well as the migration paths between the various stable configurations.

Reference data for the validation

An important question is which reference data should be used for the assessment of the atomic scale methods.

As seen in the chapters on density functional theory and empirical potentials, atomic scale methods yield equilibrium structures, cohesive energy, defect formation energies, incorporation energies for impurity atoms, migration energies through elementary or more complex processes, thermodynamic and elastic properties. Electronic structure methods also provide information on the electronic and magnetic properties. It is especially important to assess the accuracy of the energies obtained using the atomic scale methods, since these are the main data passed on to higher scale models.

The most obvious choice of reference data seems to be experimental data and an important part of the validation is done by comparing the results of the atomic scale modelling methods with experimental results. Precise experimental results from X-ray diffraction, neutron scattering or absorption, transmission electron microscopy, positron annihilation or Raman spectroscopy, calorimetry or secondary ions mass spectrometry, combined with ion or in-pile irradiations can be used.

But what happens if experimental results are lacking, if these results are uncertain (because of difficulty in obtaining them), if they are derived using several assumptions or models that may be inaccurate, if the comparison between model and experimental results can only be made through models and/or assumptions that may also be inaccurate, or, finally, if simply no technique exists that allows the property of interest to be measured? To design new and more precise experiments to get better data is a possible solution, but

it is not always applicable, either because of cost reasons or because increasing the precision would require advances in specific experimental techniques that may occur over years. Properties to measure which no technique exists may be deduced indirectly, but this generally occurs via the application of a model in which the sought property is an unknown parameter or variable while other parameters or variables are measurable: this implies *a priori* believing in the full validity of the model. An alternative is to validate against more precise calculations, which serve as reference. One of the advantages of this validation method is that specific approximations can be assessed while everything else remains equal. Often, however, reference calculations are not feasible on the systems of interest, especially complex solids. The comparison must then be done on simpler systems related to the systems of interest and the results must be extrapolated. A necessary condition for this type of validation is that a reference method must exist for the study of the specific properties investigated, even if it can only be used on model systems. This type of validation is very often used nowadays on molecular systems. However, these considerations should suffice to show that the validation of atomic level models is far from easy and no universal standard method can be identified.

Objective of the chapter

We focus here on the assessment of the description of interatomic interactions in uranium dioxide using, on the one hand, electronic structure methods, in particular in the Density Functional Theory (DFT) framework, and on the other hand, empirical potential methods. These two types of methods are complementary, the former enabling results to be obtained from a minimal amount of input data and further insight into the electronic and magnetic properties to be achieved, while the latter are irreplaceable for studies where a large number of atoms need to be considered.

We consider basic properties as well as specific ones, which are important for the description of nuclear fuel under irradiation. These are especially energies, which are the main data passed on to higher scale models. For this exercise, we limit ourselves to uranium dioxide (UO_2) because of the extensive amount of studies available on this system.

Assessment of electronic structure calculations for the description of uranium dioxide under irradiation

The DFT method with Hubbard U correction (DFT+U) has been used for several years now and is considered the most suitable one for UO_2 and other systems involving actinides. Therefore we assess this method, instead of standard DFT.

The present assessment is based:

- on the one hand, on three extensive reviews of the application of the DFT+U method (and DFT to a smaller extent) on bulk and defect properties of actinide compounds, especially UO_2 , which were published recently;
 - the assessment of various functionals (DFT, DFT+U) for the description of electronic structure and bulk properties of UO_2 done in the F-BRIDGE European project [9];

- the assessment of DFT and DFT+U for the modelling of nuclear fuel materials by Liu et al. [10], which focuses mainly on UO_2 , but also shows a few results on other actinide compounds;
- the topical review by Dorado et al. [11] on the advances made in first-principles modelling of UO_2 and its point defects;
- on the other hand, on individual studies calculating specific properties which were not included in the above-mentioned reviews.

Bulk uranium dioxide (fluorite phase)

Table 1 shows the results of the calculations by various authors using the Local Density and Generalised Gradient Approximations with the Hubbard U correction (LDA+U and GGA+U) methods of various properties of crystalline UO_2 , namely the cell parameters, the bulk modulus, the cohesive energy and the band gap, as well as the measured values. The results shown in this table are taken from Tables 1 and 2 of the review by Dorado et al. [11] and Table 1 from the article by Liu et al. [10].

Structure: Cell parameter

The fluorite phase is cubic (with $a = b = c$) and the admitted cell parameter measured at room temperature is 5.473 Å [12]. It can be seen from Table 1 that the cell parameter a is calculated to lie between 5.41 and 5.45 Å in LDA+U, and between 5.44 and 5.57 Å in GGA+U. The difference between a and c for several authors is due to the loss of symmetry induced by the approximate $1\mathbf{k}$ antiferromagnetic order considered in the calculations.

A reasonable agreement is observed between the results yielded by DFT+U and experimental data or the results from hybrid functionals or from the Self Interaction Correction (SIC) method despite a quite large span of cell parameters for similar functionals. The results show that calculation parameters beyond the exchange-correlation functional are important. As expected from the well-known overbinding character of LDA functionals [1,13], the bonds are shorter in LDA than GGA. The LDA results are below the experimental values while the GGA ones are mainly above them.

It must be stressed, however, that calculations are done at 0 K while the experimental value is for room temperature. The assumption made for the comparison of calculated and measured values, which is standard in the atomic scale modelling community, is that in solids there is only a relatively small variation of the cell parameter as a function of temperature between 0 and 300 K (see Figure 3).

Bulk modulus

As shown in Table 1 of Dorado et al. [11], the bulk modulus values measured are between 190 and 213 GPa, the most recent experimental value being 207 GPa. As shown in Table 1, the values calculated are between 196 and 222 in LDA+U; and between 180 and 209 in GGA+U, both in reasonable agreement with the experimental values.

Table 1. Properties calculated using DFT+U and LDA+U by various authors, as well as results of reference methods and experimental values

Author Year Approx	Property	a=b (Å)	c (Å)	B (GPa)	E_c (eV)	Gap (eV)
LDA+U						
Geng 2007 [15] LSDA+U		5.44	5.44	208	32.8	1.5
Andersson 2009		5.45	5.45	218		
Gryaznov 2009 LSDA+U		5.46	5.42	196	26.0	1.8
Sanati 2011 [29] LSDA+U		5.45	5.45	221		
Dorado 2013 [25] LSDA+U		5.41	5.41	222	24.8	2.3
GGA+U						
Yun 2005 PBE+U		5.44	5.44	209	20.3	1.8
Iwasawa 2006 PBE+U		5.52	5.47	190		1.8
Gupta 2007 PW91+U		5.52	5.52	209	21.7	1.8
Geng 2007 [15] PBE+U		5.55	5.55	181	28.8	1.6
Nerikar 2009 PW91+U		5.49	5.49			1.9
Gryaznov 2009 PBE+U		5.57	5.51	180	23.0	1.9
Gryaznov 2009 PW91+U		5.56	5.51	183	23.1	1.9
Yu 2009 GGA+U		5.54	5.49		21.2	1.2
Dorado 2009 PBE+U		5.57	5.49	187		2.3
Devey 2011 [26] GGA+U		5.54	5.54	197		2.6
Sanati 2011 [29] PBE+U		5.55	5.55	192		
Thompson 2011 [53] PW91+U		5.54	5.54	188		2.8
Tian 2012 PBE+U		5.55	5.55	192	21.8	2.2
Hybrid functionals						
Prodan 2006 PBE0		5.45	5.45	219		3.1
Prodan 2006 HSE		5.46	5.46	222		2.4
Jollet 2009 EECE		5.51	5.51	199		2.0
Reference methods						
Petit 2010 SIC		5.47	5.47	219		2.6
Experimental		5.47	5.47	190-213	21.9	2.0-2.5

Cohesive energy

One experimental value exists for the cohesive energy of UO_2 : 21.9 eV [14]. Table 1 shows that the LDA+U method yields cohesive energies from 24.8 to 32.8 eV, while GGA+U yields values from 20.3 to 23.1 eV with one isolated high value (28.8 eV by Geng [15]). It can be seen that the GGA results are in rather good agreement with the only available experimental value, the uncertainty on which is not assessed. In addition, the higher values yielded by LDA compared to GGA are consistent with the LDA overbinding character, as it was already the case for the cell parameter. This confirms the good description of UO_2 by the DFT+U method.

Electronic structure: Band gap

The experimental values for the band gap of UO_2 are 2.0 [20], 2.14 [16], 2.3 [17], 2.5 eV [18]. Reference calculations by Yin et al. [19] using the dynamical DFT+DMFT method yield a gap of 2.2 eV.

Table 1 shows that the calculated values lay between 1.5 to 2.8 eV, which is a quite large interval. It must be noted that the band gap width depends strongly on the values of the Hubbard interaction and the exchange parameter (U and J , respectively). In recent calculations, however, U and J are not taken as parameters as they were in earlier calculations, but drawn from experimental results or from the results of *ab initio* calculations. The fact that the gap is correctly reproduced is then an indicator of the correct description of the UO_2 bulk using DFT+U.

Electronic structure: Density of states

The density of states of UO_2 was measured by a combination of bremsstrahlung isochromat, X-ray photoemission and X-ray absorption spectroscopies (BIS, XPS and XAS, respectively) [20,21]. Comparisons between DFT calculations and experimental results were done by Yu et al. using GGA+U [21] and Jollet et al. using LDA+U [22].

As shown in Figure 1 taken from Yu et al., the GGA+U results and the corresponding optical responses agree qualitatively well with the experimental results. The DFT+U method enables one to obtain a correct description of the various bands observed. They also enable one to determine the origin of the various bands and of the hybridisation of the orbitals and to prove that UO_2 is an f-f Mott-Hubbard insulator.

In addition, a reasonable agreement is observed on the densities of states calculated at the DFT+U and DFT+DMFT [19] levels for UO_2 . This confirms the correct description obtained using GGA+U.

Magnetism

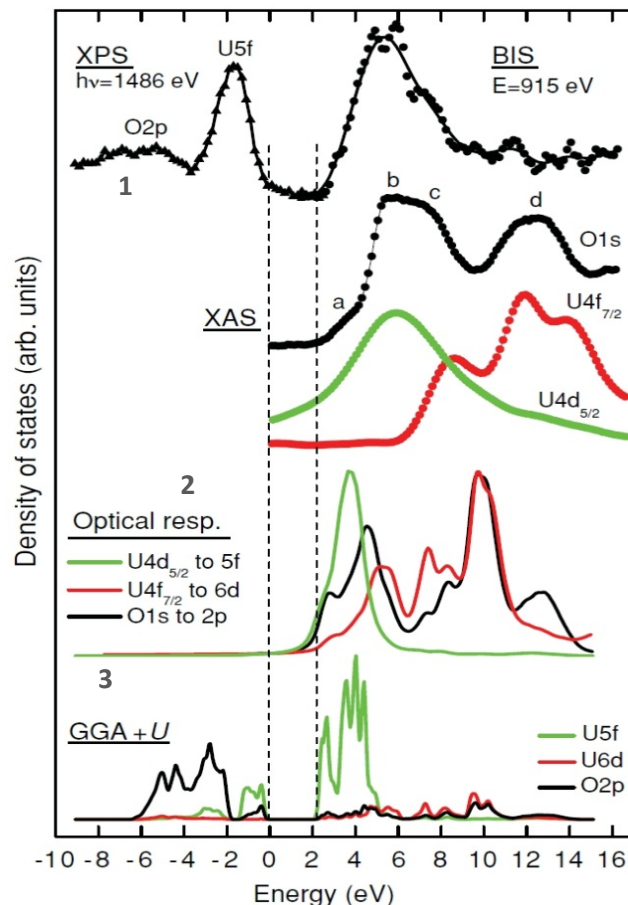
Uranium dioxide is paramagnetic above 30.8 K and antiferromagnetic below this temperature (with a static Jahn-Teller distortion). The exact magnetic ordering of UO_2 at low temperature is complicated and has long been a question of debate. The most recent experimental results indicate that UO_2 exhibits a non collinear **3k** order [23].

There are two detailed studies of the different magnetic phases of UO_2 using DFT+U.

Laskowski et al. [24] calculated the uranium electric field gradients (EFG) in **1k**, **2k** and **3k** antiferromagnetic structures. By comparison between the calculated and experimental EFG he concluded that a **3k** magnetic ordering inducing an additional

deformation of the oxygen cage is observed experimentally. The magnetic moments and the corresponding hyperfine fields agree reasonably well with the experiments. The energetic order between the various phases depends on the U and J and on other calculation parameters but the differences are very small, especially for a U parameter between 4 and 5 eV (~ 0.05 eV / 4 UO_2 units).

Figure 1. Comparison of (1) combination of XPS, BIS and XAS experimental results, (2) GGA + U optical responses for the core levels of O 1s, U 4d $5/2$, and U 4f $7/2$ and (3) GGA + UO_2 p, U 6d and U 5f partial density of states (U = 4.772, J = 0.511 eV) [21]



Dorado et al. [25] studied the **1k** antiferromagnetic, Curie-Weiss paramagnetic and ferromagnetic states of the fluorite phase. They found the paramagnetic phase to be the most stable for the fluorite without the Jahn-Teller distortion, in agreement with the experimental results above 30.8 K. The distorted AFM phase is, in turn, more stable than the non-distorted PM phase, also in agreement with the experimental results below 30.8 K. The results of these two studies show that the DFT+U method enables a correct description of the magnetic properties of bulk UO_2 .

It must be noted that most authors of UO_2 studies consider, especially for the calculation of defect properties, an approximate collinear anti-ferromagnetic order because of the very high computational costs needed for the study of the **3k** AFM or of

the paramagnetic phases. This approximation is justified by the fact that the three magnetic states exhibit only small differences in energy.

Elastic constants

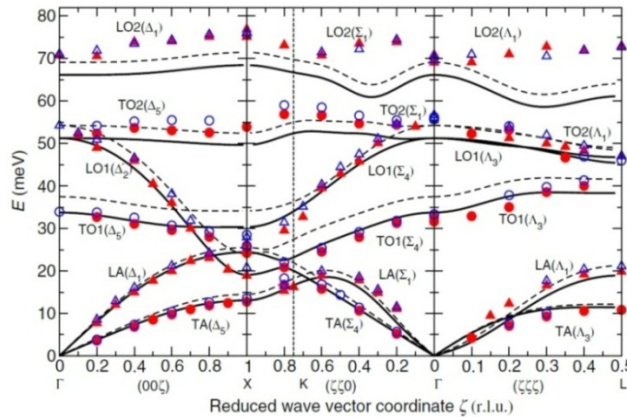
The elastic constants measured for UO_2 , taken from Dorado et al. [11], are shown in Table 2, as well as the values calculated in GGA+U by Devey [26] for the AFM order and by Dorado et al. for the AFM and PM states [25].

Table 2. Elastic constants of UO_2 calculated compared to the available experimental values

Author \ Property	c_{11} (GPa)	c_{12} (GPa)	c_{44} (GPa)
Devey 2011 [26]	361	115	64
Dorado 2013 AFM [11]	401	132	94
Dorado 2013 PM [11]	385	125	68
Exp Wachtmann 1965	396	121	64
Exp Fritz 1976 [75]	389	119	60

The elastic constants calculated are in reasonable agreement with those measured and the agreement improves significantly when a paramagnetic state is considered.

Figure 2. Phonon dispersion curves for the UO_2 fluorite phase calculated using GGA+U at 295 K (dotted lines) and 1 200 K (solid lines) compared to the experimental measurements also at 295 K (blue symbols) and 1 200 K (red symbols) using inelastic neutron scattering [28]



Phonons

The phonon dispersion curves were measured by Dolling in 1965 [27] and much more recently by Pang et al. [28]. Calculations were performed by Devey [26], Sanati et al. [29], Wang et al. [30] and Pang et al. [28]. Figure 2 shows the comparison between the phonon dispersion curves measured and calculated by Pang et al.

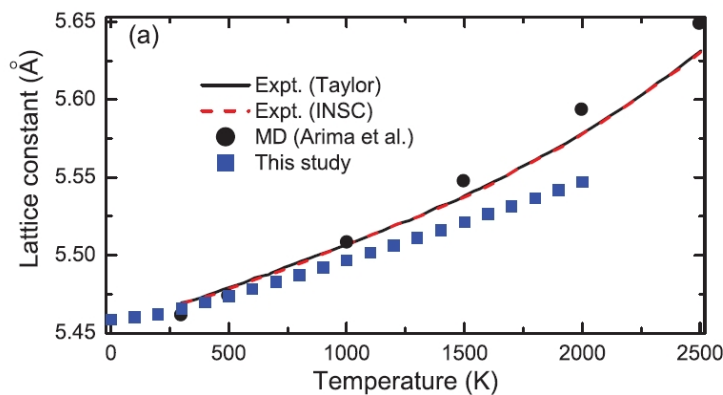
All studies show that the phonon modes and dispersion curves calculated for the UO_2 fluorite phase are in good agreement with available experimental values. They are also in good agreement with the DFT+DMFT results of Yin et al. [31]. Wang et al. have also

shown that the LO-TO splitting at the gamma point is successfully reproduced when the polarisation effects are included.

Finite T properties

Structural and energetic properties of UO_2 were measured and calculated as a function of temperature. First, the evolution of the cell parameter as a function of T was determined experimentally by Taylor [32] and calculated using GGA+U by Wang et al. [30]. The evolution of the bulk modulus was also calculated but no experimental data are available for this parameter.

Figure 3. Temperature dependence of lattice parameter of UO_2 compared to experimental data and results from classical molecular dynamics [30,33]

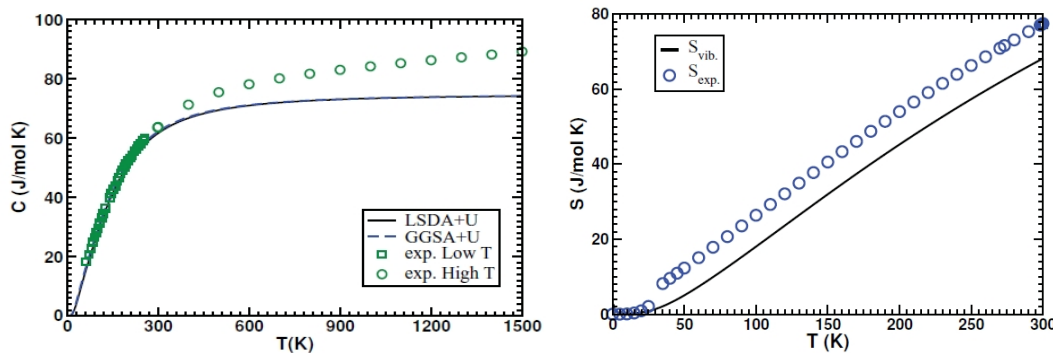


As shown in Figure 3, a good agreement is observed between the experimental and calculated evolution of the lattice parameter in the low-temperature domain. The calculated values, however, are lower than the experimental ones for temperatures higher than 800 K. The differences may come from the thermal electronic contribution and/or anharmonic effects.

Second, the evolution of the specific heat and vibrational entropy as a function of temperature was calculated from the phonon density of states and compared to experiments by Sanati et al. [29] and Wang et al. [30].

Both studies show that the specific heat of the fluorite UO_2 as calculated is in good agreement up to room temperatures. For higher temperatures, the harmonic approximation fails, and there is a significant deviation from the measured values. As for the entropy, it is systematically underestimated in a wide range of temperatures with respect to the experiments, even if its evolution with temperature is well reproduced in shape.

Figure 4. Temperature dependence of (a) specific heat at constant volume and (b) entropy of UO_2 compared to experimental data [29]



Conclusion on the description of bulk properties

Uranium dioxide is a complex material with very specific properties. The comparison of DFT+U results with more precise approximations or experimental data on a wide range of properties shows that despite its shortcomings (static approximation, U parameter, difficulty of taking into account paramagnetism) this method enables one to obtain a good description of bulk uranium dioxide at 0 K. The parameters of the calculations, however, must be well controlled. The calculations of the properties of UO_2 at finite temperature using electronic structure calculations are only beginning on this material, but the results are encouraging.

Properties of defects

The main difficulty in the evaluation of the DFT+U results on the properties of defects in uranium dioxide stems from the fact that this method is currently the most precise approximation applicable on defective systems. The assessment against more precise approximations is therefore impossible and can only be done against experimental results, which are, in turn, difficult or impossible to obtain.

Structural properties of defects

A linear decrease of the cell parameter of UO_{2+x} is observed experimentally when x increases [34]. The relationship was determined as follows: $a = (5.4705 - 0.1306x)$, i.e., a negative slope of 0.1306. The DFT+U calculations yield a decrease of the U-U distance in presence of neutral O interstitials and a slope of -0.1093 [35], which compares well with the experimental data.

In addition, the good results of the first comparison of the positron lifetimes in UO_2 calculated using DFT+U with results of Positron Annihilation Spectroscopy (PAS) shows that the volume of defects, to which the positron lifetime is particularly sensitive, is well reproduced [36].

Formation energies of defects

The formation energy is the most straightforward property to be calculated for a defect. It is, however, difficult to measure, and mostly determined through intermediate models. In addition, recent computational studies consider the various possible charge states for each defect. For charged defects, the formation energy depends not only on the stoichiometry,

but also linearly on the position of the Fermi level in the gap, i.e., the level of doping of the material. The comparison can in principle be made only with experiments at known stoichiometry and level of doping.

Actual experimental data on formation energies in UO_2 are scarce and concern only stoichiometric defects, i.e., the Frenkel pairs (association of a vacancy and an interstitial) and the Schottky defects (UO_2 trivacancy). While several studies were performed on the oxygen Frenkel pair [37,38,39,40,41,42], only one value is available for each uranium Frenkel pair and Schottky defect [39,40]. The experimental energies available taken from Table 2 of Vathonne et al. [43] are given in Table 3.

Since 2006, numerous DFT+U calculations have been performed for O and U interstitials (I_O , I_U), vacancies (V_O , V_U), Frenkel pairs (FP_O and FP_U) in the same supercell or separated, as well as infinitely separated and bound Schottky defects (ISD and BSD). The results of the various calculations for neutral and charged defects, taken from Table 3 of Dorado et al. [11] and Table 1 of Vathonne et al. [43], are also shown in Table 3.

A very large dispersion of the results on the individual defects and to a lesser extent on the stoichiometric defects can be seen in Table 3. This is due to two main reasons:

- the now well-known problem of convergence to metastable states in DFT+U (see extensive discussion in [11]);
- for individual defects, different references were used for the calculation of the defect formation energies (see the precise analysis in [43]). This reference problem disappears in the stoichiometric defects.

It can be observed that taking into account charged defects leads to much lower defect energies. UO_2 is strongly ionic, and the most stable charge for all defects is very close to their formal ionic charges. The results on stoichiometric defects calculated using the charged defects agree reasonably well with experimental data. It must be noted, however, that the comparison between calculated and experimental formation energies of defects is difficult and limited to a very small number of cases compared to all the defects calculated. This comparison should not be aimed at validation and calculation results validated through other means should ideally be used to help in the interpretation of the experimental results.

Table 3. Formation energies (in eV) of O and U interstitials, vacancies, Frenkel pairs and isolated and bound Schottky defects calculated by various authors, compared to the experimental data available [11,43]

Author \ E_f (eV)	l_o	l_u	V_o	V_u	FP_o	FP_u	ISD	BSD
Neutral defects								
Iwasawa 1965	-0.4	4.7	4.5	8.4	4.1	13.1		
Gupta 2007	-1.6	8.2	5.6	6.0	4.0	14.2	7.2	
Geng 2008					5.4	17.2	10.6	
Nerikar 2009	-1.3	6.1	5.3	9.0	4.0	15.1	7.6	
Yu 2011	-2.4	2.5	5.1	4.5	2.6	7.0	3.6	
Tiwary 2009	3.9	10.1	7.4					
Dorado 2010 [9]	-0.1	10.4	5.4	10.4	5.3	15.8	10.7	
Andersson 2011 [58]					5.3		10.2	
Hong 2012			4.9	9.7				
Charged defects								
Andersson 2011 [58]					3.3-3.4		6.0	6.4
Crocombe 2012					4.2		6.4	
Vathonne 2014 [43]					2.4-2.6	9.1-10.9	4.2	4.6
Experimental								
Clausen 1984 [37]					4.6 ± 0.5			
Murch 1987 [38]					4.1			
Matzke 1987 [39]					3.5 ± 0.5	9.5		6.5 ± 0.5
Staicu 2005					3.8 ± 0.5			
Konings 2013 [42]					3.3			

Migration energies of defects

Diffusion coefficients, i.e., activation energies to the diffusion and diffusion prefactors, are the most commonly available experimental data on defects. However, the experimental conditions, which have a significant influence on the results, are not always precisely known and models are needed for the comparison between experimental and computational results. This makes the assessment of the data calculated quite challenging.

The activation energies measured and calculated using DFT+U for the oxygen migration through vacancy and interstitial mechanisms are given in Table 4. These activation energies involve also the formation energy of the moving defect, and not only its migration energy.

Table 4. Activation energies to the oxygen self-diffusion through interstitial and vacancy mechanisms compared to the experimental data available

Ea (eV) Author	Vacancy	Interstitial
Dorado 2011 [46]	0.67	0.88
Dorado 2012 [49]	-	0.63
Experimental		
Review Belle 1969 [44]		1.0-1.3
Kim 1981 [45]	0.51 ± 0.13	-
Review Matzke 1987 [39]	0.5-0.6	0.8-1.0
Dorado 2011 [46]		0.75 ± 0.08

It can be seen from Table 4 that there is a good agreement among the most recent experimental results and between the calculated and experimental activation energies for the O self-diffusion.

Only a few studies were performed on the uranium self-diffusion. For the interstitial uranium migration, there is only one experimental value by Soullard: 0.3 eV [47] and one calculated migration energy calculated by Dorado et al.: 4.1-4.3 eV. In addition, Table 5 lists the experimental and calculated activation energies for uranium migration through a vacancy mechanism.

Table 5. Activation energies to the uranium self-diffusion (in eV) through vacancy mechanism compared to the experimental data available

Ea (eV) Author	Stoichiometric UO ₂	UO _{2+x}
Andersson 2011 [48]	7.2	4.2
Dorado 2012 [49]	3.1-3.9	
Experimental		
Review Belle 1969 [44]	2.3-4.5	3.0-4.6
Review Matzke 1987 [39]	5.6	2.6

A very large scatter is observed in both the experimental and calculated energies for the vacancy mechanism, while there is a clear mismatch between DFT+U and the experiments for the interstitial migration. An encouraging fact, however, is that the

qualitative difference between stoichiometric and hyperstoichiometric UO_2 reported by Matzke is reproduced by Andersson's calculations.

A thorough investigation of cation self-diffusion under precise experimental conditions and further calculations taking into account the migration of charged defects and various deviations of stoichiometry are needed to enable a precise assessment of the calculation results.

Conclusion on the description of defects

An encouraging agreement is observed between DFT+U and experimental data for defect formation energies and the O self-diffusion. But comparison between calculated and experimental energies of defects is extremely difficult, since it needs a detailed knowledge of the experimental conditions and involves additional models.

Incorporation and migration of rare gases

Description of bonds formed between rare gases and materials

As in the case of defects, the comparison between calculations and experiments is complicated for the behaviour of rare gases in UO_2 . In addition, it is now well known that the standard DFT approximations mainly used for solid systems (LDA, GGA, hybrid functionals) do not enable a correct description of the dispersive (van der Waals) bonds formed between rare gases [50,51]. They yield either largely overestimated binding energies or non-bonding interactions. The validity of the description of these standard functionals for interactions between rare gases and open-shell atoms which form materials is thus an open question.

A first validation study of the DFT description of the bonds between rare gases and open-shell atoms was performed on model molecular systems containing rare gases for which precise experimental data are available and reference post-Hartree-Fock calculations (CCSD(T) using large basis sets) are feasible [52].

The results of this investigation show that, when the rare gas shares density with the neighbouring atoms, the GGA functionals yield good geometries and qualitatively correct binding energies, even if these are significantly overestimated. The use of hybrid functionals enables one to obtain good geometries and satisfactory binding energies. For compounds in which the rare gas forms weak dispersive-like bonding, the accuracy yielded by the various functionals is not as good. No functional gives satisfactory binding energies for all the association compounds investigated. Several GGA and hybrid functionals yield correct geometries, even if some isomers are not obtained.

The results of this study must be confirmed on more solid systems, for instance small clusters simulating the first coordination spheres of the rare gas incorporated in a material.

Incorporation energies

Several DFT+U studies have been published on the incorporation of rare gases in UO_2 . Thompson et al. [53] studied the incorporation of He, Ne, Ar, Kr, Xe as interstitials in Schottky defects. Brillant et al. [54] determined the stability of various fission products, including Kr and Xe, as a function of stoichiometry and temperature. Geng et al. [55] investigated the stability of Xe in various defects. Finally, Liu et al. [56] studied the incorporation of Xe, Cs and Sr in various defects and segregation to other phases. No

comparison with experiments, however, was possible since no experimental incorporation energies are available.

Diffusion activation energies

The atomic diffusion of Xe in UO_2 was studied by several authors, in particular Davies, Miekeley, Cornell, Kaimal, [24,26-28], [61]. The migration of Kr was the subject of only two investigations, by Auskern [56] and more recently by Michel et al. [57].

Results of calculations are currently only available for Xe in UO_2 . A few DFT+U studies without comparison with experiments, by Andersson et al. [58], Liu et al. [59] and Thompson et al. [60], were published. An extensive investigation of the vacancy-assisted migration of Xe considering several possible traps and mobile assisting defects was, however, published recently by Andersson et al. [61]. A detailed comparison with experiments was performed taking into account the stoichiometry and the experimental chemical conditions using a specific point defect model, as well as a diffusion model. Table 6 presents a review of the activation energies measured by various authors and the lowest calculated Xe activation energies for intrinsic diffusion in $\text{UO}_{2\pm x}$ as a function of stoichiometry.

Table 6. Measured and lowest calculated Xe activation energies for intrinsic diffusion in $\text{UO}_{2\pm x}$ [61]

Ea (eV) Conditions	UO_{2-x}	UO_2	UO_{2+x}
O ₂			0.80
H ₂		2.93	
W		3.94	
Mo		3.92	
Ta	6.39		
Experimental			
Davies 1963		3.04 Mo crucible in H ₂ flow gas	
Cornell 1969		3.95 ± 0.61 Unknown crucible in H ₂ flow gas	
Miekeley 1972	6.0 ± 0.1 Ta Knudsen cell in vacuum	3.9 ± 0.4 W crucible in vacuum	1.70 ± 0.4 Pt crucible in O _{2(g)}
Kaimal 1989		2.87 Unknown crucible in He flow gas	

The experimental conditions (crucible, gas) are listed below each reference value.

The comparison between the model predictions and the available experimental data for Xe diffusion in UO_{2-x} , UO_2 and UO_{2+x} is encouraging. In particular, the calculated activation energies agree, at least qualitatively, with available experimental results. The stoichiometry of the samples, which is controlled by temperature and the chemistry of the experimental set-up, is a key parameter for Xe diffusion, since it governs the concentration and the type of assisting defects Xe trap site. In order to compare modelling and experimental results, it is critical to have a detailed knowledge of the experimental (in particular chemical) conditions. Then there are still uncertainties in the calculations of the defect energies, in particular related to the dependence on calculation parameters, the entropies and the charge state of defects and in the intermediate models used for the comparison.

Conclusion on the description of rare gas behaviour

An encouraging agreement is observed between DFT+U and experimental data for the atomic migration of Xe in UO_2 . These encouraging results, however, should be confirmed on other fission products, gaseous and non-gaseous. But, as in the case of defects, it is very complex to compare the results of the calculations on the behaviour of rare gases with experimental data.

Conclusion on DFT+U description of UO_2 under irradiation

The analysis of the numerous studies performed on uranium dioxide proves that the DFT+U method enables a good description of the structural, electronic and energetic properties of bulk UO_2 . In addition, an encouraging agreement is observed between DFT+U results and the experimental data for defect formation energies, oxygen self-diffusion and atomic diffusion of xenon in UO_2 . The comparison between calculated and experimental results on the behaviour of defects and fission products, however, is extremely difficult since it needs a detailed knowledge of the experimental conditions and involves additional models. This comparison should therefore not be really denoted as “validation”, but results of calculations should ideally be used to help in the interpretation of the experiments and in the determination of elementary mechanisms. The assessment of formation, incorporation and migration energies should be done through comparison with more precise approximations. This remains to be done since approximations beyond DFT+U are currently not applicable to the size of systems needed to investigate defects due to their computational cost. More controlled experiments involving a precise knowledge of the stoichiometric conditions and doping level are also needed.

Assessment of empirical potentials for UO_2

Structural and elastic properties of bulk fluorite UO_2

The results for structural and mechanical properties of the UO_2 fluorite phase using a large number of rigid-ion potentials are shown in Table 7.

Most of the properties like the cohesive energy E_{coh} , the lattice constant a_0 , the bulk modulus B_0 and even the derivative of the bulk modulus are well reproduced by most rigid-ion potentials. This is not a surprise as these properties are usually employed for the fitting of the potentials. A major deficiency of all rigid-ion potentials is the description of the elastic constants c_{12} and c_{44} . None of the rigid-ion potentials can properly reproduce the 2:1 ratio of the constants c_{12} and c_{44} and thus the shear modulus of UO_2 .

In contrast, core-shell models are able to fix this deficiency of the rigid-ion potentials while keeping an accurate description of the other structural and mechanical properties, as shown in Table 8.

In total, almost all core-shell potentials provide a quite satisfactory description of the considered structural and elastic properties of UO_2 . Especially, recent core-shell potentials like those of Meis [81] or Read [82] show a quite balanced description. Today’s computational power allows an exhaustive exploration of the parameter space given a functional form of the pair potentials. Hence a significant overall improvement of the results for this functional form of the empirical potential is rather unlikely, i.e., improving one property causes most likely a worsening of another one at the same time. A further

important issue is the numerical robustness of the empirical potential, especially for simulations at elevated temperatures. This is a limiting issue for core-shell potentials, because the probability for a so-called *polarisation catastrophe* increases with the kinetic energy of the atoms. Usually a shell particle stays close to its core particle, but this is no longer true for an increasing kinetic energy of the particles. A *polarisation catastrophe* can occur when two atoms get too close to each other. In this case, the strong Coulomb attraction between the core particle of one atom and the shell particle with opposite charge of the other atom can cause a collapse. Due to this fact, core-shell potentials can only be employed for UO₂ Classical Molecular Dynamics (CMD) simulations up to roughly 2 000 K. For the same reason, a direct simulation of fuel melting or of displacement cascades is not feasible using core-shell potentials.

Table 7. Structural and elastic properties of UO₂ for various rigid-ion models [62]

Potential \ Property	E_{coh} (eV)	a_0 (Å)	C_{11} (GPa)	C_{12} (GPa)	C_{44} (GPa)	B_0 (GPa)	$\frac{dB_0}{dP}$
Arima1 [63]	-103.0	5.4532	479.5	100.7	95.8	227.0	3.6
Arima2 [63]	-50.9	5.4545	435.4	113.7	106.3	220.9	5.3
Basak [64]	-43.2	5.4547	408.4	59.3	59.6	175.7	4.4
Grimes [65]	-105.6	5.4619	523.0	145.5	147.0	271.4	3.9
Karakasidis [66]	-100.6	5.4657	367.9	86.8	70.5	180.5	3.1
Lewis1 [67]	-103.6	5.3893	426.1	120.5	119.7	222.3	3.5
Morelon [68]	-65.9	5.4475	216.2	78.5	78.6	124.4	3.3
Sindzingre [69]	-100.7	5.4488	369.2	85.4	65.7	180.0	3.1
Tharmalingam [70]	-103.0	5.4104	472.2	95.3	84.5	220.9	3.5
Walker [71]	-104.1	5.3284	470.3	101.6	89.7	224.5	3.5
Yakub [72]	-37.0	5.4440	345.3	70.1	66.8	161.8	4.6
Yamada [73]	-45.6	5.4667	419.0	57.2	54.5	177.8	4.3
Experiment [74,75,76]	-106.7	5.4731	389.3	118.7	59.7	208.9	4.7

Table 8. Structural and elastic properties of UO₂ for various core-shell models [62]

Potential \ Property	E_{coh} (eV)	a_0 (Å)	C_{11} (GPa)	C_{12} (GPa)	C_{44} (GPa)	B_0 (GPa)	$\frac{dB_0}{dP}$
Busker [77]	-104.5	5.4683	531.9	120.5	119.1	257.7	3.9
Catlow1 [78]	-103.1	5.4506	419.2	124.6	66.5	222.8	3.5
Catlow2 [78]	-94.5	5.5211	434.0	99.2	57.6	210.8	3.7
Grimes [65]	-105.6	5.4619	523.0	145.5	89.4	271.3	3.9
Jackson1 [79]	-103.1	5.4479	427.8	125.0	67.1	225.9	3.9
Jackson2 [79]	-103.4	5.4516	396.8	131.1	73.8	219.7	3.4
Lewis2 [80]	-103.6	5.3900	425.9	120.4	88.7	222.3	3.5
Lewis3 [80]	-103.5	5.3815	426.0	118.3	50.1	220.9	3.5
Meis [81]	-100.8	5.4688	387.6	116.1	59.9	206.6	4.1
Read [82]	-101.9	5.4693	390.5	115.5	58.3	207.2	3.5
Experiments [74,75,76]	-106.7	5.4731	389.3	118.7	59.7	208.9	4.7

Thermal properties

Heat capacity

The value of heat capacity at constant pressure calculated by classical molecular dynamics simulation of UO₂ shows good agreement with experimental results, while there is some discrepancy between CMD simulation and experiment for PuO₂, as shown by Arima et al. [63]. Several potentials, in particular those by Kurosaki [85], Basak [64], Arima [63], and Yakub [72], are able to reproduce the variation of the lattice constant with temperature in the range from 300 to 2 500 K for UO₂, PuO₂ and U_{0.8}Pu_{0.2}O₂. The trend in the variation of the bulk modulus of UO₂ and PuO₂ with temperature is also reproduced by MD simulations [63,83].

Thermal conductivity

The calculation of the thermal conductivity κ can be performed by non-equilibrium molecular dynamics (NEMD), which involves setting up a heat source and a heat sink in the simulation cell and directly relating the heat flux to the temperature gradient [84]. Alternatively, in Equilibrium Molecular Dynamics (EMD) simulations, it is calculated from the auto-correlation of the heat current using the Green-Kubo formula, based on the fluctuation dissipation theorem [85], that reads:

$$\kappa = \frac{1}{3k_B T^2 V} \int_0^\infty \langle \mathbf{J}(t) \cdot \mathbf{J}(0) \rangle dt$$

Here k_B is the Boltzmann constant, T is the temperature, V is the volume, t is time, and $\mathbf{J}(t)$ is the heat current [63]. MD simulations tend to overestimate the thermal conductivity of UO₂ and PuO₂ at room temperature, but the agreement with experimental

data is improved in the temperature range 800 to 2 000 K [63,86]. EMD simulations of UO_{2+x} show that conductivity decreases with increasing temperature in the temperature range from 900 to 2 000 K and oxygen parameter x ranging from 0 to 0.09 [84]. The change in κ with x was attributed to scattering by excess oxygen ions, while the temperature dependence for $x = 0$ was attributed to the anharmonic Umklapp process. In real nuclear fuel, the thermal conductivity will also be influenced by voids, bubbles, grain boundaries and extended defects, which have been mostly neglected in simulations to date. A recent NEMD simulation has made a start in this direction by considering polycrystalline, albeit pure, UO_2 [84]. The simulation cell contained columnar grains with an average grain size of about 4 nm. The results were compared to findings for monocrystalline UO_2 using two different potentials. The potentials significantly overestimated the thermal conductivity of the single crystal, and the discrepancy with experimental data was reduced when an anharmonic correction was introduced. The experimentally observed decrease with increasing temperature was reproduced. The calculated κ value of the nano-crystalline sample was an order of magnitude smaller than that of the monocrystal, which shows that CMD simulations are able to capture the grain boundary scattering. However, the κ values calculated using the two potentials differ by a factor of two. This study suggests that the potential should provide a good fit to the elastic properties and thermal expansion to correctly model thermal transport [86]. A rigorous survey of 26 interatomic potentials has found that rigid-ion potentials overestimate κ , while core-shell potentials produced values of κ in good agreement with experiment [87].

Melting temperature

The simulated melting temperature T_m is another important property, because it is relevant for a reliable fuel simulation under accident conditions or for the simulation of irradiation damage (displacement cascades). In Table 9, the simulated melting temperatures of UO_2 are shown for some rigid-ion potentials. The agreement with the experimental value of about 3 140 K is reasonable, however, in general most of the potentials predict a too high melting temperature. Especially the Yamada potential gives a melting temperature which is by far too high.

Table 9. Melting temperature of bulk UO_2 for selected rigid-ion potentials [9,88]

Potential	Property	T_m (K)
Basak		3540
Morelon		3500
Sindzingre		3150
Walker		3435
Yamada		4155
Experiment [89]		3147

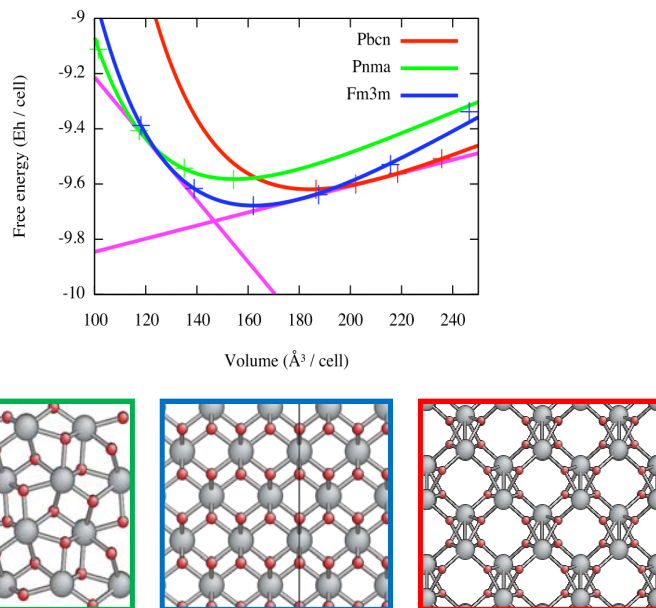
A simulation of the melting process with core-shell potentials is not feasible as explained in the previous sections. This is a major drawback of this potential type.

Relative stability of the different UO_2 phases

In addition to the influence of temperature, the behaviour of UO_2 depending on external pressure (equation of state) should be also reproduced properly by an empirical potential. It is known from experiment [90,12] that UO_2 changes from a fluorite-type structure (space group $Fm\bar{3}m$) to an orthorhombic cotunnite-type structure (space group $Pnma$) under pressure. The transition pressure is 42 GPa.

Based on theoretical and experimental results obtained for iso-structural compounds [91], uranium dioxide should transform under tensile load either into a scrutinyite-type (α - PbO_2 structure, space group $Pbcn$) or a rutile-type (space group $P4_2/mnm$) structure. The stability of the three UO_2 phases (fluorite, cotunnite, α - PbO_2) has been studied using static calculations by Fossati et al. [92]. Figure 5 shows the energy versus volume curves for these UO_2 phases obtained with the Morelon potential. The energies are normalised per UO_2 formula unit, allowing a direct comparison of the energies. The transition pressures for the α - PbO_2 and the rutile-type phase has been found to be equal to about -10 GPa. These two phases are almost energetically degenerate.

Figure 5. Free energies as a function of the volume for three different UO_2 phases, at low density the most stable phase is the α - PbO_2 structure and at high density the most stable phase is the cotunnite structure [93]



Four of the most used empirical potentials for UO_2 , namely those by Morelon, Arima, Basak, and Yakub, have been compared with DFT calculations [92]. The results are shown in Table 10. The Morelon potential has been found to be the most accurate one to describe the different uranium dioxide polymorphs. The empirical simulation results are consistent with DFT calculations and experimental data.

Table 10. Transition pressures in GPa between different UO_2 phases calculated with DFT-GGA and four empirical potentials, as well as experimental values [92]

Transition [GPa]	Morelon	Arima	Basak	Yakub	DFT	Experiment
$Fm\bar{3}m \rightarrow Pnma$	48	57	10	1.3	28	42 [12], 29 [90]
$Fm\bar{3}m \rightarrow Pb\bar{c}n$	-10	-6	-1.7	-1.4	-10	
$Fm\bar{3}m \rightarrow P4_2/mnm$	-9	-5	-1.7	-1.9	-11	

Defect formation energies

The accurate description of the formation energies of various defect types is crucial for the reliable description of the UO_2 transport properties. Tables 11 and 12 show the formation energies for oxygen and uranium Frenkel pairs (infinite distance) using various rigid-ion and core-shell potentials, respectively.

Table 11. Frenkel pair formation energies (rigid-ion models) [94,95]

Potential	E_f (eV)	FP_O	FP_U
Arima1	6.7	24.0	
Arima2	7.9	22.8	
Basak	5.8	16.7	
Grimes	9.0	32.8	
Karakasidis	4.7	19.1	
Lewis1	6.7	25.1	
Morelon	3.8	15.4	
Sindzingre	4.3	18.5	
Tharmalingam	5.9	22.0	
Walker	5.8	22.1	
Yakub	5.6	15.8	
Yamada	5.8	18.2	
DFT+U [43,48]	2.4-3.4	9.1-10.9	
Experiment [39,37]	3.0-4.0 4.6 ± 0.5	9.5	

The agreement with the experimental value for oxygen is satisfactory, but by far too high for uranium. The measurement of such defect formation energies, however, is difficult and thus the experimental value might also be unreliable. The comparison with the Frenkel pair (FP) formation energies obtained using DFT+U (see Table 3) shows that all empirical potentials overestimate the FP formation energies both for oxygen and uranium. This implies that defect configurations are excessively unstable compared to the undistorted configuration. This might be due to the fact that the empirical potentials are

mostly parameterised using properties of the ideal fluorite structure and no information about the energetics of defective configurations is directly considered during the fitting procedure.

The core-shell potentials show almost the same pattern as the rigid-ion potential (see Table 12). The O Frenkel pair formation energies are slightly lower on average. There is no qualitative change in the Frenkel pair formation energies for U. A possible explanation for this result is that current core-shell potentials consider the non-bonded interaction between the oxygen anions and in a more simplified manner between the oxygen anions and the uranium cations, but the non-bonded interactions among the uranium cations is ignored, i.e., it is reduced purely to their electrostatic interaction with the other atoms. Just the consideration of polarisability effects for the uranium cations using a core-shell model is obviously insufficient for a qualitative improvement of the FP_U formation energies. This would imply that the energetics of the U atoms in off-equilibrium positions needs the development of more suitable mathematical formalisms to be described better by empirical potentials.

Table 12. Frenkel pair formation energies for various core-shell models [94,95]

Potential	E_f (eV)	FP_O	FP_U
Busker	6.3	22.0	
Catlow1	5.0	18.3	
Catlow2	5.0	16.2	
Grimes	6.8	23.7	
Jackson1	5.1	18.5	
Jackson2	4.8	18.7	
Lewis2	5.3	20.0	
Lewis3	5.1	19.0	
Meis	4.5	17.9	
Read	4.5	17.1	
DFT+U [43,48]	2.4-3.4	9.1-10.9	
Experiment [39,37]	3.0-4.0 4.6 ± 0.5		9.5

An assessment of the Schottky defect formation energies is very difficult. There are only a few experimental data and the calculation of these energies using DFT+U is also difficult due to the limited model system sizes of a few hundreds atoms accessible by DFT+U simulations. Table 13 displays the available experimental and the currently best DFT+U results for the Schottky defect formation energies for an infinitely separated and for a bound Schottky defect. There is a clear spread in the formation energies for the

Isolated Schottky Defect (ISD) with a tendency to values larger than the ones obtained with DFT+U, whereas the Bound Schottky Defect (BSD) shows a rather fair agreement.

Table 13. Infinitely separated (ISD) and Bound Schottky Defect (BSD) formation energies for various rigid-ion models [9,96]

Potential	E _f (eV)	ISD (eV)	BSD (eV)
Arima1		10.2	4.5
Basak		10.8	5.7
Morelon		8.0	3.9
Sindzingre		6.3	2.5
Tiwary		7.1	—
Walker		8.3	3.5
Yamada		13.5	8.2
DFT+U [43,48]		4.2 - 6.0	4.6 - 6.4
Experiment [39]		—	6.5 ± 0.5

Defect migration energies

An accurate estimation of the defect migration barriers by the employed empirical potential is crucial for the reliable simulation of transport phenomena in UO₂. Table 14 lists the migration energies for the oxygen interstitial I_o , the oxygen vacancy V_o , the uranium interstitial I_U , and the uranium vacancy V_U , as well as the DFT+U values. The comparison cannot be directly made with experiments, which measure the diffusion activation energy which is generally different from the migration energy, because it includes the defect formation energy, which is moreover affected by a wide uncertainty, preventing a clear deduction of the migration energy from there.

In recent years, a fair agreement has been achieved between DFT+U simulations and experiment for the I_o and V_o migration energies (see also Table 4). Thus, for both quantities, the validation of the corresponding energies obtained with various empirical potentials can be performed on the DFT+U values. For the migration of U defects, the situation is less clear, as shown in the section on the DFT+U description of the migration of uranium defects (see also Table 5).

The rigid-ion potentials of Arima, Basak, Morelon, and Yamada give reasonable values whereas the other potentials show often a too low or even no barrier and thus these are not suited for the simulation of transport processes in UO₂. Results yielded by these potentials on U defects are also in agreement with the DFT+U results. Even the potentials failing for the O migration work reasonably for the U migration.

Table 14. Defect migration energies (in eV) for various rigid-ion models [9,62,88]

E_m (eV)	I_o	V_o	I_u	V_u
Potential				
Arima1	0.52	0.24	4.39	5.53
Arima2	1.73	0.57	4.27	5.32
Basak	1.04	0.27	3.54	4.09
Karakasidis	0.07	0.04	2.72	3.69
Lewis1	(0.69)	0.46	4.01	6.19
Morelon	0.69	0.34	2.35	3.88
Sindzingre	0.00	0.00	2.53	3.24
Tharmalingam	0.09	0.11	3.92	4.48
Walker	0.09	0.13	3.72	4.58
Yamada	0.89	0.27	3.74	4.30
DFT+U [46,49]	0.9	0.7	4.1-4.3	3.6-4.8

Table 15. Defect migration energies for various core-shell models [9,62,88]

E_m (eV)	I_o	V_o	I_u	V_u
Potential				
Busker	0.70	0.33	5.84	6.62
Catlow1	not conv.	0.54	4.44	5.18
Catlow2	0.21	0.32	4.29	4.67
Grimes	1.02	0.72	5.84	6.74
Jackson1	0.61	0.55	4.46	5.23
Jackson2	0.73	0.62	4.51	not conv.
Lewis2	not conv.	0.44	4.49	5.48
Lewis3	not conv.	0.47	3.64	4.51
Meis	0.62	0.54	3.55	4.58
Read	0.34	0.46	3.85	4.69
DFT+U [46,49]	0.9	0.7	4.1-4.3	3.6-4.8

The corresponding migration energies calculated using various core-shell potentials are shown in Table 15. The potentials of Busker, Jackson, Meis, and Read show a decent agreement with DFT+U results. The optimisation of the minimum energy path for the migration of oxygen interstitials using the climbing-image nudged elastic band (CI-NEB) method did not converge (not converged table entries) for several potentials. A closer

inspection revealed that these potentials are rather fragile with respect to close contacts between neighbouring atoms, as described above (polarisation catastrophe). Due to these instabilities, these potentials are basically not well suited for any kind of dynamical simulations.

Nevertheless, disregarding these numerical problems, all core-shell potentials describe reasonably both the oxygen and the uranium migration.

Behaviour of rare gases in UO₂

The incorporation energies of noble gas atoms into an interstitial site of UO₂ strongly depends on the size of the noble gas atom due to the strain caused by its insertion. Empirical potentials seem to overestimate the incorporation energies compared to recent calculations at the DFT and DFT+U level. On the other hand, Thompson et al. have shown that the solution energies of noble gas atoms being inserted into a pre-existing Schottky defect clusters show a reasonable agreement between empirical potential and DFT+U calculations [53].

The migration barriers of a Xe atom hopping between three types of Schottky defects were also evaluated by Thompson et al. [60]. The Arima potential overestimates all barrier energies compared to DFT+U, whereas the Tiwary potential underestimates all the barrier energies. The Morelon and the Basak potential show a fair agreement with the DFT+U diffusion barriers. Especially, the Morelon potential, which was fitted to experimental defect energetics and migration barriers, agrees well with DFT+U for both the barrier heights and the defect energetics. Adding Xe to a tetra-vacancy is electrostatically highly unfavourable.

Conclusion on the assessment of the empirical potentials

Lattice constants, bulk modulus, and the cohesive energy are well reproduced by most of the empirical potentials as these properties are usually employed for the potential fitting. The elastic constants, especially the shear modulus, are poorly described by rigid-ion potentials whereas core-shell potentials perform very well for elastic properties in general. The melting temperature is only accessible by rigid-ion potentials, by which it is usually overestimated. Core-shell potentials are not suited for simulations at higher temperatures (>2 000 K), which limits their applicability in many cases. The relative stability of various phases under tensile and compressive load is represented satisfactorily by rigid-ion potentials. The defect formation energies for UO₂ are still too high, especially for uranium, whereas the migration energies are in reasonable agreement compared to experiment and electronic structure calculations. A better description of uranium is one of the major challenges for the future development of empirical potentials. The different oxidation states of uranium and the dependence on the actual chemical environment of the U atoms have to be better reflected by the new empirical potentials, while keeping the accuracy for oxygen and the other material properties. A potential that will satisfactorily reproduce all the relevant properties of irradiated nuclear fuel appears to be out of reach at present, and one has to judiciously choose a potential that is tailored to a subset of properties of interest for the simulation.

Empirical potentials are irreplaceable for many studies that need a large number of atoms to be considered. It is therefore important to improve them and continue their assessment. The following issues remain for future development and validation:

- go beyond pure UO₂ and rare gases, e.g., consider chemical interactions with non-gaseous fission products and dopants;
- better describe deviation from stoichiometry;
- assess the potentials for atomic configurations far from equilibrium (e.g. molten fuel);
- assess the transferability of the available empirical potentials (U oxidation states, fixed U charge, preference for pristine UO₂);
- go to improved, more sophisticated empirical potentials for UO₂ systems based on alternative possibly more sophisticated functional forms like new potentials beyond the two-body approximation [97];
- construct a broader database of consolidated and reliable experimental and theoretical results.

Conclusion and future challenges

Significant work has been done on the assessment of electronic structure and empirical potential methods for the description of uranium dioxide. The analysis of the numerous studies performed on uranium dioxide proves that the DFT+U method and current empirical potentials enable a good description of the properties of bulk UO₂. In addition, an encouraging agreement is observed between modelling results and the experimental data for the defect formation energies, the oxygen self-diffusion and the atomic diffusion of xenon in UO₂. This is an important point since this is mainly what atomic scale models transfer to higher scale models.

This is a work in progress because of the complexity of the task and of the continuous improvements in the approximations. This assessment also needs to be done on other actinide compounds. Then, more controlled experiments involving a precise knowledge of the stoichiometry and doping level of the material are needed. It is important, however, that these studies are continued, since it is an important driving force for the improvement of the state-of-the-art in the calculations.

A better description of uranium ions in uranium dioxide is one of the major challenges of the atomic scale models:

- Concerning electronic structure calculations, it is necessary to go beyond the DFT+U method, even if this is only possible on model systems.
- For empirical potentials, the different oxidation states of uranium and the dependence on the actual chemical environment of the U atoms must be better reflected by the new empirical potentials, while keeping the accuracy for oxygen and the other material properties.

The comparison between calculated and experimental results on the behaviour of defects and fission products, however, is extremely difficult, since it needs a detailed knowledge of the experimental conditions and involves additional models. This comparison should not be denoted as “validation”, but calculation results should ideally be used to help in the interpretation of the experimental results and in the determination of elementary mechanisms. The assessment of formation, incorporation and migration energies should be done through comparison with more precise approximations.

Acknowledgements

The authors wish to express their gratitude to L. Malerba for valuable insight and careful reading of the manuscript. R. Devanathan was supported by the US Department of Energy (DOE) Nuclear Energy Advanced Modeling and Simulation (NEAMS) program at Pacific Northwest National Laboratory – a multiprogram laboratory operated for DOE by Battelle.

References

- [1] Koch, W., M.C. Holthausen (2000), *A Chemist's guide to Density Functional Theory*, Wiley-VCH, Weinheim.
- [2] Fulde, P. (1995), *Electron correlations in Molecules and Solids*, Springer, Berlin.
- [3] Ziegler, T. (1991), *Chemical Reviews*, 91, 651.
- [4] Ziegler, T. (1995), *Canadian Journal of Chemistry*, 73, 743.
- [5] Freysoldt, C., B. Grabowski, T. Hickel, J. Neugebauer, G. Kresse, A. Janotti, C.G. van de Walle (2014), *Reviews of Modern Physics*, 86, 253.
- [6] Rapaport, D.C. (2007), *The Art of Molecular Dynamics Simulation*, Cambridge University Press, Cambridge.
- [7] Leach, A. (2001), *Molecular Modelling: Principles and Applications*, Pearson Prentice Hall.
- [8] Tadmor, E.B., R.E. Miller (2012), *Modeling Materials: Continuum, Atomistic and Multiscale Techniques*, Cambridge University Press.
- [9] Bertolus, M. et al. (2010), “Development and assessment of atomistic modelling methods for the investigation of fuel materials under operational conditions”, *F-BRIDGE Deliverable D-221*, www.f-bridge.eu.
- [10] Liu, X-Y., D. Andersson, B. Uberuaga (2012), *Journal of Materials Science*, 47, 7367.
- [11] Dorado, B., M. Freyss, B. Amadon, M. Bertolus, G. Jomard, P. Garcia (2013), *Journal of Physics: Condensed Matter*, 25, 333201.
- [12] Idiri, M., T. Le Bihan, S. Heathman, J. Rebizant (2004), *Physical Review B*, 70, 014113.
- [13] Becke, A.D. (1995), “Exchange-correlation approximations in density-functional theory”, *Modern Electronic Structure Theory*, Part II, World Scientific, Singapore.
- [14] Kelly, P.J., M. Brooks (1987), *Journal of the American Chemical Society*, Faraday Trans. 2 83, 1189.

- [15] Geng, H.Y., Y. Chen, Y. Kaneta, M. Kinoshita (2007), *Physical Review B*, 75, 054111.
- [16] Killeen, J. (1980), *Journal of Nuclear Materials*, 88, 185.
- [17] Bates, J., C. Hinman, T. Kawada (1967), *Journal of American Ceramic Society*, 50, 652.
- [18] Myers, H., T. Jonsson, R. Westin (1964), *Solid State Communications*, 2, 321.
- [19] Yin, Q., A. Kutepov, K. Haule, G. Kotliar, S.Y. Savrasov, W.E. Pickett (2011), *Physical Review B*, 84, 195111.
- [20] Baer, Y., J. Schoenes (1980), *Solid State Communications*, 33, 885.
- [21] Yu, S.-W., J. Tobin, J. Crowhurst, S. Sharma, J. Dewhurst, P. Olalde-Velasco, W. Yang, W. Siekhaus (2011), *Physical Review B*, 83, 165102.
- [22] Jollet, F., T. Petit, S. Gota, N. Thromat, M. Gautier-Soyer, A. Pasturel (1997), *Journal of Physics: Condensed Matter* 9, 9393.
- [23] Wilkins, S.B., R. Caciuffo, C. Detlefs, J. Rebizant, E. Colineau, F. Wastin, G.H. Lander (2006), *Physical Review B* 73, 060406(R).
- [24] Laskowski, R., G.K. H. Madsen, P. Blaha, K. Schwarz (2004), *Physical Review B*, 69, 140408.
- [25] Dorado, B., P. Garcia (2013), *Physical Review B*, 87, 195139.
- [26] Devey, A. (2011), *Journal of Nuclear Materials*, 412, 301.
- [27] Dolling, G. et al. (1965), *Canadian Journal of Physics*, 43, 1397.
- [28] Pang, J.W.L. et al. (2013), *Physical Review Letter*, 110, 157401.
- [29] Sanati, M., R. Albers, T. Lookman, A. Saxena (2011), *Physical Review B*, 84, 014116.
- [30] Wang, B.-T., P. Zhang, R. Lizárraga, I. Di Marco, O. Eriksson (2013), *Physical Review B*, 88, 104107.
- [31] Yin, Q., S.Y. Savrasov (2008), *Physical Review Letter*, 100, 225504.
- [32] Taylor, D. (1984), *British Ceramic Transactions*, 83, 32.
- [33] Arima, T. et al. (2009), *Journal of Nuclear Materials*, 389, 149.
- [34] Teske, K., H. Ullmann, D. Rettig (1983), *Journal of Nuclear Materials*, 116, 260.
- [35] Dorado, B. (2010), Ph.D. thesis, Université de la Méditerranée Aix-Marseille II.
- [36] Wiktor, J., G. Jomard, M. Torrent, M.-F. Barthe, M. Freyss, M. Bertolus (2014), *Physical Review B*, 90, 184101.
- [37] Clausen, K., W. Hayes, J.E. Macdonald, R. Osborn, M.T. Hutchings (1984), *Physical Review Letter*, 52, 1238.
- [38] Murch, G.E., C.R.A. Catlow (1987), *Journal of Chemical Society, Faraday Trans. II* 83, 1157.
- [39] Matzke, Hj. (1987), *Journal of Chemical Society, Faraday Trans II* 83, 1121.
- [40] Matzke, Hj. (1990), *Journal of Chemical Society, Faraday Trans. II* 86, 1243.

- [41] Staicu, D. et al. (2010), *Journal of Nuclear Materials*, 397, 8.
- [42] Konings, R., O. Benes (2013), *Journal of Physics and Chemistry of Solids*, 74, 653.
- [43] Vathonne, E., J. Wiktor, M. Freyss, G. Jomard, M. Bertolus (2014), *Journal of Physics: Condensed Matter*, 26, 349601.
- [44] Belle, J. (1969), *Journal of Nuclear Materials*, 30, 3.
- [45] Kim, K.C., D.R. Olander (1981), *Journal of Nuclear Materials*, 102, 192.
- [46] Dorado, B. et al. (2011), *Physical Review B*, 83, 035126.
- [47] Soullard, J. (1976), *Contribution à l'étude des défauts de structure dans le bioxyde d'Uranium*, Ph.D. thesis Faculté des Sciences de Poitiers, report CEA-R-4882 CEN Fontenay-aux-Roses, France.
- [48] Andersson, D., B. Uberuaga, P. Nerikar, C. Unal, C. Stanek 92011), *Physical Review B*, 84, 054105.
- [49] Dorado, B. et al. (2012), *Physical Review B*, 86, 035110.
- [50] van Mourik, T., R.J. Gdanitz (2002), *Journal of Chemical Physics*, 116, 9620.
- [51] Zhang, Y., W. Pan, W. Yang (1997), *Journal of Chemical Physics*, 107, 7921.
- [52] Bertolus, M., M. Major, V. Brenner (2012), *Physical Chemistry Chemical Physics*, 14, 553.
- [53] Thompson, A.E., C. Wolverton (2011), *Physical Review B*, 84, 134111.
- [54] Brillant, G., F. Gupta, A. Pasturel (2011), *Journal of Nuclear Materials*, 420, 170.
- [55] Geng, H.Y., Y. Chen, Y. Kaneta, M. Kinoshita, Q. Wu (2010), *Physical Review B*, 82, 094106.
- [56] Liu, X.-Y., B.P. Uberuaga, K.E. Sickafus (2009), *Journal of Physics, Condensed Matter*, 21, 045403.
- [57] Auskern, A. (1960), US Report WAPDTM-185.
- [58] Michel, A. (2011), *Etude du comportement des gaz de fission dans le dioxyde d'uranium: mécanismes de diffusion, nucléation et grossissement de bulles*, Ph.D. thesis, Université de Caen, France.
- [59] Andersson, D.A., B.P. Uberuaga, P.V. Nerikar, C. Unal, C.R. Stanek (2011), *Physical Review B*, 84, 054105.
- [60] Liu, X.-Y., B.P. Uberuaga, D.A. Andersson, C.R. Stanek, K.E. Sickafus (2011), *Applied Physics Letters*, 98, 151902.
- [61] Thompson, A.E., C. Wolverton (2013), *Physical Review B*, 87, 104105.
- [62] Andersson, D.A. et al. (2014), *Journal of Nuclear Materials*, 451, 225.
- [63] Krack, M. (2012), *Materials Research Society Symposium Proceedings*, 1383, MRSF11-1383-a03-11.
- [64] Arima, T., S. Yamasaki, Y. Inagaki, K. Idemitsu (2005), *Journal of Alloys and Compounds*, 400, 43.

- [65] Basak, C.B., A.K. Sengupta, H.S. Kamath (2003), *Journal of Alloys and Compounds*, 360, 210.
- [66] Grimes, R.W., C.R.A. Catlow (1991), *Philosophical Transactions of the Royal Society of London A*, 335, 609.
- [67] Karakasidis, T., P.J.D. Lindan (1994), *Journal of Physics: Condensed Matter*, 6, 2965.
- [68] Lewis, G.V., C.R.A. Catlow (1985), *Journal of Physics C: Solid State Physics*, 18, 1149.
- [69] Morelon, N.D., D. Ghaleb, J.M. Delaye, L. van Brutzel (2003), *Philosophical Magazine*, 83, 1533.
- [70] Sindzingre, P., M.J. Gillan (1988), *Journal of Physics C: Solid State Physics*, 21, 4017.
- [71] Tharmalingam, K. (1971), *Philosophical Magazine*, 23, 199.
- [72] Walker, J.R., C.R.A. Catlow (1981), *Journal of Physics C: Solid State Physics*, 14, L979.
- [73] Yakub, E., C. Ronchi, D. Staicu (2007), *Journal of Chemical Physics*, 127, 094508.
- [74] Yamada, K., K. Kurosaki, M. Uno, S. Yamanaka (2000), *Journal of Alloys and Compounds*, 307, 10.
- [75] Benson, G.C., P.J. Freeman, E. Dempsey (1963), *Journal of the American Ceramic Society*, 46, 43.
- [76] Fritz, I.J. (1976), *Journal of Applied Physics*, 47, 4353.
- [77] Robach, O. et al. (2011), *Journal of Applied Crystallography*, 44, 688.
- [78] Abramowski, M., R.W. Grimes, S. Owens (1999), *Journal of Nuclear Materials*, 275, 12.
- [79] Catlow, C.R.A. (1977), *Proceedings of the Royal Society of London, Ser. A* 353, 533.
- [80] Jackson, R.A., A.D. Murray, J.H. Harding, C.R.A. Catlow (1986), *Philosophical Magazine A*, 53, 27.
- [81] Lewis, G.V., C.R.A. Catlow (1985), *Journal of Physics C: Solid State Physics*, 18, 1149.
- [82] Meis, C., A. Chartier (2005), *Journal of Nuclear Materials*, 341, 25.
- [83] Read, M.S.D., R.A. Jackson (2010), *Journal of Nuclear Materials*, 406, 293.
- [84] Arima, T. et al. (2006), *Journal of Alloys and Compounds*, 415, 43.
- [85] Watanabe, T., S.B. Sinnott, J.S. Tulenko, R.W. Grimes, P.K. Schelling, S.R. Phillpot (2008), *Journal of Nuclear Materials*, 375, 388.
- [86] Yamasaki, S., T. Arima, K. Idemitsu, Y. Inagaki (2007), *International Journal of Thermophysics*, 28, 661.
- [87] Kurosaki, K. et al. (2001), *Journal of Nuclear Materials*, 294, 160.
- [88] Chernatynskiy, A., C. Flint, S. Sinnott, S. Phillpot (2012), *Journal of Materials Science*, 47, 7693.
- [89] Govers, K., S. Lemehov, M. Hou, M. Verwerft (2008), *Journal of Nuclear Materials*, 376, 66.
- [90] Manara, D. et al. (2005), *Journal of Nuclear Materials*, 342, 148.

- [91] Benedict, U. (1994), *Journal of Alloys and Compounds*, 213-214, 153.
- [92] Sayle, T.X.T., D.C. Sayle (2010), *ACS Nano* 4, 879.
- [93] Fossati, P.C.M., L. van Brutzel, A. Chartier, J.-P. Crocombe (2013), *Physical Review B*, 88, 214112.
- [94] van Brutzel, L., P. Fossati, R. Grimes, D. Parfitt, S. Murphy (2011), “Thermo-mechanical properties of complex microstructures”, *F-BRIDGE Deliverable D-224*; www.f-bridge.eu.
- [95] Devynck, F., M. Iannuzzi, M. Krack (2012), *Physical Review B*, 85, 184103.
- [96] Krack, M. unpublished data.
- [97] Govers, K., S. Lemehov, M. Hou, M. Verwerft (2007), *Journal of Nuclear Materials*, 366, 161.
- [98] Cooper, M.W.D., M.J.D. Rushton, R.W. Grimes (2014), *Journal of Physics: Condensed Matter*, 26, 105401.

Chapter 15.

Dislocation-dynamics method

L. Van Brutzel
CEA, DEN, DPC, Centre de Saclay, France

Abstract

Dislocation-Dynamics (DD) technique is identified as the method able to model the evolution of material plastic properties as a function of the microstructural transformation predicted at the atomic scale. Indeed, it is the only simulation method capable of taking into account the collective behaviour of a large number of dislocations inside a realistic microstructure.

DD simulations are based on the elastic dislocation theory following rules inherent to the dislocation core structure often call “local rules”. All the data necessary to establish the local rules for DD have to come directly from experiment or alternatively from simulations carried out at the atomic scale such as molecular dynamics or *ab initio* calculations. However, no precise information on the interaction between two dislocations or between dislocations and defects induced by irradiation are available for nuclear fuels. Therefore, in this article the DD technique will be presented and some examples are given of what can be achieved with it.

Introduction

Usually plastic deformation of single crystals is carried out by large number of dislocations. Dislocation theory enhanced by experimental tools such as Transmission Electron Microscopy (TEM) has made significant advancements in understanding the plastic behaviour of crystalline materials. However, due to the multiplicity and complexity of the dislocation mechanisms involved, there exists a huge gap between the properties of individual dislocations and unit dislocation mechanisms at the microscopic scale and the material behaviour at the macroscopic scale. To translate the fundamental understanding of dislocation mechanisms into a quantitative physical theory for crystal plasticity, a new means of tracking the dislocation motion and interaction over large time and space evolution

is needed. In a multi-scale approach, three-dimensional Dislocation-Dynamics (DD) simulation is the only link between the atomic and the continuum aspects of plastic deformation. At the atomic scale, simulation methods such as *ab initio* or molecular dynamics allow studying very local phenomenon such as the structure of dislocation core, and the interactions between a dislocation with other point defects, dislocations or impurity. These simulations calculate directly the interactions between atoms in the crystal. Therefore, they are limited on the number of atoms that can be simulated because, in 3D, those numbers increase by the cube of the system size. They can only model small volumes ($< 10^{-6} \mu\text{m}^3$) for very small amount of time ($< 10^{-9} \text{ s}$). On the other hand, at the macroscopic scale, plastic deformation is generally treated in continuum mechanics through phenomenological laws.

In this article, we will describe the method. According to our knowledge, no DD simulation has been done in nuclear fuels, all the citations related to DD studies refer mainly to metals.

Dislocation-dynamics method

DD simulations are dedicated to the study of the plasticity mechanisms through the collective behaviour of a large number of dislocations. In DD, the discrete nature of the crystalline lattice is not explicitly described, hence the volume that can be simulated with this technique reaches $10^3 \mu\text{m}^3$ typically. This length scale is sufficient to represent the plastic deformation at the mesoscale level and to take into account the complex phenomena due to the collective properties of dislocations. It produces stress-strain curves and other mechanical properties, and allows detailed analysis of the dislocation microstructure evolution.

The basic idea of DD simulations is to compute the motion of each dislocation based on a spatial and time discretisation. The dislocation line is represented by connected discrete line segments. An effective driving force is computed for every segment according to the dislocation line tension, dislocation interaction forces and external loading. The dislocation segments respond to these forces by making discrete movement according to a mobility function that is characteristic of the dislocation type and the specific material being simulated. The dislocation mobility can be extracted from experimental data, or calculated by atomistic simulations. And the mobility is one of the key inputs to a DD simulation. Another important consideration for DD simulations is dealing with close dislocation-dislocation interactions such as annihilation and junction formation and breaking. These close interactions can be very complex and usually require special treatment. An efficient way to deal with them is to use prescribed “rules”. A bottleneck for DD simulation is the calculation of the elastic interactions between dislocations which is long range in nature. In order to perform DD simulations for realistic material plastic behaviour, efficient algorithms must be developed to enable the simulation over reasonable time and space range with a large number of dislocations.

Historically, the first DD codes, which describe the collective properties of dislocations appeared at the end of the 1980s [19,12]. These bi-dimensional simulations have shown some microstructure formation during plastic deformation with a parallel infinite dislocation lines. However, these simple two-dimensional codes are limited and do not take into account some important dislocation properties such as: dislocation

multiplication mechanisms, line tension effects or dislocation junction formation. Recently, original works have been published in order to improve these simulations [1,14]. The first tri-dimensional DD code appeared at the beginning of the 1990s [17] and demonstrated that the limitations encountered with the first simulations disappear with three-dimensional approach. Today, several three-dimensional models exist [6,16,9,13,27,34,7,32,3] and the strength and drawbacks of each model are still subject to debate [28,20,2]. Alternatively, other approaches to study dislocation properties at the mesoscale exist [8,31,33]. However, they remain marginal compared to DD simulations for which the number of users increases continuously.

Although most of the DD simulations carried out are under uniaxial load, the physical problems treated are varied. Among the problems already issued we can list for instance:

- forest hardening [5,21,24];
- nanoindentation [10];
- scaling effects [26,18];
- dislocation clustering [21];
- fatigue [25];
- temperature and strain rate effects [29,22].

Conclusions and future challenges

DD simulation is the link between atomistic scale simulations that describe the discrete local physical phenomena and the macroscopic scale that is treated with mechanics continuum method. This method gives the behaviour of the plastic deformation, which is mainly due to dislocation motion and clustering. Up to now, no DD simulation has been carried out in nuclear fuels. This is partly due to the fact that some key input parameters necessary to run DD simulations such as: dislocation mobility and dislocation interaction are missing or are not yet well described. This information is uneasy to obtain experimentally because dislocations appear mainly in nuclear fuels under irradiation. An alternative would be to conduct atomistic calculations to estimate these data. Recently, there has been a renewed interest in dislocation modelling in UO₂ exclusively with molecular dynamics simulations: [23,4,11,15]. However, these studies are still incomplete. For instance, some DFT calculations confirming the glide planes and the Peierls barriers would be useful. More investigations on the dislocation interaction forces would also be valuable. Nevertheless, with some assumptions, some DD simulations could be performed with success.

References

- [1] Benzerga, A. et al. (2004), “Incorporating three-dimensional mechanisms into two-dimensional dislocation dynamics”, *Modelling and Simulation in Materials Science and Engineering*, 12, 159-196.
- [2] Bulatov, V.V. (2002), “Current developments and trends in dislocation dynamics”, *Journal of Computer-Aided Materials Design*, 9, 133-144.

- [3] Bulatov, V.V. et al. (2004), “Scalable line dynamics in paradis”, *SperComputing*.
- [4] Deng, B. et al. (2012), “Effects of edge dislocations on thermal transport in UO₂”, *Journal of Nuclear Materials*, 434 (1-3) 203-209.
- [5] Devincre, B., L.P. Kubin (1994), “Simulations of forest interactions and strain-hardening in FCC crystals”, *Modelling and Simulation in Materials Science and Engineering*, 2, 559-570.
- [6] Devincre, B. (1996), *Computer Simulation in Materials Science* , ed: H.O. Kirchner, V. Pontikis, L. P. Kubin, Kluwer Academic Publishers, Amsterdam, North-Holland, 309.
- [7] Devincre, B. et al. (2001), “Mesoscopic simulations of plastic deformation”, *Materials Science and Engineering A*, 309-310, 211-219.
- [8] El-Azab, A. (2000), “Statistical mechanics treatment of the evolution of dislocation distributions in single crystals”, *Physical Review B*, 61, 11956-11966.
- [9] Fivel, M. et al. (1997), “3D simulation of a nanoindentation test at a mesoscopic scale”, *Materials Science and Engineering A*, 234-236, 923-926.
- [10] Fivel, M., G.R. Canova (1998), “Developing rigorous boundary conditions to simulations of discrete dislocation dynamics”, *Modelling and Simulation in Materials Science and Engineering*, 7, 753-768.
- [11] Fossati, P., L. van Brutzel, B. Devincre (2013), “Molecular dynamics simulation of dislocations in uranium dioxide”, *Journal of Nuclear Materials*, 443, 359-365.
- [12] Ghoniem, N.M., R. Amodeo (1988), *Solid State Phenomena*, 3-4, 377.
- [13] N. M. Ghoniem, M. Bacaloni (1997), *Eng. Rept Ucla/Matmod*, 1.
- [14] Gómez-García, D., B. Devincre, L. Kubin (2006), “Dislocation patterns and the similitude principle: 2.5D mesoscale simulations”, *Physical Review Letters*, 96, 125503.
- [15] Goyal, A. et al. (2013), “Segregation of ruthenium to edge dislocations in uranium dioxide”, *Journal of Nuclear Materials*, 441, 96-102.
- [16] Hirth, J.P., M. Rhee, H.M. Zbib (1996), *Computational Materials Design*, 3, 164.
- [17] Kubin, L.P. et al. (1992), “Three-dimensional simulations of plastic-flow in crystals”, *Solid State Phenomena*, 23-24, 455.
- [18] Lefebvre, S., B. Devincre, T. Hoc (2007), “Yield stress strengthening in ultrafine-grained metals: A two-dimensional simulation of dislocation dynamics”, *Journal of the Mechanics and Physics of Solids*, 55, 788-802.
- [19] Lépinoux, J., L.P. Kubin (1987), “The dynamic organization of dislocation-structures - a simulation”, *Scripta Metallurgica*, 21, 833-838.
- [20] Madec, R. et al. (2001), “Materials Research Society Symposium Proceedings”, Materials Research Society, 653, Z1.8.1.
- [21] Madec, R. et al. (2002), “On the nature of attractive dislocation crossed states”, *Computational Materials Science*, 23, 219-224.

-
- [22] Monnet, G., B. Devincre, L.P. Kubin (2004), “Dislocation study of prismatic slip systems and their interactions in hexagonal close packed metals: Application to zirconium”, *Acta Materialia*, 52, 4317-4328.
 - [23] Parfitt, D., C. Bishop, M. Wenman, R. Grimes (2010), “Strain fields and line energies of dislocations in uranium dioxide”, *Journal of Physics: Condensed Matter*, 22, 175004.
 - [24] Queyreau, S. (2008), PhD thesis, Université Pierre et Marie Curie, France.
 - [25] Shin, C.S. et al. (2005), “Dislocation dynamics simulations of fatigue of precipitation-hardened materials”, *Materials Science and Engineering A*, 400-401, 166-169.
 - [26] Schwarz, K.W., J. Tersoff (1996), “Interaction of threading and misfit dislocations in a strained epitaxial layer”, *Applied Physics Letters*, 69, 1220.
 - [27] Schwarz, K.W. (1997), “Interaction of dislocations on crossed glide planes in a strained epitaxial layer”, *Physical Review Letters*, 38, 4785-4788.
 - [28] Schwarz, K.W. (1999), “Simulation of dislocations on the mesoscopic scale, I. Methods and examples”, *Journal of Applied Physics*, 85, 108.
 - [29] Tang, M. et al. (1998), “Dislocation mobility and the mechanical response of BCC single crystals: A mesoscopic approach”, *Acta Materialia*, 46, 3221-3225.
 - [30] Tapasa, K. et al. (2007), “Computer simulation of carbon diffusion and vacancy-carbon interaction in alpha-iron”, *Acta Materialia*, 55, 1-11.
 - [31] Wang, Y.U. et al. (2001), “Phase field microelasticity theory and modeling of multiple dislocation dynamics”, *Applied Physics Letters*, 78, 2324-2326.
 - [32] Weygand, D. (2003), “Proc. IUTAM Symposium, Osaka, Japan”.
 - [33] Xiang, Y., L. T. Cheng, D. J. Srolovitz, E. Weinan (2003), “A level set method for dislocation dynamics”, *Acta Materialia*, 51, 5499-5518.
 - [34] Zbib, H.M., T. Diaz de la Rubia, M. Rhee, J. P. Hirth (2000), “3D dislocation dynamics: Stress-strain behavior and hardening mechanisms in FCC and BCC metals”, *Journal of Nuclear Materials*, 276, 154-165.

Chapter 16.

Phase field

B. Radhakrishnan¹, S.B. Gorti¹, K. Clarno¹, M.R. Tonks²

¹Oak Ridge National Laboratory, US,

²Idaho National Laboratory, US

Abstract

In this work, the phase-field method and its application to microstructure evolution in reactor fuel and clad are discussed. The examples highlight the capability of the phase-field method to capture evolution processes that are influenced by both thermal and elastic stress fields that are caused by microstructural changes in the solid-state. The challenges that need to be overcome before the technique can become predictive and material-specific are discussed.

Introduction

The phase-field technique is an efficient simulation approach for modelling microstructural evolution. A distinct advantage of the technique is that there is no need to explicitly track complex evolution of interfaces, such as grain boundaries or bubble surfaces. Therefore, it was originally developed for the simulation of liquid-solid transformations associated with solidification to capture the morphological evolution of single/multiple dendrites [2]. Since then, it has been used to model a large range of physical phenomena ranging from sintering [3,4] to fracture [5].

The phase-field model has been used to model microstructure evolution in fuel since 2009 [14]. It has proven to be well suited to the application due to the ease with which multiple physics can be coupled to account for the impact of the large stress and temperature gradients that form within the reactor fuel. It has also been used to model hydride formation in the cladding. This report summarises the phase field method and discusses its application to model reactor fuel and cladding.

Methodology

In the phase-field method, the individual phases and their crystallographic variants are described by a set of non-conserved order parameters. The interface between two phases

has a gradient in one of the order parameters that varies from 0 to 1 at the corresponding interface. Therefore, the technique is called a “diffuse interface” model as opposed to the sharp interface front-tracking models. In addition to the gradient in the order parameter, there are also gradients in the local concentrations at the diffuse interface from one phase to another. The order parameter and the concentration gradients are coupled at the interface. Microstructure evolution simulation involves solving for the time-dependent order parameters and concentrations within the simulation domain that is driven by a reduction in the total energy of the system. The total system energy is represented by the functional, F given by:

$$F = \int f_{\text{bulk}} + f_{\text{gr}} + f_{\text{el}} \quad (1)$$

where f_{bulk} is the local bulk free energy density of the phases that exist, f_{int} is the interfacial energy at the phase boundaries associated with gradients in concentration or order parameter, and f_{el} is the elastic energy associated with the lattice volume misfit between the two phases. The local bulk free energy density is the free energy per unit volume of the bulk phases that exist at a given temperature usually expressed in terms of a function of the concentrations and the non-conserved order parameters, whose coefficients are obtained by fitting thermodynamic data for the phases at the temperature of interest. The form of the free energy curve depends on the problem of interest.

The second term in the free energy expression is the gradient energy, which is an energy penalty associated with gradients in the long-range order parameters and/or concentrations, represented as:

$$f_{\text{gr}} = \sum_{p=1}^n \frac{\alpha_p}{2} (\nabla \eta_p(r))^2 + \frac{\beta}{2} (\nabla C)^2 \quad (2)$$

where α and β are the gradient energy coefficients for the order parameter and concentration, respectively, and p refers to the n non-conserved order parameters in the system. In the case of grain boundaries belonging to the same phase, the gradient energy term arises mainly due to gradients in the non-conserved order parameter that gives rise to grain boundary (GB) energy.

The last term in Equation 1 is the elastic energy, f_{el} , which is specific to microstructure evolution in the solid-state due to mismatch in the lattice parameter and heterogeneous elastic properties between the precipitate and the matrix phases. The contribution to the total elastic energy comes from the lattice inhomogeneous strains, transformation strain or the Eigenstrain due to the difference in the specific volumes of the matrix and the precipitate, bubble pressure and external strain. Various methods have been developed to vary the local elasticity tensor as a function of the composition [16,29,1,8]. However, each of these interpolation schemes is unable to reproduce analytical predictions of the elastic strain and strain energy profile at the diffuse interface [9]. While the total elastic energy calculation becomes relatively simple for the homogeneous elasticity approximation where the lattice inhomogeneous strain is zero, the elasticity solution becomes more complicated for the inhomogeneous elasticity cases. In such cases, a perturbation technique [12] can be used to compute the displacement fields in the matrix and precipitate phases.

The evolution equations for phase-field simulations include the time-dependent Ginzburg-Landau (TDGL) equation for evolving the non-conserved long-range order

parameters, and the Cahn-Hilliard (CH) equation for evolving the conserved concentration field. The TDGL equation is given by:

$$\frac{\partial \eta_p}{\partial t} = -L_p \frac{\delta F}{\delta \eta_p} \quad (3)$$

where L_p is a kinetic coefficient for the matrix-precipitate interface related to the interface mobility, and the derivative on the right hand side is the functional derivative of the free energy expression in Equation 1 with respect to the order parameter. The CH equation is given by:

$$\frac{\partial C(r,t)}{\partial t} = M \nabla^2 \frac{\delta F}{\delta C(r,t)} \quad (4)$$

where M is a kinetic coefficient for atomic mobility related to solute diffusion.

The nucleation of the precipitate is not carried out explicitly in the phase-field simulations because of the small length and time scales involved. It is possible to incorporate analytical nucleation and nuclei growth models based on the local conditions of thermodynamic undercooling, temperature and interfacial energies [27]. Alternatively, a Langevin noise term can be added to the TDGL and CH equations that is related to fluctuations in the long-range order parameter and concentrations to form a second phase from a supersaturated parent phase [19].

Phase-field models can be made quantitative and material-specific by relating the phase-field parameters to real physical quantities. The interfacial energy is related to the interface width and the energy barrier associated with the interface. For a specific material, since the energy barrier and the interfacial energy are fixed, the interface width is also fixed. Typically, the interface width in real materials is of the order of Angstroms. If the interface has to be defined by a minimum number of spatial locations, the total physical system size that can be simulated becomes extremely small given that the size of other microstructural features (precipitate, grain, etc.) is much larger than the interface width. The usual approach is to artificially increase the interface width by having an additional degree of freedom to keep the interfacial energy constant [25]. The kinetic parameter in the simulations is the phase-field mobility, which is obtained using an analytical expression that relates mobility to the interface width, interfacial energy, gradient coefficient, interface concentrations and the solute diffusion coefficient [17].

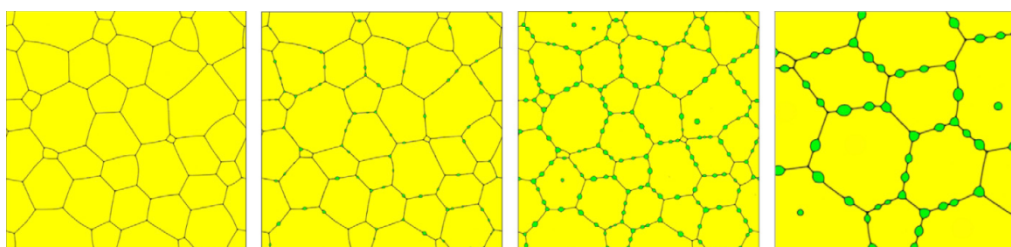
The evolution equations (3) and (4) have been solved in the simulation domain using a host of numerical techniques. The earliest phase-field simulations used a fixed grid to represent the domain, where the gradients were approximated using finite difference [6]. A semi-implicit Fourier spectral method based on second-order backward difference [7] is a well-documented approach for simulating solid-state phase transformations. The basic advantage of this approach is that partial derivatives of the order parameter and concentration are reduced to ordinary time derivatives in the Fourier space and the second order derivatives are reduced to the Fourier transform of the function multiplied by a vector in the Fourier space. Finally, the finite element method has also been used to solve the phase-field equations, due to the simplicity to couple to multiple physics and the flexibility in domain shape and boundary conditions [31,32].

Application to reactor fuel

Significant microstructure evolution takes place within the fuel during its lifetime in the reactor. This evolution degrades the material properties of the fuel, which impacts the fuel performance and can result in loss of reactor efficiency and eventual failure. The phase-field method is a powerful tool for modelling this evolution, due to its flexibility. The earliest published application of the phase-field method to nuclear fuels was in 2009 [14], in which the accumulation and transport of fission products and the evolution of gas bubbles were modelled. The model took the interaction between gas atoms and defects and elastic inhomogeneity into account. Since then, the model has been applied to gas bubble evolution [14,20], GB migration [34], gas and GB interaction [14,21], dislocation loop formation [15,18] and the impact of microstructure on thermal conductivity [32,23,34]. The application of phase field on irradiation effects is summarised in a review article [22]. Three of these efforts will be highlighted in more detail, below.

During its lifetime in a reactor, various mobile point defects are generated within the fuel. These defects include vacancies and interstitials on both the oxygen and uranium lattices, as well as gaseous fission products. The gas atoms tend to segregate to GBs and to vacancy clusters to form bubbles. The behaviour of interstitials and vacancies on the uranium lattice (the oxygen lattice is fast moving and thus was ignored) as well as gas atoms were predicted by a phase-field model, resulting in predictions of GB bubble nucleation and growth, as shown in Figure 1 [21].

Figure 1. Snapshots throughout time of the nucleation and growth of intergranular gas bubbles in a polycrystalline grain structure (the figure on the right is a close-up) (bubbles existing on GBs are lenticular shaped, whereas bubbles on triple junctions have a curved triangular shape)



The coalescence of intergranular gas bubbles is an important process in fission-gas release in nuclear fuels [21].

In addition to vacancies clustering to form voids, interstitials can cluster to form loops. These loops play an important role as segregation sites and can block dislocation and GB motion. While loops play an important role in fuels, they are also critical in the behaviour of irradiated structural materials. In [15] and [18], a phase-field model of interstitial loop formation is presented. An example of an interstitial loop simulation is shown in Figure 2. They found that elastic interactions around the loop enhance the growth kinetics.

Grain growth and GB migration also play an important role in fuel behaviour. Due to the high temperatures and large temperature gradients, GBs are mobile within reactor fuel. As the grain size impacts various phenomena, including creep, thermal conductivity and fission gas release, it is important to know how the temperature gradient impacts the grain growth within the fuel. A phase-field model of grain growth including the temperature gradient driving force has been developed [34]. A two-dimensional simulation of grain growth in the presence of various temperature gradients was conducted, showing that the

temperature gradient does not impact the change in the average grain size but does impact the grain size distribution (see Figure 3).

Figure 2. Snapshots of the morphology evolution of an interstitial loop during aging (a) in 3D, and (b) the projection on the plane of the interstitial loop [18]

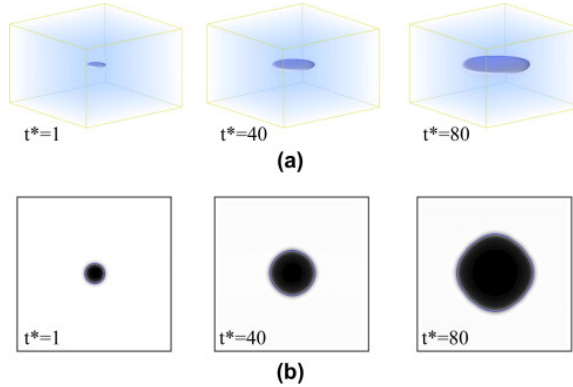
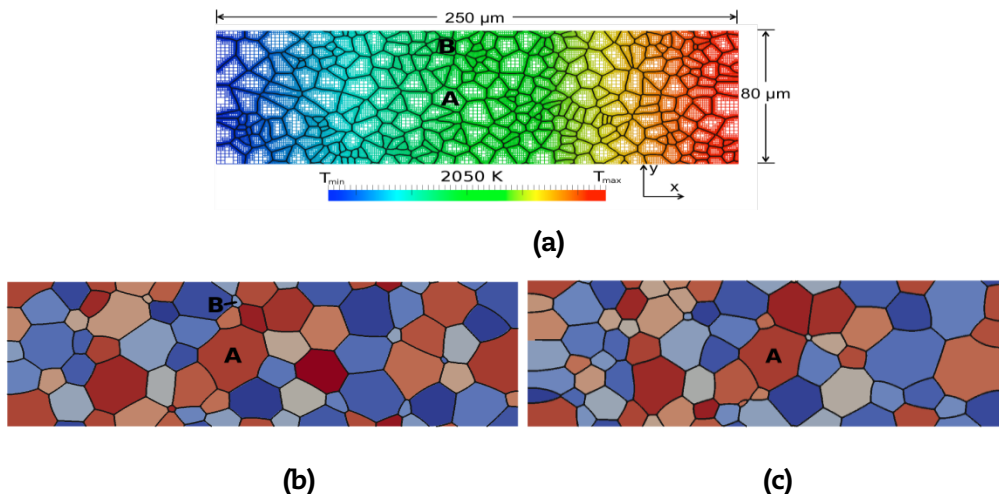


Figure 3. Polycrystal simulation domain, (a) where the initial grain configuration shows the adapted mesh



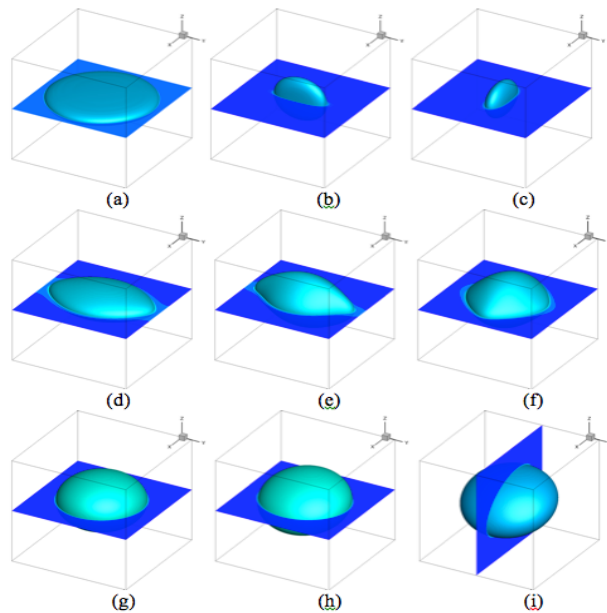
The constant temperature gradient is also shown. Note that the values for T_{\min} and T_{\max} vary for the different gradients, ranging from $T_{\min} = T_{\max} = 2050 \text{ K}$ for no gradient to $T_{\min} = 1950 \text{ K}$ and $T_{\max} = 2150 \text{ K}$ for $\nabla T = 0.8 \text{ K}/\mu\text{m}$. The final grain configuration after 2000 minutes is shown in (b) with no temperature gradient and in (c) with a gradient of 0.8 K/ μm , where grain B has disappeared. Note that with the temperature gradient, the grains are smaller on the cold side and larger on the hot side [34].

Application to fuel clad

Zircaloy clads used for nuclear fuel containment are produced using a special deformation processing approach that results in the preferential formation of hydrides in the circumferential direction in the clad [28]. However, during dry storage, the clad experiences high temperatures that may exceed the solvus temperature of the circumferential hydrides, causing the hydrides to dissolve. During subsequent cooling of the fuel-clad assembly, tensile hoop stresses develop in the sub-solvus temperature range. Under these conditions, the hydrides re-precipitate in the radial direction of the clad,

which is highly detrimental to its room temperature fracture toughness [11]. Therefore, the ability to accurately predict the conditions under which significant hydride reorientation occurs is extremely critical for the safe, long-term dry storage of cladding tubes. Previous phase-field simulations of hydride re-orientation under stress were essentially two-dimensional [19] and were confined to a specific variant, γ hydride. More recently, pseudo three-dimensional simulations have been carried out for another metastable variant of hydride, ζ hydride that was considered to respond more readily to external stress because it is coherent with the zirconium matrix [36-38].

Figure 4. Three-dimensional phase-field simulations of hydride reorientation in the presence of external strain (a) δ hydride without external strain, (b) δ hydride with 1% strain along X, (c) δ hydride with 1% strain along Y, (d) γ hydride without external strain, (e) γ hydride with 1% strain along X, (f) γ hydride with 1% strain along Y, (g) ζ hydride without external strain, (h) ζ hydride with 1% strain along X and (i) ζ hydride with 2% strain along X



Recently, full three-dimensional simulations of the growth of different variants of hydride were performed [26] using the phase-field method. Only a single variant of each hydride type was considered. Large three-dimensional simulations were carried out using parallel FFT libraries for solving the CH equation in Fourier space. The main objective was to investigate the potential for out-of-plane rotation of the growth direction from the basal plane. This is motivated by the fact that in zircaloy tubes manufactured by the pilgering process, the crystallographic texture in the axial-circumferential plane of the tube is close to basal so that the hydrides that form in the basal plane appear to be circumferential hydrides in the radial-circumferential plane. If radial hydrides form due to hoop stress, then the hydrides have to re-precipitate in an out-of-plane direction. The simulations show that of the three variants, ζ , γ and δ considered, the δ hydride has the highest propensity to reorient in the radial direction when external strain was applied in the basal plane. This was followed by γ and then by ζ . The fact that ζ shows the least tendency to rotate out of plane is due to the fact that the ratio of transformation strains in the z-direction compared to the x or y direction in the basal plane is the highest for the ζ

phase. Figure 4 shows the reorientation results obtained using three-dimensional simulations.

Conclusions and future challenges

The phase-field method is a powerful tool for modelling microstructure evolution coupled with additional physics in nuclear fuel and cladding materials. In order to develop better macroscopic models for fuel behaviour that are quantitatively informed by mesoscale models, the following barriers have to be overcome. First, many material properties and mechanisms that occur within the fuel are either not well understood or are unknown. Therefore, small-scale experiments and atomistic simulation is required to obtain this information. Second, the mesoscale models have not been well validated due to the difficulty in obtaining mesoscale data in reactor conditions. Thus, detailed separate effect experiments are needed to obtain data for validation. In addition, detailed microstructure characterisation on irradiated materials from integrated tests is also required. The application of the phase-field technique to hydride precipitation in clads is an on-going area of research that is driven by the complex materials phenomena that have not yet been fully addressed. Even though the phase-field simulations in their current form have been able to qualitatively capture the hydride reorientation under stress, significant advancement is required before predictive simulations can be performed. The approach for numerically capturing the elastic energy gradient at the diffuse interface requires accurate description of micro-plasticity effects in the vicinity of evolving precipitates, and the ability to efficiently incorporate anisotropies in the surface energy and inter-phase mobility in three-dimensional simulations. Finally, large time and length scales are needed to model the complex polycrystalline behaviour that takes place within the fuel and the clad. This can only be achieved using numerical approaches that are massively parallel and take advantage of numerical tools such as mesh and time-step adaptability.

Acknowledgements

This work was sponsored by the Department of Energy Nuclear Energy Advanced Modeling and Simulation Program and by the Laboratory Directed Research and Development Program of Oak Ridge National Laboratory (ORNL), managed by UT-Battelle, LLC for the US Department of Energy under Contract No. De-AC05-00OR22725.

References

- [1] Ammar, K. et al. (2009), *European Journal of Computational Mechanics*, 18, 485.
- [2] Boettinger, W.J. et al. (2002), *Annual Review of Materials Research*, 32, 163.
- [3] Wang, Yu. (2006), *Acta Materialia*, 54, 953.
- [4] Asp, K., J. Ågren (2006), *Acta Materialia*, 54, 1241.
- [5] Biner, S.B., S.Y. Hu (2009), *Acta Materialia*, 57, 2088.
- [6] Chen, L.Q., W. Yang (1994), *Physical Review B*, 50:21, 752.
- [7] Chen, L.Q., J. Shen (1998), *Computer Physics Communications*, 108, 147.

- [8] Durga, A. et al. (2010), *Proceedings of the ISRS – International Symposium for Research Scholars in Metallurgy, Materials Science and Engineering*, Indian Institute of Technology, Chennai, India.
- [9] Durga, A., P. Wollants, P., N. Moelans (2013), *Modelling and Simulation in Materials Science and Engineering*, 21, 055018.
- [10] Guo, X.H. et al. (2008), *Journal of Nuclear Materials*, 378, 110.
- [11] Hsu, H.H., L.W. Tsay (2011), *Journal of Nuclear Materials*, 408, 67.
- [12] Hu, S.Y., L.Q. Chen (2001), *Acta Materialia*, 49, 1879.
- [13] Hu, S., C.H. Henager (2009), *Journal of Nuclear Materials*, 394, 155.
- [14] Hu, S. et al. (2009), *Journal of Nuclear Materials*, 392, 292.
- [15] Hu, S. et al. (2012), *Modelling and Simulation in Materials Science and Engineering*, 20, 015011.
- [16] Khachaturyan, A.G. (1983), *Theory of Structural Transformations in Solids*, New York, John Wiley and Sons, pp. 201-212.
- [17] Kobayashi, H. et al. *Scripta Materialia*, 28, 689.
- [18] Li, Y. et al. (2012), *Journal of Nuclear Materials*, 427, 259.
- [19] Ma, X. et al. (2002), *Scripta Materialia*, 47, 237.
- [20] Millett, P.C. et al. (2011a), *Computational Materials Science*, 50, 949.
- [21] Millett, P.C. et al. (2011b), *Computational Materials Science*, 50, 960.
- [22] Millett, P.C., M.R. Tonks (2011), *Journal of Nuclear Materials*, 412, 281.
- [23] Millett, P.C. et al. (2013), *Journal of Nuclear Materials*, 439, 117.
- [24] Millett, P.C., M.R. Tonks (2011), “Current opinion in solid state materials science”, 15, 125, Ma, X. et al. (2002b), *Computational Materials Science*, 23, 283.
- [25] Moelans, N. et al. (2008), *Computer Coupling of Phase Diagrams and Thermochemistry*, 32, 268.
- [26] Radhakrishnan, B. et al. (2013), *Proceedings of the International High-Level Radioactive Waste Management Conference (2013 IHLRWM)*, Albuquerque, NM.
- [27] Simmons, J.P. et al. (2000), *Scripta Materialia*, 43, 935.
- [28] Singh, R. et al. (2004), *Journal of Nuclear Materials*, 325, 26.
- [29] Steinbach, I., M. Apel (2006), *Physica D*, 217, 153.
- [30] Steinbach, I., O. Shchyglo (2011), “Current opinion in solid state and materials science”, 15, 87.
- [31] Stogner, R.H. et al. (2008), *International Journal for Numerical Methods in Engineering*, 76, 5, 636.
- [32] Tonks, M.R. et al. (2012), *Computational Materials Science*, 51, 20.

- [33] Tonks, M.R. et al. (2013), *Materials Research Letters*, 2014, *Materials Research Letters*, 2, 1, 23.
- [34] Tonks, M.R. et al. (2013), *Journal of Nuclear Materials*, 440, 193.
- [35] Thuillet, L. et al. (2012), *Acta Materialia*, 60, 5311.
- [36] Thuillet, L., R. Besson (2012), *Intermetallics*, 20, 24.
- [37] Thuillet, L. et al. (2013), *Acta Materialia*, 438, 32.
- [38] Zhao, D. et al. (2008), *ASTM International*, 5, JAI101161.

Chapter 17.

Modelling microstructural evolution under irradiation

V. Tikare

Sandia National Laboratories, US

Abstract

Microstructural evolution of materials under irradiation is characterised by some unique features that are not typically present in other application environments. While much understanding has been achieved by experimental studies, the ability to model this microstructural evolution for complex materials states and environmental conditions not only enhances understanding, it also enables prediction of materials behaviour under conditions that are difficult to duplicate experimentally. Furthermore, reliable models enable designing materials for improved engineering performance for their respective applications. Thus, development and application of mesoscale microstructural model are important for advancing nuclear materials technologies. In this chapter, the application of the Potts model to nuclear materials will be reviewed and demonstrated, as an example of microstructural evolution processes.

Introduction

Microstructural evolution of nuclear fuels and claddings under irradiation is characterised by some unique features that are not typically present in other application environments. A very wide range of irradiation conditions, radiation with many different particles over a large range of energies, lead to formation of defects in crystalline materials. These defects can interact in many different ways with each other and existing defects such as grain boundaries to give rise to microstructural evolution not observed in other applications. These radiation-induced defects can alter the kinetics by enhancing diffusion. They can have more substantial effects such as void formation due to aggregation of vacancies. Under some conditions, radiation can create a large density of defects causing the crystalline material to transform to an amorphous state.

Swelling is another common consequence of radiation in many materials. The aggregation of vacancies to form voids is observed in many materials including some fuel rod claddings. The production of extra atoms by fission in nuclear fuel can strain the

lattice leading to swelling, albeit to a lesser extent. Nuclear fuels can also swell due to precipitation of fission gas (primarily Xe and Kr) into nanosized intragranular bubbles and sub-micron intergranular bubbles. The creation of extra atoms by fission or transmutation of atoms alters the chemistry of the fuel (see the next section for a detailed discussion) and results in microstructural evolution that is unique to nuclear materials.

Another feature that is unique to some nuclear materials is the large temperature gradient present in these materials that leads to different microstructural evolution in the different regions and segregation of components. Restructuring of fast reactor fuels to form an axial pore along the central axis of the fuel pellet is an example of this. Another unique feature of nuclear fuels is the accumulation of radiation damage at the outer rim of the fuels, which, in turn, drives recrystallisation in this region. Recrystallisation is virtually non-existent in most ceramics making this phenomenon most interesting in itself, but is of great importance for fuel performance. Finally, radiation-induced segregation of components in two or more component materials occurs in many materials.

All these processes unique to irradiated materials drive a number of microstructural evolution processes, which are not observed in other materials. The ability to simulate these evolution processes at the microstructural scale would enhance our ability to predict their behaviour and hence design them at the microstructural scale for optimal engineering performance. In this section, the application of Potts models to simulate microstructural evolution nuclear materials will be reviewed.

Potts kinetic Monte Carlo model

The Potts kinetic Monte Carlo (kMC) is a statistical-mechanical model that populates a lattice with an ensemble of discrete particles to represent and evolve the microstructure. The Potts kMC used for mesoscale simulations is distinct from other kinetic Monte Carlo models used for simulation of atomistic, chemical, neutronic and other materials simulations. In the following sections, the term kMC is used to refer to the Potts kMC model. The particles in the Potts kMC model represent a discrete quantity of material that is much larger than an atom, thus all atomistic information about the material system is aggregated into mesoscale model parameters. In kMC, the particles evolve in a variety of ways to simulate microstructural changes due short- and long-range diffusive processes. kMC methods have proven themselves to be versatile, robust and capable of simulating various microstructural evolution processes. They have the great advantage of being simple and intuitive, while still being a rigorous method that can incorporate all the thermodynamic, kinetic and topological characteristics to simulate complex processes. They are easy to code, readily extendable from 2D to 3D and can simulate the underlying physics of many materials evolution processes based on the statistical-mechanical nature of the model. These processes include curvature-driven grain growth [1,2], anisotropic grain growth [3], recrystallisation [4], grain growth in the presence of a pinning phase [5,6], Ostwald ripening [7], and sintering [8-10].

Representation of microstructure

The microstructure consists of an ensemble of particles that occupy a regular lattice. Recently, some kMC models have started to use non-regular or non-lattice based methods. However, the vast majority of kMC models use regular lattices and for the purpose of this

work, we will confine our discussion to regular lattices. The particles can be considered to be a discrete amount of material that is much larger than an atom; thus all atomistic characteristics are aggregated into discrete extensive thermodynamic quantities such as mass and energy for each particle. For the simplest case of grain growth, the microstructure is represented by particles identified by an integer value signifying membership in a particular grain. This membership integer value is simply a distinct degenerate state identifying each particle as belonging to a certain grain with no other physical significance. In a two-phase system such as a porous material, the solid material can be assigned one set of spins and all the porosity a single distinct membership value. In a two-phase system consisting of two solid components such as a eutectic material, each phase can be represented by a set of membership integer values. Lattices can be two-dimensional triangular or square, three-dimensional cubic or face-centered cubic or other geometries. The most commonly used geometries are two-dimensional square and three-dimensional cubic lattices.

Energy and thermodynamics

Since kMC uses a discrete ensemble of particles to represent the microstructure, it follows that the total volumetric energy is the sum of energies of each particle. In addition, interfacial energies must also be included in the calculation of the total free energy of the system. Interfaces in kMC are defined by neighbouring particles with unlike membership. Different types of interfaces with different energies can be defined. Neighbouring particles belonging to two different grains would define a grain boundary or grain particles forming an interface with pore particles would define a pore surface. Each of these can be given its own energy value. The total interfacial energy of the system is then the length in 2D or area in 3D of each interface multiplied by its interfacial energy per unit length or area. Thus, the sum of all unlike neighbour interaction energies of all the particles is E_{int}

$$E_{int} = \sum_{i=1}^N \sum_{j=1}^n J_{qi,qj}$$

where i is each particle, N is the total number of particles, j is the neighbouring particle, n is the total number of neighbours being considered, qi is the spin of particle i and J is the interaction energy between particles i and j of spins qi and qj . The bulk energy of the system is the sum of the inherent energy of each particle and does not depend on its neighbours.

$$E_{vol} = \sum_{i=1}^N V_i$$

where V_i is the volumetric energy of particle i . Examples of volumetric energy may be the volumetric chemical free energy, elastic strain energy or the irradiation damage energy stored in the nuclear fuel. The interfacial and volumetric energies are very versatile and can be formulated to match virtually any energy that is characteristic of real materials. They can be functions of microstructure or materials, so that as the system evolves due to changing chemistry or accumulation of irradiation or other damage, the particle energies can reflect their current thermodynamic state. This ability to easily tailor particle energies

makes kMC models highly versatile and widely applicable to many materials evolution processes.

Evolution and kinetics

kMC models have been shown to correctly simulate complex path-dependent evolutionary processes. They yield images with great detail of the microstructure and its evolution in response to a given set of starting conditions and applied conditions. The microstructure evolves in response to local conditions such as curvature, radiation damage, temperature, etc. These local conditions may also be changing with time and position. The basic mechanisms for change in a kMC model are the changes in membership of particles from one grain or phase to another or transport of the particles to a different lattice positions by exchanging places with neighbouring particles. These types of changes can be used to simulate many types of transport mechanisms such as grain boundary motion, surface and bulk diffusion, dissolution and precipitation and other mechanisms. The spin change event frequencies are determined using the standard Metropolis algorithm with Boltzmann statistics. A spin change event is identified. The change in total energy of a spin change event is calculated using the equation of state described in the previous section. The probability of this change is:

$$P = 1 \quad \Delta E \leq 0$$

$$P = \exp \frac{-\Delta E}{k_B T} \quad \Delta E > 0$$

where k_B is the Boltzmann constant, and T is the simulation temperature. The change is performed with this probability by choosing a random number R , uniformly distributed from 0 to 1. If $R < P$, then the event is accepted and a change is made. If not then no change is made, and the original spin is restored. kMC models reduce the total free energy of the system and, when implemented correctly, reduce free energy along the correct kinetic path of microstructural evolution. These characteristics make the Potts model well suited for studying microstructural evolution in nuclear materials.

Application of kMC model to nuclear materials

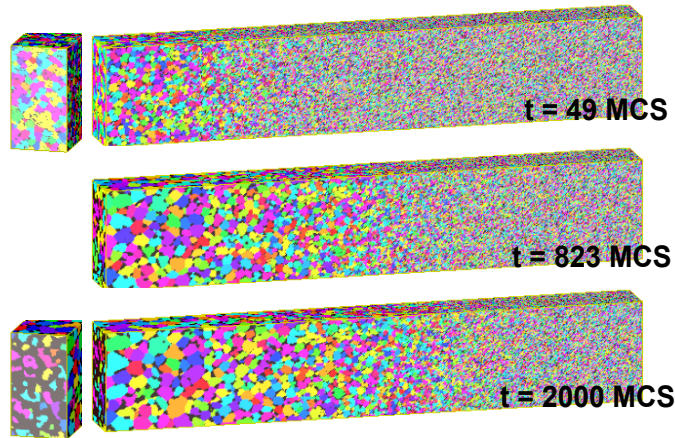
The kMC model has been applied to a variety of processes that are relevant to the simulation of nuclear fuel, clads and other materials. Grain growth was the first and has been the most extensively studied microstructural evolution process. It has been shown that this model simulates curvature-driven grain growth with the expected kinetics of $R^2 - R_0^2 = kt$, where R is the average grain radius and R_0 is the average grain radius at time $t = 0$ and k is a kinetic constant related to grain boundary diffusivity. Grain growth in systems with immobile, mobile and evolving pinning phases are important processes for nuclear fuels.

Nuclear fuels are often porous at the start of their service and become more so as fission gases are produced during in-reactor service. This porosity can move and coarsen as the matrix coarsens as well. Solid fission products often segregate to grain boundaries and pin them to effectively reduce or stop grain growth. This process has been extensively studied using the kMC model. Other fission products can segregate to grain boundaries

and pin them so that grain growth is suppressed even at high temperatures. This two-phase pinning model is described in detail elsewhere [6] and shown to incorporate all the processes necessary to simulate coarsening in a two-phase system such as that found in nuclear fuels. These processes include curvature driven grain growth mediated by pore drag on the grain boundaries, which leads to different grain boundary motion behaviours: slower grain boundary motion due to pore drag, grain boundary break away from very slow pores or complete stagnation of the grain boundary by pores.

In materials that have temperature gradients, particularly the large gradients seen in nuclear materials, microstructural evolution in different regions can vary greatly depending on the local temperature. Thermally activated processes such as grain boundary motion, and surface and bulk diffusion, occur at a faster rate at higher temperatures with the temperature-dependent rate or mobility $M(T)$ given by the Arrhenius relationship $M = M_0 \exp\left(\frac{-Q_A}{k_B T}\right)$ where M_0 is a pre-exponential constant and Q_A is the activation energy for that process. In nuclear fuels and clads, most processes are indeed thermally activated, although a few are enhanced by radiation-induced defects as well. The thermally activated processes are treated in the kMC model by varying their mobility as a function of the local temperature. For example, grain growth. The grain boundary velocity v is proportional to the driving force (curvature) and mobility as $v = M\kappa$ where κ is the grain boundary curvature. This mobility term is introduced very easily in the kinetic equation as $PM = M(T)P$ where PM is the temperature-dependent probability term and P is the original probability. It has been shown by Garcia et al. [11] that under continuously varying temperature gradients, the kinetics and topology of the grain growth are locally normal. The local grain size and grain size distribution are the same in the temperature gradient as they would be at the same temperature in an isothermal grain growth simulation. This method for simulation of temperature gradients is correct as long as the mechanism for microstructural evolution and the corresponding activation energy remain constant over the entire temperature range. In two-phase systems, the Soret effect that segregates phases is important. This, too, can be simulated in the Potts model by introducing a heat of transport term, Q^* into the energy of the system. An example that combines all the processes described above has been combined in one simulation for illustrating the model capability. Coarsening in a two-phase system with a thermal gradient applied is shown in Figure 1. Curvature-driven grain growth with a mobile pinning phase, in this case gas, is evolving in a temperature gradient. The gas pockets coarsen by coalescence and move by surface diffusion. As can be seen, coarsening is much faster at the high temperature region and the gas preferentially diffuses to the higher temperature region as this lowers the total free energy of the system.

Figure 1. Coarsening of grains and pores in a thermal gradient



Grains and pores coarsen more quickly at higher temperatures. Pores migrate to the high temperature end due to the Soret effect as shown by the difference in pore volume at the high-temperature edge between time $t = 49$ and 2,000 MCS.

Recrystallisation is an important phenomenon observed in LWR and some other fuels. Rollet et al. [12] developed a recrystallisation model and later used it to study abnormal growth [13]. Further evolution of this model was used to study dynamic recrystallisation [14]. A preliminary application of kMC model to study recrystallisation in the high burn-up rim region of LWR fuels was recently presented by Oh [15] and more developed by Madison et al. [16]. Another very important microstructural evolution process is swelling. This mechanism is very similar to densification during sintering of crystalline materials. A validated kMC model for sintering has been demonstrated by comparison to detailed experimental three-dimensional images of microstructural evolution in Cu powder compacts [17]. While almost all the basic microstructural evolution processes at the mesoscale have been simulated to varying degrees using kMC methods, their application to nuclear fuel and cladding is in its infancy. In order to make significant advances, the models have to be adapted to the specific application conditions of nuclear fuels and coupled so that many different processes (i.e., fission gas generation, diffusion, bubble formation accompanied by swelling and recrystallisation) can occur simultaneously. The adaptation of kMC models to the specific processes relevant to nuclear materials and development of coupled models is not trivial. However, the previous use of kMC models to correctly simulate various processes including coupled processes suggests that kMC is a powerful and useful method for modelling microstructural evolution in nuclear materials.

Current trends and future development of Potts models

Continued model development of the kMC model has taken the form of developing hybrid models that couple multiple materials physics that the kMC model cannot inherently treat. One of the early examples of this type of modelling was a sintering model that treated all the processes active during solid state sintering, except densification by annihilation using kMC. Densification, however, was simulated by a unique method of addressing global shrinkage based on the local microstructural configuration [17]. This is another example for simulation of recrystallisation. Application of the Potts model alone

with a volumetric free energy modified to include the strain energy density of dislocations in the metal could not simulate the kinetics of recrystallisation correctly. Rollett and Raabe [18] showed that a hybrid Potts cellular automaton model correctly simulated the kinetics of recrystallisation and Madison et al. [19] extended this model and applied it to simulate dynamic recrystallisation in the high-burn-up rim region of UO₂ fuels. In contrast, the phase-field model has remained essentially the same model. Its development has been in the form of introducing new phase fields to represent new physics. The numerical implementation of additional coupled fields has limited the advancement of phase-field models. Coupling phase fields which introduce additional physics is difficult as the development of free energy functionals that are numerically stable and converge to the correct solution is difficult. The evolution of the phase-field model is improved in numerical techniques to enable larger simulations with more coupling of the physics. Adaptation and use of advanced numerical solver that converges to solutions with less computation has been a large effort to improve phase-field model performance. Development of adaptive meshes that reduces computation in stable non-evolving areas away from the interfaces has been the focus of model improvement. Another is reassignment of degenerate grain orientation locally to both reduce the number of phase fields required and to prevent the artefacts introduced by having a limited number of grain orientations. An exciting development in mesoscale modelling has been the introduction of a hybrid model that couples phase-field with Potts model [20].

This type of hybrid combines the inherent efficiency and stability of the Potts model with the ability to treat continuously varying materials characteristics such as composition in the phase-field model to enable simulation of microstructural evolution in a new class of materials. One area of microstructural evolution problems has remained challenging. Models that can simulate microstructural evolution that is driven partially by mechanical stresses are the focus of much research. While, some solutions have been found under a limited set of conditions, the development of modelling techniques that would enable simulation microstructural evolution that is partially driving by mechanical stresses has not been achieved. The problems of interest to nuclear materials are swelling in nuclear fuels due to fission gas bubble formation, interactions between clad and pellet, hydride reorientation in cladding during long-term storage and many others.

Acknowledgements

Sandia National Laboratories is a multi-program laboratory managed and operated by Sandia Corporation, a wholly owned subsidiary of Lockheed Martin Corporation, for the US Department of Energy's National Nuclear Security Administration under contract DE-AC04-94AL85000.

References

- [1] Anderson, M.P., D.J. Srolovitz, G.S. Grest, P.S. Sahni (1984), *Acta Metallurgica*, 32, 783-791.
- [2] Holm, E.A., J.A. Glazier, D.J. Srolovitz, G.S. Grest (1991), *Physical Review A: Atomic, Molecular and Optical Physics*, 43, 2662-2668.
- [3] Holm, E.A., G.N. Hassold, M.A. Miodownik (2001), *Acta Materialia*, 49, 2981-2991.

- [4] Holm, E.A., M.A. Miodownik, A.D. Rollett (2003), *Acta Materialia*, 51, 2701-2716.
- [5] Miodownik, M., J.W. Martin, A. Cerezo (1999), *Philosophical Magazine A*, 79, 203-222.
- [6] Tikare, V., M. Miodownik, E.A. Holm (2001), *Journal of the American Ceramic Society*, 84, 1379-1385.
- [7] Tikare, V., J.D. Cawley (1998), *Acta Materialia*, 46, 1343-1356.
- [8] Hassold, G.N., I.-W. Chen, D.J. Srolovitz (1990), *Journal of the American Ceramic Society*, 73, 2857-2864.
- [9] Tikare, V., M. Braginsky, E.A. Olevsky (2003), *Journal of the American Ceramic Society*, 86, 49-53.
- [10] Braginsky, M., V. Tikare, E. Olevsky (2005), *International Journal of Solids and Structures*, 42, 621-636.
- [11] Garcia, A.L., V. Tikare, E.A. Holm (2008), *Scripta Materialia*, 59(6), 661-664.
- [12] Rollett, A.D., D.J. Srolovitz, M.P. Anderson, R.D. Doherty (1992), *Acta Metallurgica*, 40, 3475-3495.
- [13] Holm, E.A., M.A. Miodownik, A.D. Rollett (2003), *Acta Materialia*, 51, 2701-2716.
- [14] Rollett, A.D., M.J. Luton, D.J. Srolovitz (1992), *Acta Metallurgica*, 40, 43-55.
- [15] Oh, J.Y. (2009), “Potts model for simulating main characteristics of high burnup structure in UO₂ nuclear fuels”, MMSNF-8, Albuquerque, NM.
- [16] Madison, J., V. Tikare, E.A. Holm (2012), *Journal of Nuclear Materials*, 425, 173-180.
- [17] Tikare, V., M. Braginsky, D. Bouvard, A. Vagnon (2010), *Computational Materials Science*, 48, 317-325.
- [18] Rollett, A.D., D. Raabe (2001), *Computational Materials Science*, 21, 69-78.
- [19] Madison, J., V. Tikare, E.A. Holm (2012), *Journal of Nuclear Materials*, 425, 173-180.
- [20] Homer, E.R., V. Tikare, E.A. Holm (2013), *Computational Materials Science*, 69, 414-423.

Chapter 18.

Rate theory

S. Maillard¹, R. Skorek¹, P. Maugis², M. Dumont²

¹CEA, DEN, DEC, Centre de Cadarache, France,

²Aix-Marseille Université, Université de Toulon, IM2NP UMR CNRS, France

Abstract

This chapter presents the basic principles of cluster dynamics as a particular case of mesoscopic rate theory models developed to investigate fuel behaviour under irradiation such as in UO_2 . It is shown that as this method simulates the evolution of the concentration of every type of point or aggregated defect in a grain of material. It produces rich information that sheds light on the mechanisms involved in microstructure evolution and gas behaviour that are not accessible through conventional models but yet can provide for improvements in those models.

Cluster dynamics parameters are mainly the energetic values governing the basic evolution mechanisms of the material (diffusion, trapping and thermal resolution). In this sense, the model has a general applicability to very different operational situations (irradiation, ion-beam implantation, annealing) provided that they rely on the same basic mechanisms, without requiring additional data fitting, as is required for more empirical conventional models.

This technique, when applied to krypton implanted and annealed samples, yields a precise interpretation of the release curves and helps assess migration mechanisms and the krypton diffusion coefficient, for which data is very difficult to obtain due to the low solubility of the gas.

Cluster dynamics, a complementary method to mean-field models used in fuel performance codes for gas behaviour simulation

The behaviour of fission gases in fuel rods has been studied for decades and several performance codes [18,19,15,12]) have been developed to account for gas release and fuel swelling. These codes rely on “mean-field models” of a single grain (or a slab) considered as a “locally homogeneous” material for which diffusion-precipitation-resolution equations describe the evolution of the concentrations of fission gas atoms and bubbles

(xenon and krypton are the most abundant fission gases). The spatial variations of the concentrations across the grain can be taken into account to some extent, but very small scale variations, e.g., in close vicinity to bubbles or irradiation cascades, are smoothed, which justifies the terms “mean-field models” and “locally homogeneous”. As an example, a set of equations (Equation 1a to Equation 1d) are shown below, similar to those solved by the Margaret code to model the behaviour of Xe in UO_2 [12]:

$$\partial_t(c + m) = \beta + D\Delta c \quad (1a)$$

$$\partial_t N = kc^2 - WN \quad (1b)$$

$$\partial_t m = 2kc^2 + 4\pi \frac{R}{\delta} RDNc - (W + w)m \quad (1c)$$

$$\partial_t m_v = \left(2kc^2 + 4\pi \frac{R}{\delta} RDNc - wm \right) + 4\pi RD_v N \delta c_v - Wm_v \quad (1d)$$

where c , N , m stand for the concentrations of dissolved Xe, nano-bubbles, and total precipitated Xe (in atoms or bubbles/cm³), respectively, $m_v = \frac{4\pi R^3}{3\Omega} N$ is the total number of vacancies present in bubbles per unit volume (vacancies/cm³, the same dimension as c , N and m), so that $m_v \Omega$ is the porosity of the material. β is the Xe source term, D the Xe diffusion coefficient, R the average radius of the bubbles. W and w are ballistic rates, the first one for bubble destruction and the second one for gas resolution (in s⁻¹). δc_v is a vacancy concentration differential explained below. δ is a distance characterising the gas capture.

Specifically:

- Equation 1a is the mass balance for Xe and describes total concentration changes through creation or diffusion.
- Equation 1b shows that the total number of bubbles (only nano-bubbles are addressed in this simplified example) changes through nucleation, which occurs when two Xe atoms encounter each other, or ballistic dissolution, when a fission spike reaches a bubble.
- Equation 1c accounts i) for the increase in the total concentration of precipitated Xe when a new bubble is created or when an existing bubble attracts an extra Xe atom; and ii) for its decrease when a bubble is destroyed or partially dissolved by a fission fragment.
- Equation 1d is similar to Equation 1c, taking into account the fact that the volume of the bubbles can grow through vacancy capture, proportional to $\delta c_v = c_v^{eq}(\infty) - c_v^{eq}(R)$, assuming that the bulk vacancy concentration follows the thermodynamic law ($c_v^{eq}(\infty) = \Omega^{-1} \exp(-E_v^f/kT)$), and the vacancy concentration near the bubble depends on the bubble pressure P and surface energy γ ($c_v^{eq}(\infty) = \Omega^{-1} \exp\left(-\left(E_v^f + \Omega(P - 2\gamma/R)\right)/kT\right)$).

This kind of performance code relatively well reproduces the main operational features and post-irradiation observations resulting from the fuel evolution, in particular the gas concentration and release, swelling and porosity [4]. Many phenomena, however,

are included as empirical laws that do not depend upon a satisfactory and/or comprehensive understanding, thus reducing the reliability of the code when extrapolated beyond observations. For instance, at relatively high burn-up, a second type of bubbles of larger size appears at the centre of the fuel pellet [11]. In the model, this population does not appear as a result of nano-bubble evolution but is created according to an empirical relation. The analysis proposed in [4] shows that improvements in understanding should be achieved by taking into account the fact that the bubbles may exhibit distributed sizes and a gas content departing from the average. The bubble distribution could even be bimodal. Furthermore, a more realistic description of the bubble size and content evolution could be obtained by better accounting for the contribution of the isolated and aggregated self-defects generated in the material through the irradiation process. To our knowledge, no model including all these features has been applied to UO₂ in a PWR, especially in performance codes. Similar approaches are yet reported in [18] for high temperature of FBR fuel evolution. For instance, in the authors' own model, the bubbles are described by a discretised two-dimensional distribution function for radius and gas content, satisfying kinetic equations. The main mechanisms involved are bubble resolution and random or biased migration; the stoichiometry evolution is addressed as well and subsequent swelling and gas release are finally evaluated. In PWR fuels, [15] for instance, calculated the interstitial and vacancy bulk concentrations, as well as bubble average size and gas content, but not size distribution; [5] developed a cluster dynamics model that deals with the dislocation loop size distribution, but gas atoms and bubbles were not included in the model.

To improve the current operational models, a Cluster Dynamics (CD) model can be developed, aiming at calculating the time evolution of the concentration of clusters with various gas atom contents and sizes, as determined by elementary point defects (vacancies or self-interstitials).

Principle of cluster dynamics

Cluster dynamics is a chemical kinetics or rate theory method adapted to the simulation of the evolution of point defects, solutes and defect clusters (dislocation loops or bubbles) in materials at the grain scale [1]. In this method, the system investigated is seen as a gas of clusters of vacancies, interstitials and solute atoms; these clusters can show various sizes (including monomers). The properties of the system are spatially averaged and the positions of atoms or clusters are not considered, but spatial evolution of the cluster concentrations can be (but not described here). The evolution of the system is described by a set of differential equations on cluster concentrations and the model enables one to compute the evolution of the concentrations of all these clusters with time according to the various chemical reactions involved. Cluster Dynamics models have been extensively used in metallic systems, for example to study the behaviour of solid solutions in irradiated or non-irradiated metals [1].

Due to its low computer cost, cluster dynamics can handle long-term evolution that cannot be investigated through atomistic methods. Cluster dynamics enables the development of more general and precise models than standard operational rate theory models previously applied to nuclear fuels, which basically rely on the same physics, but make significant and poorly justified approximations on the cluster size distribution. In

comparison, the complete and unbiased description of the cluster size distribution can be computed by cluster dynamics as a natural consequence of input parameters such as formation and migration energies. Thus, such a model, as it addresses size and time scales relevant to industrial issues, appears as a natural framework for utilising atomic scale studies.

A drawback of the method is the loss of space correlations between the elements in the material microstructure which is the price to pay for the substantial decrease in computational cost compared to atomistic methods. Nevertheless, the improved description compared to earlier rate theory models comes with an increased complexity of numerical resolution. Finally, while cluster dynamics has been extensively applied to metallic systems, there are very few applications reported for ceramic fuels [5].

A cluster dynamics model for Kr behaviour in UO₂

The results presented below are from the European F-BRIDGE Project [14]. The goal was the first application of cluster dynamics modelling to the behaviour of fission gases, and especially Kr, in UO₂.

The CD model is devoted to calculating the time evolution of the concentration $C_{n,p}$ of aggregates of $|n|$ elementary point defects (vacancies or self-interstitials) and p gas atoms (xenon or krypton); with the spatial dependence of these quantities not taken into account. By convention n is negative for vacancies, i.e., when clusters are voids or bubbles, and positive for self-interstitials, i.e., when clusters are dislocation loops. Loops incorporating gas atoms are not considered here. Because UO₂ is a diatomic material, several types of elementary defects should, in principle, be considered, as V_O, V_U, V_U(V_O)₂ for vacancies and O_i, U_i, U_i(O_j)₂ for interstitials. However the technique does not yet account for two different sub-lattices, so, in this study, we have assumed that vacancy and interstitial defects are V_U(V_O)₂ and U_i(O_j)₂ respectively, that is Schottky and anti-Schottky trios (or defects). Indeed, these defects are thought to be among the most favoured in the situations addressed here, namely close to stoichiometry [2]. Both elementary self-defects are supposed to be mobile and therefore likely to react with other point defects or clusters. The gas atoms are assumed to be mobile in two configurations, namely interstitial (i.e., (0,1) or Kr) or combined with a di-vacancy (i.e., (-2,1) or V₂Kr), as considered for various solutes in metals.

The evolution of each cluster concentration C(n,p) is controlled by a Master Equation [1,6]:

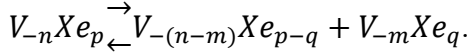
$$\begin{aligned} \partial_t C_{n,p} = & \sum_{(m,q)\text{mobile}} J_{(n-m,p-q)+(m,q)} \rightarrow (n,p) - \sum_{(m,q)\text{mobile}} J_{(n,p)+(m,q)} \leftarrow (n+m,p+q) + G_{(n,p)} - \\ & K_{(n,p)} \end{aligned} \quad (2)$$

where the first and second terms are the sums of the net cluster fluxes to and from the (n,p) cluster population, respectively. The third and fourth terms are the source and sink terms which account for the production of (n,p) defects inside the displacement cascades and their elimination to sinks (eg., free surfaces and grain boundaries) if they are mobile.

Each flux can be decomposed into absorption and emission rates:

$$J_{(n-m,p-q)+(m,q)\leftarrow(n,p)} = B_{(n-m,p-q)+(m,q)\rightarrow(n,p)} C_{(n-m,p-q)} C_{(m,q)} - A_{(n,p)\rightarrow(n-m,p-q)+(m,q)} C_{(n,p)} \quad (3)$$

$B_{(n-m,p-q)+(m,q)\rightarrow(n,p)} C_{(n-m,p-q)} C_{(m,q)}$ is the absorption rate of the mobile cluster (m,q) by the cluster (n-m,p-q), yielding an (n,p) type cluster and $A_{(n,p)\rightarrow(n-m,p-q)+(m,q)} C_{(n,p)}$ is the emission rate of a mobile (m,q) cluster by an (n,p) type cluster, yielding an (n-m,p-q) type cluster. The flux $J_{(n-m,p-q)+(m,q)\leftarrow(n,p)}$ can thus be related to the rates of a formal chemical reaction for $V_{-n}Xe_p$ dissociation (conventionally n<0 for vacancy containing clusters and n>0 for loops):



$A_{(n,p)\rightarrow(n-m,p-q)+(m,q)}$ and $B_{(n-m,p-q)+(m,q)\rightarrow(n,p)}$ are absorption and emission coefficients, defined as:

$$\begin{aligned} B_{(n-m,p-q)+(m,q)\rightarrow(n,p)} &= 4\pi(R_{(n-m,p-q)} + R_{(m,q)} + \delta R)(D_{(n-m,p-q)} + D_{(m,q)}) \\ A_{(n,p)\rightarrow(n-m,p-q)+(m,q)} &= (B_{(n-m,p-q)+(m,q)\rightarrow(n,p)}/\Omega) \exp\left(-\frac{F_{(n-m,p-q)+(m,q)\rightarrow(n,p)}^b}{kT}\right) \end{aligned} \quad (4)$$

where, the R's are the radii of the various clusters, δR a capture radius allowing for small cluster recombination, the D's the diffusivities of the clusters and Ω the volume of the lattice unit cell. The right-hand side of Equation 4 is derived from the mass action law applied to the reaction. The binding free energy between the clusters, F^b , has been estimated on the basis of a conventional thermodynamic model, generalising Equation 9 [1]. A gas equation of state derived from a hard sphere model has been used in this model (Equation 29 [16]). The source term is evaluated with classical molecular dynamics [8].

Simulation of an annealing experiment using cluster dynamics

The cluster dynamics model as included in the code CRESCENDO [6] has been tested in Thermal Desorption Spectroscopy (TDS) experiments [9]. UO₂ samples have been irradiated at room temperature with 250 keV Kr ions at a very low fluence (0.5 s at a flux of 10¹² Kr/cm²/s). The samples have then been annealed at 1 250, 1 350, or 1 450°C for about 800 minutes and the Kr release was monitored during the process. Because of the very low fluence, a rather small amount of irradiation vacancies are created; this partly prevents gas trapping and enhances the migration and release which benefits diffusivity measurements.

The krypton release curves from the annealing experiments at three temperatures are shown in Figure 1. Two release regimes can be distinguished: an initial burst (1st regime) is followed by a release roughly proportional to the annealing duration (2nd regime). Only the second follows the Fick's law.

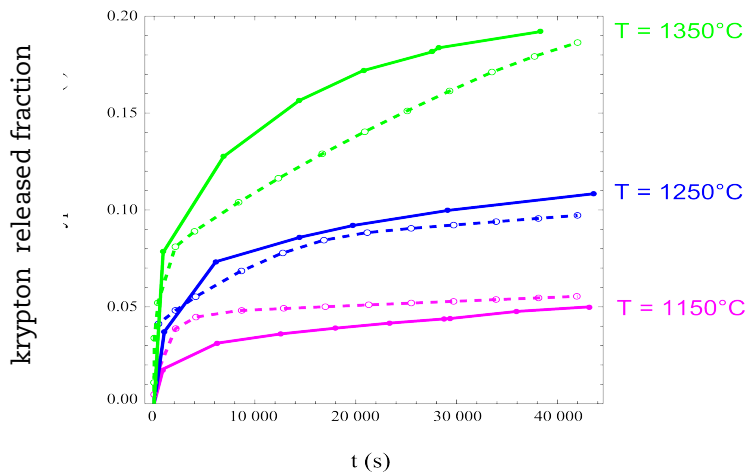
If we focus on the second regime and neglect the initial bulk trapping of the mobile krypton, the fractional release, F , can be fitted by the approximate expression $F = Dt/L^2$ (D being the gas diffusivity, L the implantation depth).

A SRIM [17] simulation yields $L = 70$ nm, and from a subsequent numerical fitting, an average value of the krypton migration energy of ~ 4.5 eV has been obtained, according to the equation $D = v a^2 \exp(-E_m/kT)$, v being the Debye frequency (10^{13} Hz) and a the lattice parameter. Since DFT determination [7] of the Xe migration energy (1.6 eV) suggests that interstitial gas atoms are highly mobile, we assumed in this work, as developed below, that this rather low experimental diffusion coefficient corresponds to another mobile species, assumed to be V₂Kr. The released gas variation K of Equation 4 for a mobile krypton simply yields: $K = D C/L^2$ (C being the concentration of the corresponding krypton migrating species).

As stated above, the source term is evaluated on the basis of classical molecular dynamics simulations [8]. The cascade resulting from the implantation of a single ion (250 keV krypton ion or a fission product) is assumed to break down into 25 lower energy independent sub-cascades of ~ 10 keV each producing on average 20 Frenkel pairs: 3 cavities of 3 vacancies ((-3,0) or V₃), 3 loops of 3 self-interstitials ((3,0) or I₃), and 11 additional isolated interstitials ((1,0) or I) and vacancies ((-1,0) or V). Krypton is assumed to be inserted into an interstitial position during implantation ((0,1) or Kr).

A first CD simulation of the implantation yields the initial cluster concentrations. Two steps are calculated: the first one results from the 0.5 s implantation and simply reflects the production rates integrated over the implantation time; the second one is obtained after an annealing period at room temperature during which the very mobile self-interstitial defects (see Table 1) migrate to the free surface or other vacancies and annihilate.

**Figure 1. Fraction of krypton released during the annealing experiment
(solid lines: experiments, dotted lines: from fitting)**



The formation and migration energies used in the model for the different elementary clusters are reported in Table 1. The formation energy of the self-interstitial is set at a very high value, practically preventing any thermal formation of Frenkel pairs while the other formation energies were taken from [3]. The migration energies are estimated by numerical fitting of the TDS experiments; initial estimates were based on atomistic

calculations of Xe migration energy [7] (assuming Kr and Xe have similar values) and on the Fickian analysis of the release curves for V₂Kr of Figure 1.

Table 1. Energetic and kinetic input parameters of the base defects (eV)

Defects	V (-1,0)	I (1,0)	Kr (0,1)	VKr (-1,1)	V ₂ Kr (-2,1)
Formation energies E _f *	2.5	10	7	3.8	Thermodynamic model
Migration energies E _m *	3	0.7	2.2	not mobile	4.5

Figure 2 shows the evolution of the different kinds of defects during annealing at 1 350°C. The figure and the corresponding reaction rates computed by CD reveal the following main features:

- The vacancies (green line) drive the system evolution, as they start to be mobile around 1 000°C: they aggregate to produce cavities (V_n) or bubbles (V_nKr_p) (summed for n>1 and represented by the thick green line); they also react with the loops and progressively “erode” them, finally yielding isolated interstitials according to reactions such as $nV + I_{n+1} \rightarrow I$. Eventually ($t \sim 10^4$ s), the vacancy concentration converges to the equilibrium value (dotted green line).
- The self-interstitials I, produced through loop “erosion” by vacancies, represent an appreciable concentration (red line) as long as loops (thick red line) exist in the material (seen up to 1 000 s). This concentration has an important impact on the initial gas release.
- Indeed, gas atoms, initially implanted in interstitial position (Kr, cyan dotted line), are rapidly trapped, mostly by vacancies (in 10^4 s), yielding VKr (blue dotted line), which is not mobile. Further vacancy captures produce V₂Kr clusters (darker blue dotted line), which are again mobile. Both mobile species yield the cumulative krypton release of the doted black lines (Kr is thin, V₂Kr is thick).

The mechanisms of krypton release need some further analysis. Indeed, the very first burst of release is simultaneous with the trapping of interstitial krypton (Kr) by vacancies, and corresponds to its rapid migration to the grain free surface (first 10^{-4} s). An estimation of the time scale of Kr trapping by vacancies is $\tau = (4\pi RDC_V)^{-1} \approx 10^{-4}$ s, which confirms that there should be no more Kr released after this period. A careful analysis of the higher reaction rates reveals an intense “kick-out” reaction involving an SIA the ejection of a substitutional Kr into an interstitial site by a SIA according to the reaction Kr: $VKr + I \xrightarrow{\text{Kr}} Kr$. This reaction accounts for Kr presence as long as free interstitial atoms exist, i.e., until complete annihilation of the loops by the mobile vacancies ($t \sim 2 000$ s). To summarise, krypton release can be explained by three successive mechanisms:

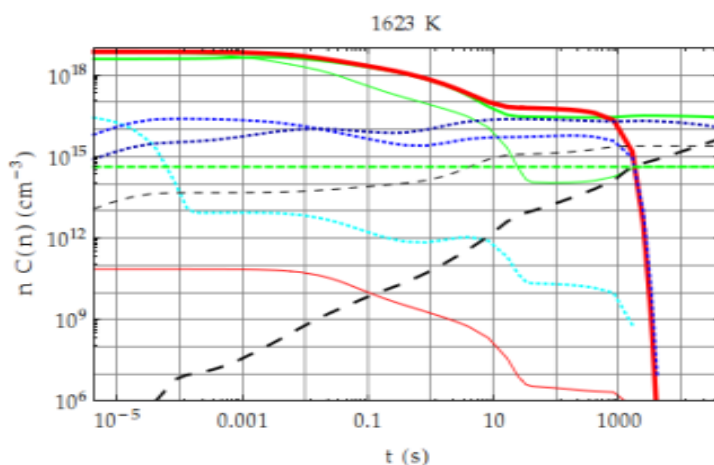
- $t < 10^{-4}$ s: immediate release due to the migration of the initial interstitial krypton (Kr) while the rest remain trapped;
- $10^{-4} s < t < 2 \times 10^3$ s: release caused by interstitial krypton (Kr) produced by the kick-out reaction;

- $2. \times 10^3 \text{ s} < t$: release caused by the substitutionally mobile (V_2Kr).

In conclusion, this first application of cluster dynamics to the interpretation of a TDS experiment yields interesting information, concerning mainly mechanisms, and, to some extent, energetic data.

- First, in such a modelling framework, two distinct krypton migration mechanisms (one interstitial and one substitutional) are necessary to explain the complex release curves, namely the initial burst.
- Second, migration energy can also be evaluated. For the krypton in substitutional position, the CD approach confirms the diffusivity evaluation obtained with a simple diffusion model applied to the late period of the experiments [9]. For the interstitial krypton, the fitting procedure yields a simultaneous and global estimation of the migration energies of all the remaining mobile species (I, V, Kr), which is less precise and should certainly be improved, for example through *ab initio* calculations or devoted experiments.
- Third, another important mechanism is evidenced as the “kick-out” reaction in which a self interstitial is replaced by a krypton atom in interstitial position. This mechanism basically relies on thermodynamic characteristics of the species involved in the reaction (i.e., the self-interstitial is much less soluble than the krypton), which motivates to determine more precisely the formation energy of the self-interstitial (i.e., anti-Schottky).

Figure 2. Concentration evolution of the main classes of clusters for the annealing experiment at 1 350°C



Conclusion and future challenges

Although cluster dynamics has long been applied to precipitation issues in metals, few examples exist concerning the behaviour of fission gas in PWR nuclear fuel. However, in this section, it has been demonstrated that the technique sheds light on aspects, and in particular mechanisms, which cannot be addressed with standard mesoscopic models used in fuel performance codes.

Cluster dynamics computes the evolution of the concentration of every type of point defect or cluster in a grain of material without any *a priori* choice concerning clusters or their reactions. As an interesting result of that, we have identified a potentially important “kick-out” mechanism that had not been anticipated prior to the calculations. Indeed, in-pile modelling of fission gas behaviour usually invokes ballistic gas resolution based on Nelson analysis [10] to account for the high dissolved concentration necessary to explain the gas release observed in irradiated UO₂. According to a recent evaluation of this resolution term [13] based on more precise techniques (coupled Monte Carlo/Molecular Dynamics), the gas resolution calculated by Nelson is 50 times too high; it can thus be inferred that this mechanism cannot alone explain the in-pile observed gas release. The kick-out mechanism, pointed out in this study, might be an additional possibility and should indeed be assessed in future work. In particular, CD should be validated on material undergoing irradiation.

Cluster dynamics, when applied to krypton implanted and annealed samples, yields a precise interpretation of the release curves and helps in assessing migration mechanisms. It also aids in the estimation of krypton diffusion coefficients, for which data are very difficult to obtain due to the low solubility of the gas.

Standard mesoscopic models are heavily phenomenological and rely on a rather limited set of effective parameters fitted from complex experiments, yet CD by contrast is based on a set of physical parameters (formation or migration energies of small clusters) describing the basic mechanisms (diffusion, capture, emission...) controlling the material’s evolution; these parameters can be evaluated by atomistic methods or dedicated experiments. An advantage of the CD approach is that the same basic mechanisms describe various operational phenomena (ion implantation, neutron irradiation, annealing...), allow a unique set of parameters to be valid for all these situations. In the same way, the impact of minor changes in material characteristics (composition...) could ideally be assessed by CD based on separated effects experiments in which these physical parameters are determined. Ion-irradiation experiments could be used for such an initial assessment, prior to a more complex neutron irradiation. This would simplify the material’s design process. Nevertheless, a temporary drawback of the approach is that the basic data necessary to assess the gas behavior in the material under irradiation remain difficult to obtain. Critical data may be missing or poorly known (migration energies of Kr, I, V, formation energy of I and I₂). More generally, a better knowledge of the real defects present in the material as a function of the stoichiometry is needed, so that the simplifying assumption of self-defects being equivalent to Schottky or anti-Schottky is better justified or improved. Indeed, in the near future, one can expect that basic data will be routinely available, from either atomistic calculations or dedicated experiments.

References

- [1] Barbu, A., E Clouet (2007), *Solid State Phenomena*, 129, 51-58.
- [2] Barthe, M.-F. et al. (2012), COSIRES, Santa Fe.
- [3] Dorado, B. (2010), PhD Thesis, University of Aix Marseille II.
- [4] Garcia, P. et al. (2011), NIMB, 227, 98.
- [5] Jonnet, J. et al. (2008), NIMB, 266(12-13), 3008-3012.

- [6] Jourdan, T. et al. (2014), *JNM*, 444(1-3), 298313.
- [7] Liu, X.Y. et al. (2011), *Applied Physics Letter*, 98, 151902.
- [8] Martin, G. et al. (2010), *Physics Letters A*, 374(30), 3038-3041.
- [9] Michel, A. (2011), PhD Thesis University of Caen.
- [10] Nelson, R.S. (1969), *Journal of Nuclear Materials*, 31(2), 153161.
- [11] Noirot, J., Noirot, L. et al. (2004), *Proceedings of the 2004 International Meeting on LWR Fuel Performance*, Orlando, Florida.
- [12] Noirot, L. (2011), *Nuclear Engineering and Design*, 241(6), 2099-2118.
- [13] Schwen, D. et al. (2009), *Journal of Nuclear Materials*, 392(1), 3539.
- [14] Skorek, R. (2013), PhD Thesis, University of Aix-Marseille.
- [15] Veshchunov, M. S. et al. (2006), *Nuclear Engineering and Design*, 236(2), 179200.
- [16] Volkov, A.E., A.I., Ryazanov (1999), *Journal of Nuclear Materials*, 273(2), 155-163.
- [17] Ziegler, J.F. et al. (2012), *The Stopping and Range of Ions in Matter*.
- [18] Griesmeyer, J.M. et al. (1979), “A dynamic intragranular fission gas behaviour model”, *Nuclear Engineering and Design*, 55.
- [19] Losonen, P. (2002), “Modelling intragranular fission gas release in irradiation of sintered LWR UO₂ fuel”, *Journal of Nuclear Materials*, 304.

Chapter 19.

Thermochemical modelling of multi-component systems

B. Sundman¹, C. Guéneau²

¹KTH Royal Institute of Technology, Sweden,

²CEA, DEN, DPC, Centre de Saclay, France

Abstract

Computational thermodynamic, also known as the Calphad method, is a standard tool in industry for the development of materials and improving processes and there is an intense scientific development of new models and databases. The calculations are based on thermodynamic models of the Gibbs energy for each phase as a function of temperature, pressure and constitution. Model parameters are stored in databases that are developed in an international scientific collaboration. In this way, consistent and reliable data for many properties like heat capacity, chemical potentials, solubilities etc. can be obtained for multi-component systems. A brief introduction to this technique is given here and references to more extensive documentation are provided.

Introduction

This text intends to introduce the Calphad method used to model thermodynamics for multicomponent systems. The implications when it concerns dealing with many components and phases with strong deviations from ideality will be clarified. For an extended text please refer to Saunders [15], Hillert [6] or Lukas et al. [10].

The most important implication of thermodynamics is the second law, which defines the equilibrium state of a system. Thermodynamics gives relations between many observable properties like temperature, volume and heat. Some of these properties are also state variables, i.e., they are independent how the system reached its current state. With models how these state variables depend on temperature, pressure and composition, using experimental and theoretical data for a system, one can assess parameters which make it possible to calculate how a multi-component system will behave when changing different external variables. Such calculations are in principle only valid at the equilibrium

state but, as will be explained below, with a consistent thermodynamic modelling one can extrapolate the thermodynamic state variables and properties also very far from the equilibrium state.

Some important relations

In the basic thermodynamics, we learned that many observables, like temperature T , pressure P and volume V , are also variables of the state of the system, i.e., they are independent how that state was reached.

We then introduced several additional state variables (or functions) that are not observables but define important relations between them. The state variable mostly used for thermodynamic modelling is the Gibbs energy, G which is a function of temperature T , pressure P and the amount of the components of the system N_i , where i specifies the component.

$$G = G(T, P, N_i) \quad (1)$$

The Gibbs energy G has a minimum, i.e., $dG = 0$, at the equilibrium of a system kept at constant T, P and amount of components N_i and we express dG as:

$$dG = \left(\frac{\partial G}{\partial T} \right)_{P, N_i} dT + \left(\frac{\partial G}{\partial P} \right)_{T, N_i} dP + \left(\frac{\partial G}{\partial N_i} \right)_{T, P, N_{j \neq i}} dN_i \quad (2)$$

Partial derivatives are an important part of thermodynamics and from the derivation of the Gibbs energy we know that:

$$S = - \left(\frac{\partial G}{\partial T} \right)_{P, N_i} \quad (3)$$

$$V = - \left(\frac{\partial G}{\partial P} \right)_{T, N_i} \quad (4)$$

$$\mu_i = - \left(\frac{\partial G}{\partial N_i} \right)_{T, P, N_{j \neq i}} \quad (5)$$

where S is the entropy and μ_i the chemical potential of component i .

In order to model the thermodynamic properties of a system, we must consider that all thermodynamic systems consist of several phases and each phase must be modelled separately. As the Gibbs energy is an extensive property, we can formulate it also as a sum of the contributions from all stable phases:

$$G = \sum_{\alpha} N^{\alpha} G_m^{\alpha}(T, P, x_i^{\alpha}) \quad (6)$$

where N^{α} is the number of moles of components in phase α per mole formula unit of the phase and G_m^{α} is the molar Gibbs energy of the phase. The molar Gibbs energy depends on T, P and the mole fractions of the components of the phase, x_i^{α} . The total amount of each component is also obtained by summing over all phases:

$$N_i = \sum_{\alpha} N^{\alpha} x_i^{\alpha} \quad (7)$$

The sum of mole fractions is unity both in each phase and for the whole system as we have:

$$x_i = \frac{N_i}{\sum_j N_j} \quad (8)$$

The separation of the Gibbs energy into the sum over all stable phases is important as it makes it possible to model each phase separately.

The chemical potential of a component was defined above as:

$$\mu_i = \left(\frac{\partial G}{\partial N_i} \right)_{T, P, N_{j \neq i}} \quad (9)$$

For an expression of the molar Gibbs energy, we can convert this to:

$$\mu_i = G_m + \left(\frac{\partial G_m}{\partial x_i} \right)_{T, P, x_{j \neq i}} - \sum_j x_j \left(\frac{\partial G_m}{\partial x_j} \right)_{T, P, x_{j \neq i}} \quad (10)$$

The difference is due to the fact that the molar Gibbs energy is for a system with fixed size and the x_i are not independent as their sum is unity.

When we use this equation for a component i of a single phase, we will call it a partial Gibbs energy and denote it G_i . At equilibrium, the partial Gibbs energy for the components must be the same in all stable phases and equal to the chemical potentials of the components.

Modelling the molar Gibbs energy

In this section, the basic techniques to model the molar Gibbs energy of a phase depending on its structure will be explained. Advanced topics such as magnetic contributions and short-range ordering are found in the references.

In the models, the Gibbs energy for a phase normally extends all the way to the pure elements even if the element is not stable for that particular phase. Estimates of the relative stability of such phases, known as “lattice stabilities” are very important in the modelling. Also for stable phases, like the liquid, extrapolations of the Gibbs energy to temperatures where the phase is not stable are important.

The configurational entropy is very important especially at dilute solutions or for systems with strong short order (sro). In Calphad, a simple ideal mixing of the constituents on the different types of sites in the phase is used in most cases. This has been one of the main criticisms of the Calphad technique for long time but for systems with 10-15 components the Calphad models are the only realistic method due to other uncertainties in the modelling. With better data and faster computers in the future more elaborate configurational entropy expressions may become more common.

Based on these estimates, the Calphad technique has an assessment procedure to fit the model parameters for the Gibbs energies for the phases in a system to experimental data on chemical potentials, enthalpies of mixing and transformation, heat capacities, etc. recalculating the same data from the model with varying the parameters to minimise the difference.

Modelling the gas phase

The Gibbs energy of formation of each gas molecule j as a function of T and relative to some reference states (SER) of the elements i in the molecule (usually the stable state at 298.15 K and 1 bar) is denoted ${}^\circ G_j(T)$:

$${}^\circ G_j(T) = G_j - \sum_k b_{ji} H_i^{\text{SER}}(298.15) \quad (11)$$

where b_{ji} is the stoichiometric ratio of element i in the molecule j . As there is no zero point for the enthalpy, the individual values of G_j and $H_i^{\text{SER}}(298.15)$ are meaningless. The pre-superscript “ ${}^\circ$ ” indicates that the parameter is for a single pure molecule. For gas molecules, such Gibbs energies are today calculated by first principle techniques taking into account all vibrational and rotational degrees of freedom of the molecule. There are several databases available with values of ${}^\circ G_j(T)$ for several 1 000 different molecules.

The molar Gibbs energy of an ideal gas is the sum of these Gibbs energies, weighted by the fraction of each molecule, y_j , an ideal configurational entropy of mixing and the total pressure P :

$$G_m = \sum_j y_j ({}^\circ G_j(T) + RT \ln(y_j)) + RT \ln(P) \quad (12)$$

where R is the gas constant. This can be derived from the equation of state for one mole of a single component gas $PV = RT$ as:

$$G_m = \int_{P_0}^P V dP = \int_{P_0}^P \frac{RT dP}{P} = RT \ln\left(\frac{P}{P_0}\right) \quad (13)$$

and the partial pressure of a gas molecule, P_j in an ideal gas is given by Dalton's law:

$$P_j = P y_j \quad (14)$$

At equilibrium, the chemical potential of a gas molecule j is equal to the sum of the chemical potentials of the components i multiplied with the stoichiometric factor, b_{ji} :

$$\mu_j = \sum_i b_{ji} \mu_i \quad (15)$$

As an example, the chemical potential of A_2B is given by:

$$\mu_{A_2B} = 2\mu_A + \mu_B \quad (16)$$

Modelling a crystalline solid phase

In the gas phase, we did not include any interactions between the molecules. For the condensed phases, this must be made and we have also other contributions, so we will write the general expression for the molar Gibbs energy as:

$$G_m = {}^{srf}G_m - T^{\text{cfg}}S_m + {}^E G_m + {}^{\text{phys}}G_m \quad (17)$$

where ${}^{srf}G_m$ is called the surface of reference for the phase, ${}^{\text{cfg}}S_m$ is the configurational entropy, ${}^E G_m$ is the excess Gibbs energy and ${}^{\text{phys}}G_m$ are special contributions due to ferromagnetic transitions or other particular physical properties of the phase.

Surface of reference and end-members

We will first discuss how the surface of reference and the configurational entropy can be modelled for different phases.

A solid phase normally has a well-defined crystalline structure and each such structure is treated as a separate phase. The model for the phase takes into account as much as possible the specific structure but considering that the modelling should extrapolate to 10-15 components, some simplifications are often used. This is not only due to the speed of computation but also because of lack of experimental or theoretical data in many binary and ternary systems. In particular, if the phase is not stable in these systems but may dissolve significant amount of these elements in higher order systems.

For a phase with a single set of lattice sites, we can use a substitutional solution of the constituents i and the surface of reference is:

$${}^{srf}G_m = \sum_i x_i {}^G_i \quad (18)$$

For example, for a phase where the A atoms occupy an FCC lattice and the interstitial B atoms another octahedral sublattice. We must take into account which constituents occupy the different sublattices in the modelling and for a system like A-C-B, the A and C atoms occupy the normal FCC lattice sites whereas B and vacancies (denoted “Va”) occupy the interstitial sites. We have:



The surface of reference for this ternary system has four terms:

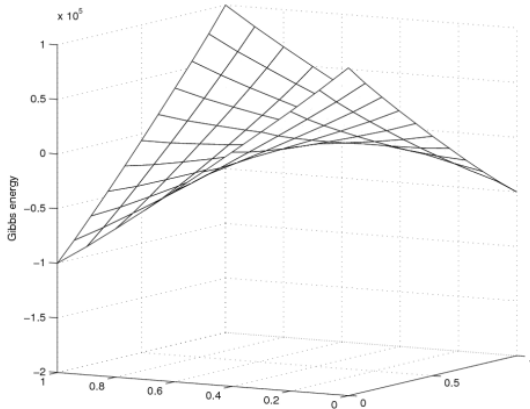
$${}^{srf}G_m = y_A y_{Va} {}^G_{A:Va} + y_C y_{Va} {}^G_{C:Va} + y_A y_B {}^G_{A:B} + y_C y_B {}^G_{C:B} \quad (20)$$

This model has four end-members representing the possible combinations of one constituent in each sublattice. The end-member represents a pure compound with fixed composition and this is the reason for the name Compound Energy Formalism (CEF). For the system above, (A:Va) represents pure A in the FCC lattice and ${}^G_{A:Va}$ is its Gibbs energy function relative to the selected reference state for A. The same for (C:Va) even if FCC-C is never stable at normal temperatures and pressures. The end-member (C:B) represents the stoichiometric cubic phase that is stable in the C-B system and ${}^G_{C:B}$ is its

Gibbs energy relative to the reference states for C and B. Finally, the end-member (A:B) represents a meta-stable phase in the A-B system.

A possible Gibbs energy surface of reference is shown in Figure 1.

**Figure 1. The sublattice model (A,C)₁(B,Va)₁ for the fcc phase in the A-C-B system:
The Gibbs energy surface of reference for a reciprocal system**



The configurational entropy

In CEF, the configurational entropy assumes ideal mixing on each sublattice and this is simply:

$$^{cfg}S_m = -R \sum_s a_s \sum_j y_i^{(s)} \ln(y_i^{(s)}) \quad (21)$$

As the configurational entropy is evaluated separately for each sublattice, it will be zero for each end-member, i.e., when the phase has perfect long range order. There are more elaborate forms of the configurational entropy proposed by Cluster Variation Method (CVM) developed by Kikuchi [9] that also describes short-range ordering.

The excess Gibbs energy

The excess Gibbs energy is used to model the remaining part of the Gibbs energy needed to describe the difference between the real Gibbs energy and the contributions from the surface of reference and the configurational entropy. As we cannot measure the Gibbs energy directly we can only use indirect data like chemical potentials, enthalpies and solubilities.

For the simplest type of models with a single substitutional lattice, the excess Gibbs energy can be written as a sum of terms multiplied with two or more fractions:

$$^E G_m = \sum_i x_i \sum_{j>i} x_j \left(L_{ij} + \sum_{k>j} x_k L_{ijk} \right) \quad (22)$$

where L_{ij} and L_{ijk} are, respectively binary and ternary interaction parameters. It is possible to have quaternary parameters or higher order parameters but rarely used. These parameters often depend linearly on temperature and, in many cases, also on composition.

The composition dependence of the binary parameters is most often described by a Redlich-Kister series:

$$L_{ij} = \sum_{v=0}^n (x_i - x_j)^v v L_{ij} \quad (23)$$

The upper limit of the sum, n , should never exceed 3 as higher powers will extrapolate badly to multi-component systems for the composition dependence of ternary parameters [10].

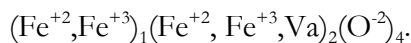
For phases modelled with several sublattices, we can have the same kind of interactions on each sublattice. For the A-C-B system, the excess Gibbs energy will be:

$$\begin{aligned} {}^E G_m = & y_A y_C y_{Va} L_{A,C,Va} + y_A y_{Ci} y_B L_{A,C,B} + y_A y_B y_{Va} L_{A,B,Va} + y_C y_B y_{Va} L_{C,B,Va} \\ & + y_A y_C y_{Va} y_B L_{A,C,B,Va} \end{aligned} \quad (24)$$

The first four terms represent binary interactions. They can be composition dependent as in Equation 23. The last term is known as the reciprocal parameter and is important to describe the contribution to the Gibbs energy due to short-range ordering.

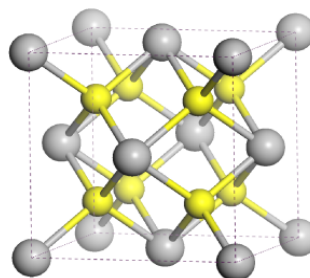
Ionic constituents

In spinels and other oxide phases, the constituents have a net charge. Even if the electrons can jump easily from one ion to another it is possible to use ions as constituents and include them in the configurational entropy. For the spinel phase in the Fe-O system, called magnetite with the ideal stoichiometry Fe_3O_4 , the following model has been adopted [13]:



In a normal spinel we have only di-valent ions on the first sublattice and only tri-valent on the second but magnetite is an inverse spinel at low temperature with mainly Fe^{+3} on the first and equal fraction of Fe^{+2} and Fe^{+3} on the second. At higher temperature, the magnetite becomes more random and can also have deviations in stoichiometry towards higher oxygen content. This is modelled, according to experimental data, with an increase fraction of Fe^{+3} ions and addition of vacant sites on the second sublattice. Another example is the $\text{UO}_{2\pm x}$ phase that has the C1 structure (Figure 2).

Figure 2. C1 structure (CaF₂ type) of UO₂



A complete modelling of the thermodynamic properties of the $\text{UO}_{2\pm x}$ fuel was performed by Guéneau et al. [4]. The simplest sublattice model including interstitial oxygen in the octahedral sites is: $(\text{U}^{+3}, \text{U}^{+4}, \text{U}^{+5})_1 (\text{O}^{-2}, \text{Va})_2 (\text{O}^{-2}, \text{Va})_1$. The three-sublattice

model leads to 12 end-member parameters to be determined from experimental data. New relationships were proposed by Sundman et al. [14] in order to relate these parameters to the energies of formation of point defects (interstitial and oxygen vacancies, as well as electrons and holes).

This model has been applied for the description of oxygen potential data in AmO_{2-x} by Besmann [17]. The model on $\text{UO}_{2\pm x}$ fuel developed by Guéneau et al. has been extended to the description of $(\text{U},\text{Pu})\text{O}_{2\pm x}$ fuels by Guéneau et al. [4] and $(\text{Pu},\text{Am})\text{O}_{2\pm x}$ fuels by Gotcu et al. [18].

Magnetic and other physical contributions

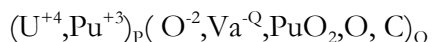
In some phases, there is a significant contribution to the Gibbs energy due to ferromagnetic transitions. This depends on the value of the Curie temperature and the Bohr magneton number, both of which depend on the temperature. This has been modelled with a phenomenological model proposed by Inden [8]. The details are given in [10].

Modelling the liquid

The liquid is the most complicated phase to model. There are no fixed lattice sites in liquids. Anyway, many use a quasichemical model with an unphysical value of 2 for the number of bonds per atom. The reason a more physical value cannot be used is that we will then have a negative configurational entropy when the short-range order is so strong the phase would like to have long-range ordering, but is prevented to transform to such a state, because there are no sublattices [11,7].

Another approach is to model the liquid with molecules, known as associates, representing the compositions for short-range ordering. This sometimes gives wrong values for the partial enthalpies (and entropies) at dilute solutions.

Another model is to accept sublattices in the liquid, not assuming any fixed positions in space but only that cations and anions would never occupy the same positions. This is the one preferred as it has consistent extrapolations to simple regular models as well as strongly ionic ones. The main problem with this model is that it creates spurious miscibility gap in the liquid, mainly due to the lack of experimental information to determine reliable model parameters. This kind of model is used, for example, to model the liquid phase in the U-Pu-O-C system [4] using the following constituents:



where the first sublattice contains the cations and the second one is filled with anions, hypothetical charged vacancies and neutral species. P and Q, the site numbers for the two sublattices, vary with the composition of the liquid to maintain electrical neutrality.

Calculation of equilibria and phase diagrams

With models of the molar Gibbs energy for the relevant phases, the equilibrium can be calculated by minimising Equation 6 for the relevant set of conditions. According to Gibbs phase rule one must set one condition for each component and two more for T and P :

$$f = n + 2 - p \quad (25)$$

where f is the degrees of freedom, n is the number of components and p is the number of stable phases. If P is constant the 2 must be replaced by 1 and if also T is constant by zero. A unary system with $n = 1$ has no degrees of freedom if three phases are stable, we have an invariant equilibrium. If one changes T or P from this point one of the three phases will disappear.

When we have many components, the number of phases that must be stable to have an invariant equilibrium increases. For a binary system with fixed P , the most common conditions for phase diagrams, we have also three phases stable at an invariant equilibrium.

All general softwares for thermodynamic calculations (Thermo-Calc [1], FACTSAGE [2], PANDAT [3], MTDATA [5], Gemini) also allow conditions to be set on the chemical potentials or activities of the components. The activity, a_i of a component i is simply related to its chemical potential G_i as:

$$a_i = \exp\left(\frac{G_i}{RT}\right) \quad (26)$$

The reference state for the element must be specified for both chemical potentials and activities.

The assessment procedure

The Calphad technique is based on experimental data and its aim is to get a description of these experimental data as accurate as possible. The methodology is explained in Figure 3.

The first step consists in the critical analysis of the available data in the literature. Three kinds of data have to be analysed: the phase diagram data (phase boundaries), thermodynamic quantities such as chemical potential, heat capacity, enthalpy of formation and crystallographic data to define the sublattice model to describe the solid phases. The data are selected with an evaluation of their uncertainty.

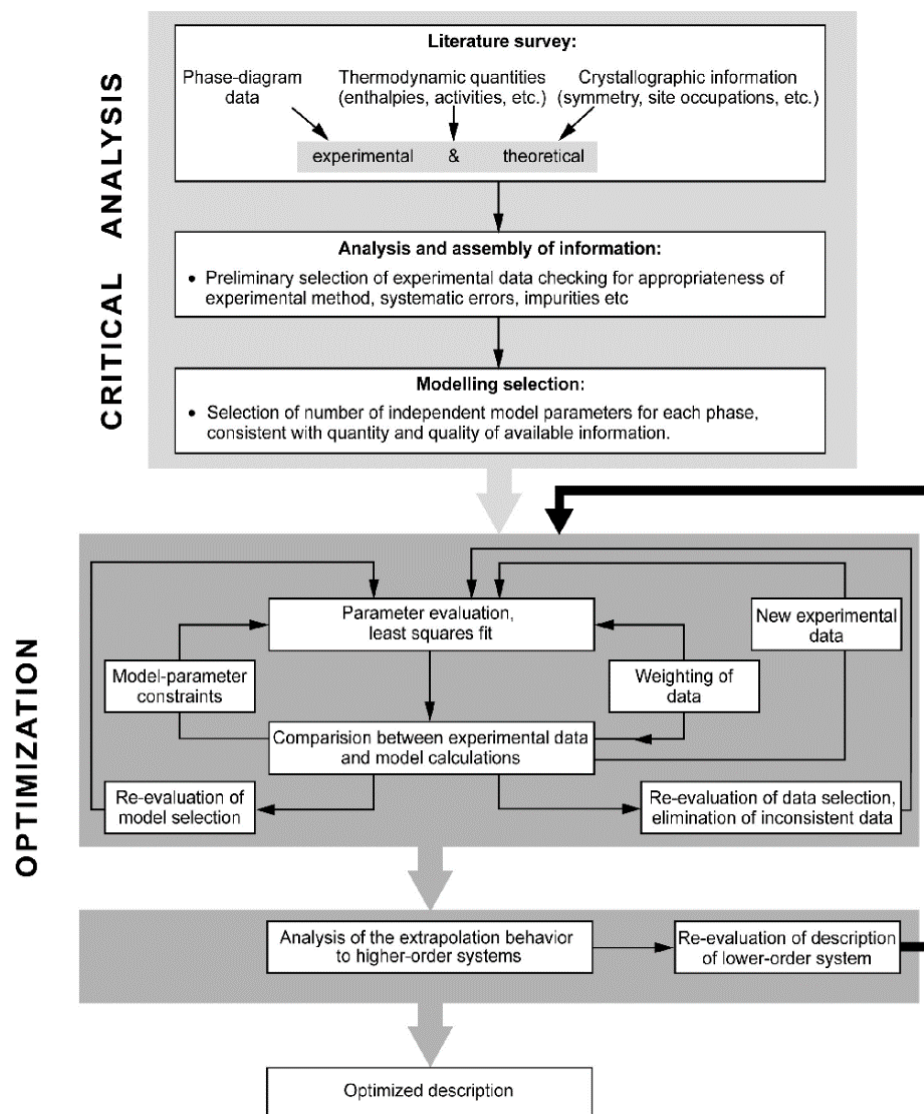
The thermodynamic parameters corresponding to the sublattice model for each phase are then selected to be optimised using an iterative least square method to minimise the difference between the experimental and the calculated data from the model.

The main limitation of the Calphad method occurs when there is a lack of experimental data on some systems which are difficult to investigate experimentally. In that case, first-principle calculations can be useful to determine, for example, data of enthalpy of formation at 0 K for some phases. Examples of such studies on actinide systems by Turchi et al. can be found, for example, on the Pu-Am system [16].

Databases using the Calphad method are developed for nuclear material applications. A review was recently published by T. Besmann [20]. Among them, the NUCLEA and MEPHISTA databases are developed by Thermodata in Grenoble, France, for severe accident applications (thermodata.online.fr). The FUELBASE is a database for advanced nuclear fuel applications developed in CEA France in collaboration with European partners [4]. The NEA Project on Thermodynamics of Advanced Fuels International Database (TAF-ID) was started in 2013 among six countries such as Canada, France, Japan, Korea, the Netherlands and the US, co-ordinated by the NEA [21]. The objective

is to develop a thermodynamic database covering different types of fuels including minor actinides, fission products and structural materials. Databases on metallic fuels are developed in the US by P. Turchi et al. [16] and in Japan by Kurata [19].

Figure 3. Methodology to develop a thermodynamic database using the Calphad method [10]



References

- [1] Andersson, J.O. et al. (2002), *Calphad*, 26, 273-312.
- [2] Bale, C.W. et al. (2002), *Calphad*, 26, 189-228.
- [3] Chen, S.L. et al. (2002), *Calphad*, 26, 175-188.
- [4] Guéneau, C. et al. (2011), *Journal of Nuclear Materials*, 10.1016/j.jnucmat.2011.07.033.
- [5] Davies, R., A. Dinsdale, J. Gisby, J. Robinson, S. Martin (2002), *Calphad*, 26, 229-271.
- [6] Hillert, M. (2008), Phase Equilibria, *Phase Diagrams and Phase Transformations*, 2nd edition, Cambridge University Press.
- [7] Hillert, M., B. Sundman, M. Selleby (2009), *Acta Materialia*, 57, 5237-5244.
- [8] Inden, G. (1981), *Physica* 103B, 82-100.
- [9] Kikuchi, R. (1951), *Physical Review* 81, 988-1003.
- [10] Lukas, H.L., S.G. Fries, B. Sundman (2007), *Computational Thermodynamics, The Calphad Method*, Cambridge University Press.
- [11] Pelton, A.D., P. Chartrand (2001), *Metallurgical and Materials Transactions A*, 32A, 1355-1383.
- [12] Sundman, B., J. Agren (1981), *Journal of Physics and Chemistry of Solids*, 42, 297-301.
- [13] Sundman, B., T. Mohri (1991), *Z Metallkunde*, 81, 251-254.
- [14] Sundman, B., C. Guéneau, N. Dupin (2011), *Acta Materialia*, 59, 6039-6047.
- [15] Saunders, N., P. Miodownik (1998), *Calphad*, Oxford Pergamon Press.
- [16] Turchi, P.E.A., A.I. Landa, P.A. Söderlind (2011), *Journal of Nuclear Materials*, 418, 165.
- [17] Besmann, T.M. (2010), *Journal of Nuclear Materials*, 402, 25.
- [18] Gotcu-Freis, P., J.Y. Colle, C. Guéneau, N. Dupin, B. Sundman, R.J.M. Konings (2011), *Journal of Nuclear Materials*, 414, 408.
- [19] Kurata, M. (2010), IOP Conference: *Materials Science and Engineering*, 9, 012022 and 012023.
- [20] Besmann, T.M. (2012), “Computational thermodynamics: Application to nuclear materials”, *Comprehensive Nuclear Materials*, edited by R.J.M. Konings Elsevier.
- [21] <https://www.oecd-nea.org/science/taf-id/>.

Chapter 20.

Peridynamics

D. Littlewood

Sandia National Laboratories, US

Abstract

Peridynamics, a nonlocal extension of continuum mechanics, is a natural framework for capturing constitutive response and modelling pervasive material failure and fracture. Unlike classical approaches incorporating partial derivatives, the peridynamic governing equations utilise integral expressions that remain valid in the presence of discontinuities such as cracks. The mathematical theory of peridynamics unifies the mechanics of continuous media, cracks, and discrete particles. The result is a consistent framework for capturing a wide range of constitutive responses, including inelasticity, in combination with robust material failure laws. Peridynamics has been implemented in a number of computational simulation codes, including the open source code Peridigm and the Sierra/SolidMechanics analysis code at Sandia National Laboratories.

Introduction to peridynamic theory

Peridynamics is a nonlocal extension of continuum mechanics [1-3]. In contrast to the classical approach, the balance of linear momentum is formulated as an integral equation that remains valid in the presence of material discontinuities such as cracks. In peridynamics, a material point \mathbf{x} interacts directly with all neighbouring material points \mathbf{x}' within a finite distance, δ , termed the horizon. The vectors connecting the point \mathbf{x} to its neighbours \mathbf{x}' are referred to as bonds.

The peridynamic balance of linear momentum at time t for the point \mathbf{x} in the body B is given by:

$$\begin{aligned} \rho(\mathbf{x})\ddot{\mathbf{u}}(\mathbf{x}, t) &= \mathbf{L}_u(\mathbf{x}, t) + \mathbf{b}(\mathbf{x}, t) \quad \forall \mathbf{x} \in \mathcal{B}, \quad t \geq 0, \\ \mathbf{L}_u(\mathbf{x}, t) &= \int_{\mathcal{B}} \{ \underline{\mathbf{T}}[\mathbf{x}, t] \langle \mathbf{x}' - \mathbf{x} \rangle - \underline{\mathbf{T}}'[\mathbf{x}', t] \langle \mathbf{x} - \mathbf{x}' \rangle \} \, dV_{\mathbf{x}'}, \end{aligned} \quad (1)$$

where ρ is the material density, u denotes displacement, and b is an external body force. The force density at point x due to direct interactions with neighbours x' is given by the term $L_u(x, t)$. Here, $T[x, t]$ denotes the peridynamic force state for point x at time t , described below, and dVx' is the volume associated with neighbour x' . Peridynamics is an extension of continuum mechanics in that the classical (local) equations are recovered in the limit as the horizon approaches zero, assuming the deformation field is sufficiently smooth [4].

One approach to discretising Equation 1 is the mesh-free approach of Silling and Askari [5]. Under this approach, the strong form of the balance of linear momentum is solved numerically by dividing the body B into a finite number of cells, each tracked using a single node located at its centre. The integral expression in Equation 1 is replaced by a summation, yielding the discrete equation:

$$\rho(\mathbf{x})\ddot{\mathbf{u}}_h(\mathbf{x}, t) = \sum_{i=0}^N \left\{ \underline{\mathbf{T}}[\mathbf{x}, t] \langle \mathbf{x}'_i - \mathbf{x} \rangle - \underline{\mathbf{T}}'_i[\mathbf{x}'_i, t] \langle \mathbf{x} - \mathbf{x}'_i \rangle \right\} \Delta V_{\mathbf{x}'_i} + \mathbf{b}(\mathbf{x}, t), \quad (2)$$

where N is the number of cells in the neighborhood of x , \mathbf{x}_i is the position of the node centred in cell i , and $\Delta V_{\mathbf{x}'_i}$ is the volume of cell i .

Equation 2 requires evaluation of the pairwise forces $\underline{\mathbf{T}}[\mathbf{x}, t](\mathbf{x}' - \mathbf{x})$ and $\underline{\mathbf{T}}'[\mathbf{x}', t](\mathbf{x} - \mathbf{x}')$, where the force states $\underline{\mathbf{T}}[\mathbf{x}, t]$ and $\underline{\mathbf{T}}'[\mathbf{x}', t]$ are, in general, functions of the deformations of all nodes within the neighbourhoods of x and x' , respectively. A constitutive model is a relation that determines the force state $\underline{\mathbf{T}}[\mathbf{x}, t]$ in terms of the deformation state in the neighbourhood of x and possibly other variables as well. Constitutive models for peridynamics generally fall into one of three categories: bond-based material models, state-based material models, and non-ordinary state-based material models (e.g., classical material models adapted for use within a peridynamic framework).

Bond-based material models

Bond-based material models are constitutive laws in which the pairwise force acting between material points x and x' is purely a function of their relative displacements [1,6]. In addition, this pairwise force always acts along the direction of the bond connecting x and x' . Bond-based material models have the advantages of being computationally inexpensive and robust, making them a good choice for large-deformation simulations involving pervasive material failure. The most significant disadvantage of bond-based constitutive laws is their restriction to relatively simple two-point interactions. A notable consequence is the restriction of Poisson's ratio to one quarter.

An example of a bond-based material model is the microelastic model proposed by Silling [1]. The magnitude of a force state for the microelastic material model is determined as:

$$\underline{\mathbf{T}} = \frac{18k}{\pi\delta^4} \underline{s}, \quad (3)$$

where k is the bulk modulus, δ is the peridynamic horizon, and s is the bond stretch, defined as:

$$\underline{s} = \frac{\underline{y} - \underline{x}}{\underline{x}}. \quad (4)$$

Here, \underline{x} is the length of the bond ($\underline{x}' - \underline{x}$) in the undeformed configuration, and y is the bond length in the current configuration. The net force acting on a material point x is the sum of the pairwise forces between x and each of its neighbors x' , where the magnitude of each pairwise interaction is computed by Equation 3 and the direction is given by the bond connecting x and x' .

State-based material models

State-based material models are those in which the pairwise force between material points x and x' is a function of the deformations of all the material points within the neighborhoods of x and x' , and possibly other variables as well [2,7]. State-based constitutive laws are significantly more general than bond-based constitutive laws. This allows for the modelling of highly complex material response, but may result in greater computational expense.

The linear peridynamic solid material model is one example of a state-based constitutive law [2]. It is an ordinary material model, meaning that the action of the force state at x on the bond ($x' - x$) is directed along the bond:

$$\underline{\mathbf{T}}[\mathbf{x}, t] \langle \mathbf{x}'_i - \mathbf{x} \rangle = \underline{t} \underline{\mathbf{M}}[\mathbf{x}, t] \langle \mathbf{x}'_i - \mathbf{x} \rangle, \quad (5)$$

where the magnitude is given by \underline{t} , and $\underline{\mathbf{M}}[\mathbf{x}, t]$ ($\mathbf{x}' - \mathbf{x}$) is the unit vector pointing from the deformed position of x to the deformed position of x' .

The magnitude, t , in a linear peridynamic solid is given by:

$$\underline{t} = \frac{-3p}{m} \underline{\omega} \underline{x} + \frac{15\mu}{m} \underline{\omega} \underline{e}^d, \quad p = -k\theta, \quad (6)$$

where the p is the peridynamic pressure, θ is the peridynamic dilatation, m is the weighted volume at x , $\underline{\omega}$ is the value of the influence function between cells x and \underline{x}' , x is the length of the bond ($x' - x$) in the undeformed configuration, \underline{e}^d is the deviatoric part of the extension \underline{e} , and μ and k are material constants (the shear modulus and bulk modulus, respectively).

Non-ordinary state-based material models

A means for adapting classical material models for use with peridynamics was developed by Silling, et al. [2]. The approach is based on the evaluation of an approximate deformation gradient, $\bar{\mathbf{F}}$, at x :

$$\bar{\mathbf{F}} = \left(\sum_{i=0}^N \underline{\omega}_i \underline{\mathbf{Y}}_i \otimes \underline{\mathbf{X}}_i \Delta V_{\mathbf{x}_i} \right) \mathbf{K}^{-1}, \quad (7)$$

F

where \mathbf{K} is the shape tensor, defined as:

$$\mathbf{K} = \sum_{i=0}^N \underline{\omega}_i \underline{\mathbf{X}}_i \otimes \underline{\mathbf{X}}_i \Delta V_{\mathbf{x}_i}. \quad (8)$$

Here, \mathbf{X} denotes a vector directed from \mathbf{x} to \mathbf{x}' in the reference configuration, \mathbf{Y} denotes a vector directed from \mathbf{x} to \mathbf{x}' in the deformed configuration, $\underline{\omega}$ is the value of the influence function between cells \mathbf{x} and \mathbf{x}' , and $\Delta V_{\mathbf{x}}$ is the volume of cell \mathbf{x} . \otimes operator denotes a dyadic product. The approximate deformation gradient, as defined in Equation 7, allows for the computation of a strain measure or, alternatively, a strain increment, that can be passed to a classical (local) material model. The classical material model is expected to return stress which is then transformed into pairwise forces as follows:

$$\underline{\mathbf{T}} \langle \mathbf{x}' - \mathbf{x} \rangle = \underline{\omega} \boldsymbol{\sigma} \mathbf{K}^{-1} \langle \mathbf{x}' - \mathbf{x} \rangle, \quad (9)$$

where $\boldsymbol{\sigma}$ is the Piola stress.

Constitutive models developed specifically for peridynamics are generally more robust than classical constitutive models that have been adapted for use within peridynamics, particularly in analyses involving extreme deformation and pervasive fracture. In addition, zero-energy modes are possible in the calculation of the approximate deformation gradient $\bar{\mathbf{F}}$. Zero-energy modes may result in nonphysical motion of cells within a simulation, typically manifesting as rapid oscillations. The suppression of zero-energy modes is possible through a penalty approach analogous to hourglass control in classical finite element analysis [8,9].

Modelling fracture

Peridynamics includes a natural mechanism for modelling fracture through the breaking of peridynamic bonds. In an undamaged material, bonds connect a given cell \mathbf{x} to each cell \mathbf{x}' within its neighbourhood in the reference configuration. A damage law dictates the conditions under which individual bonds are broken. Material discontinuities, such as cracks, form as a result of the accumulation of broken bonds.

The critical stretch damage model is one example of a peridynamic bond failure law [5]. The critical stretch model assigns a damage value of zero (unbroken) or one (broken) as a function of the maximum stretch obtained by a bond and a critical stretch material parameter, s_{crit} . The damage value, ϕ , is given by the:

$$\phi = \begin{cases} 0 & \text{for } s_{\text{max}} < s_{\text{crit}} \\ 1 & \text{for } s_{\text{max}} \geq s_{\text{crit}}, \end{cases} \quad (10)$$

where s_{max} is the maximum stretch,

$$s_{\text{max}} = \frac{y_{\text{max}} - \underline{x}}{\underline{x}}. \quad (11)$$

Here, \underline{y}_{\max} is the maximum distance between the bonded cells x and \underline{x} achieved over the duration of the simulation, and \underline{x} is the distances between x and x' in the reference configuration. The use of the maximum distance, \underline{y}_{\max} , ensures that the breaking of bonds is irreversible.

Example applications

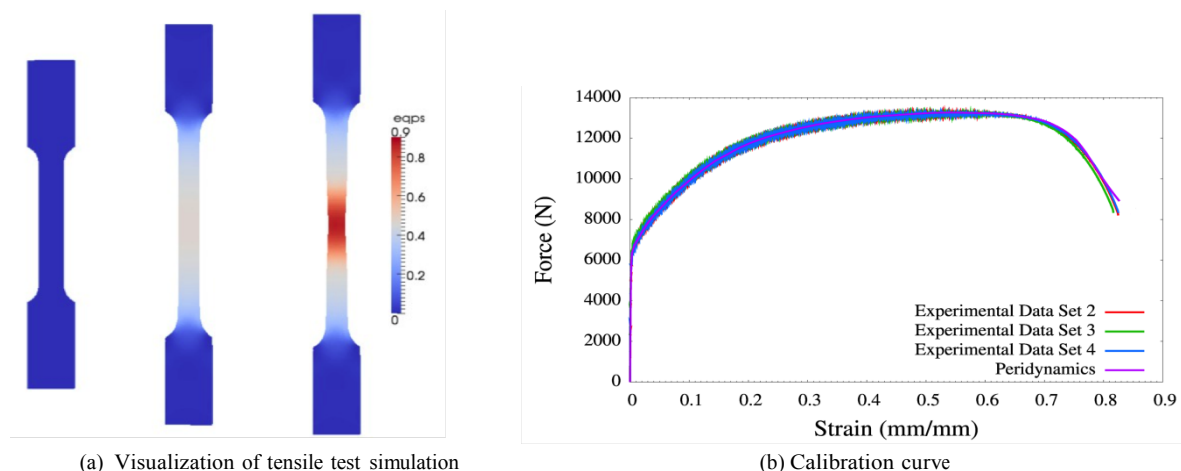
Peridynamics has been implemented in a number of computational simulation codes, including the open-source code Peridigm and the Sierra/SolidMechanics analysis code at Sandia National Laboratories [10,11]. The following example simulations, carried out in Sierra/SolidMechanics, demonstrate the modelling capabilities of peridynamics. The first is a calibration simulation carried out under quasi-static loading conditions. The second is a transient dynamics simulation involving pervasive material failure.

Simulation of a tensile test for model calibration

The calibration of a peridynamic constitutive model against experimental data from a standard tensile test is illustrated in Figure 1. The simulation was carried out using a classical elastic-plastic material model with piece-wise linear hardening adapted for peridynamics via the non-ordinary state-based approach. The specimen material is annealed 304 L stainless steel. Experimental data was provided by Brad Boyce [12].

The peridynamic model was successful in reproducing both the measured force-strain response and the observed necking behaviour. Engineering strain, measured with a half-inch strain gauge located at the specimen centre, recorded strains in excess of 80%, demonstrating the ability of peridynamics to model large-deformation plasticity.

Figure 1. Tensile test simulation

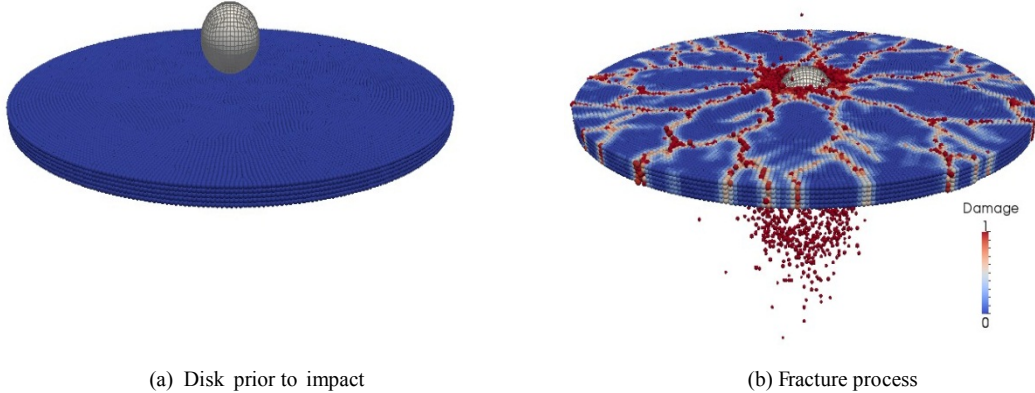


Brittle failure of an elastic disk resulting from impact

Peridynamics is particularly well suited for the modelling of pervasive material damage [5,13]. Figure 2 illustrates peridynamics as a means to simulate dynamic fracture resulting from the impact of an elastic sphere with a brittle disk. The disk was modelled using the linear peridynamic solid material model. The projectile was modelled as linear elastic using

classical finite elements. Interaction of the sphere and disk was achieved using the Sierra/SolidMechanics contact algorithm.

Figure 2. Simulation of fragmenting disk



Application of peridynamics to nuclear fuels

The cracking of nuclear fuel has direct, and often profound, impact on thermal conductivity and the release of fission products. The importance of capturing crack growth and fuel pellet fragmentation motivates the use of peridynamics, primarily because evolving material discontinuities are handled naturally within the peridynamic framework. Multi-scale and multi-physics peridynamic modelling are active areas of research. Recent applications of peridynamics to thermal-mechanical analyses, for example, provide an approach for capturing the swelling and subsequent cracking of fuel pellets due to high-thermal gradients through a straightforward inclusion of thermal strains in the peridynamic model. It is currently unknown, however, to what extent existing peridynamic models would need to be specialised to provide models of sufficient detail and accuracy to inform nuclear fuel fabrication and use. While significant research remains to be done, the inherent ability of peridynamics to model crack growth suggests a viable modelling strategy for nuclear fuels.

Conclusions and future challenges

Peridynamics is a consistent mathematical theory for modelling the initiation and propagation of cracks. There is significant potential to apply peridynamics to the modelling of nuclear fuels, in particular to the evolution of cracks in fuel pellets. Peridynamic modelling of nuclear fuels, however, will require the resolution of several open questions. The selection and calibration of peridynamic constitutive models and bond-failure laws for modelling specific fuel materials must be addressed. In addition, while peridynamics has been applied to thermal-mechanical phenomena and to coupled mechanics-diffusion scenarios, the application of peridynamics within the multi-physics environments affecting nuclear fuels remains an open area of research.

Acknowledgements

Sandia National Laboratories is a multi-programme laboratory managed and operated by Sandia Corporation, a wholly owned subsidiary of Lockheed Martin Corporation, for the US Department of Energy's National Nuclear Security Administration under contract DE-AC04-94AL85000. SAND 2013-1128P.

References

- [1] Silling, S.A. (2000), "Reformulation of elasticity theory for discontinuities and long-range forces", *Journal of the Mechanics and Physics of Solids*, 48(1):175-209.
- [2] Silling, S., M. Epton, O. Weckner, J. Xu, E. Askari (2007), "Peridynamic states and constitutive modeling", *Journal of Elasticity*, 88(2):151-184.
- [3] Silling, S.A., R.B. Lehoucq (2010), "Peridynamic theory of solid mechanics", *Advances in Applied Mechanics*, 44:73-168.
- [4] Silling, S.A., R.B. Lehoucq (2008), "Convergence of peridynamics to classical elasticity theory", *Journal of Elasticity*, 93(1):13-37.
- [5] Silling, S.A., E. Askari (2005), "A meshfree method based on the peridynamic model of solid mechanics", *Computers and Structures*, 83(17-18):1526-1535.
- [6] Macek, R.W., S.A. Silling (2007), "Peridynamics via finite element analysis", *Finite Elements in Analysis and Design*, 43:1169-1178.
- [7] Mitchell, J.A. (2011), *A Nonlocal, Ordinary, State-based Plasticity Model for Peridynamics*, SAND Report 2011-7597, Sandia National Laboratories, Albuquerque, NM and Livermore, US.
- [8] SIERRA Solid Mechanics team (2011), *Sierra/Solid Mechanics 4.22 User's Guide*, SAND Report 2011-7597, Sandia National Laboratories, Albuquerque, NM and Livermore, US.
- [9] Littlewood, D.J. et al. (2012), "Peridynamic simulation of damage evolution for structural health monitoring", *Proceedings of the ASME 2012 International Mechanical Engineering Congress and Exposition (IMECE)*, Houston, Texas, US.
- [10] Peridigm. <https://software.sandia.gov/trac/peridigm/>.
- [11] Sandia Advanced Simulation and Computing (ASC). <http://www.sandia.gov/asc/>.
- [12] Boyce, B.L. (2012), Personal correspondence.
- [13] Littlewood, D. (2010), "Simulation of dynamic fracture using peridynamics, finite element modeling, and contact", *Proceedings of the ASME 2010 International Mechanical Engineering Congress and Exposition (IMECE)*, Vancouver, British Columbia, Canada.

Chapter 21.

Micromechanical modelling of fuel viscoplastic behaviour

R. Masson¹, V. Blanc¹, J.M. Gatt¹, J. Julien¹, R. Largenton², B. Michel¹

¹CEA, DEN, DEC, Centre de Cadarache, France,

²Electricité de France R&D, France

Abstract

To identify the effect of microstructural parameters on the viscoplastic behaviour of nuclear fuels, micromechanical (also called homogenisation) approaches are used. These approaches aim at deriving effective properties of heterogeneous material from the properties of their constituents. They stand on full-field computations of representative volume elements of microstructures as well as on mean-field semi-analytical models. For light water reactor fuels, these approaches have been applied to the modelling of the effect of two microstructural parameters: the porosity effects on the thermal creep of dioxide uranium fuels (transient conditions of irradiation) as well as the plutonium content effect on the viscoplastic behaviour (nominal conditions of irradiations) of mixed oxide fuels (MOX).

Introduction

To assess the structural integrity of fuel elements, finite element computations are most of the time needed. These finite element computations require modelling the fuel element geometry, the loading imposed on its boundary as well as permanent strains occurring during the irradiation (thermals strains, irradiation induced swelling, etc.). In addition, the mechanical behaviours of the materials constituting the fuel elements have also to be known. For many structural components, elastic properties (Young modulus and Poisson ratio) as well as limit criteria (plastic stress or/and toughness) are often sufficient to assess the integrity of the considered component. Unfortunately, due to the high temperature experienced by the fuel element, the mechanical study takes the longest to know the mechanical behaviour of its constituents in the viscoplastic range. The viscoplastic range corresponds to the occurrence of inelastic strains called viscoplastic strain. A viscoplastic model allows computing these strains as a function of time, temperature and stress. These

viscoplastic models are generally derived from experimental tests like uni-axial creep tests or displacement controlled tests [1]. For instance, the steady-creep regime is often modelled by a power law relation between the viscoplastic uni-axial strain rate and the applied stress.

More recently, deductive approaches have been developed to represent the effect of microstructural parameters in mechanical models, for instance, porosity, grain orientation, and plutonium distribution (in mixed oxide fuels) are microstructural parameters considered hereafter. These deductive models are based on micromechanical approaches (also called homogenisation) which are shortly described in the first parts of this chapter. The second part is devoted to examples of application of such methods to nuclear fuels.

A short review of micromechanical approaches

Hereafter we consider a heterogeneous material whose heterogeneities are small compared with the dimension of a representative volume element (RVE) for which the mechanical model has to be established (scale separation). This is the case of cavities in UO_2 fuels: for usual fuels, voids length never exceeds the size of the grains while the dimensions of the RVE are about ten times larger. In the same way, for usual MOX fuels, we observe a heterogeneous distribution of plutonium: agglomerates length must stay above the characteristic length of the RVE.

To derive the macroscopic mechanical behaviour of the RVE, homogeneous stress or strain boundary conditions are classically imposed on the RVE boundary. The strain and stress-field solutions of this well-posed boundary value problem have to be chosen consistently with these boundary conditions. For such boundary conditions, the volume averages of the strain (stress) field equals to the macroscopic strain (stress) tensor applied at its boundary:

$$\bar{\varepsilon} = \frac{1}{V} \int \varepsilon(x) dV \quad \text{and} \quad \bar{\sigma} = \frac{1}{V} \int \sigma(x) dV$$

V denotes the volume of the RVE. More details on the foundations of micromechanics can be found in [2].

Several micromechanical approaches are commonly used:

- full-field approaches consist in modelling a representative microstructure of the material and to solve numerically the boundary value problem described previously;
- mean-field approaches are based on analytic (or semi-analytic) solutions of an elementary problem modelling a simplified heterogeneity in an infinite medium;
- transformation-field analyses approaches use a decomposition of the microscopic anelastic strain-field on a finite set of transformation fields.

Full-field approaches

Full-field approaches consist in modelling a representative microstructure of the material and solving numerically the boundary value problem described previously. Apart from periodic microstructures encountered in some specific situations, general microstructures are disordered with two limit situations:

- Matrix-inclusions microstructures: one of the phases is geometrically continuous throughout the RVE (the matrix) and embeds inclusions. UO₂ fuel can be considered as a continuous UO₂ matrix containing voids (porosity), and MOX fuel can be as well considered as a continuous (U-Pu)O₂ matrix containing UO₂ and (U-Pu)O₂ inclusions. In that situation, tri-dimensional microstructures are modelled by positioning randomly inclusion centres in the matrix (see the random sequential adsorption algorithm (RSA) described in [3]).
- Polycrystalline microstructures: the heterogeneous material is made of a very high number of phases, no phase playing any prominent morphological role. In that situation, grains are generated thanks to a Voronoi mosaic [4].

The next stage consists in meshing the model of RVE and solving the associated boundary value problem. For instance, if the mechanical behaviour is linearly elastic at each point of the RVE:

$$x \in V^r, \sigma_{ij}(x) = 2\mu^r \varepsilon_{ij}(x) + \lambda^r \varepsilon_{kk}(x) \quad (1)$$

(summation on repeated indices). This relation corresponds to an isotropic behavior depending on the Lamé coefficients (μ^r, λ^r) for each phase (r). The effective properties of the RVE are determined by its effective strain energy function:

$$\bar{W}(\bar{\varepsilon}) = \min_{\varepsilon \in K} \left[\frac{1}{V} \int \frac{1}{2} \sigma(x) \varepsilon(x) dV \right] \quad (2)$$

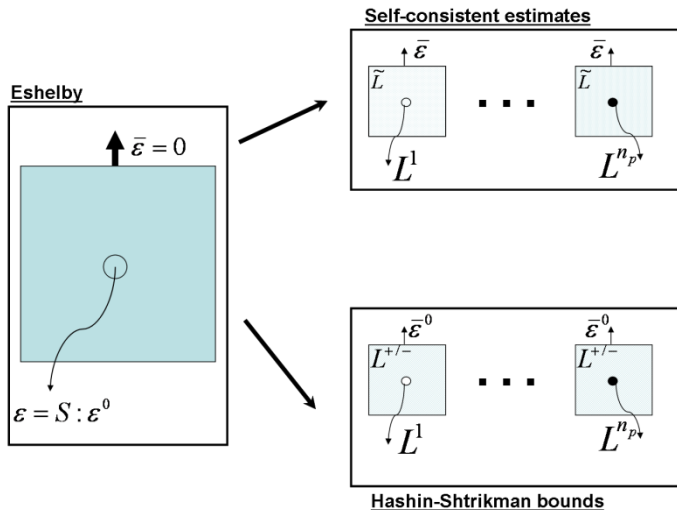
where K denotes a set of kinematically admissible strain field with the macroscopic strain $\bar{\varepsilon}$.

For periodic boundary conditions, a resolution based on the Fast Fourier Transform (FFT) can also be used [5,6] for matrix-inclusions and polycrystalline microstructures, respectively). Main advantage of this method as compared to finite element resolution relies on the fact that it avoids the meshing of the microstructure.

Mean-field approaches

When the different phases constituting the RVE of the considered heterogeneous material obey to a linear elastic behaviour (for instance relation (1) in the isotropic case), bounds as well as estimates of the effective behaviour are available. Various estimates have been derived from the solution of the Eshelby's problem [22] considering an elliptic inclusion submitted to an uniform strain free stress ε^0 and embedded in an infinite medium (see Figure 1). The Mori-Tanaka estimates [8], well suited to matrix-inclusions microstructures, are derived by considering that each phase is surrounded by an infinite medium whose elastic behaviour is the matrix one. The self-consistent estimates [7], well suited to polycrystalline microstructures, are derived by considering that each phase (elastic modulus $L^i, 1 \leq i \leq n_p$) is surrounded by an infinite medium whose elastic behaviour is the effective one (\tilde{L}).

Figure 1. Estimates and bounds of the effective properties of the heterogeneous material derived by the use of Eshelby's solution



Bounds for the effective elastic modulus (or the effective compliance) can also be derived by considering the minimum potential energy theorem (respectively the complementary energy theorem). The sharpness of these bounds depends on the knowledge of the spatial distribution of the phases:

- Voigt and Reuss bounds are the bounds available if only the volume fractions of each phase are known. Voigt bound can be easily deduced from relation (2) by considering the kinematically admissible uniform strain field: $\forall x \in V, \varepsilon(x) = \bar{\varepsilon}$. This yields the well-known mixture laws on the effective shear and bulk modulus.
- Hashin-Shtrikman type bounds [23] are available when the spatial distribution of the phases is isotropic [9] (for an ellipsoidal distribution of phases) and correspond to Mori-Tanaka estimates in particular situations.

Closed-form expressions of bounds and estimates are given in [2]. Additional methods used to derive bounds and estimates are also depicted in this paper.

When phases obey a linear viscoelastic behaviour, the total strain field can be decomposed as an elastic and a viscous field:

$$x \in V, \varepsilon(x) = \varepsilon_e(x) + \varepsilon_v(x).$$

The deviatoric parts of the strain (ε) - stress (s) relation is linear, for instance:

$$x \in V, \dot{\varepsilon}(x, t) = \frac{1}{2\mu_e} \dot{s}(x, t) + \frac{1}{2\mu_v} s(x, t) \quad (3)$$

The constitutive law (3) corresponds to a Maxwellian behaviour, representative of situations encountered for nuclear fuels (nominal irradiation conditions). The classical method to solve such a problem (the so-called Lee-Mandel correspondence principle) leads to a fictitious elastic problem in the Laplace-Carson domain:

$$x \in V, \hat{e}(x, p) = \frac{1}{2\hat{\mu}(p)} \hat{s}(x, p),$$

the Laplace-Carson of a given time function is given by: $\hat{f}(p) = p \int_0^{+\infty} f(t) e^{-pt} dt$. Usual homogenisation methods can then be applied to estimate the Laplace-Carson transform of the effective creep or relaxation functions. The time-responses are then deduced by the inversion of the Laplace-Carson transform. For instance, the deviatoric part of the macroscopic stress-strain relation (isotropic effective behaviour) is given by the following integral relation (Stieljes convolution product):

$$\bar{s}(t) = \int_0^t \tilde{\mu}(t-u) \dot{\bar{e}}(u) du, \quad (4)$$

where $\tilde{\mu}(t)$ is given by the inversion of its Laplace-Carson transform. In general, this inversion is performed numerically with a collocation method which consists in approximating the original functions as a sum of exponentials.

Extension to nonlinear behaviours remains a field of intensive researches [10], dedicated to the effective behaviour of viscoplastic polycrystals. In that situation, the strain-stress relation is nonlinear, for instance:

$$x \in V, \dot{e}(x, t) = \frac{1}{2\mu_e} \dot{s}(x, t) + \frac{3K}{2} (\sigma_{eq})^{n-1} s(x, t),$$

the viscoplastic part of the strain being a power law function of the stress. The case of porous material is of particular interest for nuclear fuels. In this last situation, the so-called elliptic potential [11] has been proved to be very efficient to predict the effect of the porosity on the steady creep of viscous materials obeying to a power law steady-creep behaviour. If the steady creep at nil porosity reads:

$$\dot{\bar{\varepsilon}}_{(vp)eq} = K \sigma_{eq}^n$$

the (macroscopic) viscoplastic strain of the porous material is derived from a macroscopic dissipation potential:

$$\dot{\bar{\varepsilon}}_{vp} = \frac{\partial \bar{\Psi}}{\partial \underline{\sigma}}(\bar{\sigma}, f) \text{ with } \bar{\Psi}(\bar{\sigma}, f; K, n) = \frac{K(d, T)}{n+1} \left(\frac{9A(f)}{4} \sigma_m^2 + B(f) \sigma_{eq}^2 \right)^{\frac{n+1}{2}} \quad f \text{ denotes the porosity.}$$

Transformation-field approaches

Transformation-field analysis [12] approximates local heterogeneous fields by piecewise uniform transformation fields $\underline{\varepsilon}_k^{vp}$:

$$\underline{\underline{\varepsilon}}_{vp}(x, t) = \sum_{k=1}^m \chi_k(x) \underline{\varepsilon}_k^{vp}(t)$$

where m is the number of subdomains and χ_k the characteristic function of the subdomain (equal to one in the subdomain, and zero outer), and $\underline{\varepsilon}_k^{vp}$ are internal tensorial variables.

The need for a finer subdivision of the phases stems from the intrinsic nonuniformity of the plastic strain field which can be highly heterogeneous even within a single material phase. To reproduce accurately the actual effective behaviour of the composite, it is important to capture correctly the heterogeneity of the viscoplastic strain field. This observation has motivated the method called nonuniform transformation-field analysis, proposed in [13], where the viscoplastic strain decomposition lay on plastic modes μ_k , which are nonuniform (not even piecewise uniform). These modes are identified numerically or analytically, along monotone loading paths in the space of macroscopic stresses corresponding to uniaxial tension and pure shear.

$$\varepsilon_{vp}(x,t) = \sum_{k=1}^M \mu_k(x) \varepsilon_k^{vp}(t)$$

Where M is the number of plastic modes, $\mu_k(x)$ are tensorial plastic modes (viscoplastic strain field), and ε_k^{vp} are internal scalar variables.

Application to the fuel mechanical behaviour

For light water reactor fuels, we report here recent advances to derive the effective properties of two microstructural parameters: the porosity in uranium dioxide fuels as well as the plutonium content distribution in mixed oxide fuels.

Porosity effects on the steady creep of UO₂ fuels

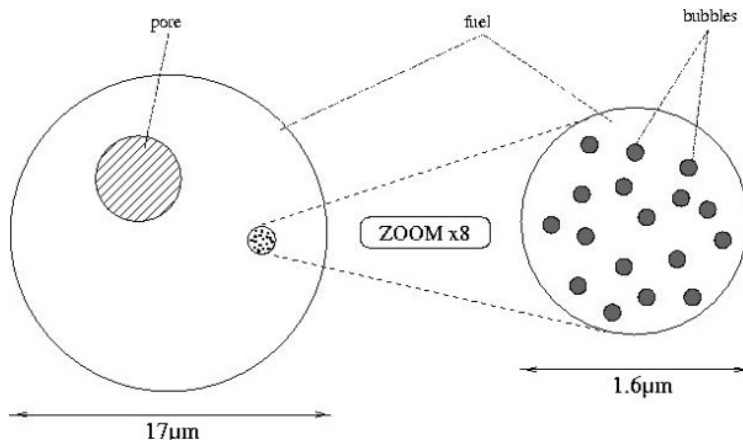
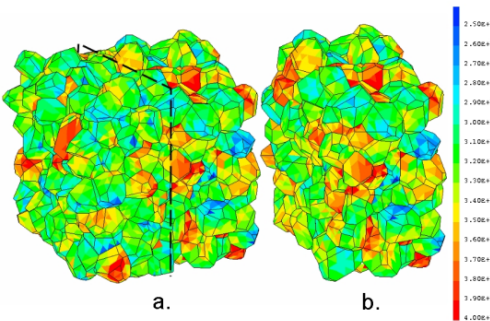
Starting from the elliptic potential (see Section "Mean-field approaches"), Monerie and Gatt [14] have proposed the following viscoplastic dissipation potential well adapted to UO₂ fuel:

$$\bar{\Psi}(\bar{\sigma}, f) = (1 - \Theta) \bar{\Psi}(\bar{\sigma}, f; K_1, n_1) + \Theta \bar{\Psi}(\bar{\sigma}, f; K_2, n_2)$$

with Θ a function of the stress and temperature. (K_1, n_1) are material coefficients corresponding to low values of temperature and stress ($\Theta = 0$) while (K_2, n_2) corresponds to high values of temperature and stress ($\Theta = 1$). If the pores are submitted to an internal pressure p_{int} (elaboration process, gaseous fission product), the hydrostatic stress have to be shifted to $\sigma_m + p_{int}$ in this last expression.

More recently, improvements of this modelling have been proposed in two complementary directions:

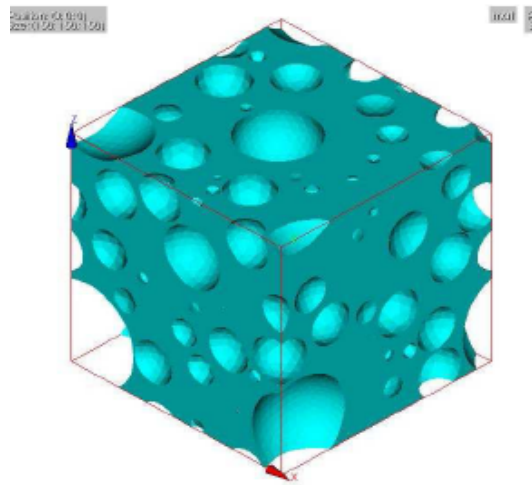
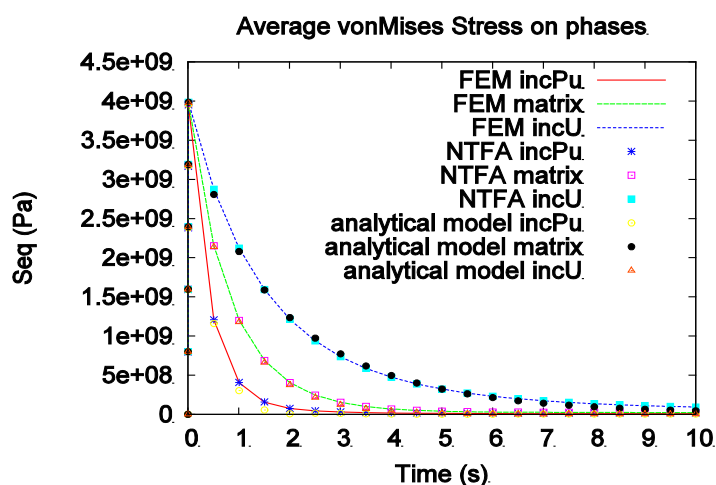
- a mean-field approach has been developed to represent the effect of two populations of voids of different sizes (see Figure 2a and [15,16]);
- full-field simulations of UO₂ polycrystals have been achieved to represent the effect of crystal misorientations on the intergranular stress-field throughout a RVE (see Figure 2b and [17]).

Figure 2a. Two populations of voids of different sizes**Figure 2b. Stress field occurring in a UO₂ polycrystal**

Mixed oxide fuels

Mixed oxide fuels display matrix-inclusions type microstructures whose behaviour in nominal conditions can be modelled as a linear viscoelastic one, the viscous strain in each phase depending linearly on the stress. In addition, this viscoelastic behaviour is ageing due to the temperature and irradiation dependencies of the creep. To derive effective properties in that particular situation, the classically used integral formulation of the effective behaviour (see relation (4)) is far less convenient than internal variables formulations with respect to computational aspects as well as theoretical extensions to ageing viscoelasticity. Recent works [18] have proposed to take advantage of the usual Prony series expansion of the effective properties to reduce the integral formulation to an equivalent internal variables formulation. Such formulation can lead to exact results for some particular situations as the ones studied for mixed oxide fuels considered as a two-phase [18] or three-phase [19] heterogeneous material. Direct extension to ageing viscoelastic behaviour is done by the use of an incremental formulation.

In parallel, full-field approaches have also been developed to compare mean-field approximated solutions to reference solutions (see Figure 3) while developments of an alternative approach based on these full-field simulation are in progress [20].

Figure 3a. Simulated microstructures of MOX fuels: Spatial repartition of the matrix (three phases) [21]**Figure 3b.** Average equivalent stress in MOX phases obtained by full-field simulations (“FE model”), NTFA method and mean-field approach (“analytic model”)

Conclusions

Through this chapter, mean-field and full-field approaches used to derive the overall viscoplastic behaviour of nuclear fuels have been shortly presented. Examples reported here are limited to light water reactor fuels but it should be noted that HTR fuels [21] and metallic uranium [24] have also been studied with such methodology.

References

- [1] Gatt, J.M., JC Menard (2007), “Overall viscoplastic behaviour of uranium dioxide”, *SMIRT 19 Div C*, Toronto, Canada.

- [2] Zaoui, A. (2002), “Continuum micromechanics: Survey”, *Journal of Engineering Mechanics*, pp. 808-816.
- [3] Rintoul, M.-D., S. Torquato (1997), “Reconstruction of the structure of dispersions”, *Journal of Colloid and Interface Science* 186.467-476.
- [4] Barbe, F., L. Decker, D. Jeulin, G. Cailletaud (2001), “Intergranular and intragranular behavior of polycrystalline aggregate -Part 1: F.E. Model”, *International Journal of Plasticity*, 17, 513-136.
- [5] Moulinec, H., P. Suquet (1998), “A numerical method for computing the overall response of nonlinear composites with complex microstructures”, *Computer Methods in Applied Mechanics and Engineering*, 157, 69-94.
- [6] Lebensohn, R. (2001), “N-site modelling of a 3D viscoplastic polycrystal using Fast Fourier Transform”, *Acta Metallurgica et Materialia* 49, 2723-2732.
- [7] Kröner, E. (1958), “Berechnung der elastischen Konstanten des Vielkristalls aus den konstanten des Einkristalls”, *Zeitschrift für Physik*, 151, 504-518.
- [8] Mori, T., K. Tanaka (1973), “Average stress in the matrix and average elastic energy of materials with misfitting inclusions”, *Acta Metallurgica*, 21, 571-574.
- [9] Willis, J.R. (1977), “Bounds and self-consistent estimates for the overall properties of anisotropic media”, *Journal of the Mechanics and Physics of Solids* 25, 185-202.
- [10] Lebensohn, R., C.N. Tomé, P. Castañeda (2007), “Self-consistent modelling of the mechanical behaviour of viscoplastic polycrystals incorporating intragranular field fluctuation”, *Philosophical Magazine*, 87, 28, 4287-4322.
- [11] Michel, JC., P. Suquet (1992), “The constitutive law of nonlinear viscous and porous materials”, *Journal of the Mechanics and Physics of Solids* 40, 783-812.
- [12] Dvorak, G.J. (1992), “Transformation field analysis of inelastic composite materials”, *Proceedings of the Royal Society of London A*, 437:311-327.
- [13] Michel, JC., P. Suquet (2003), “Nonuniform transformation field analysis”, *International Journal of Solids and Structures* 40, 6937-6955.
- [14] Monerie, Y., J.M. Gatt (2006), “Overall viscoplastic behavior of non-irradiated porous nuclear ceramics”, *Mechanics of Materials* 38, Issue 7, 608-619.
- [15] Julien, J., M. Garajeu, JC. Michel (2011), “A semi-analytical model for the behavior of saturated viscoplastic materials containing two populations of voids of different sizes”, *International Journal of Solids and Structures* 48, Issue 10, 1485-1498.
- [16] Vincent, P.G., Y. Monerie, P. Suquet (2009), “Porous materials with two populations of voids under internal pressure: I. Instantaneous constitutive relations”, *International Journal of Solids and Structures* 46, 480-506.
- [17] Pacull, J., B. Michel, O. Debordes (2010), “Polycrystalline aggregate model for the behavior of oxide fuels”, *IV European Conference on Computational Mechanics (Solides, Structures and Coupled Problems in Engineering)*, Paris, France.

- [18] Ricaud, JM., R. Masson (2009), “Effective properties of linear viscoelastic heterogeneous media: internal variables formulation and extension to ageing behaviours”, *International Journal of Solids and Structures* 46, 1599-1606.
- [19] Blanc, V., L. Barbie, R. Largenton, R. Masson (2011), “Homogenization of linear viscoelastic three phase media: internal variable formulation versus full-field computation”, *International Congress on the mechanical behavior of Materials*, Côme, Italie.
- [20] Largenton, R., JC. Michel, P. Suquet, R. Masson (2011), “Modélisation du comportement effectif du combustible MOX par une analyse micromécanique en champs de transformation non uniformes”, *CSMA, 10e Colloque National en Calcul des Structures*, Presqu’île de Giens, France.
- [21] Blanc V. et al. (2008), “Coated particle fuel modelling by multiscale approach”, *ANS 2008: American Nuclear Society (ANS) Annual Meeting*, Anaheim, Etats-Unis.
- [22] Eshelby, J.D. (1957), “The determination of the elastic field of an ellipsoidal inclusion, and related problems”, *Proceedings of the Royal Society of London A: Mathematical, Physical and Engineering Sciences* 241, 1226, 376-396.
- [23] Hashin, Z., S. Shtrikman (1963), “A variational approach to the theory of the elastic behaviour of multiphase materials”, *Journal of the Mechanics and Physics of Solids*, 11(2), 127-140.
- [24] McCabe, R.J. et al. (2010), “Deformation of wrought uranium: Experiments and modelling”, *Acta Materialia*, 58(16), 5447-5459.

Chapter 22.

Finite element modelling

M.R. Tonks¹, R. Williamson¹, R. Masson²

¹Idaho National Laboratory, US,

²CEA, DEN, DEC, Centre de Cadarache, France

Abstract

The Finite Element Method (FEM) is a numerical technique for finding approximate solutions to boundary value problems. While FEM is commonly used to solve solid mechanics equations, it can be applied to a large range of BVPs from many different fields. FEM has been used for reactor fuels modelling for many years. It is most often used for fuel performance modelling at the pellet and pin scale, however, it has also been used to investigate properties of the fuel material, such as thermal conductivity and fission gas release. Recently, the United States Department Nuclear Energy Advanced Modelling and Simulation Program has begun using FEM as the basis of the MOOSE-BISON-MARMOT Project that is developing a multi-dimensional, multi-physics fuel performance capability that is massively parallel and will use multi-scale material models to provide a truly predictive modelling capability.

Introduction

The Finite Element Method (FEM) is a numerical technique for finding approximate solutions to Boundary Value Problems (BVP). In FEM, the domain is discretised into a number of small subdomains called elements, allowing for the generation of a system of discretised equations that can be combined to represent the continuous solution of the BVP. While FEM is commonly used to solve solid mechanics equations, it can be applied to a large range of BVPs from many different fields.

FEM has been used for reactor fuels modelling for many years. It is most often used for fuel performance modelling at the pellet and pin scale, and has been very successful. In addition, it has been used to investigate properties of the fuel material, such as thermal conductivity and fission gas release.

More recently, FEM is the basis of the US Department of Energy's MOOSE-BISON-MARMOT (MBM) suite of fuel performance codes under development at Idaho National Laboratory (INL). MOOSE (the multi-physics object-oriented simulation environment) is a finite element-based numerical framework for solving partial differential equations (PDEs) and forms the basis for BISON and MARMOT. BISON is the macroscale fuel performance code that can model a large range of fuel geometries and fuel materials in 1D, 2D and 3D. MARMOT is a mesoscale simulation tool that predicts the impact of microstructure evolution on fuel properties to develop more mechanistic material models of radiation damage for use in BISON.

In this report, we summarise the past use of FEM for fuel performance modelling. We then summarise work using FEM to investigate fuel properties. Finally, we describe the MBM suite of codes and the application to fuel performance modelling.

FEM for macroscale fuel performance modelling

The goal of a fuel performance code is to calculate the internal temperature and mechanical state of the fuel and cladding while under reactor conditions, in order to establish quantitative operation guidelines to mitigate fuel duty-related failures. Fuel operates in an extreme environment that induces complex and often tightly coupled multi-physics behaviour. Adding to this complexity, important aspects of fuel behaviour are inherently multi-dimensional, examples include pellet-clad mechanical interaction, fuel fracture and non-axisymmetric neutronics and cooling.

Early fuel performance codes, such as FRAPCON [1], TRANSURANUS [2] and ENIGMA [3], focused on LWR fuel rods and approximated this complex behaviour using an axisymmetric, axially-stacked, one-dimensional radial representation (often referred to as 1½D) and finite difference numerical methods. Similar 1½D codes evolved that used FEM, such as FEMAX [4] and CYRANO [5].

EPRI's FALCON code was the first 2D FEM-based fuel performance code developed in the US [6,7]. It models the thermal, mechanical and chemical behaviour of a single fuel rod during irradiation and can be applied to steady or transient operation. CEA's first-generation fuel performance code METEOR 1D code, as well as TOUTATIS 3D, has been implemented in the PLEIADES platform [8]. PLEIADES has been under development for ten years and includes the multi-dimensional finite element solver CAST3M. ALCYONE is the PWR fuel performance code in the PLEIADES platform, and 3D simulations with ALCYONE are used to investigate localised fuel behaviour such as pellet clad mechanical interaction [9].

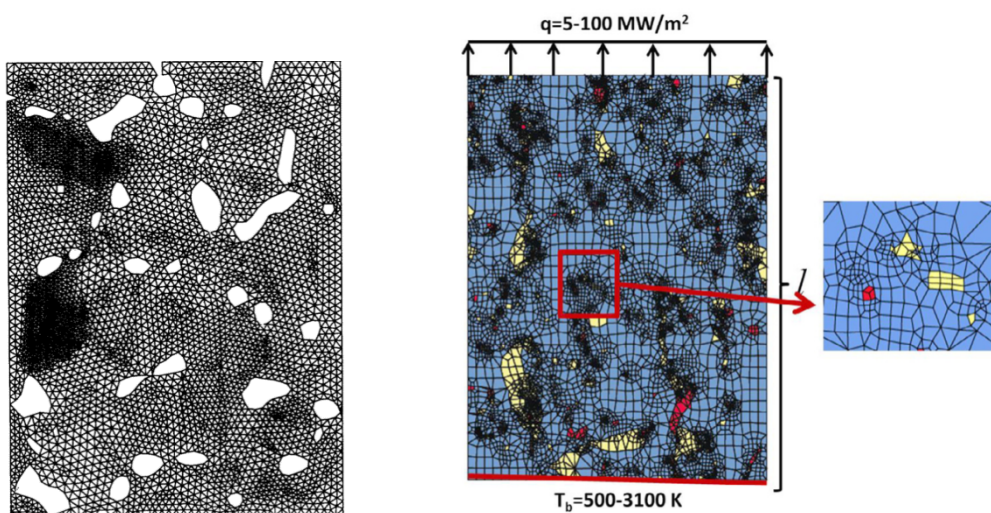
While FEM is used to solve for the thermomechanical behaviour of the fuel, materials models are required to set the various material properties and their evolution throughout the lifetime of the fuel. Historically, many of these models were developed by fitting to experimental data. However, since the 1980s' researchers have also used FEM simulations of the fuel microstructure to elucidate its properties and how they change with radiation damage.

FEM for fuel property modelling

The earliest use of FEM as a tool for investigating UO_2 fuel properties found by the authors was by Oguma [10]. In this paper, a 2D mechanics FEM code was used to investigate the fracture pattern in UO_2 pellets after reactor start-up for various power levels. Since then, one paper has used FEM to investigate fission gas release using a 1D spherical approximation of a UO_2 grain [11], where the diffusion equation was solved via FEM. The impact of porosity and Pu content on the fuel viscoplastic behaviour has also been studied with FEM analysis (see Section III.09). However, the most common use of FEM has been to investigate the impact of the bubble and grain structures within the fuel on the fuel thermal conductivity.

Bakker et al. have written two papers in which bubble structures were reconstructed from micrographs of irradiated fuel and meshed for FEM analysis. 2D heat conduction simulations were then conducted using FEM across the reconstructed meshes to determine the effective thermal conductivity [12,13] (an example of the FEM mesh is shown in Figure 1a). Microstructures from SEM and EDS data on high burn-up MOX fuel were reconstructed as 2D FEM meshes [14]. Again, heat conduction simulations were used to determine the effective thermal conductivity of the microstructures, including the impact of metallic precipitates (see Figure 1b).

Figure 1. FEM-based simulations investigating the impact of radiation damage on fuel thermal conductivity, where (a) is a FEM mesh with reconstructed bubble structure [12] and (b) shows the reconstructed microstructure [14] where metallic precipitates are in red, porosity in yellow and UO_2 in blue



MOOSE-BISON-MARMOT

The United States Department Nuclear Energy Fuels Modeling and Simulation (NEAMS) Program recognised a need for a modern, advanced 3D fuel performance capability that can model LWR accident conditions and new fuel and reactor concepts. The legacy US fuel performance codes have been under development for many years, and thus use older, serial code architectures. In addition, they are typically restricted to 1½D or 2D representations of LWR geometry. Finally, they employ materials models that are

empirical fits to experimental data and thus cannot be extrapolated outside the test conditions. Thus, NEAMS has funded a team of researchers from the Idaho and Los Alamos National Laboratories to develop the MOOSE-BISON-MARMOT, or MBM, suite of fuel performance codes.

MOOSE (Multi-physics Object-Oriented Simulation Environment) is a numerical framework that facilitates the rapid development of multi-physics simulation tools that solve systems of partial differential equations using FEM [15]. MOOSE uses modern object-oriented architecture and is massively parallel without requiring the user to write any parallel code. Though initially developed for fuel performance modelling, MOOSE now has users at laboratories, universities and industry across the world to develop advanced FEM-based simulation tools.

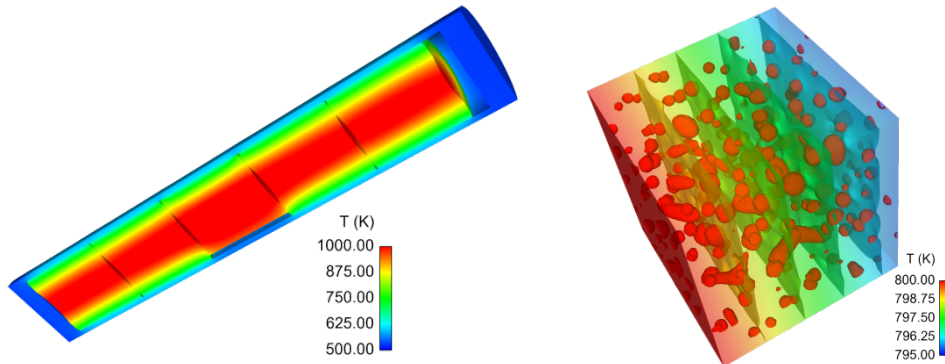
BISON is the NEAMS flagship fuel performance code and is based on the MOOSE framework [16]. BISON is a multi-dimensional code that can be run in 1D, 2D or 3D to represent desired fuel behaviour. It has been used to model LWR fuel, as well as TRISO [17] and metallic fuel. BISON models the thermomechanical behaviour of the fuel and cladding, as well as species diffusion. The pellet-cladding interaction is modelled with advanced contact algorithms that function with parallel computing and implicit time integration. BISON has been coupled to neutronics and coolant flow codes for full core simulations and to mesoscale codes to represent the impact of radiation damage. An example of a 3D BISON simulation is shown in Figure 2a.

BISON was initially developed using traditional materials models, however advanced mechanistic models are under development using multi-scale modelling and simulation to supplement difficult to perform experiments. Simulations at the atomistic and mesoscales are used to predict the radiation-induced microstructure evolution and the impact of the microstructure on the fuel properties. These results are then used in the development of mechanistic materials models correlated to evolving variables that describe the current state of the microstructure [18]. When complete, these new materials models will provide a predictive fuel performance modelling capability.

The MOOSE-based MARMOT code has been developed to model the co-evolution of microstructure and properties due to applied load, temperature and radiation damage. The microstructure evolution is modelled with the phase-field method fully coupled with computational mechanics and heat conduction equations. This set of multi-physics equations is solved with FEM using MOOSE [19]. The models are quantitative and use material properties from experiments or from atomistic simulation (molecular dynamics and density functional theory). MARMOT has been used to investigate microstructure evolution, including bubble growth and migration [19,20] and grain boundary migration and grain growth [21,22]. It has also been used to investigate the impact of GB bubbles on the fuel thermal conductivity [18,23]. An example of a MARMOT simulation is shown in Figure 2b.

Though the MBM codes are still under development, they are already being used to understand and predict fuel performance for a wide range of different types of reactors. As this work progresses, it will become a powerful tool for modelling fuel performance from its initial assembly, lifetime in the reactor and final disposition.

Figure 2. Examples of simulations using the MBM suite of codes, where (a) shows a three-dimensional BISON simulation of a five pellet rodlet with a manufacturing defect in the centre pellet [16] and (b) shows a three-dimensional MARMOT calculation that predicts the effective thermal conductivity during bubble growth in UO₂ [19]



Conclusion and future challenges

FEM is a powerful numerical tool that has been used for many years in a large range of applications. For fuel modelling, FEM has been effectively used to model fuel performance and to investigate the impact of radiation damage on the fuel material behaviour. Now, the US NEAMS project is using FEM as the basis of the MBM project that is developing a multi-dimensional, multi-physics fuel performance capability that is massively parallel and will use multi-scale materials models to provide a truly predictive modelling capability. Though FEM has been successfully applied to fuels modelling, there are challenges. For macroscale fuel performance modelling, one challenge is in directly modelling the fragmentation of the fuel pellet, as discrete crack formation and propagation is difficult with FEM. Generalist FE codes, like CAST3M FE, can model this behaviour to some extent, as demonstrated in [24] in which a viscoplastic law for creep is coupled with a multi-surface plastic softening law for cracking to represent crack development in PWR fuel pellets. A challenge comes in being able to perform massively parallel simulations with such models. Another challenge is modelling the contact between fuel and cladding, especially in 3D. An additional challenge arises as efforts are made to concurrently couple microstructure FEM models with fuel performance codes, due to difficulties in bridging the disparate length and timescales.

References

- [1] Berna, G.A., C.E. Beyer, K.L. Davis, D.D. Lanning (1997), FRAPCON-3: *A Computer Code for the Calculation of Steady-state, Thermal-Mechanical Behavior of Oxide Fuel Rods for High Burnup*, Technical Report NUREG/CR-6534 Vol. 2, PNNL-11513.
- [2] Lassmann, K., A. Schubert, J. van de Laar (2003), *TRANSURANUS Handbook*, Technical Report Document Number Version 1 Modification 1, (V1M1J2003).
- [3] Kilgour, W.J., J.A. Turnbull, R.J. White, A.J. Bull, P.A. Jackson, I.D. Palmer (1992), “Capabilities and validation of the ENIGMA fuel performance code”, *Proceedings of the ENS Meeting on LWR Fuel Performance*, Avignon, France.

- [4] Ito, K., M. Ichikawa, T. Okubo, Y. Iwano (1983), “FEMAXI-III, a computer code for fuel rod performance analysis”, *Nuclear Engineering Design*, 76, 3-11.
- [5] Baron, D., P. Thevenin, R. Largentot, R. Masson, S. Pujet, R. Arnaud (2008), “Cyrano 3 the EDF fuel performance code especially designed for engineering applications”, *Water Reactor Fuel Performance Meeting Proceeding*, Seoul.
- [6] Rashid, Y., R. Dunham, R. Montgomery (2004), *Fuel Analysis and Licensing Code: FALCON MOD01*, Technical Report EPRI 1011308, Electric Power Research Institute.
- [7] Rashid, J., S. Yagnik, R. Montgomery (2011), “Light water reactor fuel performance modeling and multi-dimensional simulation”, *JOM-International Journal of Minerals, Metallurgy and Materials S*, 63, 81–88.
- [8] Michel, B., C. Nonon, J. Sercombe, F. Michel, V. Marelle (2013), “Simulation of pellet-cladding interaction with the PLEIADES fuel performance software environment”, *Nuclear Technology*, 182(2), 124-137.
- [9] Thouvenin, G., B. Michel, J. Sercombe (2007), “Multidimensional modeling of a ramp test with the PWR fuel performance code ALCYONE”, *Proceedings of the 2007 International LWR Fuel Performance Meeting*, San Francisco, California, US.
- [10] Oguma, M. (1983), “Cracking and relocation behavior of nuclear fuel pellets during rise to power”, *Nuclear Engineering and Design*, 76, 35-45.
- [11] Ito, K., R. Iwasaki, Y. Iwano (1985), “Finite element model for analysis of fission gas release from UO₂ fuel”, *Journal of Nuclear Science and Technology*, 22(2) 129-138.
- [12] Bakker, K. et al. (1995), EHP Cordfunke, “Determination of a porosity correction factor for the thermal conductivity of irradiated UO₂ fuel by means of the finite element method”, *Journal of Nuclear Materials*, 226, 128-143.
- [13] Bakker, K. (1997), “Using the finite element method to compute the influence of complex porosity and inclusion structures on the thermal and electrical conductivity”, *International Journal of Heat and Mass Transfer*, 40(15) 3503-3511.
- [14] Teague, M., M.R. Tonks, S. Novascone, S Hayes (2013), “Microstructure modeling of thermal conductivity of high burn-up mixed oxide fuel”, *Journal of Nuclear Materials*.
- [15] Gaston, D., C. Newman, G. Hansen, D. Lebrun-Grandie (2009), “MOOSE: A parallel computational framework for coupled systems of nonlinear equations”, *Nuclear Engineering and Design*, 239, 1768-1778.
- [16] Williamson, R., J. Hales, S. Novascone, M. Tonks, D. Gaston, C. Permann, D. Andrs, R. Martineau, J. Nucl. Mater. 2012, 423, 149–163.
- [17] Hales, J.D. et al. (2013), “Multidimensional multiphysics simulation of TRISO particle fuel”, *Journal of Nuclear Materials*, 443, 531-543.
- [18] Tonks, M.R. et al. (2013), “Multiscale development of a fission gas thermal conductivity model: Coupling atomic, meso and continuum level simulations”, *Journal of Nuclear Materials*, 440, 193-200.

-
- [19] Tonks, M.R. et al. (2012), “An object-oriented finite element framework for multiphysics phase field simulations”, *Computational Materials Science*, 51, 20-29.
 - [20] Zhang, L. et al. (2012), “Phase-field modeling of temperature gradient driven pore migration coupling with thermal conduction”, *Computational Materials Science*, 56, 161-165.
 - [21] Tonks, M.R. et al. (2013), “Guidance to design grain boundary mobility experiments with molecular dynamics and phase-field modeling”, *Acta Materialia*, 2013, 61, 1373-1382.
 - [22] Tonks, M.R., Y. Zhang, X. Bai, P.C. Millett (2013), “Demonstrating the temperature gradient impact on grain growth in UO₂ using the phase field method”, *Materials Research Letters*, 2013, in press.
 - [23] Millett, P.C. et al. (2013), “Three-dimensional calculations of the effective Kapitza resistance of UO₂ grain boundaries containing intergranular bubbles”, *Journal of Nuclear Materials*, 439, 117-122.
 - [24] Michel, B. et al. (2008), “3D fuel cracking modelling in pellet cladding mechanical interaction”, *Engineering Fracture Mechanics*, 75(11), 3581-3598.

Chapter 23.

Evaluation of thermal conductivity of multi-component and multi-phase nuclear fuels by the finite element method

K. Kurosaki

Osaka University, Japan

Abstract

The effects of the shape and distribution state of voids on the thermal conductivity of UO_2 , and the temperature distribution and heat flow within the irradiated MOX fuel were evaluated by finite element analysis. Although the work is still in progress, some preliminary results are presented.

Introduction

Among the various properties of a nuclear fuel, thermal conductivity is considered to be one of the most important for determining fuel temperature. The thermal conductivities of uranium dioxide (UO_2) and mixed oxide (MOX) ($(\text{U},\text{Pu})\text{O}_2$) fuels have been investigated by a number of researchers thus far [1].

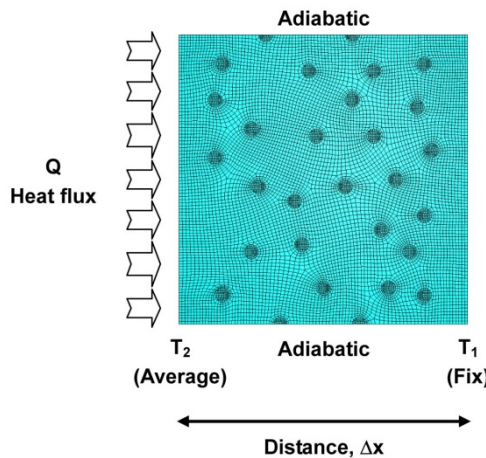
The thermal conductivity of a nuclear fuel is affected by a number of factors. In particular, accumulation of fission products (FP) and structural rearrangement occur in fuel pellets under irradiation, and the thermal conductivity of the fuel pellets changes significantly.

Solid FPs show complex behaviour depending on the environment of the fuel. Specifically, they directly react with UO_2 or $(\text{U},\text{Pu})\text{O}_2$, and form compounds with other associated FPs. Solid FPs present within a nuclear fuel, depending on their form, can be classified into three categories, a fuel matrix phase (for example, $(\text{U},\text{Pu},Ln)\text{O}_2$, Ln = rare-earth element), an oxide precipitate phase (for example, BaZrO_3), or a metal precipitate phase (Mo-Ru-Rh-Pd alloy) [2-4]. On the other hand, pronounced structural rearrangement occurs in fast reactor fuel, which has a high fuel pellet centre temperature and a sharp temperature gradient. As a result of vapourisation and translocation of various chemical species within the fuel, the structure of irradiated fuel pellets is extremely complex. In other words, a nuclear fuel after irradiation can be called a multi-component

fuel consisting of various phases and components, with a complex microstructure. However, there have been no detailed studies on the properties of such a multi-component fuel, particularly its thermal conductivity.

Accordingly, in this research, we attempted to evaluate the thermal conductivity of multi-phase, multi-component systems using finite element analysis. This evaluation was done in two stages. In stage 1, a case was assumed wherein various shaped voids are distributed in UO_2 , and together with evaluating the validity of the computational method, the effects of these voids on the thermal conductivity of UO_2 were assessed. In stage 2, a part was cut out from a metallographic photograph of an MOX fuel actually irradiated in the experimental fast reactor JOYO. The effects of the accumulation of a FP precipitated phase and the complex microstructure on the temperature distribution and heat flow within the fuel pellet were then evaluated.

Figure 1. Evaluation of thermal conductivity by finite element analysis



Thermal conductivity evaluation by finite element method

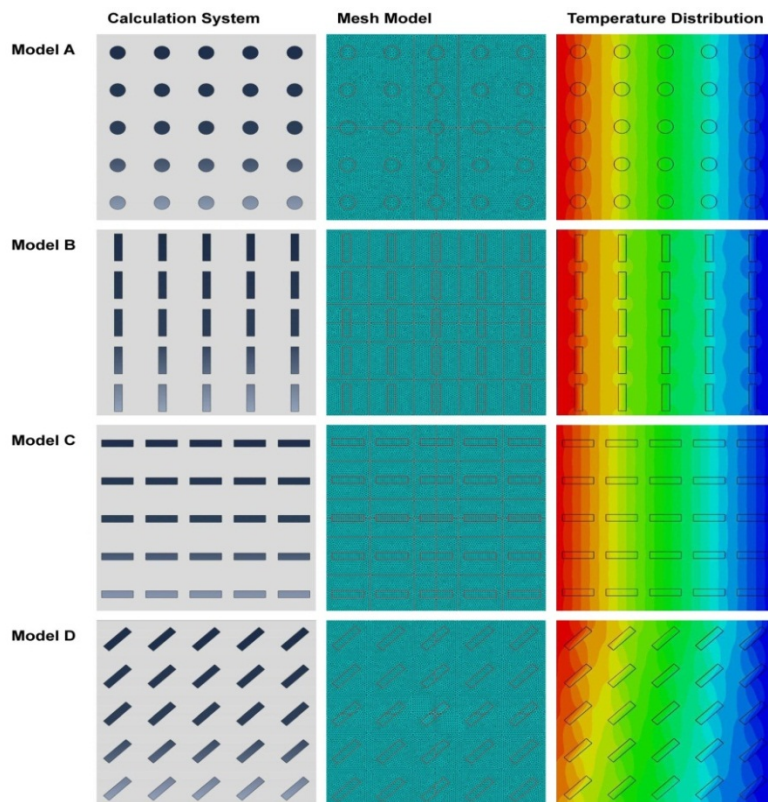
We briefly summarise here the method used for evaluating the thermal conductivity by finite element analysis. The method is shown in Figure 1. The computational system assumes a two-dimensional surface. An adiabatic state is assumed at the upper and lower ends of the computational system, and a given value of surface heat flux Q is applied uniformly. The temperature at the right end in Figure 1 is fixed at T_1 , and the average temperature at the left end, when it has risen and reached a steady state, is T_2 . In addition, the distance between the left and right ends is Δx . The heat flux value is set so that the temperature of the left side becomes a few $^{\circ}\text{C}$ to a few tens of $^{\circ}\text{C}$ higher than the fixed right-side temperature. At this point, the thermal conductivity of the system κ can be evaluated from the following equation:

$$Q = \kappa \frac{T_2 - T_1}{\Delta x}. \quad (1)$$

In assessing the thermal conductivity of such a multi-phase system, it was assumed that each phase tightly adhered to the other, and that there was no temperature difference at the boundaries. In addition, in performing the finite element analysis, thermal conductivity values for each phase were needed as input data; in order to meet the

objectives of the calculation, therefore, thermal conductivity values selected from the literature data [5] and measured values previously obtained by our group [6, 7] were used as input data.

Figure 2. The four types of computational systems used for evaluating thermal conductivity by finite element analysis, the mesh models thereof, and the temperature distributions of the system obtained by computation



Effect of porosity on the thermal conductivity of uranium dioxide

In order to prove the validity of the method for evaluating the thermal conductivity by finite element analysis, the shape and dispersion state of voids that affect the thermal conductivity of UO_2 were evaluated. Here, the thermal conductivity for UO_2 reported by Washington [5] (Equation 2) was used as the input data. In addition, the thermal conductivity of Ar was used as the thermal conductivity for the voids.

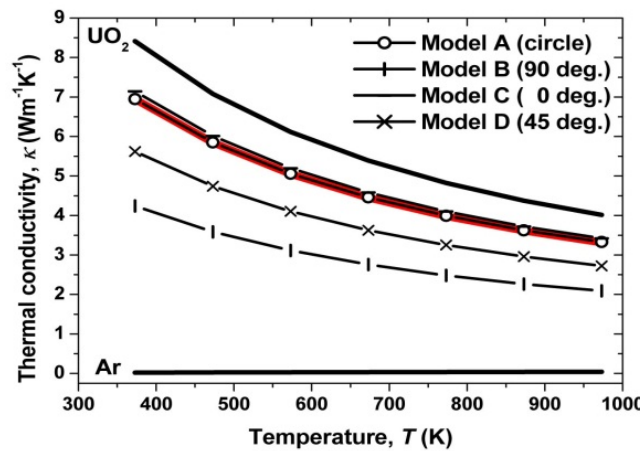
$$\kappa_{\text{UO}_2} = (0.035 + 2.25 \times 10^{-4} T_K)^{-1} + 83.0 \times 10^{-12} T_K^3 \quad (2)$$

The computational systems used in this study are shown in Figure 2. Four systems were constructed, and the temperature dependence of the thermal conductivity was evaluated for each. In all of the systems, the porosity was assumed to be 10%, and two types of void shapes, circular and rectangular, were assumed. For the rectangular shaped voids, cases were assumed wherein their long axis was aligned vertically, horizontally, and 45° to the heat flow. The diagrams shown in the centre column in Figure 2 show the

mesh partitions used in the finite element analysis of the computational system. Thermal conductivity data for UO_2 were input into the mesh at the locations corresponding to the matrix phase, and thermal conductivity data for Ar were input into the mesh at the locations corresponding to the voids. The diagrams shown in the right column in Figure 2 show the temperature distribution for the case where a specified heat flux was input from the left side of the system, and a steady state was reached.

The temperature dependence of the thermal conductivity for each computational system obtained by finite element analysis is shown in Figure 3. The thermal conductivity for UO_2 and Ar used as input data are also shown for reference. It is seen that reasonable results were obtained for the thermal conductivity of all four computational systems in that the values obtained were between the thermal conductivities of UO_2 and Ar. In addition, in looking in detail at the distribution state of the rectangular shaped voids, it was seen that the thermal conductivity became smaller in descending order of the case with voids positioned horizontal to the heat flux (Model C), then the case with voids positioned at 45° (Model D), and finally the case with voids positioned vertical (Model B). On the other hand, the value determined for the circular-shaped voids (Model A) was between that of Model C and Model D.

Figure 3. Temperature dependence of the thermal conductivity of UO_2 containing 10% voids (Ar) obtained by finite element analysis (comparison of results obtained for computational systems A through D; the red line represents computed values determined using Formula (3))



A number of formulas exist for expressing the porosity dependence of thermal conductivity. Here, the porosity dependence of the thermal conductivity of UO_2 was evaluated using the representative formula (Equation 3) shown below [8], and this was compared to results from finite element analysis shown previously.

$$\kappa_p = \kappa_0 (1 - P)^{1.5} \quad (3)$$

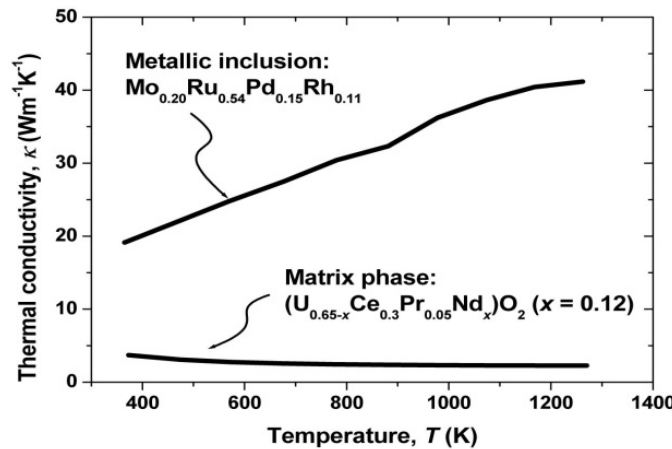
In Formula 3, κ_p is the thermal conductivity for the case containing voids, κ_0 is the thermal conductivity for the case where porosity is zero, and P is the porosity. The red line in Figure 3 shows results for calculations using Formula 3 of the thermal conductivity of UO_2 with 10% voids. The values calculated from Formula 3 were confirmed to be in good agreement with the results for Model A that had circular shaped voids.

From the above, it was confirmed that the porosity dependence of the thermal conductivity of UO_2 in response to various void shapes and distribution states could be evaluated by finite element analysis. In addition, the results obtained agreed well with the results of established formulas expressing the porosity dependence of thermal conductivity reported in the past.

Thermal conductivity evaluation of high burn-up mixed oxide fuel

In evaluating the thermal conductivity of irradiated MOX fuel, finite element analysis was carried out by constructing a computational system from three phases: a matrix phase, a precipitate phase, and voids (cracks), and inputting the thermal conductivities for the respective phases. In this analysis, the actual thermal conductivity values previously measured by our group [6,7] were used for the thermal conductivities of the fuel matrix phase and the metal precipitate phase. Thermal conductivity data were obtained for three types of samples with a composition represented by $(\text{U}_{0.65-x}\text{Ce}_{0.3}\text{Pr}_{0.05}\text{Nd}_x)\text{O}_2$ ($x = 0.01, 0.08, 0.12$) as the simulated matrix phase [6], and here, results obtained for $x = 0.12$ were used, which have the maximum FP content. On the other hand, thermal conductivity data were obtained for Mo-Ru-Rh-Pd alloys of various compositions for the metal precipitate phase [7], and of these, the actual measured values for the metal precipitate phase of the composition exhibiting the highest thermal conductivity among these were chosen as the input data. For voids (cracks), the thermal conductivity of Ar was used, similar to the evaluation of the porosity dependence of UO_2 . The temperature dependence of thermal conductivity is shown in Figure 4 for the matrix phase, $(\text{U}_{0.53}\text{Ce}_{0.3}\text{Pr}_{0.05}\text{Nd}_{0.12})\text{O}_2$, and the metal precipitate phase, Mo-Ru-Rh-Pd alloy, used as input data.

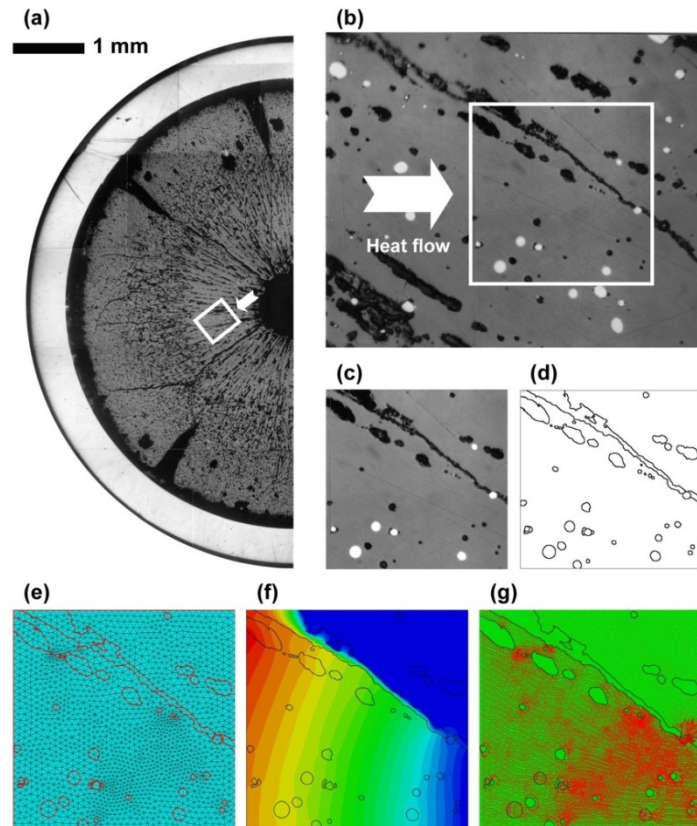
Figure 4. Temperature dependence of thermal conductivity of the matrix phase [4] and the metal precipitate phase [5] used as input data



For evaluating the thermal conductivity of the irradiated MOX fuel, we attempted to construct a computational system for finite element analysis from metallographic photographs of the MOX fuel that had been actually irradiated in a fast reactor to the point of high burn-up. A metallographic photograph of the cross-section of an irradiated high burn-up MOX fuel pellet is shown in Figure 5(a). This photo was obtained after irradiation of the MOX fuel pellet that reached a maximum high burn-up (approximately 144 GWd/t) in the experimental fast reactor JOYO [4]. Characteristics of the structure of

this fuel include a continuously changing structure in the radial direction of the fuel pellet, the shape of the outermost periphery of the pellet being severely uneven and the clear presence of a gap between the fuel pellet and cladding tube, and the precipitation of a coarsened white metal phase from near the centre hole to the radial intermediate area of the fuel pellet.

Figure 5. A cut-out of the computational system obtained from an irradiated high burn-up MOX fuel and evaluation of thermal conductivity by finite element analysis (heat is assumed to flow from left to right in the computational system)



- (a) Metallographic photograph of a cross-section of an irradiated high burnup MOX fuel pellet
- (b) Computational object cut out from photo (a)
- (c) Computational object cut out from photo (b)
- (d) Computational system prepared based on photo (c)
- (e) Mesh model prepared based on photo (d)
- (f) Temperature distribution of the computational system
- (g) Vector diagram of heat flow in the computation system

Figure 5(b) shows a cut-out of part of the metallographic photo in Figure 5(a). The region enclosed within the white lines in this figure was the object of finite element analysis. A constant quantity of heat was assumed to flow from the left of observer, and we attempted to visualise the temperature distribution and heat flow of the system. The cut-out region enclosed by the white lines in Figure 5(b) is shown in Figure 5(c). In

Figure 5(d), the regions representing the matrix phase, the metal precipitate phase, and voids (cracks) are outlined based on the image analysis of Figure 5(c). The regions in Figure 5(d) partitioned into a mesh are shown in Figure 5(e). In Figure 5(c), the regions indicated by the white round shapes correspond to the metal precipitate phase, the regions represented by black correspond to voids and cracks, and the other gray-colored regions correspond to the matrix phase.

The temperature distribution of the computational system and a heat flow vector diagram are shown in Figure 5(f) and (g), respectively. In Figure 5(f), it was confirmed that the temperature rose due to the heat flux from the left end of the computation system and that there was a temperature gradient from left to right. In addition, it was confirmed that there was practically no temperature rise in the region at the top right of the computational system. On the other hand, from Figure 5(g), it was confirmed that the heat flow was impeded by the large cracks cutting across the top part of the computational system at a slant. This is the reason why almost no temperature rise occurred in the upper right region of Figure 5(f). Also, it was found that while heat had been assumed to flow into the upper right region of the computational system via the metal precipitate phase present at the cracks, since the region through which heat could flow was narrow, the heat flow stagnated. Not only the chemical make up and components but also the microstructure of the fuel was found to have large effects on the thermal conductivity of fuel pellets.

From the above analysis, it became clear that in multi-component fuels having complex microstructures such as irradiated fuels, the temperature distribution of fuel pellets and the heat flow within the fuel change significantly due to the presence of the FP precipitate phase, voids, cracks, and similar defects.

Conclusion and future challenges

In this research, the effects of the shape and distribution state of voids on the thermal conductivity of UO_2 , and the temperature distribution and heat flow within the irradiated MOX fuel were evaluated by finite element analysis. The results obtained were reasonable in all cases. From this work, upon evaluating the thermal conductivity of irradiated fuels having complex phase states and microstructures, it was confirmed that the finite element analysis is extremely useful. In addition, this technique is not limited to just evaluating the thermal conductivity of fuel pellets. For example, because this technique could be used for applications such as evaluating the mechanical properties of light water reactor cladding tubes in which hydrides have precipitated, its use in broad-ranging fields is anticipated in the future.

References

- [1] Carbajo, J.J., G.L. Yoder, S.G. Popov, V.K. Ivanov (2001), *Journal of Nuclear Materials*, 299, 181-198.
- [2] Kleykamp, H., J.O. Paschoal, R. Pejsab, F. Thümmler (1985), *Journal of Nuclear Materials*, 130, 426-433.
- [3] Kleykamp, H. (1985), *Journal of Nuclear Materials*, 131, 221-246.

-
- [4] Kurosaki, K., K. Tanaka, M. Osaka, Y. Ohishi, H. Muta, M. Uno, S. Yamanaka, *Progress in Nuclear Science and Technology*, in press.
 - [5] Washington, A.B.G. (1973), *UKAEA Report TPG Report 2236(D)*.
 - [6] Kurosaki, K., K. Tanaka, M. Osaka, H. Muta, M. Uno, S. Yamanaka (2009), *Journal of Nuclear Materials*, 389, 85-88.
 - [7] Yamanaka, S., K. Kurosaki (2003), *Journal of Alloys and Compounds*, 353, 269-273.
 - [8] Schulz, B. (1981), *High Temp.-High Press*, 13, 649.

Chapter 24.

Use of advanced simulations in fuel performance codes

P. Van Uffelen

European Commission, JRC-Institute for Transuranium Elements, Germany

Abstract

The simulation of the cylindrical fuel rod behaviour in a reactor or a storage pool for spent fuel requires a fuel performance code. Such tool solves the equations for the heat transfer, the stresses and strains in fuel and cladding, the evolution of several isotopes and the behaviour of various fission products in the fuel rod. The main equations along with their limitations are briefly described. The current approaches adopted for overcoming these limitations and the perspectives are also outlined.

Main equations

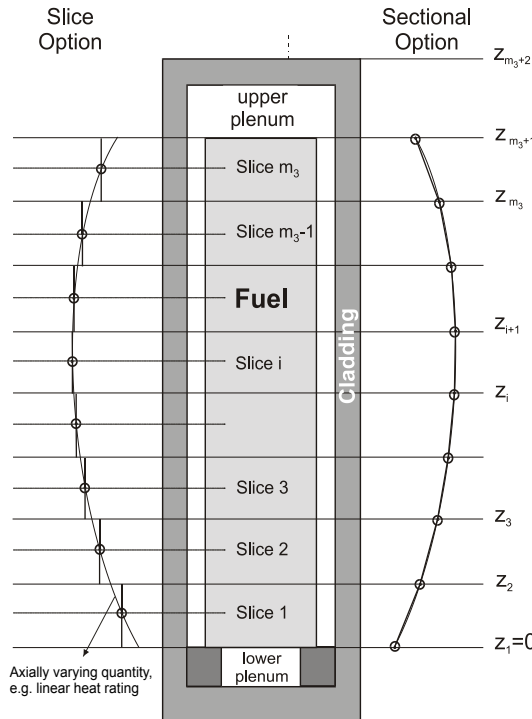
The ultimate goal of simulating nuclear fuel is to predict a fuel rod's behaviour and lifetime in a reactor. Doing so requires taking into account the coupled effects of heat transfer, the mechanical interaction between the fuel and its surrounding protection, the isotopic evolution caused by the irradiation and the chemical interactions between fuel, fission products, cladding and coolant [1-3]. The simulation of the fuel behavior requires therefore fuel performance codes, which are being used by safety authorities, research organisations and fuel vendors.

In view of the strong interactions between the various aspects of fuel performance and the resulting mathematical problems, several assumptions are introduced for rendering the set of equations amenable to an accurate numerical solution after a reasonable computation time. The first important assumption deals with the rod geometry. Most fuel performance codes consider a cylindrical geometry and assume axisymmetry [2]. For example, Figure 1 shows a computational domain consisting of a cylindrical UO_2 fuel pellet and zircaloy cladding separated by a helium gap. Furthermore, the radial temperature gradient is considered to be much larger in comparison with the axial temperature gradient. As a result, a majority of the codes represent the cylindrical

fuel rod in a so-called one-and-a-half dimension, whereby all transport processes are solved in one (radial) dimension, and the axial segments are coupled via balance equations.

The heat transfer is generally solved in a section of slice of fuel as a sequence of heat transfers between different heat resistances: the fuel, the fuel-to-cladding gap, the cladding (and its outer corrosion layer) and finally the barrier between the cladding surface and the bulk of the coolant [3]. Apart from the fuel and the cladding, in which the Fourier equation is solved with the fission rate density or the gamma heating providing the main heat source, all thermal resistances are represented by heat transfer coefficients. The heat transfer in the gap is both important and very delicate to assess as it is very sensitive to the gap size and the gas composition, hence it is strongly affected by the uncertainties pertaining to the other aspects of the fuel behaviour. The boundary conditions usually applied consist of the Dirichlet boundary condition at the cladding surface and the Neumann boundary conditions at the fuel pellet centre because of symmetry [3].

Figure 1. Typical schematic representation of a rod in a fuel performance code



The assessment of the stresses and strain in a section of the fuel rod is usually based on the solution of the equilibrium relation, the compatibility equation and the constitutive equations [3]. The main difficulties arise because of the cracking of the pellets and the relocation of the fuel fragments. The boundary condition at the outer surface is determined by the coolant pressure and either the rod inner gas pressure in the event of an open gap situation or the contact pressure between the fuel and the cladding when the gap is closed. The boundary condition at the pellet centre is determined by the inner gas pressure in the case of hollow pellets, and by the equality of the tangential and radial deformation in the event of solid pellets.

The fission product behaviour in each axial slice of the fuel rod is generally considered to occur in two steps [3]. The first step consists of the production and subsequent migration in the grains. This is usually dealt with by means of a diffusion equation in a sphere. The second step consists of the development of grain boundary bubbles that grow until they interlink and form a tunnel network through which the insoluble fission products can be released. Because of the large uncertainties pertaining to the parameters of interest, and in particular to the diffusion coefficient that can vary by a factor 5 up or down, simple ordinary differential equations are usually solved to describe both the fission product release and the gaseous swelling caused by insoluble fission products such as Xenon and Krypton.

Current approaches to deal with limitations

In order to cope with large local deformations, such as those occurring in the cladding, for instance, during loss of coolant accidents, some codes either provide a separate tool to analyse local deformations and stresses in two dimensions by means of finite element calculations such as the FEMAXI code [4], or a full two-dimensional mechanical computation is proposed in the FALCON code [5] whereas a three-dimensional finite element analysis is proposed in the ALCYONE code in the PLEIADES platform [6,7]. More recently, fuel performance codes are currently being developed either from scratch, or on the basis of commercial software for three-dimensional finite element method (FEM) simulations. Examples of such attempts are the BISON code [8] based on ABAQUS software and the FRA-TF_global code based on COSMOSDesignSTAR/COSMOSM system [9] or a code based on the COMSOL software [10]. The starting point for their development is to take full advantage of the improvements in hardware and software, as well as in numerical techniques since the conventional fuel performance codes - currently used by safety authorities – have been developed. Nevertheless, the increase in the number of dimensions goes along with a substantial increase of the computational costs and offers only an added value for the analysis of strong and localised pellet-cladding interactions (triple-point effect) or certain accident situations with large deformations. Indeed, for normal operational conditions, one-dimensional codes are at least as accurate in view of the numerous uncertainties, as for instance those brought about by the stochastic cracking and friction processes. The uncertainties in fuel rod powers and geometry (sphericity, pellet cracking, etc.) cannot be avoided by those multi-dimensional codes and ultimately may prevent them from replacing more simplified codes of today for licensing purposes. In any case, they will provide a deeper understanding and an excellent supporting tool for designing advanced nuclear fuels.

Apart from the main limitations caused by the geometrical assumptions, there are other limitations related to the empirical nature of material property models and some of the physical models, such as cracking and the subsequent relocation of the segments. These limitations apply to multi-dimensional codes alike. As a consequence of the use of empirical models, it is impossible to extrapolate the material properties and models beyond the range of operating conditions in which they have been fitted. Hence, when advanced materials are to be designed for innovative reactor types, new codes have to be developed for each combination. The required amount of experimental data is both time consuming and expensive. With the advent of advanced software and hardware many attempts have been made to introduce more physics-based models that enable

extrapolation to a large range of operating conditions, and to cover a large set of potential materials. This has led to the development of mesoscopic models, microscopic models and even simulations tools at the scale of the electronic structure [11]. Each simulation tool requires specific experimental data for their development and validation. There are now attempts to link the various simulations tools in what is commonly referred to as the multi-scale approach and is considered in the other parts of this report. Several examples have been published recently. In the first case, molecular dynamics computations were applied for extracting the thermal expansion and thermal conductivity of unirradiated UO₂ fuel and for implementing the correlation in the FRAPCON code [12]. In the frame of the F-BRIDGE Project, a similar molecular dynamics analysis was carried out to simulate the interaction of a He bubble with a fission fragment [13]. It is expected that this will lead to a quantitative assessment of the resolution coefficient, which remains up until now a fitting parameter in several fission gas release models of fuel performance codes. In the same project, first principles-based predictions of the migration energies for point defects in UN by means of the VASP DFT code were introduced in the thermal creep model of the TRANSURANUS fuel performance code [14].

The parameters and models required for by the fuel performance codes are subject to uncertainties. A pragmatic manner to deal with uncertainties pertaining to power histories, fabrication data and models in the current fuel performance codes consists of applying conservative or probabilistic analysis. In order to assess the technological effect of all sources of uncertainties there are various techniques that may be considered. First of all, there are various so-called sensitivity methodologies, ranging from multiple runs with input data or model parameters being varied, up to a rigorous mathematical treatment based on perturbation theory [15-17]. A second category of probabilistic approaches is the response surface technique. This is based on a careful combination of parameters called the experimental design, such as the Latin hypercube sampling or the Taguchi design [18]. A third category consists of the Monte Carlo method, which is based on random sampling of all uncertain variables that are considered, and implemented in the TRANSRANUS code [19]. A fourth category of methods is called semi-statistical and combines statistical and deterministic computations [20-22].

Perspectives

New simulation tools are being developed for a multi-dimensional rather than a one-and-half-dimensional analysis in order to take advantage of the hardware and software improvements over the last decades. They can complement the existing fuel performance codes for research purposes such as a localised pellet cladding interaction analysis, and provide a good supporting tool for the design of advanced or accident-tolerant fuels. Nevertheless, they suffer from limitations associated with uncertainties inherent in the stochastic nature of some phenomena such as fuel crack formation and input parameters such as the fuel rod power. Furthermore, they cannot (yet) be used for a full core analysis required in the fuel licensing of some countries.

In addition to improving or rewriting fuel performance codes, there is also a tendency to couple existing codes with other simulation tools like the thermohydraulic codes or the neutron transport codes. The aim of this so-called multi-physics approach is to take again advantage of the hardware and software developments for improving predictions during

transients and design-basis accidents such as reactivity-initiated accidents or loss of coolant accidents. The coupling between the TRANSURANUS code and the DYN3D code is such an example [23], where it is hoped that the more detailed fuel performance predictions will improve the overall simulation accuracy for the reactor core during an accident, at a reasonable computational costs.

Finally, the conventional as well as the advanced fuel performance codes can also be extended to assess the fuel and fission product chemistry. This will extend the application range of the codes to simulate fuel cladding chemical interaction in fast reactor conditions or stress corrosion cracking and accident behaviour in LWR fuel where the release of Cs for example is important. At the same time, it will enable the prediction of the source term required in spent fuel simulations. For this purpose, a coupling or integration of a module for the thermochemistry of the fuel system with fission products is being developed. For example, the VICTORIA code [24] is being integrated in the MFPR code [25], whereas the Thermochimica model is being coupled with integration in the AMP code [26].

References

- [1] Olander, D.R. (1976), *Fundamental Aspects of Nuclear Reactor Fuel Elements*, Technical Information Center - Energy Research and Development Administration, University of California, Berkeley.
- [2] van Uffelen, P. et al. (2010), “Analysis of reactor fuel rod behavior”, *Handbook of Nuclear Engineering*, D.G. Cacuci, Editor, Springer Science+Business Media.
- [3] van Uffelen, P., M. Suzuki (2012), “Fuel performance modeling and simulations: Oxide fuel performance and simulation”, *Comprehensive Nuclear Materials*, R.J.M. Konings.
- [4] Suzuki, M., H. Uetsuka, H. Saitou (2004), “Analysis of mechanical load on cladding induced by fuel swelling during power ramp in high burn-up rod by fuel performance code FEMAXI-6”, *Nuclear Engineering and Design*, 229, p. 1.
- [5] Rashid, J. et al. (2003), “Behavioral modeling of LWR fuel as represented in the FALCON code”, *Workshop on Materials Modelling and Simulations for Nuclear Fuel (MMSNF)*, New Orleans, US.
- [6] Sercombe, J. et al. (2009), “Multi-dimensional modeling of PCMI during base irradiation and ramp testing with ALCYONE V1.1”, *Top Fuel 2009, European Nuclear Society*, Paris, France.
- [7] Struzik, C., V. Marelle (2012), “Validation of the fuel performance CEA code ALCYONE, scheme 1D, on extensive data base”, *Top Fuel 2012, European Nuclear Society*, Manchester, UK.
- [8] Williamson, R.L. (2011), “Enhancing the ABAQUS thermomechanics code to simulate multipellet steady and transient LWR fuel rod behavior”, *Journal of Nuclear Materials*, 415, pp. 74-83.

- [9] Dostál, M., M. Valach, J. Zymák (2009), “Development and validation of the FEM based global fuel rod analyzer FRA-TF_global”, *Top Fuel 2009, European Nuclear Society*, Paris, France.
- [10] Mihaila, B. et al. (2009), “Simulations of coupled heat transport, oxygen diffusion, and thermal expansion in UO₂ nuclear fuel elements”, *Journal of Nuclear Materials*, 394, pp. 182-189.
- [11] Devanathan, R. et al. (2010), “Modeling and simulation of nuclear fuel materials”, *Energy and Environmental Science*, 3, pp. 1406-1426.
- [12] Vega, D.A. et al. (2009), “Towards an atomistically informed fuel performance code: Thermal properties using FRAPCON and molecular dynamics simulations”, *Nuclear Technology*, 165, pp. 308-312.
- [13] Parfitt, D.C., R.W. Grimes (2008), “Predicted mechanisms for radiation enhanced helium resolution in uranium dioxide”, *Journal of Nuclear Materials*, 381, pp. 216-222.
- [14] Kotomin, E.A. et al. (2009), “Implementing first principles calculations of defect migration in a fuel performance code for UN simulations”, *Journal of Nuclear Materials*, 393, pp. 292-299.
- [15] Bouloré, A., C. Struzik, F. Gaudier (2012), “Uncertainty and sensitivity analysis of the nuclear fuel thermal behavior”, *Nuclear Engineering and Design*, 253, pp. 200-210.
- [16] Lassmann, K. (1983), “Numerical noise analysis: A new probabilistic technique”, *Computer Methods in Applied Mechanics and Engineering*, 40(1), pp. 111-119.
- [17] Heins, L. et al. (1991), “Statistical analysis of QC data and estimation of fuel rod behaviour”, *Journal of Nuclear Materials*, 178(2-3), pp. 287-295.
- [18] Gardiner, W.P., G. Gettinby (1998), *Experimental Design Techniques in Statistical Practice: A Practical Software-based Approach*, Woodhead Publishing.
- [19] Lassmann, K., C. O'Carroll, J. van de Laar (1994), “Probabilistic fuel rod analyses using the TRANSURANUS code”, *Technical Committee Meeting on Water Reactor Fuel Element Modelling at High Burnup and Experimental Support*, Windermere, UK.
- [20] Sauer, G., W. Besenböck (2008), “Reliable statistical fuel rod analysis”, *Water reactor fuel performance meeting*, Seoul, Korea.
- [21] Arimescu, V.I. (2008), “Best-estimate BWR fuel thermal-mechanical analysis based on non-parametric order statistics”, *Water reactor fuel performance meeting*, Seoul, Korea.
- [22] Forsberg, K. et al. (1996), “Probabilistic analysis of nuclear fuel rod behaviour using quasi Monte Carlo Method”, *Nuclear Science and Engineering*, 122, pp. 142-150.
- [23] Holt, L. et al. (2013), “Development of a general coupling interface for the fuel performance code TRANSURANUS tested with the reactor dynamic code DYN3D”, *10th International conference on WWER fuel performance, modelling and experimental support*, Bulgarian Academy of Sciences, Sandanski, Bulgaria.
- [24] Olander, D.R., V. Mubayi (1999), “Review of the materials-chemistry models in the VICTORIA code”, *Journal of Nuclear Materials*, 270(1-2), pp. 1-10.

- [25] Veshchunov, M.S. et al. (2006), “Development of mechanistic code MFPR for modelling fission product release from irradiated UO₂ fuel”, *Nuclear Engineering and Design*, 236(2), pp. 179-200.
- [26] Piro, M.H.A. et al. (2011), “Numerical verification of equilibrium thermodynamic computations in nuclear fuel performance codes”, *Journal of Nuclear Materials*, 414, pp. 399-407.

Chapter 25.

Integrated multi-scale modelling and simulation of nuclear fuels

C. Valot¹, M. Bertolus¹, L. Malerba², J. Rachid³, T. Besmann⁴,
R. Masson¹, S. Phillpot⁵, M. Stan⁶

¹CEA, DEN, DEC, Centre de Cadarache, France, ²SCK•CEN, Belgium, ³ANATECH-SI, US

⁴University of South Carolina, US, ⁵University of Florida, US,

⁶Argonne National Laboratory, US

Introduction

Nuclear fuels are very specific materials and their in-pile behaviour and performance are determined by a large number of interconnected phenomena induced by chemistry, irradiation, temperature and mechanical effects. These phenomena lead in fuels to a very large diversity of physical and chemical transformations and evolution at various scales, such as cracking, fission gas bubble precipitation, restructuring, fission product migration and interaction, as shown for ceramic oxides in Figure 1.

Figure 1. Diversity of physical, chemical, and microstructural transformations observed in ceramic oxide fuel under irradiation

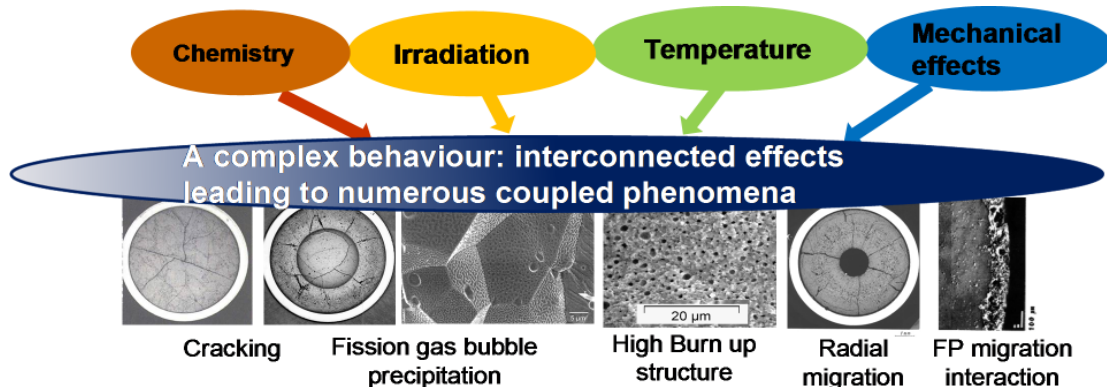
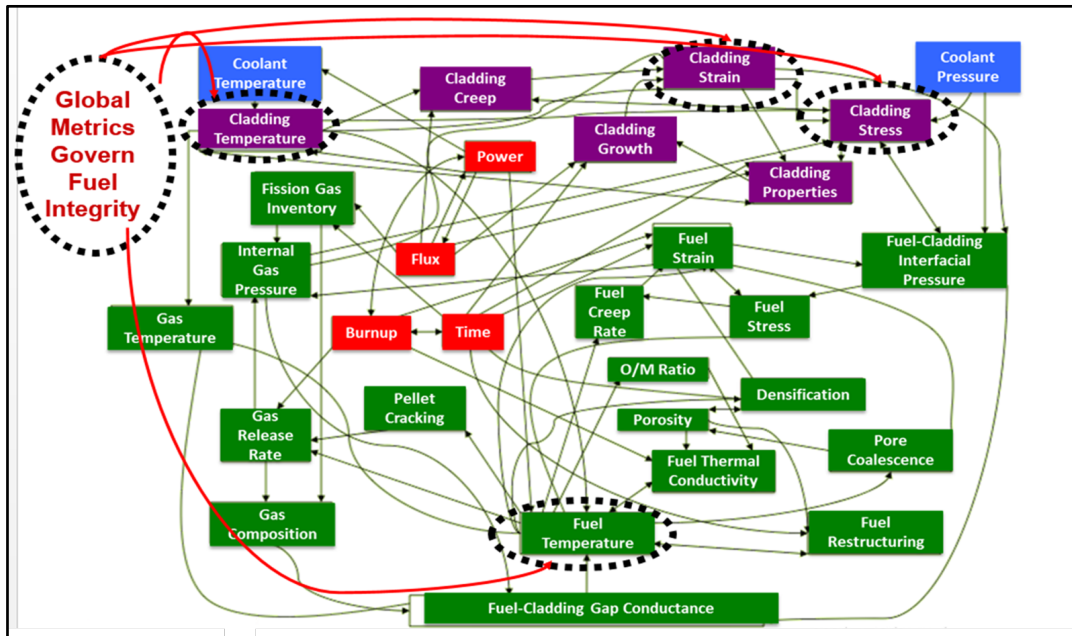


Figure 2 illustrates the numerous parameters that influence the behaviour of nuclear fuels under irradiation and that must be considered to understand their evolution in pile, as well as the relationships between them. This leads to a significantly complex

understanding and modelling of the thermomechanical and thermochemical properties and evolution of fuel.

Figure 2. Phenomena influencing the behaviour of nuclear fuels under irradiation and their interrelationships: Scope and complexity of the fuel behaviour modelling [37]



Despite this complexity, significant experience on the modelling and simulation of fuel rods behaviour at long lengths and times under irradiation has been developed around the world over the last 50 years based on semi-empirical macroscopic modelling validated by a large number of valuable in-pile experiments. Most operational regimes are well reproduced, and this understanding is the basis for the licensing of fuel in current reactors.

But because of the complex character of the fuel behaviour, an in-depth predictive knowledge of the nuclear fuel and fission products behaviour calls for a clear understanding of the underlying phenomena from the atomic to the rod scale through the mesoscopic scale, i.e., the scale of the fuel grain. Strategies based essentially on experimental irradiation approaches and empirical model developments may not be sufficient when a large number of complex conditions must be accounted for. It is then necessary to use a material science approach supported by numerical simulations performed at different time and space scales, combined with relevant analytical experiments to establish a sound scientific basis for the understanding of the evolution of nuclear fuel under irradiation.

This modelling and simulation approach has already proved its feasibility and value in materials development and uses over the last decades [1], including:

- the virtual aluminium casting project developed by Ford Motor Company to design cast aluminium components, which has led to a significant reduction in development costs, as well as improved end products [2];

- computational materials science which has enabled the rapid and efficient design of corrosion resistant ultra-high-strength steels [3];
- in the nuclear field the “virtual reactor” as developed under the PERFECT European project (2004-2007) [4] and its follow-up PERFORM-60 project (2009-2013) [5] on structural materials (reactor pressure vessel and internals steels).

To some extent, the multi-scale modelling and simulation of nuclear fuels behaviour is a more recent effort because of the specific character of fuel materials and the difficulty of investigations at the lower scales. The atomic scale modelling methods, however, are now mature enough to study fuel materials with adequate accuracy (see Chapter 14) and several important national and international initiatives have focused on the construction of consistent multiscale/multi-physics modelling approaches. Some examples include:

- in Europe, the F-BRIDGE project (2008-2012) [6-8];
- in the US, the Nuclear Energy Advanced Modelling and Simulation (NEAMS) Program [9], the Consortium for Advanced Simulation of Light Water Reactors (CASL) [10], the Center for Material Science of Nuclear Fuels (CMSNF) [11];
- specifically in France the PLEAIDES platform (CEA) [12];
- the NXO Project in Japan [14].

This chapter aims at discussing the objectives, implementation and integration of multi-scale modelling approaches applied to nuclear fuel materials. We will first show why the multi-scale modelling approach is required, due to the nature of the materials and by the phenomena involved under irradiation. We will then present the multiple facets of multi-scale modelling approach, while giving some recommendations with regard to its application. We will also show that multiscale modelling must be coupled with appropriate multi-scale experiments and characterisation. Finally, we will demonstrate how multi-scale modelling can contribute to solving technology issues.

Multi-scale modelling is required to capture the multi-scale character of materials and of the phenomena occurring under irradiation

As the modern understanding of matter has taught us, while they appear continuous at a macroscopic scale, materials are discrete and made of atoms or, more precisely, of atomic nuclei (ions) surrounded by electrons. Despite their discrete nature, for most applications the approximation of describing them as a continuum with uniform properties is appropriate. This is commonly done for solids for instance in continuum mechanics to calculate stress and strain fields, or for determining the temperature field, in all parts of a material subjected to a given external mechanical and/or thermal load. The finite element method is used in this context to study the behaviour of fuel under irradiation (strain, cracking, temperature distribution, fuel-pellet interaction, etc.) (see Chapter 22).

However, under increased magnification, intermediate structures/microstructures can be identified revealing discontinuities without even going down to the atomic level. In solids, grains and subgrains can be identified. In fuel, fission gas behaviour as well as the mechanical properties depend enormously on how these grains are structured and change under in-reactor conditions (irradiation, mechanical or thermal load).

Although grains appear as single crystals in which atoms are distributed according to the material's crystallographic structure, yet they are in reality defective poly-crystals. Point defects, i.e., vacancies (missing atoms) or interstitials (atoms in excess), as well as dislocations, play a key role in determining the materials' properties. Exogenous atoms such as dopants added in the fabrication process and fission products generated during irradiation also contribute to crystal imperfection and have an impact on properties.

Below the grain-level structure, the description of many physical phenomena requires that materials be described as a set of discrete atoms. For example, optical, magnetic or thermal, as well as chemical behaviour, depend on the electronic structure of the material, and diffusion mechanisms in solids also depend on atomic structure.

Behaviour under irradiation (i.e., radiation damage) in solids represents an extreme case in materials science, because the almost instantaneous ballistic displacement of atoms by an energetic impinging particle (e.g., neutron or fission product), localised in a region of a few nanometres repeated several times at different points in the material over time, is a source of changes of material properties. In nuclear fuel, the accumulation of defects and fission products, especially gases, produces cavities and bubbles, which generate particular microstructural changes and cause macroscopic swelling, which, in turn, leads to cracking. Thus, the behaviour of materials under irradiation is such that atomic- or even nuclear-level processes can lead to changes in the way large components, such as fuel pins, respond to loads.

In theory, the behaviour of a material described as a set of atoms under given conditions could be predicted exactly by solving the time dependent Schrödinger equation for all the ions and electrons that compose it. This is the principle of *ab initio* calculations. In practice, such calculations are only possible in simple cases that involve a few ions and electrons. In fact, even if the atomic and discrete nature of materials can be taken into account, approximations/models need to be devised to describe the properties at the atomic level. The discrete modelling tools that describe atomic-level processes in solids can be classified as:

- approximated quantum-mechanical electronic structure calculations (also called first-principles or even *ab initio*) [15], (see Chapter 12);
- molecular dynamics [16] either based on electronic structure calculations or more frequently on the use of classical empirical interatomic potentials [17], (see Chapter 13);
- models treating the evolution of defects derived from the underlying atomic structure, such as kinetic Monte Carlo, rate theory (see Chapter 18), dislocation dynamics (see Chapter 15).

These tools have been progressively developed in the last decades [18] and rely heavily on the use of high-performance computing for simulations. They have become increasingly widespread because of the growing power of computers and have been extensively applied to nuclear materials in the last decade.

In summary, in order to be able to describe the behaviour of materials and especially of nuclear fuels under irradiation, beyond and in complement to an empirical approach based on data obtained by integral irradiations, it is necessary to develop models at various scales for:

- atomic scale processes: diffusion of chemical species and defects, cascades of atomic displacements;
- nano- and microscale processes: creation of fission gas bubbles or aggregates, segregation of chemical species that influence local properties, development and movement of nanostructural features such as dislocations that govern plastic deformation, changes in grain boundary behaviour;
- macroscale processes: continuum thermomechanical calculations of stress and strain field, fission gas release, pellet-clad interaction.

It also requires that the information based on relevant mechanisms about the behaviour of the fuel at a particular scale somehow informs the higher scales, so that the models at the higher level can be more physically representative and more accurate.

Choosing multi-scale modelling approaches

There exists a multiplicity of motivations and possible implementations of multi-scale modelling. It is thus of paramount importance to define precisely the objective for the development of such an approach and the type of approach needed. The challenges that are to be met will be at various levels starting from building a link between scales, providing information to the next level, and to the Holy Grail of a 3D simulation integrating codes over large scales of time and length.

It is also important to distinguish between modelling, simulation and prediction which are different, yet complementary activities. A model is a logical description of how a system (fuel in our case) performs. Models can be empirical or theory-based. A simulation is the process of conducting mathematical experiments or running computer programs to reproduce in a simplified way the behaviour of a system along a certain coordinate (in the case of fuels, for instance time or burn-up). Prediction can be defined as the use of a simulation tool (built either on empirical or theory-based models) applicable inside a validation domain to describe the behaviour of a given fuel. Empirical modelling requires the analysis to remain inside the validated domain, whereas theory-based models are key for predictions even slightly outside the validated domain. From such definitions we can have an initial understanding of how experiments, modelling and simulation are closely linked, and on how challenging it is to obtain a predictive capability.

Table 1 lists various possible objectives and various ways to utilise multi-scale modelling.

When generating a plan for the development of (multi-scale) physical models to investigate a given phenomenon, it is extremely important to keep in mind its feasibility based on the knowledge of the state-of-the-art and as much as possible the expected timeframe. Modern modelling tools are not all-powerful, irrespective of the power of available computers. With the increasing capability of high-performance computing it is not impossible that computer scientists can ultimately, cleverly combine different established models to provide integrated codes that are capable of giving answers about materials behaviour under given conditions. However, this should not be regarded as the main, and certainly not the only, goal of the development of multi-scale models. One should not assume that everything can be obtained *ab initio*, even though electronic

structure calculations are a very powerful and by now essential tools in our hands; it is not by attempting the simulation of a very complex phenomenon including all the complexities of the system that one understands and quantifies the most important underlying physical mechanisms.

Table 1. Various possible objectives and utilisation of multiscale modelling

Various objectives/motivations
<ul style="list-style-type: none"> • improve understanding of the underlying mechanisms and processes that control behaviour; • help in the selection, preparation and interpretation of irradiation tests to optimise results; • improve predictive capability for licencing; • contribute to the design of new fuel materials with limited property information (i.e., materials by design).
Possible utilisation /plans for development
<ul style="list-style-type: none"> • couple experiments and modelling to select relevant phenomena that are to be used for the simulation; • promote exchange between disciplines and provide information/mechanisms/data from the lower scales to the higher scales; • perform multi-disciplinary modelling (thermomechanical, physico-chemical, thermochemical, etc); • computationally couple the various codes used in multi-scale modelling approaches.

A modelling plan should address problems that are sufficiently well-understood, based on experimental data, so that a reasonable conceptual model exists already that can be used to actually build a quantitative computational model. In this case, the physical model can actually provide added value to cast some light on still unclear issues. Often the problem is so complicated that empirical correlations are the only way to find out which variables play a role and the determination of these variables corresponds to the very first step in rationalising experimental observations: without this knowledge, no further steps can be taken and we would be deluded in thinking that all aspects of the problem can be elucidated by trying to simulate it in a computer. The development of physical models and the application of computer simulation should be undertaken with precise questions in mind that seems to be answerable with the available tools. Often, even if it cannot be directly validated by experiments, atomistic models allow different possible mechanisms to be explored which may reveal unexpected mechanisms.

The Cartesian effort to split the problem into parts that are simpler to address is not an obsolete practice: it remains key to designing a modelling plan. Consistent with what is noted above, the plan should also always include feasible experiments that involve the use of a combination of characterisation techniques, so that physical mechanisms can be deduced from the experimental work. A final model will have to include these mechanisms and the data will be usable for the validation of the model.

The tools to be used to develop models should be identified and related to the scale they encompass to allow the selection of that most suitable from a fairly wide choice. Sometimes the difference between tools lies only in very technical and subtle details; however, these small differences can be important. It may be that the development of new modelling tools is necessary. Developing tools that allow more “realistic” simulations to be performed and the complexity of real systems to be better represented is a stimulating challenge and part of the path to be followed to obtain steady progress.

Unfortunately, experience shows that the development of new tools or approaches is time consuming. It is frequently not as easy as one might think at the beginning, and it always requires proceeding step-by-step, often leading to the need to address numerical or mathematical problems that might require years to solve. Thus, in the case of an especially complex phenomenon, one should not rely too much on the development of revolutionary modelling tools. Instead, key questions amenable to modelling with existing or foreseeable tools should be identified. It is of course possible to think of an ambitious plan that relies on new developments at all scales, but in the short-to-medium term the investigation should rely mainly on existing modelling tools that only need to be adapted, following an incremental approach.

Modelling fuel across scales

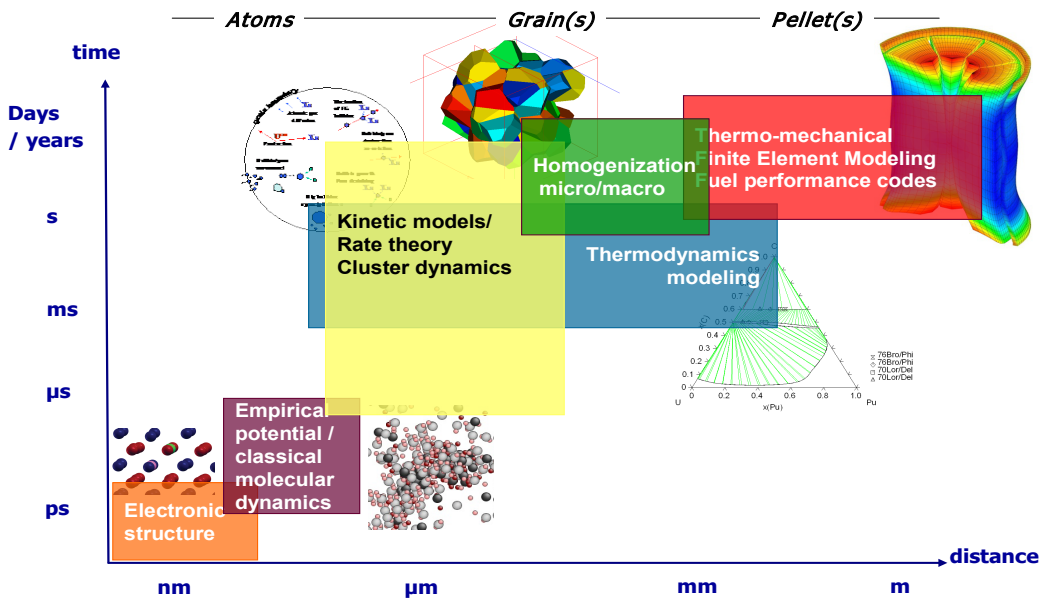
Figure 3 shows a schematic view of the multi-scale modelling and simulation approach for understanding the thermomechanical, physical and chemical evolution of nuclear fuels from the atomic scale through the intermediate grain size scale up to the pellet/rod scale. Although not discussed in this chapter, fuel behaviour modelling should also be coupled with neutronics and thermal-hydraulics for a full multi-physics simulation of a reactor.

Currently the vast majority of researchers involved in multi-scale modelling are operating at either end of the spectrum. At the macroscale end are those using widespread continuum thermomechanical tools to develop models used also at industrial level. At the other end are those performing atomic scale calculations, e.g., electronic structure calculations and empirical potential methods which are tools now commonly used for a variety of purposes and studies [8,20].

To balance the efforts at the macroscopic and atomic scales more attention needs to be addressed to the intermediate scale, also termed the mesoscopic scale, which encompasses time and length scales too large to be addressed using atomistic methods, but too small for fully continuum models. This is the case for materials in general, and nuclear fuels are no exception. It has, however, been demonstrated, for example during the F-BRIDGE project [7], that a key scale in fuel behaviour is the mesoscopic grain scale, because it allows one to aggregate information yielded by atomic scale calculations and form the foundation for macroscopic modelling. This scale therefore enables the real transfer of information from the lower to the higher scales.

A key challenge for the future is to enrich the already existing multi-scale modelling and simulation approach by developing models at the mesoscopic scale to further strengthen links between the atomic and macroscopic scales and systematically address the problem of transferring information from one scale to another.

Figure 3. A schematic view of the multi-scale modelling and simulation approach (inspired from [19]) for understanding the thermomechanical, physical and chemical evolution of nuclear fuels from the atomic scale to the pellet and rod scale



Interactions between multi-scale modelling and experimental characterisation

An idea often raised is that modelling could replace experiment, thereby saving time and money in the research activities. This becomes an especially convincing argument when expensive experiments such as irradiation or characterisation of irradiated fuels are involved. This, however, is a false economy, as modelling can of course help in rationalising experiments and can support their interpretation, but without experiments modelling remains divorced from reality and has little utility.

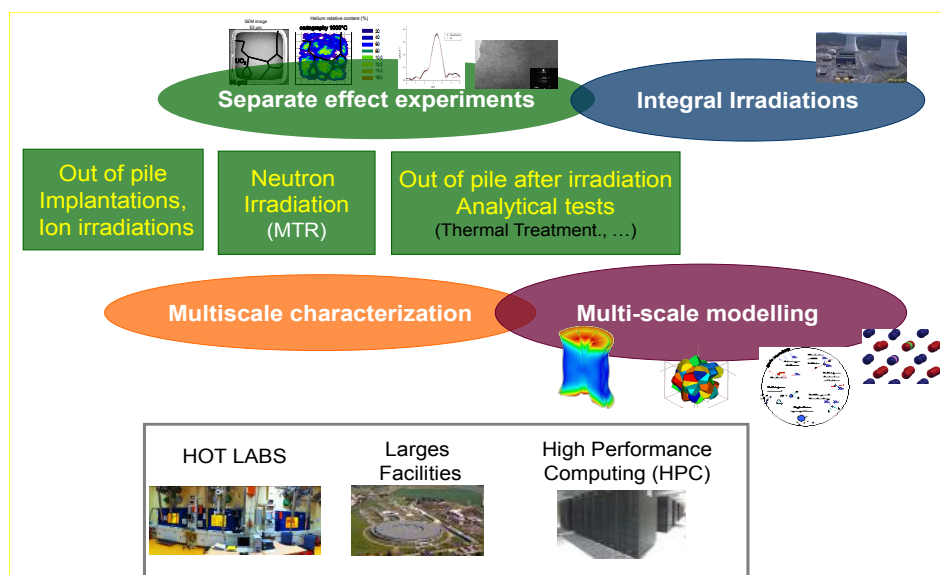
In opposition to modelling and simulation is the view that these are not necessary because, in the end, an integral irradiation test for the validation of fuel behaviour is required. Of course, this is not entirely correct either. First of all, the main contribution of modelling is precisely to insure that what is observed in integral irradiation tests is well explained and justified, meaning that the physical phenomena are well understood and modelled to reproduce the experimental results. In addition, validation of fuel behaviour cannot only be done through an integral test, because all the main underlying phenomena can only be validated as separate effects (at various scales) in parallel with integral validation.

As described in Figures 4 and 5, the correct approach is to couple experiments and modelling across scales. Experiments have to include in parallel integral irradiation as well as separate effect experiments (out-of-pile with ion irradiation and implantation, out-of-pile after neutron irradiation with thermal treatment for instance, subscale in pile irradiation...)

Experimental validation of models is not the only link between modelling and experiment. Modelling and experiment should not be performed sequentially but in

parallel to inform each other: the experiment provides modelling with basic data, modelling helps to prepare/interpret the experiment. More than individually, intelligently coupling modelling and experiment allows crucial information on phenomenology and relevant mechanisms to be revealed. More than “experimental validation” of models, what is needed is a “combination of state-of-the-art models and experiments in order to better understand reality”.

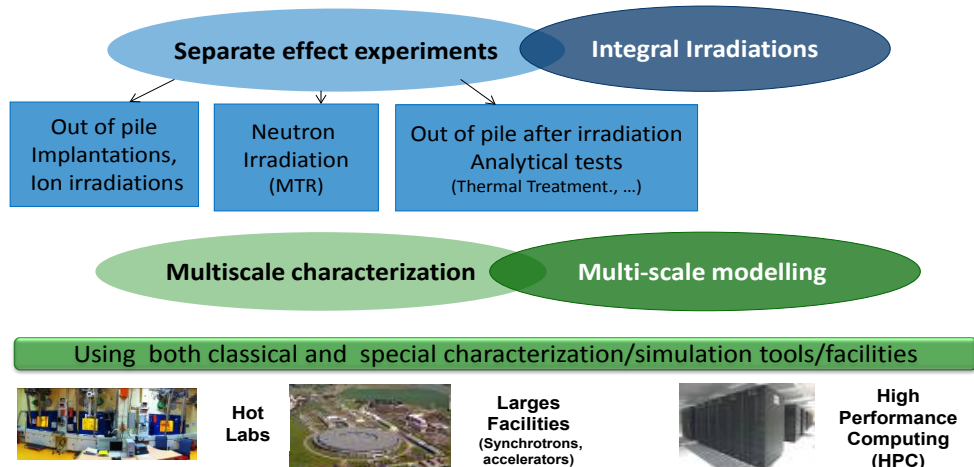
Figure 4. Coupling experiments (both separate effects and integral irradiations), characterisation and modelling in a multi-scale approach



Even models that start from quantum chemical calculations are not developed in a separate world and then brought down to earth so as to be compared with experiments, to be tested to “see if they work” (i.e., validated). No model with the ambition of helping interpret experimental data for a given phenomenon can be conceptually designed and built without a significant understanding of the experimental phenomenology. One should know which problems should be studied, have as much experimental evidence as possible on the mechanisms involved, and obtain and analyse sufficient data to develop a *conceptual* model to guide the creation of actual *mathematical* models. This is thus very different from “experimental validation”.

The assumptions made in models must either be suggested by experiments, or deduced from more fundamental models. The first objective in the process of model development is not to make predictions to be verified experimentally, but to make sure that the model reproduces satisfactorily a set of available experiments, providing a key for their rationalisation and interpretation. These experiments must be as complete and detailed as possible, so that all or most of the model’s aspects can be developed and verified. In other words, what a physical model is chiefly expected to do is explain the experimental data. The fact that experimental data are correctly reproduced by a physical model is likely to mean that the relevant mechanisms have been properly identified and quantified.

Figure 5. Schematic description of the interrelations between experiments and modelling



The identification of relevant mechanisms can trigger a series of considerations on what can be done to keep a given phenomenon under control or to exploit it for given purposes. Only at an advanced level of development may one attempt *predictions* with the model outside the initial data set and plan experiments to validate the prediction. Eventually, science-based models can be used to explore a spectrum of conditions that cannot be explored entirely experimentally, providing hints for the interpretation and rationalisation of experimental results, and importantly also anticipating experimental results for yet unexplored conditions. In this sense, they definitely achieve some level of predictive capability.

The characterisation techniques listed in Table 2 currently applied to as-fabricated or irradiated fuels, are at the cutting edge of the techniques, despite the great difficulties associated with the handling of actinide and irradiated materials.

These characterisation techniques are now invaluable tools in the development of physical models that describe fuel behaviour under irradiation, because of the detailed information they provide from the macroscale down to the lower scales.

One should finally consider that advanced physical models and modelling tools are divided into two categories: those developed to investigate phenomena that cannot be observed experimentally and those developed to reproduce experimental results, with which they can be compared directly to help in their interpretation.

Table 2. Main characterisation methods currently applied to nuclear fuels

Atomic scale
<ul style="list-style-type: none"> • HR-TEM (high resolution-transmission electronic microscopy) for the study of irradiation damage, dislocations; • XRD (X-ray diffraction) for crystallographic structure; • PAS (Positron annihilation spectroscopy), Raman spectroscopy, electrical conductivity for point defect characterisation; • XAS (X-ray analysis spectroscopy) for the local atomic environment and oxidation states.
Microstructure /Grain scale
<ul style="list-style-type: none"> • optical as well as well as scanning electron microscopy (SEM) for microstructure characterisation; • EPMA (electron probe microanalysis) for chemical analysis; • XRD for the microstructure analysis (crystallite size, microdistortion); • TEM for the study of fission gas bubbles nucleation growth; • EBSD (electron back scatter diffraction) for grain orientation; • Micromechanics characterization (micro/ nanoindentation); • X-ray tomography (using synchrotron radiation); • high-temperature X-ray diffraction for phase diagram studies; • NRA (Nuclear reaction analysis), Knudsen cell mass spectrometry for gas analysis such as fission products or He; • SIMS (secondary ion mass spectroscopy) and TDS (thermal desorption spectroscopy) for the characterisation of gas contained in fuels down very low concentrations.
Pellet scale
<ul style="list-style-type: none"> • diffusivity or melting temperature measurements for the thermal properties; • thermal transport properties; • mechanical testing (compression, bending for creep, toughness, fracture properties).

An obvious example of a model that cannot be validated is that from atomistic simulation techniques to study the evolution of displacement cascades, i.e., the almost instantaneous displacement of thousands of atoms triggered by the collision of an impinging energetic particle (e.g., a neutron or a fission atom) with an atomic nucleus. Most of what is known of displacement cascades comes from atomistic simulations and, to date, no experimental device or technique has been developed that is able to follow the evolution of the cascade in space (a few nanometers) and in time (a few picoseconds), because of the scales involved. Even if the model cannot be validated, it is however sometimes possible to correlate information from this type of modelling with those obtained experimentally. Although not directly comparable, vacancy cluster simulations of displacement cascades in UO₂ can be correlated with regard to size with nanobubbles of fission gas observed in fuel by transmission electronic microscopy [21,22]. The coupling of experiments and electronic structure calculations has also enabled the determination of oxygen [23] and xenon [24] diffusion mechanisms in UO₂. Atomistic simulation

techniques are therefore a tool, on the same footing as experimental measurement, to obtain data and identify mechanisms. While atomistic simulations might be not fully accurate, just as experimental measurements are affected by uncertainties not always fully quantifiable, they do produce data that help rationalise observed phenomena.

Examples of models that can be directly experimentally validated include those developed to simulate the fission gas release from nuclear fuels. Rate theory models such as those in the Margaret code developed at CEA [25], or phase-fields models [26], are built based on information from experiments and whenever possible from models at lower scales. Such a type of model, by being in principle directly comparable with experiments, can be later used to indirectly validate “experimentally unvalidatable” models. On the other hand, a model of this type, however, accurate and physically justified, will always contain assumptions that are not fully proven, or coefficients and parameters that are not fully known, no matter how much effort is made to obtain them from experimental measurements or atomistic modelling.

The process of validation requires that one utilises data coming from a wide range of experimental techniques, because there is rarely one experimental technique that can provide all the required information. Experiments supporting multi-scale modelling can be delicate and time-consuming. Often they require that specimens of the same materials, or even better of *model* materials in which a certain phenomenon is separately observed and thus complexity reduced, are tested and analysed using various techniques, and in different laboratories. Eventually, the results must be consistent and integrated with the help of the models.

It is important to stress that it is hardly ever possible to obtain experimental information for every aspect of a physical model. For example, while it is possible to obtain experimental information on microscopic fission gas bubbles using SEM or even nanobubbles using TEM [27], the same cannot be said yet about the impact of the interaction of fission gas and point defects on gas release. Rate theory models such as cluster dynamic can help identify the most probable clusters of defects/gas that lead to the release as a function of temperature (see Chapter 18). Those models are themselves informed by data from atomistic models (electronic structure calculations). This is why more fundamental models are useful and necessary, otherwise there would be no information on the invisible atomistic processes.

Multi-scale modelling approach: Using materials science to solve technological issues

The ultimate goal of the multi-scale modelling approach applied to nuclear fuels is to obtain physically informed fuel performance and safety codes. These codes are used in technological contexts to improve existing fuels and design future fuels with increased performance and safety features. Therefore, the multi-scale approach not only builds links between scales but also between various technical areas of expertise, as well between basic research and technology. It provides the opportunity to make engineers who use models at large scales and scientists who investigate the physical mechanisms at the origin of the fuel behaviour under irradiation work together.

It is inherent to the complexity of the issues to be solved that, in some cases mid- or long-term basic research activities requiring many years before getting to the point of

solving particular issues are needed, and anticipation is necessary to provide key tools and answers for future challenges. But basic research is now mature enough to bring relevant answers to operational issues. In addition, a top-down approach, i.e., the definition of the main technological issues where further understanding is needed to increase safety and operational margins and the translation into scientific investigations can ensure that the multiscale approach meets the needs of the end-users.

The main objectives of the R&D necessary to improve current fuels and design new ones are as follows:

- improve the flexibility of power reactors as well as their manoeuvrability preventing material failure risk in normal and off-normal operating conditions;
- propose innovative concepts and breakthrough technology to gain significant performance margins with regards to safety requirement;
- accelerate the design process of new, innovative fuels.

The improvement of the prediction capabilities of fuel performance and safety codes by a physics-based multi-scale modelling and simulation approach at the relevant scales will of course help reach these objectives. There are many issues where multi-scale modelling can improve existing engineering models for current reactors. Then, for Gen-IV reactors, a thorough understanding of basic processes governing the behaviour of advanced fuels is necessary since it is complicated to extrapolate empirical models to new conditions outside the domains in which they were developed.

During in-reactor irradiation, actinide fission produces large quantities of fission products, volatile and non-volatile, which have a significant influence on the chemical composition, as well as on the structural and mechanical properties of nuclear fuels. In parallel, nuclear interactions with neutrons and fission products induce atomic displacements and disturb the crystalline structure, while electronic excitations disturb the chemical bonds and transport phenomena assisted by temperature and irradiation modify the microstructure. The interaction between fission products and the various defects created govern a large number of operational properties and processes: cracking, gas bubble nucleation, radial migration or corrosive fission product availability at the fuel-cladding interface. Margins to melting, evolution of point and extended defects, fission product chemistry, evolution and release, swelling, microstructure evolution under irradiation, including the evolution to high burn-up structure, the mechanical integrity, as well as the cladding corrosion, are only some of the key issues to be investigated by materials'science. One can mention in particular the following points:

- One strong objective of the studies relative to safety is to determine the margins to fuel melting. The fuel melting temperatures is very dependent on composition, defects present and microstructure. The changes due to irradiation in the present formulations are more or less empirical and must be thoroughly investigated. The fuel thermal conductivity is also a key parameter as it determines the fuel temperature in the pin, especially at its centre, and therefore impacts strongly all the thermally activated processes, as well as fuel melting in off-normal situations.
- Fuel fragmentation and pulverisation during a loss of coolant accident (LOCA) is another safety-related behaviour issue. The effect of high temperature on the

fission gas pressure in the gas bubbles within the grains and on the grain boundaries in the pellet centre and in the highly porous high burn-up structure on the pellet periphery, combined with the loss of confinement due to cladding ballooning, causes instability in the fuel matrix. This is an ideal target for performing multi-scale modelling that couples the grain-scale with the macro/continuum scale. For example, one of the questions that are of critical importance for LOCA safety analyses, and for which satisfactory answers are presently elusive, is to quantify the thermal conductivity of fragmented/pulverised pellet, which can only be provided through multi-scale modelling (see Chapter 7).

- The numerous point (vacancies, interstitials) and extended (dislocations, fission gas bubbles, grain boundaries) defects created under irradiation will impact significantly the fuel and fission product behaviour. The cation self-diffusion determines for example the creation of sinks for insoluble fission products, in particular gases, but also grain growth and the creep properties. In addition, the mechanisms of creation and growth of extended defects, such as dislocation lines or large cavities and bubbles, must be better understood in view of modelling the formation and the behaviour of the high burn-up structure and of understanding the effect of pressurised bubbles on the fuel matrix. While most of the existing knowledge was obtained in a semi-empirical way, significant advances can be expected from the development of increasingly more reliable atomic scale simulations associated with experiments (see Chapter 7).
- The evolution of fission rare gases in fuels is closely coupled to fuel performance and limits the maximal burn-up they can be submitted to. These fission gases, because they are chemically inert and particularly insoluble, tend either to form small nanometre size clusters by interaction with vacancies or to be released from the fuel. This induces an over-pressurisation of the rod, which increases the pressure on the clad and extensive fuel swelling, which leads to mechanical interaction with the clad and increases the probability for clad breach [28]. Retained fission gas bubbles also decrease the thermal conductivity of the fuel and consequently contribute to limiting the operating temperature and the degree of burn-up. Understanding and modelling the elementary mechanisms of the solubility of gas in fuel lattice and in bubble are of paramount importance to predict the proportion of gas remaining in the fuel and the quantity released [29] and could help in developing solutions to mitigate the consequences of the formation and evolution of these large quantities of gas.
- The microstructural changes (see Chapter 1) and mechanical behaviour (see Chapter 2) of nuclear fuels under irradiation are of course central to predicting the structural integrity of fuel elements. Although three-dimensional thermomechanical modelling is now becoming widely available, current modelling in fuel performance codes relies mainly on mechanical behaviour laws that have been obtained from integral in-pile experiments. Extrapolation of these laws to materials or irradiation conditions is often tenuous. One need is therefore to draw on recent experimental and modelling advances to develop and improve elastic, plastic, creep and fracture models. Fuels are polycrystalline materials, therefore grain boundaries play an important role in fuel mechanical integrity. Microstructure features such as

porosities or fission gas bubbles appearing under irradiation, as well as the high burn-up structure, also play an important role on the fuel behaviour. Grain boundaries have an influence on defect [30], gas diffusion [31, 32] and on the consequence of irradiation damage [33]. Progress in the modelling of the microstructure (grain aggregates, gas bubbles or porosity network) has been made over these last years and are to be used to model the behaviour at the grain level [34]. Recent advances proposed to model grain boundaries at the atomistic scale will also contribute to a better modelling of the microstructure and their influence on mechanical properties at higher scales.

- Finally, the fuel-cladding interaction (see Chapter 3) is a very important safety issue since it can lead to cladding corrosion and failure. The knowledge of thermodynamic data for fuel and fission product is a major requirement to derive reliable thermodynamic models and fission product speciation, especially for off-normal situations. Specific needs concern the consideration of the highly oxidising conditions, the gas phase species and the effects of interactions with structural materials, cladding or absorber rod. Moreover, the coupling between mechanics and thermochemistry [35,36] is a promising approach to investigate the fuel-cladding interaction, in particular in transient or accidental conditions.

Conclusions and recommendations

The multi-scale modelling and simulation approach has the objective to describe the thermomechanical, physical and chemical evolution of nuclear fuels and combines modelling tools from the atomic scale through the intermediate grain scale all the way up to the pellet/rod scale (engineering scale). It relies on the idea that, in order to describe beyond empiricism the behaviour of materials and especially of nuclear fuels under irradiation, it is necessary to use the proper tool to model a given phenomenon at the appropriate scale. It also requires that the information and relevant mechanisms relating to the behaviour of fuel at a certain scale inform the neighbouring scale, so that models at each scale can be more physically representative and more accurate. It is important to stress that the multi-scale approach does not only build links between scales but also between various technical areas of expertise, as well as between basic research and applied technology. It is an effective tool for translating technological issues into scientific questions and scientific understanding into practical descriptions.

Multi-scale modelling does not aim at replacing experiments. The objective is to couple modelling with experiments performed at the relevant scales to obtain further insight into the basic phenomena of fuel behaviour under irradiation. Models need to be informed by experiment at many different scales, using combinations of the most advanced materials characterisation techniques. In turn, modelling helps to design optimal experiments and contributes to an improved interpretation of the results.

It has been shown that a key scale in fuel behaviour is the grain or mesoscopic scale because it aggregates atomic scale descriptions and, in turn, acts as the foundation for macroscopic modelling and therefore bridges the two extreme scales. This scale therefore enables the real transfer of information from the lower to the higher level. Although they are absolutely essential, macroscopic and atomic scales should not absorb all the effort of the multi-scale modelling. The challenge for the future is to enrich the already existing

multi-scale modelling and simulation approach by developing models at the mesoscopic scale to further strengthen links between the atomic and macroscopic scales. This needs to be done by systematically addressing the problem of transferring information from one scale to another.

The multi-scale modelling future is of course intimately connected with advances in computer power and high-performance computing. The integration of experiments, modelling and high-performance computing will, in the near future, open the doors for increased modelling and simulation capability with greater application of physics-based models integrated into fuel performance codes. In the longer term, this will pave the way towards computer-assisted materials discovery and design and enable us to obtain more efficiently innovative fuels with improved performance and safety features. Modelling and simulation will also accelerate regulatory approval for new fuel systems.

References

- [1] Malerba, L., M. Bertolus (2014), Conference Proceedings FISA 2013, 8th European Conference on Euratom research and training in reactor systems.
- [2] <http://www.tms.org/pubs/journals/jom/0611/allison-0611.html>.
- [3] Kuehmann, C. et al. (2008), “Computational design for ultra high-strength alloy”, *Advanced Materials and Processes*, 37.
- [4] <ftp://ftp.cordis.europa.eu/pub/fp6-euratom/docs/perfect-final-report.pdf>.
- [5] http://cordis.europa.eu/result/rcn/57044_en.html.
- [6] Valot, C., M. Bertolus, R. Konings, J. Somers, S. de Groot (2011), *Nuclear Engineering Design*, 241, 3521.
- [7] F-BRIDGE Final report [\(2013\)](http://cordis.europa.eu/publication/rcn/16699_en.html).
- [8] F-BRIDGE deliverable D226 (2012), <http://www.f-bridge.eu>.
- [9] <http://www.ne.anl.gov/NEAMS/>.
- [10] <http://www.casl.gov/>.
- [11] inlportal.inl.gov/portal/server.pt/community/center_for_materials_science_of_nuclear_fuel.
- [12] http://www.materials.cea.fr/PDF/PlateformePLEIADES_2012-fr.pdf.
- [13] http://www.materials.cea.fr/PDF/PlateformePLEIADES_2012-fr.pdf.
- [14] <http://www.nxo.jp>.
- [15] Martin, R.M. (2004), *Electronic Structure: Basic Theory and Practical Methods*, Cambridge University Press.
- [16] Rapaport, D.C. (2007), *The Art of Molecular Dynamics Simulation*, Cambridge University Press, Cambridge.
- [17] Leach, A. (2001), *Molecular Modelling: Principles and Applications*, Pearson Prentice Hall.

- [18] Malerba, L. (2010), “Multi-scale modelling of irradiation effects in nuclear power plant materials”, *Understanding and mitigating ageing in nuclear power plants: Materials and operational aspects of plant life management (PLiM)*, P.G. Tipping Ed., Woodhead Publishing Ltd., 456.
- [19] Stan, M. (2009), *Materials Today*, 12.20.
- [20] Bertolus, M. et al. (2010), “Development and assessment of atomistic modelling methods for the investigation of fuel materials under operational conditions”, *F-BRIDGE Deliverable D-221*, <http://f-bridge.eu/>.
- [21] Martin, G. et al. (2010), *Physical Letters A* 374, 3038.
- [22] Sabathier, C. et al. (2014), *Nuclear Instruments and Methods B* 326, 247.
- [23] Dorado, B. et al. (2011), *Physical Review B* 83, 035126.
- [24] Andersson, D.A. et al. (2014), *Journal of Nuclear Materials*, 451, 225.
- [25] Noirot, L. (2012), *Journal of Nuclear Science and Technology*, 43, 1149.
- [26] Hu, S.H. et al. (2009), *Journal of Nuclear Materials*, 392, 292.
- [27] Michel, A., C. Sabathier, G. Carlot, O. Kaitasov, S. Bouffard, P. Garcia, C. Valot (2012), *Nuclear Instruments and Methods B* 272, 218.
- [28] Olander, D.R. (1975), *Fundamental Aspects of Nuclear Reactor Elements*, NTIS, ERDA.
- [29] Garcia, P. et al. (2012), *Nuclear Instruments and Methods in Physics Research B* 277, 98.
- [30] Vincent-Aublant, E., L. van Brutzel, J.M. Delaye (2009), *Journal of Nuclear Materials*, 392, 114.
- [31] Nerikar, P.V. et al. (2011), *Physical Review B*, 84, 174105.
- [32] Govers, K., S.E. Lemehov, M. Verwerft (2012), *Defect Diffus Forum*, 323-325, 215.
- [33] van Brutzel, L., E. Aublant-Vincent (2009), *Nuclear Instruments Methods B* 267, 3013.
- [34] Soulacroix, J., B. Michel, J.-M. Gatt , R. Kubler, L. Barrallier (2014), *International Journal of Plasticity* 62, 121.
- [35] Baurens, B. et al. (2014), *Journal of Nuclear Materials*, 452, 578.
- [36] Piro, M., J. Banfield, K. Clarno, S. Simunovic, T. Besmann, B. Lewis, W. Thompson (2013), *Journal of Nuclear Materials*, 441, 240.
- [37] Rashid, J.Y, R.O. Montgomery (2014), “The perils and pitfalls of multi-scale modelling of nuclear fuel: Future expectations from a historical perspective”, NEA/WPMM meeting, *Special Session on Contribution of Mesoscale and Atomistic scale to Fuel Performance and Structural Materials Modelling*.

Conclusion

The *State-of-the-Art Report on Multi-scale Modelling of Nuclear Fuels* describes the state of fundamental materials models that can represent fuel behaviour, the methodologies for obtaining material properties, and modelling principles as they can be implemented in fuel performance codes. This report, while far from being a detailed assessment of nuclear fuel modelling, provides a recognition of the approaches to the significant aspects of fuel modelling and examples of their application. Fuel behaviour phenomena are discussed that are applicable across the spectrum of fuel forms, from conventional LWR oxide pellets to MOX, carbide, and metal SFR fuel, to coated particle fuel for gas-cooled reactors. A key issue is microstructural evolution during burn-up, and the state of understanding of that phenomenon is considered at length. Covered in the discussions are the basic material properties of heat capacity, free energy, and thermal conductivity and diffusion. Also included are the more functional effects of restructuring, bubble formation, constituent redistribution, fuel and clad oxidation, and fuel clad and environmental interactions. Fuel fabrication is considered as are many material modelling challenges, such as representing injection casting of metallic fuels, as seen in the preparation of nuclear fuel. The last set of contributions covered the basic principles for modelling phenomena and determining fundamental materials properties, a look at the state of fuel performance codes and a last note about integrating across multiple scales.

There has been substantial progress in the development of fundamental materials models and properties for nuclear fuels. These include free energies, thermal conductivity, heat capacity, thermal expansion, and mechanical properties of single crystal materials or polycrystalline fuels. Traditional materials processing approaches have been successfully applied to fuel fabrication, and new simulation tools have enhanced capabilities. Models for sintering, for example, currently support oxide fuel fabrication. Advanced simulations of casting are being used to aid fabrication of metal fuel elements for proposed SFRs.

Microstructural evolution during irradiation presents some of the most complex problems in modelling, and while progress in relating defect formation and transport to a changing microstructure is significant, it is hampered by a lack of basic knowledge of a number of actinide phase properties. Some in-reactor behaviour, such as swelling and creep, have relatively well developed representations, albeit with empirical values needed for determining the relations. The progress in modelling radiation effects has been substantial when using tools such as MD and DD. The effect of defect generation on thermal transport can thus be represented. Grain growth can also be modelled utilising approaches such as Potts kMC and phase field. Rate theory has proven its ability to illuminate mechanisms in microstructural evolution and fission gas behaviour, although basic data necessary to assess gas behaviour is still needed as well as a better knowledge of real defects as a function of the stoichiometry.

Interactions among components are more complex, whose relations can be developed, but are less accurately predictive. These include pellet-clad mechanical interactions where we can reproduce behaviour, but not predict it well. And bubble formation, migration, and consolidation, where we have interesting simulations, but are yet far from reproducing observations. It is also possible to compute chemical interactions between fuel and clad from fundamental thermochemical models and understanding of transport between fuel and clad. Yet, the rate of internal oxidation of the clad by oxide fuel for example, cannot be determined from only fundamental properties.

The computational determination of values and modelling of the fundamental information on materials used in the simulation of fuel behaviour has seen remarkable progress in recent years. Molecular dynamics has contributed substantially to determining thermal expansion through describing atomic-scale processes. New methods for determining thermal conductivity that improve upon Debye-based approaches are allowing more realistic first-principles determinations. Techniques such as kinetic MD are providing baseline diffusive transport properties in fuel materials. Measurements of free energies and heat capacity, as well as properties computed from first principles via techniques like DFT, are yielding needed thermodynamic values as input for the eventual representation of the complex phase behaviour seen in fuels that have undergone high burn-up, and generated substantial solutes and second phases. Mean-field formulations are being used to determine crystal elasticity and plasticity allowing calculation of the mechanical properties of polycrystalline materials. To a greater or lesser extent, all these approaches to the development of nuclear fuel properties have been successful in moving from highly idealised systems, often single-crystal, to more practical systems that are polycrystalline, and often multi-phase/heterogeneous. These all serve as input to broader fuel models and simulation codes.

The various modelling and computational techniques used for both determining fundamental properties and in representing fuel behaviour from the atomistic through the micro- to the mesoscale are generally fairly recent. With the exception of thermodynamic and traditional finite elements, they are approaches that required the advent of substantial computing power. These are methods such as DFT, MD, DD, phase field, and kMC. While the success of the techniques, especially for relatively simplified systems, is remarkable, they still need further development to obtain more accurate results, such as better interatomic potentials or means for better describing 5f electron materials by DFT.

The integration of the materials properties and models into codes such as BISON, TRANSURANUS, PLEIADES, or FRAPCON needs to be an on-going endeavour supported by benchmarking and comparison to separate effects testing. While current fuel performance codes provide valuable insight, it will be well into the future before they can reliably *a priori* provide a three-dimensional picture of fuel evolution. Yet, as we evolve the codes with better materials properties and simulations, they can provide us with ever improving guidance with regard to in-reactor behaviour, development of new fuel strategies and an understanding of safety performance.

Finally, one of the greatest challenges facing multi-scale modelling of fuels is the integration of the representations of properties and behaviour across a broad range of time and length scales. Atomistic models need to inform the mesoscale, dealing with issues such as grain growth and species migration. And these and other phenomena

should provide properties and relations to the macroscale, allowing simulation of behaviour such as cracking, fission product release and morphology of the high burn-up region.

Development and incorporation of multi-scale models into fuel simulations will continue to be a substantial, long-term process. The combination of the need to generate new information and understanding at multiple scales, the coupling of those improved models across the various scales, and the inclusion of these representations in fuel performance codes and simulations are daunting tasks. Great progress has been made, however, and the point has been reached where the path forward is becoming clear. It is now necessary to persevere in the efforts at all levels so that the ultimate goal of having tools that provide sufficiently accurate simulations of nuclear fuels for predicting processing and in-reactor behaviour can be achieved.